



**HAL**  
open science

**Study of the  $J/\psi$  production in pp collisions at  $\sqrt{s} = 5.02$  TeV and of the  $J/\psi$  production multiplicity dependence in p-Pb collisions at  $\sqrt{s_{NN}} = 8.16$  TeV with ALICE at the LHC**

Jana Crkovská

► **To cite this version:**

Jana Crkovská. Study of the  $J/\psi$  production in pp collisions at  $\sqrt{s} = 5.02$  TeV and of the  $J/\psi$  production multiplicity dependence in p-Pb collisions at  $\sqrt{s_{NN}} = 8.16$  TeV with ALICE at the LHC. High Energy Physics - Experiment [hep-ex]. Université Paris-Saclay, 2018. English. NNT : 2018SACLS343 . tel-01952850

**HAL Id: tel-01952850**

**<https://theses.hal.science/tel-01952850>**

Submitted on 12 Dec 2018

**HAL** is a multi-disciplinary open access archive for the deposit and dissemination of scientific research documents, whether they are published or not. The documents may come from teaching and research institutions in France or abroad, or from public or private research centers.

L'archive ouverte pluridisciplinaire **HAL**, est destinée au dépôt et à la diffusion de documents scientifiques de niveau recherche, publiés ou non, émanant des établissements d'enseignement et de recherche français ou étrangers, des laboratoires publics ou privés.

# Study of the $J/\psi$ production in pp collisions at $\sqrt{s} = 5.02$ TeV and of the $J/\psi$ production multiplicity dependence in p-Pb collisions at $\sqrt{s_{NN}} = 8.16$ TeV with ALICE at the LHC

Thèse de doctorat de l'Université Paris-Saclay  
préparée à l'Université Paris-Sud

Ecole doctorale n°576 Particules, Hadrons, Energie et Noyau :  
Instrumentation, Image, Cosmos et Simulation (PHENIICS)  
Spécialité de doctorat : Physique des particules

Thèse présentée et soutenue à Orsay, le 30/10/2018, par

**Jana Crkovská**

Composition du Jury :

M. Raphaël Granier de Casagnac Directeur de recherche, Ecole polytechnique (LLR)	Président
M. Andreas Morsch Directeur de recherche, CERN	Rapporteur
M. Michael Schmelling Professeur, Max-Planck-Institut für Kernphysik	Rapporteur
Mme Roberta Araldi Chargé de recherche, INFN Torino	Examineur
M. Francesco Prino Chargé de recherche, INFN Torino	Examineur
M. Klaus Werner Professeur, Université Nantes (SUBATECH)	Examineur
M. Bruno Espagnon Professeur, Université Paris-Saclay (IPNO)	Directeur de thèse



## ACKNOWLEDGEMENTS

There are many people who supported me thorough my PhD in one way or another and to whom I would like to express my gratitude. It is beyond my power to list all of you here, but just know this: Thank you.

I would like to thank the ALICE group at the Institut de Physique Nucléaire d'Orsay for giving me the opportunity to join their ranks for these three years. To my thesis advisor Bruno Espagnon, thank you for your advice and many, many corrections to this dissertation. To my co-advisor Zaida Conesa del Valle, thank you for your helpful advice and comments to the analysis, for giving me hints and ideas on what to improve and how. To Christophe Suire for your help with the thesis and with overcoming the administration puzzles. To Cynthia Hadjidakis and Laure Massacrier, I enjoyed our discussions be they about Physics or not. To my old and new officemates - Mohamad Tarhini, Chun-Lu Huang, and Sizar Aziz - for making my time in the lab more fun. To all of you, I am most thankful for your friendship and support during these three years, and for all the help you gave me.

Special thanks go to the members of my jury - Raphaël Granier De Cassagnac, Andreas Morsch, Michael Schmelling, Roberta Araldi, Francesco Prino, and Klaus Werner. Thank you for accepting to take a part in the defence of this thesis and for all the suggestions you gave me before and during the defence.

Huge shout out to Markinen, Anastasia, Renata, Irène, Tona, Pedrito, Alice, Liss, Florent, and to all my friends be they in Prague, Paris or elsewhere. Thanks for all the good times and morale boosting.

Last but not least, lots of love and thanks to my family - mum, Verča, Jirka, Emma, and Sofi. Bez vás bych se na to dávno vykašlala.

Díky! Merci! Thank you!



# CONTENTS

<b>Contents</b>	<b>8</b>
<b>1 Introduction</b>	<b>9</b>
1.1 Standard Model of particle physics . . . . .	9
1.1.1 Quarks, confinement and asymptotic freedom . . . . .	10
1.2 The Quark-Gluon Plasma . . . . .	12
1.2.1 QCD phase diagram . . . . .	12
1.3 Experimental study of the QGP . . . . .	13
1.3.1 Evolution of a heavy ion collision . . . . .	13
1.3.2 Collision geometry . . . . .	13
1.4 Signatures of QGP formation in heavy-ion collision . . . . .	15
1.4.1 Examples of soft probes . . . . .	15
1.4.1.1 Anisotropic flow . . . . .	15
1.4.1.2 Electromagnetic probes . . . . .	16
1.4.1.3 Particle yields and ratios . . . . .	16
1.4.2 Examples of hard probes . . . . .	17
1.4.2.1 Weak bosons . . . . .	17
1.4.2.2 Jet quenching . . . . .	17
1.4.2.3 Heavy flavour production . . . . .	18
<b>2 <math>J/\psi</math> production in ultrarelativistic hadron collisions</b>	<b>19</b>
2.1 Introduction to quarkonia . . . . .	19
2.1.1 Discovery of $J/\psi$ . . . . .	19
2.1.2 Charmonia family . . . . .	20
2.2 Charmonia in pp . . . . .	22
2.2.1 Theoretical description of $J/\psi$ production . . . . .	22
2.2.1.1 Colour Evaporation Model . . . . .	24
2.2.1.2 Colour Singlet Model . . . . .	24
2.2.1.3 Colour Octet Mechanism and Non-Relativistic QCD . . . . .	24
2.2.2 Production measurement in pp . . . . .	25
2.2.2.1 Results from Tevatron and RHIC . . . . .	25
2.2.2.2 Measurements at LHC energies . . . . .	26
2.3 Charmonia in nucleus-nucleus collisions . . . . .	29
2.3.1 $J/\psi$ as a probe of the Quark-Gluon Plasma . . . . .	29
2.3.2 Models . . . . .	30
2.3.2.1 Statistical Hadronisation Model . . . . .	31
2.3.2.2 Transport models . . . . .	31
2.3.2.3 Comovers model . . . . .	31
2.3.3 Experimental results . . . . .	32
2.3.3.1 Results from the SPS and RHIC . . . . .	32
2.3.3.2 Results from the LHC . . . . .	33
2.4 Charmonia in proton-nucleus collisions . . . . .	35
2.4.1 Cold nuclear matter effects . . . . .	35
2.4.1.1 Gluon (anti)shadowing . . . . .	35

2.4.1.2	Gluon saturation . . . . .	36
2.4.1.3	Coherent parton energy loss . . . . .	38
2.4.1.4	Nuclear absorption . . . . .	38
2.4.2	Experimental results from proton-nucleus measurements . . . . .	38
2.4.2.1	Results from RHIC . . . . .	38
2.4.2.2	Results from the LHC . . . . .	41
<b>3</b>	<b>Multiplicity dependence of heavy flavour production</b>	<b>45</b>
3.1	Correlation of hard and soft particle production . . . . .	45
3.1.1	What can we learn from multiplicity studies? . . . . .	45
3.1.2	Theoretical models . . . . .	47
3.2	$J/\psi$ and D-meson production measurements . . . . .	50
3.2.1	Proton-proton collisions . . . . .	50
3.2.2	Proton-lead collisions . . . . .	51
3.3	$\Upsilon$ production measurement . . . . .	54
3.4	Digression towards multiplicity dependence of strangeness production . . . . .	55
<b>4</b>	<b>Experimental Setup</b>	<b>59</b>
4.1	The Large Hadron Collider . . . . .	59
4.2	A Large Ion Collider Experiment . . . . .	61
4.2.1	Central Barrel detectors . . . . .	61
4.2.1.1	Inner Tracking System . . . . .	61
4.2.1.2	Time Projection Chamber . . . . .	64
4.2.1.3	Transition Radiation Detector . . . . .	65
4.2.1.4	Time Of Flight . . . . .	65
4.2.2	Forward detectors . . . . .	66
4.2.2.1	V0 detector . . . . .	66
4.2.2.2	T0 detector . . . . .	67
4.2.2.3	Zero Degree Calorimeter . . . . .	69
4.3	The Muon Spectrometer . . . . .	69
4.3.1	Detector design . . . . .	69
4.3.1.1	Absorbers and shielding . . . . .	69
4.3.1.2	Tracking Chambers . . . . .	71
4.3.1.3	Trigger Chambers . . . . .	72
4.3.2	Reconstruction of muon tracks . . . . .	75
4.4	Trigger and Data Acquisition . . . . .	75
4.4.1	Trigger system . . . . .	76
4.4.2	Data reconstruction . . . . .	77
<b>5</b>	<b>Efficiency studies of the Muon Tracking Chambers</b>	<b>79</b>
5.1	Acceptance and efficiency of the Muon Spectrometer . . . . .	79
5.2	Method to estimate the acceptance-efficiency of the Muon Spectrometer . . . . .	80
5.2.1	Sources of systematic uncertainty on acceptance-efficiency . . . . .	82
5.3	Tracking efficiency of the Muon Spectrometer . . . . .	82
5.3.1	Method to estimate tracking efficiency . . . . .	83
5.3.2	Limitations due to dead zones in the detector . . . . .	84
5.4	Method to estimate the uncertainty on the tracking efficiency . . . . .	84
5.5	Systematic uncertainty on the tracking efficiency in p-Pb data at $\sqrt{s_{NN}} = 8.16$ TeV . . . . .	88
5.5.1	Systematic uncertainty of the muon tracking efficiency in the p-Pb period . . . . .	88
5.5.2	Systematic uncertainty of the muon tracking efficiency in the Pb-p period . . . . .	88
<b>6</b>	<b>Measurement of inclusive <math>J/\psi</math> production at forward rapidity in pp collisions at <math>\sqrt{s} = 5.02</math> TeV</b>	<b>93</b>
6.1	Event and track selection . . . . .	93
6.1.1	Event selection criteria . . . . .	93
6.1.2	Track selection criteria . . . . .	94
6.2	Signal extraction . . . . .	94
6.2.1	Systematic uncertainty on signal extraction . . . . .	97
6.2.1.1	Fitting the $p_T$ and $y$ integrated spectrum . . . . .	97

6.2.1.2	Fitting the $p_T$ and $y$ differential spectrum . . . . .	98
6.3	Acceptance and efficiency correction . . . . .	99
6.3.1	Systematic uncertainty on acceptance-efficiency . . . . .	99
6.3.1.1	Uncertainty on Monte Carlo input . . . . .	99
6.3.1.2	Uncertainty on tracking efficiency . . . . .	104
6.3.1.3	Uncertainty on trigger efficiency . . . . .	104
6.3.1.4	Uncertainty on trigger-track matching . . . . .	106
6.4	Event normalisation . . . . .	107
6.4.1	Dimuon trigger event normalisation . . . . .	107
6.4.1.1	Methods to calculate the normalisation factor . . . . .	107
6.4.1.2	Correction for pile-up . . . . .	108
6.4.1.3	Normalisation factor $F_{\text{norm}}$ in pp at 5.02 TeV . . . . .	109
6.4.2	Luminosity . . . . .	111
6.5	Systematic uncertainty . . . . .	111
6.6	Inclusive $J/\psi$ production in pp at $\sqrt{s} = 5.02$ TeV . . . . .	111
6.6.1	Cross section . . . . .	111
6.6.2	Mean transverse momentum . . . . .	113
6.6.3	Comparison with theory . . . . .	115
6.7	Energy dependence of forward $J/\psi$ production in pp . . . . .	117
<b>7</b>	<b>Measurement of forward <math>J/\psi</math> production as a function of charged particle multiplicity at midrapidity in p–Pb collisions at <math>\sqrt{s_{\text{NN}}} = 8.16</math> TeV</b> . . . . .	<b>121</b>
7.1	Definition of observables . . . . .	121
7.2	Event and track selection . . . . .	122
7.2.1	Event selection criteria . . . . .	122
7.2.1.1	Pile-up rejection via a centralised ALICE task . . . . .	122
7.2.1.2	Custom pile-up rejection for the multiplicity analysis in p–Pb at 8.16 TeV . . . . .	123
7.2.1.3	Verification of pile-up rejection with the Custom Physics Selection . . . . .	127
7.2.1.4	SPD vertex selection criteria . . . . .	128
7.2.2	Muon track selection criteria . . . . .	130
7.3	Multiplicity measurement . . . . .	130
7.3.1	Data-driven correction method . . . . .	131
7.3.1.1	Correction with Poissonian smearing . . . . .	131
7.3.1.2	Choice of the reference value . . . . .	134
7.3.1.3	Correction with binomial smearing . . . . .	134
7.3.2	Constructing the multiplicity axis . . . . .	135
7.3.2.1	Comparison between the data and the MC . . . . .	135
7.3.2.2	Correcting the difference between the data and the MC . . . . .	135
7.3.2.3	Correlation between the number of corrected tracklets and charged particles $N_{\text{ch}} - N^{\text{corr}}$ . . . . .	144
7.3.3	The denominator $\langle dN_{\text{ch}}/d\eta \rangle$ . . . . .	147
7.3.4	Systematic uncertainty on the multiplicity measurement . . . . .	147
7.3.4.1	Uncertainty on the multiplicity axis construction . . . . .	147
7.3.4.2	Uncertainty on the multiplicity bin-flow and pile-up . . . . .	149
7.3.4.3	Estimation of the possible remaining pile-up contamination . . . . .	149
7.3.4.4	Total systematic uncertainty . . . . .	150
7.3.5	Charged particle multiplicity . . . . .	150
7.4	$J/\psi$ yields extraction . . . . .	152
7.4.1	$J/\psi$ signal extraction . . . . .	152
7.4.1.1	Invariant mass fit . . . . .	152
7.4.1.2	Fits in bins of multiplicity . . . . .	156
7.4.1.3	Relative $J/\psi$ signal . . . . .	156
7.4.2	Event normalisation . . . . .	158
7.4.2.1	Methods to compute $F_{\text{norm}}$ . . . . .	158
7.4.2.2	Normalisation factor $F_{\text{norm}}$ . . . . .	161
7.4.3	Event selection efficiency . . . . .	163
7.4.3.1	Multiplicity integrated event selection efficiency . . . . .	163

7.4.3.2	Event selection efficiency compared between ESD and AOD . . . . .	164
7.4.3.3	Event selection efficiency in bins of multiplicity . . . . .	165
7.4.4	Impact of the choice of the $\langle N_{\text{tr}} \rangle (v_z)$ equalisation reference value and the randomisation method . . . . .	166
7.4.5	Systematic uncertainty on the $J/\psi$ yields extraction . . . . .	166
7.4.5.1	Uncertainty in the signal extraction . . . . .	166
7.4.5.2	Uncertainty on the trigger class normalisation . . . . .	167
7.4.5.3	Uncertainty on the vertex equalisation . . . . .	167
7.4.5.4	Uncertainty on the bin-flow and pile-up . . . . .	168
7.5	Multiplicity differential relative $J/\psi$ yields . . . . .	174
7.5.1	Comparison of invariant yields with $R_{\text{pPb}}$ analysis . . . . .	176
7.5.2	Comparison with results from the centrality dependent analysis . . . . .	176
7.6	Comparison with other multiplicity dependent results . . . . .	179
<b>8</b>	<b>Mean transverse momentum measurement in p–Pb collisions at <math>\sqrt{s_{\text{NN}}} = 8.16</math> TeV</b>	<b>181</b>
8.1	Acceptance-efficiency correction . . . . .	181
8.2	Mean transverse momentum extraction . . . . .	182
8.2.1	Absolute $\langle p_{\text{T}} \rangle$ signal extraction . . . . .	183
8.2.2	Relative $\langle p_{\text{T}} \rangle$ signal extraction . . . . .	186
8.3	Systematic uncertainty on $\langle p_{\text{T}} \rangle$ . . . . .	186
8.3.1	Systematic uncertainty on signal extraction . . . . .	187
8.3.2	Systematic uncertainty on MC input . . . . .	187
8.4	Results . . . . .	190
<b>9</b>	<b>Conclusions and outlook</b>	<b>195</b>
	<b>Resumé en français</b>	<b>199</b>
	<b>Bibliography</b>	<b>205</b>
	<b>List of Figures</b>	<b>227</b>
	<b>List of Tables</b>	<b>230</b>
<b>A</b>	<b>Fit functions</b>	<b>231</b>
A.1	Extended Crystal-Ball . . . . .	231
A.2	NA60 . . . . .	231
A.3	Variable Width Gaussian . . . . .	231
A.4	Double exponential . . . . .	232
<b>B</b>	<b>Important formulæ</b>	<b>233</b>
<b>C</b>	<b>Lists of analysed runs</b>	<b>235</b>
C.1	LHC15n: pp data at $\sqrt{s} = 5.02$ TeV . . . . .	235
C.2	LHC16r: p–Pb data at $\sqrt{s_{\text{NN}}} = 8.16$ TeV . . . . .	235
C.3	LHC16s: Pb–p data at $\sqrt{s_{\text{NN}}} = 8.16$ TeV . . . . .	235
<b>D</b>	<b>Validation of general event Monte Carlo productions</b>	<b>237</b>

## INTRODUCTION

In this introduction, we will address few general concepts which will help us in later chapters. We shall start from the very beginning by briefly describing the standard model of particle physics. We will present the state of matter existing at very high energy densities and temperatures - the Quark-Gluon Plasma (QGP). Such a state of matter is believed to have existed in the primordial Universe after the Big Bang. QGP is probed (not only) by the ALICE experiment at the LHC in CERN. As last, we will explain how heavy ion collisions serve to study the QGP in laboratory conditions.

### 1.1 Standard Model of particle physics

The Standard Model (SM) is a theory describing the electromagnetic, weak, and strong interaction among particles. It is an incomplete theory as it does not cover the gravitational interaction. The elementary particles in the SM are depicted in Fig. 1.1 and can be classified into two main groups according to their spin: i) fermions with half integer spin and ii) bosons with integer spin. The fermions can be split into quarks and leptons. The bosons (photon  $\gamma$ , vector gauge bosons  $W^\pm$  and  $Z^0$ , and gluon  $g$ ) serve as mediators of the three interactions.

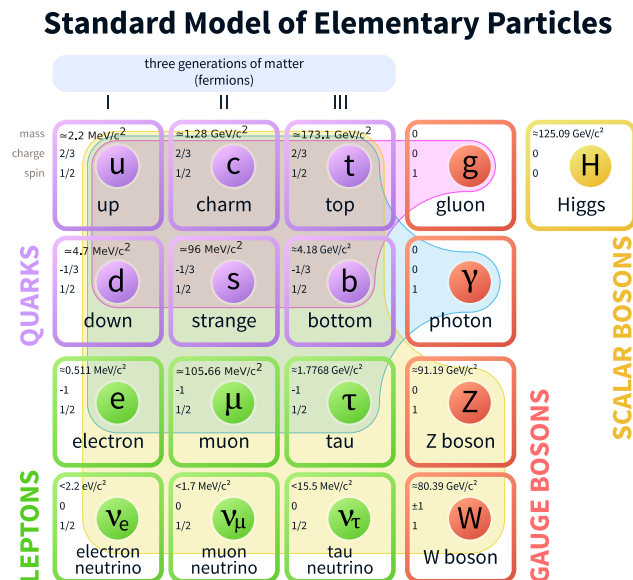


Figure 1.1: Elementary particles of the Standard Model [1].

**Leptons** carry an integer charge and subject to the electromagnetic and weak interactions. Three generations of leptons are known, each including one negatively charged lepton ( $e^-$ ,  $\mu^-$ , and  $\tau^-$ ) and one neutral left-handed neutrino ( $\nu_e^L$ ,  $\nu_\mu^L$ ,  $\nu_\tau^L$ ). Their antiparticle counterparts are positively charged

antileptons ( $e^+$ ,  $\mu^+$ , and  $\tau^+$ ) coupled to a right-handed neutrino with corresponding flavour ( $\nu_e^R$ ,  $\nu_\mu^R$ ,  $\nu_\tau^R$ ).

**Quarks** have a non-integer electric charge and a colour charge. They interact via any of the three interactions in the SM. There are six flavours of quarks (up  $u$ , down  $d$ , strange  $s$ , charm  $c$ , bottom/beauty  $b$ , top  $t$ ) and antiquarks ( $\bar{u}$ ,  $\bar{d}$ ,  $\bar{s}$ ,  $\bar{c}$ ,  $\bar{b}$ ,  $\bar{t}$ ), which are grouped into three generations. Each generation contains a pair of quarks and a their respective antiquarks. Each couple consist of a (anti)quark with charge  $q = 2/3$  ( $u$ ,  $c$ ,  $t$ ) and a (anti)quark with charge  $q = -1/3$  ( $d$ ,  $s$ ,  $b$ ). In normal matter, quarks are always bound into colourless hadrons.

For both leptons and quarks, the generations follow an increasing mass hierarchy. The ordinary matter consist only of the first generation particles. The higher mass particles are highly unstable and decay quickly into the stable states if produced.

Concerning the interactions included in the SM:

**The electromagnetic interaction** governs the interaction among two elementary particles with an electric charge. Hence charged leptons and quarks are subject to it while neutrinos are not. It is mediated by a photon, which is massless and electrically neutral. The theory describing the electromagnetic interaction is Quantum Electrodynamics (QED).

**The weak interaction** is mediated by the massive vector gauge bosons  $W^\pm$  ( $M_W \approx 80 \text{ GeV}/c^2$ ) and  $Z^0$  ( $M_Z \approx 90 \text{ GeV}/c^2$ ). Due to the high mass of its mediators, the weak interaction has limited range to  $\sim 10^{-18} \text{ fm}$ . The charged interaction changes flavour and is thus responsible for nuclear decays. The weak interaction is unified with the electromagnetic interaction in the electroweak theory.

**The strong interaction** occurs among particles with colour charge. The interactions is mediated by gluons, which themselves carry a a combination of colour and anticolour charge. The strong interaction is described by a non-Abelian  $SU(3)$  symmetry group, meaning its gauge bosons also interact. We will address the consequences of this phenomenon in the upcoming sections. The theory describing the strong interaction is Quantum Chromodynamics (QCD).

interaction	electromagnetic	weak	strong
range (m)	$\infty$	$10^{-18}$	$\leq 10^{-15}$
mean life-time (s)	$10^{-20}$	$10^{-10}$	$10^{-23}$
boson intermediator	photon	$W^\pm, Z^0$	gluon
spin ( $\hbar$ )	1	1	1
mass ( $\text{GeV}/c^2$ )	0	80.2, 91	0

Table 1.1: Properties of the fundamental interactions in the Standard Model [2].

The basic characteristics of the fundamental interactions included in the SM are summed up in Tab. 1.1. Recall that the gravitational interaction is not included. In the SM formalism, the particles gain mass through interactions with the Higgs field. The quantum of the Higgs field is the Higgs boson, discovered in 2012 by ATLAS [3] and CMS [4] experiments in CERN.

### 1.1.1 Quarks, confinement and asymptotic freedom

The quarks are fermions, which means no two identical quarks can co-exist in the same state. This puts certain constraints on how quarks combine into hadrons. We distinguish two kinds of hadrons according to their number of valence (constituent) quarks: i) mesons, which are the bound states of a quark and antiquark pair of opposite colour charge (e. g. red and antired), and ii) baryons, the bound states of three (anti)quarks of different colour each. However, as long as two (anti)quarks do not carry the same quantum numbers, other states such as tetraquarks ( $q\bar{q}q\bar{q}$ ) or pentaquarks ( $qqqq\bar{q}$ ) are allowed. It was only recently that likely candidates of these states were reported. In particular, Belle announced an observation of a resonance named  $Z^\pm(4430)$  [5], which may well be a double charmed tetraquark. LHCb reported observation of two pentaquark candidates  $P_c(4380)^+$  and  $P_c(4450)^+$  [6]. Likewise, the QCD also predicts existence of glueballs - bound states of multiple gluons. No clear proof of glueball observation existed at the time of writing of this work.

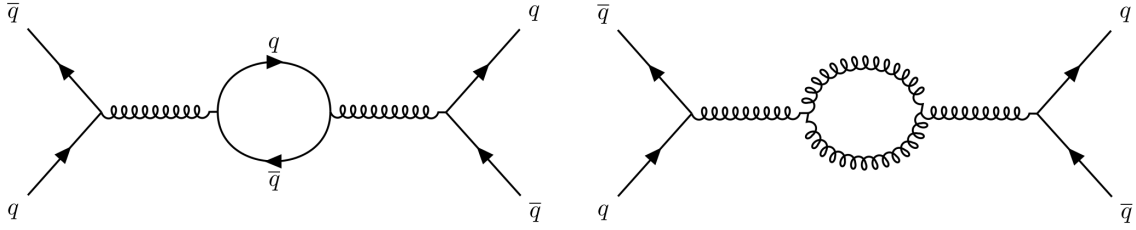


Figure 1.2: Feynman diagrams showing vacuum fluctuations at the lowest order in QCD.

The polarisation of vacuum in QED results in many virtual electron-positron pairs  $e^+e^-$ . Such pairs are felt by other charged particles, whose interactions are thus diminished. The screening decreases with increasing distance (or decreasing momentum transfer  $Q$  of the interaction). Analogical effect exist in QCD too, where both virtual quark-antiquark  $q\bar{q}$  pairs and gluon pairs can be produced in the vacuum excitations, see Fig. 1.2 [7]. The  $q\bar{q}$  act very much like the  $e^+e^-$  pairs in QED, since they are all fermions, and screen other coloured charges. The gluon however are bosons, leading to an antiscreening effect. The antiscreening from gluons outweighs the screening from quarks. In other words, the interactions grows stronger with increasing distance (smaller  $Q$ ) and weaker with decreasing distance (larger  $Q$ ).

Fig. 1.3 shows the evolution of the strong coupling constant  $\alpha_s$  with the energy scale  $Q$ . At high transferred energies (short distances), the coupling  $\alpha_s$  asymptotically decreases and the quarks behave as quasi-free particles. This regime is called **asymptotic freedom**. On the other hand, at low energy (long distances), the strong coupling  $\alpha_s$  increases. This phenomenon is called **confinement** and explains why at normal energies the quarks are always bound into colourless hadrons with integer charge.

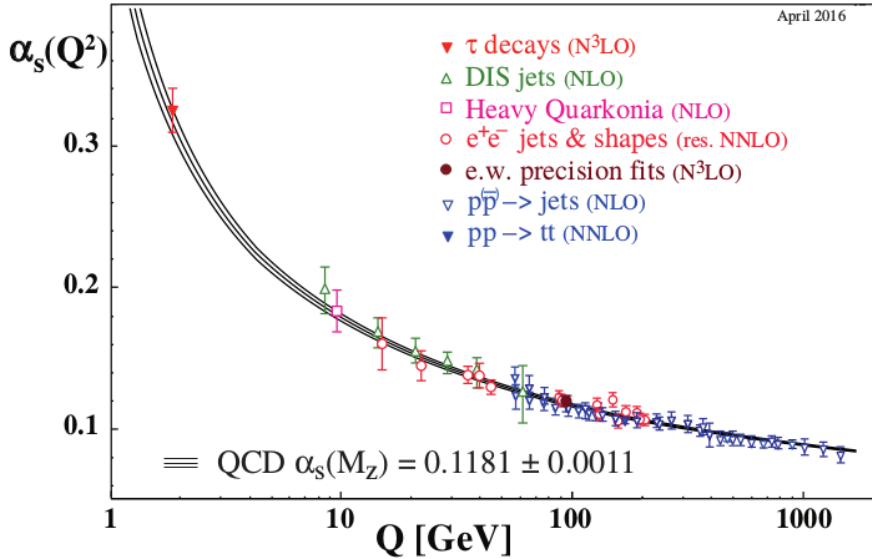


Figure 1.3: Summary of measurements of  $\alpha_s$  as a function of the energy scale  $Q$ . Taken from [1].

Another implication of the running  $\alpha_s$  is that at high energies, a perturbative approach can be used. Such framework is referred to as perturbative QCD (pQCD). The interaction is dealt with as a perturbative series in powers of  $\alpha_s$ . However at low energies,  $\alpha_s$  is too large and pQCD breaks. One needs to use instead effective theories, or lattice QCD (lQCD). Lattice QCD had proven to be a powerful tool to calculate the thermodynamical properties of the QCD matter in the non-perturbation regime. In the lQCD framework, the QCD Lagrangian is discretised to a lattice of finite space-time points at which the Lagrangian can be solved.

## 1.2 The Quark-Gluon Plasma

After the Big Bang, the primordial Universe is believed to have been in the state composed of deconfined quarks and gluons - the Quark-Gluon Plasma (QGP). As the medium expanded and cooled down, the QGP underwent a transition into the hadronic matter that we know today.

Similar conditions can be recreated at smaller scales in laboratory by colliding beams of heavy ions. Such collisions release a sizeable energy into a very limited space, resulting in extreme energy densities and elevated temperatures. In such conditions the hadrons start to overlap, and the strong interaction among their constituents becomes weak. The matter experiences transition into a state of deconfined quarks and gluon, the QGP.

### 1.2.1 QCD phase diagram

The different phases of the QCD matter can be characterised in the  $(T, \mu_B)$  phase-space, where  $\mu_B$  is the baryon chemical potential and  $T$  denotes the temperature. A schema of such a phase-space diagram is depicted in Fig. 1.5. The potential  $\mu_B$  is related to the net baryon density. Presumably, equal amounts of matter and antimatter were produced during the Big Bang so that  $\mu_B = 0$  for the early Universe. Nowadays, we observe an abundance of matter over antimatter, corresponding to  $\mu_B > 0$ .

The nature of the transition of the QGP into hadrons and vice-versa is still a subject of debate. One possible scenario would be a phase transition of  $n^{\text{th}}$  order, manifested by a discontinuity of derivatives of free energy  $F$  up to the  $n^{\text{th}}$  order. Another possibility would be a cross-over with no discontinuous derivative.

Multiple experimental facilities investigate the transition between hadrons and QGP at different collisions energies: e. g. the lowest energy studied in the RHIC Beam Energy Scan (BES) phase 1 is  $\sqrt{s_{\text{NN}}} = 7$  GeV while the highest energy so far achieved is  $\sqrt{s_{\text{NN}}} = 5.02$  TeV at the LHC. With increasing energy, the temperature of the created system increases while its net baryon density decreases. This enables us to probe different part of the  $(T, \mu_B)$  phase-space. Current experiments at RHIC and at the LHC observe matter at  $\mu_B \sim 0$ . According to lQCD calculations, the QGP created at such conditions should then cross over into hadronic gas at a critical temperature  $T_c \sim 170$  MeV [8]. With increasing  $\mu_B$ , the nature of the transition is expected to change into a first-order transition at a critical point [9].

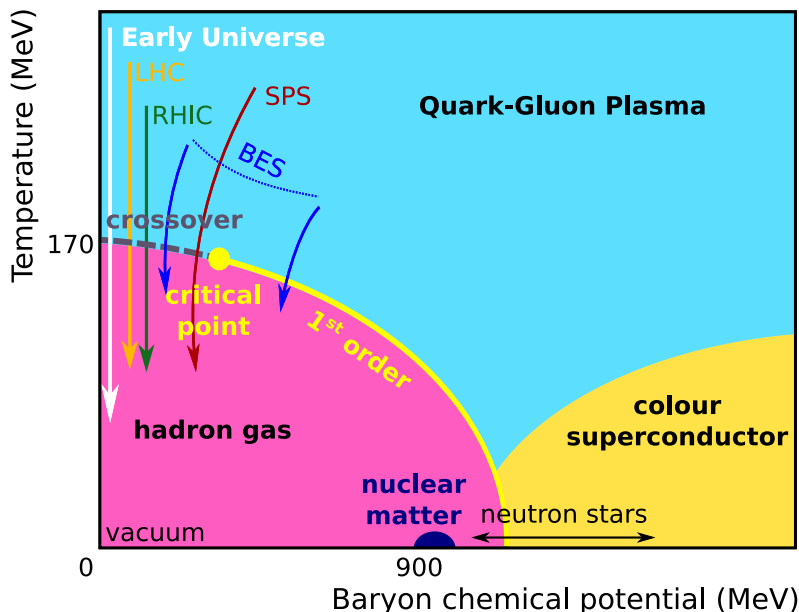


Figure 1.4: The QCD phase-space diagram. Modified from [10].

## 1.3 Experimental study of the QGP

### 1.3.1 Evolution of a heavy ion collision

A schematic representation of a heavy ion collision and its space-time evolution in the Bjorken scenario [11] can be found in Fig. 1.5. The collision takes place at  $\tau = 0$  and undergoes the following stages<sup>1</sup>:

1.  $\tau < 1 \text{ fm}/c$ : At the beginning of the collision, the multiple hard scatterings between the partons of the nuclei take place. We say that the system is in **pre-equilibrium**.
2.  $1 < \tau < 10 \text{ fm}/c$ : Rescatterings of the partons lead to thermalisation of the system. If the energy density of the system is high enough, the system reaches equilibrium and the **QGP** is formed. The hot medium further expands and cools down.
3.  $10 < \tau < 20 \text{ fm}/c$ : As the expanding system continues to cool down, the quarks and gluons start to form hadrons once the temperature reaches  $T \leq T_c$ . This transition can happen instantaneously or through a **mixed phase**. A **chemical freeze-out** occurs when no more inelastic scatterings take place and the number of particles is fixed.
4.  $\tau > 20 \text{ fm}/c$ : The hadronic matter continues its expansion. Once the density of the matter becomes too low, the elastic scatterings among the hadrons cease. The system reaches the **kinetic freeze-out**. The hadrons decouple and their momenta are fixed.

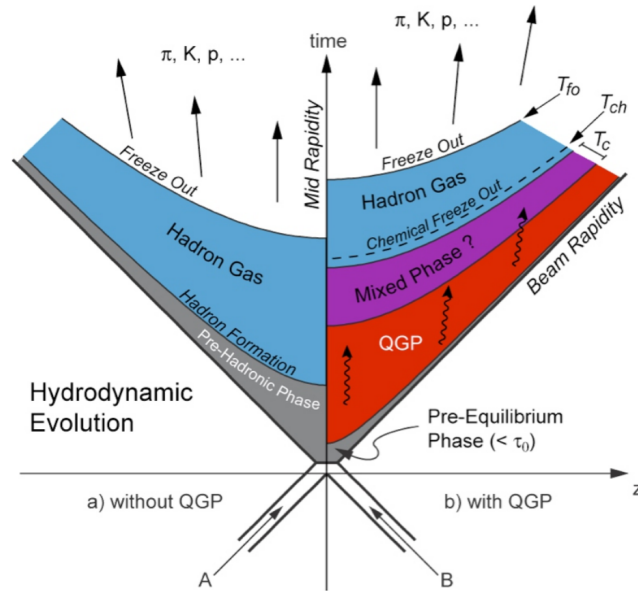


Figure 1.5: Space-time evolution of a collisions of heavy-ion. Taken from [8].

### 1.3.2 Collision geometry

Nuclei are objects of finite size and as such the area in which the collision takes place will vary from event to event. Schema on Fig. 1.6 depicts a typical collisions of two heavy nuclei. The axes of the the two nuclei are separated by a distance  $b$ , called the **impact parameter**.

There exist two noteworthy scenarios:

- A head-on collision during which the centres of the two nuclei move on the same trajectory, i.e. at  $b \approx 0$ . Such collision is referred to as **central**.
- A collisions during which the two centres move along parallel trajectories displaced by a distance  $0 \ll b < R_A + R_B$ , where  $R_i$  denotes the radius of either nucleus. Collision of such kind is called **peripheral**.

<sup>1</sup>The proper time  $\tau = \sqrt{t^2 - z^2}$  given for each phase is only approximative and can change from source to source.

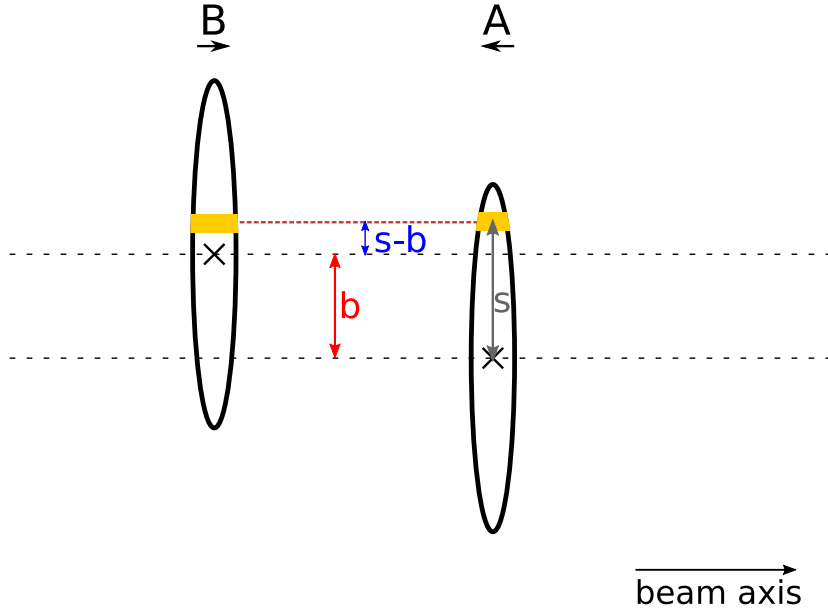


Figure 1.6: Schematic view of the initial geometry of a collisions of nuclei A and B at the impact parameter  $b$ . Modified from [12].

The conditions during the collision change with the initial geometry. The more central the collisions is, the higher the energy density of the system and the more likely the QGP forms. Since we measure sets of many collisions, we can qualify the properties of the created system by the **centrality** of the collision. The impact parameter  $b$  is the physical measure of the centrality. In hadronic collisions,  $b$  can take any value starting from zero up to the sum of the radii of the two nuclei

$$0 \leq b \leq R_A + R_B. \quad (1.1)$$

However,  $b$  cannot be measured in experiment and must be instead determined from Monte Carlo by comparing simulations with data. The centrality can be estimated from observables monotonically varying with  $b$ . ALICE uses the charged particle multiplicity and the energy carried by particles travelling along the beam axis as centrality estimators [13].

The Glauber model [12] relates the centrality of the collisions to the number of nucleons undergoing at least one binary collision (i. e. participant nucleons)  $N_{\text{part}}$ , and to the number of binary nucleon-nucleon collisions  $N_{\text{coll}}$ . We can also define the number of spectator  $N_{\text{spec}}$ , i. e. nucleons that do not participate in the collisions:

$$N_{\text{spec}} = A + B - N_{\text{part}}, \quad (1.2)$$

where  $A$  and  $B$  are atomic mass numbers of the two colliding nuclei. In the Glauber model, the nucleus-nucleon collisions are treated as a superposition of multiple independent nucleon-nucleon collisions.

The probability of a nucleon in A to be located at a distance  $s$  from the centre of A can be expressed using the nucleus density distribution  $\rho(s, z)$  as [14]

$$T_A(b) = \int dz \rho(s, z). \quad (1.3)$$

$T_A(b)$  is the nuclear thickness function. Note that integrating Eq. (1.3) over the full volume gives  $\int db T_A(b) = A$ . Similarly we can define for a nucleon in B at a distance  $(s - b)$  from the centre of B

$$T_B(s - b) = \int dz \rho(s - b, z). \quad (1.4)$$

The effective overlap area at which a given nucleon in A can interact with nucleons in B can be written in terms of the nuclear overlap function  $T_{AB}$

$$T_{AB}(b) = \int d^2s T_A(s) T_B(s - b). \quad (1.5)$$

The number of nucleon-nucleon collisions  $N_{\text{coll}}$  at given impact parameter can be computed from the product of this effective overlap area and the inelastic nucleon-nucleon scattering cross section  $\sigma_{inel}^{NN}$

$$N_{\text{coll}}(b) = \sigma_{inel}^{NN} T_{AB}(b). \quad (1.6)$$

The inelastic cross section  $\sigma_{inel}^{NN}$  grows with collision energy and hence  $N_{\text{coll}}$  too.

To calculate number of participants in the collisions, we shall start by deriving the formula of  $N_{\text{part}}$  from nucleus A. The probability of a given nucleon in A scattering once with any nucleon in B is

$$P_1^A = \frac{T_B(s-b)}{B} \sigma_{inel}^{NN}.$$

Then the probability that the nucleon in A will not scatter with any of the nucleons in B is

$$P_0^A = (1 - P_1^A)^B.$$

Consequently the probability of at least one collisions taking place can be written as

$$P_{\geq 1}^A = 1 - P_0^A = 1 - (1 - P_1^A)^B.$$

The number of participants in A at a given impact parameter  $b$  (i. e. nucleons that interact at least once and are located in the given volume of A) can be calculated from

$$N_{\text{part}}^A(b) = \int d^2s T_A(s) P_{\geq 1}^A, \quad (1.7)$$

from where we can see that the total number of participants reads as

$$\begin{aligned} N_{\text{part}}(b) &= N_{\text{part}}^A(b) + N_{\text{part}}^B(b) \\ &= \int d^2s T_A(s) \left[ 1 - \left( 1 - \frac{T_B(s-b)}{B} \sigma_{inel}^{NN} \right)^B \right] + \int d^2s T_B(s) \left[ 1 - \left( 1 - \frac{T_A(s)}{A} \sigma_{inel}^{NN} \right)^A \right]. \end{aligned} \quad (1.8)$$

## 1.4 Signatures of QGP formation in heavy-ion collision

The QGP, being extremely short-lived<sup>2</sup>, cannot be directly observed in experiment. Instead, one needs to find other indirect observables. We can classify the different probes into two main groups based on their momentum scales:

- The **hard probes** originate in processes with high transferred momentum and can thus be only created in hard scatterings during the first stages of the collision. Examples of hard probes are jets, heavy flavour hadrons, or weak bosons.
- The **soft probes** typically involve low momentum transfers. Unlike hard probes, they can be created at all stages of the collisions. Examples of soft probes are anisotropic flow of charged particles, modification of particle yields and ratios, or electromagnetic probes (photons and thermal dileptons).

The list of hereby discussed probes is incomplete as it would be impossible to mention all possible probes of QGP. The literature in this section is non-exhaustive, just to give some sort of general idea to the reader.

### 1.4.1 Examples of soft probes

#### 1.4.1.1 Anisotropic flow

As the medium created in a heavy ion collision thermalises through secondary collisions of its constituents, pressure developed in the system creates an outward motion of the matter. In a peripheral collision, the initial anisotropy of the overlap regions results in an anisotropy in momentum distribution of the final states as illustrated in Fig. 1.7. The strongest pressure gradient in the initial elliptic overlap zone is along the direction with the least amount of matter in the way. Most matter will move in this direction due to least resistance from the medium and will gain most momentum. Particles

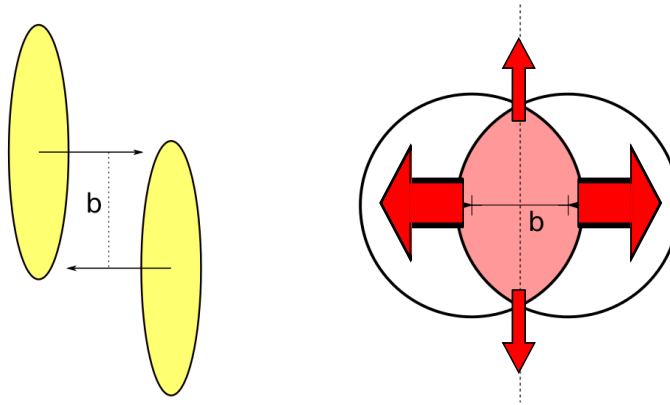


Figure 1.7: A sketch of a peripheral heavy ion collisions. The asymmetric overlap region gives rise to momentum anisotropy.

moving perpendicular to this direction will struggle more to exit the zone, gaining significantly less momentum.

The anisotropy can be studied by expanding the azimuthal distribution of particles into a Fourier series with respect to the reaction plane  $\Psi_{RP}$ <sup>3</sup> [15]:

$$\frac{dN}{d\varphi} \propto 1 + \sum_{n=1}^{\infty} 2v_n \cos(n\varphi - n\Psi_{RP}) \quad (1.9)$$

$$v_n = \langle \cos(n\varphi - n\Psi_{RP}) \rangle,$$

where  $\varphi$  is the azimuthal angle. The first term represent isotropic expansion of the matter, the sum describes its anisotropic expansion. The odd flow coefficients relate to the nucleon fluctuations in the overlap zone, while the even coefficients originate from the initial anisotropy. Flow measurements provide information on the hydrodynamical properties of the medium such as its shear viscosity  $\eta/s$  or temperature. For instance, results from LHC experiments favour a scenario in which the QGP is not an ideal gas (i. e.  $\eta/s = 0$ ) but rather an ideal liquid ( $\eta/s > 0$ ) [16–18].

#### 1.4.1.2 Electromagnetic probes

The electromagnetic probes, i. e. direct thermal photons and leptons, are tools to measure the thermodynamic properties of the created medium [19]. Both have low probability of interacting with the deconfined medium. They are produced at all stages of the collision.

Dileptons can be formed in QGP through the annihilation of quark-antiquark pair. The temperature of the produced dilepton is approximately equal to the temperature of the original  $q\bar{q}$  pair. Thus by measuring the thermal distribution of dileptons produced in collisions of heavy nuclei one can extract the temperature of the system during the time of the dilepton creation. Similarly, the thermal photons are produced through annihilation or through Compton scattering of  $q\bar{q}$  pair and carry the information on thermodynamic properties of the original pair. Another contribution to the spectra of direct photons are the prompt direct photons, which are produced in the initial scatterings and carry the information on parton distributions in the incoming nuclei. On the dilepton side, there is a number of competing processes which needs to be taken into account in the dilepton spectra, e. g. Drell-Yann or decays of hadrons.

#### 1.4.1.3 Particle yields and ratios

The production of light hadrons (i. e. containing  $u$ ,  $d$ , and even  $s$  quarks) depends on the state of the medium at the chemical freeze-out. The relative yields of hadrons in statistical models are functions of the temperature  $T$  and  $\mu_B$  [8]. By fitting the data with these two parameters, one can extract the

<sup>2</sup>See previous text for estimates of duration of its evolution. Typically the QGP lives for about  $\tau \sim 20$  fm/c.

<sup>3</sup>The reaction plane  $\Psi_{RP}$  is defined by the beam axis and the direction of the impact parameter.

critical temperature  $T_C$  and  $\mu_B$  at which the transition happened. Results at RHIC and LHC energies give  $T_c \approx 160 - 170$  MeV [20–22], which is close to lQCD predictions.

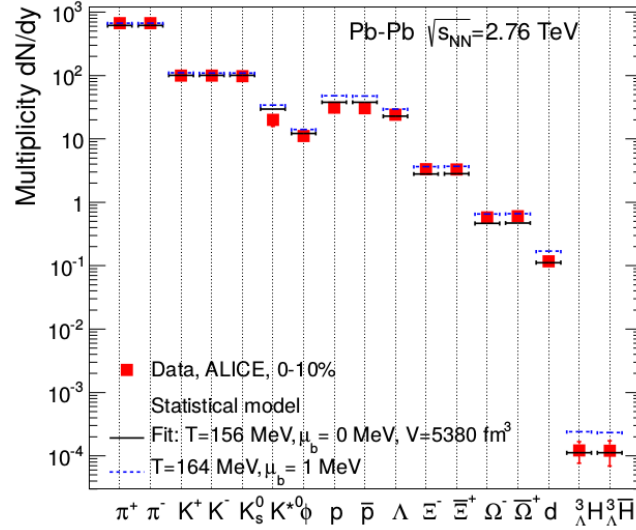


Figure 1.8: Relative particle production in central collisions at the LHC. Taken from [22].

## 1.4.2 Examples of hard probes

### 1.4.2.1 Weak bosons

The electroweak bosons  $W^\pm$  and  $Z^0$  are very massive and thus their production requires large momentum transfers. Their production happens during the initial stages of the collision. Since they do not carry colour charge, they are unaffected by the presence of the QGP. They are therefore ideal probes of the ‘cold’ nuclear matter effects not originating from the QGP formation in nucleus-nucleus collisions.

The nuclear matter effects can be quantified via the nuclear modification factor<sup>4</sup>

$$R_{AA} = \frac{1}{\langle T_{AA} \rangle} \frac{d^2 N_{AA}/dp_T dy}{d^2 \sigma^{pp}/dp_T dy} \quad (1.10)$$

$$= \frac{1}{\langle N_{\text{coll}} \rangle} \frac{d^2 N_{AA}/dp_T dy}{d^2 N_{pp}/dp_T dy},$$

where  $d^2 N_{AA}/pp/dp_T dy$  are the  $p_T$  and  $y$  differential yields of the measured boson,  $d^2 \sigma^{pp}/dp_T dy$  is the double differential cross section measurement in pp collisions,  $\langle T_{AA} \rangle$  is the mean value of the nuclear overlap function, and  $\langle N_{\text{coll}} \rangle$  denotes the mean number of the binary nucleon-nucleon collisions.

In Pb–Pb collisions, the production of  $W^\pm$  and  $Z^0$  at central rapidity was measured by ATLAS [23] and CMS [24],  $Z^0$  was also measured at forward rapidity by ALICE [25]. The CMS results from Pb–Pb at  $\sqrt{s_{NN}} = 2.76$  TeV are shown in Fig. 1.9. The  $Z^0$  boson  $R_{AA}$  is depicted as a function of centrality. In all centrality classes,  $R_{AA} = 1$  suggesting the colourless  $Z^0$  is unaffected by the QGP.

### 1.4.2.2 Jet quenching

In collider experiments, parton pairs can be produced in the initial hard parton scattering. The quark and antiquark propagate in the opposite direction while radiating gluons. The gluons can decay into more quark-antiquark pairs. If the momenta of the original pair are high, the radiated gluons and subsequent quark pairs will be highly collimated with the original fermion. Such collimated shower of particles is called a jet.

<sup>4</sup>The modification factor can be computed for any particle, not just the weak bosons. For instance, in chapter 2 we will be reviewing selected results of  $J/\psi$  nuclear modification.

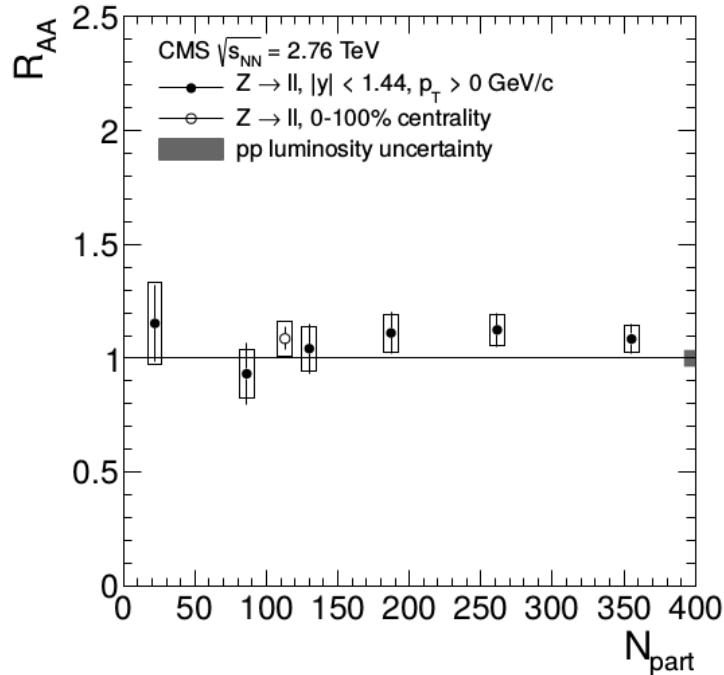


Figure 1.9: The  $Z^0$  boson  $R_{AA}$  values for the combination of the dimuon and dielectron channel as a function of the number of participants  $N_{\text{part}}$  in Pb-Pb at  $\sqrt{s_{\text{NN}}} = 2.76$  TeV. Taken from [24].

In presence of strongly interacting matter, one or both jets suffer energy loss due to collisions with the constituents of the medium and via gluon radiation. At a given energy, the number of jets reconstructed in Pb-Pb is thus effectively lowered with respect to the number reconstructed in an equal number of pp collisions.

### 1.4.2.3 Heavy flavour production

Heavy flavour (charm  $c$  and beauty  $b$ ) quarks are produced in the initial hard scatterings and are expected to experience the full evolution of the collision. However, the production of their bound states can be affected by the strongly interacting medium. We will dedicate the next chapter to the discussion of the effects that the presence of the QGP has on charmonia ( $c\bar{c}$  resonances).

## Summary

The Standard Model is a theory describing the fundamental particles and their interactions. It contains the strong interaction, which is manifested by an exchange of coloured gluon among particles with colour charge, i. e. quarks and gluons. At normal conditions, quarks are always confined inside colourless hadrons. However, due to QCD vacuum polarisation the coupling becomes weaker with increasing energy transfers in the interactions. As a result, the quarks become asymptotically free at high energies. The hadronic matter thus experiences a transition into a state of deconfined partons known as the Quark-Gluon Plasma (QGP).

The QGP existed in the primordial Universe few microseconds after the Big Bang. It can be recreated in laboratory in collisions of ultrarelativistic heavy ion. Since the QGP is very short-lived, it is impossible to measure it. Instead we measure direct and indirect signatures of formation of the deconfined medium in the collision. The suppression of  $J/\psi$  is one such signature and will be addressed in the next chapter.

---

## J/ $\psi$ PRODUCTION IN ULTRARELATIVISTIC HADRON COLLISIONS

---

This chapter discusses the topic of J/ $\psi$  and its production in relativistic hadron collisions. The general introduction is in Sec. 2.1, where we briefly explain what is a J/ $\psi$  and its discovery. Sec. 2.2 focuses on J/ $\psi$  production in pp collisions. We will review the theory describing the production and experimental results from collider experiments. We will follow up with Pb–Pb collisions in Sec. 2.3 and p–Pb collisions in Sec. 2.4 and show how J/ $\psi$  can be used to study nuclear effects.

### 2.1 Introduction to quarkonia

Quarkonia are bound states of a heavy quark-antiquark pair. Bound states of ( $c\bar{c}$ ) are called charmonia, while ( $b\bar{b}$ ) are known as bottomonia<sup>1</sup>. Their production mechanisms include both soft and hard scales of QCD and are thus used as tools to test both perturbative and non-perturbative QCD models. They are also important in QGP studies as due to their heavy mass, the heavy quarks are produced in the initial hard scattering processes in hadron collisions. In consequence, they are able to experience the full evolution of the p–Pb or Pb–Pb collisions. Moreover, the presence of nuclear matter can affect their hadronisation. Heavy flavour hadrons are hence an important tool to study suppression mechanisms in p–Pb and Pb–Pb collisions.

The subject of this thesis is the J/ $\psi$  meson, the first excited ( $c\bar{c}$ ) bound state with mass  $M_{J/\psi} = 3096.900 \pm 0.006 \text{ MeV}/c^2$  and  $J^{PC} = 1^{--}$  [1].

#### 2.1.1 Discovery of J/ $\psi$

The J/ $\psi$  was discovered in 1974 simultaneously in two experiments: one was performed with the MARK I detector from the Stanford Positron Electron Accelerating Ring (SPEAR) at the Stanford Linear Accelerator Center (SLAC) [26] and one was performed at the Alternating Gradient Synchrotron (AGS) in the Brookhaven National Laboratory [27]. The AGS group searched for new particles decaying into dilepton pairs in reaction  $p + \text{Be} \rightarrow e^+ + e^- + X$ . The group at SLAC scanned the  $e^+e^-$  collisions in the energy range  $3.1 \leq \sqrt{s} \leq 3.3 \text{ GeV}$  and studied the produced hadron and dilepton spectra. Both experiments reported an observation of a very narrow massive particle with  $M \approx 3.1 \text{ GeV}/c^2$  and width  $\Gamma \sim 0$ . Such resonance could not be explained without involving new quantum numbers and it was hinted that it could be a particle containing the recently predicted charm quark [28].<sup>2</sup> The discovery was quickly followed by an observation of another heavy particle at SPEAR, which was named  $\psi(2S)$  [31]. The particle was discovered using the same setup as for the J/ $\psi$  discovery but scanning in energy range  $3.6 \leq \sqrt{s} \leq 3.71 \text{ GeV}$ . The observed resonance had the mass  $M = 3.695 \pm 0.004 \text{ GeV}/c^2$  and a narrow width of  $\Gamma < 2.7 \text{ MeV}$ .

---

<sup>1</sup>The top quark  $t$  does not produce quarkonia as it decays before it can bind into an -onium.

<sup>2</sup>The charm quark was originally predicted as a rather elegant means to overcome the appearance of strangeness-changing neutral current in three-quark gauge theory and to achieve symmetric four-lepton-four-quark model, however it was supported by no experimental evidence [29]. Therefore the discovery of J/ $\psi$  confirmed existence of charm quark, a feat for which S. Ting from AGS and B. Richter from SPEAR were awarded the Nobel Prize in Physics in 1976 [30].

The narrow width of the  $J/\psi$  translates into its anomalously long lifetime compared to the mean lifetime of the strong interaction  $\tau_s$

$$\tau_{J/\psi} \sim 10^{-20} > \tau_s \sim 10^{-23}. \quad (2.1)$$

The OZI rule<sup>3</sup> [32–34] explains this phenomenon. In the case of a charmonium  $\psi$ , the energetically preferred strong decay is

$$\psi \rightarrow \pi^+ + \pi^0 + \pi^-.$$

The Feynman diagram of this decay is in left panel of Fig. 2.1. The  $\psi$  needs to annihilate into three gluons, which must be hard enough to fragment into hadrons. However, as was discussed in Sec. 1.1.1, gluons couple weakly at high energies. Hence the diagram is suppressed. Instead, the decay of the charmonium into a pair of the lightest charmed hadrons

$$\psi \rightarrow D^0 + \bar{D}^0$$

would be preferred as it would require emission of soft, strongly coupling gluons, see Fig. 2.1 right. This decay is however kinematically forbidden for charmonia with mass below the  $D^0$  pair mass threshold<sup>4</sup>  $M_\psi < M_{2D} \approx 3700 \text{ MeV}/c^2$ .



Figure 2.1: OZI forbidden (left) and allowed (right)  $c\bar{c}$  decay.

In case of electromagnetic decays ( $\tau_{EM} \sim 10^{-16}$ ), the  $J/\psi$  decays into a leptonic pair  $\ell^+ + \ell^-$  via a virtual photon. Due to lepton universality, the branching ratio is the same regardless whether one observes a pair of electron or muons in the final state. The latest values are [1]

$$\begin{aligned} \text{BR}_{J/\psi \rightarrow \mu^+ \mu^-} &= (5.961 \pm 0.033)\%, \\ \text{BR}_{J/\psi \rightarrow e^+ e^-} &= (5.971 \pm 0.032)\%. \end{aligned}$$

### 2.1.2 Charmonia family

Quarkonia states with masses below the threshold for production of a pair of open heavy flavour hadrons are considered stable, due to their strong decays being OZI suppressed. The stable charmonia states are shown in Fig. 2.2. The horizontal line corresponds to the  $2M_D$  threshold<sup>5</sup>. The diagram also shows hadronic and radiative decays of excited states to lower energy states. These feed-down contributions need to be taken into account in calculations of total invariant yields. The  $\psi(2S)$  for instance contributes to the  $J/\psi$  production directly via hadronic decays or by a double radiative decay via an intermediate  $\chi_c(1P)$  state. Tab. 2.1 contains the fundamental characteristics of selected stable charmonia states.

<sup>3</sup>Okubo, Zweig and Iizuka were originally trying to explain suppression of energetically convenient decay  $\phi \rightarrow 3\pi$  compared to the favoured  $\phi \rightarrow 2K$ ,  $M_{2K} > M_{3\pi}$  [2].

<sup>4</sup>The  $D^0$  meson has mass  $M_D = 1864.83 \pm 0.05 \text{ MeV}/c^2$  [1].

<sup>5</sup>Similar diagram can be drawn for  $b\bar{b}$  states, see e. g. [14].

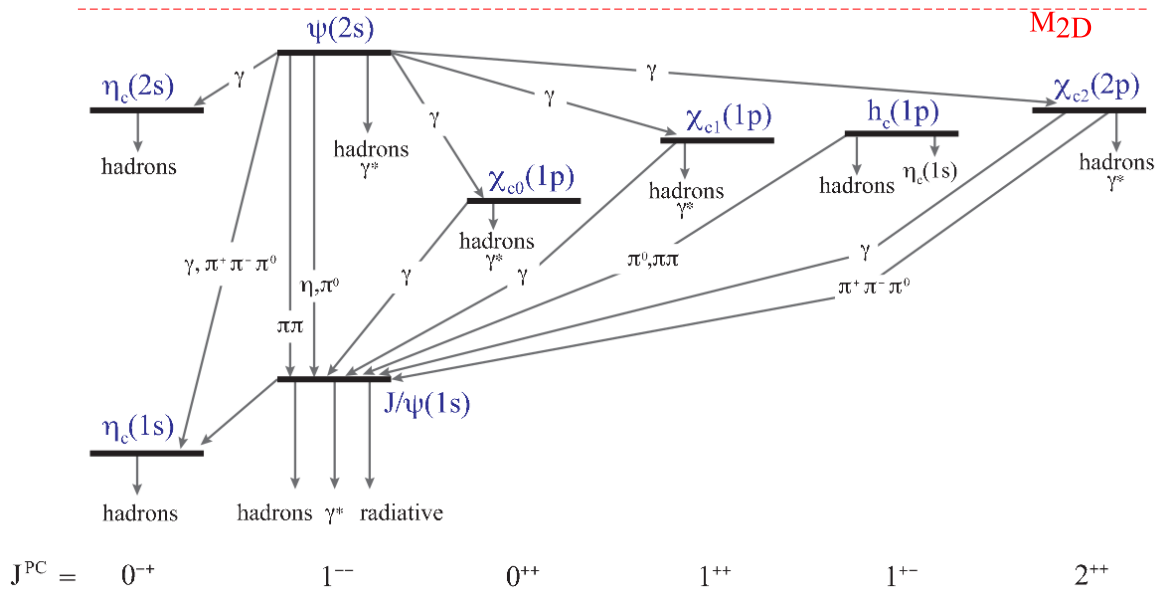


Figure 2.2: Spectroscopy of stable charmonia states.

	$\eta_c$	$J/\psi$	$\psi(2S)$	$\chi_{c0}$
$M$ (MeV/ $c^2$ )	$2983.4 \pm 0.5$	$3096.900 \pm 0.006$	$3686.097 \pm 0.025$	$3414.75 \pm 0.31$
$r$ (fm)	-	0.453	0.875	0.696

Table 2.1: Characteristics of selected stable charmonia states. Masses were taken from [1], while radii were quoted from [14].

## 2.2 Charmonia in pp

The subject of this thesis is a study of inclusive  $J/\psi$  produced at forward rapidity in ultrarelativistic hadron-hadron collisions. Inclusive studies do not discriminate between the source of  $J/\psi$  production. We distinguish three sources of  $J/\psi$ :

**Direct production** includes the  $J/\psi$  produced directly from hadronisation of the initial  $c\bar{c}$  pair.

**Production by feed-down higher charmonia states** in which the higher state charmonium is produced directly from hadronisation of the initial  $c\bar{c}$  pair. The contribution of feed-down processes  $\chi_c \rightarrow J/\psi + X$  and  $\psi(2S) \rightarrow J/\psi + X$  at forward rapidity  $2 < y < 4.5$  were measured by LHCb [35, 36].

**Production by feed-downs of  $b$ -hadrons.** The fraction of  $J/\psi$  originating in  $B$  decays depends on  $p_T$  and  $y$ . This contribution is negligible below LHC energies, see the  $b\bar{b}$  production cross section as a function of energy in Fig. 2.3. In LHC experiments, the midrapidity contribution of  $B$  feed-down  $f_b$  ranges from  $\sim 15\%$  at low and intermediate  $p_T$  of the total production up to  $\sim 70\%$  at the highest measured  $p_T \sim 70$  GeV/ $c$  [37–39]. At forward rapidity, the non-prompt sample represents  $\sim 10 - 50\%$  of the inclusive cross section in the measured  $p_T$  range [40, 41]. In all measured rapidity intervals,  $f_b \approx 15\%$  for the  $p_T$ - and  $y$  integrated cross section ratio. Examples of the mid- and forward rapidity  $f_b$  as a function of  $p_T$  can be found in Fig. 2.4.

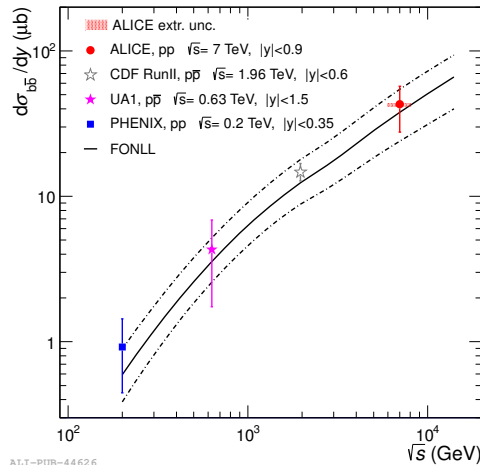


Figure 2.3: The energy dependence of the  $d\sigma_{b\bar{b}}/dy$  production cross section. Taken from [37].

Unless explicitly stated otherwise, we will discuss results of inclusive  $J/\psi$  measurements in all systems. One can also use alternative division to:

**Prompt  $J/\psi$**  which encompasses the direct production and the production via decay of higher charmonium states.

**Non-prompt production** which equates the production from feed-downs  $b \rightarrow J/\psi$ , with a typical lifetime  $c\tau_B \sim 500$   $\mu\text{m}$ . Such produced  $J/\psi$  originate in a displaced secondary vertex.

### 2.2.1 Theoretical description of $J/\psi$ production

Production of quarkonia involves both perturbative and non-perturbative scales of QCD. The heavy quark production requires high-momentum transfers at

$$m \geq 2M_Q.$$

There are multiple processes in which heavy quarks are created. Few examples are shown in Fig. 2.5 such as (i) quark annihilation, (ii) flavour creation, or (iii) gluon fusion.

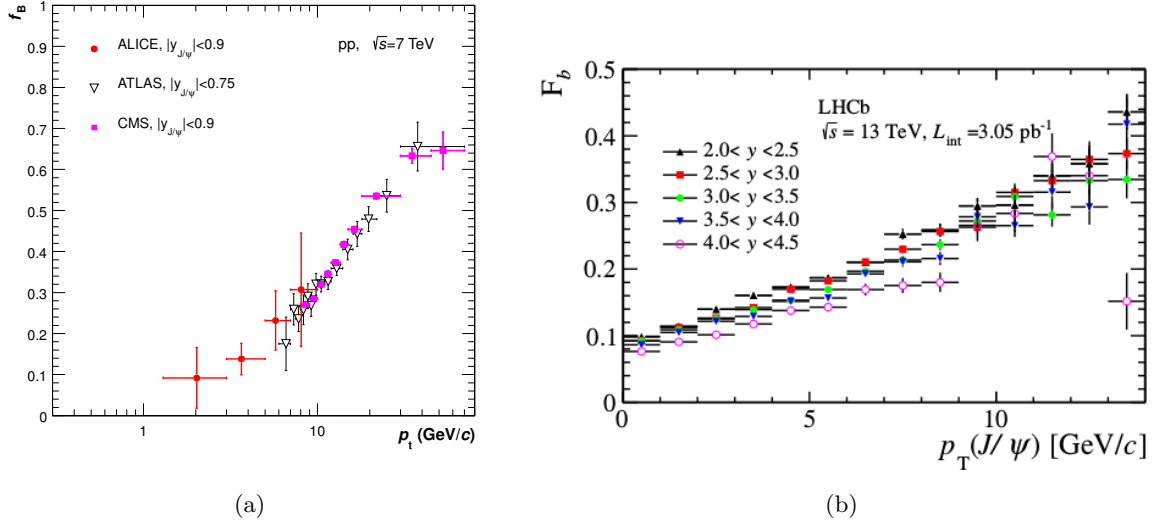


Figure 2.4: **(a)** The  $p_T$  dependence of the fraction of non-prompt  $J/\psi$   $f_b$  at midrapidity in pp at  $\sqrt{s} = 7$  TeV measured in ALICE [37], ATLAS [38], and CMS [39]. **(b)** The  $p_T$  dependence of fraction of non-prompt  $J/\psi$   $f_b$  at forward rapidity in pp at  $\sqrt{s} = 13$  TeV measured in LHCb [41].

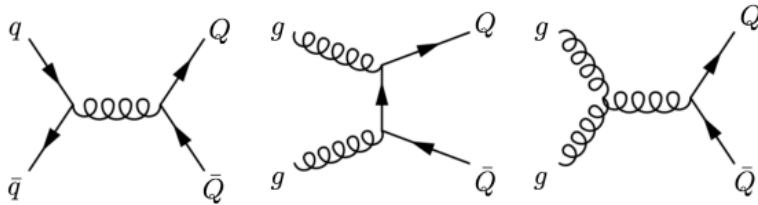


Figure 2.5: Examples of Feynman diagrams describing the charm quark pair creation in QCD.

On the other hand the evolution into the bound state is non-perturbative. The heavy quark is non-relativistic in the bound state rest frame as it occurs at typical momentum scales  $m_Q v$  where in the case of charmonium<sup>6</sup>  $v^2 \sim 0.3 c^2$  [14].

A limpid overview of models describing production of quarkonia can be found in [42]. All models consider factorisation between the high momentum (short distance) pair production and its binding into a quarkonium state, which occurs at low momentum (over long distance). In the following paragraphs, we will briefly discuss the Colour Evaporation Model (CEM), the Colour Singlet Model (CSM), and the Colour Octet Mechanism (COM), all of which differ in the treatment of the non-perturbative part. The latter two are incorporated into the Non-Relativistic QCD (NRQCD) framework to correct for some of the CSM shortcomings, which we shall explain later. The same formalism is used for both  $c\bar{c}$  and  $b\bar{b}$  states. For that sake of simplicity, we will only discuss the production of charmonia.

### 2.2.1.1 Colour Evaporation Model

In the CEM framework [14], the production cross section is directly connected to the production of the charm quark pair integrated over the mass range where the pair can hadronise into a charmonium state, i. e. starting from the mass necessary for the production to occur  $2M_c$  up to the mass of a pair of lightest open charm hadrons  $2M_D$ . Hence the production cross section reads as

$$\sigma_\psi^{\text{CEM}} = F_\psi \int_{2M_c}^{2M_D} \frac{d\sigma_{c\bar{c}}}{dm_{c\bar{c}}} dm_{c\bar{c}}. \quad (2.2)$$

The model assumes that the quantum numbers between the production and hadronisation stage can be changed via exchange of soft gluons. The factor  $F_\psi$  is purely phenomenological and represents the process independent probability of the  $c\bar{c}$  quark pair hadronising into a charmonium. On the other hand it depends on  $m_c$ ,  $\alpha_s$  and parton densities in the colliding hadrons. The factor also includes both radiative and hadronic feed-down from higher states.

### 2.2.1.2 Colour Singlet Model

Contrary to the CEM, the CSM model [43] assumes that the quantum numbers at production and at hadronisation time remain constant. The model assumes the hadronic cross section of the form

$$d\sigma_{\psi+X}^{\text{CSM}} = \sum_{i,j} \int dx_i dx_j f_i(x_i, \mu_F) f_j(x_j, \mu_F) \times d\hat{\sigma}_{i+j \rightarrow (c\bar{c})+X}(\mu_R, \mu_F) \times |\psi(0)|^2, \quad (2.3)$$

where  $f_i(x_i, \mu_F)$  and  $f_j(x_j, \mu_F)$  are parton densities in the colliding hadrons. The partonic cross section  $d\hat{\sigma}_{i+j \rightarrow (c\bar{c})+X}(\mu_R, \mu_F)$  is equivalent to the production cross section of charm quark pair with relative velocity  $v = 0$  and with the same  $J$  as the subsequently formed charmonium. The probability  $|\psi(0)|^2$  can be extracted from subsequent decays of the formed  $\psi$  state.

### 2.2.1.3 Colour Octet Mechanism and Non-Relativistic QCD

To correct for the divergences of the CSM approach, one can include colour octet contributions at *a priori* different angular momentum  $L$  and spin  $S$ . Within the NRQCD framework [44], an additional expansion in  $v$  is introduced on top of the one in  $\alpha_s$ . The hadronisation probability is expressed by Long Range Matrix Elements (LRME)<sup>7</sup>  $\mathcal{O}_\psi^n$ . The Eq. (2.3) is then modified to

$$d\sigma_{\psi+X}^{\text{NRQCD}} = \sum_{i,j,n} \int dx_i dx_j f_i(x_i, \mu_F) f_j(x_j, \mu_F) \times d\hat{\sigma}_{i+j \rightarrow (c\bar{c})_n+X}(\mu_R, \mu_F, \mu_\Lambda) \times \langle \mathcal{O}_\psi^n \rangle. \quad (2.4)$$

Unlike in the CSM, the LRMEs cannot be fixed neither from decay-widths nor from lattice calculations except for the leading order, which corresponds to the CSM cross section.

The matrix elements are obtained from fitting  $p_T$  spectra at different energies. Various models differ in the number of LRMEs used to fit data and also in the dataset used in the fitting. They largely disagree in  $J/\psi$  polarisation. Measurements of  $J/\psi$  polarisation thus present a vital test of theoretical calculation and could help by either confirming or refuting the existing QCD approach.

<sup>6</sup>For bottomia,  $v^2 \sim 0.1 c^2$ .

<sup>7</sup>Or Long Distance Matrix Elements (LDME)

## 2.2.2 Production measurement in pp

The production of quarkonia, namely  $J/\psi$ , has been thoroughly measured in ultrarelativistic proton collisions. Highlights from the Tevatron and RHIC will be discussed in the first part of the section. We shall also briefly mention a comparison of measurements at LHC energies with theoretical calculations. More in-depth discussion of the LHC results at large rapidities will be given in Sec. 6.7, which is dedicated to the energy dependence of forward  $J/\psi$  production.

### 2.2.2.1 Results from Tevatron and RHIC

In the Tevatron Run 1 data taking campaign, the CDF Collaboration published results on  $J/\psi$  measurement in  $p\bar{p}$  collisions at  $\sqrt{s} = 1.8$  TeV [45]. The measurement was carried out at midrapidity. The results were compared to leading order (LO) and next-to-leading order (NLO) CSM predictions available at the time. The calculations severely underestimated the  $p_T$ -differential cross section. The colour octet contribution was later included to improve the description of the data [46]. Comparison of experimental data with colour singlet and colour octet contributions and with their sum can be found in Fig. 2.6a. The newly introduced NRQCD was also able to describe the  $p_T$  spectra of other charmonium states, namely  $\psi(2S)$  and  $\chi_c$ . However, the models were less successful in describing the polarisation measurement [47], see Fig. 2.6b. The polarisation, integrated over the azimuthal angle, was determined from angular distributions of muons from  $J/\psi$  decays

$$\frac{dN}{d(\cos\theta)} = \frac{3}{2(\alpha + 3)}(1 + \alpha \cos^2\theta), \quad (2.5)$$

where  $\theta$  is the angle between the  $\mu^+$  direction in the  $J/\psi$  rest frame and the  $J/\psi$  direction in the lab frame. The parameter  $\alpha$  gives the level of polarisation:  $\alpha = 0$  for unpolarised  $J/\psi$ ,  $\alpha = \pm 1$  for full transverse and longitudinal polarisation respectively. The same method was applied to muons from  $\psi(2S)$  decays. The used CSM models worked with a hypothesis of the  $J/\psi$  and  $\psi(2S)$  being increasingly more transversely polarised with  $p_T$  [48, 49]. However, it can be seen from Fig. 2.6b that the high- $p_T$  results are consistent with unpolarised charmonia. The  $J/\psi$  calculation fails to describe the observed behaviour qualitatively, but agrees with the data in the low- $p_T$  range.

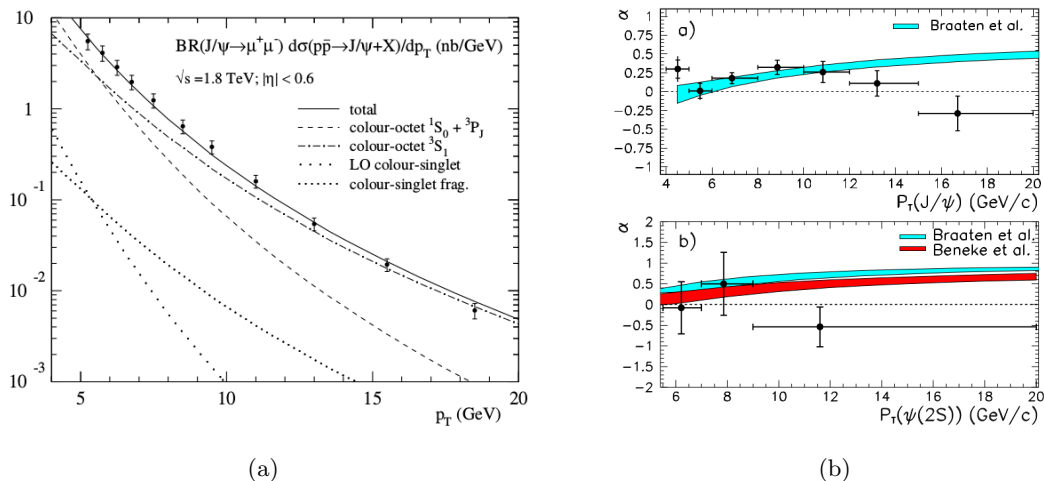


Figure 2.6: **(a)**  $p_T$  dependence of direct  $J/\psi$  production in  $p\bar{p}$  collisions at  $\sqrt{s} = 1.8$  TeV at the Tevatron [45]. Visualised are colour singlet, colour octet and total contributions. Figure taken from [46]. **(b)** Polarisation of prompt  $J/\psi$  (top) and  $\psi(2S)$  (bottom) from 1.8 TeV  $p\bar{p}$  collisions at the Tevatron. The coloured bands show different NRQCD predictions [48, 49]. Figure taken from [47].

At RHIC, the inclusive  $J/\psi$  cross section at midrapidity was measured in  $pp$  collisions at  $\sqrt{s} = 200$  and 500 GeV. Results of the 200 GeV measurement from both STAR [50–52] and PHENIX [53] are shown in Fig. 2.7a. The different measurements are in good agreement among each other as well as with prompt CEM [54, 55] and NLO NRQCD [56] predictions. At low  $p_T$ , a Colour Glass Condensate (CGC) component is added to the NRQCD calculation to account for the small- $x$  gluons in the incoming protons [57].

The polarisation measurement at 200 GeV in both experiments [58, 59] hint at an increase of the longitudinal polarisation with  $p_T$ . In this case, the  $\alpha$  parameter from Eq. (2.5) is instead denoted as  $\lambda_\theta$ , i. e.

$$\frac{dN}{d(\cos\theta)} \propto 1 + \lambda_\theta \cos^2\theta.$$

The sum of the RHIC data was compared with next-to-leading-order (NLO<sup>+</sup>) CSM calculation with and without the feed-down contribution [60] and with LO NRQCD [61]. Both kinds of calculations agree with the data within uncertainties.

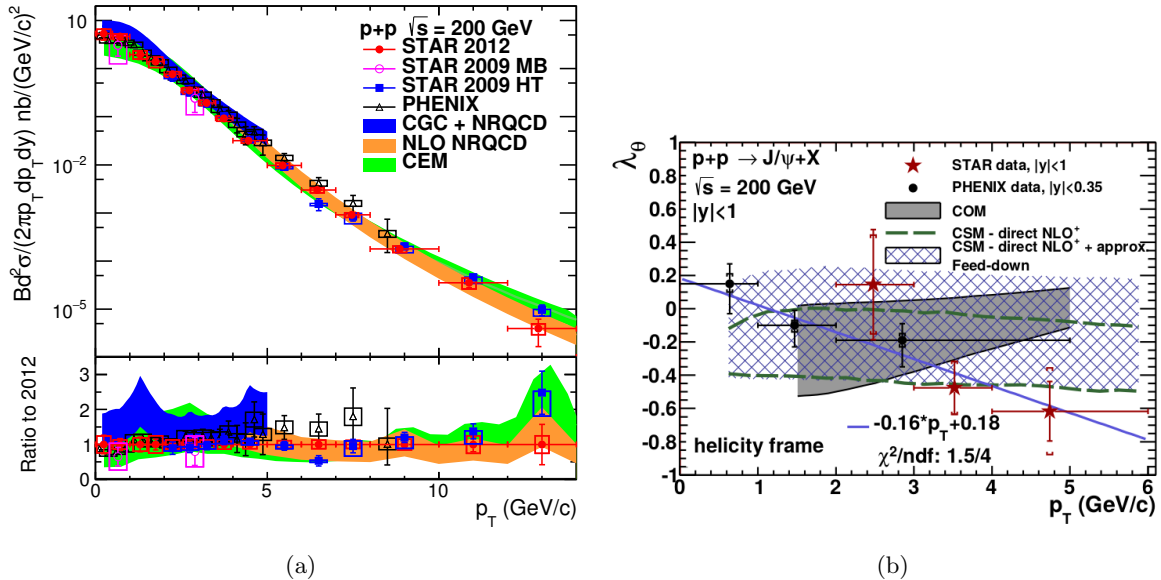


Figure 2.7: The  $p_T$  differential  $J/\psi$  cross section in pp collisions at  $\sqrt{s} = 200$  GeV at the RHIC. Recent STAR results [52] are compared with previous STAR data [50, 51] and PHENIX data [53] at the same energy. Comparison with theoretical calculations [54–57] are shown. Figure taken from [52].

### 2.2.2.2 Measurements at LHC energies

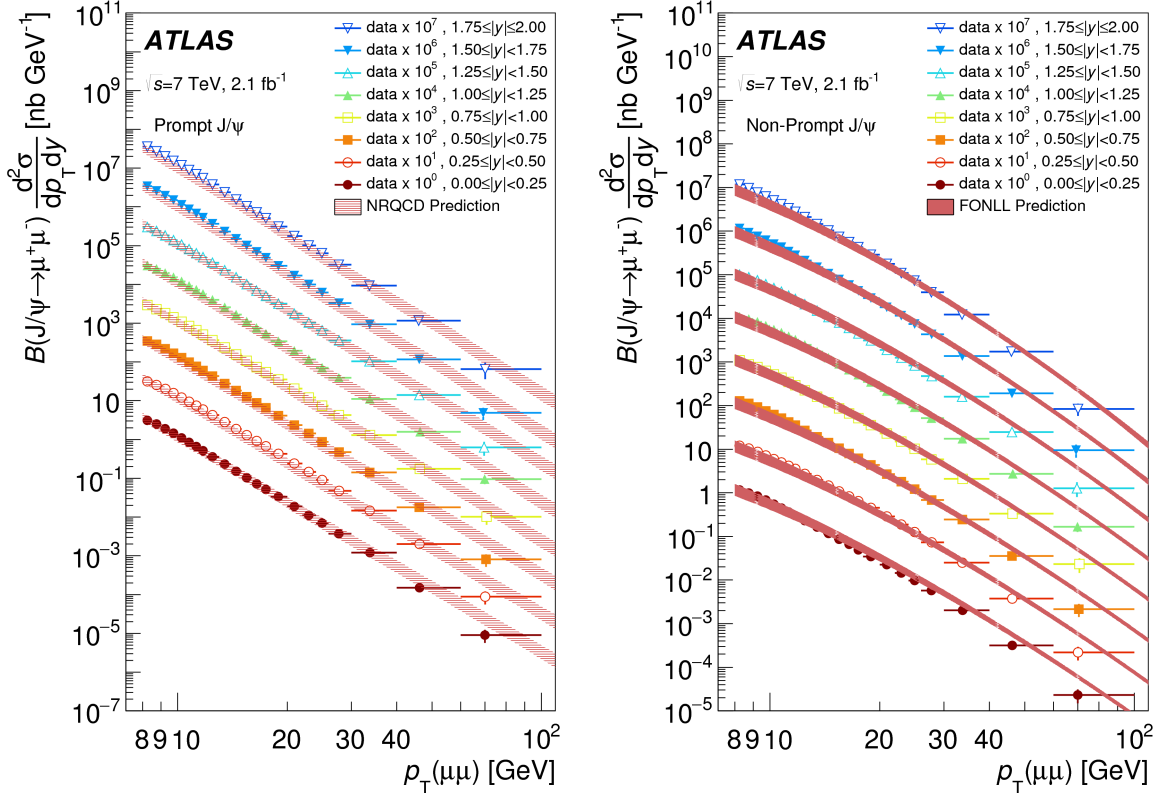
$J/\psi$  production is studied in all four main LHC experiments. ATLAS and CMS perform the high- $p_T$  measurement at midrapidity and separate the prompt and non-prompt contribution to the inclusive  $J/\psi$  cross section. LHCb has also the ability to separate prompt and non-prompt  $J/\psi$ , but does so at forward rapidity. ALICE measures  $J/\psi$  in two separate rapidity intervals: i) at midrapidity, where prompt and non-prompt contribution can be separated, and ii) in the forward rapidity region, where inclusive  $J/\psi$  are measured.

One of the analyses discussed in this manuscript is the analysis of the inclusive  $J/\psi$  production in the forward rapidity region with ALICE. These results will be discussed in a dedicated chapter (see Sec. 6.7).

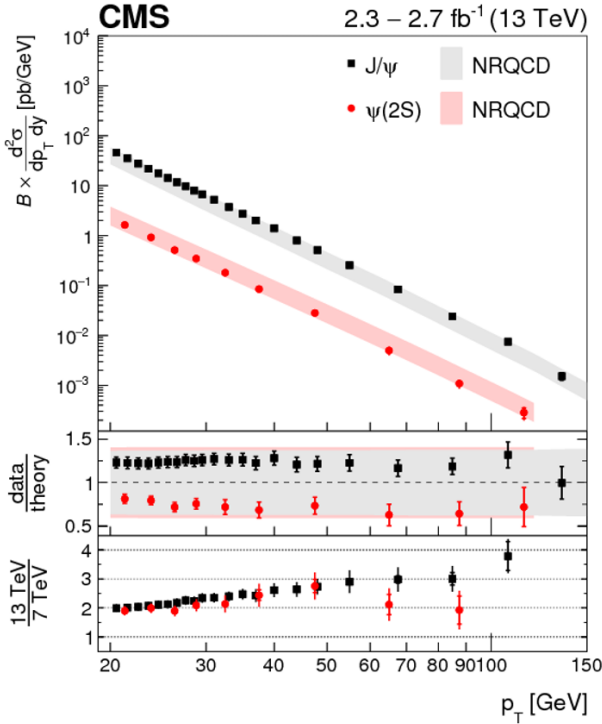
ATLAS, CMS, and ALICE are able to measure the prompt and non-prompt  $J/\psi$  at midrapidity. The first two measure the charmonia at high  $p_T$  from their decays into  $\mu^+\mu^-$  pairs. The advantages are easier triggering, better signal-to-background (S/B) ratio and sizeable branching ratio. ALICE measures the decay channel  $J/\psi \rightarrow e^+e^-$  at midrapidity down to  $p_T = 0$ .

The high- $p_T$  measurements from ATLAS and CMS are compared in Fig. 2.8 [62–64]. The prompt production is well described by an NLO NRQCD calculation [65] in a vast  $p_T$  and  $y$  range and at different energies. First-order-next-to-leading-logarithm (FONLL) pQCD calculations [66, 67] agree well with the non-prompt data. The results at 7 TeV were also compared between the two experiments, they show an excellent agreement over the whole measured  $p_T$  and  $y$  range. The results of the midrapidity measurement in ALICE agrees with these high- $p_T$  results in the overlapping kinematic region and further extends the reach of the data at 7 TeV down to  $p_T \approx 1$  GeV/c [68].

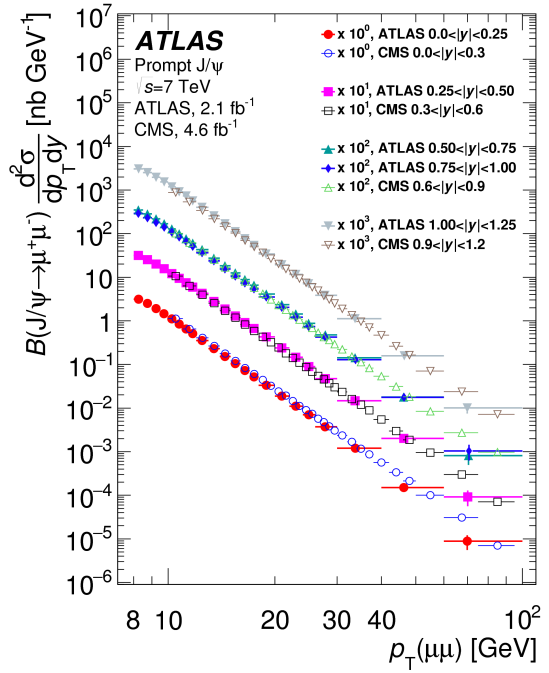
The fraction  $f_b$  of non-prompt to inclusive  $J/\psi$  measured by CMS in pp at  $\sqrt{s} = 7$  and 13 TeV [69] is shown in Fig. 2.9. At intermediate  $p_T$ ,  $f_b$  increases with  $p_T$  until it saturates at  $p_T \sim 50$  GeV/c



(a)



(b)



(c)

Figure 2.8: (a) Prompt and non-prompt  $J/\psi$  at  $\sqrt{s} = 7$  TeV measured with ATLAS [62]. Prompt  $J/\psi$  were compared with NRQCD calculation [65], non-prompt with FONLL calculation [66, 67]. (b) Prompt  $J/\psi$  and  $\psi(2S)$  at 13 TeV measured with CMS [63], compared with NRQCD calculation [65] (middle panel) and with data. at 7 TeV [64]. (c) Comparison between the ATLAS and the CMS data at  $\sqrt{s} = 7$  TeV.

around the value  $f_b \approx 0.7$ . Moreover, the two measurements give consistent results suggesting that this phenomenon is independent of energy. The measurements from ATLAS at  $\sqrt{s} = 7$  and 8 TeV also show a saturation at high  $p_T$  [62], which is constant in energy. ALICE [68] extended the measurement down to  $p_T \approx 1$  (recall Fig. 2.4b), where  $f_b \approx 0.1$ . The  $p_T$  integrated value was computed in ALICE as  $f_b \approx 0.15$ . Data from all three experiments agree in the common  $p_T$  interval.

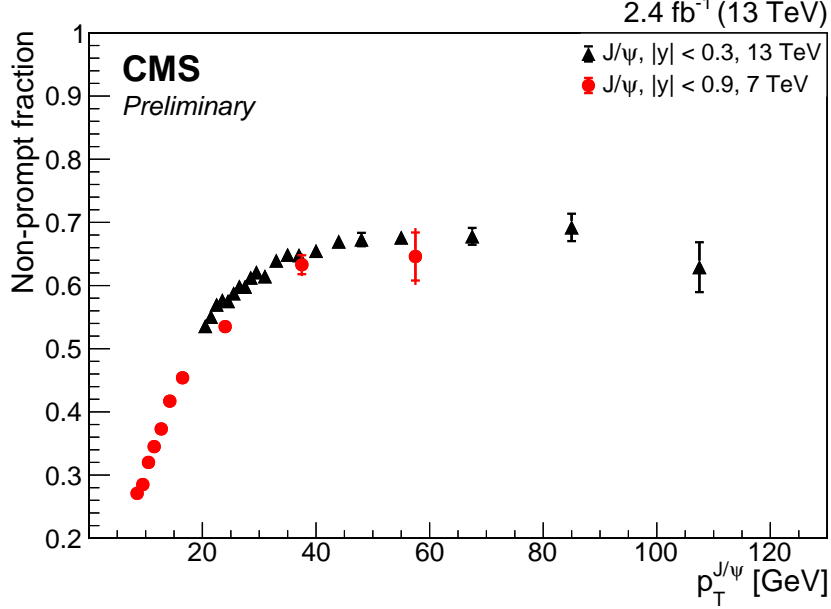


Figure 2.9: Non-prompt-to-inclusive  $J/\psi$  fraction  $f_b$  measured by CMS in pp at  $\sqrt{s} = 7$  and 13 TeV [69].

The forward  $J/\psi$  are measured with LHCb [40, 41, 70, 71] and ALICE [72–75] down to  $p_T = 0$ . The prompt  $J/\psi$  measured with LHCb at  $\sqrt{s} = 7$  TeV are compared to theoretical models in Fig. 2.10. The prompt production is well described by NLO NRQCD calculations [76, 77], which includes both the colour singlet and octet states. The direct NLO CSM fails to describe the data, however adding a NNLO approximation (denoted NNLO\*) [78, 79] bring the theoretical curve closer to data albeit in a limited  $p_T$  range.

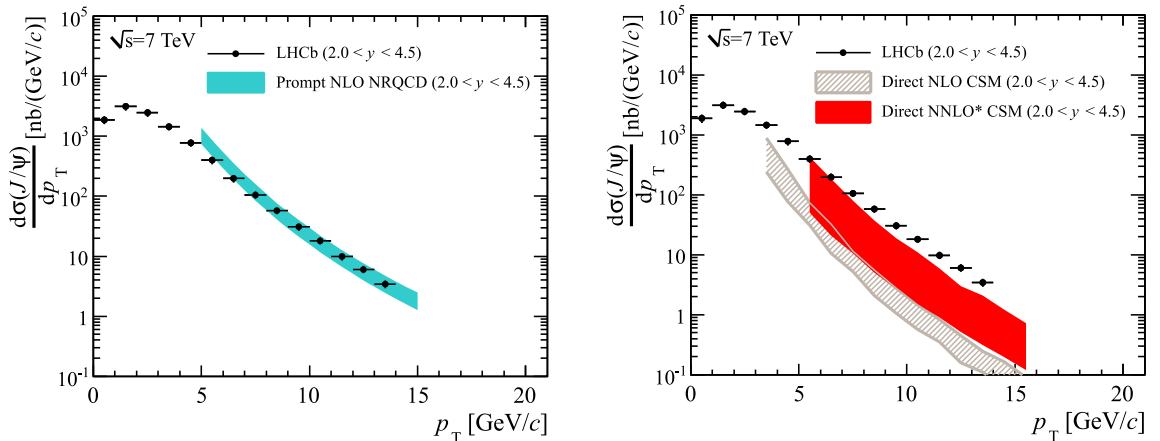


Figure 2.10: The LHCb  $p_T$ -differential prompt  $J/\psi$  production cross section in pp at  $\sqrt{s} = 7$  TeV [40] compared with theoretical calculations [76–79].

Concerning the polarisation measurements, we shall mention as an example the results from pp

data at 7 TeV measured by LHCb at forward rapidity [80], shown in Fig. 2.11. The data favour mostly unpolarised (or slightly longitudinally polarised)  $J/\psi$ . This behaviour was also observed by ALICE at 7 and 8 TeV at forward rapidity [81, 82]. The LHCb data were compared with one NLO CSM [83] and three different NLO NRQCD models [83–85], none of which is able to qualitatively reproduce the observed behaviour at low  $p_T$ .

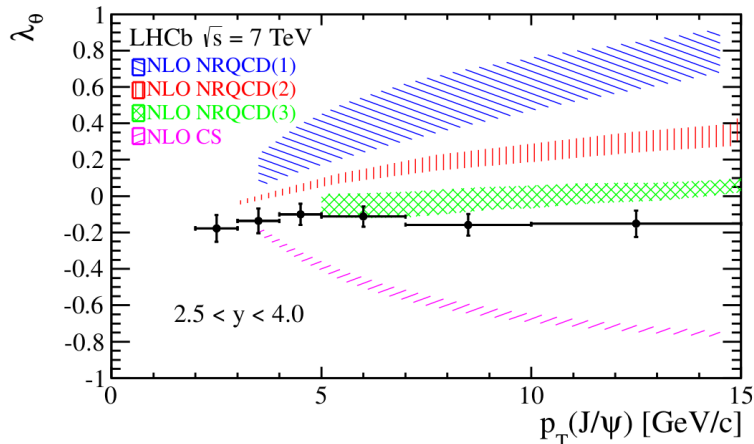


Figure 2.11: Polarisation parameter  $\lambda_\theta$  of prompt  $J/\psi$  measured by LHCb at forward rapidity [40].

To briefly sum up the discussed pp results: the  $J/\psi$  were studied at multiple energies ranging from  $\sim 0.1$  TeV up to  $\sim 10$  TeV. At the LHC energies, the  $b\bar{b}$  production cross section and in consequence the non-prompt contribution grows in importance. Three models are used to describe the production cross section of prompt  $J/\psi$ . Often the NRQCD is favoured by the experimentalists, although the CEM and CSM at higher order approximation gives also a reasonable description of the  $p_T$  spectra. Nevertheless, the polarisation data at low  $p_T$  measured at the LHC are not qualitatively described by any of them.

## 2.3 Charmonia in nucleus-nucleus collisions

### 2.3.1 $J/\psi$ as a probe of the Quark-Gluon Plasma

In 1986, Matsui and Satz [86] proposed a new signature of QGP formation. The QGP is a state with a high density of free colour charges, which are felt by the hadrons crossing the plasma. If the density of the free colour charges is large enough, they screen the interaction between the constituents of the hadrons, which ‘melt’ in consequence. Heavy quarks cannot be produced from the medium, and thus their bound states are produced in the first stages of the collisions<sup>8</sup>. Thus in presence of the QGP, we observe a suppression of bound states compared to systems without the plasma.

The QCD binding potential of quarkonia can be expressed as [14]

$$V(r) = -\frac{4}{3} \frac{\alpha_s}{r} + k \cdot r, \quad (2.6)$$

where  $r$  is the distance between the two heavy quarks,  $\alpha_s$  is the strong coupling constant and  $k$  is string tension. The first, repulsive, Coulomb-like term describes the gluon exchange between the  $Q\bar{Q}$  pair at short distances. The second, attractive term represents the confinement.

In a medium with a high density of free colour charges, quarks will only ‘see’ other quarks at a distance limited by the Debye screening radius  $r_D$ . The Debye radius is a function of temperature of the medium  $T$  and decreases with increasing  $T$ . The dissociation occurs at the dissociation temperature  $T_d$ . To accommodate the screening in the QGP, the potential in Eq. 2.6 can be written as

$$V(r, T) = -\frac{4}{3} \frac{\alpha_s}{r} \exp^{-\frac{r}{r_D}} + k \cdot r_D \left(1 - \exp^{-\frac{r}{r_D}}\right). \quad (2.7)$$

<sup>8</sup>Today we know that the reality is not so simple.

At low temperatures  $T < T_d$ ,  $r_D \rightarrow \infty$  and so  $r/r_D \rightarrow 0$ . The potential simplifies to Eq. (2.6) and no screening occurs. At temperatures  $T > T_d$ , the Debye radius decreases to  $r > r_D$  and hence

$$-\frac{4}{3} \frac{\alpha_s}{r} \exp^{-\frac{r}{r_D}} \longrightarrow -\frac{4}{3} \frac{\alpha_s}{r},$$

$$k \cdot r_D \left(1 - \exp^{-\frac{r}{r_D}}\right) \longrightarrow 0.$$

The confinement term vanishes and the bound state dissociates in the QGP.

The value of the Debye radius predicted by lattice QCD and quoted in [86] for  $T \approx 1.5 T_c$  is

$$r_D \sim 0.2 - 0.3 \text{ fm},$$

which is of the same order as the quarkonia radii, see Tab. 2.1. Moreover, due to the different binding energy of charmonia states, the dissociation temperature will vary from state to state. This phenomenon can be interpreted as a sort of ‘‘QGP thermometer’’. The sequential dissociation will manifest as well in the total  $J/\psi$  suppression as the higher states will break up before feeding the  $J/\psi$  yield, as illustrated in Fig. 2.12.

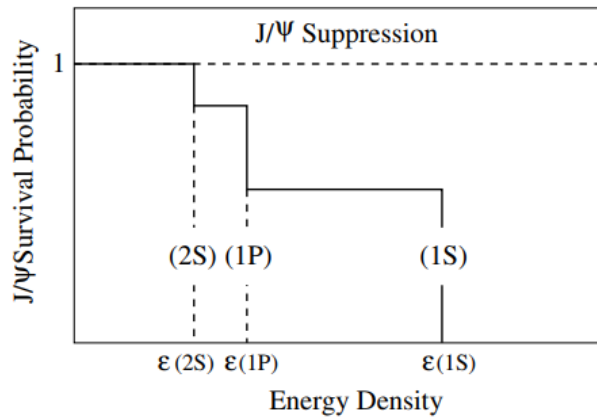


Figure 2.12: Schema of  $J/\psi$  sequential suppression. Figure taken from [42].

At high energies, a competing mechanism needs to be taken into account - the (re)generation of  $J/\psi$  in the medium [87]. Matsui and Satz originally assumed that at hadronisation the heavy quarks will mostly interact with the light quarks, which are abundant in the medium, to form open heavy flavour hadrons. These are also dissociated in the presence of the QGP. Fig. 2.13 shows the total charm-anticharm production cross section as a function of energy. At LHC energies, many  $c\bar{c}$  pairs are produced, resulting in many free  $c$  and  $\bar{c}$  (anti)quarks in the deconfined plasma. The probability that they form a bound state through coalescence increases. As a consequence, the  $J/\psi$  yield will be larger in a scenario with both suppression and (re)generation compare to when only suppression would take place.

Additional nuclear effects also need to be taken into account in studies of suppression of quarkonia due to the QGP. These are not connected to the creation of the hot and dense plasma but instead relate to the binding of the nucleons in the incoming nuclei. Such effects are commonly called the ‘‘cold nuclear matter’’ (CNM) effects. Sec. 2.4 is dedicated to discussion of these effects. These effects depend on  $p_T$ ,  $y$ , and on the  $J/\psi$  production process (prompt and non-prompt contributions are affected differently). However, they scale with the collision energy. Different CNM effects may apply at different stages of the collisions - some may affect the  $c\bar{c}$  production while some impact its subsequent evolution.

### 2.3.2 Models

In the following text, we will describe selected models describing charmonia production in A–A collisions: (i) the Statistical Hadronisation Model (SHM) [89], (ii) the Transport Models (TM1 and TM2) [90–93], (iii) and the Comovers Model (CM) [94, 95].

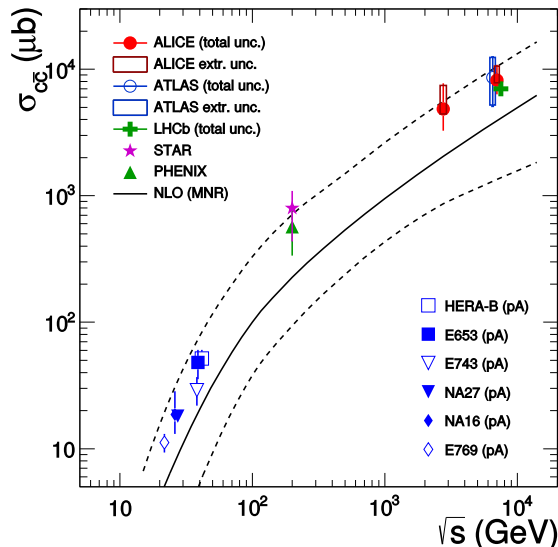


Figure 2.13: The total  $c\bar{c}$  cross section in pp collisions. Figure taken from [88].

The models include both the suppression and regeneration of the  $c\bar{c}$  pairs in the medium. An overview of all hereby presented models can be found in [42].

### 2.3.2.1 Statistical Hadronisation Model

The SHM [89] uses the grand canonical approach to describe the statistical production of hadrons at the hadronisation phase. The free parameters of the SHM are the temperature of the chemical freeze-out  $T_{ch}$ , the baryo-chemical potential  $\mu_B$ , and the volume  $V$ . These are obtained from global fit to particle yields for each collisions energy.

The SHM assumes that all  $c\bar{c}$  pairs are produced in hard scattering events and that all direct charmonia are screened in the medium. At the phase boundary, the open charm hadrons and charmonia hadronise according to the mass spectrum of charmed hadrons and their respective statistical weights. As  $T$ ,  $\mu_B$  and  $V$  are fixed from light hadron spectra, the only additional parameter that needs to be added for the charmed hadrons is the charm cross section per unity of rapidity  $d\sigma_{c\bar{c}}/dy$ .

The initial CNM effects on charmonia are not considered as the model assumes all charmonia are suppressed during the QGP phase. The shadowing, as the dominating CNM effects applicable on the  $c\bar{c}$  production cross section, is included.

### 2.3.2.2 Transport models

Transport models assume continuous dissociation and (re)generation of charmonia during the full deconfined phase. The space-time evolution of the distribution function of a charmonium state  $\psi$ ,  $f_\psi$ , is described by a relativistic Boltzmann equation

$$p^\mu \partial_\mu f_\psi(\vec{r}, \tau, \vec{p}) = E [-\Gamma_\psi(\vec{r}, \tau, \vec{p}) f_\psi(\vec{r}, \tau, \vec{p}) + \beta_\psi(\vec{r}, \tau, \vec{p})], \quad (2.8)$$

where  $E = \sqrt{p^2 + M_\psi^2}$ ,  $\tau$  is the proper time,  $\vec{r}$  is the spatial coordinate, and  $\Gamma_\psi$  and  $\beta_\psi$  correspond to the dissociation and gain terms respectively. The dissociation originates from the inelastic scatterings with the partons in the medium. Moreover, the model takes into account the modification of the nPDFs.

### 2.3.2.3 Comovers model

The Comovers Model includes dissociation of charmonia states due to interactions with the co-moving medium, which may be composed of hadrons or partons. The same dynamical approach as in TM is adopted, CM however does not assume the QGP formation. For a charmonium state  $\psi$ , Eq. (2.8) is modified to

$$dN_\psi/d\tau(b, s, y) = \frac{\sigma_{co}}{\tau} [-N^{co}(b, s, y)N_\psi(b, s, y) + N_c(b, s, y)N_{\bar{c}}(b, s, y)], \quad (2.9)$$

and is a function of the impact parameter  $b$ , the centre-of-mass energy squared  $s$ , and the rapidity  $y$ . The first term describes the dissociation of  $\psi$  due to comovers with density  $N^{\text{co}}$ , reigned by the dissociation cross section  $\sigma_{\text{co}}$ . The second term represents the recombination of dissociated  $c\bar{c}$  pairs. The nuclear shadowing is also taken into account in the CM.

### 2.3.3 Experimental results

The modification of yields due to the QGP can be quantified through the nuclear modification factor  $R_{\text{AA}}$  (defined in Eq. (1.10)). Recall that

$$R_{\text{AA}} = \frac{1}{\langle N_{\text{coll}} \rangle} \frac{d^2 N_{\text{AA}}/dp_{\text{T}}dy}{d^2 N_{\text{pp}}/dp_{\text{T}}dy},$$

where  $d^2 N_{\text{AA/pp}}/dp_{\text{T}}dy$  are the  $p_{\text{T}}$  and  $y$  differential yields of the measured particle in A-A and pp, and  $\langle N_{\text{coll}} \rangle$  denotes the mean number of the binary nucleon-nucleon collisions. The  $J/\psi$   $R_{\text{AA}}$  has been thoroughly studied at multiple energies and in various systems at the SPS, RHIC and the LHC.

#### 2.3.3.1 Results from the SPS and RHIC

The Super Proton Synchrotron (SPS) at CERN provided collisions of different nuclear systems at multiple energies. Suppression of  $J/\psi$  and  $\psi(2\text{S})$  in Pb–Pb and S–U collisions as measured by the NA50 experiment [96] at the SPS can be found in Fig. 2.14a. The plot shows the ratio of the measured yield versus the expected as a function of the crossing length  $L$ , which can be related to centrality via Glauber MC.  $L \approx 0$  corresponds to the most peripheral collisions, while  $L \approx 10$  fm represents the most central collisions. The  $J/\psi$  suppression increases with  $L$  and hence with the centrality of the collision. Moreover, the  $\psi(2\text{S})$  demonstrate stronger suppression than the  $J/\psi$ . A possible explanation is the larger  $\psi(2\text{S})$  state is less bound than the smaller  $J/\psi$  (see Tab. 2.1 for estimates of their respective radii). The observed suppression pattern thus favours the sequential suppression scenario.

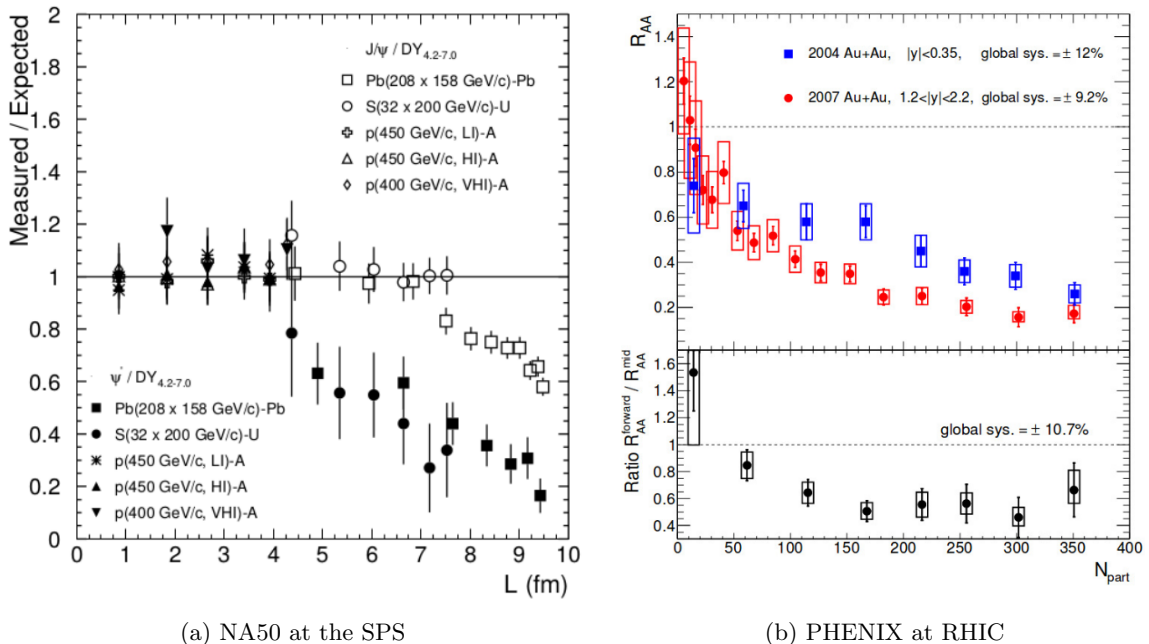


Figure 2.14: (a) Measured over expected  $J/\psi$  and  $\psi(2\text{S})$  as a function of the crossing length, which relates to centrality [96]. (b) Suppression of  $J/\psi$  at mid- and forward rapidity as a function of centrality [97].

PHENIX measured the  $J/\psi$   $R_{\text{AA}}$  at mid- and forward rapidity [97, 98]. The results from measurement in Au–Au collisions at  $\sqrt{s_{\text{NN}}} = 200$  GeV are visualised as a function of collision centrality in Fig. 2.14b. In both rapidity intervals,  $R_{\text{AA}}$  starts around unity in the most peripheral events and gradually decreases with centrality. The ratio of the mid- and forward rapidity data can be found in the bottom panel of the very same figure. In central collisions, the forward yields seem to be more

suppressed<sup>9</sup> Such observation was not expected at the time when these results were published, In contrary, due to the larger energy density at midrapidity, one would expect the midrapidity yields to be more suppressed. This observation was explained only after first results from LHC became public.

### 2.3.3.2 Results from the LHC

The forward data from ALICE measured at  $\sqrt{s_{NN}} = 2.76$  and 5.02 TeV [99, 100] were compared with forward PHENIX data at  $\sqrt{s_{NN}} = 200$  GeV in Fig. 2.15a. In the most peripheral collisions, the ALICE  $R_{AA}$  shows a decrease compatible with the PHENIX measurement. However, in central and semi-central collisions, the LHC data saturate while the RHIC data continue to decrease. The energy density increases with  $\sqrt{s_{NN}}$  and so one would expect the LHC data to lie below RHIC in suppression scenario. Another competing effect must take place to balance the screening of  $J/\psi$  in the medium. Moreover, Fig. 2.15b shows the rapidity dependence of the  $R_{AA}$  at  $\sqrt{s_{NN}} = 2.76$  TeV in ALICE [99]. As in previous measurements at RHIC energies, the midrapidity data show hints of being less suppressed than the forward rapidity yields<sup>10</sup>.

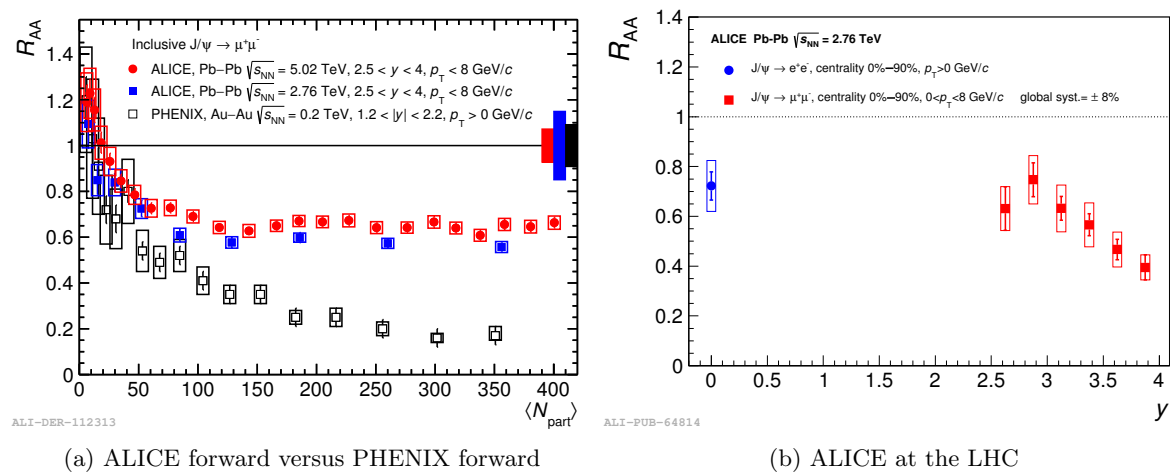


Figure 2.15: (a) Comparison of  $J/\psi$  suppression at forward rapidity between ALICE [99, 100] and PHENIX [97]. (b) Rapidity dependence of the  $J/\psi$  suppression in Pb–Pb at  $\sqrt{s_{NN}} = 2.76$  TeV measured with ALICE [99].

If the thermalised  $c\bar{c}$  pairs (re)combine at the LHC energies, they would do so at low  $p_T$ . The  $p_T$ -dependent  $R_{AA}$  measured in LHC Run 1 data at low  $p_T$  by ALICE [101] and at  $p_T > 1$  GeV/c by CMS [102] are shown in Fig. 2.16a. The LHC data decrease with increasing  $p_T$ . This behaviour is qualitatively reproduced in the transport models [90, 103, 104], which includes both suppression and (re)generation mechanisms. The PHENIX data on the other hand show a flat trend with  $p_T$  [98]. The centrality dependent data from LHC Run 2 measured with ALICE at forward rapidity show a saturation of the  $R_{AA}$  in the (semi-)central centrality interval, reproduced by models containing both suppression and (re)generation [89–91, 93–95].

The  $J/\psi$  elliptic flow  $v_2$  gives the level of thermalisation of the charm quarks and antiquarks before they are bound into a  $J/\psi$ . In Au–Au collisions at  $\sqrt{s_{NN}} = 200$  GeV, the  $v_2$  of  $J/\psi$  was measured to be consistent with zero [105], while the 2.76 TeV LHC data showed indication of positive elliptic flow [106]. Finally at 5.02 TeV, ALICE measured positive  $v_2^{J/\psi}$  with significance  $> 6\sigma$  [107] in low  $p_T$  region at forward rapidity. The  $v_2$  pattern for inclusive  $J/\psi$  at forward rapidity is similar to the one of D mesons at midrapidity measured by ALICE in the same data [108]. The behaviour is consistent with collective motion of  $c$  and  $\bar{c}$  in the plasma, which is supported by the theoretical calculations [91, 93].

<sup>9</sup>It must be said however that the large uncertainty of the measurement prevents any strong conclusion. The ratio is still consistent with unity!

<sup>10</sup>However, take note of the large uncertainties of the measurement. The two measurements are still consistent within uncertainties.

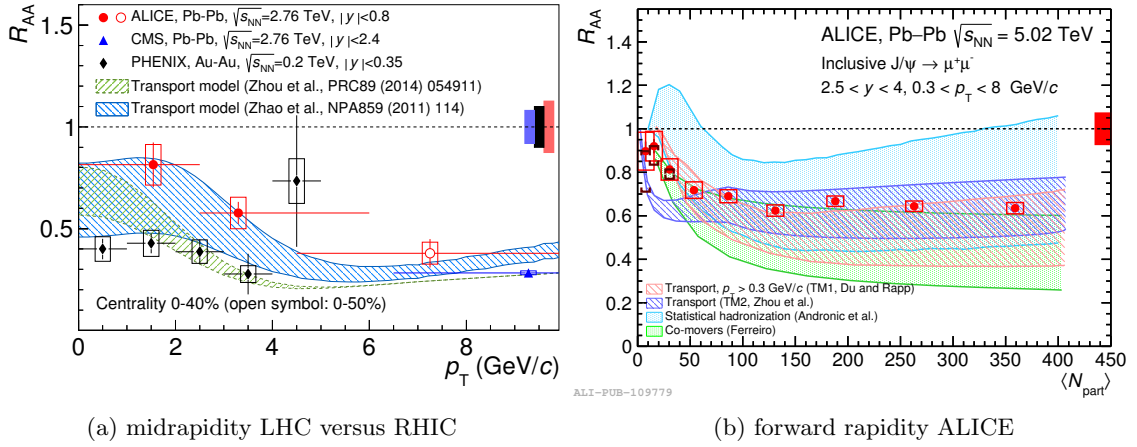


Figure 2.16: **(a)** Prompt  $R_{AA}$  at midrapidity as a function of  $p_T$  at  $\sqrt{s_{NN}} = 2.76$  TeV measured with ALICE [101] and CMS [102] compared to PHENIX results at  $\sqrt{s_{NN}} = 200$  GeV [98]. Data are also compared with available theoretical calculation [90, 103, 104]. **(b)** Centrality dependent forward rapidity  $R_{AA}$  at  $\sqrt{s_{NN}} = 5.02$  TeV [100] compared with theoretical calculations [89–91, 93–95].

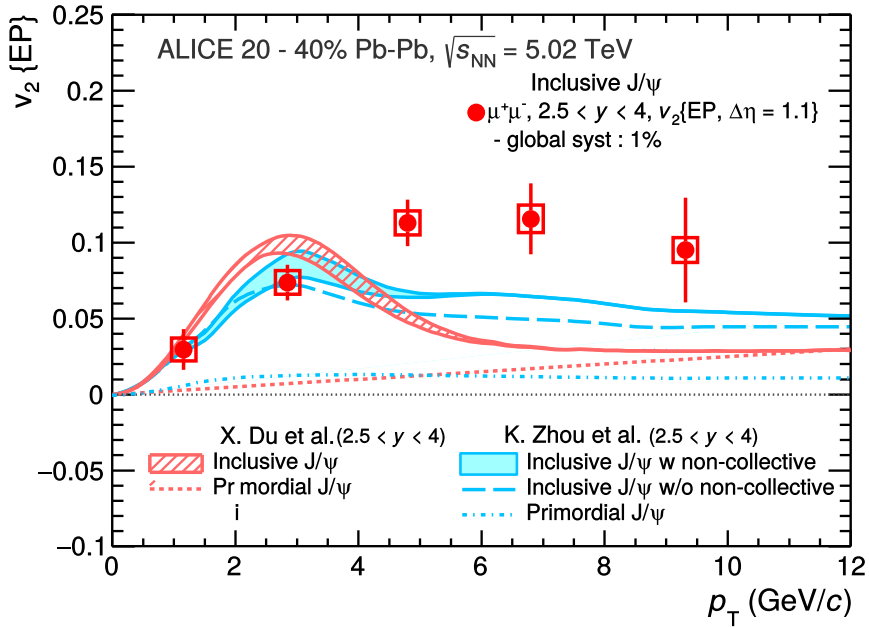


Figure 2.17: The  $p_T$  dependent  $v_2^{J/\psi}$  at forward rapidity for semi-central (20 – 40%) Pb–Pb collisions at  $\sqrt{s_{NN}} = 5.02$  TeV [107], compared with transport model calculations [91, 93].

To sum up the results reviewed in this section, the  $J/\psi$  are used as a probe of formation of the deconfined hot QCD matter. The measurements at energies of  $\mathcal{O}(0.1 \text{ TeV})$  showed that the observed  $J/\psi$  yields in A–A collisions are below the expected value, which would correspond to a superposition of multiple binary nucleon-nucleon collisions. Already at RHIC, the data showed a hints of another mechanism affecting the yields. With the recent LHC data from Run 1 and Run 2 at energies of  $\mathcal{O}(1 \text{ TeV})$ , the current understanding is that the observed suppression pattern results from an interplay of both suppression due to the deconfined medium and (re)generation from the free thermalised heavy quarks in the medium.

## 2.4 Charmonia in proton-nucleus collisions

Quantification of the effects of hot nuclear matter effects on charmonia production in nucleus-nucleus collisions requires prior understanding of how they are affected by effects stemming from the presence of nuclear matter in the collisions. These effects can be studied in collisions of proton-nucleus, where the QGP - the hot QCD matter - is not expected to form. They are hence referred to as the 'cold nuclear matter effects' (CNM effects).

In analogy to the nuclear effects in A–A collisions, the CNM effects in p–A collisions can be quantified through the nuclear modification factor. In the p–A case, the nuclear modification factor defined in Eq. (1.10) takes the form

$$R_{\text{pA}} = \frac{1}{\langle N_{\text{coll}} \rangle} \frac{d^2 N^{\text{pA}}/dp_{\text{T}}dy}{d^2 N^{\text{pp}}/dp_{\text{T}}dy}. \quad (2.10)$$

Alternative definition of the nuclear modification can be also used to express its centrality dependence [109]:

$$\begin{aligned} Q_{\text{pA}} &= \frac{1}{\langle T_{\text{pA}} \rangle^{\text{Glauber}}} \frac{d^2 N^{\text{pA}}/dp_{\text{T}}dy}{d^2 \sigma^{\text{pp}}/dp_{\text{T}}dy} \\ &= \frac{1}{\langle N_{\text{coll}} \rangle^{\text{Glauber}}} \frac{d^2 N^{\text{pA}}/dp_{\text{T}}dy}{d^2 N^{\text{pp}}/dp_{\text{T}}dy}. \end{aligned} \quad (2.11)$$

The nuclear overlap function  $\langle T_{\text{pA}} \rangle^{\text{Glauber}}$  and the number of binary collisions  $\langle N_{\text{coll}} \rangle^{\text{Glauber}}$  are obtained from the Glauber model. The different notation of  $R_{\text{pA}}$  and  $Q_{\text{pA}}$  signifies that the latter is influenced by potential biases from the centrality estimators. As a result,  $Q_{\text{pA}}$  can be different from unity even in absence of nuclear effects.

### 2.4.1 Cold nuclear matter effects

#### 2.4.1.1 Gluon (anti)shadowing

The parton distribution functions (PDFs) characterise partonic content of a nucleon. They represent a probability of finding a parton of a type<sup>11</sup>  $i$  carrying a fraction  $x$  of the nucleon's momentum at the energy scale  $Q^2$ ,  $f_i(x, Q^2)$ . The PDFs are universal - they do not depend on a specific process. This property allows the PDFs obtained through fitting the data from in deep inelastic scattering (DIS) of  $ep$  to be used to predict any hadronic processes. An example of the PDFs measured at the scale  $Q^2 = 10 \text{ GeV}$  with H1 experiment at HERA is shown in Fig. 2.18.

Due to the larger partonic density, the PDFs of a nucleons bound in a nucleus are modified with respect to the free PDFs. These nuclear PDFs (nPDFs) show dependence on both  $x$  and  $Q^2$ . The modification of PDFs for a parton type  $i$  in a nucleus  $A$  can be expressed via the nuclear modification function

$$R_i^A(x, Q^2) = \frac{f_i^A(x, Q^2)}{f_i(x, Q^2)}. \quad (2.12)$$

In absence of any nuclear effects,  $R_i^A(x, Q^2) = 1$ .

A typical distribution of the nuclear modification  $R_i^A(x, Q^2)$  is visualised in Fig. 2.19. We distinguish three main kinematic regions, each of them dominated by different effect:

<sup>11</sup>By type, we understand either a valence or a sea quark, or a gluon.

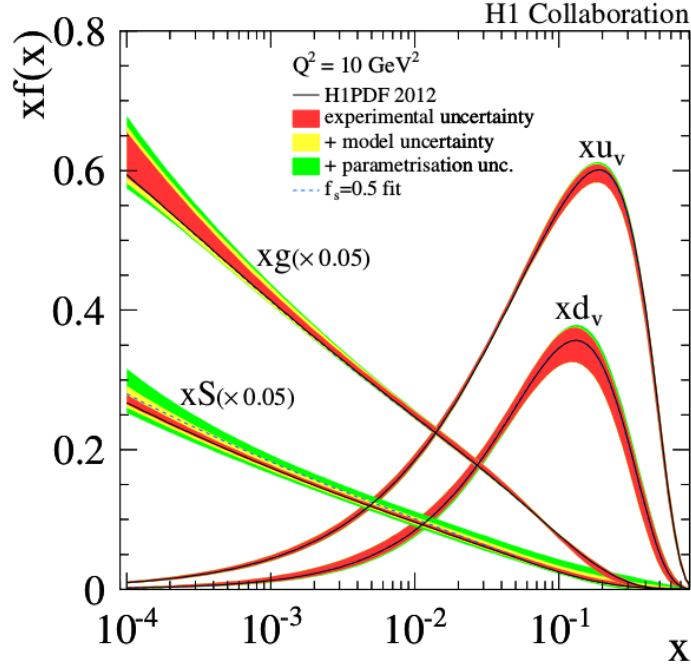


Figure 2.18: Parton distribution functions for valence quarks, sea quarks, and gluon at a scale  $Q^2 = 10 \text{ GeV}$  [110].

**Shadowing**  $R_i^A < 1$  at  $x \lesssim 10^{-2}$ . The effect can be explained through recombination of gluons due to the high phase-space density. The recombined gluon will then carry higher momentum, causing depletion in  $x$ .

**Anti-shadowing**  $R_i^A > 1$  at  $10^{-2} \lesssim x \lesssim 10^{-1}$ . This effect is complementary to shadowing and is a result of increase of gluon density due to the lower  $x$  recombination.

**EMC effect**  $R_i^A < 1$  at  $x \gtrsim 10^{-1}$ , found by the European Muon Collaboration [111]. The origin of this effect is not yet fully understood [112].

**Fermi motion** at  $x \approx 1$ . Fermi motion is born from the uncertainty principle

$$\Delta x \Delta p \geq \frac{\hbar}{2}. \quad (2.13)$$

A bound nucleon is localised in a region of space of  $\sim 5 - 10 \text{ fm}$  (nuclear radius). Using  $\hbar c \approx 200 \text{ MeV} \cdot \text{fm}$ , one gets a typical momentum of  $10 - 20 \text{ MeV}/c$ .

In relativistic collisions, production of heavy flavour, and hence  $J/\psi$ , is dominated by gluon fusion [114]. Therefore in collisions of p-Pb, their production is particularly sensitive to modification of gluon nPDFs. Fig. 2.20 shows the  $R_g^{\text{Pb}}(x, Q^2)$  at the  $J/\psi$  mass scale  $Q^2 = 10 \text{ GeV}$ . The depicted parametrisation is EPPS16 [113], which also includes LHC data. As the  $J/\psi$  production can be approximated as a  $2 \rightarrow 1$  process, the momentum fraction of the two collided hadrons  $x_1$  and  $x_2$  can be expressed at a given rapidity  $y$  and centre-of-mass energy  $\sqrt{s}$  as

$$x_{1,2} = \frac{M_{J/\psi}}{\sqrt{s}} e^{\pm y}. \quad (2.14)$$

Typical values for  $J/\psi$  at the LHC in the forward rapidity region accessible in ALICE ( $2.5 < y_{\text{lab}} < 4.0$ ) in pp and p-Pb collisions are listed in Tab. 2.2.

#### 2.4.1.2 Gluon saturation

At small  $x$  the gluon PDFs indicate a growth of the gluon density with energy. As the gluon density increases, the distance between the gluon becomes smaller, In consequence, the strong interaction

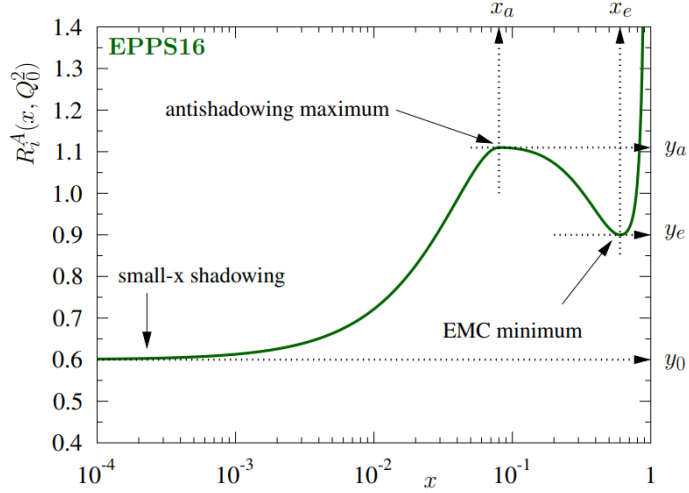


Figure 2.19: Schema of a typical  $x$  dependence of a nuclear modification function in the EPPS16 parametrisation [113].

proton-proton			
$\sqrt{s}$ (TeV)	$y_{\text{cms}}$	$x_1$	$x_2$
5.02	$2.5 < y_{\text{cms}} < 4.0$	$1.1 \cdot 10^{-5} < x < 5.1 \cdot 10^{-5}$	$7.5 \cdot 10^{-3} < x < 3.4 \cdot 10^{-2}$
13	$2.5 < y_{\text{cms}} < 4.0$	$4.4 \cdot 10^{-6} < x < 2.0 \cdot 10^{-5}$	$2.3 \cdot 10^{-3} < x < 1.3 \cdot 10^{-2}$
proton-lead			
$\sqrt{s_{\text{NN}}}$ (TeV)	$y_{\text{cms}}$	$x_{\text{Pb}}$	$x_{\text{p}}$
8.16	$2.03 < y_{\text{cms}} < 3.53$	$1.1 \cdot 10^{-5} < x < 5.0 \cdot 10^{-5}$	$2.9 \cdot 10^{-3} < x < 1.3 \cdot 10^{-2}$
8.16	$-4.46 < y_{\text{cms}} < -2.96$	$7.3 \cdot 10^{-3} < x < 3.3 \cdot 10^{-2}$	$4.4 \cdot 10^{-6} < x < 2.0 \cdot 10^{-5}$

Table 2.2: Typical momentum fractions for forward  $J/\psi$  ( $2.5 < y_{\text{lab}} < 4.0$ ) at the LHC.

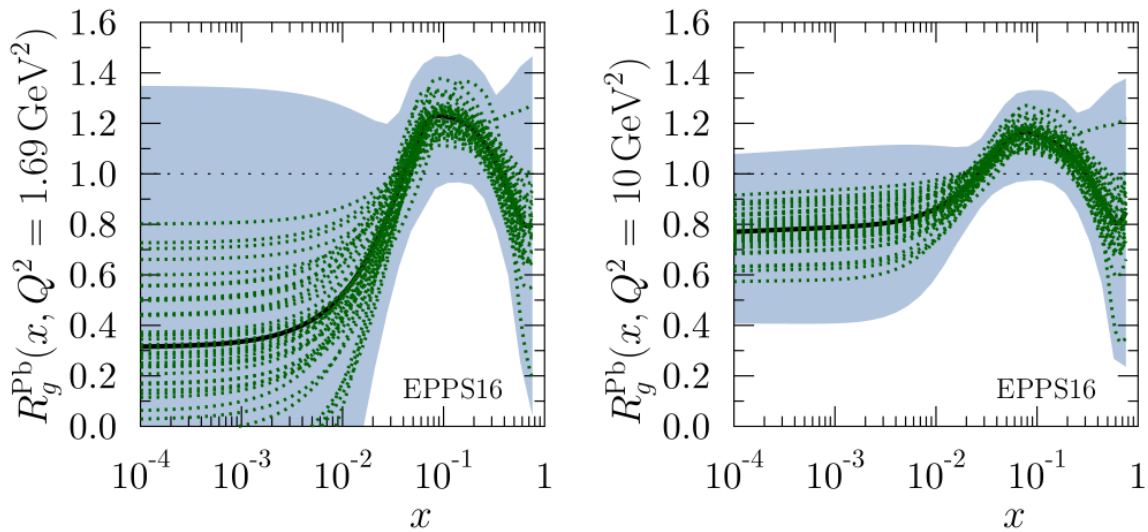


Figure 2.20: The EPPS16 nuclear modification functions for gluons in the lead nucleus at the energy scale  $Q^2 = 1.69$  and  $10 \text{ GeV}^2$  [113].

weakens. Once the maximal occupation  $\sim 1/\alpha_s$  is reached, the system saturates and the gluon density increases no more. The saturation is characterised by a saturation scale  $Q_{s,A}^2$ . The saturation can be studied within the framework of the Colour Glass Condensate (CGC) [115].

Within the CGC framework, the  $J/\psi$  are formed outside of the target nuclei described by the CEM. The saturation will manifest in a suppression of  $J/\psi$   $R_{pA}$  at forward rapidities, which probe the small  $x$  regions. The model has been constrained from deep inelastic scattering (DIS) data.

### 2.4.1.3 Coherent parton energy loss

A high energy parton travelling through a nuclear medium will experience scattering on the constituents of the matter. In case of small angle scatterings, the gluon will emit coherent soft gluon radiation.

The coherent energy loss was proposed as a tool to describe the significant  $J/\psi$  suppression observed at the SPS and RHIC at large rapidities in collisions of p–A [116]. The  $c\bar{c}$  pair is produced as a colour octet state at a time-scale  $\tau_{c\bar{c}} \sim 1/M_{Q\bar{Q}}$  and propagates through the nucleus for  $\tau \gg \tau_{c\bar{c}}$ . Then, at sufficiently large energy  $E$  of the  $c\bar{c}$  pair in the target rest frame, the charmonium can be described as a small angle scattering of a gluon on the pair. The amount of energy loss and consequently the magnitude of the energy loss depends on the nuclear matter transport coefficient and relates to the gluon distribution in the target nucleus. The transport coefficient is the only free parameter of the model and is determined from experiment.

### 2.4.1.4 Nuclear absorption

While crossing the nuclear matter, the  $c\bar{c}$  state may dissociate via interaction with the nucleus constituents. Such interaction is described by an effective absorption cross section  $\sigma_{abs}$  and is usually treated through the Glauber formalism, although simpler parametrisations can be also used (exponential or linear). The effective absorption depends on the thickness of the nuclear matter that the  $c\bar{c}$  needs to cross. Hence the effect is expected to be negligible at LHC energies as due to the Lorentz boost the formation time  $\tau_f$  of the bound state is far superior to the nuclear size. An example of  $\sqrt{s_{NN}}$  dependence of  $\sigma_{abs}^{J/\psi}$  for free proton PDFs and for three different sets of nuclear PDFs is visualised in Fig. 2.21. We see that the cross section decreases with increase in the collision energy.

## 2.4.2 Experimental results from proton-nucleus measurements

In this section, we will review selected measurement of nuclear modification of  $J/\psi$  in proton(deuteron)-nucleus collisions. Such measurements were performed at RHIC in d–Au collisions at  $\sqrt{s_{NN}} = 200$  GeV by STAR and PHENIX, and at the LHC in p–Pb collisions at  $\sqrt{s_{NN}} = 5.02$  and 8.16 TeV. We will discuss only selected results from the two colliders.

### 2.4.2.1 Results from RHIC

PHENIX measured the  $J/\psi$  nuclear modification factor  $R_{dAu}$  at midrapidity over a large rapidity range  $-2.2 < y < 2.4$  [118]. The centrality integrated results are shown in Fig. 2.22, where they were compared with two theoretical calculations: (i) a model containing shadowing and nuclear absorption, and (ii) a gluon saturation model. The data demonstrate a suppression over the full measured  $y$  range. The suppression is stronger at forward rapidity. The red line denotes the calculation using ESP09 nPDFs [119] and an effective  $\sigma_{abs}$  [120], the dotted lines show the uncertainties on the nPDFs. The calculation described is in good agreement with the data in the full measured rapidity range. The data were also compared with a saturation model [121, 122], which is applicable at  $y > 0$ . The saturation calculation is visualised by the green dashed line, and predicts a strong suppression at forward rapidity as seen in the data. However it overestimates the  $R_{dAu}$  at midrapidity.

A more detailed picture can be drawn from dividing the  $R_{dAu}(y)$  in bins of centrality, see Fig. 2.23 on left. In peripheral collisions (top panel) the data show a weak suppression in the measured rapidity interval, within the uncertainties the  $R_{dAu}$  is consistent with unity. The central collisions (middle panel) manifest a stronger suppression at forward rapidity. To better quantify the effects and to reduce systematic uncertainties on the measurement, a ratio of central-to-peripheral modification factor  $R^{CP}$  is plotted in the bottom panel.

The mid- and backward rapidity data are well described by the absorption calculation in both centrality bins. At the forward rapidity, the model agrees with the data within the uncertainties albeit

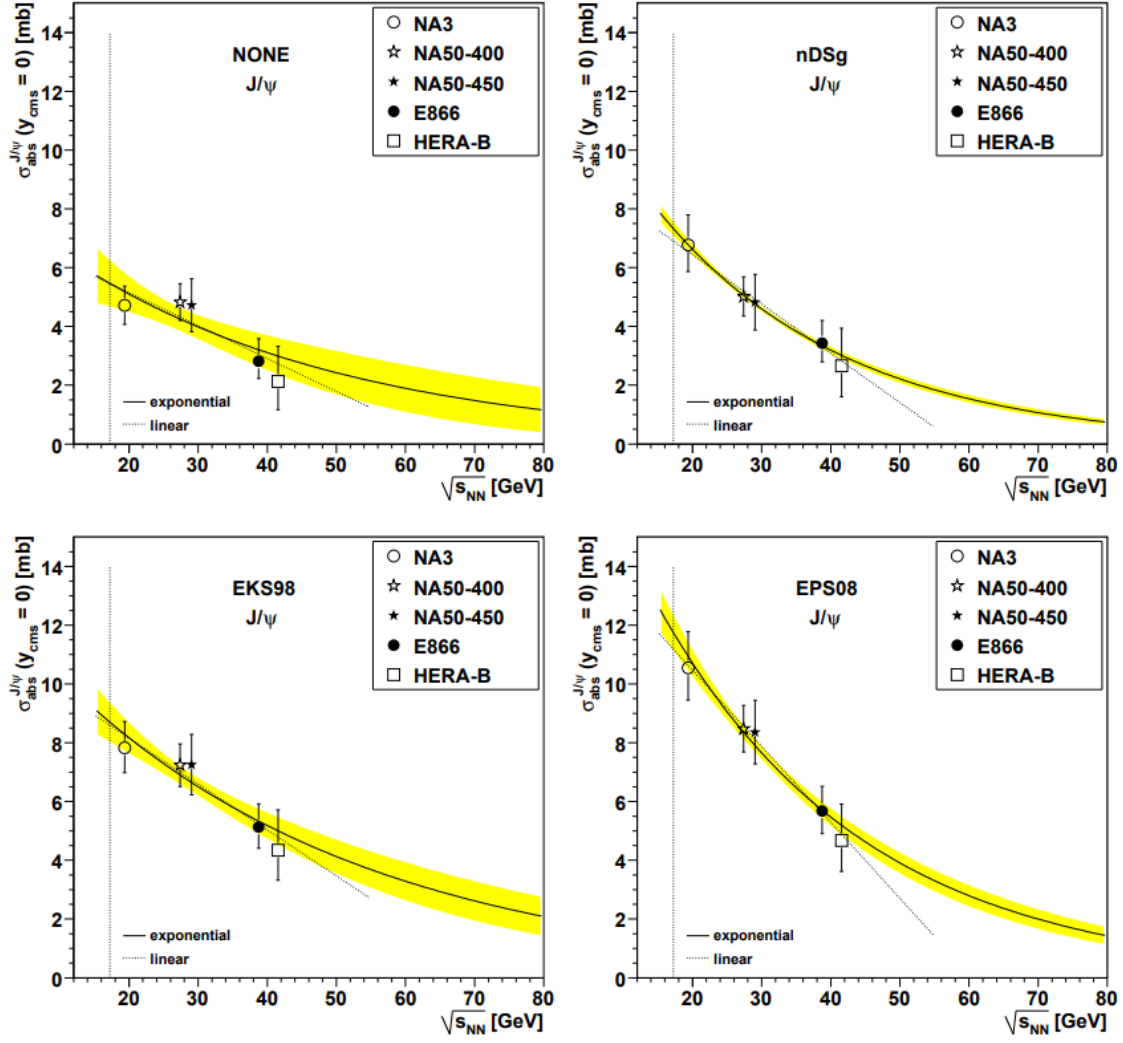


Figure 2.21: The  $J/\psi$  absorption cross section  $\sigma_{abs}^{J/\psi}$  as a function of collision energy  $\sqrt{s_{NN}}$  for free proton PDFs (top left) and for three different sets of nPDFs. Figures taken from [117].

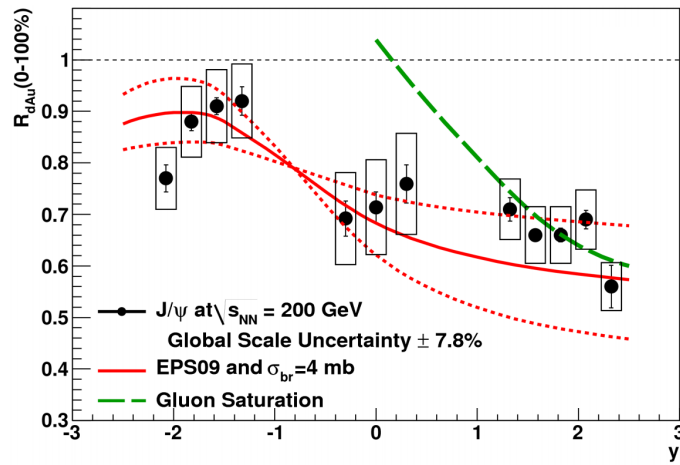


Figure 2.22: Rapidity differential  $R_{dAu}$  for  $J/\psi$  measured in minimum bias collisions at  $\sqrt{s_{NN}} = 200$  GeV with PHENIX. The data are compared to theoretical calculation combining EPS09 nPDFs with an absorption cross section (red lines) [119, 120], and with a saturation model (green lines) [121, 122]. Figure taken from [118].

it underestimates the ratio in the peripheral bin. This is then propagated into the  $R^{\text{CP}}$  comparison, where the three forward-most points are below the calculation. The saturation model agrees well with the data at forward rapidity in both centrality classes. The midrapidity data are overestimated, more so in peripheral collisions. The  $R^{\text{CP}}$  is however well described by the calculation. These results suggest that the saturation effects play an important role at forward rapidity.

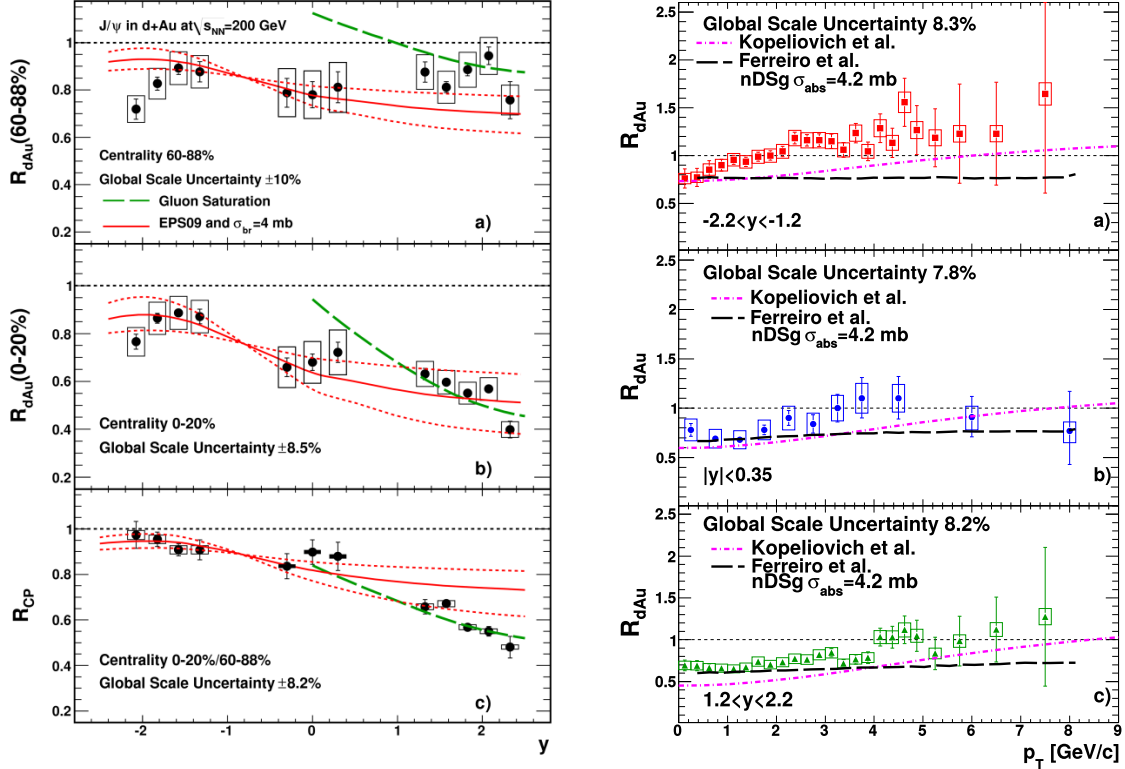


Figure 2.23: (Left) Rapidity differential  $J/\psi$   $R_{\text{dAu}}$  for peripheral (top) and central (middle) collisions at  $\sqrt{s_{\text{NN}}} = 200$  GeV measured by PHENIX. The data are compared to theoretical calculation combining EPS09 nPDFs with a absorption cross section (red lines), and with a saturation model (green lines). The ratio of the two centrality classes is shown in the bottom panel. Figure taken from [118]. (Right)  $R_{\text{dAu}}$  of  $J/\psi$  as a function of  $p_T$  for (a) backward, (b) mid- and (c) forward rapidity in minimum bias d-Au collisions at  $\sqrt{s_{\text{NN}}} = 200$  GeV measured by PHENIX. Figure taken from [123].

The minimum bias  $J/\psi$   $R_{\text{dAu}}$  was also studied as a function of  $p_T$  in the three rapidity regions. The results can be found in the right column of Fig. 2.23. In all three centrality bins, we observe an increase with the  $R_{\text{dAu}}$  with increasing  $p_T$ . At backward rapidity, the  $R_{\text{dAu}}$  is suppressed only at low  $p_T < 1.5$  GeV/c, above this value the ratio is consistent with unity with hints of enhancement at high  $p_T$ . The mid- and forward measurement show similar level of suppression at lower  $p_T$  up to  $p_T \approx 3$  GeV/c and  $p_T \approx 4$  GeV/c. The increase with  $p_T$  becomes more gradual going from backward to forward rapidity, with the crossing point moving towards higher  $p_T$  with increasing  $y$ .

The measurement was compared with two different theoretical calculations. Both models use the same set of nPDFs to describe the shadowing and they account for nuclear absorption. They however differ in the kinematics of the implemented  $J/\psi$  production. The model by Kopeliovich et al. [124, 125] considers the Cronin effect [126]. Cronin effect represents the broadening of the  $p_T$  distribution due to multiple elastic scatterings of the partons in the incoming hadrons prior to the hard scattering, in which the  $c\bar{c}$  pair is produced. This causes an enhancement at high  $p_T$ , balanced by a suppression at low  $p_T$ . The calculation by Ferreiro et al. [127, 128] does not include Cronin effect. Therefore the calculation is flat in  $p_T$ . Both models display an overall stronger suppression than what is measured, and favour similar suppression pattern in all centrality bins contrary to the data. At mid- and forward rapidity, they are in good agreement with the data. At backward rapidity, neither model reproduces the shape nor agrees with the values of  $R_{\text{dAu}}$  in the intermediate  $p_T$  region.

### 2.4.2.2 Results from the LHC

ALICE measured  $R_{pPb}$  of the inclusive  $J/\psi$  at forward and backward rapidity in p–Pb collisions at  $\sqrt{s_{NN}} = 5.02$  and  $8.16$  TeV [129, 130]. Results of the measurement as a function of rapidity can be viewed in Fig. 2.24. At backward rapidity, the data are consistent with unity. At forward rapidity, they show a suppression reaching up to 40%. Moreover, the suppression pattern is identical at the two energies, suggesting the effects at play are independent of  $\sqrt{s_{NN}}$ .

The data were compared with multiple theoretical calculations, all of which include a different combination of CNM effects [95, 131–136]. At present precision, all shown models provide a good description to experimental points.

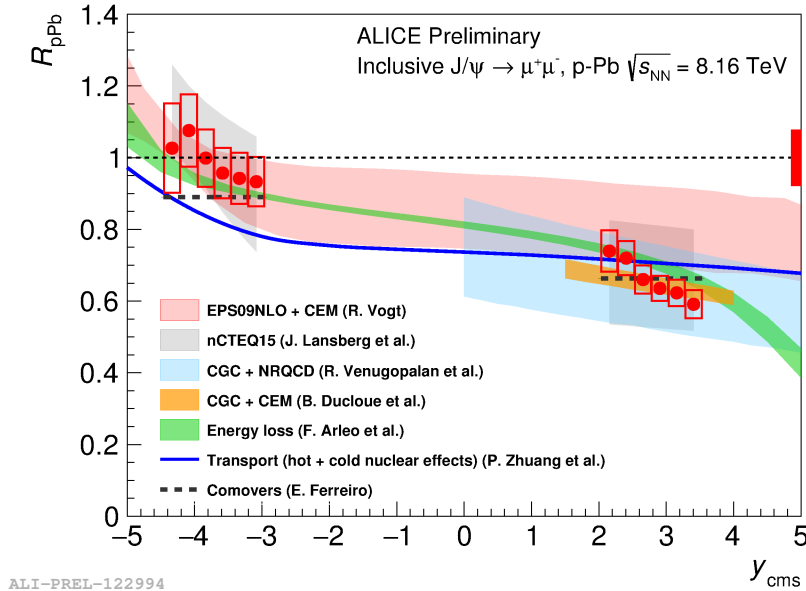


Figure 2.24: The  $J/\psi$  nuclear modification as a function of rapidity in Pb-Pb collisions at  $\sqrt{s_{NN}} = 8.16$  TeV. ALICE data are compared with available theoretical calculations. The box around unity shows the correlated uncertainty. Figure taken from [137].

The  $p_T$  differential measurement of  $R_{pPb}$  in both rapidity windows is shown in Fig. 2.25. The forward rapidity measurement is shown on left. At low  $p_T$ , the  $J/\psi$  are strongly suppressed. The ratio gradually increases with  $p_T$  until it saturates around  $R_{pPb} \approx 1$  at  $p_T \gtrsim 9$  GeV/c. At backward rapidity, the data show hints of suppression at  $p_T < 2$  GeV/c. Above this crossing point, the  $R_{pPb}$  saturates to a value systematically above the unity. Nevertheless, all along the  $p_T$  axis, the backward yields are consistent with unity. The data at 5.02 TeV [129], which also included the measurement at midrapidity, also showed the evolution of the crossing point toward higher  $p_T$  from backward to forward rapidity. All available models describe data within uncertainties in both rapidity regions.

Centrality dependence of the nuclear modification factor  $Q_{pPb}$  has been studied in ALICE in Pb-Pb at  $\sqrt{s_{NN}} = 5.02$  TeV [138]. Recall the definition of  $Q_{pPb}$  in Eq. (2.11). The modification factor was measured at mid-, forward, and backward rapidity. The results as a function of centrality, expressed as mean number of binary collisions  $N_{coll}$  are show in Fig. 2.26. The modification factor  $Q_{pPb}$  is consistent with unity at backward rapidity (left panel), although in most central collisions, the ratio shows hints of enhancement with respect to pp collisions. At midrapidity, the measurement is limited by the low statistics (middle panel). Nevertheless, the ratio shows suppression constant in centrality. The forward data are clearly suppressed (right panel). The ratio indicates stronger suppression with increasing centrality.

The data were compared with theoretical calculations including different CNM effects, namely modification of nPDFs, energy loss and a combination of nPDFs with break-up due to comovers [95, 139–141]. All shown models reproduce data within uncertainties in the three rapidity bins. At backward rapidity, the models except the one with comovers favour a suppression constant in multiplicity. The comovers model shows an increase of the  $Q_{pPb}$  of the same magnitude as indicated in the data.

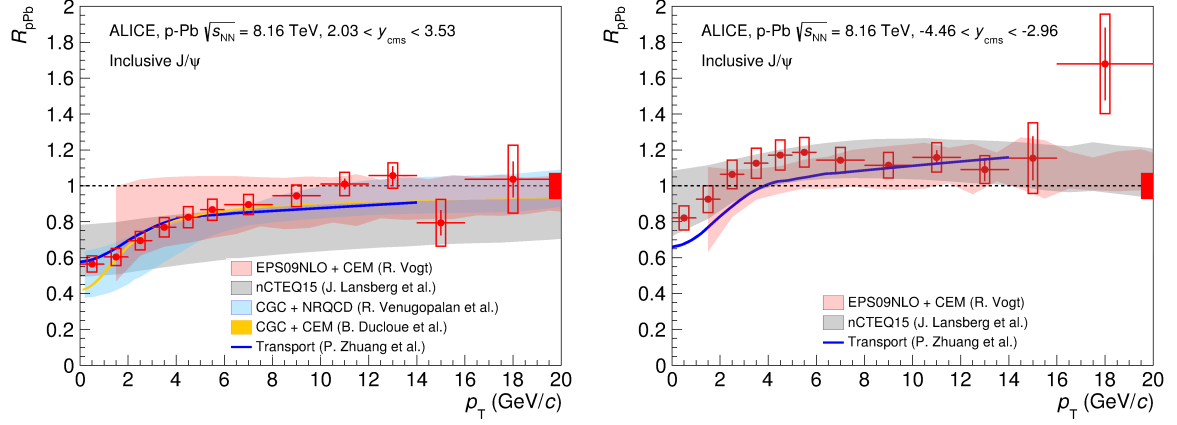


Figure 2.25: The  $p_T$  differential nuclear modification factor for inclusive  $J/\psi$  measured in ALICE in p-Pb at  $\sqrt{s_{NN}} = 8.16$  TeV. Data are well described by all available models [131–136]. Figures taken from [130].

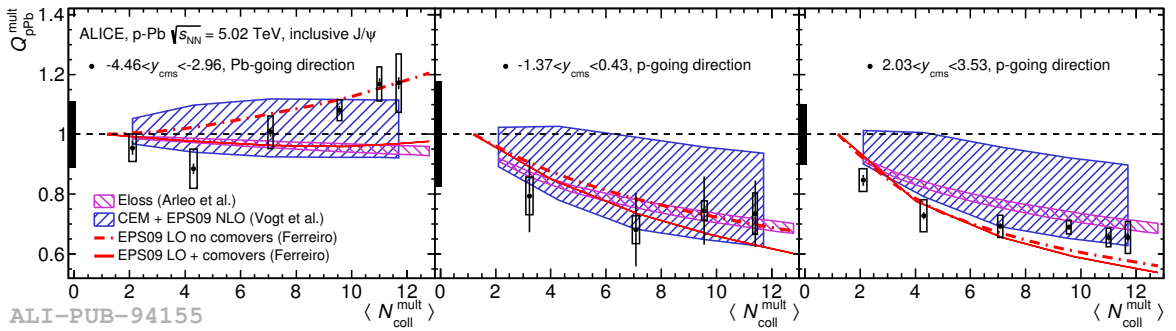


Figure 2.26: Inclusive  $J/\psi$   $Q_{pPb}$  as a function of  $\langle N_{coll} \rangle$  at backward (left), mid- (centre) and forward (right) rapidity. The boxes centred at  $Q_{pPb} = 1$  represent the relative uncertainties correlated over centrality. Comparison with theoretical calculations [95, 139–141] is shown. Figure taken from [138].

Recall that the ALICE results we have just reviewed are for inclusive  $J/\psi$ . In a similar rapidity region, LHCb separates the  $J/\psi$  to their prompt and non-prompt contributions. The  $R_{pPb}$  was measured for both at 5.02 and 8.16 TeV [142, 143]. Fig. 2.27 shows the results obtained at 8.16 TeV for prompt and non-prompt  $J/\psi$  as a function of the nucleon-nucleon centre-of-mass rapidity  $y^*$ . For the prompt  $J/\psi$ , yields are below unity over the entire rapidity range. This is reminiscent of the inclusive  $J/\psi$  measurement at RHIC (see Fig. 2.22) where the non-prompt  $J/\psi$  production is negligible. The non-prompt  $J/\psi$  on the other hand are consistent with unity in the measured rapidity interval. The suppression pattern is identical in the 5.02 TeV measurement, which is also shown in Fig. 2.27. The behaviour for both prompt and non-prompt contributions is thus independent of the energy.

The prompt  $J/\psi$  are compared with three different kinds of calculations: (i) models including modifications of nPDFs [119, 144–146], (ii) a saturation model [134, 147], and (iii) a coherent energy loss calculation by Arleo [148]. At forward rapidity, all shown calculations reproduce the measured suppression. At backward rapidity, the energy loss provides the best description of the  $R_{pPb}$  behaviour. The calculations with nPDFs agree with the data within uncertainties, but they overestimate the  $R_{pPb}$  for the two most backward points.

The non-prompt  $J/\psi$  are well described by the FONLL pQCD calculations with modifications of nPDFs [66, 119, 149].

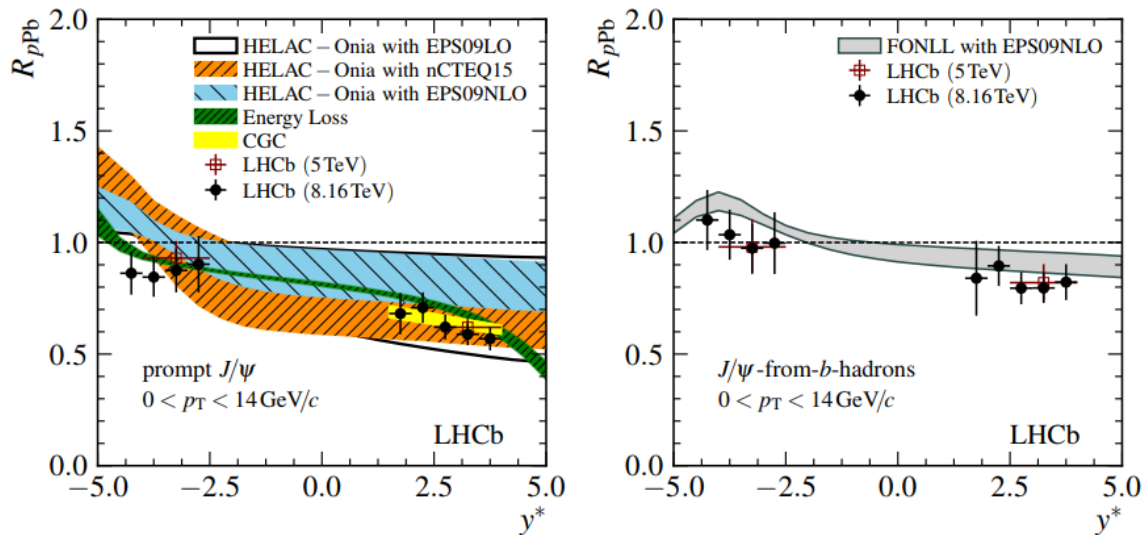


Figure 2.27: The  $p_T$  and centrality integrated  $J/\psi$  nuclear modification factor  $R_{pPb}^{J/\psi}$  in  $\sqrt{s_{NN}} = 8.16$  TeV for prompt and non-prompt  $J/\psi$  in LHCb. Figure taken from [143].

Finally we shall briefly mention the nuclear modification of high- $p_T$   $J/\psi$  measured in p–Pb collisions at  $\sqrt{s_{NN}} = 5.02$  TeV with CMS [150] and ATLAS [151]. Both experiment probed a similar kinematic region. Fig. 2.28 displays the results of prompt  $J/\psi$  measurement with CMS at midrapidity interval  $-2.40 < y_{cms} < 1.93$  and at  $6.5 < p_T < 30$  GeV/ $c$ . The measured  $R_{pPb}$  is consistent with unity in the two  $p_T$  intervals, with the most backward rapidity bins showing hints of enhancement. At forward rapidity the ratio increases with  $p_T$ . The data are qualitatively well reproduced in calculations incorporating (anti)shadowing [119, 132, 146, 152], albeit the models overall predict lower value of the ratio. Let it be stated that the  $p_T$  differential  $R_{pPb}$  for non-prompt  $J/\psi$  is consistent with unity.

We have thus seen that the  $J/\psi$  yields are modified in p(d)–A with respect to pp collisions. The observed modification depend on the production mechanism (prompt/non-prompt),  $p_T$  and rapidity of the measurements, but seem to scale in energy. Such modifications are caused by the cold nuclear matter effects. These include the modification of PDFs in the nucleus, saturation of gluons at small  $x$ ,  $p_T$  broadening, or energy loss due to gluon radiation. Models with different combinations of CNM effects successfully reproduce the measured suppression/enhancement patterns, at current precision none of them is favoured by the data.

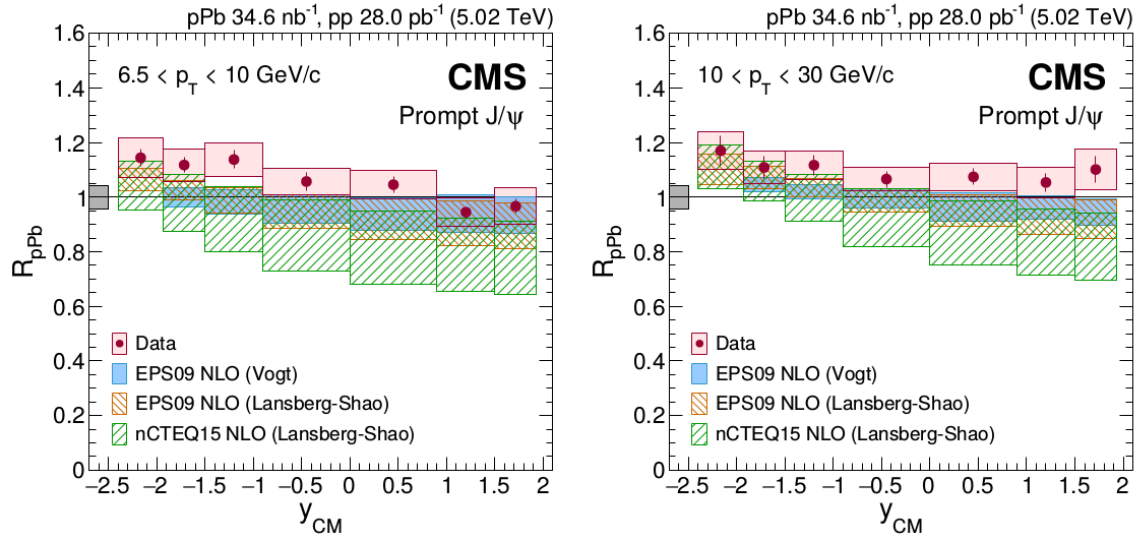


Figure 2.28: The nucleus-nucleon centre-of-mass rapidity dependence of  $R_{pPb}$  for prompt  $J/\psi$  in p-Pb at  $\sqrt{s_{NN}} = 5.02$  TeV measured by CMS. Data were compared with models including (anti)shadowing [119, 132, 146, 152]. Taken from [150].

## Summary

$J/\psi$  and other charmonia has been extensively studied in collider experiments in pp, p-A, and A-A collisions. In proton-proton collisions, their production combines the processes at large and small momentum transfers. Measurements of the yields of different charmonia states in given kinematic ranges is necessary to better constrain theoretical calculations describing the measured cross section and polarisation. The latter in particular present a challenge for the present day models.

In nucleus-nucleus collisions, the charmonia serve as a probe of the deconfined medium. The bound states of  $c\bar{c}$  are screened in the QGP. Furthermore, the regeneration of the charmonia from the free charm (anti)quarks in the medium becomes more important with increasing energy of the collision and plays an important role at the LHC energies.

In proton-nucleus collisions, the modification of yields due to cold nuclear matter effects is studied. The observed suppression and enhancement patterns ranging from RHIC to LHC energies is reproduced in the models accounting for different CNM effects. However, at present precision none of the effects is favoured by the data. More precise and/or differential measurements would be needed to disentangle which effects play the major role at which conditions.

## MULTIPLICITY DEPENDENCE OF HEAVY FLAVOUR PRODUCTION

In this chapter, we will briefly discuss the physics behind multiplicity studies in proton-proton collisions and in collisions involving heavy nuclei. We will review selected result on multiplicity dependent heavy flavour production at LHC and RHIC energies. In the last part of the chapter, we will also tackle the subject of strangeness production as a function of event activity.

### 3.1 Correlation of hard and soft particle production

A complete pp event contains an interplay of hard and soft processes. It can be split into two components - hard scattering and the underlying event. The hard scattering can be described by pQCD as it involves large  $Q^2$  transfer. Examples of hard processes are production of hadrons containing heavy quarks or jets. The underlying event comprises production of all the final states associated with the hard scattering, such as the multiple parton interactions, soft hadron processes (hadronisation, decays), or fragmentation of beam remnants [153]. A sketch of a typical pp collisions at LHC energies can be found in Fig. 3.1.

In such event, the production of heavy quarks can be affected by Multiple Parton Interactions (MPI). MPIs are defined as multiple uncorrelated parton-parton scatterings in a single event. MPI is a general term and includes two noteworthy cases which we shall mention and which are visualised in Fig. 3.2. The first is the single parton scattering (SPS), when a parton from one hadron interacts with a parton from the other hadron. The second is the double parton scattering (DPS) meaning two partons from one colliding hadron interact with two partons from the other incoming hadron. The DPS grow in importance in the small  $x$  regions probed in collisions at the LHC energies [154]. Maciula et al. [155] predict that the charm production cross section in DPS is of the same order as the cross section in SPS at the top LHC energies  $\sqrt{s} \sim 10$  TeV.

Furthermore, we can also investigate correlations of produced heavy flavour hadrons with other heavy flavour hadrons or with all charged hadrons. There are multiple contributions to heavy flavour production, all of which lead to a different angular correlation between the heavy quark pair [114]. Therefore by studying the angular correlation of heavy flavour hadrons with charged particles, be they heavy or light, one can unveil information on relative contributions of the individual processes to the total production. Angular correlations of two charmed hadrons can also provide better understanding of the DPS in which both scattering involve production of  $c\bar{c}$  [157].

#### 3.1.1 What can we learn from multiplicity studies?

In heavy ion physics, the charged particle pseudorapidity density at midrapidity is used as a measure of the initial energy density of the collisions of ultrarelativistic nuclei [11, 13]. The multiplicity of charged particles produced in pp and p-Pb collisions at LHC energies are comparable or higher to the ones measured at RHIC and SPS, see Fig. 3.3. The energy densities may even exceed those achieved in central collisions at SPS and RHIC. At such conditions, collective-like behaviour akin to effects in Pb-Pb collisions is expected to arise. Indeed, multiple measurements of effects attributed to formation of the QGP in the system were measured in pp and in p-Pb with the LHC experiments [158–162].

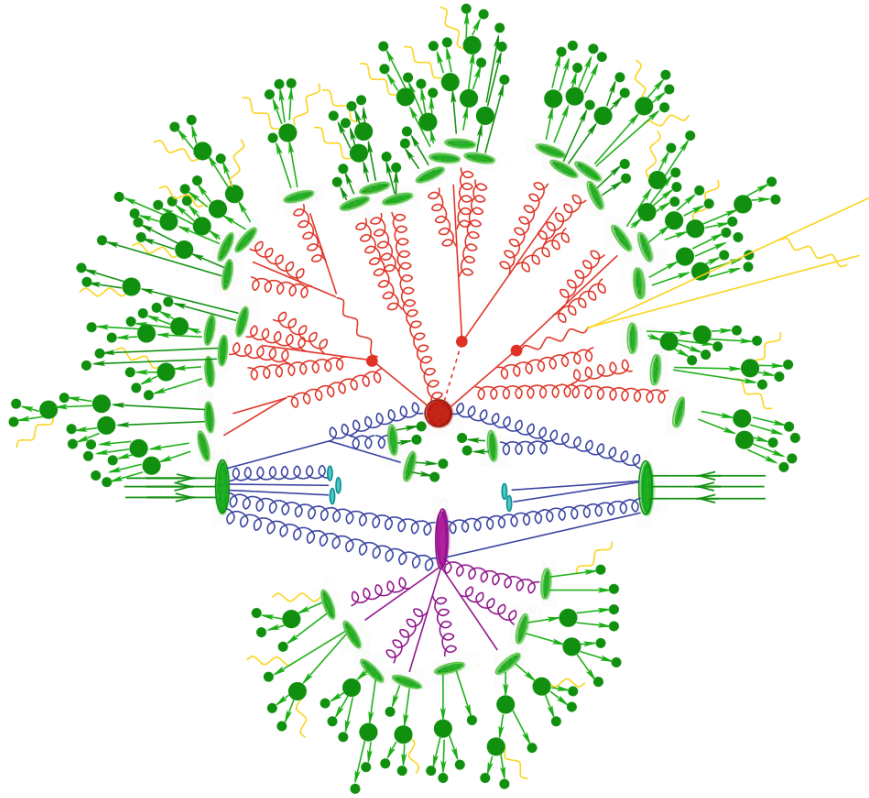


Figure 3.1: A sketch of a typical proton-proton collision at LHC. The green lines and ellipses indicate the two incoming protons, the light blue ellipses indicate the beam remnants. The event is visually separated into the hard part, which is in the top half of the figure, and the underlying event in the bottom half. The initial hard scattering, indicated by the big red blob, produces a parton shower. As the shower evolves, the products of the hard scattering decay and QCD radiation is emitted. The produced coloured partons eventually hadronise into colourless states, indicated by the light green ellipses. These states than may further decay into stable particles. The softer secondary hard scattering also produces a shower. Charged particles can also at any time emit electromagnetic radiation (yellow). Taken from [153].

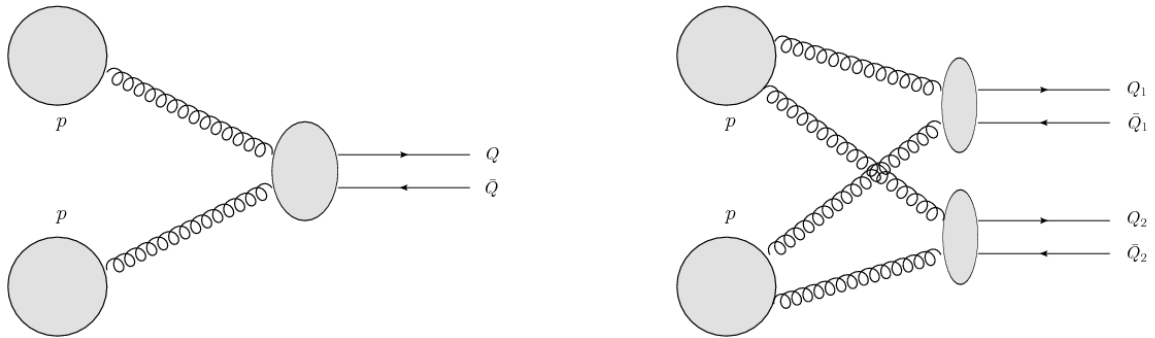


Figure 3.2: A diagram of single parton scattering (left) and double parton scattering (right). Taken from [156].

The multiplicity variable, relating to the impact parameter of the collisions, also serves as a measure of centrality of the collision. It can be used as such also in p–Pb allowing for finer slicing in centrality, and in pp<sup>1</sup>.

On the other hand, the final state effects at high multiplicity may also influence the measured yields [163].

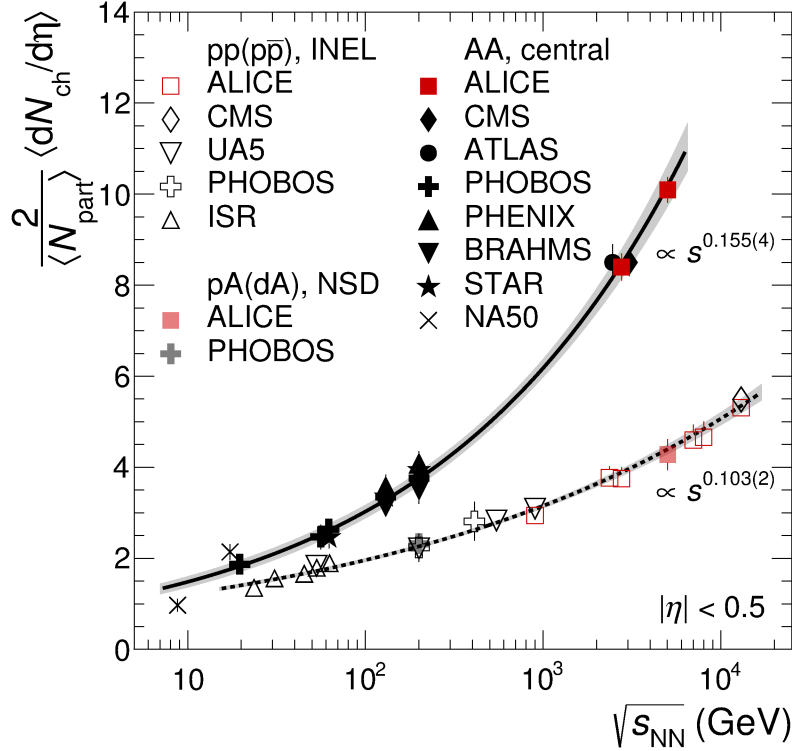


Figure 3.3: Mean charged particle density normalised by the average number of participating nucleon pairs  $\frac{2}{\langle N_{\text{part}} \rangle} \langle dN_{\text{ch}}/d\eta \rangle$  versus  $\sqrt{s_{\text{NN}}}$ . Normalisation by  $\frac{\langle N_{\text{part}} \rangle}{2}$  enables direct comparison of bulk particle production between different systems and energies. Taken from [164].

In conclusion, studying correlation of hard probes with other particles in the event is vital to advance our understanding of the elementary processes taking place in such collisions

### 3.1.2 Theoretical models

Several models study the correlation of heavy quark production with underlying multiplicity. Most of them simulate the observed behaviour of D-mesons or  $J/\psi$  via a MPI scenario [165–167]. The EPOS3 model by Werner et al. [168] also includes final state interactions, i. e. interactions of hadrons produced in the collisions which result in the collective flow. All below mentioned models are shown in Fig. 3.4 where they are compared with multiplicity dependence of inclusive  $J/\psi$  in pp collisions at  $\sqrt{s} = 13$  TeV [169]. The comparison between the data and the models will be discussed in Sec. 3.2.1, for now we only use the plot to illustrate the behaviour of each model.

**PYTHIA** [165] includes MPIs among number of other processes such as colour reconnection, soft QCD, or initial and final state radiation (ISR/FSR). They can be either combined or used separately, permitting to study their relative contribution. Concerning charm quarks, the latest version (Pythia 8.x) includes not only direct production but also production in MPIs.

The contribution of different processes to the multiplicity dependent D-meson production was studied by ALICE [170]. The results are shown in Fig. 3.5. The top left (right) panel shows the

<sup>1</sup>At high energies, the proton can be described as an extended object composed of partons. The impact parameter gives the distance between centres of the two protons. The geometry of the collision then depends in  $b$  as well as on parton distributions in the two incoming protons.

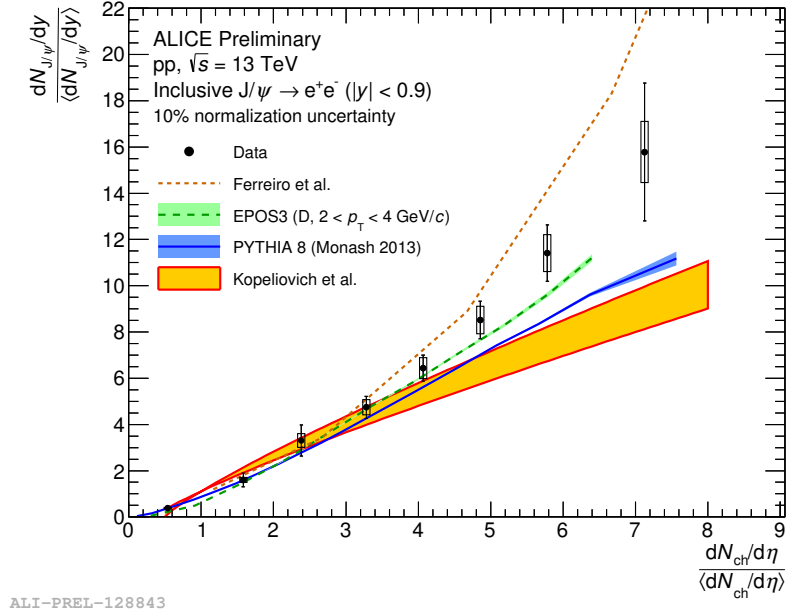


Figure 3.4: Multiplicity-dependent self-normalised inclusive  $J/\psi$  yields in pp collisions at  $\sqrt{s} = 13$  TeV, measured at midrapidity. The measurement is compared with available calculations: percolation model by Ferreiro [166], EPOS3 [168], Pythia [165] and a calculation by Kopeliovich [167] (see legend). More details are given in text. Taken from [169].

contribution of each considered process into the D-meson (B-meson) relative yields. The first, hardest scattering shows little multiplicity dependence. The contributions from subsequent hard interactions, gluon splitting and ISR/FSR demonstrate a (stronger-than-)linear increase of the yields with increasing multiplicity. The calculation suggests the slope of the increase grows steeper with the  $p_T$  of the hadron, see the bottom row.

The model predicts a linear increase of the relative  $J/\psi$  yields with multiplicity as shown by the blue curve in Fig. 3.4.

The **percolation model** by Ferreiro and Pajares [166] uses the colour string as its fundamental variable. The colour string have a finite size and can interact. A string is produced in each parton-parton interaction. The number of parton-parton interactions  $N_{coll}$  thus gives the number of strings  $N_s$ . The number of produced charmonia  $N_{J/\psi}$  is proportional to the number of collisions and thus to the number of strings

$$N_{J/\psi} \propto N_{coll} \equiv N_s.$$

In the model the number of soft particles, the multiplicity  $dN/d\eta$  is related to  $N_s$  as

$$dN/d\eta = F(\rho)N_s\mu_1,$$

where  $F(\rho) = \sqrt{1 - e^{-\rho}}/\rho$  is a string density dependent damping factor and  $\mu_1$  is the multiplicity of a single string in a given rapidity range. The string density is defined as

$$\rho = \frac{N_s\sigma_0}{\sigma}.$$

The factor  $\sigma_0$  is the transverse are of one string, while  $\sigma$  is the transverse area of the collision. Thus at large  $N_s$ ,  $\rho$  increases and consequently  $F(\rho)$  diminishes. Hence the multiplicity decreases proportionally to the damping factor. So in a collision with few parton-parton scatterings, both multiplicity and  $N_{J/\psi}$  are proportional to  $N_s$ . Therefore relative  $N_{J/\psi}$  shows a linear dependence on multiplicity

$$\frac{N_{J/\psi}}{\langle N_{J/\psi} \rangle} \propto \frac{dN/d\eta}{\langle dN/d\eta \rangle}.$$

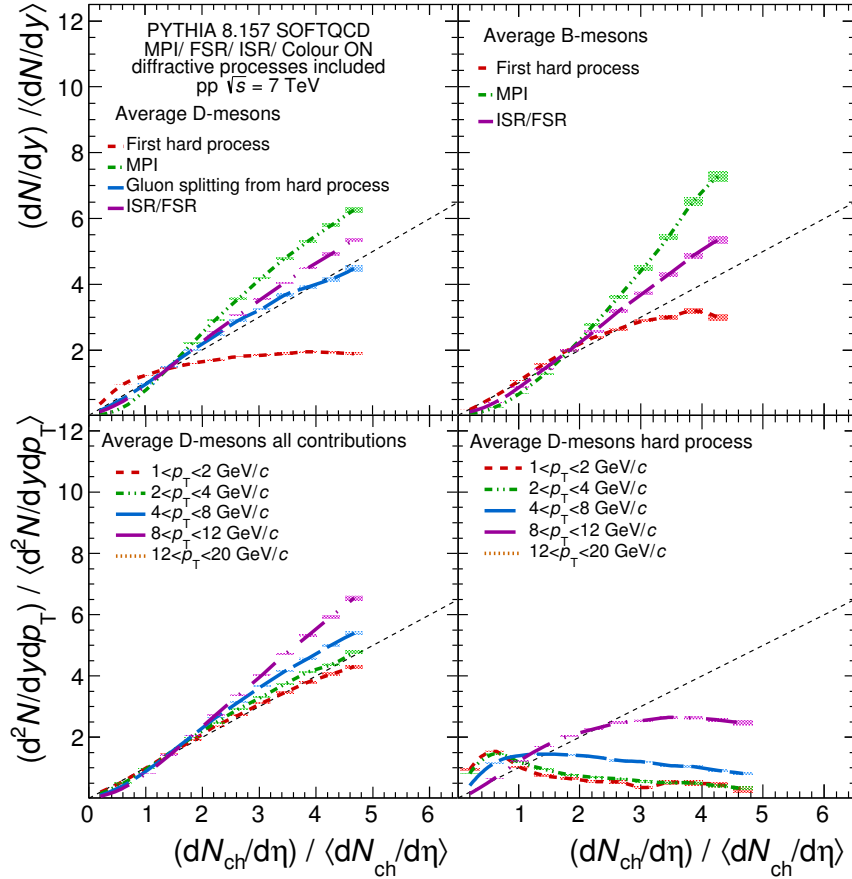


Figure 3.5: D- and B-meson relative yield as a function of the relative charged particle multiplicity at midrapidity calculated with the PYTHIA event generator [165]. The top row showcases the individual contributions to the total  $c$  and  $b$  quarks production. The bottom panel visualises the dependence of the increase on  $p_T$  of the D-meson.

With increasing  $N_{coll}$  and hence increasing  $N_s$  the damping will become important and we obtain a quadratic dependence

$$\frac{N_{J/\psi}}{\langle N_{J/\psi} \rangle} \propto \left( \frac{dN/d\eta}{\langle dN/d\eta \rangle} \right)^2.$$

The behaviour is visualised in in Fig. 3.4 by the red dashed line.

**Kopeliovich** et al. [167] draw a parallel between high multiplicity pp and p–A collisions. In pp, high multiplicities arise from multiple interactions in one collision, while in p–A they result from multiple proton-nucleon collisions.

In a boosted nucleus, which is Lorentz contracted by  $\gamma^A = m/E$ , the gluons experience a smaller contraction by  $\gamma^g = m/xE$  and thus propagate at much larger distances than is the average distance between nucleons in  $A$ . As a consequence, all transversally overlapping gluons overlap also in the longitudinal direction. They can be thus treated as a single 'gluon cloud'. Heavy flavour production is enhanced in such gluon rich environment. Therefore at higher multiplicities, where the gluon density increases, we also see an increase in  $J/\psi$  production. The model predicts linear increase of the yields with multiplicity shown by the yellow band in Fig. 3.4.

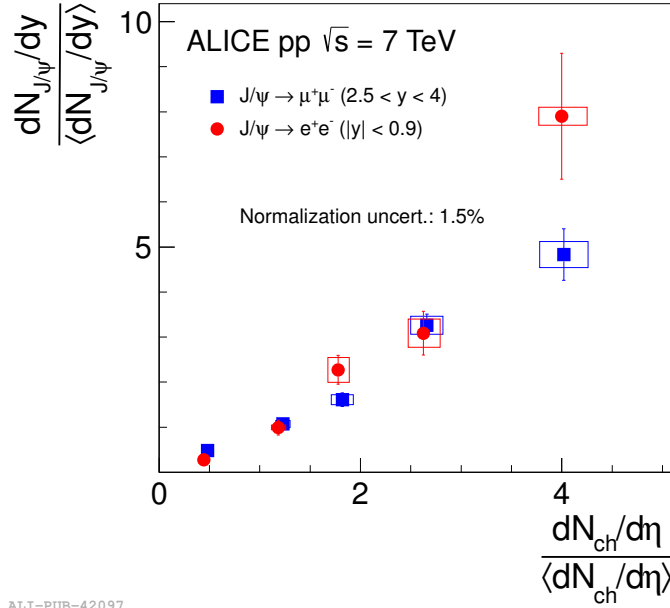
**EPOS3** [168] combines a MPI approach with a hydrodynamical treatment. The MPIs are treated via the Gribov-Regge multiple scattering framework combined with pQCD [171]. The scattering is expressed through parton ladders associated to the so-called Pomerons. The number of such Pomeron exchanges characterises the geometry of the collision. Each parton ladder is identical to a flux tube, which eventually breaks into individual strings and later into hadrons and jets. Parton saturation effects in the nucleus are summarised by a saturation scale  $Q_s$  for each Pomeron individually. The scale  $Q_s$  depends on the mass number  $A$  and can be expressed in function of the momentum fraction  $x$  or as dependent on the number of participants  $N_{part}$  (and therefore centrality). This approach gives a different scaling at low and high  $p_T$ , corresponding to a soft component scaling with  $N_{part}$  and a hard component scaling with binary collisions  $N_{coll}$ . In heavy ion collisions and in high multiplicity pp and p–A events, the high density of strings will result in a creation of a thermalised, collectively expanding bulk matter. Such bulk is referred to as 'core'. The string close to the surface of the bulk and/or with high  $p_T$  will escape the bulk and produce hadrons and jets. These segments are referred to as 'corona'. The 'core-corona' separation is a dynamical process, which provides the initial conditions for the subsequent viscous hydrodynamical evolution and allows us to describe the flow and jets at the same time.

## 3.2 $J/\psi$ and D-meson production measurements

### 3.2.1 Proton-proton collisions

ALICE reported the first measurement of multiplicity dependent inclusive  $J/\psi$  yields in pp collisions at  $\sqrt{s} = 7$  TeV [172].  $J/\psi$  were studied both at midrapidity from their di-electron channel and at forward rapidity from their decay into a muon pair. The multiplicity was measured at midrapidity  $|\eta| < 1$ . Fig. 3.6 shows the results of the two measurements. At both rapidity ranges, the relative yields demonstrate an approximately linear increase with multiplicity. According to authors of [172], a hint of stronger-than-linear increase emerges at midrapidity in the last measured point at about four times the average multiplicity. Comparing the data with PYTHIA 6 results, which includes only production of  $J/\psi$  from hard scattering via NRQCD [172], cannot explain the measured increase. The percolation model [166] on the other hand successfully reproduces the increase at mid- and forward rapidity in the measured multiplicity range and predicts a stronger-than-linear increase at higher multiplicity [166].

The 13 TeV data sample collected in 2016 provided the needed statistics to extend the measurement to higher multiplicities [169]. A dedicated high multiplicity trigger was defined, extending the reach up to about eight times the average multiplicity. Recall the results for the relative  $J/\psi$  yields shown in Fig. 3.4. Both observables were measured at midrapidity:  $J/\psi$  at  $|y| < 0.9$  from their dielectron decay channel and multiplicity at  $|\eta| < 1$ . The behaviour measured at 7 and 13 TeV is similar in the common multiplicity interval. The increase is thus independent of the energy of the collision. The increase observed in the 13 TeV data is consistent with the predicted stronger-than-linear increase,



ALI-PUB-42097

Figure 3.6: Self-normalised  $J/\psi$  yields at mid- and forward rapidity as a function of relative charged particle multiplicity in pp collisions at  $\sqrt{s} = 7$  TeV. Taken from [172].

favoured by percolation and EPOS3<sup>2</sup> models [166, 169]. However, the linear increase seen in PYTHIA and model by Kopeliovich also agree with the measurement within uncertainties [167, 173].

The 13 TeV yields also show a hint of  $p_T$  dependence [174]. The slope seems to steepen with increasing  $p_T$ , albeit the yields in all  $p_T$  bins are consistent within uncertainties. Such  $p_T$ -dependence is expected in PYTHIA and EPOS models [165, 168].

We learned from recent midrapidity STAR results [52, 175] that this behaviour also emerges at lower energies of  $\sqrt{s} = 200 - 500$  GeV. STAR did not reach as high multiplicities as ALICE did, however the statistics allowed for separation of the data into three  $p_T$  bins. Hints of steepening of the increase with higher  $p_T$  consistent with theory were reported.

The multiplicity differential D production at midrapidity  $|y| < 0.5$  was studied in ALICE with respect to event activity determined both at midrapidity  $|\eta| < 1$  and at forward rapidity from combined charge collected in two scintillator arrays at  $-3.7 < \eta < -1.7$  and  $2.8 < \eta < 5.1$  [170]. The latter measurement introduces an  $\eta$  gap between the yield and the multiplicity. This allows for a study of the possible auto-correlation effects. The average D-meson yields in Fig. 3.7, measured at  $|y| < 0.5$  in pp at  $\sqrt{s} = 7$  TeV, display a qualitatively identical increase regardless of whether the  $\eta$  gap is introduced or not in the multiplicity estimation.

Comparing the results of open charm hadrons with prompt and non-prompt  $J/\psi$  can tell us about the possible dependence on hadronisation process and therefore at which stage the correlation is born. Fig. 3.8a reveals that for midrapidity yields, the behaviour is consistent for D-mesons and inclusive  $J/\psi$ . The inclusive  $J/\psi$  yields are dominated by the prompt production. The non-prompt contribution is set side by side with open charm yields in Fig. 3.8b. These three hadrons differ in their hadronisation process. This suggests that the correlation between the relative yields and the charged particle multiplicity is related to the production of the heavy quark pair, and that the behaviour is identical for  $c$  and for  $b$  quarks.

### 3.2.2 Proton-lead collisions

In p-Pb at  $\sqrt{s_{NN}} = 5.02$  TeV, ALICE measured the open charm yields at  $-0.96 < y_{cms} < -0.04$  as a function of both mid- and forward rapidity multiplicities,  $|\eta_{lab}| < 1$  and  $2.8 < \eta_{lab} < 5.1$  respectively. The introduction of an  $\eta$  gap is important in p-Pb collisions as the multiplicity at large rapidities

<sup>2</sup>The EPOS3 provides calculations for open charm hadrons. The  $J/\psi$  measurement was compared with D-meson calculation at  $2 < p_T < 4$  GeV/c. The  $J/\psi$   $\langle p_T \rangle$  falls into this  $p_T$  interval.

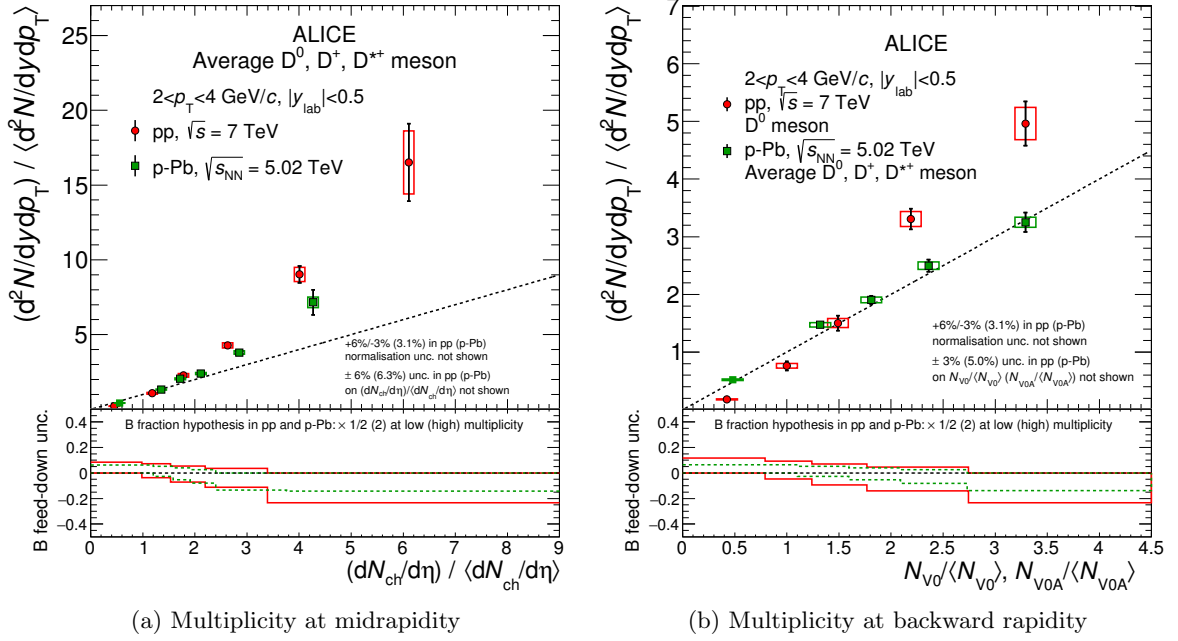


Figure 3.7: Average relative D-meson yields in  $|y| < 0.5$  as a function of the relative charged particle multiplicity at midrapidity (a), and at backward rapidity (b). Compared are data measured in pp at  $\sqrt{s} = 7$  TeV and p-Pb  $\sqrt{s_{NN}} = 5.02$  TeV. The diagonal is shown as dashed line to draw the line. The bottom panel shows uncertainty on the B feed-down fraction. Taken from [176].

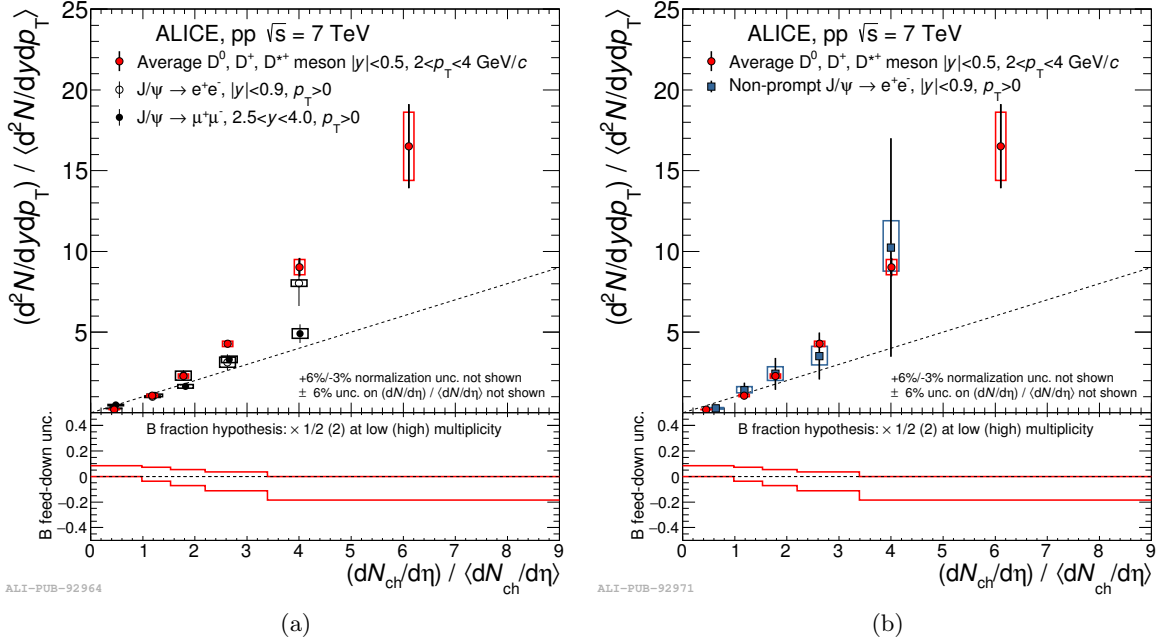


Figure 3.8: Relative yields of charmed hadrons as a function of  $dN_{ch}/d\eta / \langle dN_{ch}/d\eta \rangle$  in pp collisions at  $\sqrt{s} = 7$  TeV. (a) shows inclusive  $J/\psi$  at mid- and forward rapidity versus prompt D. (b) shows non-prompt  $J/\psi$  at midrapidity versus prompt D. Taken from [170].

scales differently compared to midrapidity [109]. At midrapidity, it scales with  $N_{\text{part}}$  and thus relates to initial effects. At large rapidities, scaling with  $N_{\text{coll}} = N_{\text{part}} - 1$  and hence with parton-parton interactions was found. As a result we observe different behaviour in case the multiplicity is measured at midrapidity (see Fig. 3.7a) and in case the multiplicity is measured at forward rapidity (see Fig. 3.7b). Contrast with pp measurement at  $|y_{\text{cms}}| < 0.5$  drawn in the same figures which show no such difference.

In Fig. 3.9, both p–Pb measurements were compared with corresponding EPOS 3.116 calculations [168, 171] with and without viscous hydrodynamical evolution of the collisions for four D-meson transverse momentum bins within  $1 < p_T < 12$  GeV/c. In either rapidity window, both calculations agree with the measured yields within uncertainties, albeit the curve including the hydrodynamical evolution reproduces better the yields at high multiplicity. The difference in the nature of the observed increase could be thus explained by stronger influence of flow on charged particles close to  $\eta = 0$ , while its role at large rapidities is minor.

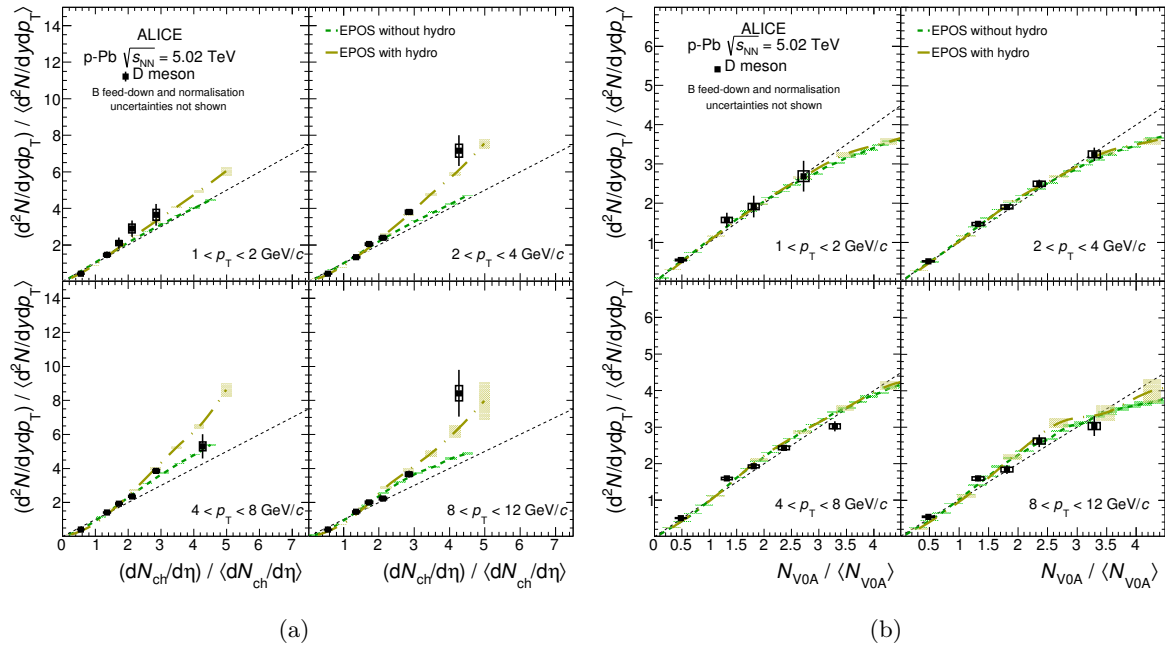


Figure 3.9: Average relative D-meson yields in  $|y_{\text{LAB}} < 0.5|$  as a function of the relative charged particle multiplicity at midrapidity (a), and at backward rapidity (b) measured in p–Pb  $\sqrt{s_{\text{NN}}} = 5.02$  TeV. Data are compared to EPOS calculation with and without hydrodynamical evolution [168, 171]. The dashed line represents the diagonal  $y = x$  and is shown to draw the eye. Taken from [176].

Unlike the D-mesons<sup>3</sup>, the  $J/\psi$  were measured in p–Pb at  $\sqrt{s_{\text{NN}}} = 5.02$  TeV in three different kinematic regions:  $J/\psi \rightarrow e^+e^-$  at midrapidity corresponding to  $-1.37 < y_{\text{cms}} < 0.43$ , and  $J/\psi \rightarrow \mu^+\mu^-$  at forward rapidity  $2.03 < y_{\text{cms}} < 3.53$  and at backward rapidity  $-4.46 < y_{\text{cms}} < -2.96$  [177]. The relative yields are plotted as a function of charged particle multiplicity at midrapidity  $|\eta_{\text{lab}}| < 1$  in Fig. 3.10a. At low multiplicities, the relative yields experience a linear increase with multiplicity. Starting at  $dN_{\text{ch}}/d\eta / \langle dN_{\text{ch}}/d\eta \rangle \approx 1.5$ , the trend seems to depend on the  $J/\psi$  rapidity. The backward rapidity  $J/\psi$  continue to increase in a linear fashion whilst the forward rapidity yields grow at a decreasing rate. The midrapidity  $J/\psi$  suffer from the limited statistics - within the large uncertainty, the highest multiplicity data point is consistent with the stronger-than-linear increase of D mesons as well as with linear increase of the backward  $J/\psi$ . Run 2 data are hoped help to solve this conundrum thanks to the increase in statistics. The stronger suppression of forward yields is consistent with expected suppression due to the CNM effects applicable in the small  $x$  region. CMS measured the ratio between the forward and backward  $J/\psi$  yields at  $p_T > 6.5$  GeV/c in p–Pb collisions at  $\sqrt{s_{\text{NN}}} = 5.02$  TeV [150], separating the prompt and non-prompt  $J/\psi$ . They also

<sup>3</sup>In ALICE, the D-mesons are measured only at midrapidity. Therefore they do not profit much from having the beam configuration reversed.

observed a suppression of forward yields with respect to the backward one, which depend on the multiplicity (estimated from the transverse energy  $E_T$ ), the rapidity window in which the measurement is performed, and on the  $J/\psi$  production process.

Furthermore, the relative mean transverse momentum  $\langle p_T \rangle^R$  was studied in [177]. In each multiplicity bin  $i$ ,  $\langle p_T \rangle^R$  is defined as the ratio of the  $\langle p_T \rangle$  of  $J/\psi$  in the given multiplicity interval divided by the multiplicity integrated value:

$$\langle p_T \rangle^R = \langle p_T \rangle^i / \langle p_T \rangle^{\text{MB}}. \quad (3.1)$$

Fig. 3.10b shows the measurement for backward and forward  $J/\psi$  yields. Both data sets show similar behaviour. At low multiplicities  $dN_{\text{ch}}/d\eta / \langle dN_{\text{ch}}/d\eta \rangle < 1$ , we observe a steep increase of the ratio. From average multiplicity  $dN_{\text{ch}}/d\eta / \langle dN_{\text{ch}}/d\eta \rangle \approx 1$  onwards, the yields saturate around unity. The results of measurement for midrapidity charged hadrons at  $|\eta_{\text{cms}}| < 0.3$  [178] in p-Pb is shown in the same plot. We see that the behaviour of particles created in soft processes at midrapidity is different to the one measured in studies of particles created in hard processes at forward or backward rapidity. The origin of this difference is not fully understood, one of the possible reasons may be the autocorrelations in the midrapidity measurement.

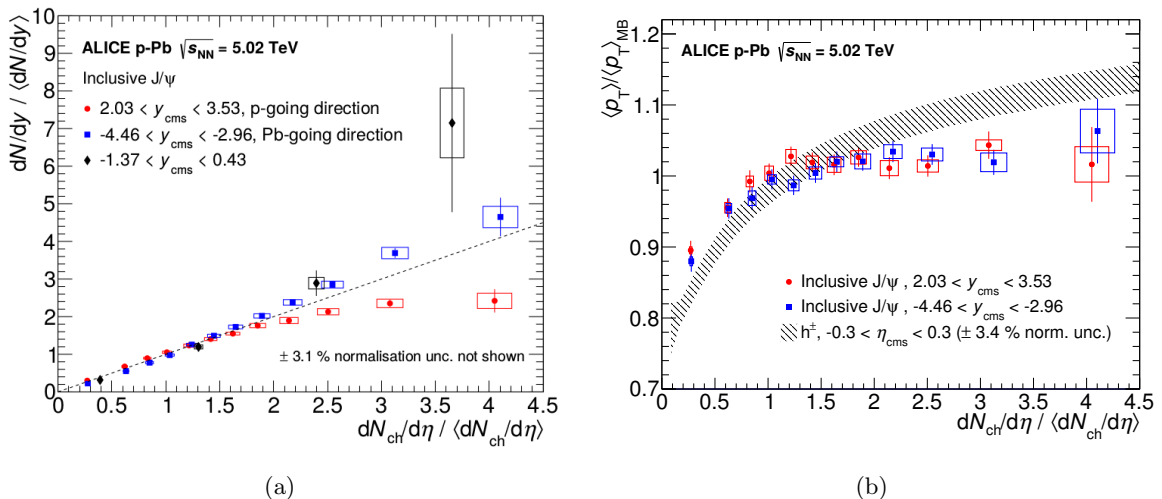


Figure 3.10:  $J/\psi$  at forward, mid-, and backward rapidity as a function of charge particle multiplicity measured at  $|\eta| < 1$ . (a) Relative  $J/\psi$  yields as a function of multiplicity. The diagonal is shown as dashed line to draw the line. (b) Relative  $\langle p_T \rangle$  as a function of multiplicity at forward and backward rapidity, compared with results for charged hadrons at  $|\eta_{\text{cms}}| < 0.3$  [178]. Taken from [177].

### 3.3 $\Upsilon$ production measurement

CMS measured the vector bottomonia states  $J^{CP} = 1^{--}$  - i. e.  $\Upsilon(1S)$ ,  $\Upsilon(2S)$ , and  $\Upsilon(3S)$  - in pp, p-Pb and Pb-Pb collisions at LHC energies [179]. The  $\Upsilon$  production at  $|y_{\text{cms}}| < 1.93$  was studied as a function of transverse energy at large rapidity  $4 < |\eta_{\text{lab}}| < 5.2$  and as a function of the charged particle tracks at midrapidity  $|\eta_{\text{lab}}| < 2.4^4$ .

Results of the measurements are plotted in Fig: 3.11. The top row shows the dependence on self-normalised transverse energy (therefore with  $\eta$  gap between the multiplicity estimator and the yields rapidity regions). The bottom row shows the midrapidity tracklets dependence. Each panel shows self-normalised yields in pp, p-Pb, and Pb-Pb for one given bottomonium state - from left to right the order goes as  $\Upsilon(1S)$ ,  $\Upsilon(2S)$ , and  $\Upsilon(3S)$ . When the  $\eta$  gap is introduced, all three states show a consistent linear increase with multiplicity regardless of the size of the system. In the case of midrapidity multiplicity dependence, the yields measured in pp demonstrate a stronger-than-linear increase.

<sup>4</sup>Note that the event activity used by CMS in this study is much different from the one used by ALICE and in theory calculations. Alas, direct comparison with charmed hadrons measured by ALICE and/or theory predictions is thus impossible.

Recall that the non-prompt  $J/\psi$ , discussed in the previous section, are produced from decays of B-mesons. We concluded that their behaviour with multiplicity in an overlapping rapidity region is consistent with a stronger-than-linear increase (see Fig. 3.8b). Open and hidden charm displays identical behaviour as open and hidden beauty. The phenomenon is thus independent of the flavour of the heavy quark pair.

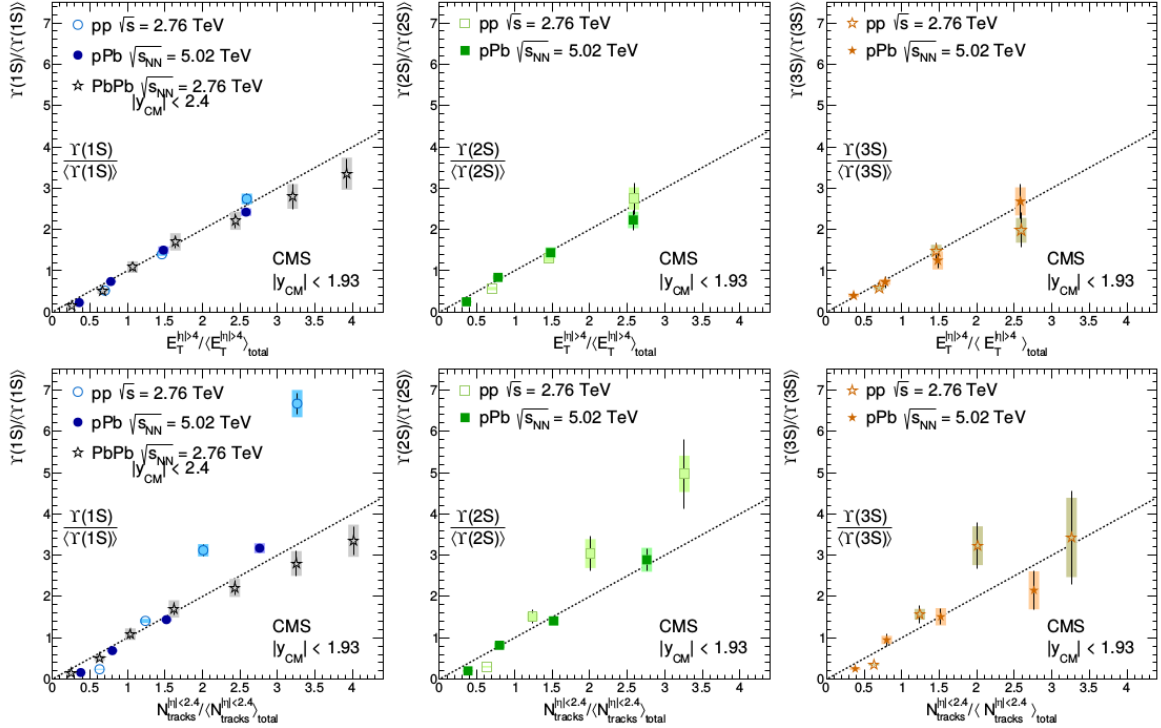


Figure 3.11: The  $\Upsilon(nS)$  relative cross section versus transverse energy measured at forward rapidity  $4 < |\eta| < 5.2$  (top row) and versus charged track multiplicity at midrapidity  $|\eta| < 2.4$  (bottom row). The cross section was measured at midrapidity  $|y_{cms}| < 1.93$  in pp collisions at  $\sqrt{s} = 2.76$  TeV and in p–Pb collisions at  $\sqrt{s_{NN}} = 5.02$  TeV. For  $\Upsilon(1S)$ , the results for Pb–Pb measurement at  $\sqrt{s_{NN}} = 2.76$  TeV is also shown. Taken from [179].

### 3.4 Digression towards multiplicity dependence of strangeness production

Strangeness enhancement is another of the typical heavy ion phenomena observations measured also in high multiplicity pp and p–Pb events. In heavy ion collisions, enhancement of strangeness production is observed with respect to pp events. ALICE studied the relative enhancement of hadrons containing one ( $K_S^0$ ,  $\Lambda$ ,  $\bar{\Lambda}$ ) or multiple strange quarks ( $\Xi^-$ ,  $\Xi^+$ ,  $\Omega^-$ ,  $\Omega^+$ ) with respect to pions in pp collisions at  $\sqrt{s} = 7$  TeV [180]. The measured multiplicity dependent relative yields  $h/(\pi^+ + \pi^-)$  were compared with results from p–Pb at  $\sqrt{s_{NN}} = 5.02$  TeV [181, 182] and Pb–Pb at  $\sqrt{s_{NN}} = 2.76$  TeV [183] in Fig. 3.12. With increasing  $\langle dN_{ch}/d\eta \rangle$ , the relative yields increase smoothly from low multiplicity pp events to high multiplicity p–Pb collisions, where they reach a value measured in Pb–Pb. This finding is non-trivial, as the observed charged particle multiplicity is in general related to different underlying physics in each system. According to the authors of [180], this measurement shows that the charged particle multiplicity  $dN_{ch}/d\eta$  has the potential to be a good variable to bridge the gap between the different colliding systems.

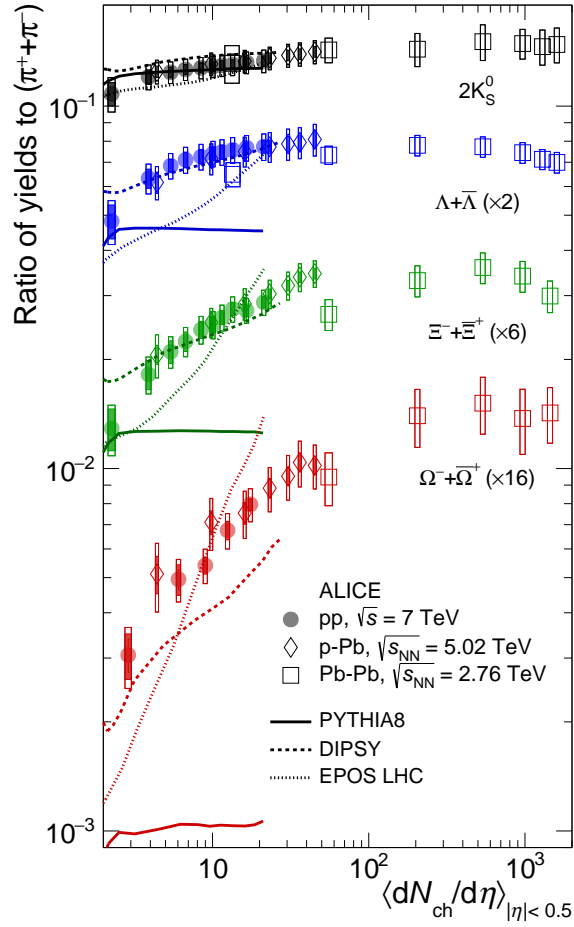


Figure 3.12: The relative yields of strange hadron compared to charged pions as a function of mean charged particle multiplicity  $\langle dN_{\text{ch}}/d\eta \rangle$ . The shown yields were measured in pp, p-Pb, and Pb-Pb collisions. Taken from [180].

## Summary

Since the start of LHC operation, it became clear that proton-proton collisions are more complex than previously considered. Multiple hard scatterings can take place in one such collision. Yet the pp collisions remain to be the best baseline for studies of more complex events in p–A and A–A collisions. Therefore it is necessary to have a good grasp of the processes taking place in pp events.

Correlations of heavy flavour hadrons with the underlying event and/or other hard and soft processes is vital to better constrain the models describing the production of hard probes. They can also help us to understand in more details the elementary processes taking place in one proton-proton event.

There are multiple theoretical models that study the multiplicity dependent production of charm in pp and p–A collisions. Models discussed in this work employ the MPIs in some way to achieve a good agreement with the data. They also include other hard and soft processes which contribute to the observed behaviour in their own way. More measurements at increased precision are necessary in order to discriminate between the available models.

Measurement of open and closed charmed and beauty hadrons in pp collisions showed that the multiplicity dependence is independent of the hadronisation processes. It can be instead linked to the production of the heavy quark pair. To investigate the possible auto-correlations in case when the hadrons and multiplicity are measured at the same rapidity, studies with  $\eta$ -gap were introduced. The results on open charmed hadrons at midrapidity showed that the introduction of  $\eta$ -gap in pp measurements has no effect on the nature of the increase of the yields. In contrary, the  $\Upsilon$  results from CMS suggest that in pp collisions, the yields are sensitive to the rapidity interval at which the multiplicity is measured. Furthermore, the  $\eta$ -gap does play a role in p–Pb collisions. The open charmed hadrons show a stronger increase when the rapidity window of the yields and multiplicity measurements overlap. This difference can be understood to originate in the collective effects taking place in p–Pb collisions that are more pronounced in the midrapidity region.

Up to date there exist no measurement of closed charmed hadrons at midrapidity versus forward multiplicity. However, ALICE measures forward and backward rapidity  $J/\psi$  as a function of charged particle multiplicity at midrapidity. Such a measurement enables us to study CNM effects at small  $x$ . The large  $x$  (backward) measurement shows an increase consistent with midrapidity D-mesons. CMS data also show a stronger suppression of forward yield in high multiplicity events, which is attributed to the presence of CNM effects in the forward region. The suppression differs between prompt and non-prompt  $J/\psi$ , hinting at different CNM effects affecting each contribution. At present, no measurement of forward (backward)  $J/\psi$  was shown as a dependence of forward (backward) multiplicity. Such measurement will provide another piece to this interesting puzzle.

On a side note, ALICE also studied the dependence of strange hadrons on multiplicity of the collisions and observed a smooth transition from low multiplicity pp events up to central Pb–Pb collisions. However, the observed strangeness enhancement with event activity is not attributed to multiple hard scatterings, as it is in the case of charm and beauty, but instead to higher energy density available for particle production.



## EXPERIMENTAL SETUP

In this chapter we will briefly present the Large Hadron Collider and A Large Ion Collider Experiment (ALICE). Selected ALICE subdetectors will be described. Particular focus will be given to the Muon Spectrometer as it is the main system used in hereby presented analyses.

### 4.1 The Large Hadron Collider

The Large Hadron Collider (LHC) [184], with its 27 km of circumference, is the largest and the most powerful particle accelerator built to date. It consist of  $\sim 1200$  supraconductive magnets that provide a magnetic field of 8 T to bend the beams. The beams are kept in two separate beams, which share the same magnet and cross at four points along the collider. The four main experiments are located each at one of these crossing points:

**A Toroidal LHC Apparatus (ATLAS)** [185] and the **Compact Muon Solenoid (CMS)** [186] are general purpose physics experiments, designed to search for (and possibly study) 'New Physics': Higgs boson(s), Dark Matter, and Supersymmetry to name a few<sup>1</sup>. ATLAS and CMS shared the Higgs boson discovery in 2012 [3, 4].

**Large Hadron Collider beauty (LHCb)** [187] experiment is designed to study the CP violation in decays of heavy flavour hadrons. Such measurements are motivated by our lack of understanding of the Matter-Antimatter asymmetry in our Universe. CP violation may be one of the pieces of this puzzle.

**A Large Ion Collider Experiment (ALICE)** [188] was designed to study the hot and dense medium created in collisions of ultrarelativistic nuclei. This thesis is dedicated to analyses of charm probes in ALICE. The detector will be described in upcoming sections.

The LHC primarily collides proton beams but also collides ion beams or proton-ion. The maximal nominal energy to which protons can be accelerated is  $E_p = 7$  TeV. In the case of lead ions  $^{208}_{82}\text{Pb}$ , the maximal energy of the beam can be computed in the following way: as only charged particles can be accelerated, the neutrons will be dragged by the protons in the nucleus and hence only  $Z/A$  nucleons will contribute to the overall acceleration. The maximal nominal energy per nucleon in the ion is then  $E_{Pb} = Z/A \cdot E_p = 2.75$  TeV.

The LHC is a part of the CERN accelerator complex which is shown in Fig. 4.1. The proton beams are produced by stripping electrons from a hydrogen gas by an electric field, which also serves to accelerate the proton beam up to 750 keV. The protons are then injected into the Linac 2 and accelerated up to 50 MeV. Subsequently they are accelerated up to a total energy of 450 GeV by a series of circular accelerators - in order Proton Synchrotron Booster (PSB), Proton Synchrotron (PS), and Super Proton Synchrotron (SPS) - to be finally injected into the LHC with a spacing of 25 ns between consecutive bunches. In LHC they are accelerated up to 6.5 TeV.<sup>2</sup>

---

<sup>1</sup>The two experiments may share their goals but use vastly different set-ups to perform their work.

<sup>2</sup> After the Long Shutdown 1 (2012-2014), it would take much longer to establish conditions to run at 14 TeV (7 TeV/beam) than at 13 TeV (6.5 TeV/beam), which would mean shorter physics programme. Nice explanation can be found at the LHC site <https://home.cern/about/engineering/restarting-lhc-why-13-tev>.

CERN's Accelerator Complex

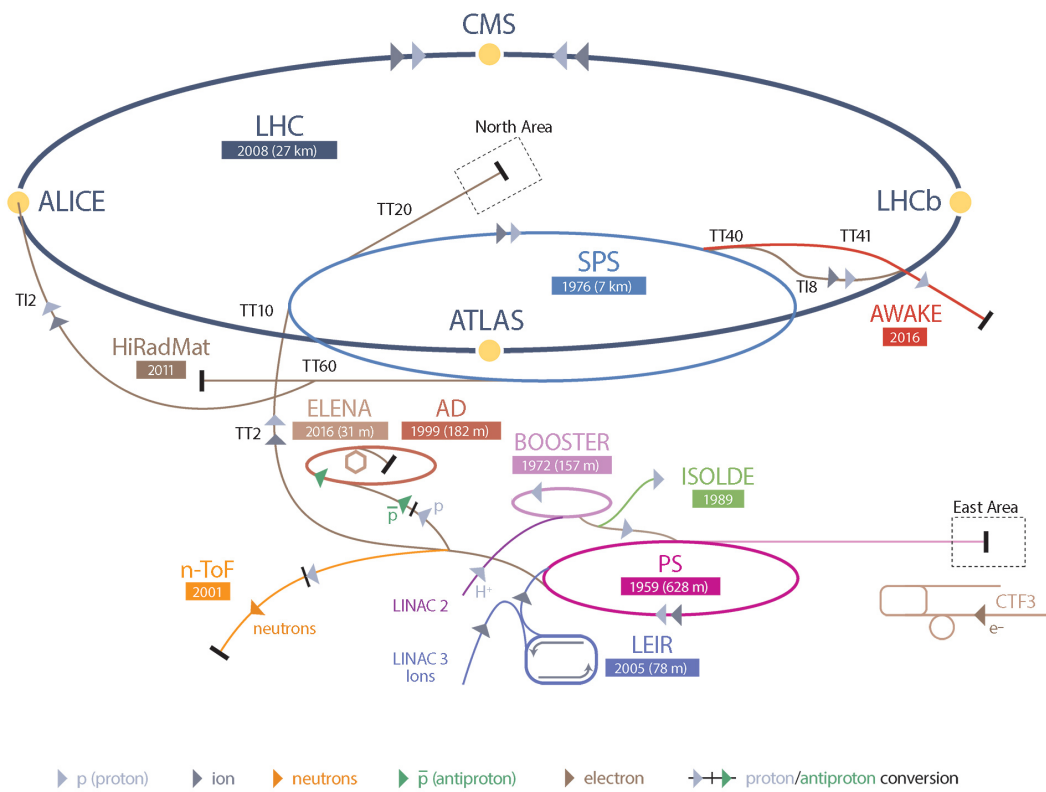


Figure 4.1: The CERN accelerator complex.

The Pb ions are produced by ionising the vaporised lead and delivered by Linac 3 to the Low Energy Ion Ring (LEIR). Their energy is then ramped up to 72 MeV. The beam is subsequently injected into the PS, from where it follows the same acceleration chain as protons. In the LHC, Pb beams are accelerated up to 522 TeV (or 2.51 TeV per nucleon) with spacing of 152 ns between individual bunches.

## 4.2 A Large Ion Collider Experiment

ALICE [188] is a dedicated heavy-ion experiment and is thus optimised to measure the high charged particle densities up to  $dN/d\eta \sim 8000$ . ALICE also collides pp and p–Pb primarily as a reference for the Pb–Pb measurements but also as a standalone physics programme. For instance, charmonia are extensively studied in pp and p–Pb collisions in ALICE, as we discussed in Chapters 2 and 3.

ALICE consists of 18 subsystems that can be grouped into two main parts:

**Central Barrel detectors** at midrapidity, surrounding the interaction point (IP) and encapsulated by the L3 magnet, which provides a 0.5 T solenoidal magnetic field. Detectors that can be listed in this group are the Inner Tracking System (ITS), the Time Projection Chamber (TPC), the Time Of Flight (TOF), the Transition Radiation Detector (TRD), the High Momentum Particle Identification detector (HMPID), the Electromagnetic Calorimeter (EMCal), the Di-jet Calorimeter (DCal), the Photon Spectrometer (PHOS), and the Photon Multiplicity Detector (PMD).

**Forward detectors** which include V0, T0, the Zero Degree Calorimeters (ZDC), the ALICE Diffractive (AD) and the Muon Spectrometer.

The system is completed by the ALICE Cosmic Ray Detector (ACORDE) - a scintillator array positioned on top of the L3 magnet. A schema of the ALICE detector is shown in Fig. 4.2. In the following section, we will briefly describe only detectors that are in some way relevant for quarkonia analyses at mid- or forward rapidity.

### The ALICE beam-pipe

The ALICE beam-pipe is a beryllium cylinder with a diameter of 6 cm and wall thickness of 800  $\mu\text{m}$  [189]. Beryllium is a very light material. Its low atomic mass decreases the risk of interaction with the particles produced in the collision. The beam-pipe is supported by the first layers of ITS, hence no relative movement can occur during runtime.

### 4.2.1 Central Barrel detectors

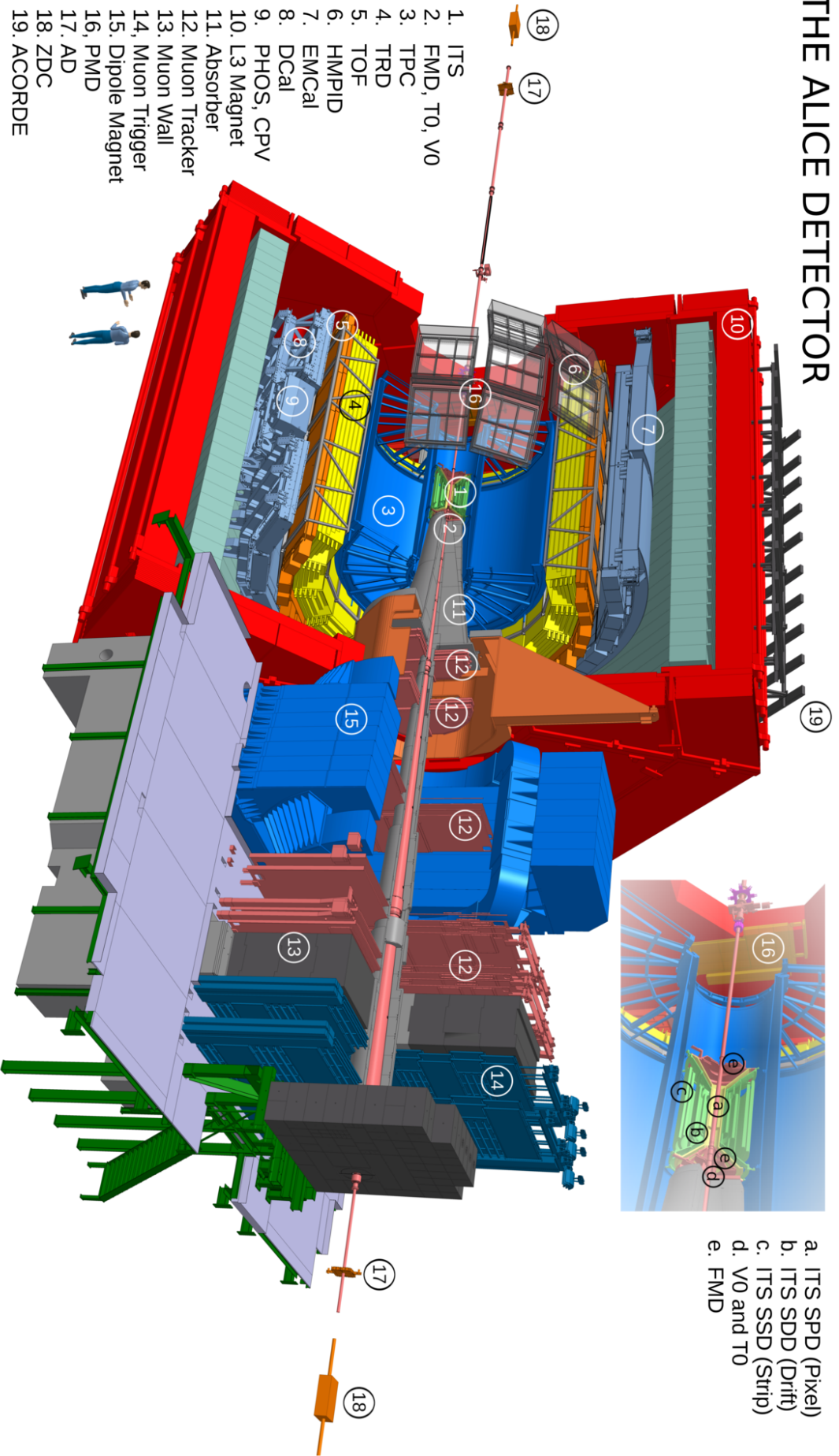
#### 4.2.1.1 Inner Tracking System

The Inner Tracking System (ITS) [190] is the innermost detector immediately surrounding the beam-pipe, covering the pseudorapidity range of  $|\eta| < 0.9$ . It consists of 6 layers of silicon detectors, divided into three subsystems: the Silicon Pixel Detector (SPD), the Silicon Drift Detector (SDD), and the Silicon Strip Detector (SSD). Each of the subdetectors uses different technology so that the granularity is highest in the layers closest to the interaction point and decreases with distance from the beam-pipe. Tab. 4.1 lists the dimensions of each of the ITS layers. The minimal radius is limited by the beam-pipe and the maximal radius was chosen to optimise the matching of tracks from the ITS to the TPC. A schema of the different ITS subsystems is shown in Fig. 4.3.

layers	$r_{\text{in}}$ [cm]	$r_{\text{out}}$ [cm]	$ \eta_{\text{in}} $	$ \eta_{\text{out}} $
SPD (1,2)	3.9	7.6	2.0	1.4
SDD (3,4)	15.0	23.9	0.9	0.9
SSD (5,6)	38.0	43.0	1.0	1.0

Table 4.1: Dimensions of individual layers of ITS [191].

# THE ALICE DETECTOR



1. ITS
2. FMD, T0, V0
3. TPC
4. TRD
5. TOF
6. HMPID
7. EMCal
8. DCal
9. PHOS, CPV
10. L3 Magnet
11. Absorber
12. Muon Tracker
13. Muon Wall
14. Muon Trigger
15. Dipole Magnet
16. PMD
17. AD
18. ZDC
19. ACORDE

- a. ITS SPD (Pixel)
- b. ITS SDD (Drift)
- c. ITS SSD (Strip)
- d. V0 and T0
- e. FMD

Figure 4.2: The ALICE experiment in Run 2.

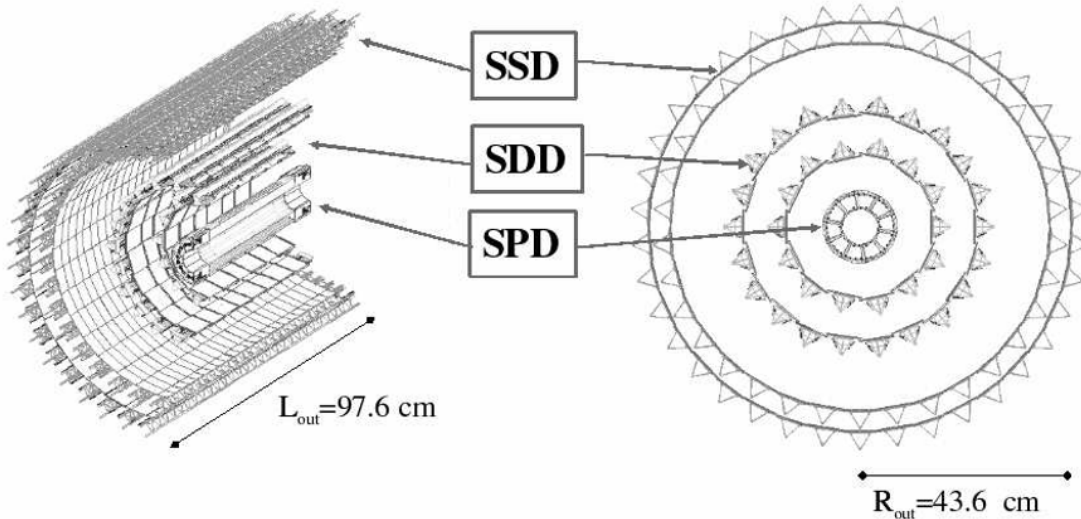


Figure 4.3: Layout of the ITS detector. Taken from [188].

The ITS serves to reconstruct primary vertices, secondary vertices from decays of strange and heavy flavour hadrons, and primary tracks in the Central Barrel and in the Muon Spectrometer. The SSD, consisting of the two outer-most layers, measures the specific energy loss per unit path length  $dE/dx$ , thus enabling identification of low momentum particles with  $p_T < 200$  MeV/ $c$  or passing through dead regions of the TPC. The SPD provides, among other, multiplicity estimator relevant for the analysis described in Chapter 7. Therefore we will give it a bigger focus compared to the SDD and the SSD.

### Silicon Pixel Detector

The Silicon Pixel Detector (SPD) is formed by the two layers closest to the beam-pipe. The SPD pseudorapidity range is extended with respect to the rest of the ITS to  $|\eta| < 1.98$  as it was built to provide, together with the FMD, a continuous charged particle multiplicity coverage. The SPD serves as a trigger detector and is used to identify in-bunch pile-up events, i. e. events in which more than one pp collisions from the same bunch crossing took place. The information from the SPD is used in analyses of centrality or charged particle multiplicity dependence of particle production.

We will briefly explain the SPD vertex and tracklets reconstruction algorithms. The SPD vertex is necessary in muon trigger operations (more details in Sec. 4.3.1.3) and in reconstruction of muon tracks in the Muon Spectrometer (see Sec. 4.3.2). The information on the SPD vertex and on the SPD tracklets are used in analyses of charged particle multiplicity.

There are two algorithms to reconstruct the SPD vertex [192]:

1. **3D vertexer** that reconstruct  $x$ ,  $y$ , and  $z$  position of the interaction vertex. The method is multiplicity dependent and its resolution improves with increasing multiplicity. The algorithm reconstructs *tracklet candidates* by connecting reconstructed points between the two layers of the SPD within a small azimuthal window from the expected interaction point. A distance of closest approach (DCA) cut is then applied on pairs of tracklets. Pairs with crossing point in the fiducial interaction region are kept and their coordinates are calculated. The coordinates of the vertex are first estimated from the distributions of the coordinates of individual crossing points. A second reconstruction is performed, removing tracklets that are displaced from the vertex reconstructed in the first iteration. The coordinates of the vertex are then recomputed from the remaining tracklets.
2. **1D vertexer** that reconstructs the  $z$ -coordinate of the SPD vertex when the 3D vertexer fails. The  $x$  and  $y$  coordinates are taken from the online measurements<sup>3</sup>. The algorithm calculates

<sup>3</sup>The coordinates and spreads of the interaction diamond are reconstructed online and are stored in the Offline

the intersection point  $z_i$  with the beam axis or each candidate tracklet  $i$ . The error  $\sigma_i$  is also calculated. Assuming that  $z_i$  follow the Gaussian distribution, a first estimate of the  $z$ -vertex coordinate  $\langle z \rangle$  is computed in a region around the peak from all tracklets  $N_{tr}$

$$\langle z \rangle = \frac{\sum_{i=1}^{N_{tr}} z_i / \sigma_i}{\sum_{i=1}^{N_{tr}} 1 / \sigma_i}.$$

The value of  $\langle z \rangle$  is iteratively recomputed. The iteration stops when all used tracklets come from a symmetric region around the mean value  $\langle z \rangle$ .

The SPD tracklets are reconstructed by correlating the SPD vertex with a cluster in both layers [193]. A schema of the algorithm is depicted in Fig. 4.4. The algorithm considers a straight line from the vertex to a cluster in the inner layer. Another line is drawn to a cluster in the outer layer of the SPD. The differences in the azimuthal and polar angles  $\Delta\varphi$  and  $\Delta\theta$  are computed. Combinations with all clusters in the outer layer are considered. Only candidates in a given  $\Delta\varphi$  and  $\Delta\theta$  window are accepted.

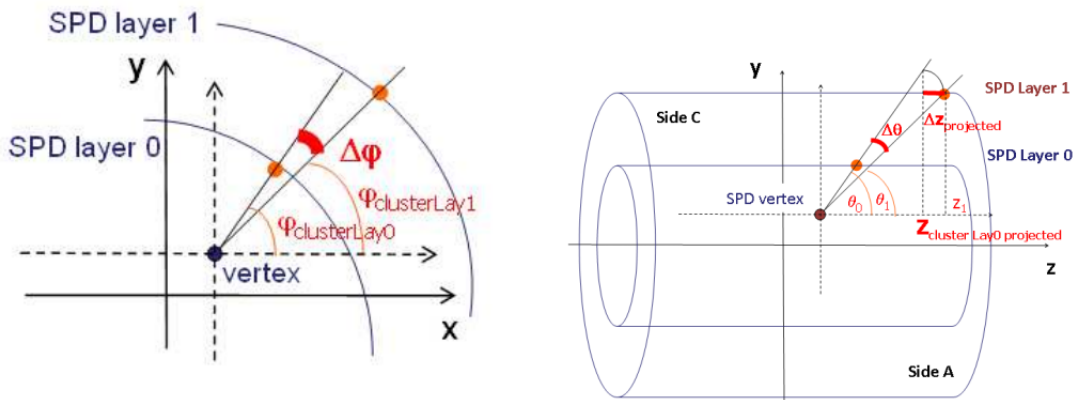


Figure 4.4: Schematic drawing of the tracklet reconstruction algorithm principle. Taken from [193].

#### 4.2.1.2 Time Projection Chamber

The Time Projection Chamber (TPC) [194] is the main tracking and PID detector in ALICE. It covers a  $2\pi$  azimuthal angle, and a pseudorapidity  $|\eta| < 0.9$  for fully reconstructed tracks or  $|\eta| \lesssim 1.5$  for tracks with reduced track length. The TPC is a cylindrical unit surrounding the beam-pipe and the ITS, with an inner and an outer diameter of 85 and 247 cm respectively. It has a length of 5 m along the beamline and its volume is separated by a cathode membrane in the middle. The cathode is under high voltage of 100 kV, meaning the inner electric field of the volume is 400 V/cm. While passing the chamber filled with gas, particles ionise the gas. The ionisation produces secondary electrons. These then drift to the read-out caps. The read-out caps are split into 18 sectors. Each sector is radially segmented into two chambers: an inner and outer read-out chamber. Each chamber constitutes of several pads with varying size, optimised for the radially dependent track density. The  $x$  and  $y$  coordinates of the track are reconstructed from the pad signal of drifting electrons hitting the cap. The  $z = v_e \Delta t$  coordinate is calculated as a product of the drift time  $\Delta t$  of the electron cluster and the average electron drift velocity  $v_e$ . The average drift velocity in the TPC is  $v_e = 2.78$  cm/ $\mu$ s, resulting in the maximum drift time of  $\approx 90$   $\mu$ s.

The TPC records tracks of produced particles, measures their momenta and their ionisation energy loss  $dE/dx$  to identify the particles. The TPC has the ability to measure wide range of particle momenta - from 100 MeV/c to about 100 GeV/c with good momentum resolution. At  $p_T = 1$  GeV/c, the momentum resolution is about  $\sigma_{1/p_T} \approx 1\%$  [191]. Together with other detectors, the TPC also provides vertex determination. The TPC can be also used in centrality and in event plane determination.

---

Condition Database (OCDB), see Sec. 4.4.2

The particle identification in the TPC is done by the simultaneous measurement of particle momentum  $p$  and the corresponding specific ionisation energy loss  $dE/dx$ . The energy loss can be parametrised by the Bethe-Bloch formula [195]

$$\langle dE/dx \rangle = f(\beta, \gamma, C_i),$$

where  $\beta$  is the velocity of the particle,  $\gamma = \sqrt{1 - \beta^2}$ , and  $C_i$  are detector specific constants. The specific ionisation is thus related to the velocity of the particle. A particle can be identified from Bethe-Bloch without prior knowledge of its mass, just from the  $dE/dx$  and  $p$  measured in TPC. Typical momentum dependence of  $dE/dx$  can be found in Fig. 4.5.

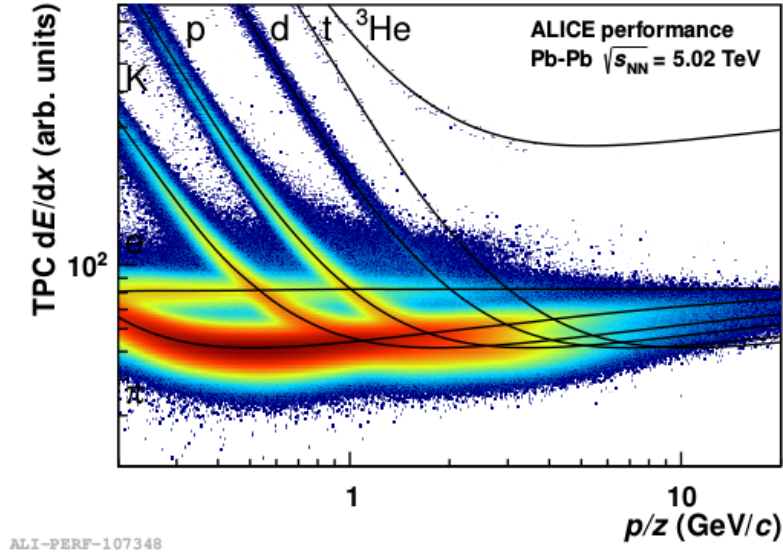


Figure 4.5: The specific ionisation energy loss  $dE/dx$  in TPC as a function of momentum in Pb-Pb collisions at  $\sqrt{s_{\text{NN}}} = 5.02$  TeV. The solid lines show the central value of the Bethe-Bloch parametrization for a given particle. Taken from the ALICE Figure Repository [196].

#### 4.2.1.3 Transition Radiation Detector

The purpose of the Transition Radiation Detector (TRD) [197] is identification of high- $p_T$  electrons. The detector covers the central pseudorapidity range  $|\eta| < 0.8$  at a radial distance of 290 – 368 cm. The TRD consists of 18 supermodules with sandwich structure, alternating between layers of 4.8 cm of radiator and 3 cm of gas (85% Xe + 15% CO<sub>2</sub>) coupled to a multi-wire proportional chamber (MWPC).

The transition radiation is a radiation that occurs at the transition between two materials with different permittivity - in this case the radiator and the gas. The wavelength of the emitted gamma depends on the particle energy. For ultra-relativistic particles with  $\gamma \geq 1000$ , the spectrum of the emitted radiation extends into the X-ray domain [198], whose conversion results in a larger energy deposit compared to conversion from ionisation. The probability of a X-ray radiation is however very small. Multiple transitions are used to increase this probability.

#### 4.2.1.4 Time Of Flight

The Time Of Flight (TOF) [199, 200] is a barrel detector mounted in a cylindrical cage with the respective inner and outer radius of 370 and 399 cm. The detector covers the pseudorapidity range of  $|\eta| < 0.9$  and has a full azimuthal coverage.

The TOF consists of  $18 \times 5$  modules of Multi-gap Resistive Plate Chambers (MRPC). A MRPC module can be described as a stack of resistive plates separated by minuscule gaps filled with gas mixture C<sub>2</sub>H<sub>2</sub>F<sub>4</sub> (93%) + SF<sub>6</sub> (7%) [201]. A passing charged particle ionises the gas in the gap. High voltage is applied to the external surface of the chamber to amplify the ionisation of the gas. This

creates an intense electric field  $E \approx 100\text{kV/cm}$ . The resistive plates quench the avalanche immediately after particle crossing.

The TOF measures the velocity of charged particles and thus contributes to particle identification of electrons, pions, kaons and protons in ALICE at low and intermediate momentum. The velocity  $\beta$  is calculated from ratio of the path length  $L$  of the particle from the vertex and the time it takes to cross this path length  $\Delta t$

$$\beta = \frac{L}{c\Delta t}. \quad (4.1)$$

The starting time  $t_0$  from which  $\Delta t$  is measured is determined by the T0 and explained in Sec. 4.2.2.2. A typical plot distribution of  $\beta$  measured in TOF as a function of particle momentum  $p$  is shown in Fig. 4.6. The TOF can separate pions and kaons up to  $2.2\text{ GeV}/c$  and kaons from protons up to  $4\text{ GeV}/c$ .

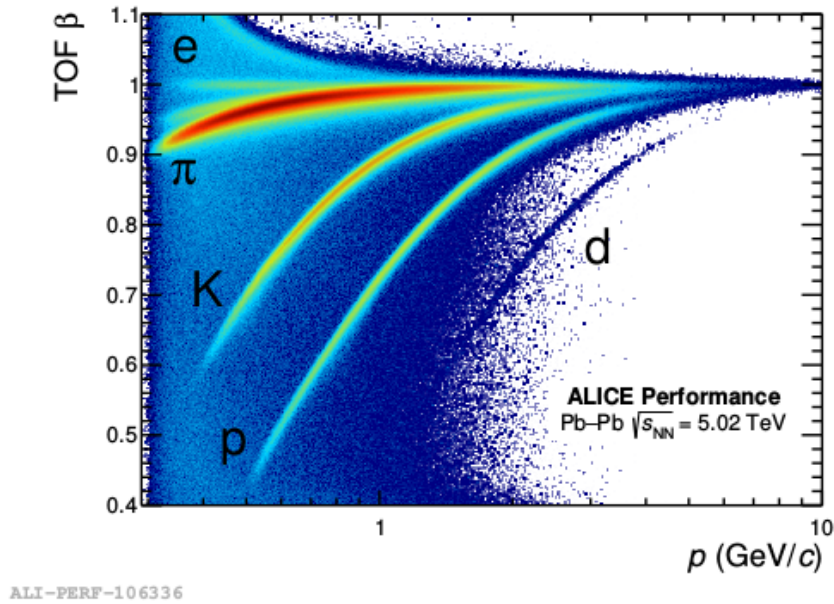


Figure 4.6: The TOF velocity  $\beta$  as a function of momentum in Pb–Pb collisions at  $\sqrt{s_{\text{NN}}} = 5.02\text{ TeV}$ . Taken from the ALICE Figure Repository [196].

## 4.2.2 Forward detectors

### 4.2.2.1 V0 detector

The V0 system [202, 203] consists of two sets of scintillator arrays located asymmetrically on either side from the nominal interaction point. The V0A is placed at  $z = +330\text{ cm}$  and covers pseudorapidity range of  $2.8 < \eta < 5.1$ , whilst the V0C sits at  $z = -90\text{ cm}$  and covers  $-3.7 < \eta < -1.7$ . The placement of the arrays within the ALICE system is depicted in Fig. 4.7.

The V0 provides a trigger for ALICE and discriminates beam-beam interactions from background events. Furthermore, the V0 is used for determination of the integrated luminosity  $\mathcal{L}_{\text{int}}$ . Analysis-wise, the V0 is used in centrality, multiplicity, and in event characterisation (e. g. flow or azimuthal correlations measurements).

The V0 was programmed to render MB trigger (pp, p–Pb, and Pb–Pb) and a centrality trigger in Pb–Pb[203]. In pp collisions, V0 has provided three types of MB triggers:

- $\text{MB}_{\text{OR}}^4$  defined as coincidence of a signal from SPD and a signal from either V0A or V0C:

$$\text{SPD} \ \&\& \ (\text{VOA} \ || \ \text{VOC}).$$

<sup>4</sup> $\text{MB}_{\text{OR}}$  was used primarily on 2009 and 2010 pp collisions at low luminosity.

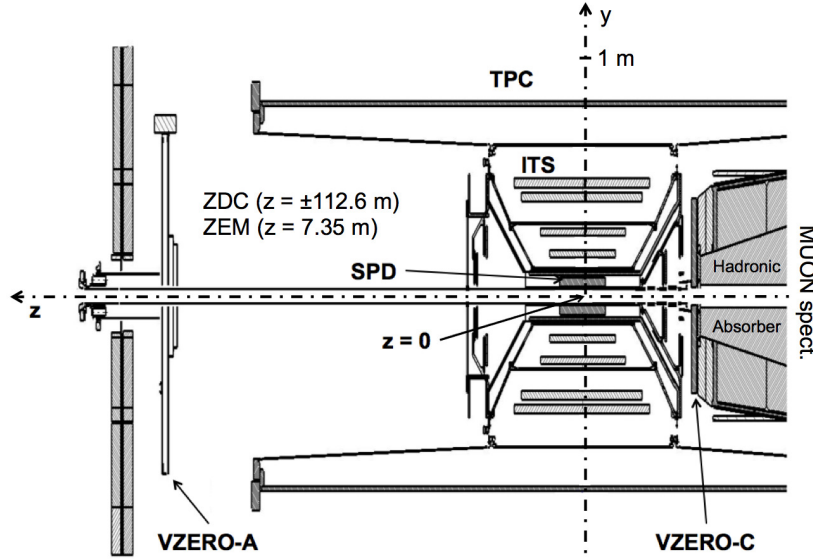


Figure 4.7: Placement of the V0A and V0C arrays within the ALICE detector. Taken from [203].

- $MB_{\text{AND}}$  defined as a coincidence of signals from both VOA and VOC and the LHC bunch crossing signal:

$$(V0A \&\& V0C) \&\& LHC_{\text{bunchX}}.$$

This trigger was used from 2011 further on after the increase of the LHC luminosity.

- $MB_{\text{AND}}$  for rare signals which is defined as coincide of previously defined  $MB_{\text{AND}}$  and a signal from detector triggering on specific rare event topology, such as the Muon Spectrometer:

$$(V0A \&\& V0C) \&\& LHC_{\text{bunchX}} \&\& MUON.$$

In Pb–Pb collisions, the V0 issues a MB trigger defined as a coincidence of V0A and V0C, and a centrality trigger for either 0 – 10% or 0 – 50% centrality range.

The beam-induced background events occur when one of the incoming beams collides with the residual gas in the beam-pipe or when the halo of one of the beams interacts with the components of the accelerator. Such events can be separated from physical interactions based on the arrival time of the produced particles into both arrays. The online selection places a coincidence window of 8 ns around the beam-beam timing from the accelerator [203]. The offline selection relies on the time of flight of each array. Only events with positive time of flight in both arrays are accepted, as illustrated in Fig. 4.8.

Finally, the integrated luminosity is calculated as a ratio of number of minimum bias triggered events  $N_{V0\text{AND}}$  and total cross section  $\sigma_{V0\text{AND}}$  extracted from the van der Meer scan [204]:

$$\mathcal{L}_{\text{int}} = \frac{N_{V0\text{AND}}}{\sigma_{V0\text{AND}}}. \quad (4.2)$$

#### 4.2.2.2 T0 detector

The T0 [202] consists of two arrays of Cherenkov detectors on either side from the IP. The T0A sits at a distance of 375 cm from the nominal IP, covering pseudorapidity range  $4.61 < \eta < 4.92$ . The T0C on the opposite side from the IP needs to be much closer due to the presence of muon absorber, at a distance of 72.7 cm from the nominal IP, translating into  $-3.28 < \eta < -2.97$ . The placement of the T0 within ALICE is shown in Fig. 4.9.

The T0 provides a start time  $t_0$  for TOF, which is computed as the average of time signals from both T0A and T0C:

$$t_0 = \frac{t_{T0A} + t_{T0C}}{2}. \quad (4.3)$$

It also separates beam-gas interactions from physics, and provides minimum bias and multiplicity triggers. The dead time of the detector must be shorter than the bunch crossing in the collider, i. e.  $< 25$  ns.

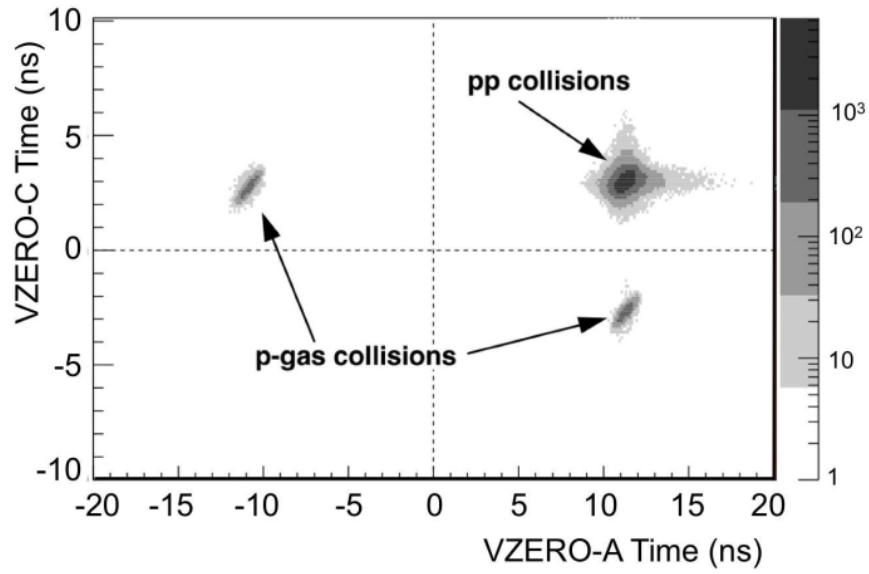


Figure 4.8: Time of flight of the particles detected in V0C versus V0A. The dashed line intersection represents the time of the collisions at the IP. Taken from [203].

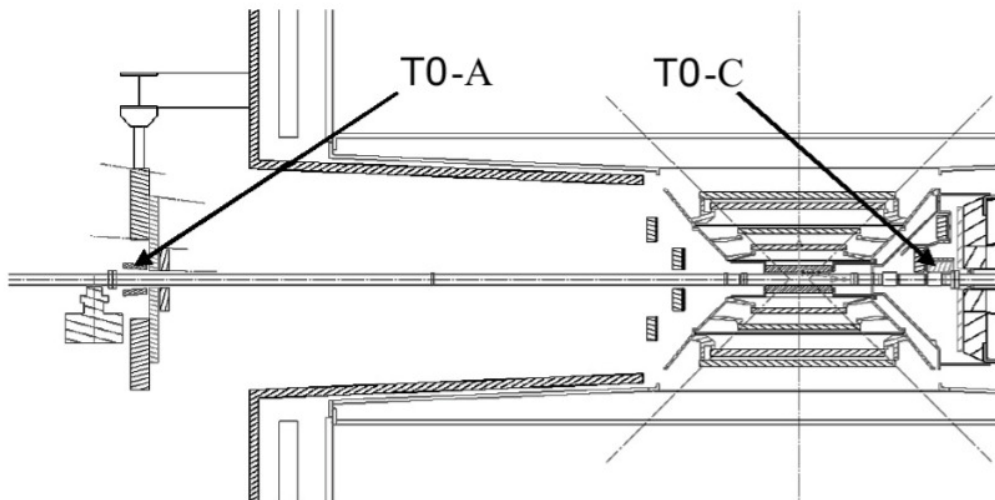


Figure 4.9: Layout of the T0 arrays inside the ALICE detector. Taken from [205].

### 4.2.2.3 Zero Degree Calorimeter

The Zero Degree Calorimeters (ZDC) [206] is a set of hadronic calorimeters at  $z = \pm 113$  m on either side of the IP [191]. Installed were two sets of hadronic calorimeters - one to measure spectator protons (ZP) and one to measure spectator neutrons (ZN). The magnetic field in the LHC deflects protons from the bunch while the neutrons continue travelling along the beam axis. Both hadronic detectors consist of quartz fibre sampling calorimeters, which combines quartz fibres coupled to PMTs with a dense tungsten (for ZN) or brass (ZP) absorber. The hadronic calorimeters are complemented by a set of electromagnetic calorimeters (ZEM) at  $z = 7$  m from IP on the opposite side from the Muon Spectrometer.

The ZDC measures the energy released by spectators to measure number of participants and thus the centrality of the collision. ZDC also provides information on the reaction plane. The ZEM help to distinguish between central and ultraperipheral collisions, as both would have a similar response in ZN and ZP. The ZEM detects energy of  $\gamma$  and  $\pi$  at forward rapidity, which has a monotonic dependence on the centrality of the collision.

## 4.3 The Muon Spectrometer

The Muon Spectrometer [207] was designed to measure the dimuon decays of heavy quarkonia (namely  $J/\psi$ ,  $\psi(2S)$ ,  $\Upsilon(1S)$ ,  $\Upsilon(2S)$ , and  $\Upsilon(3S)$ ), low mass vector mesons ( $\rho$ ,  $\omega$ ,  $\phi$ ), and the vector gauge bosons  $W^\pm$  and  $Z^0$ . The spectrometer also measures the open heavy flavour (D- and B-mesons) from their semi-leptonic muon decays.

The detector is positioned in the forward region and covers the pseudorapidity window  $-4.0 < \eta < -2.5$  and is able to reconstruct heavy flavour hadrons over a wide  $p_T$  range down to zero. The forward position with respect to the interaction point allows to probe two different rapidity and hence Bjorken  $x$  regions (recall Eq. 2.14) in asymmetric collision systems such as p-Pb.

The rapidity in the centre-of-mass frame  $y_{\text{cms}}$  in asymmetric collisions is shifted with respect to the laboratory system  $y_{\text{lab}}$  by a value depending on the charge and atomic numbers of the two nuclei

$$\Delta y = \frac{1}{2} [\ln(Z_1 A_1) - \ln(Z_2 A_2)]. \quad (4.4)$$

In p-Pb collisions, the shift is

$$\Delta y = \pm 0.465.$$

The p-Pb data are measured with ALICE in two beam configurations, a schematic view of the two cases is shown in Fig. 4.10:

- p-Pb collisions, when the proton comes towards the spectrometer and the lead ion comes from the side of the spectrometer (left panel). The centre-of-mass rapidity is  $2.03 < y_{\text{cms}} < 3.53$ . We call this the **forward rapidity** region. Alternatively, we can use the term **p-going direction** as it is the proton that comes to the spectrometer.
- Pb-p collisions, when the proton comes from the direction of the spectrometer and it is the lead ion that comes towards the spectrometer (right panel). The centre-of-mass rapidity is  $-4.46 < y_{\text{cms}} < -2.96$ . This is the **backward rapidity** region, or the **Pb-going direction**.

### 4.3.1 Detector design

Starting from the interaction point, the Muon Spectrometer consists of the following components: (i) the frontal absorber, followed by (ii) a set of ten planes of tracking chambers coupled to (iii) a dipole magnet to bend the tracks of charged particles, after which comes (iv) an iron wall that together with (v) shielding surrounding the beam axis protects (vi) a set of four planes of trigger chambers, which must be also protected from the background generated by the accelerator by (vii) a rear absorber from behind. The schema of the detector is shown in Fig. 4.11.

#### 4.3.1.1 Absorbers and shielding

The Muon Spectrometer is equipped with a set of absorbers that protect it from the high flux of secondary particles produced in central Pb-Pb collisions.

The **front absorber** is a conical structure of length  $l_{\text{abs}} \sim 4$  m, situated inside the solenoidal magnet at a distance of  $\sim 90$  cm from the IP. Its purpose is twofold:

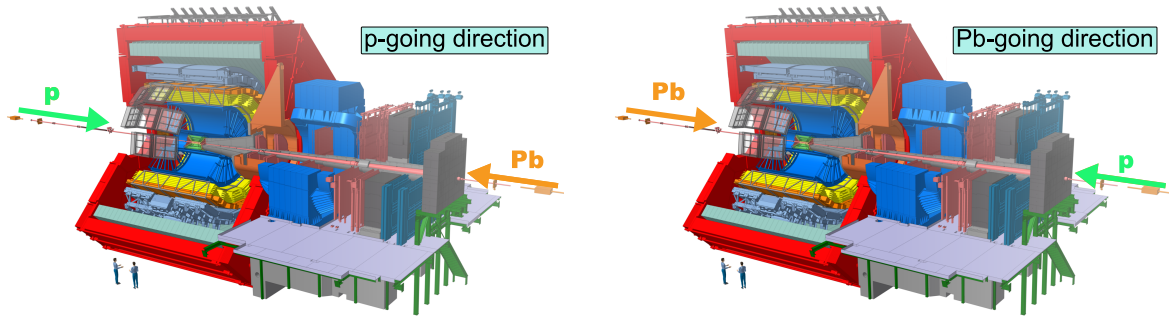


Figure 4.10: The p-Pb and Pb-p beam configuration in ALICE.

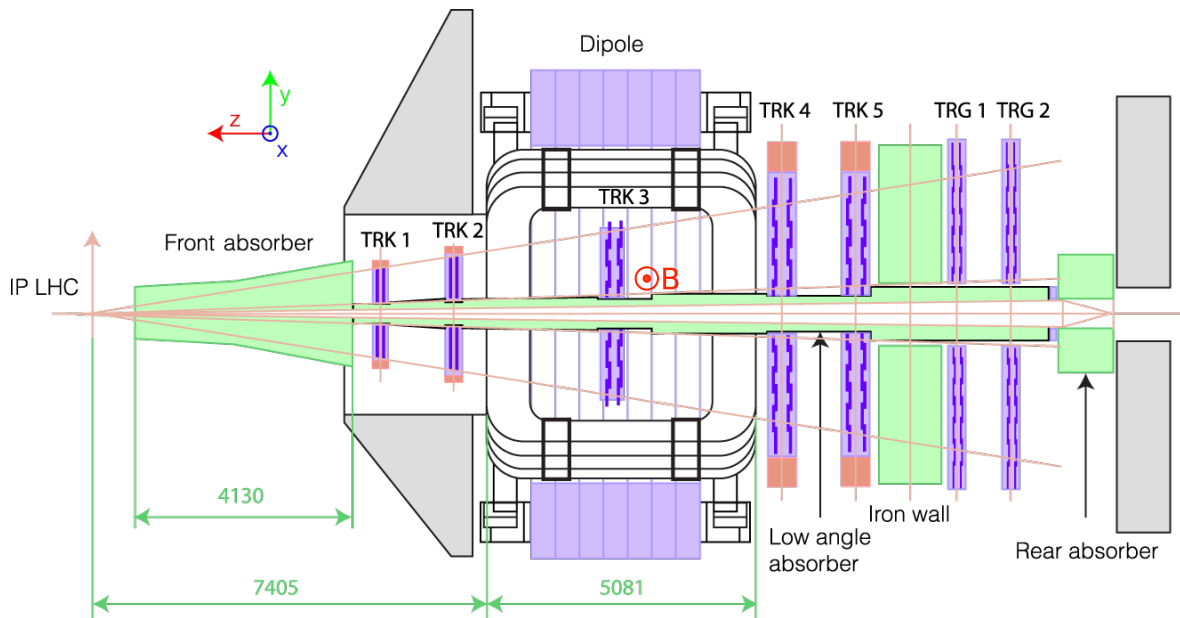


Figure 4.11: Schema of the Muon Spectrometer.

- To reduce the flux of hadrons and photons produced in the interaction vertex.
- To reduce the background of secondary muons from decays of pions and kaons, and the background from secondary particles produced in the absorber itself.

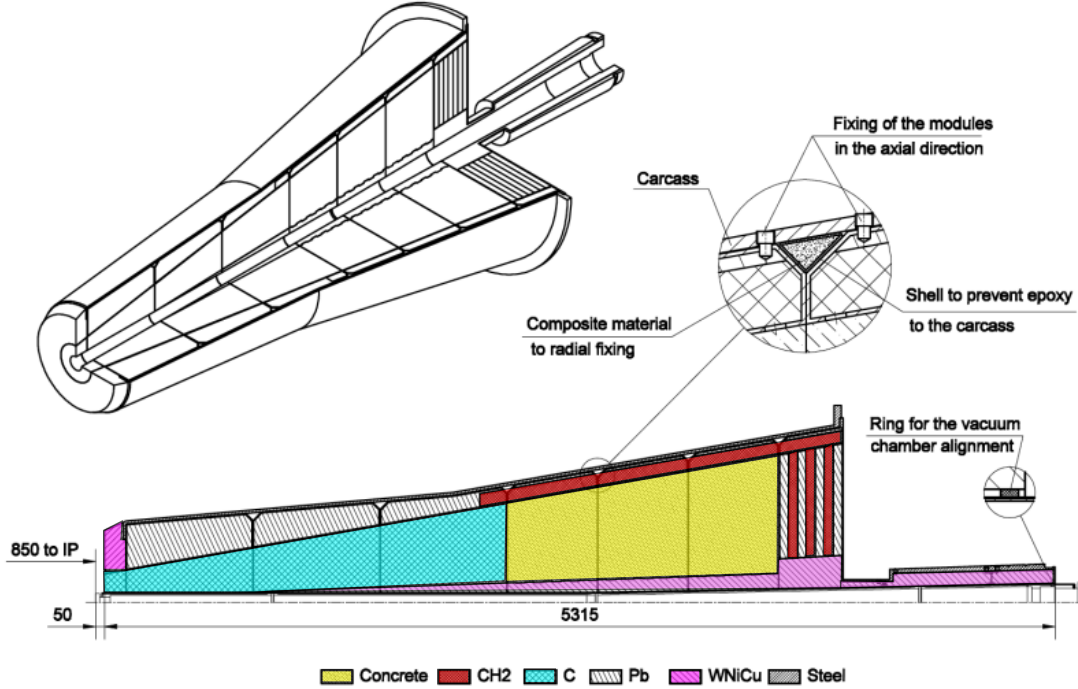


Figure 4.12: Schema of the front absorber of the Muon Spectrometer. Taken from [207].

Fig. 4.12 shows the internal structure of the absorber. The body of the absorber is composed of light materials, i. e. carbon and concrete, to limit multiple small-angle scatterings and energy loss of the muons. In contrast, the rear end of the absorber is composed of dense materials (W, Pb, steel) to filter the secondary particles produced in the absorber. The surface of the absorber is covered by lead and steel to prevent back-scattering of particles into the TPC.

The beam pipe is covered by a **beam shield** all along the length of the Muon Spectrometer. The shield comes in a form of conical tube made out of dense materials such as W, Pb and stainless steel. The shield reduces the background originating in the interactions of low angle particles with the beam pipe.

While the absorber and the beam shield are sufficient to screen the Muon Chambers (MCH), the Trigger Chambers (MTR) require additional protection. For this reason, they are separated from the MCH by a **muon filter** - an iron wall of thickness  $\sim 1.2$  m. In combination with the front absorber, the wall will prevent muons with momentum below  $p \approx 4$  GeV/ $c$  to reach the MTR.

The MTR is also protected by an iron **rear absorber** from the background generated by beam-gas interactions in the beam pipe. Such background is very high mainly during pp data taking periods, since during those LHC provides low luminosity beams. Particle production scales with luminosity while the machine induced background depends on the beam current [208].

#### 4.3.1.2 Tracking Chambers

The tracking system consists of a set of ten planes of Multi-Wire Proportional Chambers (MWPC) with cathode pad read-out, grouped into five stations. The stations are coupled to a dipole magnet of  $3 \text{ T} \cdot \text{m}$  that bends the tracks. The first two stations are located immediately downstream from the IP and the front absorber. The third station is placed inside the dipole magnet. The last two are placed between the dipole magnet and the muon filter. The active area of each station grows with the distance from the IP.

To minimise multiple scattering of the muons in the chambers, they are constructed from lightweight composite materials. This limits their thickness in terms of radiation length<sup>5</sup> to  $\sim 0.03X_0$ . Two different geometries are used for the chambers. Stations 1 and 2 have a quadrant geometry, while Stations 3, 4 and 5 have a rectangular (slat) geometry, see Fig. 4.13.

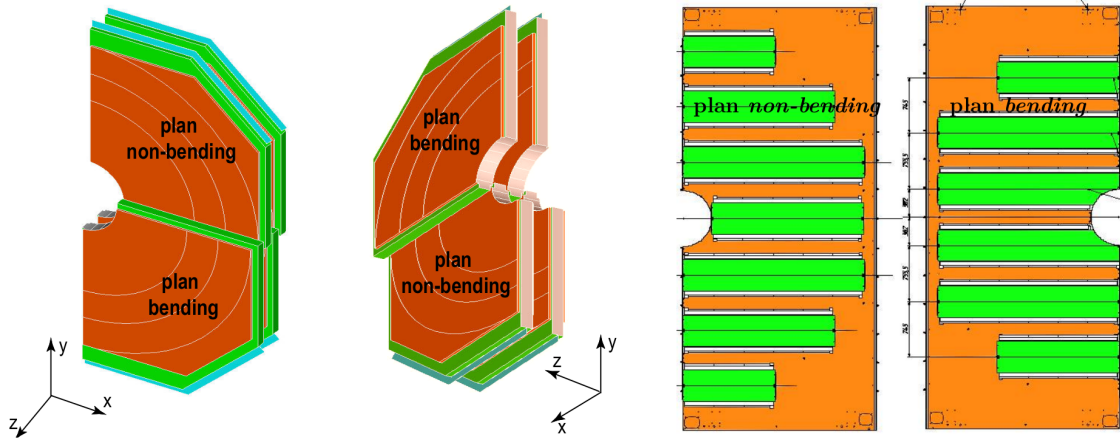


Figure 4.13: Schema of detection elements used in MCH. The quadrants used in the Stations 1 and 2 are shown on the left. The slats of the Stations 3, 4 and 5 are pictured on the right. Taken from [209].

Each MWPC constitutes of a central plane of anode wires sandwiched between two cathode planes. The space between the anode and the cathodes is filled with gas Ar + CO<sub>2</sub> (80/20). High voltage of  $\sim 1600$  V is applied to the anode plane, creating an internal electric field. The field lines are parallel and the field nearly constant in most of the volume save for the region very close to the wires where the field behaves as  $\propto 1/r$ . A schema of the field configuration is shown in Fig. 4.14a. A charged particle crossing the detector volume ionises the gas. The produced electrons travel towards the anode. In the immediate proximity of the wire, the field is high enough for the electrons to unleash an avalanche. The electrons are then captured by the anode while the ions travel towards the cathode. The cathodes are segmented in perpendicular directions as shown in Fig. 4.14b. The plane that has finer segmentation in the y-direction is called bending plane, since the dipole magnetic field bends the tracks in y-direction. The plane that has finer segmentation in x-direction is called non-bending plane. The distribution of charge in these two planes allows for 2D localisation of the hit.

Mixtures of noble gas with organic or inorganic quenchers are usually used in MWPCs. Argon is usually used as the active gas due to its low cost and higher specific ionisation. The disadvantage of using Ar is that excited atoms Ar\* produced in the avalanche may de-excite via emission of photon, which would be able to ionise the cathode and cause another avalanche. The CO<sub>2</sub> serves as a quencher, which in principle means that its molecules absorb the photons emitted by Ar\*.

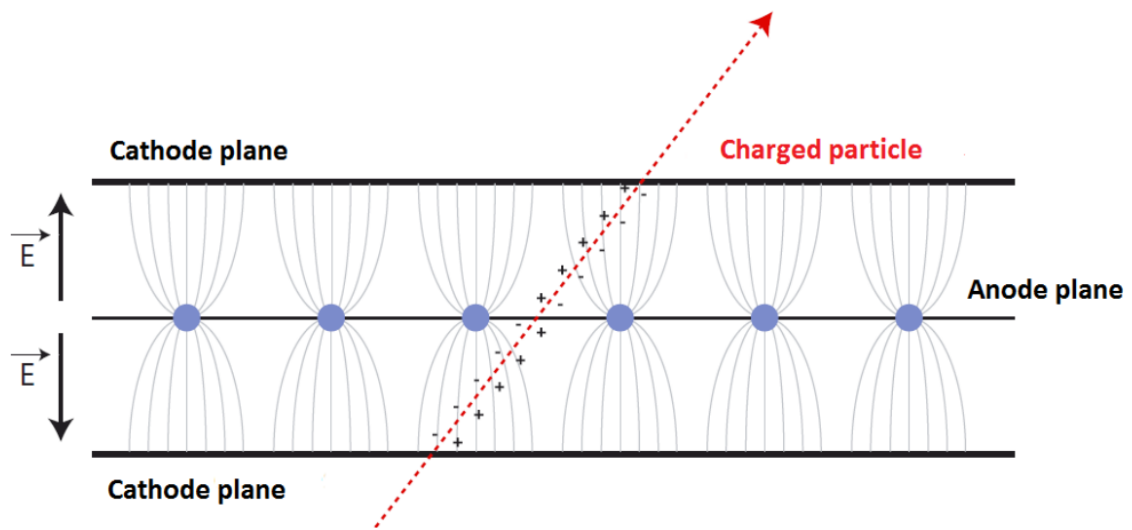
#### 4.3.1.3 Trigger Chambers

The Muon Trigger (MTR) consists of four planes of Resistive Plate Chambers (RPC) operating in streamer mode, grouped into two stations of two planes each. The stations are located behind the muon filter at a distance of  $\sim 16$  m from the IP, with a spacing of 1 m between the two stations. The chambers have spatial resolution below 1 cm, necessary to cut for low  $p_T$  muons originating in decays of pions and kaons. The timing resolution of the chambers is  $\sim 2$  ns to identify bunch crossing. The system has two programmable cuts<sup>6</sup> - low  $p_T$  cut ( $p_T^\mu \gtrsim 0.5$  GeV/c) and high  $p_T$  cut ( $p_T^\mu \gtrsim 4$  GeV/c) to reduce the combinatorial background in  $J/\psi$  and  $\Upsilon$  analyses respectively. The following trigger inputs are usually defined for muon data taking:

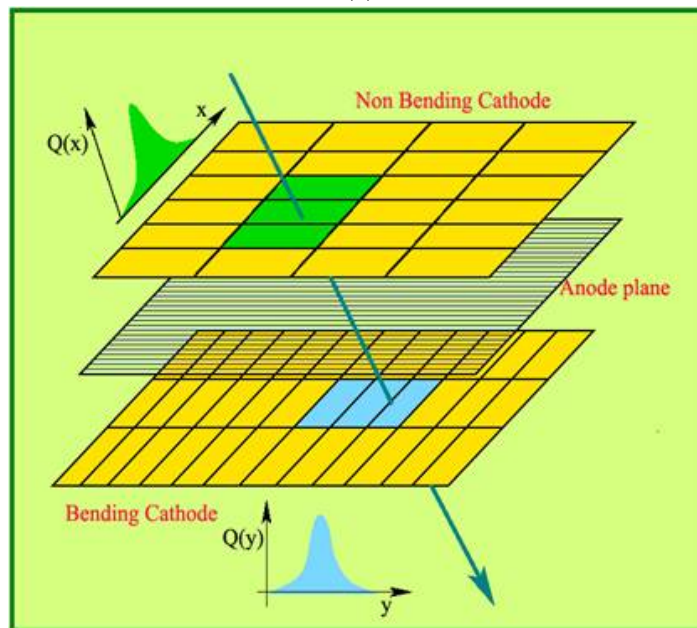
- at least one reconstructed muon satisfying the low  $p_T$  cut (0MSL),

<sup>5</sup>Radiation length  $X_0$  is a characteristic of material and denotes the distance that a charged particle moving in a straight line can travel through this material before its energy is decreased to  $1/e$  of its original value.

<sup>6</sup>The quoted online cut values were set for data taking campaigns of pp at  $\sqrt{s} = 5.02$  TeV and p-Pb at  $\sqrt{s_{NN}} = 8.16$  TeV. Each data taking period can have a priori different thresholds.



(a)



(b)

Figure 4.14: (a) Field configuration inside a MWPC. Taken from [210]. (b) Working principle of a MWPC inside the MCH. [211].

- at least one reconstructed muon satisfying the high  $p_T$  cut (0MSH),
- at least one reconstructed unlike signed dimuon pair satisfying the low  $p_T$  cut (0MUL),
- at least one reconstructed like signed dimuon pair satisfying the low  $p_T$  cut (0MLL).

RPCs are characterised by their good spatial and timing resolution and make excellent muon trigger detectors for LHC experiments. Operating in streamer mode means that the field inside the active volume is kept intense enough to generate limited discharges, which are localised in the proximity of the path of the charged particle.

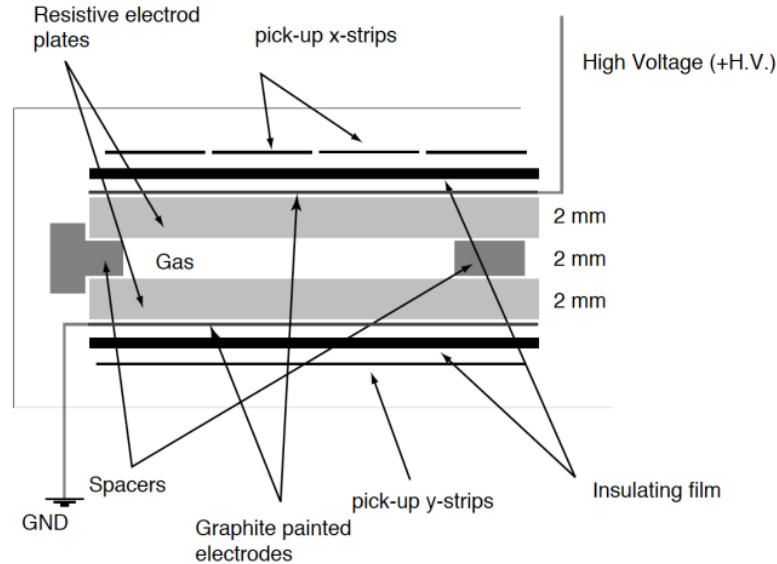


Figure 4.15: Structure of the RPC in Muon Trigger. Taken from [207].

Fig 4.15 shows the RPC design used in MTR. Each RPC consists of two parallel plates made out of low resistivity Bakelite, an anode and a cathode. The electrodes are coated with polymerised flaxseed oil<sup>7</sup> to smoothen their surface as a prevention of discharges on structures found on the plate. They are separated by  $\sim 2$  mm gap filled with a gas mixture<sup>8</sup>  $\text{Ar} + \text{C}_2\text{H}_2\text{F}_4 + \text{i-butane} + \text{SF}_6$  (50.5/41.3/7.2/1). Each electrode is covered by an insulating film connected to metal stripes. The two sets of stripes are in perpendicular direction to one another, so that one gives position along the  $y$ -direction (“bending”) and the other in  $x$ -direction (“non-bending”).

Bakelite is in general a high resistivity material<sup>9</sup>. High resistivity materials prevent the charge from spreading too much, thus enabling a better localisation. On the other hand, low resistivity materials allow for quick read-out. Low resistivity Bakelite presents a good compromise between the two and enables operation at higher particle flux.

The principle of the trigger algorithm is visualised in Fig. 4.16. The idea is to estimate the  $p_T$  of the tracks during data taking, so that tracks with  $p_T \geq p_T^{threshold}$  trigger the read-out. The algorithm projects the reconstructed position  $(X_1, Y_1, Z_1)$  from the first trigger chamber (MT1) into the second chamber (MT2), assuming infinite transverse momentum ( $p_T \rightarrow \infty$ , i. e. no deviation of track in presence of magnetic field). The “infinite momentum” track must pass through the SPD vertex. The algorithm then reconstructs the direction of the track between the two chambers from hit coordinates in both chambers MT1  $(X_1, Y_1, Z_1)$  and MT2  $(X_2, Y_2, Z_2)$ . The deviation of the two lines  $\delta_Y$  is evaluated. If the deviation is equal or greater to a pre-set threshold,  $\delta_Y \geq \delta_Y^{threshold}$ , the track is rejected.

<sup>7</sup>Flaxseed oil polymerises (“dries out”) quickly when in contact with oxygen.

<sup>8</sup> $\text{Ar} + \text{C}_2\text{H}_2\text{F}_4 + \text{i-butane}$  is often used in RPCs. Ar is the active gas while the i-butane and tetrafluoroethane act as quencher. The  $\text{SF}_6$  serves as a quencher for the streamer mode as it captures electrons and thus prevents the avalanche from expanding into a large volume.

<sup>9</sup>Resistivity range of Bakelite is at the order of  $10^9 - 10^{11} \Omega \cdot \text{m}$ .

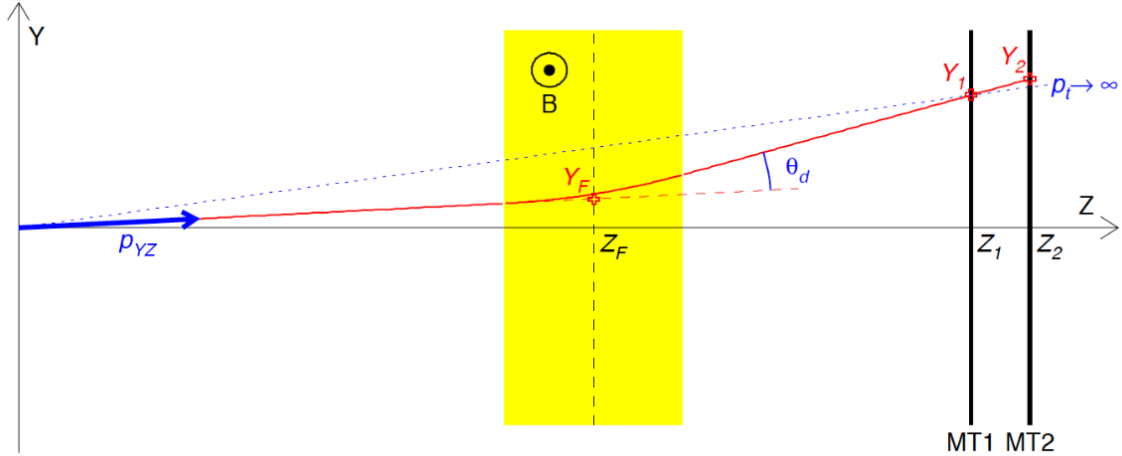


Figure 4.16: Principle of the Muon Trigger online  $p_T$  cut. Taken from [207].

### 4.3.2 Reconstruction of muon tracks

We will briefly explain how muon tracks are reconstructed - first in the MCH and then matched with a track in MTR.

The tracking algorithm [212] combines the clusters from individual MCH stations into track candidates. The reconstruction starts with cluster information from Stations 4 and 5, which are the farthest from the IP and are therefore exposed to lower track density than the Stations 1-3.

1. For all possible combination of clusters in Station 5 or 4, the hit position, momentum direction and impact parameter at IP are computed. Then the momentum is estimated assuming the tracks originated in the vertex and taking into account the average magnetic field of the dipole. All parameters are estimated with an error, which is also kept. Selected candidates must pass cuts on momentum and impact parameter. The track candidates are then extrapolated from Station 5 to Station 4 or vice-versa, after which the track parameters are recomputed. At least one cluster is required in the other station.
2. Candidates sharing identical combinations of clusters are removed. Candidates that do not pass cuts on momentum and impact parameter are also rejected.
3. The same process is repeated consecutively for Stations 3, 2, and 1. The step is successful if at least one cluster per station is compatible with the track. If several clusters per chamber are found, the track is duplicated to consider all options.
4. Tracks sharing one or more clusters are removed. Only the candidate with the largest amount of clusters or with the best fit (determined via cut on  $\chi^2$ ) in case of equal number of clusters is kept.
5. The reconstructed track is matched with a trigger track.
6. Finally the reconstructed tracks are extrapolated to the vertex (measured with the SPD). The track parameters are corrected for energy loss and multiple scattering in the front absorber.

## 4.4 Trigger and Data Acquisition

Most analyses require input from a limited number of detectors. Inputs from different detectors are combined into **clusters** - groups of detectors that are read out together. Several clusters can be read out simultaneously, at different paces. The detectors in one cluster are thus not limited by the dead time of those included in another cluster. This is particularly interesting for fast detectors (e. g. SPD, MCH, MTR, ...) which can then run at a different rate than for instance the TPC. A detector can be included in several clusters at the same time.

The trigger inputs are combined into **trigger classes**. The following trigger classes are usually defined in muon data taking:

- The dimuon trigger CMUL7-B-NOPF-MUFAST, which is given by a coincidence of signals in V0A and V0C systems and of a pair of unlike sign muons satisfying the low  $p_T$  threshold in the Muon Spectrometer.
- The low  $p_T$  single muon trigger CMSL7-B-NOPF-MUFAST, which is given by a coincidence of signals in V0A and V0C systems and of a muon satisfying the low  $p_T$  threshold in the Muon Spectrometer.
- The high  $p_T$  single muon trigger CMSH7-B-NOPF-MUFAST, which is given by a coincidence of signals in V0A and V0C systems and of a muon satisfying the high  $p_T$  threshold in the Muon Spectrometer.
- The like sign dimuon trigger CMLL7-B-NOPF-MUFAST, which is given by a coincidence of signals in V0A and V0C systems and of a pair of like signed muons satisfying the low  $p_T$  threshold in the Muon Spectrometer.

In muon data taking periods, the minimum bias (MB) triggers are usually downscaled to allocate more bandwidth to the rare triggers listed above. In this text, we will briefly list the MB triggers used in the analyses in Chapters 6 and 7:

- CINT7-B-NOPF-MUFAST, which is defined by a coincidence of signals in V0A and V0C.
- C0TVX-B-NOPF-CENTNOTRD, which is defined as a coincidence of signals in T0A and T0C and fulfilling a condition of having a T0 vertex within  $|z| < 30$  cm from the IP [213].

The name of each trigger class is formed to contain information on the trigger input (e.g. “CMUL7” means 0MUL input with V0AND), on the bunch crossing mask from LHC (“B” indicates bunches from both beams), on the online timing vetoes around the time of the actual event called *past-future protection* (“NOPF” means there is no such condition applied) and on the cluster of detectors read out. In the two datasets analysed in Ch. 6 and 7, “MUFAST” cluster includes SPD, MCH, MTR, T0, V0, AD, and in case of p-Pb also ZDC.

#### 4.4.1 Trigger system

The Central Trigger Processor (CTP) [214] generates the trigger decision based on the trigger signals from the detectors. The rates of selected events can be scaled down in order to minimise the used band-width of the Data Acquisition system (DAQ). As an example, CINT7-B-NOPF-MUFAST are scaled down to 10% in certain periods - in other words, only one in ten admissible events is accepted. The trigger inputs are evaluated once every machine clock cycle of  $\sim 25$  ns.

The CTP selects events with different features on a three level basis [191]:

**Level 0 (L0)** is the fastest trigger level. At this level, the vetoes on e. g. SPD, MTR, V0, and T0 are made. The latency of the L0 trigger, i. e. the time between the interaction to the arrival of the trigger signal to the read-out detectors, is  $\sim 0.9 \mu\text{s}$ .

**Level 1 (L1)** is supplied by inputs from TRD and ZDC in the events accepted by L0. The latency of the L1 trigger is  $\sim 6.5 \mu\text{s}$ .

**Level 2 (L2)** decision is taken after  $\sim 100 \mu\text{s}$  from the interaction. This delay corresponds to the drift time of electrons in the TPC.

The information on counts for all trigger classes at each of these levels before (L0b) and after (L0a) the CTP decision is stored in the so called **scalers**.

The instance in which the CTP does not generate the L0 signals is called the **CTP veto**. Some examples of the CTP vetoes are i) at least one detector in the cluster is busy, ii) the trigger input does not match with a bunch crossing, iii) or the downscaling of certain trigger classes to allocate more DAQ band-width to rare events.

The CTP is complemented by a software-only High Level Trigger (HLT) [215]. It allows for implementation of a more sophisticated trigger criteria than the CTP. The HLT processes already read-out data from the detectors and accepts or rejects events based on an online analysis of the output. The HLT is also dedicated to the compression of the accepted ALICE data.

### 4.4.2 Data reconstruction

The accepted events usually undergo several cycles of reconstruction called **passes**. Results of each reconstruction pass are stored in the Event Summary Data (ESD) files. These include information from the different detectors that is later used for analysis, calibration, and detector performance studies. The quality assurance (QA) analysis is performed on ESD data. The ESDs are refiltered into the Analysis Object Data (AOD) files, which contain reduced information essential for a specific type of analysis.

Calibration and alignment data are produced during the first reconstruction pass. They are stored in the Offline Condition Database (OCDB) together with scalers and information on magnetic field. The information filed in the OCDB is accessed in all reconstruction, analysis, and simulation of the data.

## Summary

ALICE is a dedicated heavy-ion experiment supplied by beams from the LHC. The detector consists of nearly twenty subsystems grouped into two main parts: the Central Barrel at midrapidity and Muon Spectrometer in the forward region  $-4 < \eta < -2.5$ . The Muon Spectrometer measures muons coming from decays of quarkonia, low mass vector mesons, from gauge vector mesons and Drell-Yan, and from decays of open heavy flavour. The spectrometer consists of a set of tracking chambers coupled to a dipole magnet, a set of trigger chambers at the further side of the interaction point and is protected by a set of absorbers. We reviewed the working principle of the tracking and trigger chambers and explained the track reconstruction.



## EFFICIENCY STUDIES OF THE MUON TRACKING CHAMBERS

This chapter shall focus on the studies of the tracking efficiency of the Muon Spectrometer. First the acceptance-efficiency will be defined and the methods how to compute it explained. Then we will review the various sources of uncertainty affecting the determination of the acceptance-efficiency. More details will be given on the tracking efficiency estimation and evaluation of its uncertainty. Finally we will discuss results of estimation of the uncertainty on tracking efficiency in p–Pb collisions at  $\sqrt{s_{NN}} = 8.16$  TeV.

### 5.1 Acceptance and efficiency of the Muon Spectrometer

In order to obtain the produced number of particles in the collision one needs to correct the data by the detector acceptance-efficiency factor  $A\varepsilon(p_T, y)$ :

$$\frac{d^2 N^{corr}(p_T, y)}{dp_T dy} = \frac{1}{A\varepsilon(p_T, y)} \frac{d^2 N^{rec}(p_T, y)}{dp_T dy}. \quad (5.1)$$

The reliability of the measured cross section thus depends on the precision with which we are able to determine these detector effects.

The acceptance-efficiency is defined as the ratio of the number of all reconstructed particles in the detector to the number of all particles produced within the detector acceptance

$$A\varepsilon = \frac{N_{reconstructed}}{N_{produced}}. \quad (5.2)$$

Acceptance is a purely geometrical factor. In the  $J/\psi$  analyses,  $A\varepsilon$  depends on the kinematics and polarisation of the  $J/\psi$  as well as on the kinematics of its daughter muons. The efficiency takes into account the response of the spectrometer, such as the state of its electronics during the data taking or the status of the high voltage applied to the chambers. It gives the ratio of all particles that are reconstructed in the detector and the number of particles produced within its acceptance. In muon analyses, the acceptance and efficiency are considered together in the combined acceptance-efficiency factor  $A\varepsilon$ . The  $A\varepsilon$  factor contains both the terms of the tracking and the trigger efficiencies.

A typical  $A\varepsilon(p_T, y)$  of the Muon Spectrometer for the  $J/\psi$  particle is shown in Fig. 5.1. In transverse momentum,  $A\varepsilon$  has the minimum at  $p_T \sim M_{J/\psi}$  which marks the point where the opening angle between the daughter muons is just large enough so that one of the particles has the largest probability to escape the spectrometer. Below this value at  $p_T \sim 0$ , the  $J/\psi$  decay is symmetric with respect to the beam axis so that either both muons escape or both pass through the detector. At  $p_T > M_{J/\psi}$  the acceptance-efficiency increases as the daughter muons tend to be proportionally more collinear with the mother particle. In rapidity, the maximal  $A\varepsilon$  is at the centre of the detector and decreases towards the edges. This is due to the  $J/\psi$  being produced close to the edge and the subsequent escape of one or both of the decay muons from the detector volume.

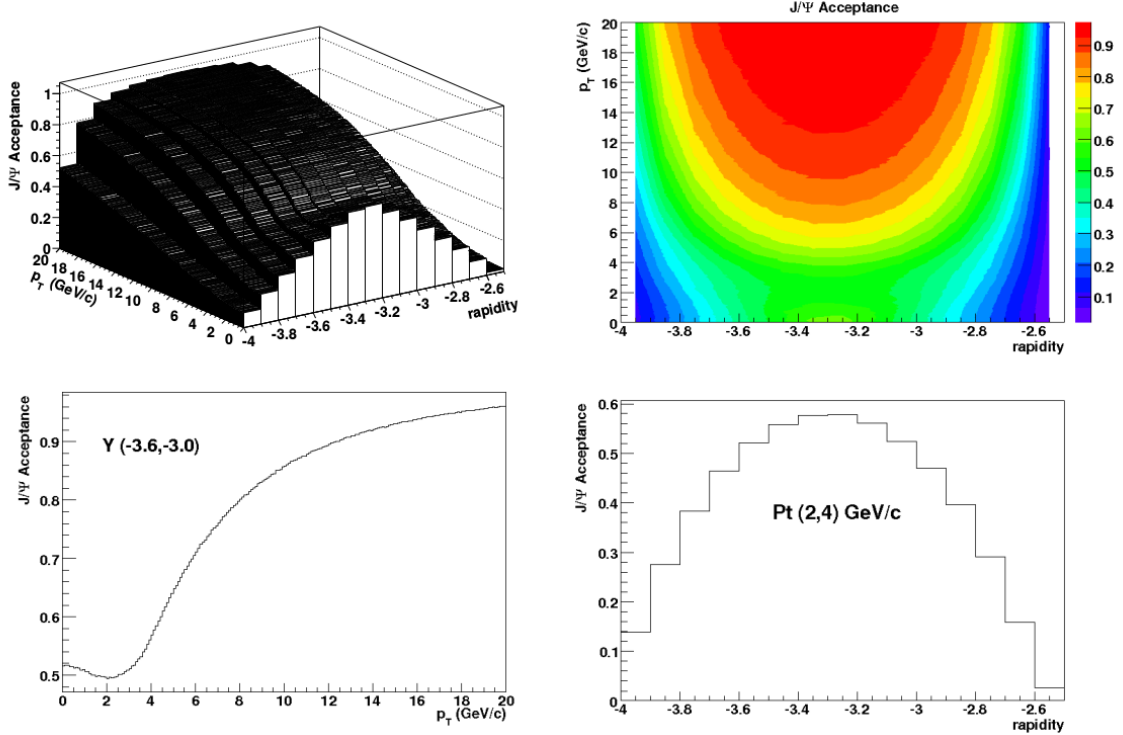


Figure 5.1: Example of  $A\varepsilon$  of the Muon Spectrometer as a function of  $p_T$  and  $y$ . The top row shows the two dimensional  $A\varepsilon(p_T, y)$ . The bottom row shows projections of  $J/\psi$  acceptance (left) into the  $p_T$  axis at  $-3.6 < y < -3.0$  and (right) into  $y$  axis at  $2 < p_T < 4$  GeV/c. Taken from [216].

## 5.2 Method to estimate the acceptance-efficiency of the Muon Spectrometer

For the  $J/\psi$ , the acceptance-efficiency  $A\varepsilon$  can be determined from Monte Carlo simulations as

$$A\varepsilon(p_T, y) = \frac{N_{MC}^{rec}(p_T, y)}{N_{MC}^{gen}(p_T, y)}, \quad (5.3)$$

where  $N_{MC}^{rec}$  stands for the number of selected<sup>1</sup> reconstructed particles in the MC and  $N_{MC}^{gen}$  denotes the number of generated particle in the MC. The number of generated  $J/\psi$  is proportional to the number of analysed events.

The generated  $J/\psi$  are decayed into muons using dedicated simulation packages. EvtGen [217] and PHOTOS [218] were used in the analysis presented in Chap. 6 of this work. The muons are then transported through a GEANT3 [219] model of the detector<sup>2</sup>. The status of the electronics and alignment of the detector during the corresponding data taking is also recovered from the Offline Condition Data Base (OCDB). The reconstructed simulated muons are then analysed using the same code as is run on data.

The  $p_T$  and  $y$  distributions of the generated  $J/\psi$  are tuned to the data using an iterative procedure, visualised in Fig. 5.2. The initial  $J/\psi$  are usually generated using a power-law distribution for  $p_T$  and a quadratic function for  $y$ . The number of generated and reconstructed  $J/\psi$  from the MC  $N_{MC}^{gen}$  and  $N_{MC}^{rec}$  are evaluated in each  $p_T$  and  $y$  bin. The efficiency is computed in each  $p_T$  and  $y$  interval from their ratio following Eq. (5.3). The corresponding number of reconstructed corrected  $J/\psi$  is computed in the data as  $N_{data}^{corr} = N_{data}^{rec}/A\varepsilon$  and is compared to  $N_{MC}^{gen}$  in the same  $p_T$  and  $y$  bin. The MC distributions, both reconstructed and generated, are then weighted by the ratio  $w = N_{data}^{corr}/N_{MC}^{gen}$ . This procedure is repeated until the ratio starts to fluctuate around unity, at which point the procedure reaches its maximal precision. New MC is finally produced using the tuned distributions, from which the  $A\varepsilon$  can be finally computed.

<sup>1</sup> $N^{rec}$  is obtained from MC using the same selection criteria and analysis task as is used on data.

<sup>2</sup>GEANT4 [220] may be also used to quantify differences that enter systematic uncertainties.

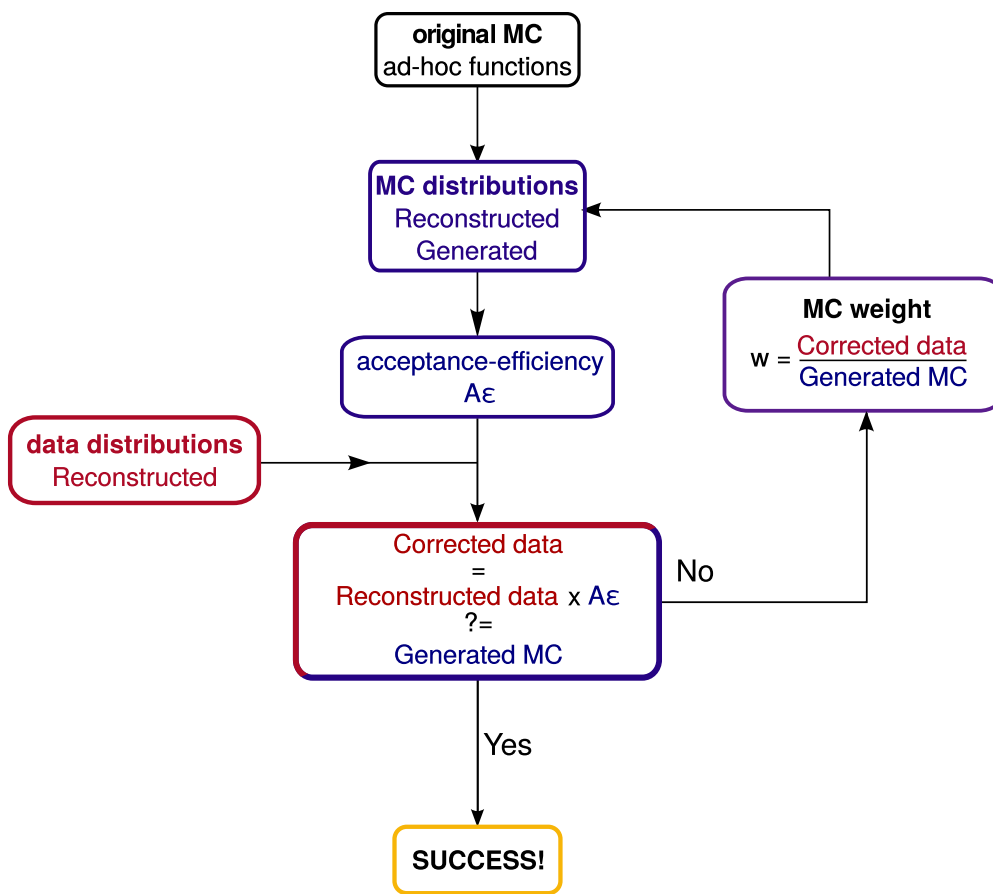


Figure 5.2: Schema of the iterative tuning of the MC.

### 5.2.1 Sources of systematic uncertainty on acceptance-efficiency

There are of course several sources of systematic uncertainty to be taken into account.

- Uncertainty on MC input. This source has several contributions:
  - (i) Run-by-run<sup>3</sup> changes of detector status can affect the final value. The  $A\epsilon$  of the detector is studied run by run to assure the detector conditions were stable.
  - (ii) One source of uncertainty on the input shape comes from the statistical uncertainty on the data points, which were used to tune the MC distributions. This uncertainty can be evaluated by randomly varying the data points around their respective central values. Such varied distributions are then one by one used to re-weight the MC and recompute the efficiency.
  - (iii) In case the low statistics of the data sample prevents multidimensional extraction in bins of  $(p_T, y)$ , the respective integration in one dimension may affect the result. To account for this source, the one dimensional  $p_T$  and  $y$  dependence can be weighted by distributions from different data samples where two dimensional extraction of signal was possible, the maximal spread of these new distributions gives the uncertainty.
- Uncertainty on tracking efficiency, described in detail in Sec. 5.3. The tracking efficiency of one chamber is defined as the number of tracked particles over the number of all traceable. The uncertainty estimation relies on comparison of these ratios between data and MC and studying the variation of this ratio using different kinematic cuts.
- Uncertainty on trigger efficiency. The trigger efficiency of a given chamber  $ch$  is defined as number of all tracks triggered in all chambers including  $ch$  over all triggerable (i. e. triggered in all three of the remaining chambers regardless of their fate in  $ch$ )

$$\epsilon_{ch} = \frac{N_{4/4}}{N_{3/4}^{ch}}.$$

The efficiency is estimated in all MTR local boards, which are its smallest detection elements (DE). An efficiency map is created from these local efficiencies.

Two contributions to the systematic uncertainty are considered:

- (i) The intrinsic efficiency is evaluated by comparing the efficiency in realistic MC simulations and MC simulation generated from modified efficiency map. The modified efficiency map is created by decreasing the efficiency in each DE by a factor  $\alpha$ . This factor is computed from the average uncertainty on the single muon  $A\epsilon$  obtained by changing the muon  $p_T$  cut on the tracks used to estimate the efficiency.
  - (ii) The other source of uncertainty is born from the application of a trigger threshold in  $p_T$ . The muon trigger has three different  $p_T$  cuts programmed:  $Ap_T$  for  $p_T^\mu \gtrsim 0.5$  GeV/ $c$ ,  $Lp_T$  for low- $p_T$  cut<sup>4</sup>, and  $Hp_T$  for high- $p_T$  cut. Two sets of weights are computed from the  $p_T$  dependent ratio of  $Lp_T$  and  $Ap_T$  in data  $\left(\frac{Lp_T}{Ap_T}\right)^{\text{data}}(p_T)$  and in MC  $\left(\frac{Lp_T}{Ap_T}\right)^{\text{MC}}(p_T)$ . These weights are then used to re-weight the  $Ap_T(p_T)$  distribution in MC. The ratio of  $N_{J/\psi}$  extracted for these two distributions is computed and its deviation from unity gives the uncertainty for single muon. The uncertainty on dimuon is taken as double the former.
- Uncertainty on tracking-trigger matching. The tracks from MCH and MTR are matched during reconstruction. The matched tracks need to pass a cut on the goodness of the fit in order to be accepted for analysis. The systematic uncertainty is estimated by changing the value of the matching cut in both data and MC and studying the effect this has on the  $A\epsilon$ .

## 5.3 Tracking efficiency of the Muon Spectrometer

The method to estimate the tracking efficiency described in this section can be used on both data and MC. The differences between the efficiency estimated in data and in MC provide a good estimate of the uncertainty on the tracking efficiency.

<sup>3</sup>A “run” corresponds to a time period of data taking during which the conditions in the experiment were stable.

<sup>4</sup>Low- and high- $p_T$  cuts are defined for each period.

### 5.3.1 Method to estimate tracking efficiency

The intrinsic efficiency of the MCH is estimated from data to verify how the simulations used to compute  $A\varepsilon$  describe reality. The method to estimate the tracking efficiency is based on the muon tracking algorithm and exploits the redundancy of chambers in the stations. The four possible options

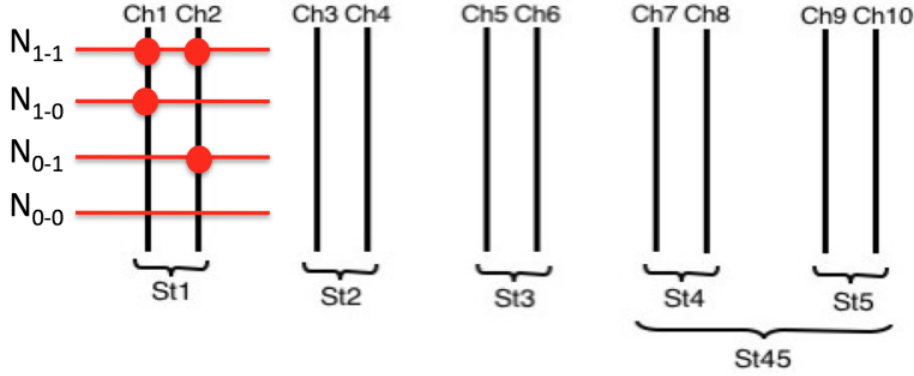


Figure 5.3: Schema of the MCH showing the arrangement of individual chambers and stations. Possible track passing responses are shown for Station 1. Stations 4 and 5 are considered as one ensemble (St45). Taken from [221].

of a station response for the first three stations are illustrated in Fig. 5.3 on the example of the first station. The tracks can leave a hit in both chambers ( $N_{ij}$ ), in one of the two chambers ( $N_{i0}$  and  $N_{0j}$ ) or it may leave no trace ( $N_{00}$ ). The total number of tracks passing the station is

$$N_{tot} = N_{ij} + N_{i0} + N_{0j} + N_{00}. \quad (5.4)$$

The efficiency of  $i$ -th chamber  $\varepsilon_i$  is independent from efficiency of  $j$ -th chamber  $\varepsilon_j$ . The number of tracks leaving a hit in both chambers  $N_{ij}$  is defined as

$$N_{ij} = \varepsilon_i \varepsilon_j N_{tot},$$

from where we can write  $\varepsilon_i$  as

$$\varepsilon_i = \frac{N_{ij}}{\varepsilon_j N_{tot}}.$$

The number of tracks leaving a hit in only the first chamber  $N_{i0}$  is defined as

$$N_{i0} = \varepsilon_i (1 - \varepsilon_j) N_{tot}.$$

Shuffling a bit the components of the last equation gives

$$\begin{aligned} \varepsilon_j N_{tot} &= N_{0j} + \varepsilon_i \varepsilon_j N_{tot} \\ &= N_{0j} + N_{ij}. \end{aligned}$$

Finally the efficiencies  $\varepsilon_i$  and  $\varepsilon_j$  can be expressed as

$$\varepsilon_i = \frac{N_{ij}}{N_{0j} + N_{ij}}, \quad (5.5)$$

$$\varepsilon_j = \frac{N_{ij}}{N_{i0} + N_{ij}}. \quad (5.6)$$

Note that all quantities in Eq. (5.5) and (5.6) can be computed from data and do not require simulations. For Stations 1-3, the efficiency of the  $m$ -th station can be then determined as probability of the muon being detected by at least one of its two chambers:

$$\varepsilon_{St(m)} = 1 - (1 - \varepsilon_i)(1 - \varepsilon_j). \quad (5.7)$$

For Stations 4 and 5, the efficiency is calculated as a whole due to the requirements of the tracking algorithm. The efficiency  $\varepsilon_{\text{St}(45)}$  is given as the probability of the muon being detected by at least three out of the four chambers:

$$\varepsilon_{\text{St}(45)} = \prod_{i=7}^{i=10} \varepsilon_i + \sum_{i=7}^{i=10} \left( (1 - \varepsilon_i) \prod_{j=7, j \neq i}^{j=10} \varepsilon_j \right). \quad (5.8)$$

The total tracking efficiency is then calculated as

$$\varepsilon_{\text{trk}} = \varepsilon_{\text{St}(1)} \varepsilon_{\text{St}(2)} \varepsilon_{\text{St}(3)} \varepsilon_{\text{St}(45)}. \quad (5.9)$$

The same exercise is used to extract the efficiency of smaller elements, e. g. individual detection elements (DE, equivalent to either a quadrant or a slat). The efficiency is estimated as a function of time or track kinematics ( $p_T, y, \varphi$ ).

### 5.3.2 Limitations due to dead zones in the detector

The method to estimate the tracking efficiency is biased by local correlations between the chambers. Two possible correlation effects may occur: correlated dead area (CDA) or anti-correlated dead area (ACDA). Both are visualised in Fig. 5.4.

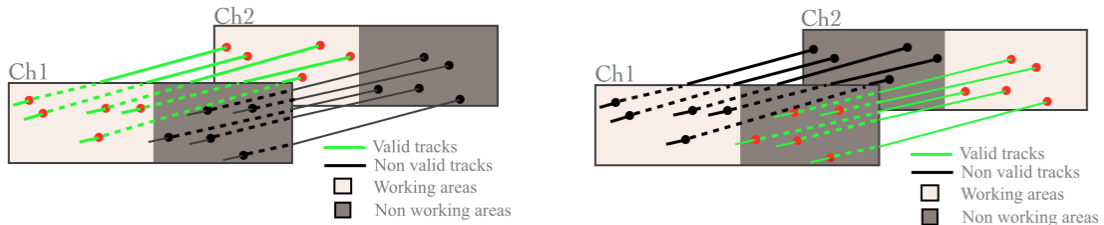


Figure 5.4: (Left) Correlated dead area and (right) anti-correlated dead area between the chambers of MCH. Taken from [221].

Suppose we want to estimate the efficiency in Station 1. Hence we study the tracks passing through Chambers 1 and 2. Now consider that half of the DEs in either chamber is not working. Therefore out of all the tracks passing St1, only half passes through the active area and the efficiency should be 50%. However, the method used to estimate tracking efficiency uses the redundancy of the chambers on the detector. In one extreme scenario, the halves which are not working overlap perfectly between the chambers (Left panel of Fig. 5.4). Therefore all tracks passing through the dead area in Ch1 pass also through the dead area in Ch2. Moreover, all tracks passing through the active area in Ch1 pass through the active area in Ch2. Now only 50% of all tracks passing through the station are detected. However, the method considers only tracks leaving at least one hit in either Ch1 or Ch2. Hence the efficiency is measured to be 100%. In the second extreme scenario, the dead and active areas in one chamber are swapped, see right side of Fig. 5.4. The active area in Ch1 overlaps the dead area in Ch2 and vice-versa. None of the tracks will be reconstructed in both chambers and the efficiency is thus measured as 0%. Clearly, the dead areas influence the measurement, the efficiency is overestimated in case of DCAs and underestimated in case of ADCAs. Correlation effects could be reduced by computing the efficiency for smaller elements than chambers (e. g. DEs). However, the current method uses simulations that carefully reproduce the dead zones in the detector during the corresponding data taking period. The same biases are thus expected in data and in MC.

## 5.4 Method to estimate the uncertainty on the tracking efficiency

The method to determine the uncertainty on the tracking efficiency of the Muon Spectrometer was developed in [222] and has been since refined [210, 221, 223]. A dedicated Twiki page was created as a part of this thesis to serve as a manual on estimation of this uncertainty [224].

First, the tracking efficiency must be computed from the data. The task code to compute the tracking efficiency is available in AliROOT<sup>5</sup>. The following kinematic cuts are applied to reject fake tracks or tracks that do not originate in the interaction vertex<sup>6</sup>:

- The track must be within the detector acceptance ( $-4 < \eta < -2.5$  and  $171^\circ < \theta_{abs} < 178^\circ$ ).
- The track from the tracking chambers must be matched with a track reconstructed in the trigger chambers with  $p_T^\mu \gtrsim 0.5$  GeV/ $c$ .
- The track must fulfil a cut on a distance of the projected muon vertex and the reconstructed vertex in the collision. The selection is applied on the  $pDCA$  distribution, which is a product of a track momentum  $p$  and the Distance of the Closest Approach (DCA), and is tuned for each data taking period. DCA is defined as the distance between the measured interaction vertex in the collision and the projected vertex of the reconstructed muon track, see Fig. 5.5. The DCA dispersion is inversely proportional to the momentum of the track  $DCA \propto 1/p$ . By putting a cut to this dispersion, one can reject fake tracks that do not originate from the IP.

Most of these cuts (except the one on  $pDCA$ ) are also applied in the analyses described in Chapters 6 and 7. The correct alignment must be also chosen from the OCDB.

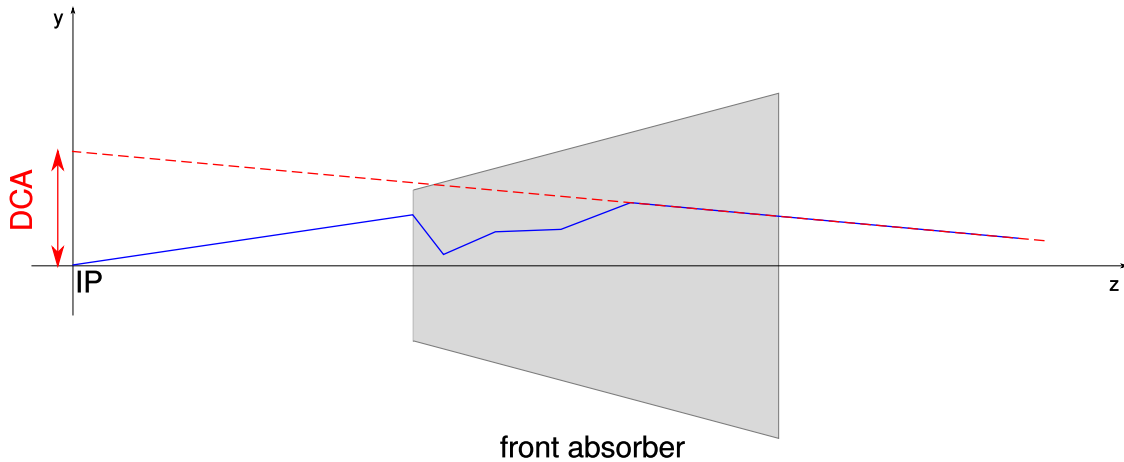


Figure 5.5: Principle of the  $pDCA$  selection criterion on the tracks reconstructed in the Muon Spectrometer.

The MC simulated data are obtained via the iterative method described in Sec. 5.2. In short, the distributions are re-weighted by a ratio of the distribution in data and in MC. This procedure is repeated until the ratio starts to fluctuate around unity when this method breaks. New MC must be produced with the tuned distributions.

To verify that the MC are well tuned to reproduces the data, one needs to examine the kinematic distributions in data and in MC. The kinematic distributions ( $p_T$ ,  $y$ , and polar angle  $\varphi$ ) and the charge distributions (proportion between positive and negative muons) must correspond to the reality. An example of such comparison is shown in Fig. 5.6, corresponding to p-Pb data at  $\sqrt{s_{NN}} = 8.16$  TeV. Both the data and the MC are shown for  $p_T > 0.5$  GeV/ $c$ . The bottom panel shows the ratio of the data over the MC. The ratios fluctuate within 5% from unity, which is the usual limit of this method. Such distributions are considered well tuned.

The efficiency is then computed in the data and in the MC using Eq. (5.7 - 5.9). An example of a tracking efficiency time dependent distribution estimated for single muons with  $p_T > 0.5$  GeV/ $c$  is shown in Fig. 5.7.

<sup>5</sup>AliROOT is a dedicated framework for ALICE experiment based on ROOT. AliROOT contains the geometry of the ALICE detector as well as libraries for simulation, reconstruction, and analysis of data. The task for tracking efficiency estimation can be found in `$ALICE_PHYSICS/PWGPP/MUON/dep/AliAnalysisTaskMuonTrackingEff.cxx`

<sup>6</sup>The same cuts are used in analyses of muon data and will be addressed in the next chapter.

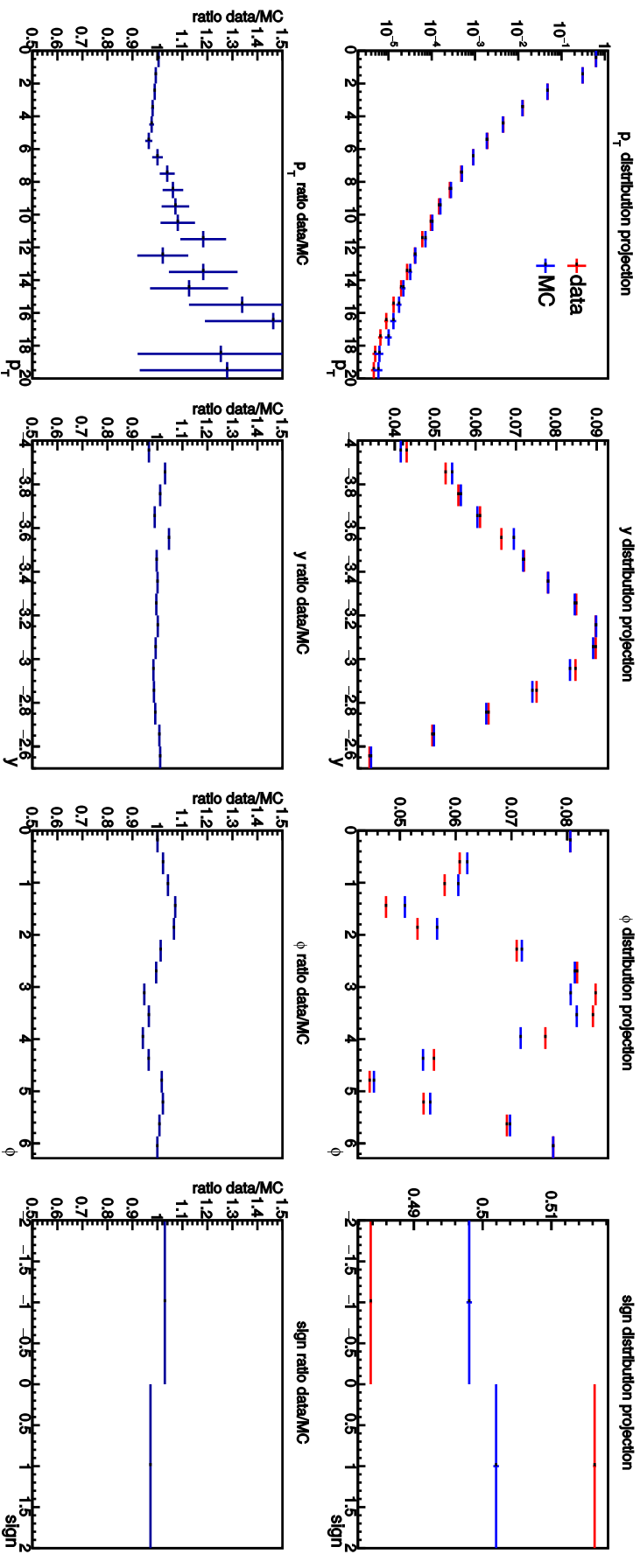


Figure 5.6: Comparison of kinematic distributions in data (red) and MC (blue). The top row shows the individual distributions as a function of  $p_T$ ,  $y$ ,  $\varphi$  and muon charge. The bottom row shows corresponding ratios of data/MC. The distributions correspond to  $p$ -Pb data at  $\sqrt{s_{NN}} = 8.16$  TeV.

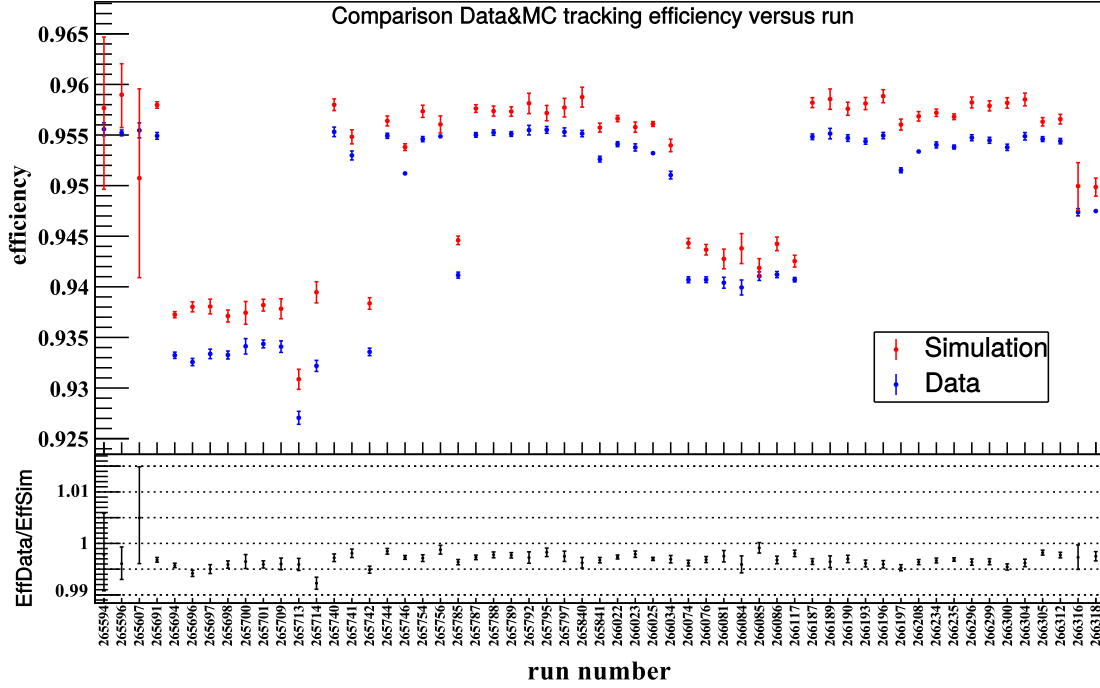


Figure 5.7: Tracking efficiency estimated as a function of run in the p–Pb period at  $\sqrt{s_{NN}} = 8.16$  TeV. The red points represent data while the blue points represent the MC.

The ratio of efficiencies estimated in data and in MC is then computed as a function of time and of kinematic variable  $p_T$ ,  $y$ ,  $\varphi$ . The ratios need to be also checked for individual stations and detection elements in each chamber to make sure no issues affecting the overall efficiency computation are present. An example of efficiency ratio for the four detection elements of Chamber 1 is shown in Fig. 5.8. If the ratio differs much from unity, it means that the behaviour of the spectrometer is not well reproduced in the MC. However, any potential improvement can be only achieved by performing a new reconstruction pass.

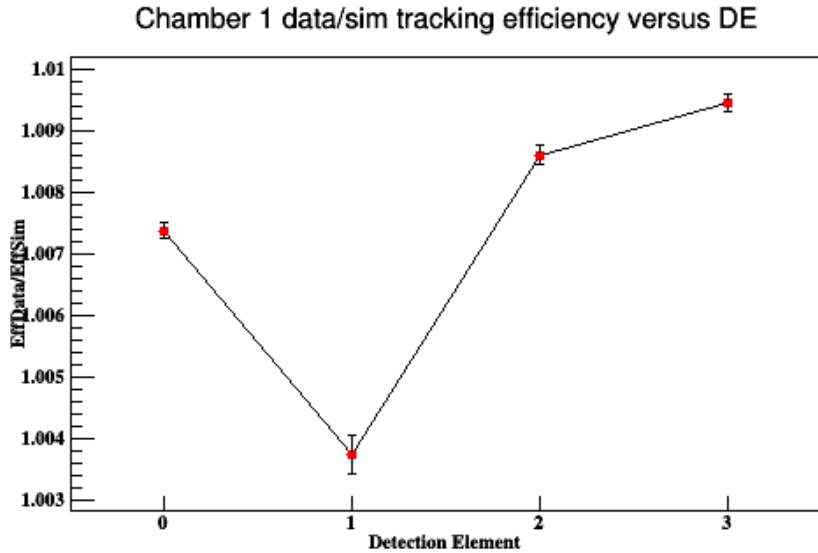


Figure 5.8: Ratio of the tracking efficiency in data and MC as a function of detection element (DE) in Chamber 1. Corresponding to the p–Pb data at  $\sqrt{s_{NN}} = 8.16$  TeV.

The systematic uncertainty is computed from the time dependence of the overall efficiency of the MCH as the standard deviation of the distribution. Moreover, the four efficiency distributions measured as a function of time,  $p_T$ ,  $y$ , and  $\varphi$  need to have all points within the  $3\sigma$  band. This gives the estimate on the uncertainty on the single muon tracking efficiency  $\sigma_{\varepsilon_{trk}}^\mu$ . For the dimuon tracking efficiency, we can assume that the two muons are fully correlated. This is not necessarily true for all pairs, but such estimate is conservative. The uncertainty on the dimuon tracking efficiency is hence computed as

$$\sigma_{\varepsilon_{trk}}^{\mu\mu} = 2 \cdot \sigma_{\varepsilon_{trk}}^\mu.$$

## 5.5 Systematic uncertainty on the tracking efficiency in p–Pb data at $\sqrt{s_{NN}} = 8.16$ TeV

In the following text, we will present results on the estimation of the tracking efficiency uncertainty on the p–Pb and Pb–p data at  $\sqrt{s_{NN}} = 8.16$  TeV, taken during Autumn 2016. The efficiency was measured for single muon data with low  $p_T$  threshold (CMSL7-B-NOPF-MUFAST trigger class). Parallel measurements were also performed in the single muon trigger with high  $p_T$  threshold (CMSH7-B-NOPF-MUFAST trigger class) and the low  $p_T$  threshold dimuon trigger (CMUL7-B-NOPF-MUFAST trigger class).

We studied the tracking efficiency in CMSL7 triggered data and in the corresponding MC as a function of run,  $p_T$ ,  $y$ , and  $\varphi$ . To investigate the stability of the result, the calculation is done using different selection of muon  $p_T$ . The effect of muon charge, i. e. selecting only  $\mu^+$  or only  $\mu^-$ , is also studied. We have used the following selection criteria:

- $p_T > 0.5$  GeV/ $c$ ,
- $p_T > 0.5$  GeV/ $c$  and selecting only  $\mu^+$ ,
- $p_T > 0.5$  GeV/ $c$  and selecting only  $\mu^-$ ,
- $p_T > 1.0$  GeV/ $c$ ,
- $p_T > 1.0$  GeV/ $c$  and selecting only  $\mu^+$ ,
- $p_T > 1.0$  GeV/ $c$  and selecting only  $\mu^-$ .

### 5.5.1 Systematic uncertainty of the muon tracking efficiency in the p–Pb period

The ratio of tracking efficiency in data and in MC for all listed cuts is shown in Fig. 5.9. All points, save for few outliers are within a  $2 - 3\sigma$  from the unity. For single muon, the tracking efficiency uncertainty was estimated as

$$\sigma_{\varepsilon_{trk}}^\mu = 0.5\%.$$

Assuming fully correlated dimuon pairs, the tracking efficiency uncertainty for dimuons is

$$\sigma_{\varepsilon_{trk}}^{\mu\mu} = 1\%.$$

This result agrees with uncertainty extracted from CMSH7 and CMUL7 triggered data [130, 225].

### 5.5.2 Systematic uncertainty of the muon tracking efficiency in the Pb–p period

The results of the second reconstruction pass for the Pb–p period are shown in Fig. 5.10. Due to frequent high-voltage trips in Station 2 during data taking, the Pb–p period has larger run-by-run fluctuations than the p–Pb period. There are also several runs in which the efficiency is not well reproduced in the MC compared to the rest of the period. This was attributed to a faulty Bus Patch in Station 3 correlated with a dead zone in Station 4. The same problem was present in studies based on the CMSH7 and CMUL7 samples [225]. The run-integrated ratios versus  $p_T$ ,  $y$ , and  $\varphi$  are however more stable.

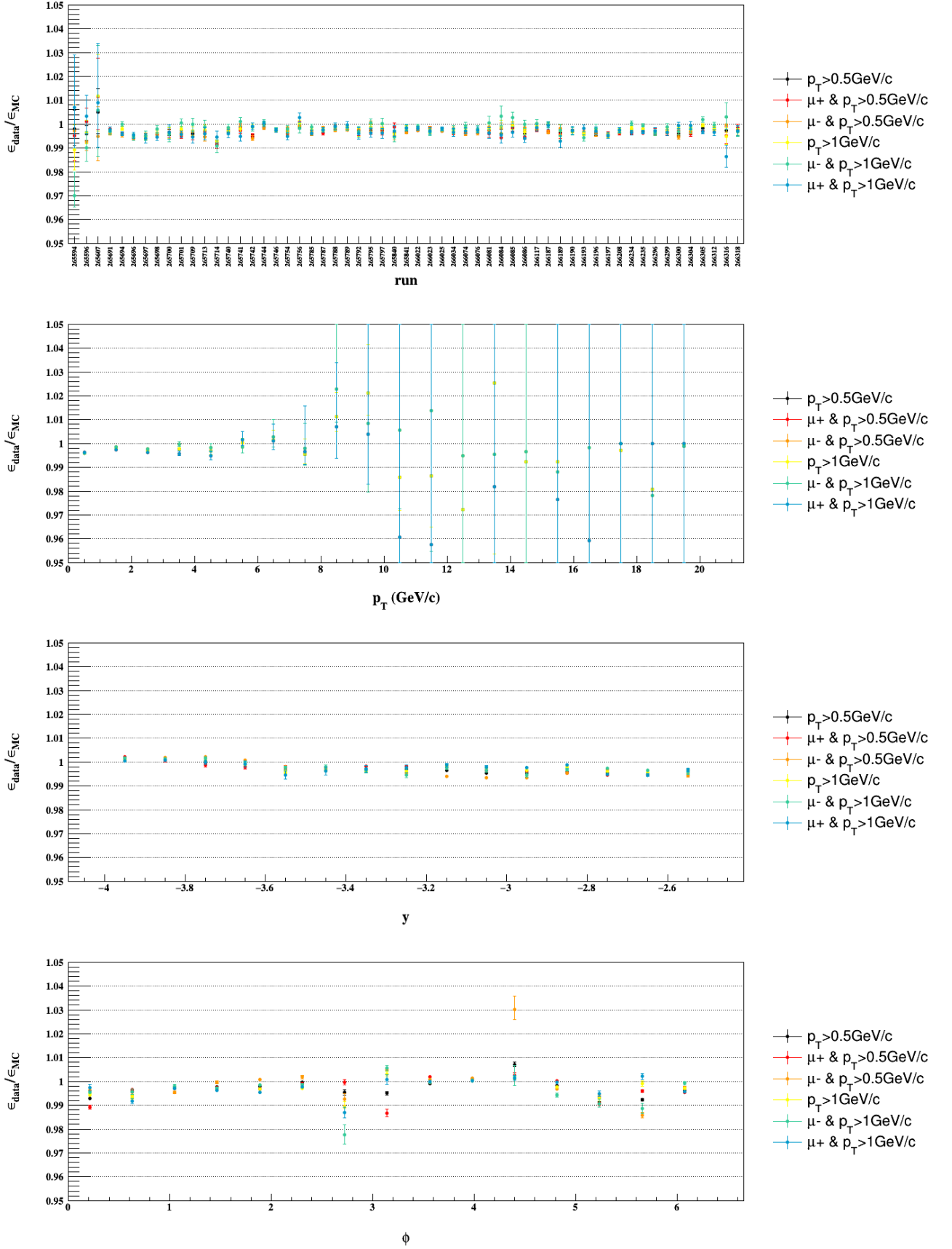


Figure 5.9: Ratio of the tracking efficiency in data and in MC in the p-Pb period as a function of run,  $p_T$ ,  $y$ , and  $\phi$ .

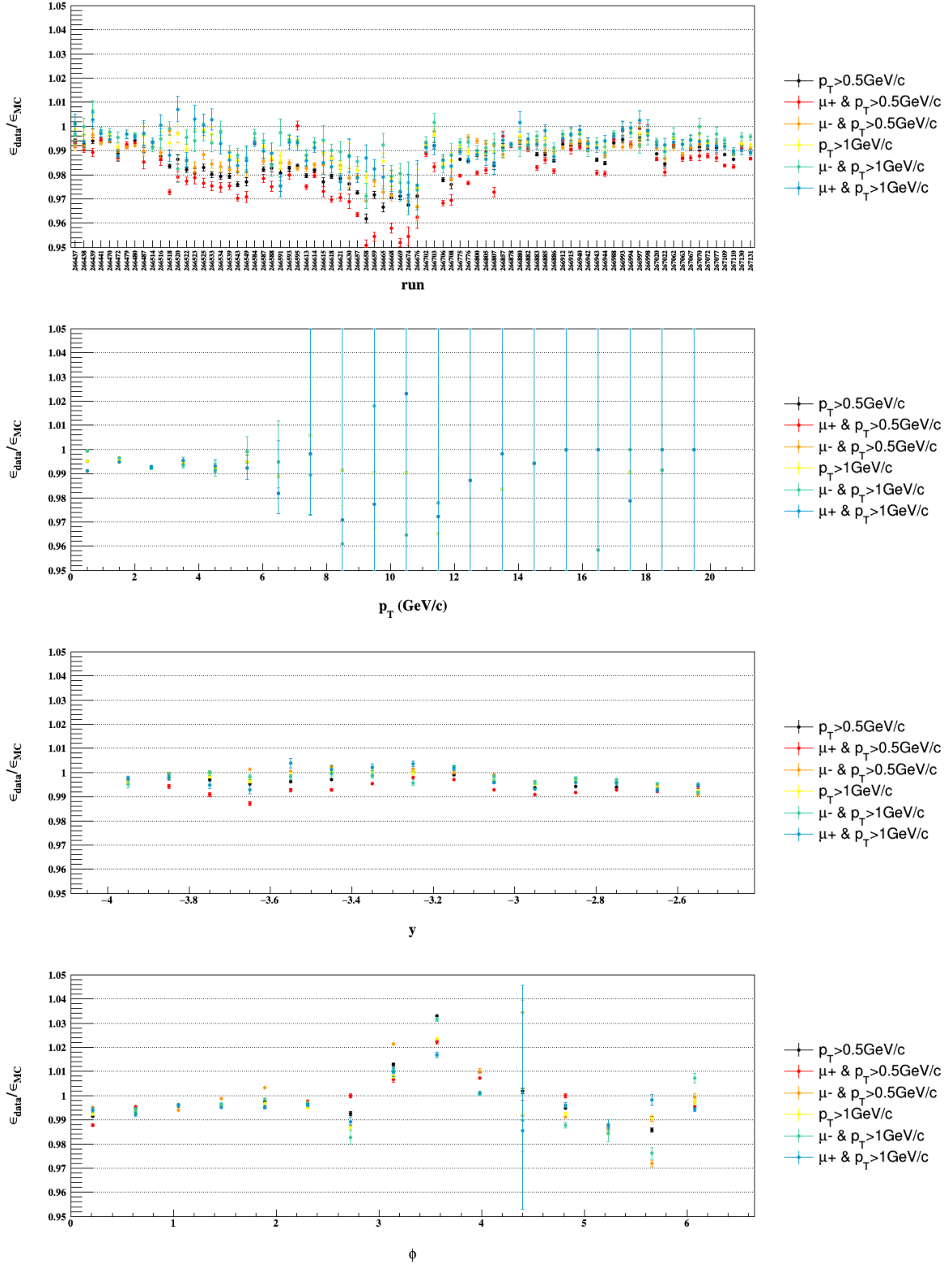


Figure 5.10: Ratio of the tracking efficiency in data and in MC in the Pb-p period as a function of run,  $p_T$ ,  $y$ , and  $\phi$ . The ratios were computed from the second reconstruction pass of the Pb-p data.

In the second reconstruction pass the uncertainty on the single muon tracking efficiency for the p–Pb period in CMSL7 trigger was estimated to

$$\sigma_{\varepsilon_{trk}}^{\mu} = 2\%.$$

Assuming fully correlated dimuon pairs, the tracking efficiency uncertainty for dimuons was estimated to

$$\sigma_{\varepsilon_{trk}}^{\mu\mu} = 4\%.$$

The results for the CMSH7 and CMUL7 trigger classes gave similar estimate [225].

### Improving the results

Another reconstruction of data was performed for the Pb–p period, taking into consideration the observed problems. An improvement was done in describing the status of the detector in the simulations [225]. The faulty Bus Patch was the main contributor to the discrepancy between the previous reconstruction pass of the data and the MC.

The study based on the new reconstruction pass in CMSL7, CMUL7, and CMSH7 triggers estimated the single muon tracking uncertainty to

$$\sigma_{\varepsilon_{trk}}^{\mu} = 1\%$$

and hence the dimuon tracking uncertainty to

$$\sigma_{\varepsilon_{trk}}^{\mu\mu} = 2\%$$

[130]. As an example, we show in Fig. 5.11 the time,  $p_T$ ,  $y$ , and  $\varphi$  dependence of the tracking efficiency uncertainty estimated for the third reconstruction pass of the CMSL7 trigger class in the Pb–p data.

## Summary

The Muon Spectrometer, introduced in the previous chapter, is among other dedicated to studies of charmonia and bottomia from their dimuon decays. To compute the production cross section of these particles, we need to compute the acceptance-efficiency  $A\varepsilon$  of the spectrometer with the corresponding uncertainties. There are several sources to the uncertainty - the uncertainty in the MC input used to compute the  $A\varepsilon$ , the uncertainty on tracking, the uncertainty on trigger, and the uncertainty on the trigger-track matching. In this thesis, we explained the estimation of uncertainty on the tracking efficiency and presented results of the uncertainty considered for the p–Pb data period at  $\sqrt{s_{NN}} = 8.16$  TeV.

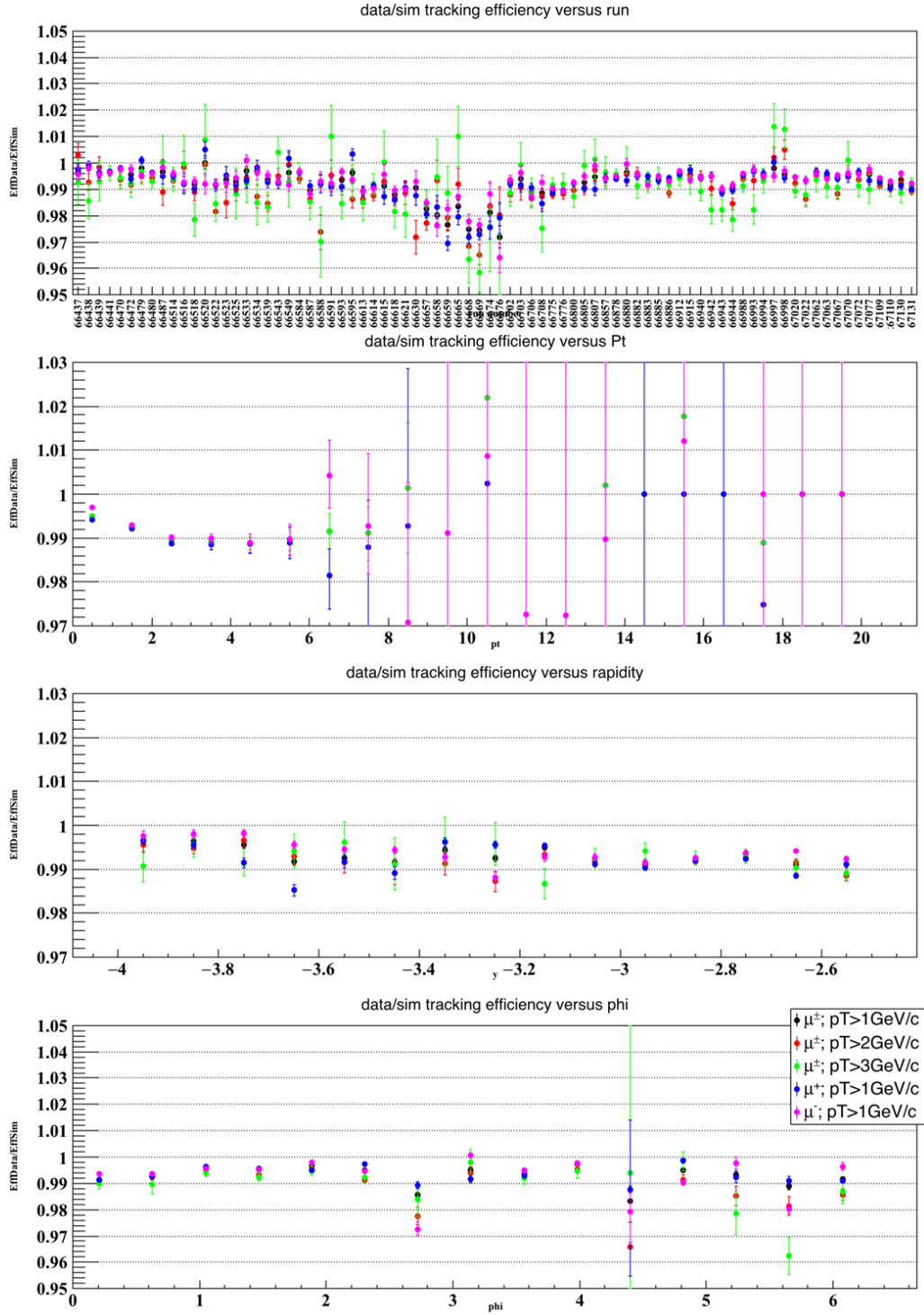


Figure 5.11: Ratio of the tracking efficiency in data and in MC in the Pb-p period as a function of run,  $p_T$ ,  $y$ , and  $\phi$ . The ratios were computed from the third reconstruction pass of the Pb-p data. Courtesy of Philippe Pillot.

## MEASUREMENT OF INCLUSIVE $J/\psi$ PRODUCTION AT FORWARD RAPIDITY IN pp COLLISIONS AT $\sqrt{s} = 5.02$ TeV

In this chapter, we shall present the analysis of inclusive  $J/\psi$  production from its dimuon decay channel in pp collisions at  $\sqrt{s} = 5.02$  TeV. The  $J/\psi$  are reconstructed with the Muon Spectrometer in the rapidity range  $2.5 < y < 4$  and in the transverse momentum range  $p_T < 12$  GeV/ $c$ . We will start by explaining the observables, which we will discuss in the following text, to then introduce the analysed data sample. We will explain step by step the extraction of ingredients needed to compute the cross section as well as assessment of relevant uncertainties. Finally, we will discuss the results of the measurement, what can we learn by studying them together with other available ALICE results at different collisions energies ranging from 2.76 to 13 TeV [73], and how they compare with a previously used interpolation of pp data at  $\sqrt{s} = 2.76$  and 7 TeV to 5.02 TeV [226].

The differential  $J/\psi$  production cross section at a given  $y$  and  $p_T$  range is defined as

$$\frac{d^2\sigma_{J/\psi}}{dp_T dy} = \frac{1}{\Delta p_T \Delta y} \frac{N_{J/\psi}^{raw}}{A\varepsilon(p_T, y) \text{BR}_{J/\psi \rightarrow \mu^+\mu^-} \mathcal{L}_{\text{int}}}, \quad (6.1)$$

where  $N_{J/\psi}^{raw}$  stands for the raw<sup>1</sup> reconstructed number of  $J/\psi$  in the dimuon sample,  $A\varepsilon$  is the acceptance-efficiency factor introduced in Chapter 5,  $\text{BR}_{J/\psi \rightarrow \mu^+\mu^-} = (5.961 \pm 0.033)\%$  [1] gives the ratio of all produced  $J/\psi$  decayed into a pair of muons, and  $\mathcal{L}_{\text{int}}$  is the integrated luminosity of the data sample in question.

Luminosity gives the interaction rate and is defined<sup>2</sup> as a ratio of the number of events in the selected data sample  $N_{\text{evt}}$  and the cross section of the process we want to study  $\sigma$

$$\mathcal{L} = \frac{N_{\text{evt}}}{\sigma}. \quad (6.2)$$

The analysis was performed on pp data at  $\sqrt{s} = 5.02$  TeV taken during four days in Autumn 2015. The data sample consists of a set of 25 runs, which are good for muon analyses. The full runlist can be found in App. C. The final and intermediate results were compared with a parallel analysis on the same data sample [223].

## 6.1 Event and track selection

### 6.1.1 Event selection criteria

The  $J/\psi$  were analysed in the low  $p_T$  dimuon triggered data sample. Two different MB triggers were used for normalisation purpose. An overview of the trigger classes used in this analysis can be found in Tab. 6.1. The trigger classes 1 and 2 correspond to minimum bias triggers. The trigger classes 3 (4) allow us to select muon (dimuon) data samples.

The beam-beam interactions (“physics events”) are selected through timing cuts on signals in V0A and V0C, and T0A and T0C. The beam-gas and beam-collider interactions usually take place outside

---

<sup>1</sup>In other words not corrected by acceptance and efficiency.

<sup>2</sup>We already encountered the luminosity once in this work, when discussing the V0 detector, see Eq. (4.2).

	trigger class	description
1	CINT7-B-NOPF-MUFAST	V0A && V0C
2	C0TVX-B-NOPF-CENTNOTRD	T0A && T0C && T0 vertex within $ z  < 30$ cm
3	CMSL7-B-NOPF-MUFAST	V0A && V0C && low- $p_T$ muon ( $p_T^\mu \gtrsim 0.5$ GeV/ $c$ )
4	CMUL7-B-NOPF-MUFAST	V0A && V0C && low- $p_T$ dimuon ( $p_T^\mu \gtrsim 0.5$ GeV/ $c$ )

Table 6.1: Definition of trigger classes used in  $J/\psi$  analysis in pp collisions at  $\sqrt{s} = 5.02$  TeV.

of the nominal interaction points and are hence delayed with respect to the beam-beam events. The process of discriminating between beam-beam and either beam-gas or beam-collider interactions is called 'Physics Selection (PS)' and the selected events are referred to as 'physics selected'.

### 6.1.2 Track selection criteria

To make sure all accepted tracks are muons reconstructed within the detector acceptance, we required the following criteria to be fulfilled by each individual track:

1. The track must be within pseudorapidity window  $-4 < \eta < -2.5$  (in the laboratory frame<sup>3</sup>).
2. The track must pass through the absorber. This is verified by putting limits on the angle between the beam axis and the line connecting the position of the track immediately after absorber to the vertex. The angle must fall within  $2^\circ < \theta < 10^\circ$ . Using the small angle approximation, the angle can be related to the radial transverse position  $R_{\text{abs}}$  of the track and to the distance from vertex to the end of the absorber  $L$  as  $\theta = R_{\text{abs}}/L$ . Usually, this cut is expressed as a function of  $R_{\text{abs}}$ , with the limits being  $17.6 < R_{\text{abs}} < 89.5$  cm.
3. The track reconstructed by the tracking chambers must match a trigger track reconstructed in the trigger chambers with  $p_T^\mu \gtrsim 0.5$  GeV/ $c$ .

The selected muons are then combined into dimuon pairs. Candidates that do not meet the following criteria are rejected:

1. The two muons must have opposite charge. In this thesis we consider only pairs of opposite sign.
2. The dimuon must be reconstructed within the rapidity window  $2.5 < y < 4.0$  in the detector frame.
3. In the pp 5.02 TeV study, we also imposed an upper  $p_T$  threshold to limit the study on a region where we have enough statistics,  $p_T^{\mu\mu} < 12$  GeV/ $c$ .

## 6.2 Signal extraction

For each of the selected dimuon pairs, the invariant mass  $M_{\text{inv}}$  of the pair is computed as

$$M_{\text{inv}} = \sqrt{2m_\mu^2 + 2E_{\mu 1}E_{\mu 2}(1 - \cos\theta_{12})}. \quad (6.3)$$

Here  $m_\mu$  is the mass of the muon,  $E_{\mu 1}$  and  $E_{\mu 2}$  denote the energies of the two daughter muons, and  $\theta_{12}$  is the angle between the momenta of the muons. Schematic depiction of a decay of  $J/\psi \rightarrow \mu^+\mu^-$  can be found in Fig. 6.1.

Fig. 6.2 shows the invariant mass spectrum of all selected dimuon pairs in the pp 5.02 TeV data in the region  $1.5 < M_{\text{inv}} < 6$  GeV/ $c^2$ . We clearly see a peak emerging above the continuum at  $M_{\text{inv}} \sim 3.1$  GeV/ $c^2$ , which is the  $J/\psi$  mass region. The continuum consists of uncorrelated pairs of unlike sign muons originating mainly from decays of light mesons ( $\pi$  and K) or of open charm and beauty mesons (D and B). In the mass region of  $M_{\text{inv}} \sim 3.7$  GeV/ $c^2$  one can perceive a hint of a peak originating from decays of  $\psi(2S) \rightarrow \mu^+\mu^-$ .

<sup>3</sup>The laboratory frame coincides with the centre-of-mass frame of a pp collision. However, the distinction is important in p-Pb collisions.

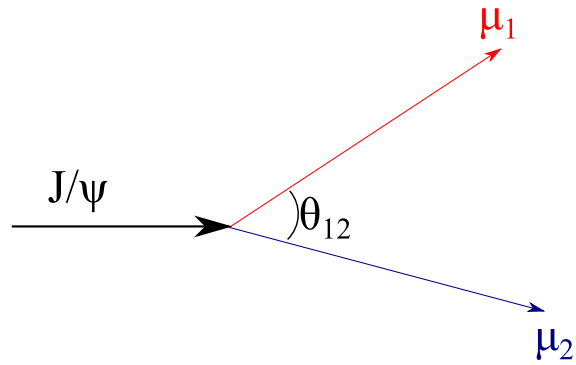


Figure 6.1: Schema of a decay of  $J/\psi$  into a pair of opposite sign muons in the laboratory frame.

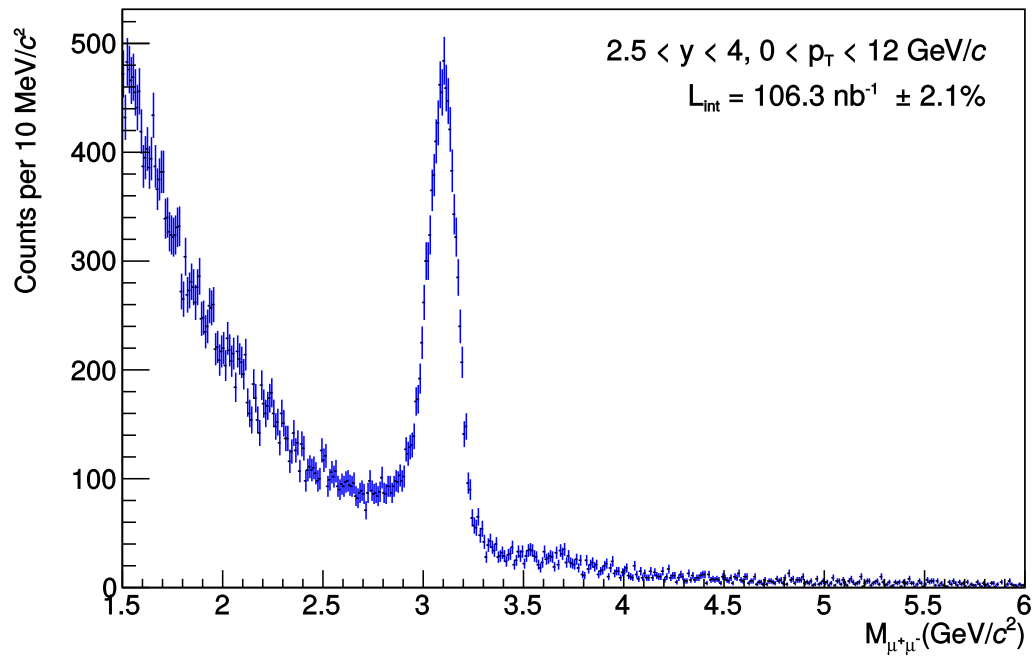


Figure 6.2: The dimuon invariant mass spectrum in pp collisions at  $\sqrt{s} = 5.02 \text{ TeV}$ .

The raw number of  $J/\psi$  was extracted by fitting the invariant mass spectrum by a sum of functions describing the  $J/\psi$  peak<sup>4</sup> and the combinatorial background. The functions were chosen empirically, using multiple functions for each ingredient. All of them can be found in App. A.

### Signal functions

The functions used to characterise the  $J/\psi$  signal consist of a Gaussian core with power-law tails added on either side of the mean of the peak. In ideal case, the signal would be characterised by a delta function at the mass of  $J/\psi$ . However, the detector resolution causes broadening of the signal into a Gaussian shape. In case of the Muon Spectrometer, we need to consider additional effect which deteriorate the resolution. These are:

1. The alignment of the detector. This effect is symmetric and contributes to both left and right tail.
2. Multiple Coulomb scatterings in the front absorber and in the tracking chambers. These phenomena increase the energy loss and contribute to the left (lower mass) tail.
3. Radiative decays and energy loss in the front absorber. These also contribute to the left tail only.

The  $\psi(2S)$  needs to be considered in the fit too as its proximity to the  $J/\psi$  peak means that the low-mass tail of  $\psi(2S)$  may affect the  $J/\psi$  high-mass tail. The two peaks are described with the same function. Moreover, the parameters of the two functions are correlated. The mass  $M_{\psi(2S)}$  and width  $\sigma_{\psi(2S)}$  of the  $\psi(2S)$  are fixed to the mass  $M_{J/\psi}$  and width  $\sigma_{J/\psi}$  of the  $J/\psi$ :

$$M_{\psi(2S)} = M_{J/\psi} + (M_{\psi(2S)}^{\text{PDG}} - M_{J/\psi}^{\text{PDG}}), \quad (6.4)$$

$$\sigma_{\psi(2S)} = \sigma_{J/\psi} \times \frac{M_{\psi(2S)}^{\text{PDG}}}{M_{J/\psi}^{\text{PDG}}}, \quad (6.5)$$

where PDG denotes the values given by the Particle Data Group [1].

The two functions used to describe the  $J/\psi$  peak in the Muon Spectrometer were extended double Crystal Ball<sup>5</sup> (CB2) function (see Sec. A.1) and the double NA60<sup>6</sup> function (see Sec. A.2). Given the number of parameters, which is 8 in case of CB2 and 12 in case of NA60, the tail parameters were fixed when fitting the invariant mass spectrum. The low statistics in pp at 5.02 TeV would prevent a fit with all free parameters from converging. Of course, the tail parameters cannot be fixed just to any value. One reasonable choice was to use the tails extracted from fitting a larger data sample - in our case the 13 TeV pp data, taken also in 2015 [73]. The detector conditions were stable during the 2015 data taking, therefore the characteristics of the  $J/\psi$  peak should be the same in 5.02 TeV as in the 13 TeV data. However, only CB2 tails were successfully extracted from the pp 13 TeV data. Another possibility, which we also explored, was to extract the parameters from dedicated Monte Carlo simulations, which were described in Sec. 5.2.

In total, we used one set of CB2 tails extracted from data, one set of tails CB2 tails extracted from MC of pure  $J/\psi \rightarrow \mu^+\mu^-$  at 5.02 TeV, and one set of NA60 tails extracted from the same MC.

### Background functions

We tested multiple ad hoc parametrisations of background. Ideally they should have the least number of parameters (to better constrain them at high  $p_T$  where the data are scarce). We finally settled for two functions: a Variable width Gaussian function (VWG) and a ratio of first order and second order polynomial (Pol12).

<sup>4</sup>We also consider the  $\psi(2S)$  peak, but we fix its parameters to those of the  $J/\psi$  peak. See further text.

<sup>5</sup>The function was christened after the Crystal Ball detector, originally located at the SPEAR in SLAC. The detector was designed to study the charmonia and was the one to discover the  $\eta_c$  resonance [227].

<sup>6</sup>Named after the NA60 experiment at the SPS in CERN [228]. The experiment studied "prompt dimuons and charm production with proton and heavy ion beams."

## 6.2.1 Systematic uncertainty on signal extraction

### 6.2.1.1 Fitting the $p_T$ and $y$ integrated spectrum

Using multiple fits to the spectrum allowed us to extract the systematic uncertainty associated to the signal extraction. We also varied the invariant mass fit range to make sure the results were not affected by e. g. some structures at the edges of the used fit ranges. We have considered two different ranges: (i)  $2.1 < M_{\text{inv}} < 4.5 \text{ GeV}/c$  and (ii)  $1.7 < M_{\text{inv}} < 4.8 \text{ GeV}/c$ . All in all, we used the following variations:

- two different background functions,
- two different signal functions,
- two sets of tail parameters from MC (one for CB2 and one for NA60) and one set extracted from data (CB2),
- two different  $M_{\text{inv}}$  fit ranges.

Fig. 6.3 shows an example of a fit to the invariant spectra, integrated in  $p_T$  and  $y$ , in the mass range  $2.1 < M_{\text{inv}} < 4.5 \text{ GeV}/c$ . The shown combination is CB2+VWG with a set of tails extracted from MC.

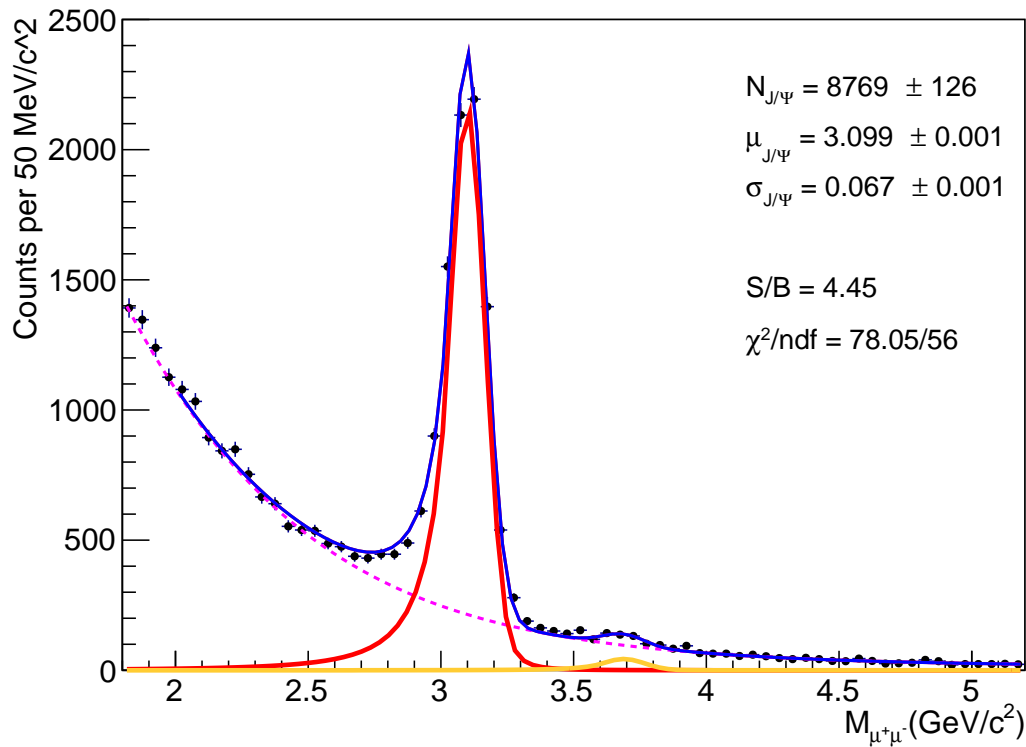


Figure 6.3: Example of CB2+VWG fit to the dimuon invariant mass spectrum over the range  $2.1 < M_{\text{inv}} < 4.5 \text{ GeV}/c$  in pp collisions at  $\sqrt{s} = 5.02 \text{ TeV}$ .

It was found that the MC gave consistently narrower peak than the data. As a large fraction of uncertainty comes from the difference between the data and MC tails, this could have potentially biased the results. To prevent biasing the results, we assigned double the weight to the fits with data parameters. The spread of  $N_{J/\psi}^{\text{raw}}$  in each fit can be found in Fig. 6.4.

The signal  $N_{J/\psi}^{\text{raw}}$  was computed as the weighted average over all tests. The statistical uncertainty associated to the signal extraction was defined as the weighted average of uncertainties associated to each individual fit. The systematic uncertainty was given by the spread of individual fit results around

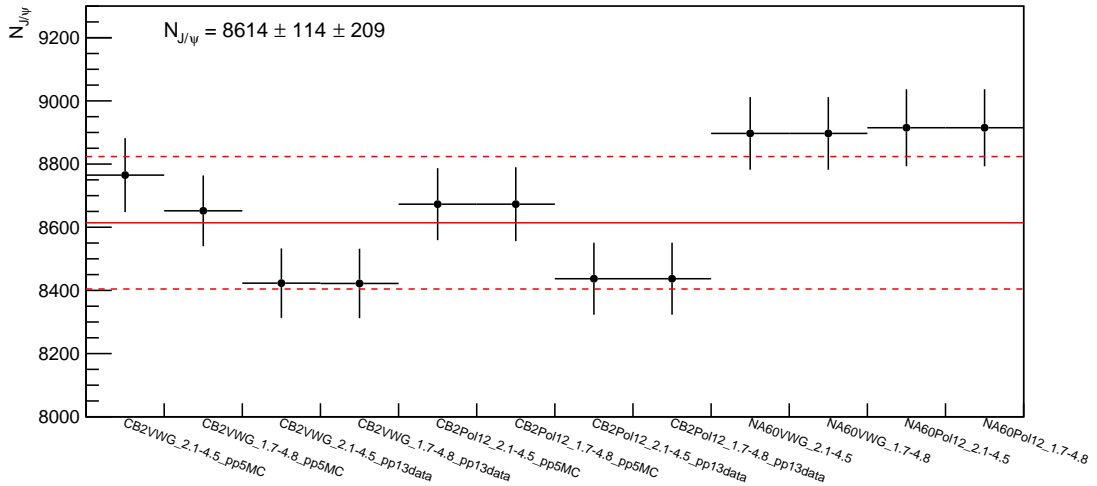


Figure 6.4: Number of  $J/\psi$  integrated in  $p_T$  and rapidity as a function of the fit trial in pp collisions at  $\sqrt{s} = 5.02$  TeV. The solid red line shows the mean value averaged over all trials. The dashed lines show the standard deviation.

the average  $N_{J/\psi}^{\text{raw}}$ . The extracted number of  $J/\psi$  integrated over  $p_T < 12$  GeV/c and  $2.5 < y < 4.0$  was

$$N_{J/\psi}^{\text{raw}} = 8614 \pm 114(\text{stat.}) \pm 209(\text{syst.}), \quad (6.6)$$

in agreement with [223].

### 6.2.1.2 Fitting the $p_T$ and $y$ differential spectrum

We also extracted  $N_{J/\psi}^{\text{raw}}$  integrated in  $2.5 < y < 4.0$  in 10  $p_T$  bins in the range  $0 < p_T < 12$  GeV/c, and  $N_{J/\psi}^{\text{raw}}$  integrated in  $0 < p_T < 12$  GeV/c in 6  $y$  bins in the rapidity range of the spectrometer. The  $p_T$ -differential and  $y$ -differential results are reported in Tab. 6.2.

The systematic uncertainty in  $p_T$  ranged mostly between 0.8 – 8.9%, with 31.3% for  $9 < p_T < 10$  GeV/c. The  $y$  differential uncertainty varied between 2.5 – 3.1%. The extracted  $N_{J/\psi}$  agree with values from the parallel analysis [223]. In most bins, the systematic uncertainty quoted here is below the uncertainty from [223]. The discrepancy was studied, however no apparent issue was found. The relative systematic uncertainty in  $9 < p_T < 10$  GeV/c is large compared to all other bins as the functions were not well constrained by the spectrum in this particular  $p_T$  bin.

$p_T$ (GeV/c)	$N_{J/\psi} \pm \text{stat.} \pm \text{syst.}$		
0 – 1	$1442 \pm 69 \pm 38$		
1 – 2	$2523 \pm 98 \pm 38$		
2 – 3	$1991 \pm 72 \pm 35$		
3 – 4	$1189 \pm 52 \pm 17$		
4 – 5	$635 \pm 30 \pm 10$		
5 – 6	$390 \pm 28 \pm 3$		
6 – 7	$208 \pm 16 \pm 6$		
7 – 8	$116 \pm 11 \pm 7$		
8 – 9	$56 \pm 9 \pm 5$		
9 – 10	$32 \pm 6 \pm 10$		
10 – 12	$32 \pm 6 \pm 1$		
		$y$	$N_{J/\psi} \pm \text{stat.} \pm \text{syst.}$
		3.75 – 4.00	$415 \pm 25 \pm 11$
		3.50 – 3.75	$1358 \pm 46 \pm 42$
		3.25 – 3.50	$2109 \pm 59 \pm 53$
		3.00 – 3.25	$2318 \pm 62 \pm 70$
		2.75 – 3.00	$1848 \pm 55 \pm 54$
		2.50 – 2.75	$563 \pm 31 \pm 17$

Table 6.2: Number of  $J/\psi$  extracted in  $p_T$  bins integrated over  $2.5 < y < 4$  and in bins of  $y$  integrated in  $p_T$ .

### 6.3 Acceptance and efficiency correction

The acceptance-efficiency correction factor was computed from the same MC, which were used for extraction of the tail parameters. The method used to extract the factor was described in Sec. 5.2. Here we will only briefly remind the steps.

The factor was estimated from MC.  $J/\psi$  were generated with realistic  $p_T$  and  $y$  distributions (tuned to the data), their number being kept proportional to the number of analysed CMUL events on a run-by-run basis. The  $J/\psi$  were then decayed to muons. The muons were propagated through the detector using GEANT3. The  $J/\psi$  were then reconstructed from the muons using the same cuts as in the analysis of data. The acceptance-efficiency was computed in a given  $p_T$  or  $y$  range as a ratio of reconstructed over all generated  $J/\psi$  ( $A\varepsilon = N_{J/\psi}^{rec}/N_{J/\psi}^{gen}$ , see Eq. (5.3)).

The average acceptance-efficiency in the rapidity range  $2.5 < y < 4.0$  and for  $p_T < 12$  GeV/c amounted to

$$A\varepsilon = 0.2434 \pm 0.0003.$$

Fig. 6.5 shows the value of  $A\varepsilon$  as a function of run. Computing the acceptance-efficiency as a function of run allows us to study the evolution of detector conditions in time. We see that the detector was stable as the  $A\varepsilon$  does not change much from run to run, the variations being within 1.5%. We also studied the evolution of  $A\varepsilon$  with  $p_T$  (hence integrated in  $y$  and time) and with  $y$  (integrated in  $p_T$  and time). The distributions are shown in Fig. 6.6. The  $p_T$  distribution reaches its minimum around  $p_T \approx 2 - 3$  GeV/c, where the probability of at least one muon escaping from the detector is maximal, and increases with  $p_T$ . The  $y$  dependence shows that the  $A\varepsilon$  decreases at the edges of the detector. The  $p_T$  and  $y$  differential values can be found in Tab. 6.3.

#### 6.3.1 Systematic uncertainty on acceptance-efficiency

The total  $A\varepsilon$  uncertainty has several contributions, which were generally discussed in Sec. 5.2.1. Here we will detail the contributions in case of the pp sample at  $\sqrt{s} = 5.02$  TeV.

##### 6.3.1.1 Uncertainty on Monte Carlo input

We considered two sources of uncertainty on MC input:

1. Uncertainty on the kinematic input shape originating from the statistical uncertainty on the data points. The MC shapes were tuned on data, hence the limited statistics of the datasample will influence the precision of the input.
2. Uncertainty on the shape due to existing  $p_T - y$  correlations, which are not taken into account in the generation function. The pp sample at  $\sqrt{s} = 5.02$  TeV does not allow us to extract the signal in bins of  $(p_T, y)$ .

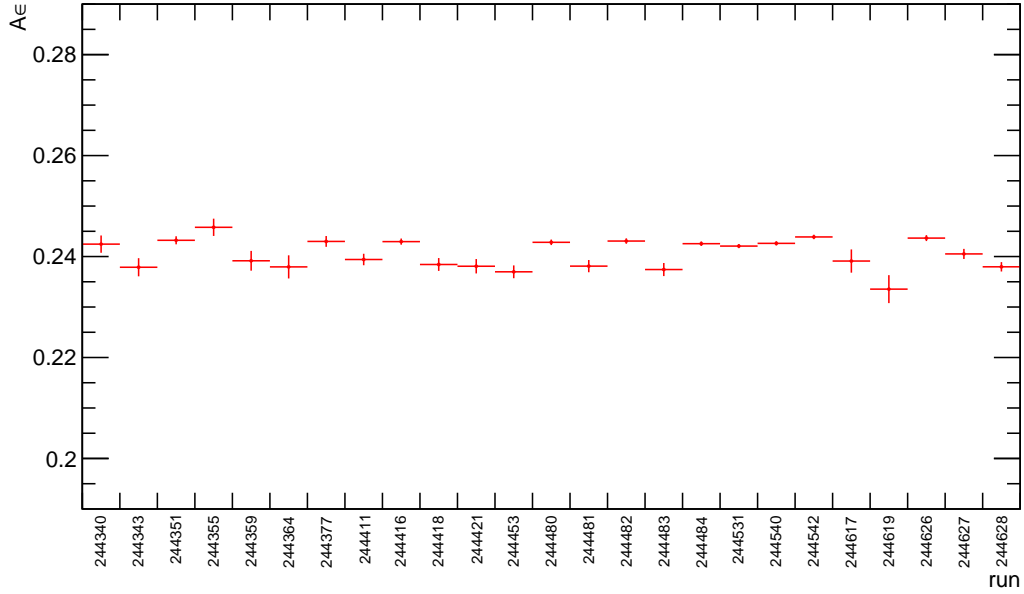


Figure 6.5: The evolution of  $A\varepsilon$  with time in pp collisions at  $\sqrt{s} = 5.02$  TeV.

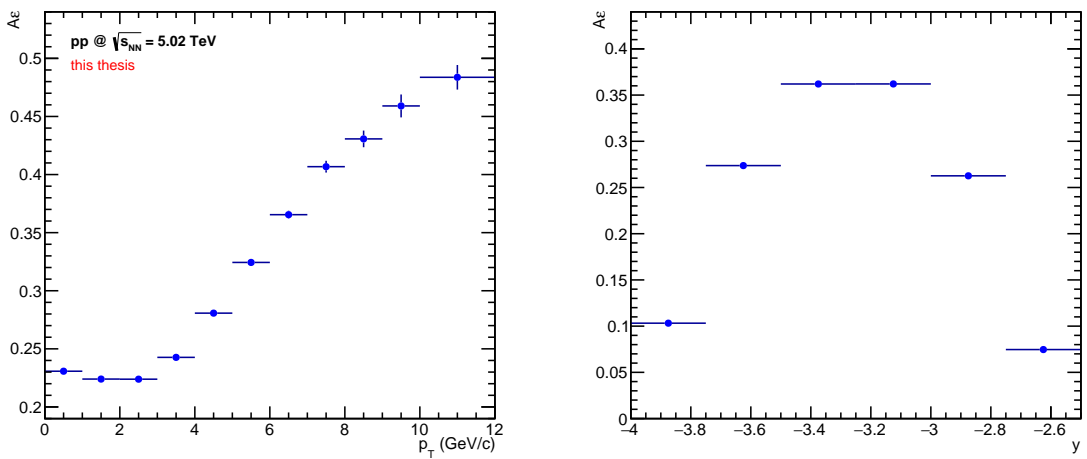


Figure 6.6: The  $p_T$ - and  $y$  differential  $A\varepsilon$  in pp collisions at  $\sqrt{s} = 5.02$  TeV. (Left)  $A\varepsilon$  as a function of  $p_T$ , integrated over  $2.5 < y < 4.0$ . (Right)  $A\varepsilon$  as a function of  $y$ , integrated over  $0 < p_T < 12$  GeV/c.

$p_T$ (GeV/c)	$A\varepsilon \pm \text{stat.}$		
0 – 1	$0.2307 \pm 0.0008$		
1 – 2	$0.2240 \pm 0.0005$		
2 – 3	$0.2239 \pm 0.0006$		
3 – 4	$0.2427 \pm 0.0009$		
4 – 5	$0.2807 \pm 0.0014$		
5 – 6	$0.3244 \pm 0.0022$		
6 – 7	$0.3655 \pm 0.0034$		
7 – 8	$0.4068 \pm 0.0051$		
8 – 9	$0.4307 \pm 0.0072$		
9 – 10	$0.4591 \pm 0.0099$		
10 – 12	$0.4837 \pm 0.0106$		
		$y$	$A\varepsilon \pm \text{stat.}$
		3.75 – 4.00	$0.1032 \pm 0.0006$
		3.50 – 3.75	$0.2737 \pm 0.0009$
		3.25 – 3.50	$0.3620 \pm 0.0010$
		3.00 – 3.25	$0.3620 \pm 0.0010$
		2.75 – 3.00	$0.2626 \pm 0.0008$
		2.50 – 2.75	$0.0746 \pm 0.0004$

Table 6.3: The  $J/\psi$  acceptance-efficiency in  $p_T$  bins integrated over  $2.5 < y < 4.0$  and in bins of  $y$  integrated in  $p_T$ .

### Limitations due to statistical uncertainty on data

The shape of the MC was obtained by comparing the  $N_{J/\psi}^{\text{corr}} = N_{J/\psi}^{\text{raw}}/A\varepsilon$  computed from data to the  $N_{J/\psi}^{\text{gen}}$  generated in the MC. The MC were tuned so that these distributions were at the best possible agreement. However, we did not compare the distributions directly, we compared the fits to these distributions. These fits were free to vary within the statistical uncertainty on the datapoints. Therefore we studied the influence of this freedom within the uncertainty on the final result.

We used the following method:

- All points were randomly shifted within their uncertainty. We assumed the uncertainty is uncorrelated, i. e. each point can vary independently of the rest. We assumed the errors follow the Gaussian distribution, where the mean of each was given by the central value and the width defined the uncertainty on the data.
- The new distribution was fit by a function of the same form that was used to generate the MC sample.
- The new shape was used to re-weight the MC simulations (applied both on generated and reconstructed level).
- We recalculated  $A\varepsilon$  from the re-weighted MC.

We repeated the procedure enough times to assure we had a large enough sample to study. In this case we used 50 trials. The fits to the varied data were plotted in top row of Fig. 6.7. We then computed the average  $A\varepsilon$  in each bin and the corresponding RMS. The uncertainty was computed as the ratio of RMS over the average, see bottom row of Fig. 6.7. The uncertainty was  $< 0.1\%$  in all bins. Hence the effect of statistical variation was not considered in the final systematic uncertainty estimation.

### Limitations due to $p_T - y$ correlations

The function used to generate the  $p_T$  shape were extracted from  $y$  integrated  $N_{J/\psi}$  distribution and vice-versa, and thus neglected any possible  $p_T - y$  correlation. This could be handled by extracting the  $p_T$  distribution on different  $y$  bins and the  $y$  distributions in different  $p_T$  bins. The limited statistics of the data at 5.02 TeV however prevented two dimensional extraction. Instead, we used the distributions from pp data at  $\sqrt{s} = 13$  TeV, which were measured in the same kinematic domain. All combinations of the  $p_T$  and  $y$  shapes from 13 TeV data were used to re-weight the 5.02 TeV MC distributions and the  $A\varepsilon$  was recomputed for each combination. The original  $A\varepsilon$  correction at 5.02 TeV, i. e. prior any weighting, was taken as the central value. The systematic uncertainty was taken as the maximal spread of the recomputed  $A\varepsilon$  corrections in each bin normalised to the central value. The re-weighted distributions and the spread with respect to the central correction can be found in Fig. 6.8.

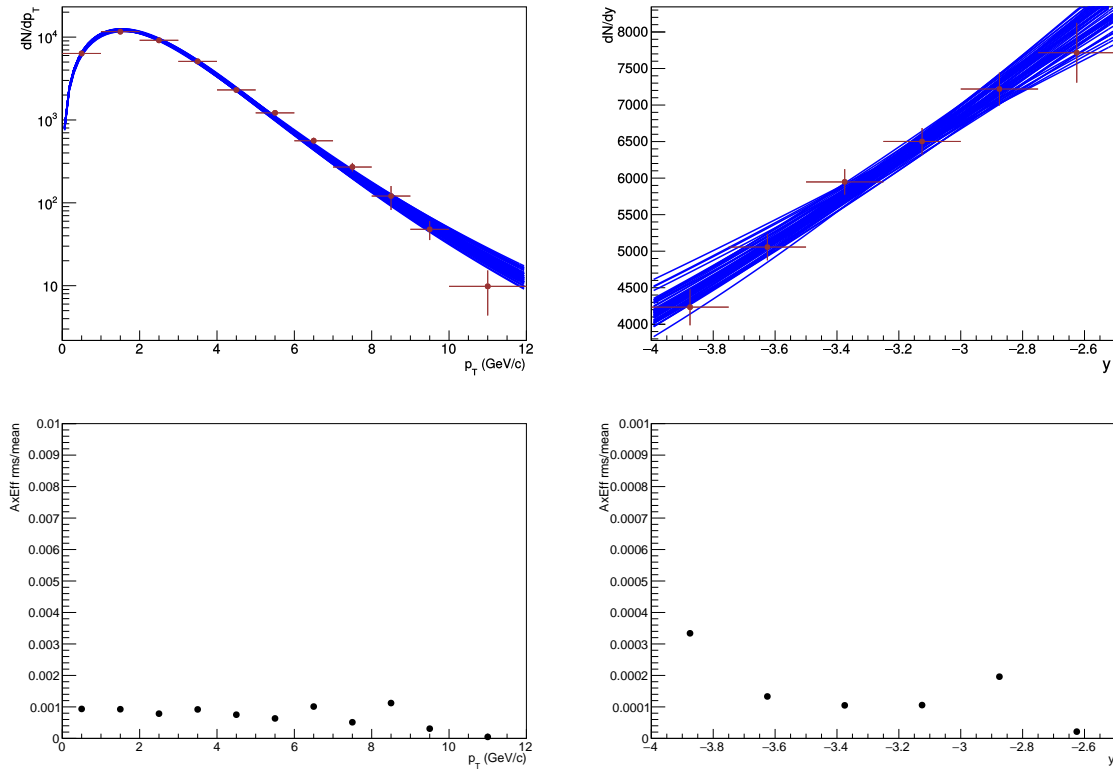


Figure 6.7: Variation of MC shape within statistical uncertainty on data. Top row shows the  $N_{J/\psi}^{\text{corr}}$  as a function of  $p_T$  (left) and  $y$  (right). The lines represent variations of the shape assuming Gaussian uncertainty, which are used to re-weight the MC. Bottom row shows the ratio of RMS over average of all re-weighted  $A\varepsilon$ . More details in text.

The  $p_T$  and  $y$  integrated uncertainty was of 2%. The  $p_T$  differential uncertainty varied between 0.7 – 1.5%. The  $y$  differential uncertainty ranged between 0.5 – 2.5%. Values can be found in Tab. 6.4.

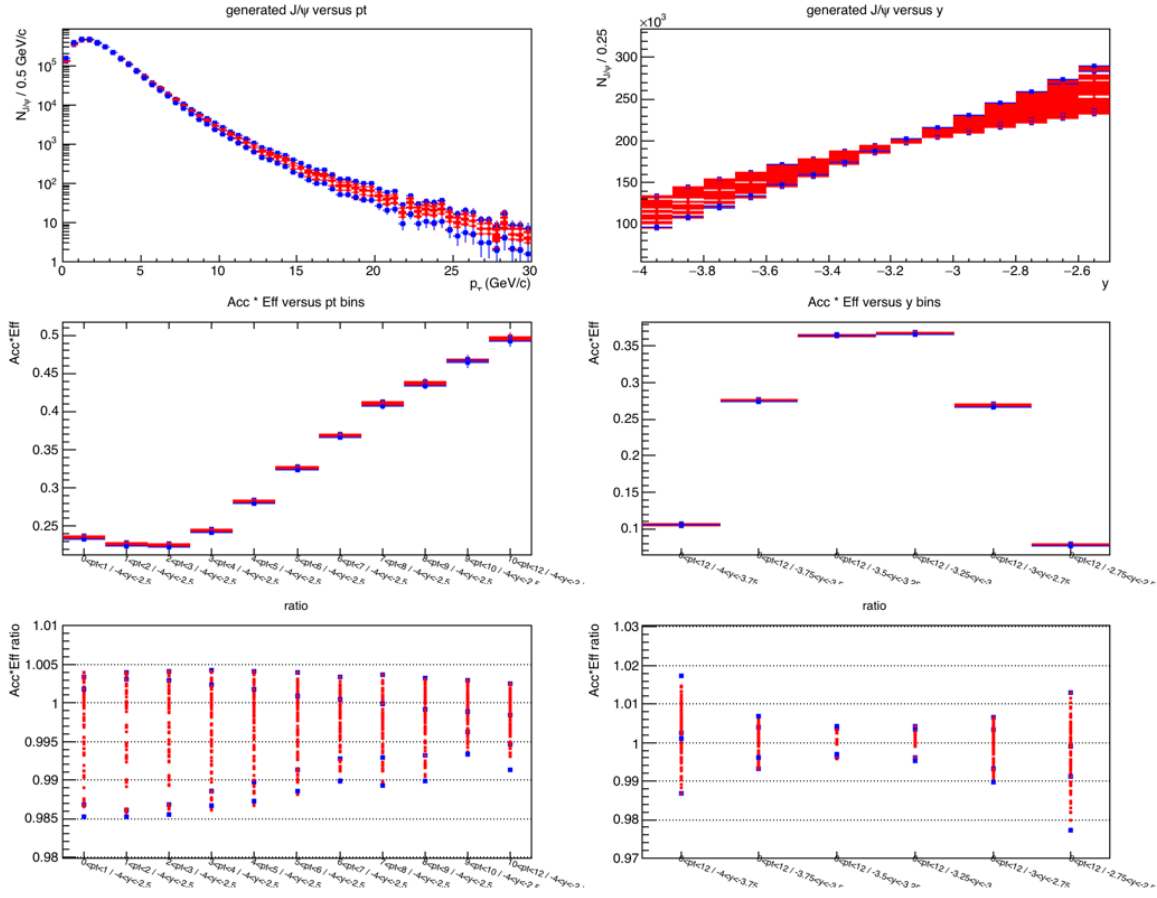


Figure 6.8: The systematic uncertainty on  $A\varepsilon$  associated to the MC input shape in pp collisions at  $\sqrt{s} = 5.02$  TeV. The left column shows the  $p_T$  differential uncertainty, while the right one shows the  $y$  differential. The blue points correspond to the combinations of the extreme shapes. Courtesy of Philippe Pillot.

$p_T$ GeV/c	Syst. Unc. (%)
0 – 1	1.5
1 – 2	1.5
2 – 3	1.5
3 – 4	1.4
4 – 5	1.3
5 – 6	1.2
6 – 7	1.0
7 – 8	1.0
8 – 9	1.0
9 – 10	0.7
10 – 12	0.9

$y$	Syst. Unc. (%)
3.75 – 4.00	2.5
3.50 – 3.75	1.0
3.25 – 3.50	0.5
3.00 – 3.25	0.5
2.75 – 3.00	1.0
2.50 – 2.75	2.5

Table 6.4: The systematic uncertainty on  $A\varepsilon$  associated to the MC input shape as a function of  $p_T$  (left) and  $y$  (right).

### 6.3.1.2 Uncertainty on tracking efficiency

The tracking efficiency uncertainty was extracted using the same method as on p-Pb data at  $\sqrt{s_{NN}} = 8.16$  TeV. See Sec. 5.3 for detailed description. The uncertainty in pp 5.02 TeV data was estimated from CMSL7 triggered data.

The run-dependent estimated tracking efficiency in data and in MC are compared in Fig. 6.9. The distribution shows little variation in time with exception of one run. However this drop in efficiency is well reproduced in the MC. The ratio of estimated tracking efficiencies in data and in MC was

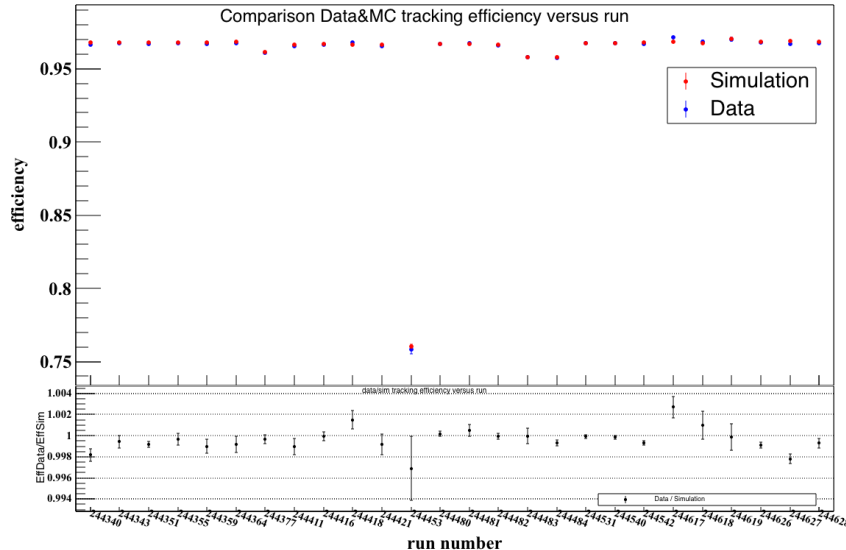


Figure 6.9: Estimated tracking efficiency in data and in MC in pp collisions at  $\sqrt{s} = 5.02$  TeV. Courtesy of Benjamin Audurier and Philippe Pillot.

recomputed varying  $p_T$  and charge selection to study the stability of the method. Fig. 6.10 shows the variation of ratio with these selection criteria as a function of  $p_T$ ,  $y$ , and  $\varphi$ . The single muon uncertainty is computed as the standard deviation of the ratio from the unity over all runs. The  $p_T$ ,  $\varphi$ , and  $y$  ratios must fall within  $\pm 3\sigma$ . The uncertainty on the tracking efficiency on single muon level amounts to

$$\sigma_{\varepsilon_{trk}}^{\mu} = 0.5\%,$$

meaning on  $J/\psi$  level it is

$$\sigma_{\varepsilon_{trk}}^{\mu\mu} = 1\%.$$

### 6.3.1.3 Uncertainty on trigger efficiency

The method to estimate the uncertainty on trigger efficiency is briefly explained in Sec. 5.2.1. Here we will detail an alternative method used in pp analysis at  $\sqrt{s} = 5.02$  TeV [223] to estimate the effect of the  $p_T$  cut. The original method could not have been used as in pp at 5.02 TeV  $Lp_T = 0.5$  GeV/c =  $Ap_T$ .

The  $p_T$  dependent ratio of  $Lp_T/All$  was evaluated instead of  $Lp_T/Ap_T$ . *All* represent all muons selected without requiring tracking-trigger matching. The  $Lp_T/Ap_T$  was evaluated from Pb-Pb data recorder later during the same year, where  $Lp_T = 1$  GeV/c  $\neq$   $Ap_T$ . This was done under the assumption that the efficiency maps are constant in time and that the ratio of data/MC is the same regardless whether  $Lp_T = 1$  GeV/c or  $Lp_T = 0.5$  GeV/c. The ratio  $Lp_T/Ap_T$  from Pb-Pb was then propagated to  $Lp_T/All$  from pp in order to estimate the expected trigger response in pp data. From there on, the usual procedure was followed. The propagation was executed using two different methods:

- Via stretch factor method, which relies on the stretch factor

$$s = \frac{p_T^{cut|MC}_{Pb-Pb}}{p_T^{cut|MC}_{pp}}. \quad (6.7)$$

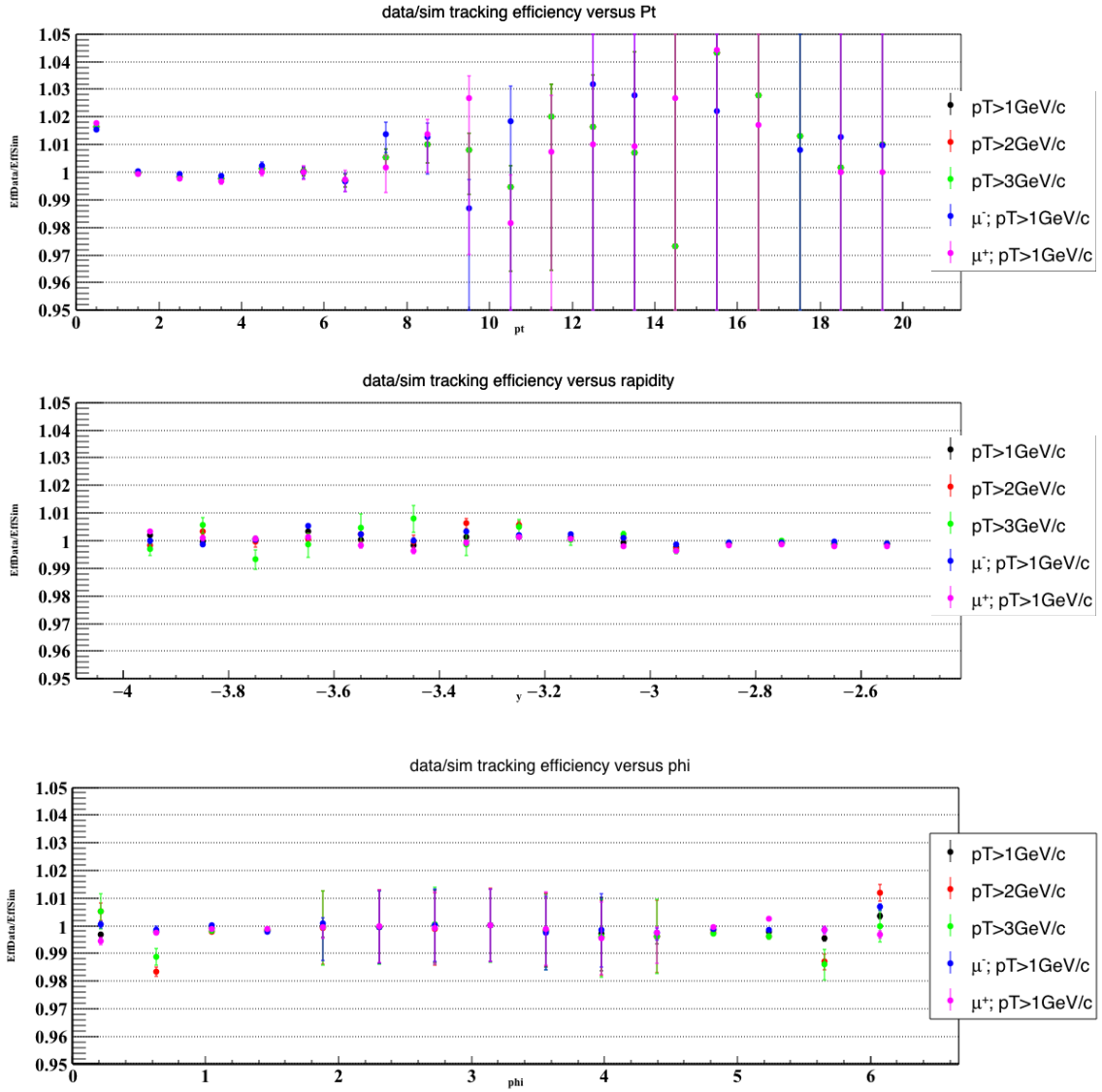


Figure 6.10: Ratio of estimated tracking efficiency in data and in MC versus  $p_T$  (top),  $y$  (middle), and  $\phi$  (bottom) in pp collisions at  $\sqrt{s} = 5.02$  TeV. Courtesy of Benjamin Audurier.

Here  $p_T^{cut}$  is defined as the  $p_T$  value for which the trigger reaches 50% of the difference between its maximum and the minimum. The  $Lp_T/Ap_T$  ratio from Pb–Pb is then propagated to  $Lp_T/All$  in pp as

$$\frac{Lp_T}{All}\bigg|_{pp}^{\text{data}}(p_T) = \frac{Lp_T}{All}\bigg|_{pp}^{\text{MC}}(p_T) \times \frac{\left(\frac{Lp_T}{Ap_T}\bigg|_{\text{Pb-Pb}}^{\text{data}}(s \cdot p_T)\right)}{\left(\frac{Lp_T}{Ap_T}\bigg|_{\text{Pb-Pb}}^{\text{MC}}(s \cdot p_T)\right)}.$$

- Via fitting the  $\frac{Lp_T}{Ap_T}\big|_{\text{Pb-Pb}}$  in data and MC with an error function

$$F^X(p_T, \langle p_T \rangle, \sigma) = 1 + p_0 \times \left\{ \text{erf} \left( \frac{p_T - \langle p_T \rangle}{\sqrt{2}\sigma} \right) \right\},$$

where  $X$  represent the type of sample (data or MC). Modifying the fit parameters by the stretch factor defined in Eq. (6.7), the  $Lp_T/Ap_T$  ratio from Pb–Pb is propagated to  $Lp_T/All$  in pp as

$$\frac{Lp_T}{All}\bigg|_{pp}^{\text{data}}(p_T) = \frac{Lp_T}{All}\bigg|_{pp}^{\text{MC}}(p_T) \times \frac{F^{\text{data}}(p_T, \langle p_T \rangle / s, \sigma / s)}{F^{\text{MC}}(p_T, \langle p_T \rangle / s, \sigma / s)}.$$

The intrinsic uncertainty of the muon trigger was evaluated to 1.5%. The integrated effect of the muon  $p_T$  cut amounted to 1%. The  $p_T$  and  $y$  differential values can be found in Tab. 6.5. Summing the two contributions, the final result for  $p_T$  and  $y$  integrated uncertainty was 1.8%. The  $p_T$  differential uncertainty ranged between 1.5 – 1.8% and the  $y$  differential uncertainty varied between 1.5 – 2.3%.

$p_T$ GeV/ $c$	Syst. Unc. (%)		
0 – 1	0.8		
1 – 2	1.0		
2 – 3	1.0		
3 – 4	0.9		
4 – 5	0.7		
5 – 6	0.6		
6 – 7	0.4		
7 – 8	0.4		
8 – 9	0.3		
9 – 10	0.2		
10 – 12	0.2		
		$y$	Syst. Unc. (%)
		3.75 – 4.00	0.2
		3.50 – 3.75	0.6
		3.25 – 3.50	0.8
		3.00 – 3.25	0.8
		2.75 – 3.00	1.0
		2.50 – 2.75	1.7

Table 6.5: The systematic uncertainty on trigger efficiency associated to the muon  $p_T$  cut threshold in pp collisions at  $\sqrt{s} = 5.02$  TeV.

### 6.3.1.4 Uncertainty on trigger-track matching

The matching efficiency between a track reconstructed in the tracking chambers and a track reconstructed in the trigger chambers depends on the  $\chi^2$  cut. The results for the matching efficiency as a function of  $\chi^2$  cut for different track and momentum selection are shown in Fig. 6.11. The uncertainty at dimuon level amounted to 1%.

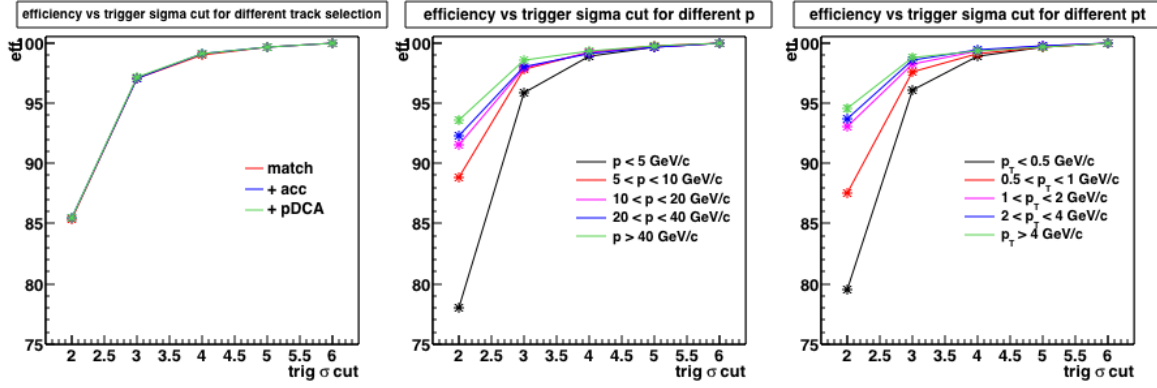


Figure 6.11: The matching efficiency as a function of the matching  $\chi^2$  cut for different track selection (left), for different  $p$  selection (middle), and for different  $p_T$  selection (right) in pp collisions at  $\sqrt{s} = 5.02$  TeV. Courtesy of Benjamin Audurier.

## 6.4 Event normalisation

### 6.4.1 Dimuon trigger event normalisation

In our analysis, we extracted the yields from a sample of events collected triggering on a pair of muons. However, such events constitute only a fraction of all statistics. Using such triggers therefore introduces a bias into the data. In order to compare the results with other experiments and theory, we needed to correct for this bias. We achieved this by normalising the yields to the event sample collected with minimum bias trigger. As minimum bias, we considered the trigger classes CINT7-B-NOPF-MUFAST and C0TVX-B-NOPF-CENTNOTRD, described in Sec. 4.4. We will refer to them in the following as CINT7 and C0TVX respectively, and will be denoted as MB in the following. The MB triggers are usually downscaled during dimuon data taking to allow more bandwidth for the rare events.

#### 6.4.1.1 Methods to calculate the normalisation factor

The equivalent number of MB events  $N_{\text{MB}}^{\text{eq}}$  in run  $i$  can be computed from the dimuon triggered sample  $N_{\text{CMUL7}}$  as

$$N_{\text{MB}}^{\text{eq},i} = F_{\text{norm}}^i \times N_{\text{CMUL7}}^i. \quad (6.8)$$

There are two approaches to calculate the normalisation factor  $F_{\text{norm}}$ :

1. First is to use the **offline method**, which exploits the offline information for different trigger classes combined with the CTP input. The normalisation in run  $i$  can be defined in an *one-step method* as

$$F_{\text{norm}}^{\text{off1},i} = \frac{N_{\text{MB}}^i}{N_{\text{MB}\&0\text{MUL}}^i}, \quad (6.9)$$

where  $N_{\text{MB}}^i$  and  $N_{\text{MB}\&0\text{MUL}}^i$  denote the number of counts corresponding to the given MB trigger class with the latter also having the 0MUL input fired. 0MUL is fired when at least one pair of opposite sign dimuons is reconstructed in the event. Note that it is implied that all the samples used in offline  $F_{\text{norm}}$  calculation are physics selected, meaning they originate in beam-beam interactions.

To improve the precision of the method, we can redefine the normalisation in a *two-step method* by using an intermediate trigger with higher statistics such as the single muon trigger  $N_{\text{CMSL7}}$

$$F_{\text{norm}}^{\text{off2},i} = \frac{N_{\text{MB}}^i}{N_{\text{MB}\&0\text{MSL}}^i} \times \frac{N_{\text{CMSL7}}^i}{N_{\text{CMSL7}\&0\text{MUL}}^i}. \quad (6.10)$$

Here  $N_{\text{MB}\&0\text{MSL}}$  gives the number of MB triggered events with at least one reconstructed low- $p_T$  single muon (0MSL input fired).  $N_{\text{CMSL7}\&0\text{MUL}}$  then denotes the subsample of  $N_{\text{CMSL7}}$  that contains also the 0MUL input. The idea is that the CMSL7 trigger is usually less downscaled than MB.

2. The **online method** relies on the information from L0b scalars stored in the OCDB. L0b means that we use information from the L0 trigger before the CTP decision (recall Sec. 4.4.1). The benefit of the online method is that the online scalars contain large statistics than the offline counters. The physics selection cannot be applied to the online scalars. The purity factor  $F_{\text{purity}}$ , computed from the offline counters, is applied to correct for the ratio of physics selected events in the sample:

$$F_{\text{purity}}^i = \frac{N_{\text{PhysSel}}^i}{N_{\text{ALL}}^i}.$$

The purity factor of the T0, and hence the class C0TVX, is 100 %. The run-by-run purity factor for the CINT7 and CMUL7 trigger class are shown in Fig. 6.12.

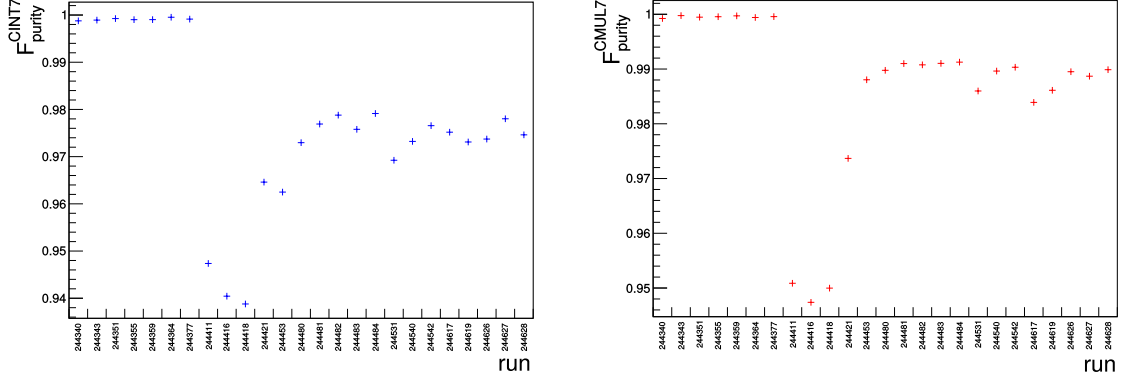


Figure 6.12: Purity factor for CINT7 and CMUL7 trigger classes in pp at  $\sqrt{s} = 5.02$  TeV as a function of time.

The normalisation can be then computed from the ratio of MB and CMUL7 scalars as

$$F_{\text{norm}}^{\text{online},i} = \frac{F_{\text{purity}}^{\text{MB},i} \text{L0b}_{\text{MB}}^i}{F_{\text{purity}}^{\text{CMUL7},i} \text{L0b}_{\text{CMUL7}}^i}. \quad (6.11)$$

#### 6.4.1.2 Correction for pile-up

In LHC Run 2 pp collisions, several collisions can be piled up into a single event. To take into account such events in our normalisation, we introduced a per-run pile-up factor

$$F_{\text{PU}}^i = \frac{\mu^i}{1 - e^{-\mu^i}}, \quad (6.12)$$

where  $i$  denotes the run. The interaction rate  $\mu$  can be computed from online information in the OCDB as

$$\mu = -\ln \left( 1 - \frac{F_{\text{purity}}^{\text{MB},i} \text{L0bRate}_{\text{MB}}^i}{N_{\text{bunches}}^i f_{\text{LHC}}} \right), \quad (6.13)$$

where  $\text{L0bRate}_{\text{MB}}^i$  is the number of  $\text{L0b}_{\text{MB}}^i$  counts per hour,  $N_{\text{bunches}}^i$  gives the number of colliding bunches, and  $f_{\text{LHC}} = 11245$  kHz is the LHC frequency. Fig. 6.13 shows the pile-up factor for the CINT7 and C0TVX trigger classes.

We applied this factor to all formula to compute  $F_{\text{norm}}$ . Hence for the one-step offline method, we got from Eq. (6.9)

$$F_{\text{norm}}^{\text{off1},i} = F_{\text{PU}}^i \frac{N_{\text{MB}}^i}{N_{\text{MB\&0MUL}}^i}. \quad (6.14)$$

Similarly for the two-step offline method, Eq. (6.10) changed to

$$F_{\text{norm}}^{\text{off2},i} = F_{\text{PU}}^i \frac{N_{\text{MB}}^i}{N_{\text{MB\&0MSL}}^i} \times \frac{N_{\text{CMSL7}}^i}{N_{\text{CMSL7\&0MUL}}^i}. \quad (6.15)$$

Finally, the online normalisation changed from Eq. (6.11) into

$$F_{\text{norm}}^{\text{online},i} = F_{\text{PU}}^i \frac{F_{\text{purity}}^{\text{MB},i} \text{L0b}_{\text{MB}}^i}{F_{\text{purity}}^{\text{CMUL7},i} \text{L0b}_{\text{CMUL7}}^i}. \quad (6.16)$$

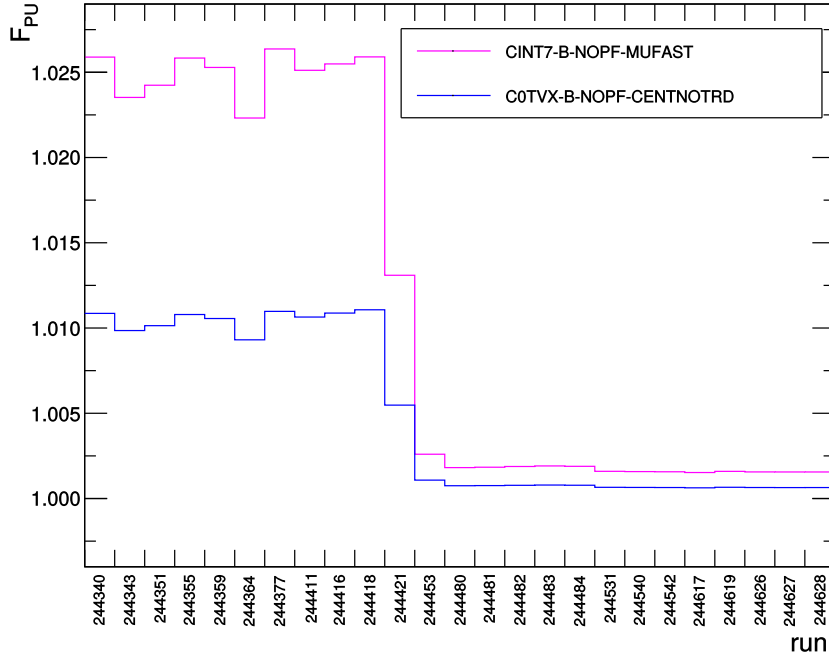


Figure 6.13: Pile-up factor for CINT7 and C0TVX trigger classes in pp at  $\sqrt{s} = 5.02$  TeV as a function of time.

### 6.4.1.3 Normalisation factor $F_{\text{norm}}$ in pp at 5.02 TeV

We computed the normalisation  $F_{\text{norm}}$  from CINT7 trigger class, using the two-step offline method (see Eq. (6.15)). The one-step method was also considered but was not ultimately chosen for final values due to limited statistics. The online method (Eq. 6.16) was used to calculate  $F_{\text{norm}}$  from the C0TVX triggered data. The results of the two calculations are visualised in Fig. 6.14.

The run averaged normalisation factor was calculated as

$$F_{\text{norm}} = \frac{\sum_{\text{run}=i} F_{\text{norm}}^i \times N_{\text{CMUL7}}^i}{\sum_{\text{run}=i} N_{\text{CMUL7}}^i}. \quad (6.17)$$

For the CINT7 trigger, we calculated

$$F_{\text{norm}}^{\text{CINT7}} = 4736.87 \pm 60.29.$$

The online method for C0TVX trigger gave

$$F_{\text{norm}}^{\text{C0TVX}} = 1960.18 \pm 1.67.$$

To allow us to compare the two methods, we computed the cross section of the CMUL7 class in run  $i$  as

$$\sigma_{\text{MUL}}^i = \frac{\sigma_{\text{vdM}}}{F_{\text{norm}}^i}, \quad (6.18)$$

where  $\sigma_{\text{vdM}}$  is the cross section measured in the van der Meer scan for the corresponding MB trigger class. The vdM scan gave  $\sigma_{\text{vdM}}^{\text{V0}} = 51.17 \pm 1.18$  mb and  $\sigma_{\text{vdM}}^{\text{T0}} = 21.55 \pm 0.45$  mb to be used together with CINT7 and C0TVX class respectively. From Fig. 6.15 we see that the two methods and the two trigger classes give consistent results. The online method using C0TVX is however more precise. We will hence use it in the final correction calculation.

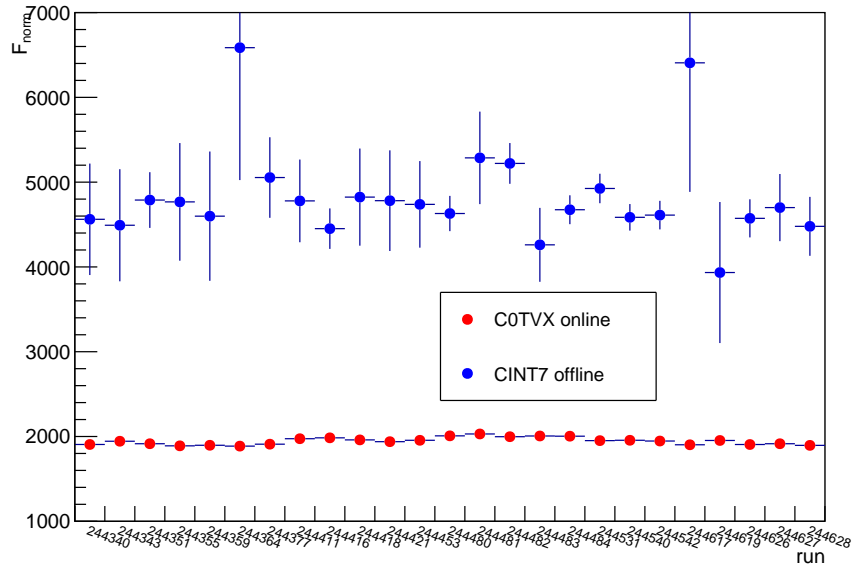


Figure 6.14: Pile-up factor for CINT7 and C0TVX trigger classes in pp at  $\sqrt{s} = 5.02$  TeV as a function of time.

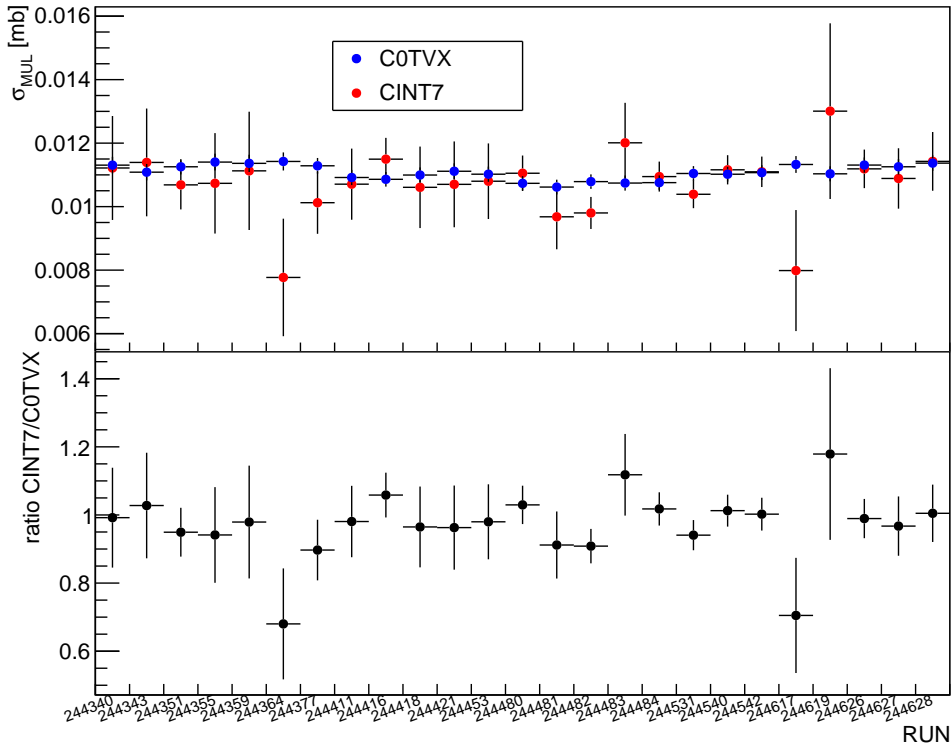


Figure 6.15:  $\sigma_{MUL}$  calculated from the CINT7 and C0TVX trigger classes in pp at  $\sqrt{s} = 5.02$  TeV as a function of time.

## 6.4.2 Luminosity

The integrated luminosity for our data sample can be computed as

$$\mathcal{L}_{\text{int}} = \frac{N_{\text{CMUL7}}^{\text{tot}}}{\sigma_{\text{MUL}}} = \frac{N_{\text{CMUL7}}^{\text{tot}} \times F_{\text{norm}}}{\sigma_{\text{vdM}}}. \quad (6.19)$$

Our total dimuon event count was  $N_{\text{CMUL7}}^{\text{tot}} = 1168316$ . We used the vdM cross section for T0 and the corresponding  $F_{\text{norm}}$ . Putting these ingredients together into Eq. (6.2), we got

$$\mathcal{L}_{\text{int}} = 106.27 \pm 0.10(\text{stat.}) \pm 2.22(\text{syst.}) \text{ nb}^{-1}.$$

The systematic uncertainty was taken as a square sum of systematic uncertainty on  $F_{\text{norm}}$  and on  $\sigma_{\text{vdM}}$ .

## 6.5 Systematic uncertainty

The various contributions to the overall systematic uncertainty are summarised in Tab. 6.6. The dominant uncertainty comes from the signal extraction. Thanks to the low luminosity and the consequent low pile-up during the data taking, the detector was in a good condition, resulting in small uncertainties.

source	integrated	vs $p_{\text{T}}$	vs $y$
signal extraction	2.4%	0.8 – 31.3%	2.5 – 3.1%
MC input	2%	0.1 – 1.5%	0.5 – 2.5%
tracking efficiency	1%	1%	1%
trigger efficiency	1.8%	1.5 – 1.8%	1.5 – 2.3%
matching efficiency	1%	1%	1%
luminosity	2.1%	2.1%*	2.1%*
BR	0.5%	0.5%*	0.5%*

Table 6.6: Summary of systematic uncertainties on  $J/\psi$  cross section. Values marked with asterisk are correlated in  $p_{\text{T}}$  and  $y$ .

## 6.6 Inclusive $J/\psi$ production in pp at $\sqrt{s} = 5.02$ TeV

### 6.6.1 Cross section

We calculated the inclusive  $J/\psi$  cross section  $\sigma_{J/\psi}^{pp}$  integrated in  $p_{\text{T}} < 12$  GeV/ $c$  and  $2.5 < y < 4$  from Eq. (6.1) as

$$\frac{d^2\sigma_{J/\psi}}{dp_{\text{T}}dy} = \frac{1}{\Delta p_{\text{T}}\Delta y} \frac{N_{J/\psi}^{\text{raw}}}{A\varepsilon(p_{\text{T}}, y)\text{BR}_{J/\psi \rightarrow \mu^+\mu^-}\mathcal{L}_{\text{int}}}.$$

The integrated cross section amounted to

$$\sigma_{J/\psi}^{pp} = 5.60 \pm 0.07(\text{stat.}) \pm 0.26(\text{syst.}) \mu\text{b}.$$

The differential cross section as a function of  $p_{\text{T}}$  and of  $y$  are plotted in Fig. 6.16 and Fig. 6.17 respectively. The values can be found in Tab. 6.7. The results are consistent with a parallel analysis of  $J/\psi \rightarrow \mu^+\mu^-$  in pp 5.02 TeV data [223].

The integrated and  $p_{\text{T}}$  differential cross section were used in the calculation of the nuclear modification factor  $R_{\text{AA}}$  in Pb–Pb at  $\sqrt{s_{\text{NN}}} = 5.02$  TeV [100]. The  $R_{\text{AA}}$  results can be found in Fig. 2.15a and Fig. 2.16b.

Due to the back-then unavailability of pp 5.02 TeV data, an interpolation was used as a reference in the analysis of p–Pb data at  $\sqrt{s_{\text{NN}}} = 5.02$  TeV taken in 2013 instead. The interpolation was a

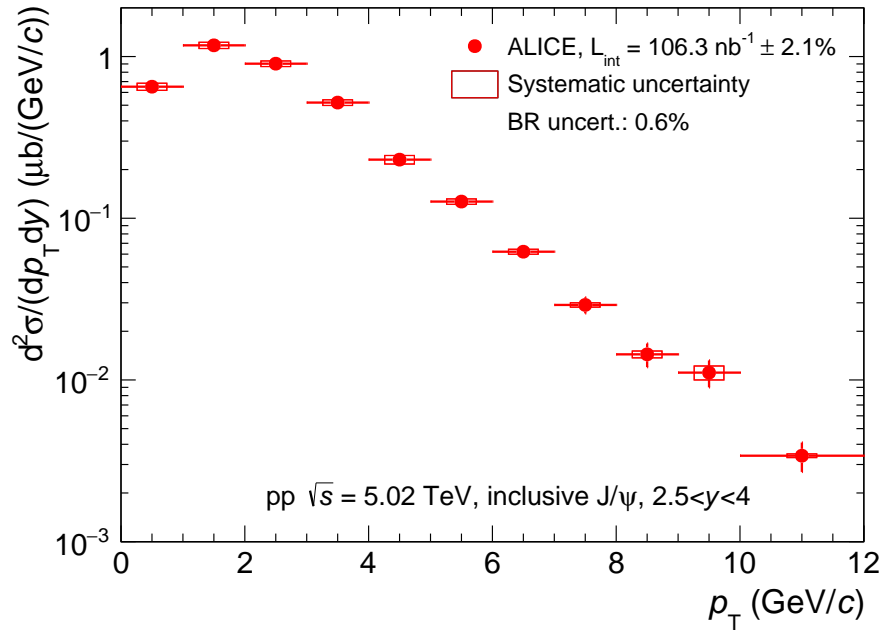


Figure 6.16: Differential inclusive  $J/\psi$  cross section as a function of  $p_T$  in pp at  $\sqrt{s} = 5.02$  TeV [73].

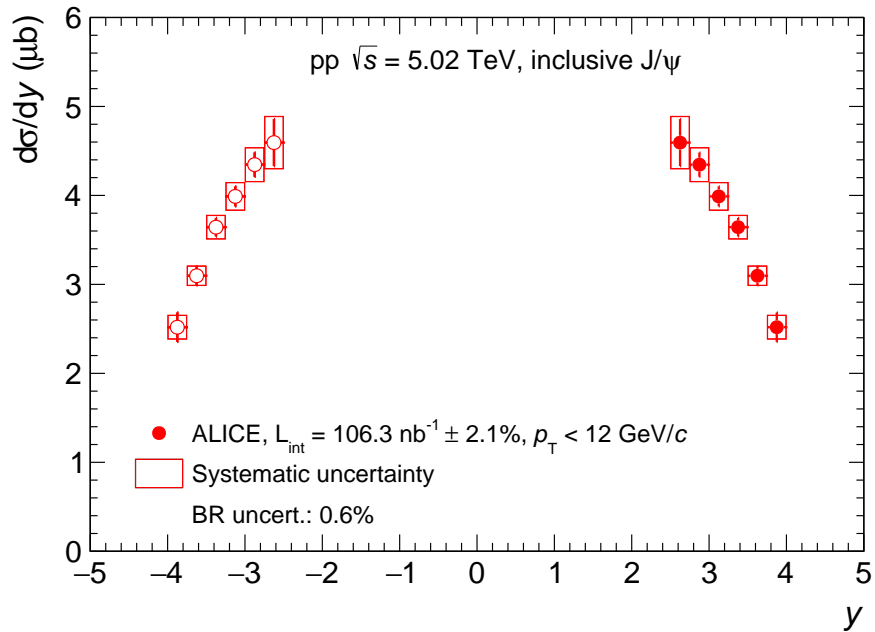


Figure 6.17: Differential inclusive  $J/\psi$  cross section as a function of  $y$  in pp at  $\sqrt{s} = 5.02$  TeV [73]. Filled and open markers denote the measured and mirrored points respectively.

$p_T$ GeV/c	$d^2\sigma_{J/\psi}^{pp}/dp_T dy$ ( $\mu\text{b}$ )		
0 – 1	$0.6578 \pm 0.0315 \pm 0.0177$		
1 – 2	$1.1854 \pm 0.0461 \pm 0.0326$		
2 – 3	$0.9358 \pm 0.0339 \pm 0.0258$		
3 – 4	$0.5156 \pm 0.0226 \pm 0.0138$		
4 – 5	$0.2381 \pm 0.0112 \pm 0.0062$		
5 – 6	$0.1265 \pm 0.0091 \pm 0.0032$		
6 – 7	$0.0599 \pm 0.0046 \pm 0.0015$		
7 – 8	$0.0300 \pm 0.0028 \pm 0.0008$		
8 – 9	$0.0137 \pm 0.0022 \pm 0.0004$		
9 – 10	$0.0073 \pm 0.0014 \pm 0.0002$		
10 – 12	$0.0035 \pm 0.0007 \pm 0.0001$		
		$y$	$d\sigma_{J/\psi}^{pp}/dy$ ( $\mu\text{b}$ )
		3.75 – 4.00	$2.539 \pm 0.153 \pm 0.107$
		3.50 – 3.75	$3.133 \pm 0.106 \pm 0.122$
		3.25 – 3.50	$3.679 \pm 0.103 \pm 0.125$
		3.00 – 3.25	$4.043 \pm 0.108 \pm 0.153$
		2.75 – 3.00	$4.444 \pm 0.132 \pm 0.171$
		2.50 – 2.75	$4.765 \pm 0.262 \pm 0.228$

Table 6.7: The differential J/ $\psi$  cross section extracted in  $p_T$  bins integrated over  $2.5 < y < 4$  and in bins of  $y$  integrated in  $p_T$ .

common work of ALICE and LHCb, as both detectors cover a similar rapidity coverage at forward rapidity ( $2.5 < y < 4$  for ALICE and  $2 < y < 4.5$  for LHCb) [226]. The interpolated reference in reality was obtained through interpolation of integrated cross section from available pp data (2.7, 7 TeV, and in case of LHCb also 8 TeV), followed by an extrapolation in rapidity to obtain the same rapidity range as p-Pb data ( $2.03 < y_{\text{cms}} < 3.53$  for p-Pb  $-4.46 < y_{\text{cms}} < -2.96$  and Pb-p). The interpolated cross section covers the full  $y_{\text{cms}}$  and goes up to  $p_T < 8$  GeV/c.

Fig. 6.18 shows the  $p_T$ - and  $y$ -differential spectrum, compared with the points obtained from interpolation. The two are in a good agreement within uncertainty. The cross section measured from data is more precise than the interpolation.

## 6.6.2 Mean transverse momentum

We evaluated the  $\langle p_T \rangle$  by fitting the  $p_T$ -differential yields with the following function:

$$f(p_T) = C \frac{p_T}{\left(1 + (p_T/p_0)^2\right)^n}. \quad (6.20)$$

The three parameters  $C$ ,  $p_0$ , and  $n$  were left free in the fitting process. Example of the fit to the  $p_T$  spectrum is shown in Fig. 6.19.

The  $\langle p_T \rangle$  and the mean transverse momentum squared  $\langle p_T^2 \rangle$  were calculated as the first and second order moment of  $f(p_T)$  respectively:

$$\langle p_T^k \rangle = \frac{\int p_T^k f(p_T) dp_T}{\int f(p_T) dp_T} \quad (6.21)$$

The errors on the  $\langle p_T^k \rangle$  were evaluated by multiplying the covariance matrix (Cov) by the fit Jacobian  $J = (0, \partial \langle p_T \rangle / \partial p_0, \partial \langle p_T \rangle / \partial n)$  on each side:

$$\sigma_{\langle p_T \rangle} = \sqrt{J(\text{Cov})J^T}. \quad (6.22)$$

Two scenarios were considered in the error calculation. In the first case, we performed the fit using only statistical and only systematic uncertainties on the data in order to extract statistical and systematic uncertainty on  $\langle p_T \rangle$  respectively. In the second case, the quadratic sum of the two uncertainties was considered. Both yield consistent results.

The final  $\langle p_T \rangle$  and  $\langle p_T^2 \rangle$ , truncated between  $0 < p_T < 12$  GeV/c, are

$$\begin{aligned} \langle p_T \rangle &= 2.37 \pm 0.02 \pm 0.02 \text{ GeV}/c, \\ \langle p_T^2 \rangle &= 8.07 \pm 0.14 \pm 0.12 \text{ GeV}^2/c^2. \end{aligned}$$

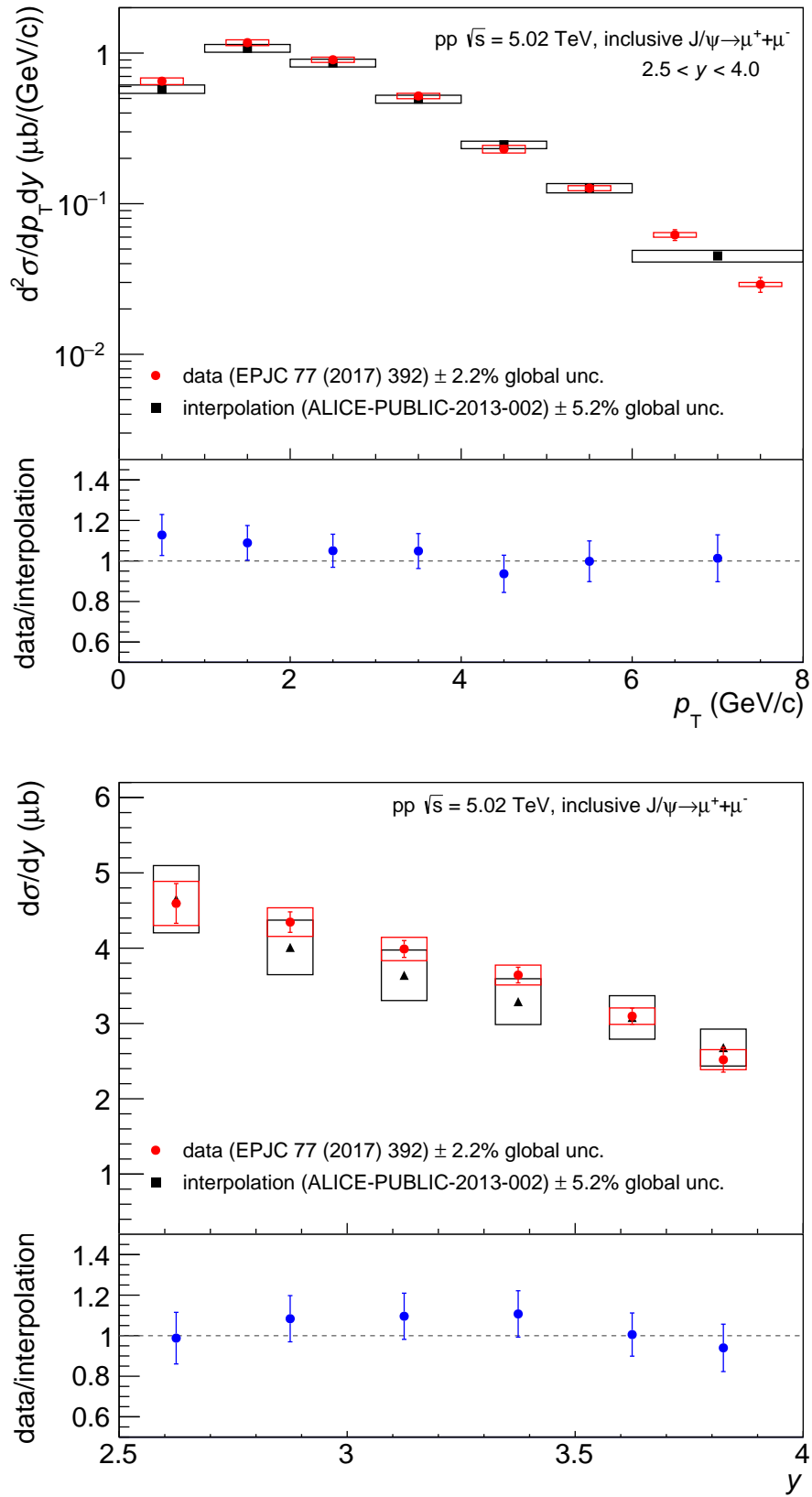


Figure 6.18: Differential inclusive  $J/\psi$  cross section in pp collisions at  $\sqrt{s} = 5.02$  TeV as a function  $p_T$  and  $y$  compared with interpolation done by ALICE and LHCb [226].

The central values were extracted by fits with combined statistical and systematic uncertainties, while the statistical (systematic) uncertainties were taken from fits with only statistical (systematic) uncertainties taken into account.

The results were cross-checked by applying an alternative method [223], which will be in further detail described in the Ch. 8. The invariant mass method consists of fitting the  $A\varepsilon$ -corrected dimuon  $\langle p_T \rangle$  distribution as a function of the dimuon invariant mass  $M_{\mu\mu}$  by

$$\begin{aligned} \langle p_T \rangle (M_{\mu\mu}) &= \alpha^{J/\psi}(M_{\mu\mu}) \langle p_T \rangle^{J/\psi} \\ &+ \alpha^{\psi(2S)}(M_{\mu\mu}) \langle p_T \rangle^{\psi(2S)} \\ &+ (1 - \alpha^{J/\psi}(M_{\mu\mu}) - \alpha^{\psi(2S)}(M_{\mu\mu})) \langle p_T \rangle^{\text{bkgd}}(M_{\mu\mu}). \end{aligned} \quad (6.23)$$

In the above equation,  $\langle p_T \rangle^{J/\psi}$  and  $\langle p_T \rangle^{\psi(2S)}$ ,  $\alpha(M_{\mu\mu}) = S/(S + B)$  were extracted from fitting the  $A\varepsilon$ -corrected invariant mass spectra. Both methods gave compatible values of  $\langle p_T \rangle$ .

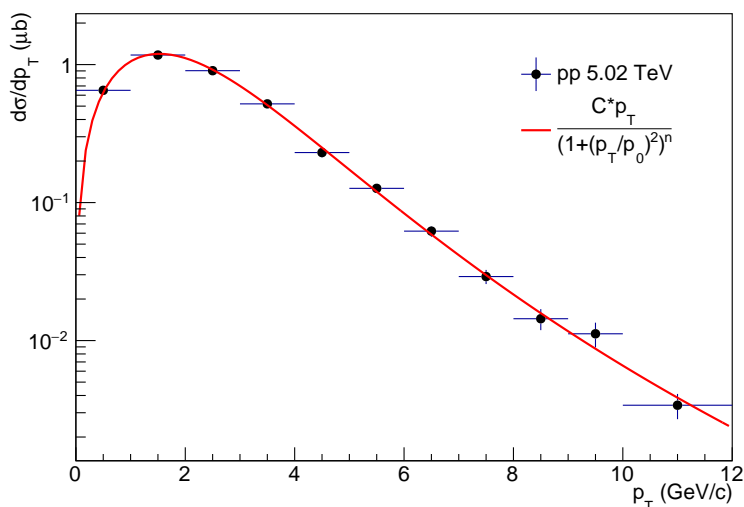


Figure 6.19: Example fit of the function in Eq. (6.20) to the  $p_T$  differential spectrum in pp collisions at  $\sqrt{s} = 5.02$  TeV.

### 6.6.3 Comparison with theory

We remind that at forward rapidity, ALICE measures the inclusive cross section, i. e. the prompt and non-prompt contributions are not separated. For this reason, we considered both contributions when comparing data to theory. We used three different NRQCD calculations for prompt  $J/\psi$ : a high- $p_T$  next-to-leading-order (NLO) NRQCD calculation from Ma et al. [65], a low- $p_T$  calculation by Ma and Venugopalan [57] coupling NLO NRQCD with Colour Glass Condensate (CGC) to describe gluon saturation at low- $x$ , and a high- $p_T$  NLO NRQCD model by Butenschön and Kniehl [229]. The non-prompt  $J/\psi$  were described by fixed-order-next-to-leading-logarithm (FONLL) calculation by Cacciari et al. for open beauty [67].

The FONLL calculation was added to each of the NRQCD. The errors of the given two calculations were considered uncorrelated, the final error was taken as their quadratic sum. It was considered that while NRQCD describes the production of bound charm quark pairs, the FONLL relates to the production of beauty quarks and thus they could be taken as uncorrelated.

The main differences between the NLO NRQCD calculations stem from the treatment of colour octet (CO) long distance mass elements (LDME). The calculation by Butenschön and Kniehl [229] uses three different matrix elements while the calculation by Ma et al. [65] uses two linear combinations of the three matrix elements. The limitation for the latter comes from the fitting of  $\psi(2S)$ . Other differences include the data sets used in the matrix elements fits, the lower  $p_T$  cut-off above which the calculation is applicable, and the treatment of  $\chi_c$  and  $\psi(2S)$  decaying into  $J/\psi$ . In the NLO+CGC

calculation by Ma and Venugopalan [57], all three matrix elements for  $\psi(2S)$  could be determined from a global fit. The calculation is valid at  $p_T < 8$  GeV/c. At higher  $p_T$ , the calculation starts to disagree with the data for prompt J/ $\psi$  production. According to the authors, this was expected and originates from the initial conditions used in the CGC calculation.

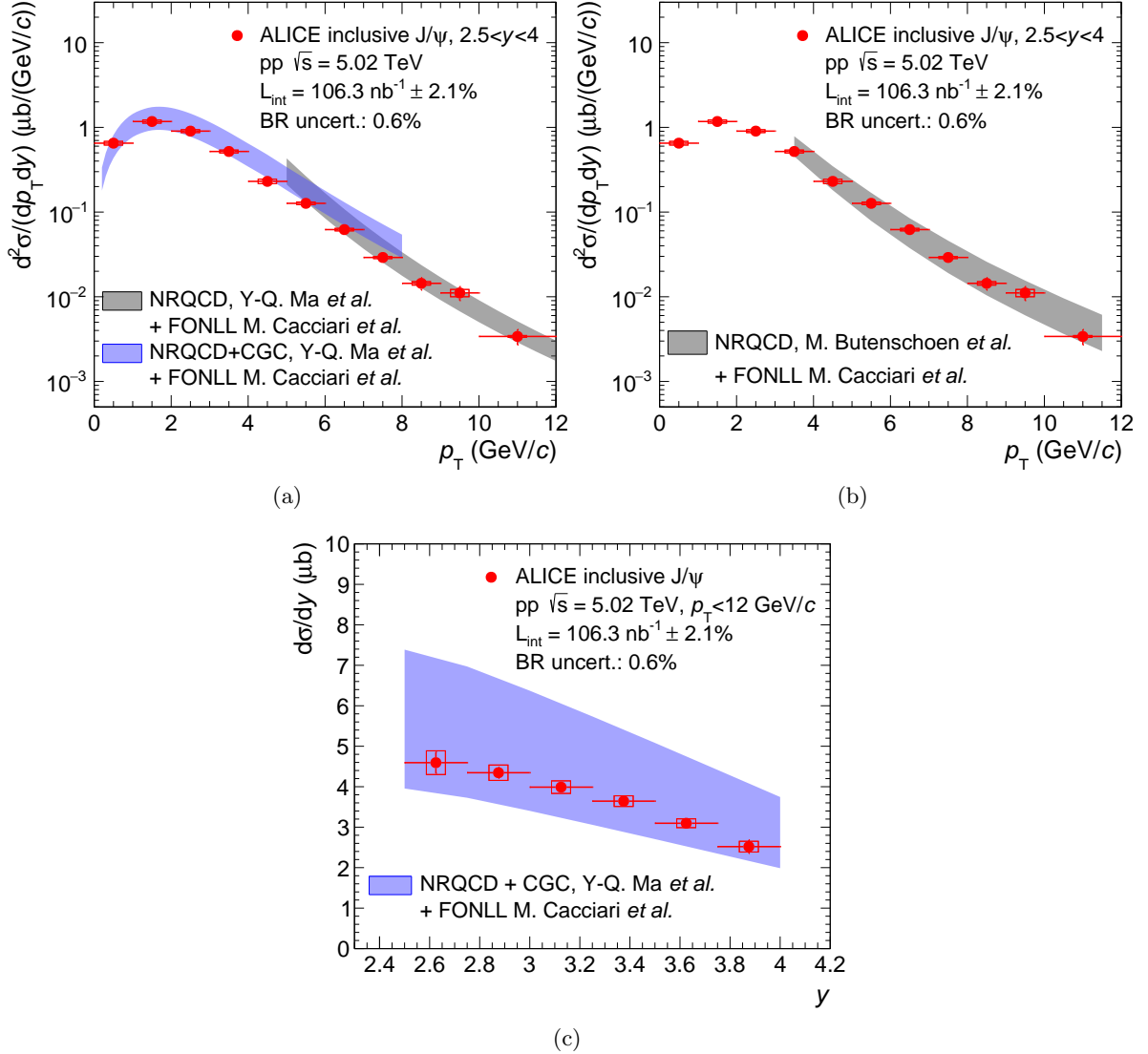


Figure 6.20: Differential inclusive J/ $\psi$  cross section in pp collisions at  $\sqrt{s} = 5.02$  TeV. Taken from [73].

The inclusive J/ $\psi$  cross section was compared with theoretical curves in Fig. 6.20. The NLO NRQCD calculation by Ma *et al.* [65] is shown in grey in Fig. 6.20a. The blue band shows the NLO NRQCD+CGC by Ma and Venugopalan [57]. We remind that both curves were summed with a FONLL calculation by Cacciari *et al.* [67]. The theory curves describe the data rather well. In the combined NRQCD+CGC framework, the calculation overestimates the data at  $p_T \gtrsim 4$  GeV/c. As was discussed in the previous paragraph, the NRQCD+CGC was expected to overestimate the data. Moreover, the non-prompt contribution at  $p_T > 4$  GeV/c in the forward rapidity region in pp at 7 TeV [40] and 13 TeV [41] is  $> 10\%$ . We can expect the same to be true also at 5.02 TeV, meaning part of the disagreement can come from this source. The NRQCD calculation at  $p_T > 5$  GeV/c summed with the FONLL describes the data well at high  $p_T$ . At the lower limit, the data lie below the band. As the non-prompt contribution is low in this  $p_T$  region, the difference most likely comes from the  $p_T$  cut-off used in fitting the LDMEs. For  $p_T > 3.5$  GeV/c we also compared the data with the calculation by Butenshön and Kniehl [229] summed with FONLL by Cacciari *et al.* [67], see Fig. 6.20b. We observed a good agreement over the full valid  $p_T$  range.

The results of the NRQCD+CGC calculation were integrated in  $p_T$  and compared with the  $y$ -differential  $J/\psi$  cross section. The calculation is only valid for  $p_T < 8$  GeV/ $c$ , however the contribution of  $J/\psi$  with  $p_T > 8$  GeV/ $c$  is in order of percent and can be neglected. We observed a good agreement between the theory and the data.

## 6.7 Energy dependence of forward $J/\psi$ production in pp

In this section, we will discuss the energy dependence of the  $\sigma_{J/\psi}^{pp}$  at forward rapidity. ALICE measured the inclusive  $\sigma_{J/\psi}^{pp}$  at forward rapidity at multiple energies, namely at  $\sqrt{s} = 2.76, 5.02, 7, 8,$  and  $13$  TeV [72–75]. Furthermore, the inclusive cross section of the  $\psi(2S)$  was measured at  $\sqrt{s} = 7, 8,$  and  $13$  TeV [73–75]. Therefore when possible, the  $\psi(2S)$ -to- $J/\psi$  ratio was computed and compared to theory in addition to the corresponding cross sections.

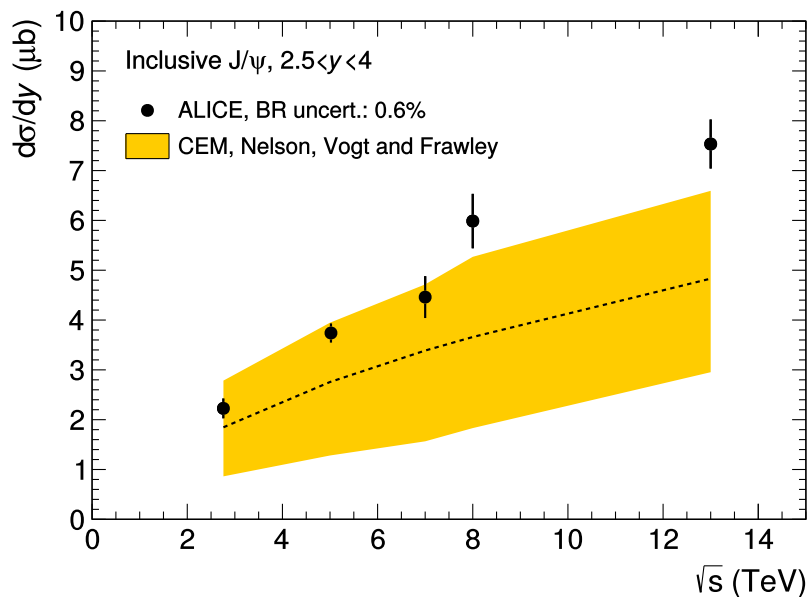


Figure 6.21: Inclusive  $J/\psi$  cross section at forward rapidity as a function of collisions energy  $\sqrt{s}$ . The band represents CEM calculation by Nelson et al. [230]. Taken from [73].

Fig. 6.21 shows the integrated  $\sigma_{J/\psi}^{pp}$ . The cross section increases with the  $\sqrt{s}$  as more energy is available for  $J/\psi$  production. The errorbars show the square sum of statistical and systematic uncertainty of each measurement. The data were compared with CEM calculation by Nelson et al. [230]. The calculation is compatible with the data within uncertainties, however at all  $\sqrt{s}$ , the measurement lies systematically at the upper limit or above the CEM band. Furthermore, the relative difference between the measurement and the calculation seems to grow with increasing  $\sqrt{s}$ . This could be partially attributed to the absence of non-prompt contribution in the theoretical band.

The evolution of the  $p_T$  and  $y$  differential cross section is visualised in Fig. 6.22. For better visibility, the  $p_T$  spectra were multiplied by factors of  $10^n$ , as indicated in the legend. The measurable  $p_T$  range increases with energy of the collision. Moreover, we observe a hardening of the spectra - in other words increase of  $\langle p_T \rangle$  of measured  $J/\psi$  - with increasing  $\sqrt{s}$ . One of the possible reasons may be the relative increase of the non-prompt contribution. With more energy available more B-hadrons can be produced. Another contributing factor may be that in more energetic collisions, the produced  $J/\psi$  themselves are harder. The  $\langle p_T \rangle$  as a function of collision energy can be found in Fig. 6.23. We observe a steady increase with  $\sqrt{s}$ . The dashed line corresponds to the same data but with truncating at all energies to the smallest available  $p_T$  range ( $p_T < 8$  GeV/ $c$ ). The solid line corresponds to extrapolating all data to the widest available  $p_T$  range ( $p_T < 30$  GeV/ $c$ ). ALICE measurements are compared with available lower energy pp ( $p\bar{p}$ ) measurements from CDF [231], PHENIX [232], and NA3 [233]. The midrapidity measurements are systematically above the forward measurements at the same (or similar)  $\sqrt{s}$ . It was argued in the PHENIX paper [232] that one of the contributions to this phenomenon may be relative decrease in  $p_T$  due to the stronger boost at forward rapidity.

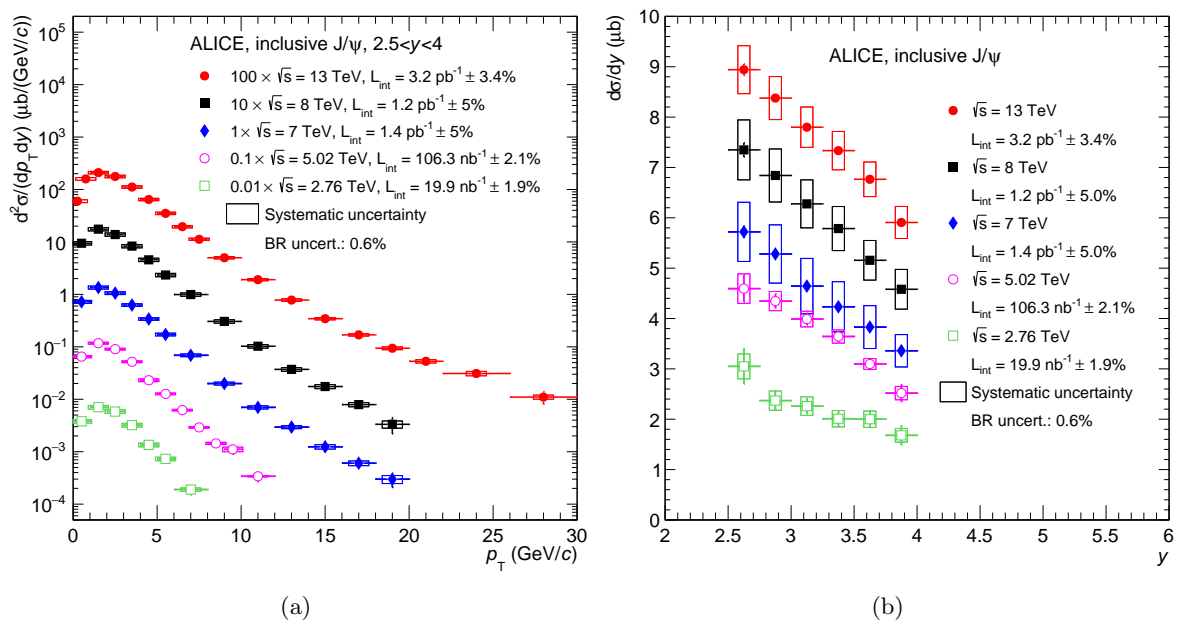


Figure 6.22: Inclusive  $J/\psi$  cross section at forward rapidity as a function of (a)  $p_T$  and (b)  $y$ . Taken from [73].

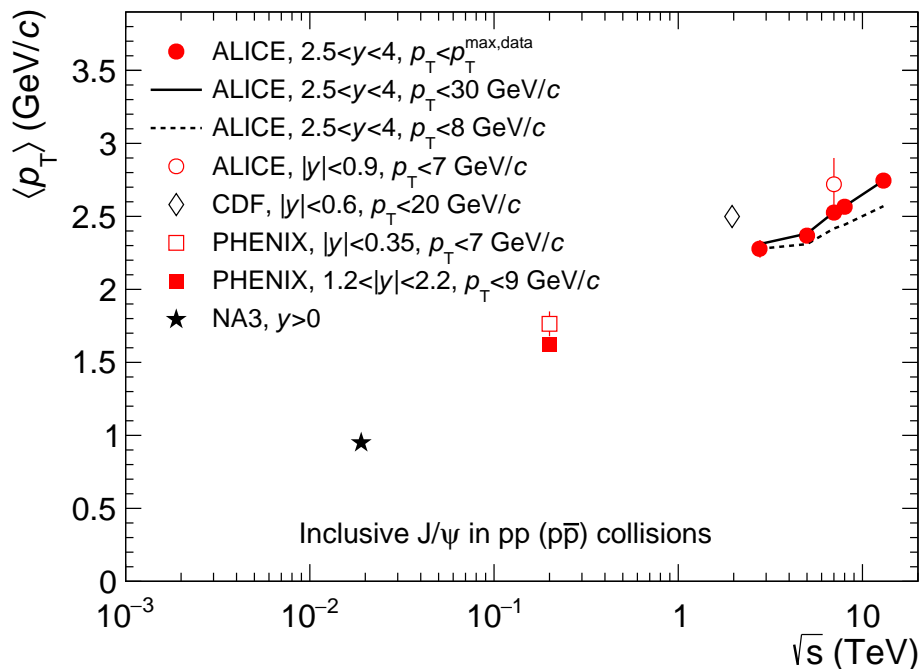


Figure 6.23:  $\langle p_T \rangle$  as a function of  $\sqrt{s}$ . ALICE measurements at forward (full points) and midrapidity (open points) are compared with lower energy results from CDF [231], PHENIX [232], and NA3 [233]. Figure taken from [73]

$\psi(2S)$  was measured in ALICE at forward rapidity in pp at  $\sqrt{s} = 7, 8,$  and 13 TeV. As some of the systematic uncertainties on the cross section are shared between  $J/\psi$  and  $\psi(2S)$ , computing a ratio of the two allows us to eliminate these contributions to the overall uncertainty. The contributions in question are uncertainty on tracking efficiency, trigger efficiency, tracking-trigger matching, and luminosity. Moreover, the non-prompt contribution to both charmonia states cancels out too.

The authors of high- $p_T$  NRQCD calculations [65, 229] also provided a calculation for the  $\psi(2S)$ -to- $J/\psi$  ratios as a function of  $p_T$ . The comparison of data and theory for the ratio at 13 TeV is shown in Fig. 6.24a for the calculation by Ma et al. [65] and in Fig. 6.24b for the calculation by Butenschön and Kniehl [229]. The model by Ma et al. overestimates the measurement at intermediate  $p_T$  by more than  $2\sigma$ . The model by Butenschön and Kniehl only achieves better agreement due to much larger uncertainty band. Both models overestimate the  $p_T$  spectrum of the  $\psi(2S)$  near the low- $p_T$  validity limit.

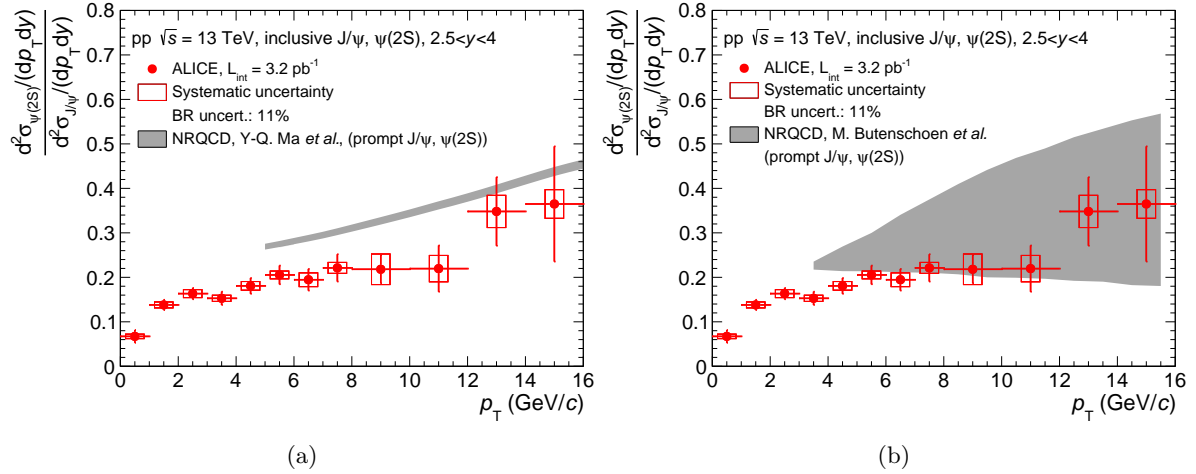


Figure 6.24:  $\psi(2S)$ -to- $J/\psi$  ratio as a function of  $p_T$  in pp at  $\sqrt{s} = 13$  TeV, compared with NRQCD calculations [65, 229]. Figure taken from [73].

## Summary

In this chapter, we reviewed the analysis of inclusive  $J/\psi$  production in pp collisions at  $\sqrt{s} = 5.02$  TeV. The inclusive  $J/\psi$  cross section was measured in the forward rapidity region  $2.5 < y < 4.0$  and up to  $p_T = 12$  GeV/ $c$ . The differential results were compared with a sum of NRQCD + FONLL calculations to account for the non-prompt contribution in the data. The results were also compared with other forward ALICE measurements at energies between  $2.76 \leq \sqrt{s} \leq 13$  TeV. The cross section shows a steady increase with  $\sqrt{s}$ . Moreover, the  $p_T$  and  $y$  integrated and  $p_T$  differential cross sections were used as a reference for  $R_{AA}$  measurement at  $\sqrt{s_{NN}} = 5.02$  TeV.



## MEASUREMENT OF FORWARD $J/\psi$ PRODUCTION AS A FUNCTION OF CHARGED PARTICLE MULTIPLICITY AT MIDRAPIDITY IN p–Pb COLLISIONS AT $\sqrt{s_{\text{NN}}} = 8.16$ TeV

This chapter focuses on the analysis of multiplicity differential  $J/\psi$  yields in p–Pb collisions at  $\sqrt{s_{\text{NN}}} = 8.16$  TeV. As in the previous chapter, the  $J/\psi$  were analysed from their decays into a pair of opposite sign muons in the Muon Spectrometer at forward rapidity  $2.5 < y_{\text{lab}} < 4.0$ . The multiplicity was estimated from the SPD data at midrapidity  $|\eta_{\text{lab}}| < 1$ . In the following we will briefly introduce the observables used in this analysis and described the analysed data samples. We will explain the multiplicity estimation first. Description of the  $J/\psi$  yields extraction will follow next. We will compare the results at 8.16 TeV with results from previous multiplicity differential analysis in p–Pb at  $\sqrt{s_{\text{NN}}} = 5.02$  TeV [177] and also discuss the comparison with results from centrality analysis at 8.16 TeV [234]. We will complete the chapter by scrutinising the possible outlook of the analysis.

### 7.1 Definition of observables

We shall begin by defining the observables. The goal of the analysis was to study the evolution of self-normalised  $J/\psi$  yields as a function of the relative charged particle pseudorapidity density  $dN_{\text{ch}}/d\eta / \langle dN_{\text{ch}}/d\eta \rangle$ . The measurement is performed in the sample of the non-single diffractive (NSD) events.

The self-normalised (or relative)  $J/\psi$  yield in multiplicity bin  $i$  is defined as

$$Y_{J/\psi}^{R, i} = \frac{Y_{J/\psi}^i}{Y_{J/\psi}^{\text{tot}}} = \frac{N_{J/\psi}^i}{N_{J/\psi}^{\text{tot}}} \times \frac{N_{\text{MB}}^{\text{eq,tot}}}{N_{\text{MB}}^{\text{eq},i}} \times \frac{\varepsilon_{\text{MB}}^i}{\varepsilon_{\text{MB}}}, \quad (7.1)$$

where  $i$  loops over bins in multiplicity,  $N_{J/\psi}$  is the number of  $J/\psi$ ,  $N_{\text{MB}}^{\text{eq}}$  is the equivalent number of minimum bias events corresponding to the analysed data sample, and  $\varepsilon_{\text{MB}}$  is the vertex selection efficiency in non-single diffractive (NSD) events. The factor  $\varepsilon_{\text{MB}}$  accounts for selection of the NSD sub-sample from all reconstructed events and for selection of events with reconstructed vertex.

As was mentioned in Chapter 3, the relative yields ease the comparison between results at different energies, from different experiments, and with theory. Moreover, we can compare Eq. (7.1) with the previously defined  $J/\psi$  cross section in Eq. (6.1). We note that several factors in the latter are constant in multiplicity and hence cancel out in the ratio, namely the acceptance-efficiency  $A\varepsilon$ , branching ratio, and minimum bias cross section in the luminosity calculation. This also cancels out the corresponding sources of systematic uncertainty.

The multiplicity is estimated from SPD information. The SPD reconstruct the so called tracklets. A tracklet is defined as a track segment connecting a pair of clusters, each in one layer of the SPD, aligned with the primary vertex within a given angular window. The charged particle multiplicity at midrapidity is assumed to be proportional to the number of charged tracklets  $N_{\text{tr}}$  reconstructed in the SPD at  $|\eta_{\text{lab}}| < 1$ :

$$\frac{dN_{\text{ch}}}{d\eta} \propto \frac{N_{\text{tr}}}{\Delta\eta}. \quad (7.2)$$

The proportionality factor needs to be determined from MC simulations. In fact, the relation between  $N_{\text{tr}}$  and  $N_{\text{ch}}$  was studied in detail as will be explained in Sec. 7.3.2. The self-normalised charged particle pseudorapidity density at midrapidity  $|\eta_{\text{lab}}| < 1$  can be then calculated as

$$\frac{dN_{\text{ch}}/d\eta}{\langle dN_{\text{ch}}/d\eta \rangle} \propto \frac{1}{\Delta\eta} \frac{\langle N_{\text{tr}} \rangle^i}{\langle dN_{\text{ch}}/d\eta \rangle}. \quad (7.3)$$

The superscript  $i$  denotes the multiplicity bin and  $\langle dN_{\text{ch}}/d\eta \rangle$  is the average charged particle multiplicity for NSD events.

## 7.2 Event and track selection

### 7.2.1 Event selection criteria

As in the previous analysis, the  $J/\psi$  yields were analysed in the low  $p_{\text{T}}$  dimuon triggered data. The multiplicity on the other hand was analysed in the minimum bias sample from the MUFASST cluster. Tab. 7.1 lists all triggers used in this analysis. We also used additional triggers for normalisation of the yields. Namely, we used minimum bias trigger from the CENT cluster. The advantage is that the CENT trigger was less downscaled compared to the MUFASST minimum bias trigger. For completeness, the CENT cluster reads out the following detectors: SPD, SDD, SSD, TPC, TOF, HMPID, PHOS, CPV, FMD, T0, V0, ZDC, EMCal, AD, PMD, TRD.

trigger class	description
CINT7-B-NOPF-MUFASST	V0A && V0C
CINT7-B-NOPF-CENT	V0A && V0C
CMSL7-B-NOPF-MUFASST	V0A && V0C && low- $p_{\text{T}}$ muon ( $p_{\text{T}}^{\mu} \gtrsim 0.5 \text{ GeV}/c$ )
CMUL7-B-NOPF-MUFASST	V0A && V0C && low- $p_{\text{T}}$ dimuon ( $p_{\text{T}}^{\mu} \gtrsim 0.5 \text{ GeV}/c$ )

Table 7.1: Definition of trigger classes used in  $J/\psi$  multiplicity analysis in p-Pb collisions at  $\sqrt{s_{\text{NN}}} = 8.16 \text{ TeV}$ .

The beam-beam interactions were selected using a dedicated Physics Selection task included in the ALICE analysis framework. Through the rest of the document we will refer to the task as AliPhysicsSelection (APS). The task removes the machine induced background through a series of SPD selection criteria and V0 and ZDC timing cuts. The Physics Selection task also allows one to apply a set of predefined cuts to remove pile-up events. These are tuned for each period separately. For reasons that will be explained later, we did not use the predefined selection. Instead, we applied a set of modified selection criteria that were tailored to our analysis.

We will first review the APS selection criteria, to then explain why we chose to use a custom selection instead.

#### 7.2.1.1 Pile-up rejection via a centralised ALICE task

The AliPhysicsSelection Task includes the following cuts for pile-up rejection:

1. Correlation of V0 clusters with SPD tracklets.
2. Past-future protection for out-of-bunch pile-up in the V0 time window.
3. Correlation of online and offline information in the V0.
4. Correlation of online and offline information in the SPD.
5. Correlation of the sum and difference of the ZNA and ZNC time.
6. Cut on SPD in-bunch pile-up with  $N_{\text{contributor}} = 5$  and vertex distance  $d = 0.8 \text{ cm}$ .

7. Correlation of number of clusters  $N_{CL}^1$  and tracklets  $N_{tr}$  in the SPD.

The cuts were validated by ALICE and were used in other analyses of the p–Pb samples (e. g. [234]). Examples of the listed distributions 1. and 3.-5. and the corresponding selection criteria can be found in Fig. 7.1. We will describe the last two cuts in more detail in the next section as their modified versions were used in our Custom Physics Selection.

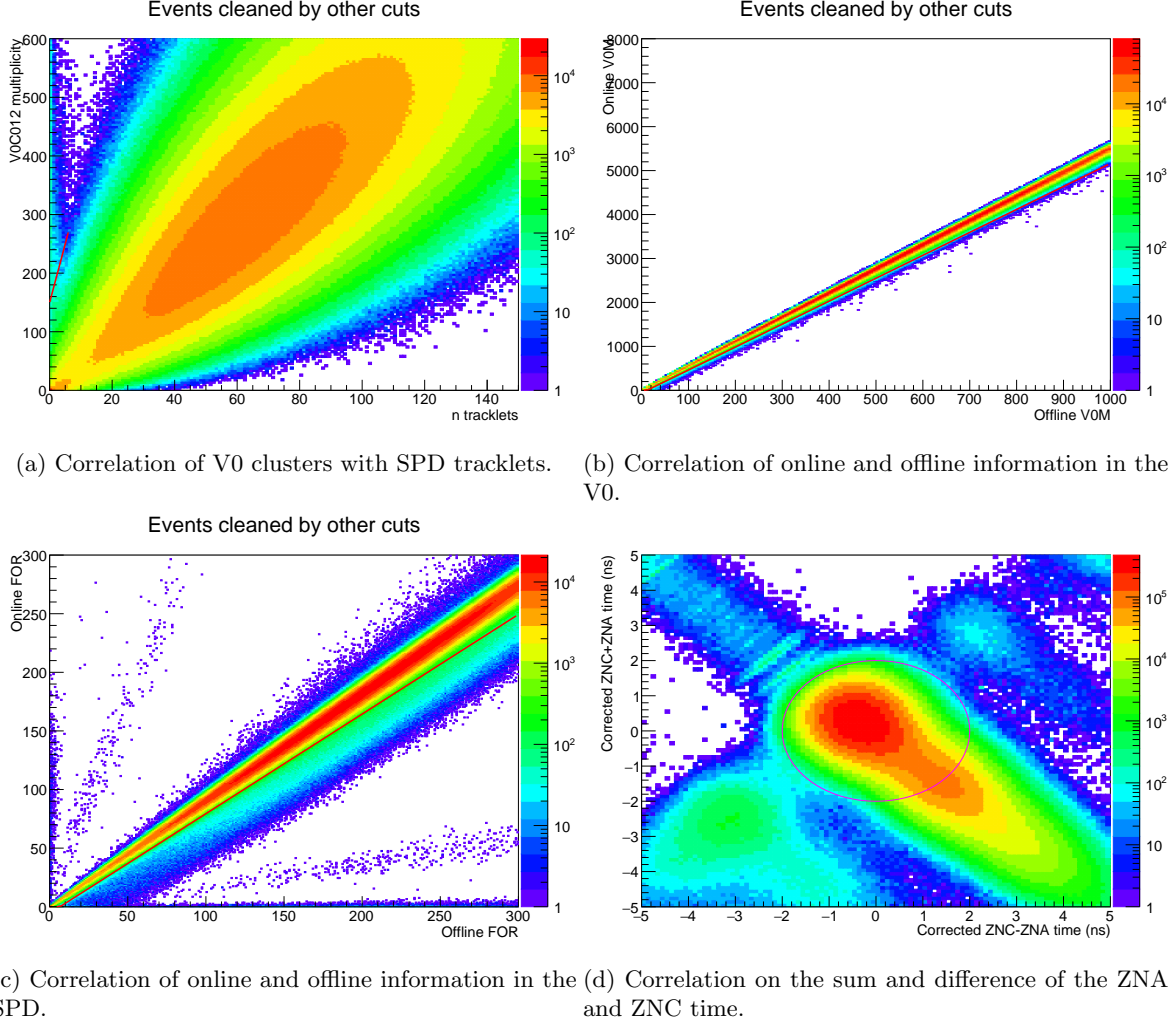


Figure 7.1: . Pile-up selection criteria included in the AliPhysicsSelection. The red (magenta) curve shows the default cut used in the APS to clean the pile-up. Exemplar distributions corresponding to the Pb–p period.

### 7.2.1.2 Custom pile-up rejection for the multiplicity analysis in p–Pb at 8.16 TeV

The default APS pile-up rejection cuts were not tuned for the dimuon triggered data in p–Pb and Pb–p periods. Muon tracks reconstructed in the spectrometer usually originate in hard events [235]. Hard events produce on average more charged particles than minimum bias events and their multiplicity is thus higher. It may then happen that rejection criteria tuned for minimum bias events remove a large portion of good hard events in the dimuon sample.

First, we shall describe the cuts used in our Custom Physics Selection (CPS). Then we will compare them to the APS selection to explain the reason to use the CPS instead of the APS.

For most part, the CPS used the same cuts as the APS (namely 1.-5.), see the list in Sec. 7.2.1.1. The last two cuts in the APS were modified to better discriminate pile-up in high multiplicity p–Pb

<sup>1</sup>Cluster is the SPD information from one layer. Individual clusters in both layers are combined into tracklets. In SPD,  $N_{tr} \propto N_{CL}$ . If  $N_{CL}$  is too large with respect to  $N_{tr}$ , it probably comes from piled up events.

and Pb–p events.

### In-bunch SPD pile-up selection criterion

The ALICE analysis software contains an algorithm to reconstruct the in-bunch pile-up in the SPD. The function identifies the main vertex in the SPD in a single event. Then it loops over all secondary vertices in the same event. If the secondary vertex has more than a given number of contributing tracklets  $N_{\text{contributor}}$  and the distance between the primary and the secondary vertex is longer than a given threshold value  $d$ , the event is rejected as pile-up.

Three variations of this function are commonly used, although in principle one can chose any  $N_{\text{contributor}}$  and  $d$  thresholds. Commonly used are:

- $N_{\text{contributor}} > 3$  and  $d > 0.6$  cm,
- $N_{\text{contributor}} > 5$  and  $d > 0.8$  cm,
- a multiplicity dependent cut, which applies  $N_{\text{contributor}} > 3$  and  $d > 0.6$  cm for events with  $N_{\text{tr}} < 50$  and  $N_{\text{contributor}} > 5$  and  $d > 0.8$  cm for the rest.

This cut was tuned for pp data, which in principle reach lower multiplicities than p–Pb. The function contains a cut-off on maximal number of clusters/tracklets. The cut-off is around  $N_{\text{CL}} \sim 300$  or  $N_{\text{tr}} \sim 100$ . Therefore it has no effect at high multiplicity where we expect most of the pile-up. This cut-off was introduced to optimise the algorithm time in pp data.

The default function used in the APS was the second one, i. e.  $N_{\text{contributor}} > 5$  and  $d > 0.8$  cm. The CPS used the third, multiplicity dependent option.

### Correlation of number of clusters $N_{\text{CL}}$ and tracklets $N_{\text{tr}}$ in the SPD

We studied the effect of this cut in the APS, therefore all cuts used in this subsection refer to those included in the APS. Fig. 7.2 shows the correlation between  $N_{\text{CL}}$  and  $N_{\text{tr}}$  reconstructed in the SPD in the two periods, after all the other pile-up selection criteria included in the APS were applied. Shown are the CMUL7-B-NOPF-MUFAST (from now on 'CMUL7') triggered events in the top row and the CINT7-B-NOPF-MUFAST triggered events ('CINT7') in the bottom row. The black line shows the cut implemented in the APS task, which is defined by a linear function

$$N_{\text{CL}} = 65 + 4 \cdot N_{\text{tr}}. \quad (7.4)$$

Although the distributions were already cleaned of a fraction of the total pile-up, we still see structures around  $N_{\text{tr}} \sim 0$  and  $N_{\text{tr}} > 60$ , which we suspected originated from pile-up events. The default APS cut removes this events, but also cuts a fraction of the main linear shape. Notice that in the MB triggered events, that reach lower multiplicities, the linear shape is unaffected by the APS cut.

We have therefore tried to relax this cut so that it does not reject events from the linear shape in the dimuon sample. To contain the linear shape around  $N_{\text{CL}} = 4 \cdot N_{\text{tr}}$ , we have defined the following cut:

$$N_{\text{CL}} = \begin{cases} 65 + 5.5 \cdot N_{\text{tr}} - 0.009 \cdot N_{\text{tr}}^2 & \text{for } N_{\text{tr}} < 165 \\ 65 + 4 \cdot N_{\text{tr}} & \text{for } N_{\text{tr}} \geq 165 \end{cases}$$

Hence for multiplicities  $N_{\text{tr}} < 165$ , the cut adopts a less strict quadratic form, represented in Fig. 7.2 by the magenta line. At  $N_{\text{tr}} \geq 165$ , the cut follows the default linear function. Recall that the CINT7 triggers classes are downscaled in the MUFAST cluster, therefore the bottom plots contain visibly less events than the top ones.

Tab. 7.2 lists the number of events passing each of the physics selection cuts. Here the 'Physics Selection' without any adjective denotes the timing cuts used to reduce the machine induced background. The table gives values for both CMUL7 and CINT7 samples.

Three cuts removed most of the pile-up:

- the multiplicity dependent SPD pile-up cut,
- the correlation between the sum and difference of the ZNA and ZNC time, and
- the correlation  $N_{\text{CL}} - N_{\text{tr}}$  in the SPD.

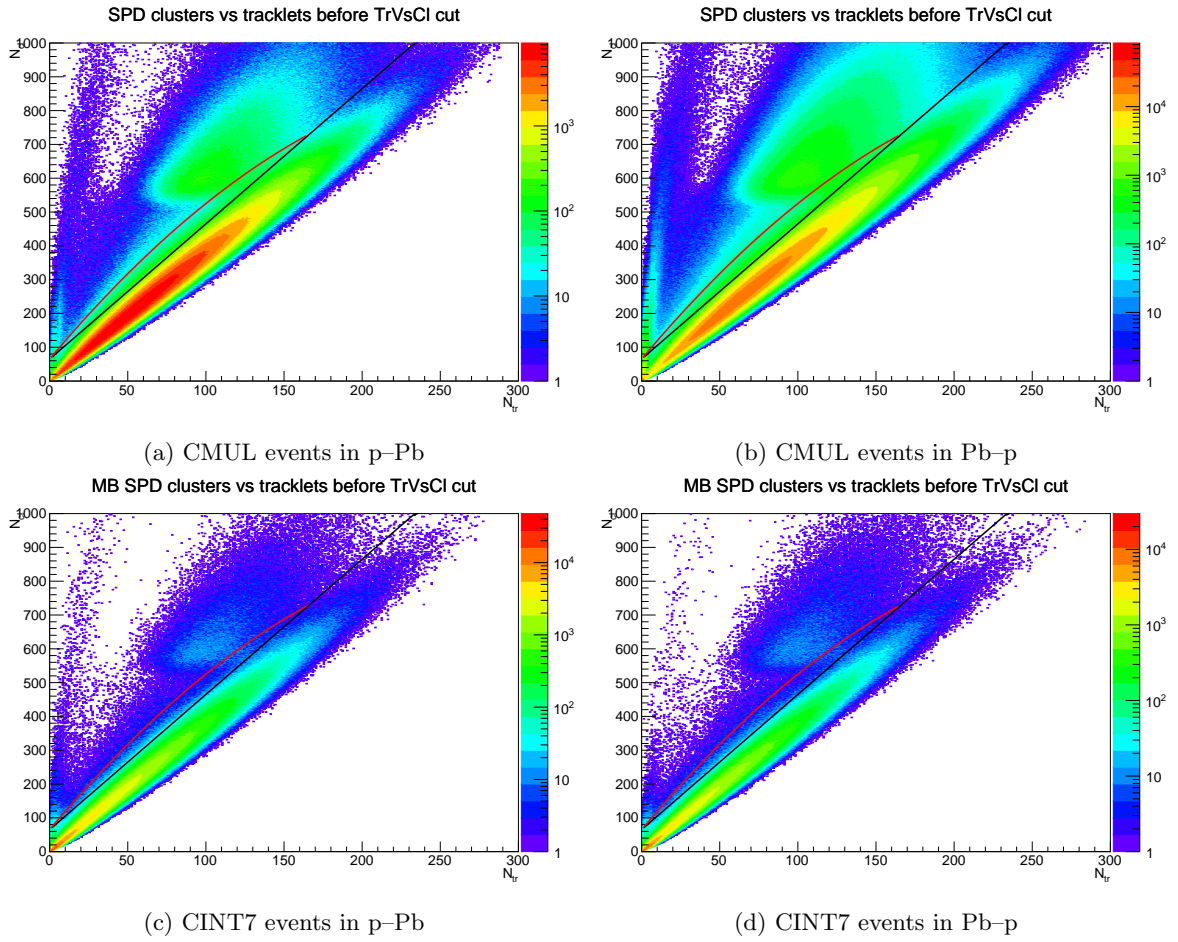


Figure 7.2:  $N_{CL}$  versus  $N_{tr}$  SPD pile-up cut. The black line represents Eq. (7.4) and red line the alternative polynomial form proposed in Eq. (7.2.1.2) for the intermediate tracklet range.

event cut	p-Pb		Pb-p	
	events passed	events passed/all events	events passed	events passed/all events
CMUL7-B-NOPF-MUFAST				
all events	26100170	1	69640275	1
Physics Selection	25805931	0.989	68702067	0.987
past-future protection in V0	25805931	0.989	68702067	0.987
mult. dependent SPD pile-up cut	23928644	0.917	63648667	0.914
Online-Offline in V0	23928644	0.917	63648667	0.914
Online-Offline in SPD	23928644	0.917	63648667	0.914
ZNA+ZNC vs ZNA-ZNC	23115811	0.886	63592897	0.913
correlation $N_{\text{CL}}^{V0} - N_{\text{tr}}^{\text{SPD}}$	23115811	0.886	63592897	0.913
SPD $N_{\text{CL}} - N_{\text{tr}}$	22041220	0.844	59605457	0.856
CINT7-B-NOPF-MUFAST				
all events	7240547	1	3959725	1
Physics Selection	7070747	0.977	3893936	0.983
past-future protection in V0	7070747	0.977	3893936	0.983
mult. dependent SPD pile-up cut	6766879	0.935	3660573	0.924
Online-Offline in V0	6766879	0.935	3660573	0.924
Online-Offline in SPD	6766879	0.935	3660573	0.924
ZNA+ZNC vs ZNA-ZNC	6602121	0.912	3657669	0.924
correlation $N_{\text{CL}}^{V0} - N_{\text{tr}}^{\text{SPD}}$	6602121	0.912	3657669	0.924
SPD $N_{\text{CL}} - N_{\text{tr}}$	6466701	0.893	3556374	0.898

Table 7.2: Number of events in CMUL7 and CINT7 trigger samples in p-Pb and Pb-p after each pile-up cut. The cuts are applied sequentially, i. e. application of each of the cuts implies also application of the previously listed cuts.

Their effect is visualised in Fig. 7.3. Prior to pile-up removal, the p–Pb distribution in particular has a long  $N_{\text{tr}}$  tail, which originates from the pile-up (see yellow points in Fig. 7.3a). Each of the cuts was added on top of the previous ones and the resulting  $N_{\text{tr}}$  distribution was divided by the one with pile-up. The ratios are shown in Fig. 7.3b. The multiplicity dependent SPD pile-up cut (in blue) removed pile-up at low and intermediate multiplicities below the cut-off value  $N_{\text{tr}} \sim 100$ . Above his value, we see that the cut had no effect. Adding the ZDC timing criterion (in green) removes pile-up in the whole multiplicity range. Yet the distribution still contains remains of the pile-up tail. Finally, adding the condition on the correlation  $N_{\text{CL}} - N_{\text{tr}}$  in the SPD removes the tail. Similar situation was observed i the Pb–p period, see Fig. 7.3c and 7.3d.

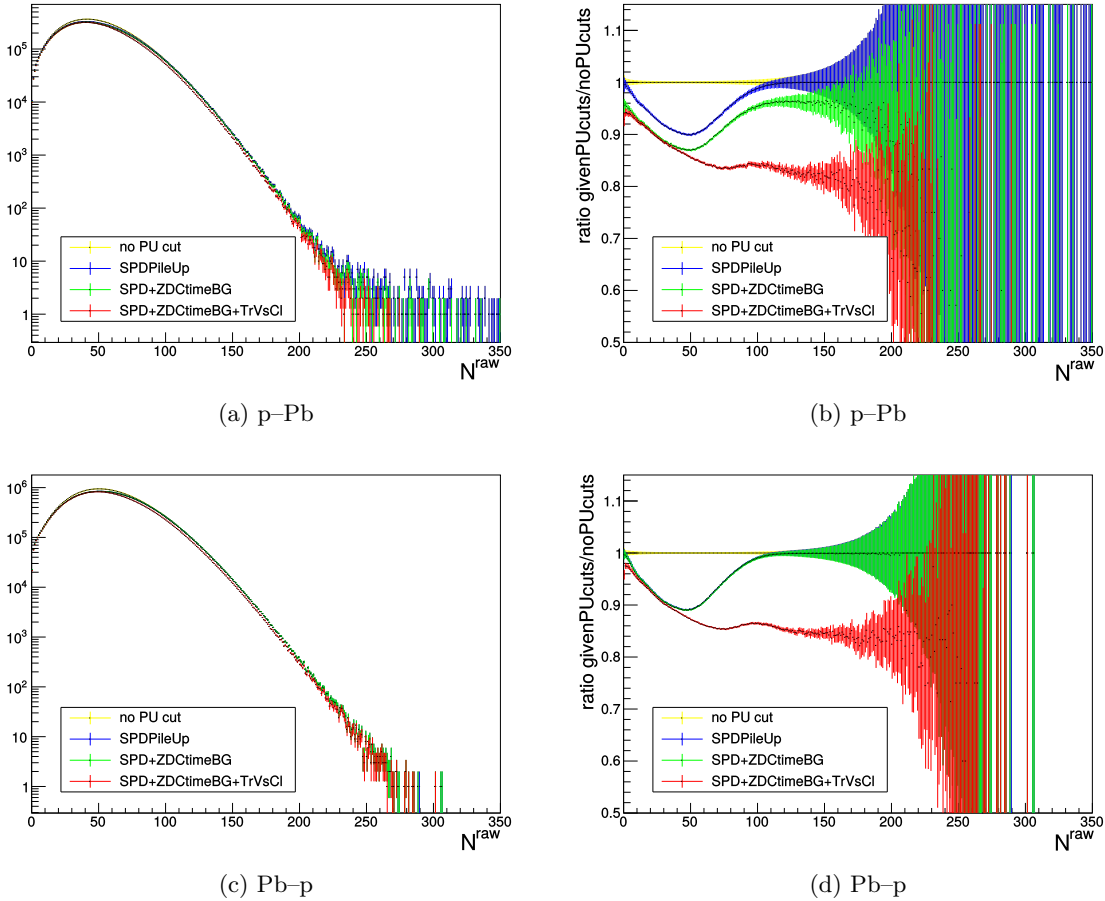


Figure 7.3: Custom Physics Selection pile-up rejection cuts for CMUL events.

### 7.2.1.3 Verification of pile-up rejection with the Custom Physics Selection

Assuming the detector was stable during the entire p–Pb and Pb–p run, we expect the mean number of raw tracklets  $\langle N_{\text{tr}} \rangle$  to be constant in time. However, pile-up events can cause large fluctuations and structures in the time dependence of  $\langle N_{\text{tr}} \rangle$ , as we may expect more pile-up at the beginning of the fill.

One of the reasons we did not use the APS was that it was removing too much of potentially good events at high multiplicity. However, it did successfully remove pile-up from the data. Therefore we compared the  $\langle N_{\text{tr}} \rangle$  as a function of run between our CPS and the APS. The results are to be seen in Fig. 7.4. While there was still some residual structure present in the CPS distributions, the run-by-run ratios of the two were close to unity. The standard deviation weighted by number of CMUL7 events per run in either period amounted to 0.4%. This test validated the use of our CPS in the analysis. This difference is included in the uncertainty on residual pile-up which will be explained further in the text.

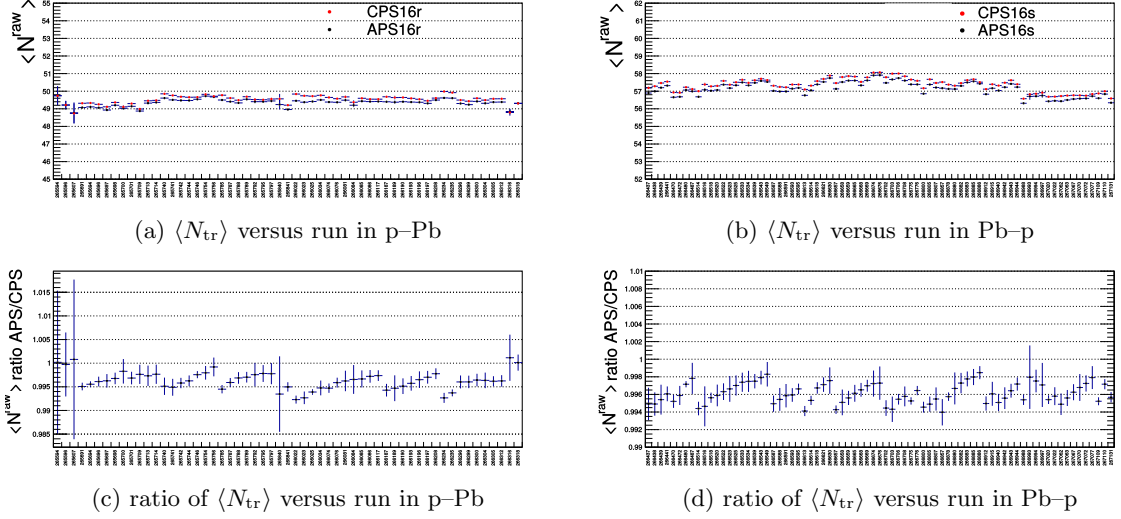


Figure 7.4: Comparison of  $\langle N_{tr} \rangle$  extracted with CPS and APS in p-Pb and Pb-p in dimuon events. The top row shows the  $\langle N_{tr} \rangle$  as a function of run with APS and with CPS. The bottom row shows the ratio of the CPS/APS distributions.

#### 7.2.1.4 SPD vertex selection criteria

The multiplicity analysis relies on accurate determination of vertex in the SPD. Hence we required the following 'Quality Assurance' selection criteria on the SPD vertex:

- The event must have a reconstructed vertex in the SPD.
- The SPD vertex must have at least one contributing track  $N_{contributor} > 0$ .
- The resolution of the  $z$ -coordinate of the SPD vertex must be below  $\sigma_{v_z} < 0.25$  cm.
- The vertex must be reconstructed within a distance  $|v_z| < 10$  cm from the nominal interaction point (IP) to assure proper reconstruction of tracklets taken into account in this study.

The effect of the above listed cuts on CMUL7 and CINT7 events in the two periods can be found in Tab. 7.3. Most of the events are removed by the condition on the distance from the nominal IP. This selection criterion removes  $\sim 7\%$  of all physics selected (PS) events in the CMUL7 sample. The reason behind this is the shift of the  $v_z$  maximum, see Fig. 7.5. The mean of the vertex is shifted to  $v_z \sim 1.4$  cm.

event cut	p-Pb		Pb-p	
	events passed	events passed/all events (%)	events passed	events passed/all events (%)
	CMUL7-B-NOPF-MUFAST			
Physics Selection	22041220	84.4	59605457	85.6
reconstructed SPD vertex	22041220	84.4	59605457	85.6
$N_{\text{contributor}} > 0$	22032612	84.4	59556285	85.5
$\sigma_{v_z} < 0.25$ cm	22027865	84.4	59546708	85.5
$ v_z  < 10$ cm	20332171	77.9	55086811	79.1
	CINT7-B-NOPF-MUFAST			
Physics Selection	6466701	89.3	3556374	89.8
reconstructed SPD vertex	6466701	89.3	3556374	89.8
$N_{\text{contributor}} > 0$	6399922	88.4	3516845	88.8
$\sigma_{v_z} < 0.25$ cm	6381962	88.1	3506736	88.6
$ v_z  < 10$ cm	5916507	81.7	3250402	82.1

Table 7.3: Number of CMUL7 and CINT7 triggered events in p-Pb and Pb-p after each SPD vertex QA cut.

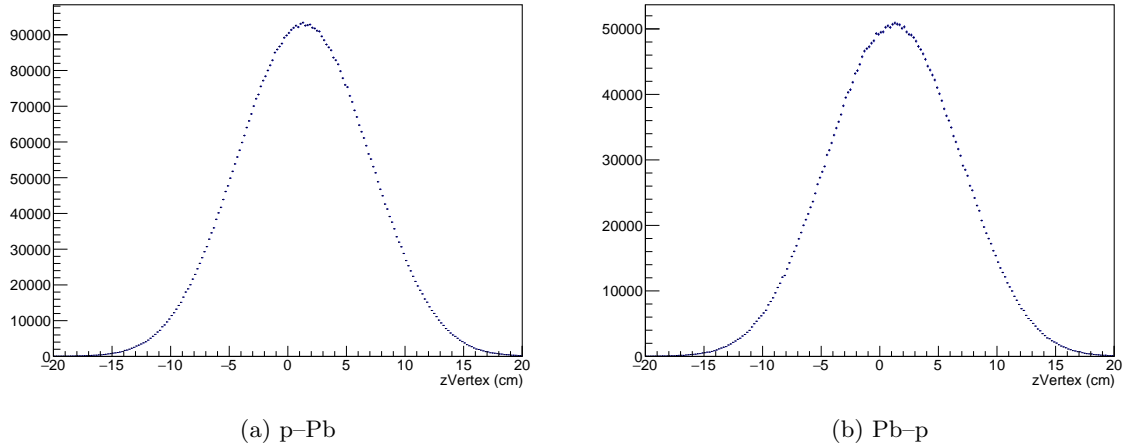


Figure 7.5: The  $z$ -coordinate of the SPD vertex in p-Pb and Pb-p. The maximum of the distribution is shifted in both period with respect to the nominal interaction point.

## 7.2.2 Muon track selection criteria

Most of the track selection criteria are identical to those applied in previous analysis, see Sec. 6.1.2. However, we will list all for completeness.

The following single track selection criteria are required:

- $-4 < \eta_{\text{lab}} < -2.5$ , i. e. the track must pass through the Muon Spectrometer.
- The reconstructed track in the tracking chambers must match a trigger track in the trigger chambers with  $p_{\text{T}}^t \gtrsim 0.5 \text{ GeV}/c$ .
- $17.6 < R_{\text{abs}} < 89.5 \text{ cm}$ , where  $R_{\text{abs}}$  is the radial transverse coordinate of the track at the end of the front absorber.

On the dimuon level, we required:

- $2.5 < y_{\text{lab}} < 4$ , i. e. that the dimuon was within the spectrometer acceptance.

## 7.3 Multiplicity measurement

We chose the charged particle pseudorapidity density to be our estimator of event multiplicity. To obtain the  $dN_{\text{ch}}/d\eta$ , we used the number of tracklets  $N_{\text{tr}}$  from the SPD. The tracklets are counted at midrapidity  $|\eta| < 1$ . We expected  $N_{\text{tr}}$  to be proportional to  $N_{\text{ch}}$ .

During the data taking, the SPD acceptance varies as dead regions may appear in the detector. The dead zones will naturally affect the tracklet information in the given part of the SPD. In order to properly evaluate the multiplicity of the event, one needs to correct for the missing acceptance. The SPD efficiency also needs to be taken into account. Only then can one convert the number of tracklets  $N_{\text{tr}}$  into the corresponding number of charged particles  $N_{\text{ch}}$ .

Up until now, we only used the notation  $N_{\text{tr}}$  to signify the number of tracklets. From now on, we will be distinguishing between two different related quantities:

- **Number of raw tracklets**  $N^{\text{raw}}$ , i. e. the quantity reconstructed in the SPD as it is in the data files.
- **Number of corrected tracklets**  $N^{\text{corr}}$ , which corrects the  $N^{\text{raw}}$  by a procedure described in the following sections.

In case the notation  $N_{\text{tr}}$  is used, it means that we talk about tracklets as general without distinguishing whether the correction took place or not.

This section is structured as follows:

1. In Sec. 7.3.1, we describe the acceptance correction of  $N^{\text{raw}}$  into  $N^{\text{corr}}$ . We use a data driven method which does not require the use of MC simulations. Two variations of the method are considered.
2. In Sec. 7.3.2, we describe the efficiency correction of  $N^{\text{corr}}$  into  $N_{\text{ch}}$ . The efficiency correction is evaluated from the  $N_{\text{ch}} - N^{\text{corr}}$  correlation. We expect a linear correlation with slope  $> 1$ . The correlation is studied in dedicated MC. In this case, the MC had to be re-weighted in order for it to correspond to the data as best as possible.
3. Systematic uncertainties are scrutinised in Sec. 7.3.4.
4. The relative multiplicity  $dN_{\text{ch}}/d\eta / \langle dN_{\text{ch}}/d\eta \rangle$  defined in Eq. (7.3) is computed in Sec. 7.3.5. In the denominator, we used a value obtained in an independent analysis of charged particle pseudorapidity density<sup>2</sup>.

### 7.3.1 Data-driven correction method

#### 7.3.1.1 Correction with Poissonian smearing

Dead regions in the SPD will result in reduced acceptance. The average raw number of reconstructed tracklets  $\langle N^{\text{raw}} \rangle$  will then depend on the region of the SPD in which it was reconstructed. The blue data points in Fig. 7.6 shows a typical dependence of  $\langle N^{\text{raw}} \rangle$  on the  $z$ -coordinate of the reconstructed vertex. Recall that  $z$ -axis coincides with the beam direction. However, we expect the physical properties of a single event to remain the same regardless of where in the detector the collision took place. In case of uniform detector acceptance, we expect a flat  $\langle N_{\text{tr}} \rangle$  distribution along the SPD  $z$ -axis similar to the one shown in the Fig. 7.6 in red.

The method used to equalise the  $\langle N_{\text{tr}} \rangle$  along the SPD was used for instance in the multiplicity dependent  $J/\psi$  analysis in p-Pb at  $\sqrt{s_{\text{NN}}} = 5.02$  TeV [177]. Brief overview of the method is given in this thesis. We limited the analysis to events with  $|v_z| < 10$  cm.

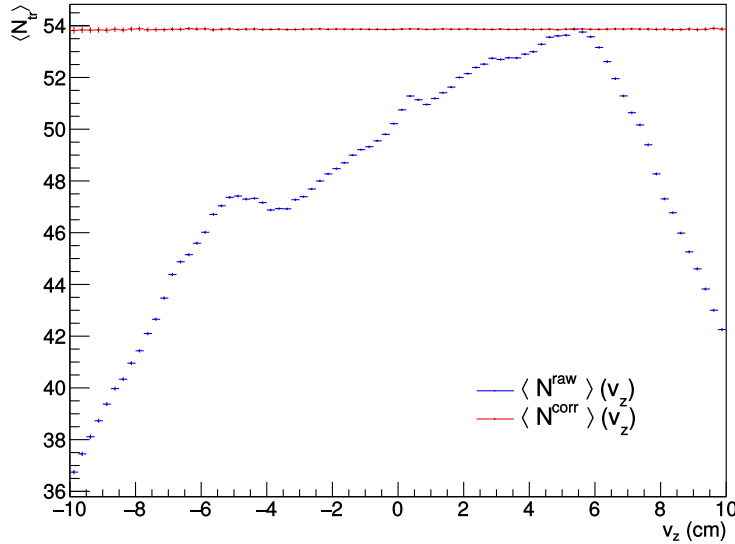


Figure 7.6: Event averaged number of tracklets  $\langle N_{\text{tr}} \rangle$  versus  $z$ -coordinate of the SPD vertex  $v_z$  before (blue) and after (red) the Poissonian correction using  $v_z^0 = \text{Max}\{-10, 10\}$ .

For each event, we computed the number of missing or excessive tracklets  $\Delta N$  with respect to a reference  $\langle N^{\text{raw}} \rangle(v_z^0)$  defined as

$$\Delta N = N^{\text{raw}}(v_z) \frac{\langle N^{\text{raw}} \rangle(v_z^0) - \langle N^{\text{raw}} \rangle(v_z)}{\langle N^{\text{raw}} \rangle(v_z)}. \quad (7.5)$$

<sup>2</sup>The paper was being prepared for publication during writing of this thesis.

We then randomised  $N^{\text{raw}}$  by Poisson smearing the excess  $\Delta N$  to obtain the number of corrected tracklets  $N^{\text{corr}}$

$$N^{\text{corr}} = N^{\text{raw}} \pm \text{gRandom} \rightarrow \text{Poisson}(\Delta N). \quad (7.6)$$

Fig. 7.7 shows comparison of  $N^{\text{raw}}$  and  $N^{\text{corr}}$  in the p-Pb periods

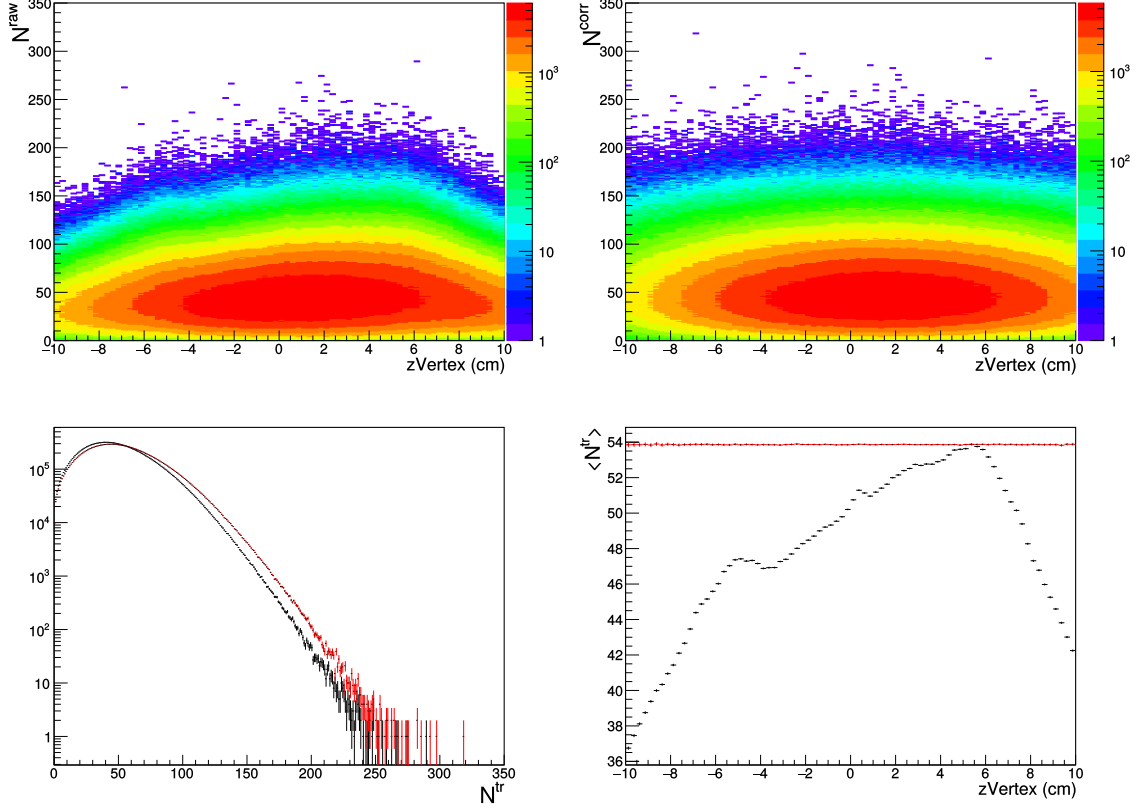


Figure 7.7: Number of tracklets  $N_{tr}$  versus  $v_z$  in CMUL7 triggered events in the p-Pb period. The top left (right) panel shows the distribution of raw (corrected) tracklets  $N^{\text{raw}}$  ( $N^{\text{corr}}$ ). The bottom left plot shows projection of the top 2D distributions into the tracklets axis ( $N^{\text{raw}}$  in black or  $N^{\text{corr}}$  in red, commonly denoted as  $N_{tr}$ ). The bottom right plot shows the projections into the  $v_z$  axis ( $N^{\text{raw}}$  in black or  $N^{\text{corr}}$  in red).

$N^{\text{corr}}$  is however not a measure of the true multiplicity as the SPD efficiency at the reference value is not necessarily 100%. This efficiency loss correction is tackled in Sec. 7.3.2.

We used different reference values for each of the two data periods in consideration. Values for maximal and minimal  $\langle N_{tr} \rangle(v_z)$  for the two periods can be found in Tab. 7.4. We listed separately the values for minimum bias and dimuon triggered data samples. The  $N^{\text{raw}}(v_z)$  distributions for the two period and for the two triggers can be found in Fig. 7.8. The difference between the CMUL7 distributions in p-Pb and Pb-p is expected and results from the rapidity shift of the beam. Moreover, we select for events containing tracks in the Muon Spectrometer which is in the Pb-going direction in Pb-p. In the CINT7 triggered samples on the other hand, the distributions are similar and hence the minimum and maximum are similar.

Fig. 7.8e and Fig. 7.8f show the comparison of the  $N^{\text{raw}}(v_z)$  profiles of the CMUL7 and CINT7 triggered data in p-Pb and Pb-p respectively. The distributions were normalised to unity. Their ratios in either period are visualised in the bottom panel of each corresponding plot. We see that the ratios are flat within the statistical fluctuations. Therefore it is safe to apply the same profile to correct both CMUL7 and CINT7. The obvious choice would be to use the CINT7 data, as they are the least biased. However, the CMUL7 datasample is larger and thus the distributions experience lower statistical fluctuations. We opted to use the CMUL7 profiles to correct all datasets to minimise the statistical uncertainty.

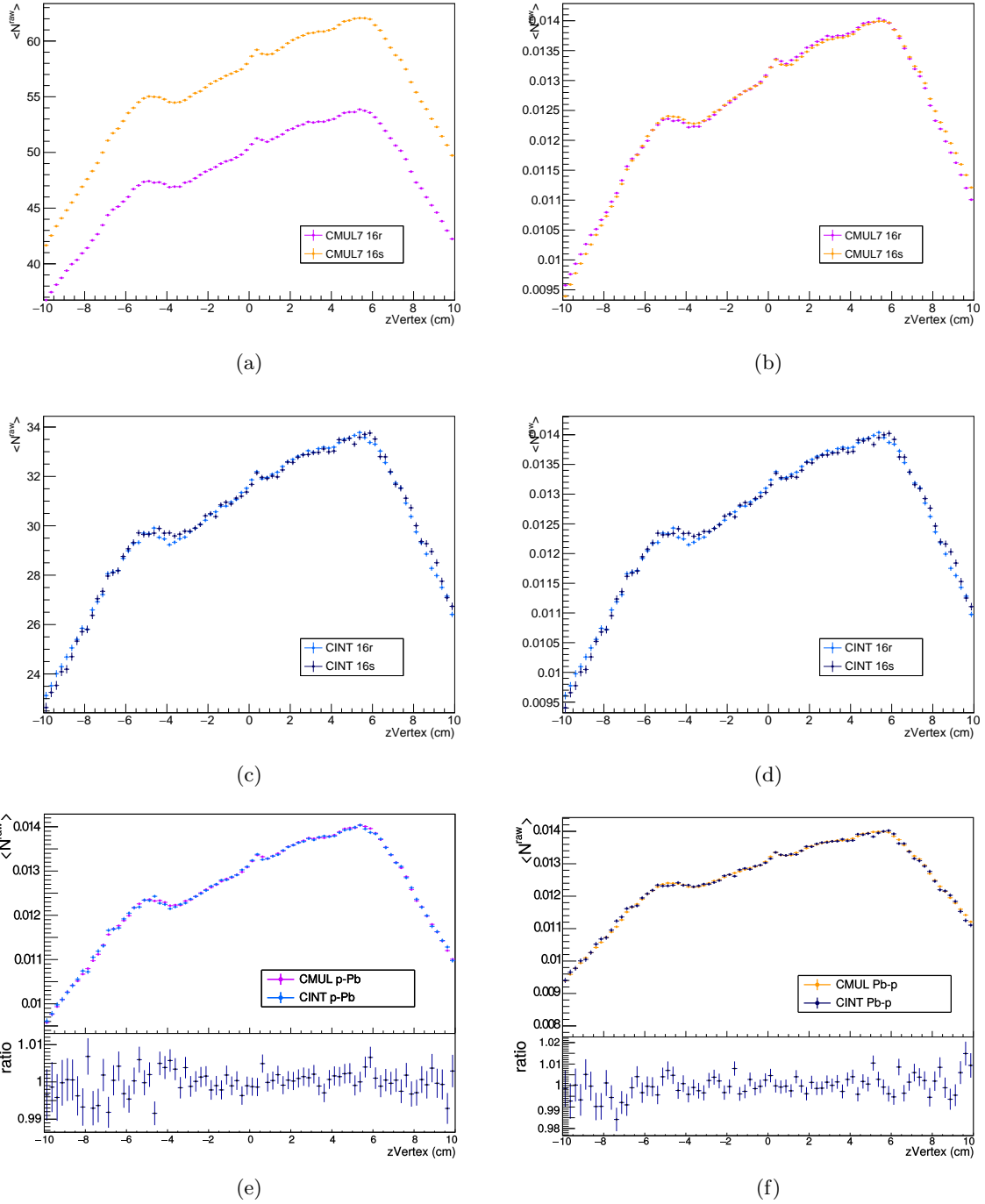


Figure 7.8: Event averaged number of tracklets  $\langle N^{\text{raw}} \rangle$  versus  $v_z$  in CMUL7 and CINT7 triggered event samples. (a)  $\langle N^{\text{raw}} \rangle$  vs  $v_z$  in CMUL7 triggered events in p-Pb (LHC16r) and Pb-p (LHC16s) periods. The LHC16s period has overall larger multiplicity than LHC16r, which is the usual case in Pb-p collisions compared to p-Pb. (b)  $\langle N^{\text{raw}} \rangle$  vs  $v_z$  in CMUL7 triggered events in LHC16s periods renormalised to unity. (c)  $\langle N^{\text{raw}} \rangle$  vs  $v_z$  in CINT7 triggered events in LHC16s periods. (d)  $\langle N^{\text{raw}} \rangle$  vs  $v_z$  in CINT7 triggered events in LHC16s periods renormalised to unity. (e, f) Comparison between renormalised  $\langle N^{\text{raw}} \rangle$  vs  $v_z$  in CMUL7 and CINT7 events in LHC16r and LHC16s respectively. The bottom panel shows the ratio of the two histograms. The ratio being consistent with unity, we apply the same correction to both CMUL7 and CINT7 in given period.

	CMUL7		CINT7	
	Min	Max	Min	Max
p-Pb	36.74	53.86	23.12	33.78
Pb-p	41.66	62.06	22.64	33.76

Table 7.4: Minimal and maximal values of  $\langle N_{\text{tr}} \rangle(v_z)$  in CMUL7 and CINT7 triggered data.

### 7.3.1.2 Choice of the reference value

Three possible cases were considered: correction with respect to the minimum, mean<sup>3</sup> and maximum of the distribution, see Fig. 7.9. Each of them came with different advantages but always at a certain cost. We examined three factors to help us choose: (i) the resolution of the correlation of  $N^{\text{raw}}$  with  $N^{\text{corr}}$ , (ii) the effect the correction has at low multiplicities, and (iii) the difficulty to optimise the multiplicity slicing to extract  $J/\psi$  yields in all bins while reaching high enough multiplicities. The authors of the previous work [221] argued that correction with respect to minimum of the  $\langle N^{\text{raw}} \rangle$  results in the best resolution of  $N_{\text{ch}}$  from the three studied cases, at least in absolute value. However, correcting low multiplicity events with respect to the minimum of  $N^{\text{raw}}$  may result in creation of corrected events with non-physical properties. By construction, the method described in Eq. 7.6 will always yield  $\Delta N < 0$ . Depending on the  $N^{\text{raw}}$  in the event, it may happen that  $N^{\text{corr}} < 0$ . To prevent creation of events with non-physical  $N_{\text{tr}} < 0$ , we opted for correcting the distribution with the maximum of the corresponding period. It must be nevertheless mentioned that using the maximum reference value for the correction widens the  $N^{\text{corr}}$  distribution and can deteriorates the  $N_{\text{ch}} - N^{\text{corr}}$  distribution.

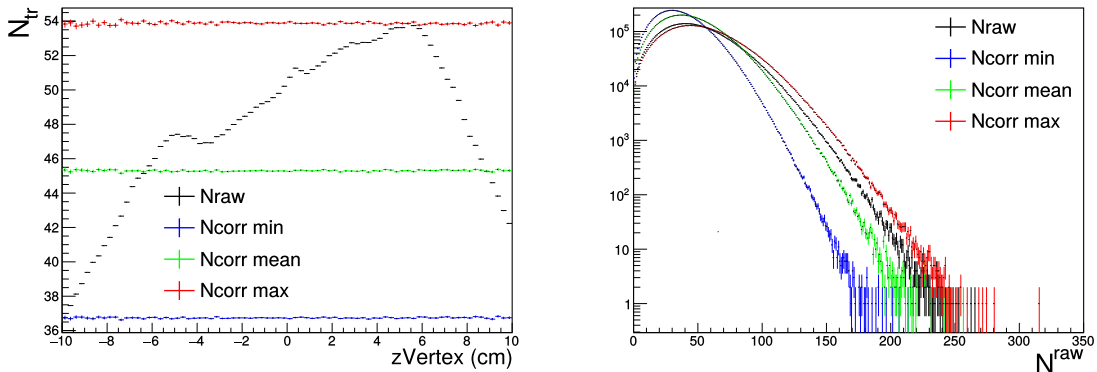


Figure 7.9: Left:  $\langle N_{\text{tr}} \rangle$  as a function of  $v_z$  in the p-Pb data sample. The  $\langle N^{\text{raw}} \rangle(v_z)$  distribution (black) is compared to  $\langle N^{\text{corr}} \rangle(v_z)$  corrected using minimum (blue), mean (green), and maximum (red). Comparison of  $N^{\text{raw}}$  (black) distribution and  $N^{\text{corr}}$  obtained using minimum (blue), mean (green), and maximum (red) in the p-Pb period.

### 7.3.1.3 Correction with binomial smearing

Another correction method was proposed to enable the correction by the minimum of  $\langle N^{\text{raw}} \rangle$  and to prevent the creation of events with  $N^{\text{corr}} < 0$ . The new method uses binomial correction. For each event with a given  $N^{\text{raw}}(v_z)$ , the binomial distribution ranges between 0 and  $N^{\text{raw}}(v_z)$ :

$$N^{\text{corr}} = \text{gRandom} \rightarrow \text{Binomial} \left( N^{\text{raw}}(v_z), \frac{\langle N^{\text{raw}} \rangle(v_z^0)}{\langle N^{\text{raw}} \rangle(v_z)} \right). \quad (7.7)$$

The main results presented in this thesis were obtained from the Poissonian correction with respect to the maximum of  $\langle N^{\text{raw}} \rangle$ . We performed an additional cross-check of the results by correction by

<sup>3</sup>Mean of the distribution was taken as the mean of the minimum and maximum:  $\text{mean} = \frac{\text{min} + \text{max}}{2}$ .

the minimum and applying the binomial smearing. The discussion of the two sets of relative yields and of the corresponding systematic uncertainty is to be found in Sec. 7.4.4.

### 7.3.2 Constructing the multiplicity axis

At first approximation we assumed that the number of tracklets and the number of charged particles created in the collisions were perfectly proportional:

$$N_{\text{ch}} = \alpha \cdot N_{\text{tr}}. \quad (7.8)$$

However, we cannot investigate the correlation in data to verify this assumption. Instead we need to rely on general event Monte Carlo simulations. In the simulations, a given number of charged particles is generated for each event and then let to propagate through the model of the detector. The charged particles then may or may not leave charge in the SPD.

#### 7.3.2.1 Comparison between the data and the MC

ALICE produced two sets of simulations for our analysis, each set consists of generated data for p–Pb and for Pb–p period. The two sets differ in the employed generator. Thus we have in total four different samples, two for each period. One set was produced using a DPMJET Monte Carlo event generator [236]. The other was produced with EPOS-LHC Monte Carlo event generator [237]. We validated the suitability of the two MC productions before using them in our analysis. The validation consisted of comparing the kinematic distributions between the data and the MC, namely distributions in  $\eta_{\text{lab}}$ ,  $\varphi$ ,  $v_z$ , and  $N^{\text{raw}}$ . Details and comparison plots can be found in App. D. In this section we will only show one example for each variable, comparing p–Pb data with corresponding DPMJET production.

- The  $\eta_{\text{lab}}$  distributions were compared in the interval  $|\eta_{\text{lab}}| < 1$ . All MC agreed with the corresponding data within  $\sim 5\%$ . See example comparison in Fig. 7.10a.
- The  $\varphi$  distributions were compared over the full range  $0 < \varphi < 2\pi$ . The ratio of data/MC  $\varphi$  distributions was weighted by the number of MB events in each  $\varphi$  bin and averaged over the full  $\varphi$  range. The weighted average was within 3.5% from unity for all productions. See Fig. 7.10b
- The  $v_z$  distributions were compared in  $-10 < v_z < 10$  cm. The vertex in MC is narrower than in data. In Pb–p period, the vertex is also shifted into positive values, see Fig. D.3 in App. D. We correct for these differences, more details can be found in the next section.
- The  $N^{\text{raw}}$  distributions were compared over the full  $N^{\text{raw}}$  range. The MC agree with the data rather well at low multiplicity. At  $N^{\text{raw}} \gtrsim 60$ , they start to differ considerably. The MC distribution does not reach as high  $N^{\text{raw}}$  as the data. The MC distributions also show a steeper decrease than what is observed in the data, see Fig. 7.10d.

Complementary to comparison of tracklets and  $v_z$  distributions, we also compared the  $N^{\text{raw}}$  profiles between data and each of the generators - results can be seen in Fig. 7.11 for p–Pb and 7.12 for Pb–p. In both periods, the MC profiles differ from the data profiles to the point of showing a visible structure along the  $v_z$ -axis. When compared among themselves, DPMJET and EPOS give the same profiles within uncertainties, without the presence of any systematic behaviour. This suggests that the detector is not perfectly described in the simulations.

As a result, the  $\langle N^{\text{corr}} \rangle (v_z)$  is not flat for none of the available MC productions, albeit the deviation is within a few percent. The  $\langle N^{\text{raw}} \rangle$  and  $\langle N^{\text{corr}} \rangle$  profiles for both generators in the two periods can be found in Fig. 7.13. The structure in the corrected profile is reminiscent of the structures in Fig. 7.11 and 7.12.

#### 7.3.2.2 Correcting the difference between the data and the MC

To correct the differences between data and MC, we have defined the following set of weights:

- A run-by-run weight to correct for the different relative number of events between data and MC. We took the trigger class CINT7-B-NOPF-MUFAST as a reference, as the multiplicity is extracted from the MB data. The weight is defined as a ratio of CINT7 from data and number of events in the MC in each run and is assigned per run. The distributions for the four available MC samples are shown in Fig. 7.14.

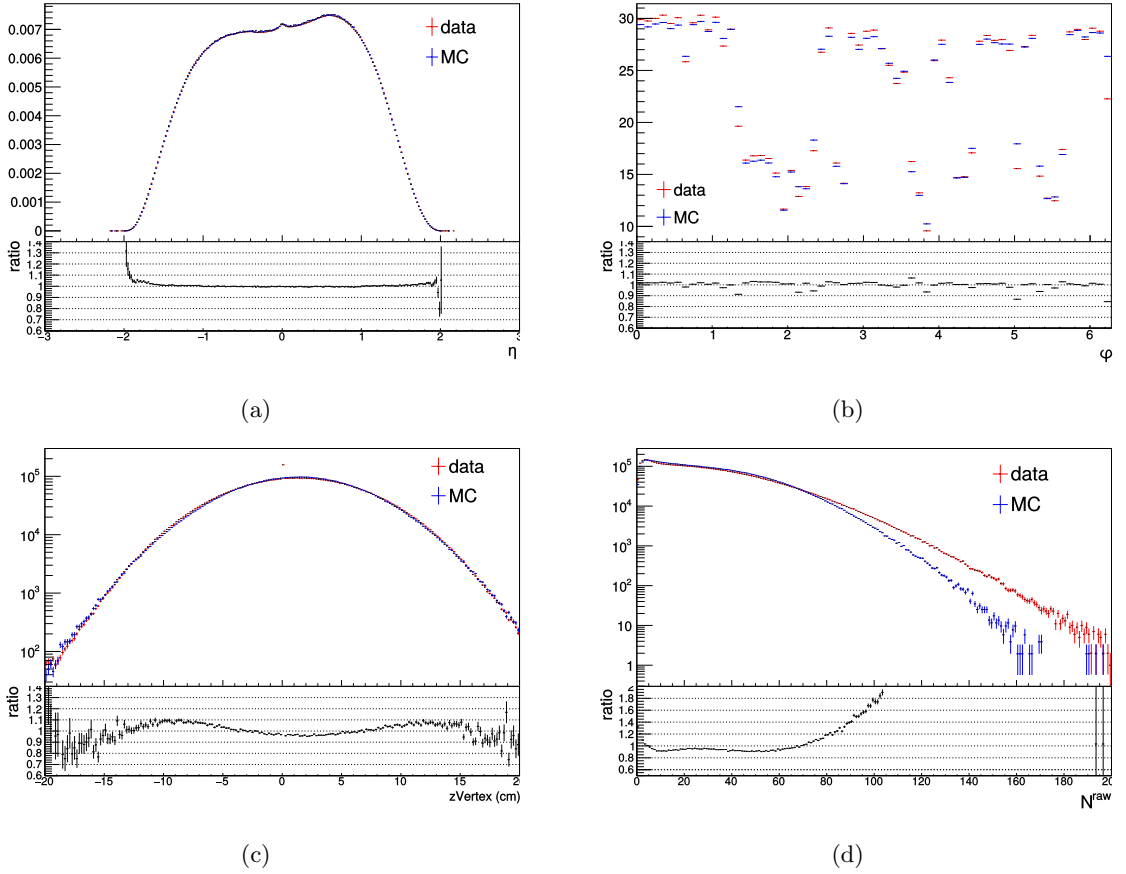


Figure 7.10: Comparison of p-Pb data (red) and the corresponding DPMJET MC production (blue). In each plot, the bottom panel shows ratio of data/MC unless stated otherwise. (a)  $\eta_{\text{lab}}$  distribution of reconstructed tracklets. (b)  $\varphi$  distribution of reconstructed tracklets. The bottom panel shows weighted ratio of data/MC; weights were number of MB events in each  $\varphi$  bin. (c)  $v_z$  distribution in  $-20 < v_z < 20$  cm. (d)  $N^{\text{raw}}$  distribution.

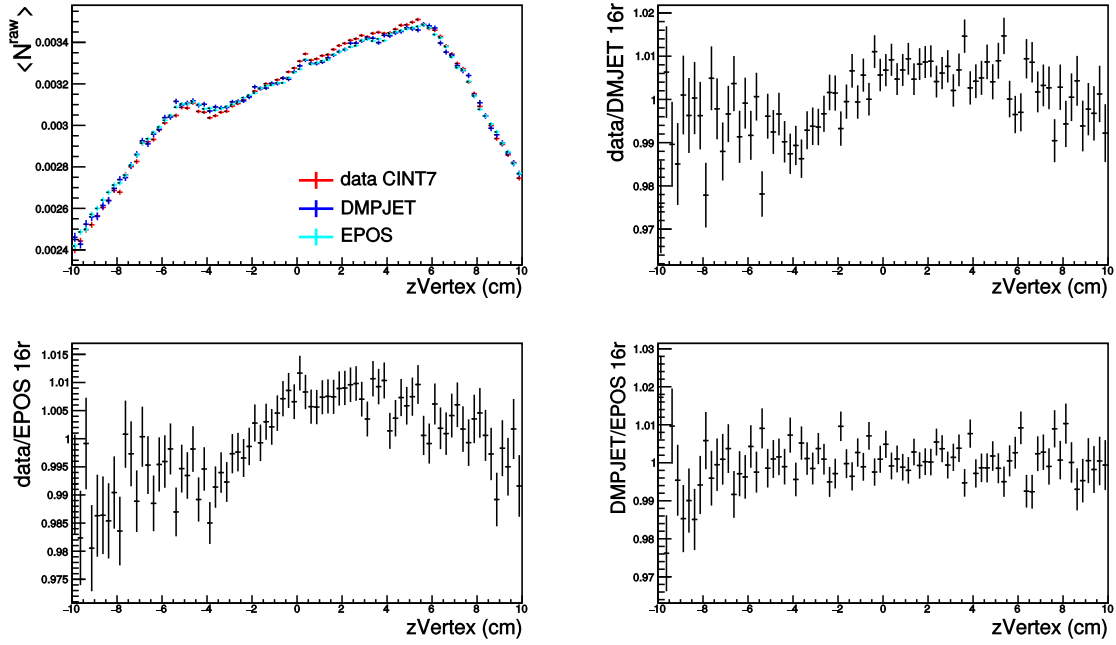


Figure 7.11:  $\langle N^{\text{raw}} \rangle (v_z)$  profiles in p-Pb period. The top left plot shows the profiles compared between data and the two sets of MC. The top left shows ratio of data/DPMJET with a visible non-flat structure. Bottom left the same for data/EPOS, again a structure is present along z-vertex. Bottom right compares the two generated samples - we see that profiles from different MC are similar.

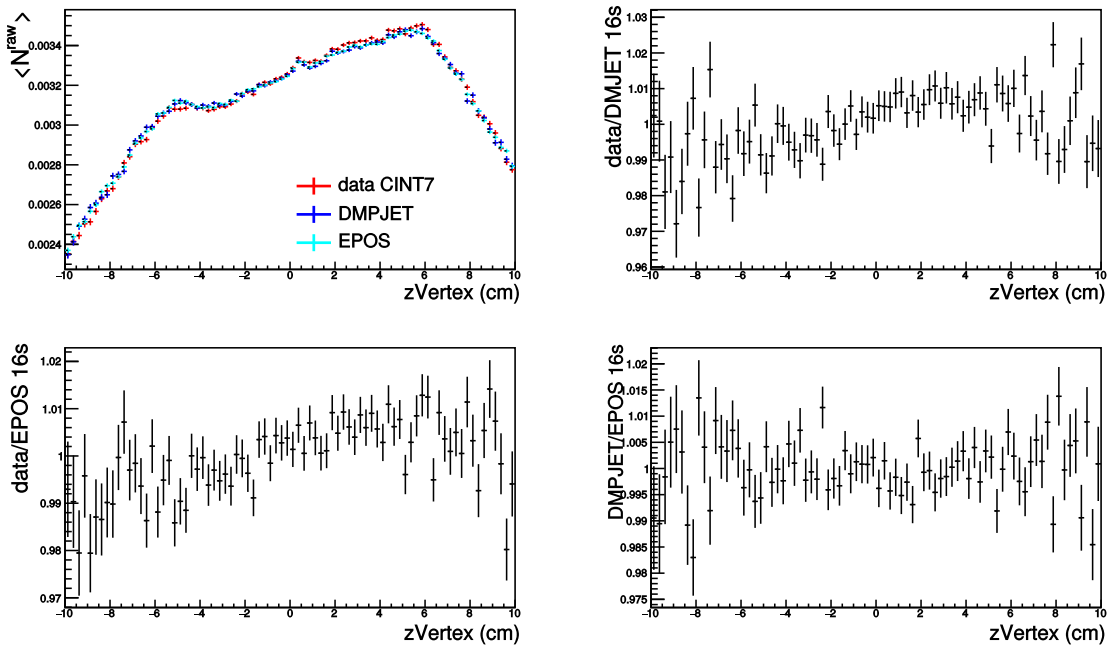
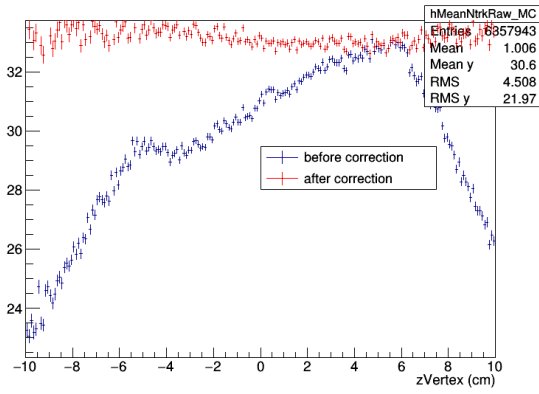
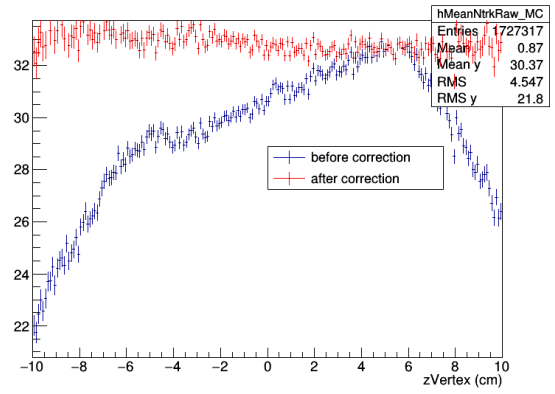


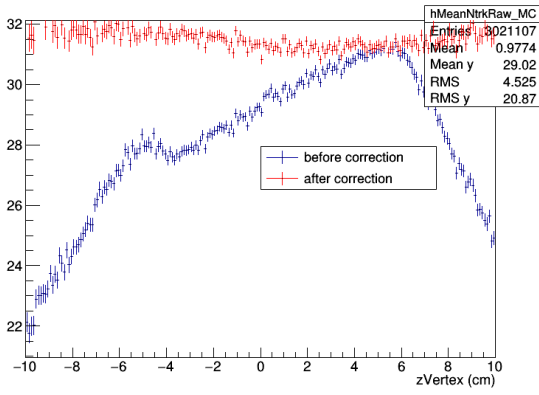
Figure 7.12: Same as Fig. 7.11 but for Pb-p period.



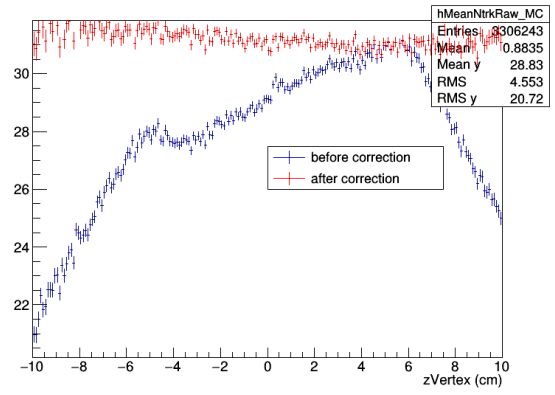
(a) DPMJET p-Pb



(b) DPMJET Pb-p



(c) EPOS p-Pb



(d) EPOS Pb-p

Figure 7.13:  $\langle N^{\text{raw}} \rangle (v_z)$  (blue) and  $\langle N^{\text{corr}} \rangle (v_z)$  (red) in DPMJET and EPOS Monte Carlo.

- A  $z$ -vertex weight, to correct for the difference and the systematic shift in  $v_z$ . The weight is defined as a polynomial fit to the ratio of the distribution in data/MC. We used “pol4” function and performed the fit at a larger range  $-15 < v_z < 15$  cm than what we use in the analysis to control effects at the edges of the distribution. The results of the fit are shown in Fig. 7.15.
- A  $N^{\text{raw}}$  weight, to correct for the different shape of  $N^{\text{raw}}$ , and by extension  $N^{\text{corr}}$  distribution. The weight was defined from a ratio of data/MC distributions. At low multiplicity  $N^{\text{raw}} < 80$ , the weight is directly taken as the value of the ratio at given  $N^{\text{raw}}$ . At  $N^{\text{raw}} \geq 80$ , the ratio shows significant fluctuations. Therefore at high multiplicity, we used the value of the fit to the ratio at a given  $N^{\text{raw}}$  as the weight. We used two different parametrisations - a double exponential (“expo+expo”) and an exponential multiplied by a quadratic function (“expo\*pol2”) function, see Fig. 7.16. To ensure smooth transition between weights taken from the ratio and from the fit, we fitted the distribution in the range of  $60 < N^{\text{raw}} < 165$ . At  $N^{\text{raw}} \geq 165$ , we set the weight equal to 1.

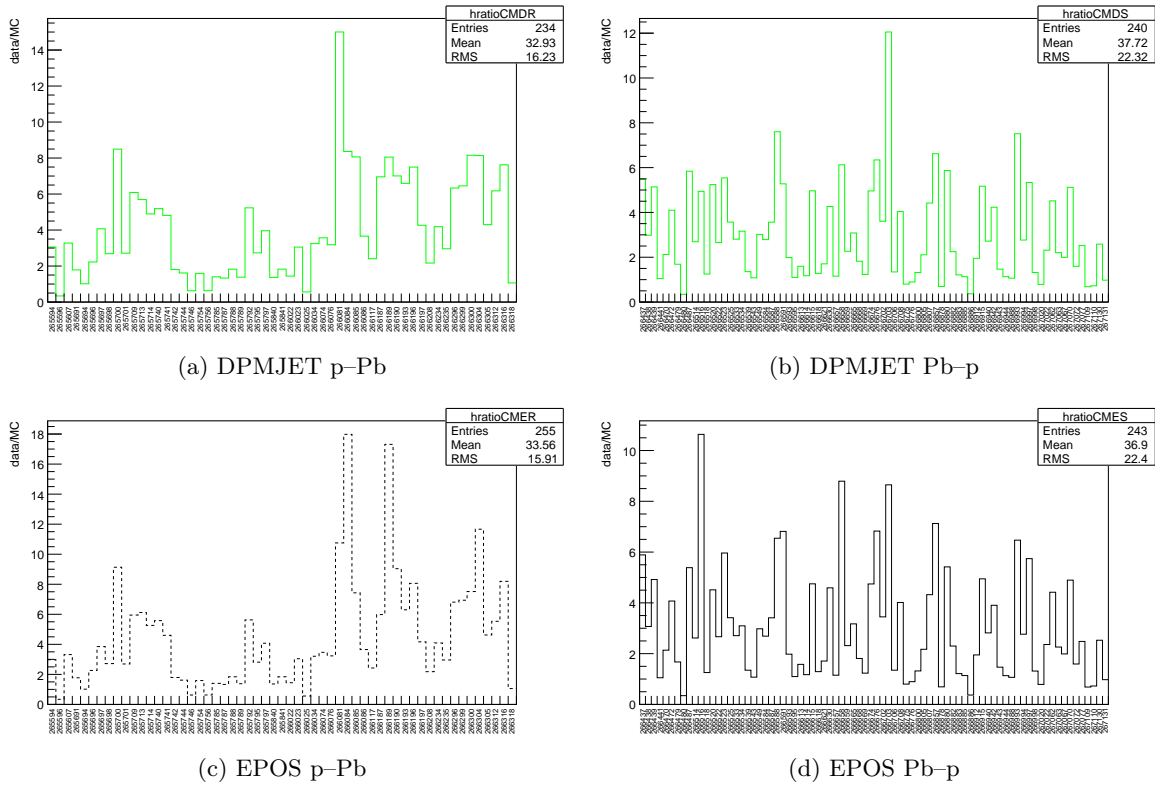


Figure 7.14: Ratio of MB events per run in data/MC.

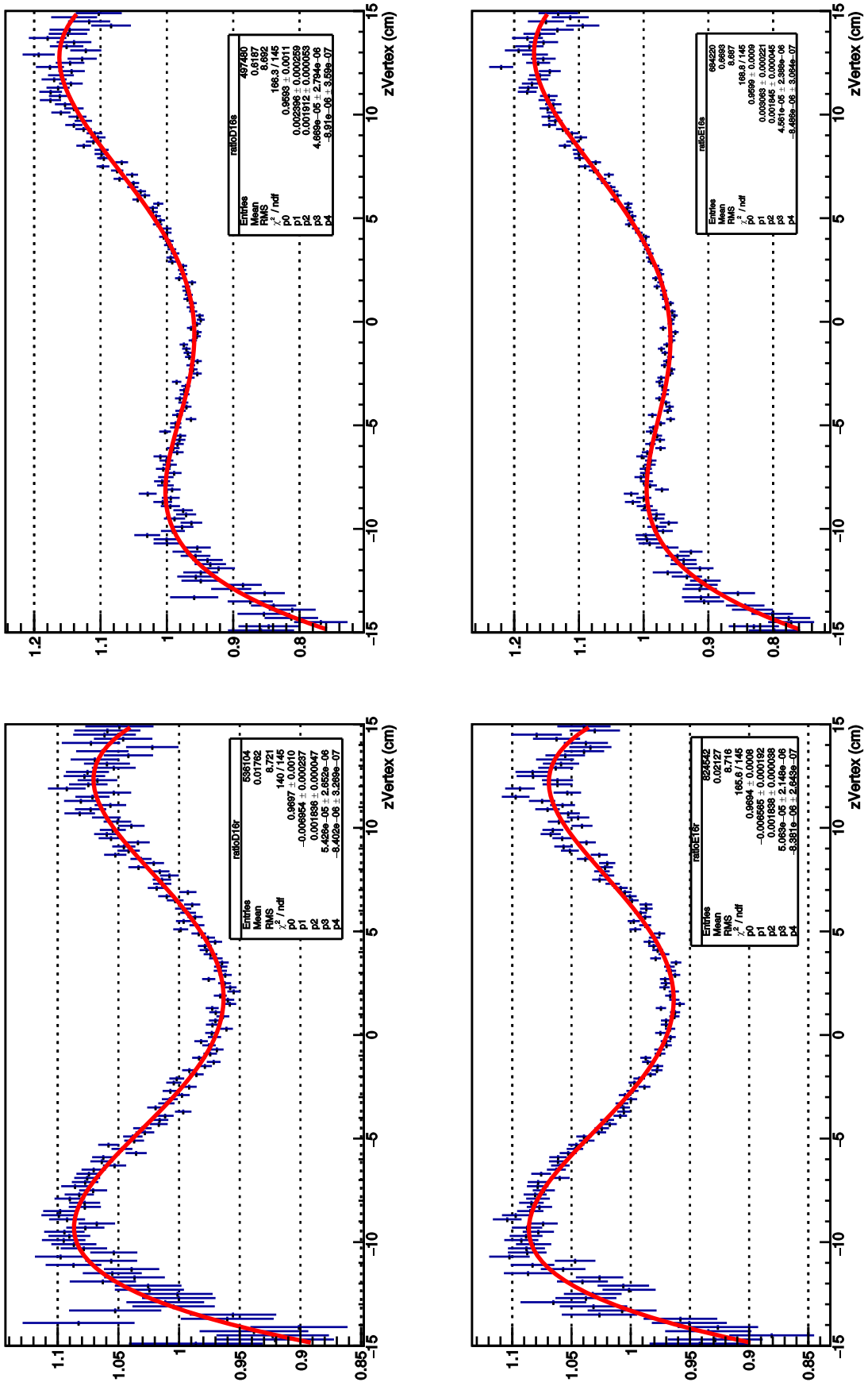
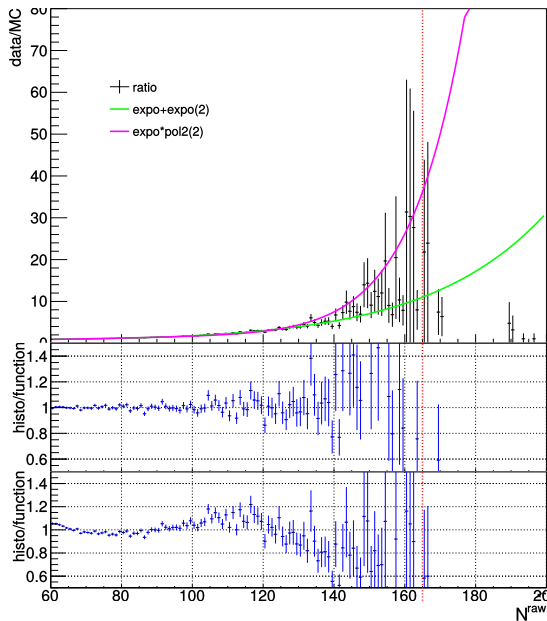
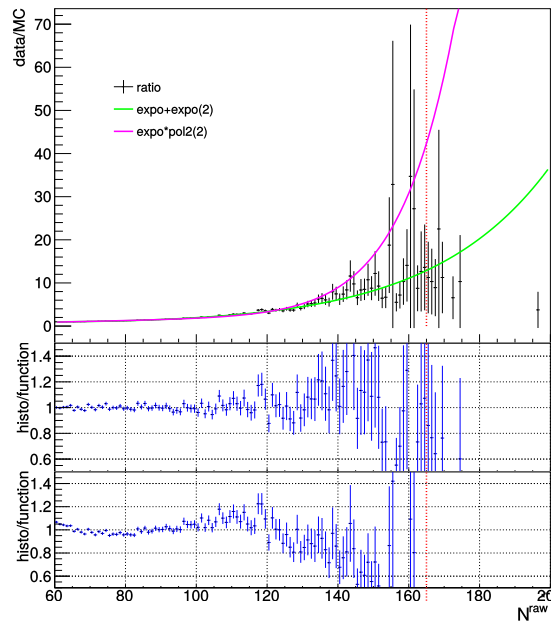


Figure 7.15: Ratio of data/MC of  $z$ -vertex distributions. The red line shows the  $\text{pol4}$  fit to the ratio. The fit was done over an extended range  $-15 < v_z < 15$  cm to prevent edge effects at  $v_z = \pm 10$  cm. Top left panel shows DPMJET p-Pb, bottom left EPOS p-Pb, top right panel DPMJET Pb-p, and bottom right EPOS Pb-p.

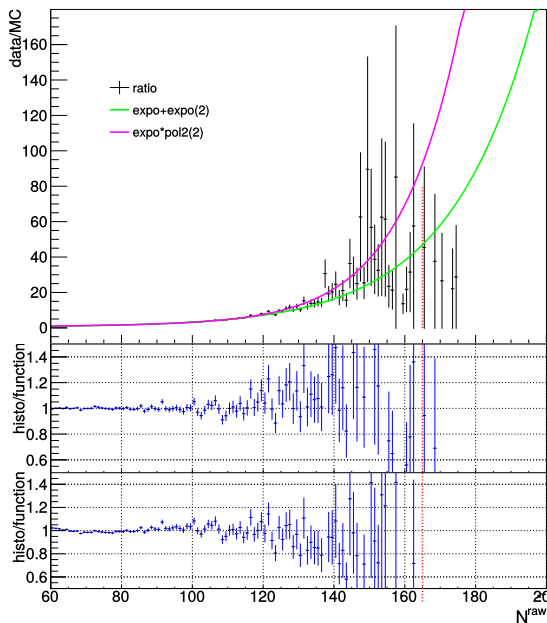
The double exponential function describes the ratio of  $N^{\text{raw}}$  data/MC better than the product of exponential and quadratic function. Therefore we used the double exponential function for the central results. We kept the other function to help us to assess the systematic uncertainty issued from using the  $N^{\text{raw}}$  weights.



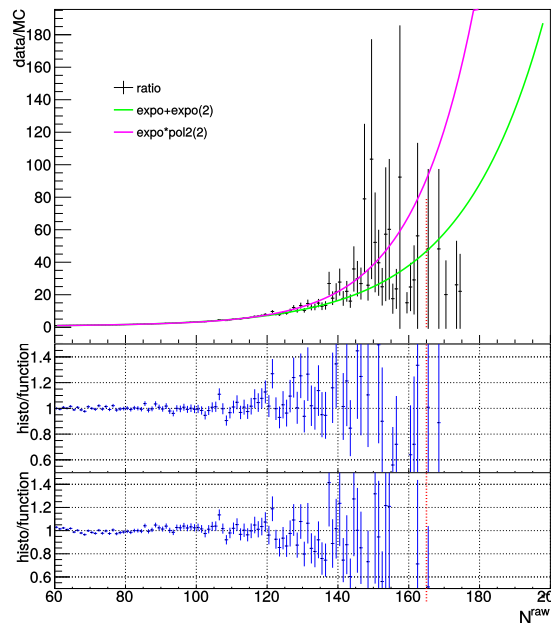
(a) DPMJET p-Pb



(b) DPMJET Pb-p



(c) EPOS p-Pb

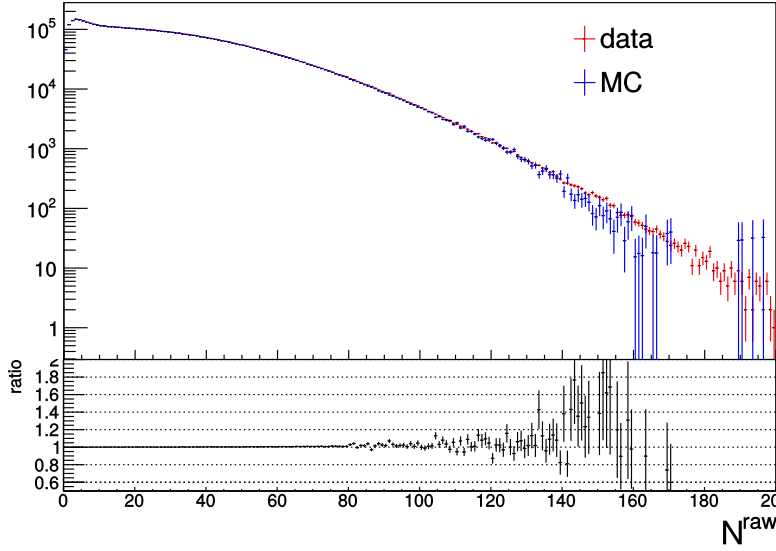


(d) EPOS Pb-p

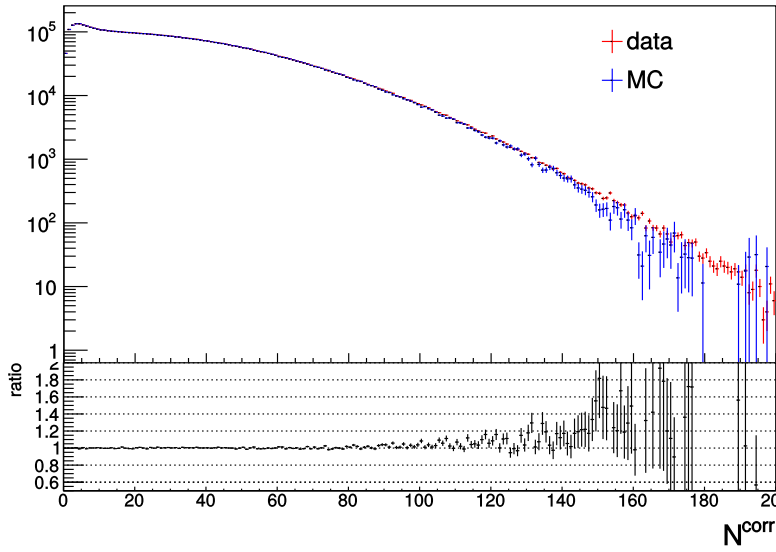
Figure 7.16: Function weights to correct  $N^{\text{raw}}$  in the MC. Green line denotes the expo\*expo fit. Both functions are fit in the range  $60 < N^{\text{raw}} < 165$ . The vertical red chequered line shows the cut-off at  $N^{\text{raw}} = 165$  above which the weights are set to 1. The middle panel shows the ratio of data/MC ratio histogram and the expo\*expo function. The bottom panel shows the ratio of histogram and the expo\*pol2 function.

Each event was corrected by a combined weight `runWeight*zVtxWeight*NrawWeight`. Example of weighted  $N^{\text{raw}}$  and  $N^{\text{corr}}$  for DPMJET p-Pb is shown in Fig. 7.17. We conclude that the weights

bring the tracklets distributions sufficiently close to the data. While the original assumption was to use the  $N^{\text{raw}}$  as to avoid possible bias coming from the correction, it was pointed out that this could also bias the results due to the prevalent  $z$ -vertex dependence. For this reason, we test-weighted the DPMJET p–Pb distribution by a weight obtained from  $N^{\text{corr}}$  ratio. We used the same method to define the weight as for  $N^{\text{raw}}$ . The final weighted  $N^{\text{raw}}$  and  $N^{\text{corr}}$  distributions are consistent with those obtained by applying  $N^{\text{raw}}$  weights and we get consistent  $N_{\text{ch}} - N^{\text{corr}}$  correlation (shall come in Sec. 7.3.4.1).



(a)  $N^{\text{raw}}$  DPMJET p–Pb



(b)  $N^{\text{corr}}$  DPMJET p–Pb

Figure 7.17: Weighted  $N^{\text{raw}}$  and  $N^{\text{corr}}$  distributions in MC compared with the data. Used double exponential  $N^{\text{raw}}$  weight.

To understand the effects each weight has on the distributions, we plotted  $N^{\text{raw}}$ ,  $\langle N^{\text{raw}} \rangle (v_z)$ ,  $N^{\text{corr}}$ , and  $\langle N^{\text{corr}} \rangle (v_z)$  weighted by a different set of weights in Fig. 7.18. We studied the following cases:

1. No weights were applied.
2. Only  $v_z$  weight was applied.

3. Only  $N^{\text{raw}}$  weight was applied.

4. Product of run,  $v_z$ , and  $N^{\text{raw}}$  weights was applied:  $\text{runWeight} * z\text{VtxWeight} * \text{NrawWeight}$ .

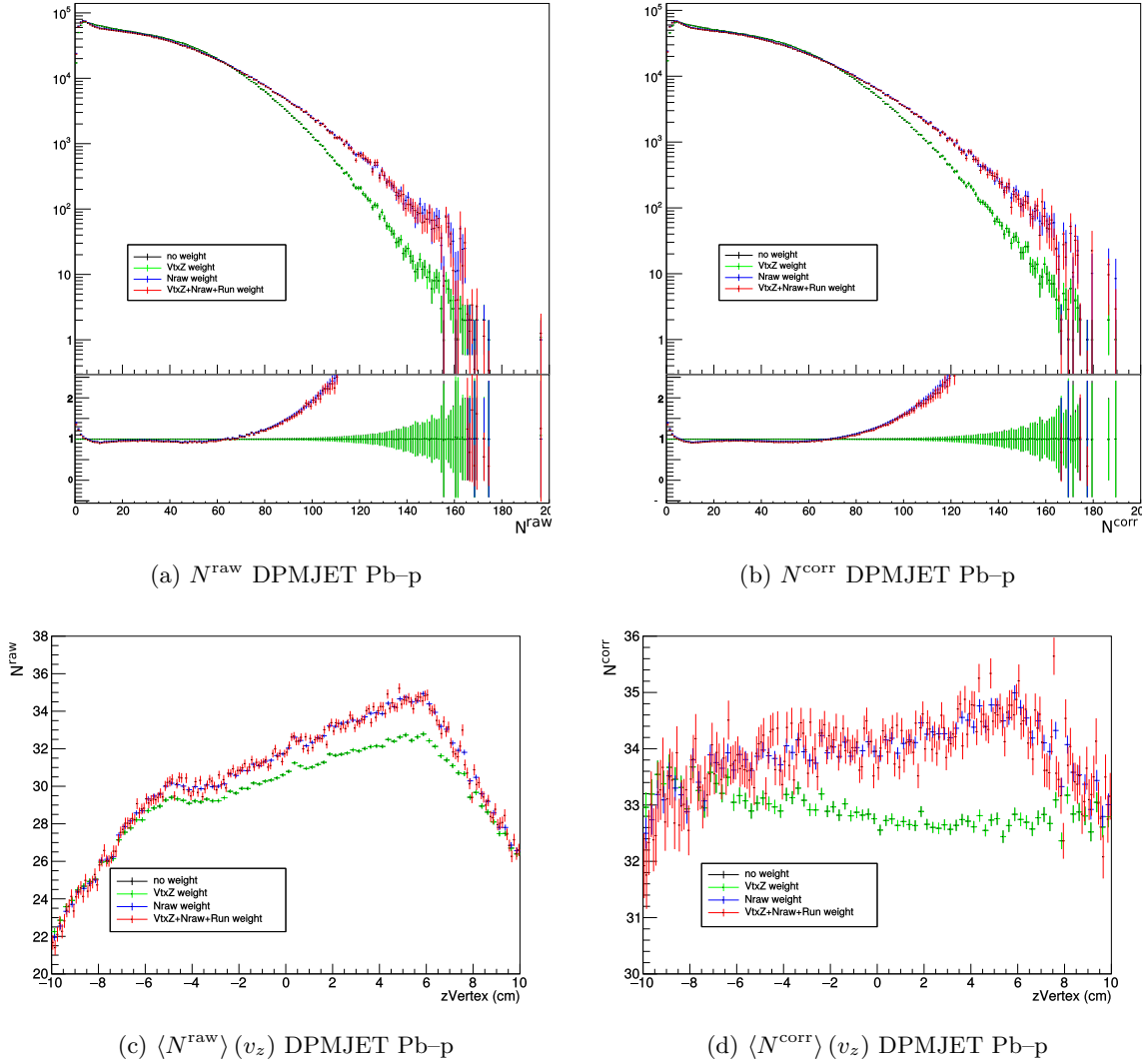


Figure 7.18: Effect of run,  $z$ -vertex and  $N^{\text{raw}}$  weights on tracklets distributions and profiles. Example shows DPMJET Pb-p. Note that black (no weight) points are hidden below the green ( $z$ -vertex weight) ones. Top row shows the  $N^{\text{raw}}$  (left) and  $N^{\text{corr}}$  distributions, the respective bottom panels show the ratio of the weighted distributions with respect to the unweighted one. Bottom row shows the  $\langle N^{\text{raw}} \rangle (v_z)$  (left) and  $\langle N^{\text{corr}} \rangle (v_z)$  (right).

The  $v_z$  weighted distributions in Fig. 7.18 overlap the unweighted distributions. This was expected for  $N_{\text{tr}}$  distributions, in case of  $\langle N_{\text{tr}} \rangle (v_z)$  profiles this suggests that these weights had very little effect on the distributions. The  $N^{\text{raw}}$  weight bring the tracklet distributions up. The combined weight gives a distribution overlapping with the former. We concluded that the  $N^{\text{raw}}$  weight plays the biggest role in the correction of the MC production. However, we also needed to verify the effect of the weights on the profiles. The corrected profiles prior to weighting (recall Fig. 7.13) were not flat. Hence we inspected if the situation was improved after weights were applied. As in the case of the tracklets distributions, the  $N^{\text{raw}}$  weight played the biggest role on the raw and corrected profiles. Moreover, the  $\langle N^{\text{corr}} \rangle (v_z)$  weighted by either  $N^{\text{raw}}$  or the combined weight shows larger deviation from uniformity. We will come back to this residual  $v_z$  dependence. To conclude on this section, the weights improve the  $N_{\text{tr}}$  distributions but deteriorate  $\langle N_{\text{tr}} \rangle$  profiles. We opted to use the weight anyway as they allowed us to improve our reach in multiplicity and enabled us to better determine the  $N_{\text{ch}} - N^{\text{corr}}$  correlation in high multiplicity bins.

### 7.3.2.3 Correlation between the number of corrected tracklets and charged particles

$$N_{\text{ch}} - N^{\text{corr}}$$

The conversion from  $N_{\text{ch}}$  into  $N^{\text{corr}}$  was done by extracting the correlation function from a  $N^{\text{corr}}$  profile of the 2D  $N_{\text{ch}} - N^{\text{corr}}$  correlation. Two different approaches were used to cross-check the obtained values of  $N_{\text{ch}}$ :

- Fitting the 2D distribution, both integrated and in bins of  $N^{\text{corr}}$ . We then computed the values for each multiplicity bin as

$$\langle N_{\text{ch}} \rangle_i = f(\langle N_i^{\text{corr}} \rangle).$$

Uncertainty is taken from the uncertainty on the fit. The spread between different fits (see later text) served to evaluate uncertainty coming from deviation of the linearity of the correlation.

- Projecting the  $N^{\text{corr}}$  bin into the  $N_{\text{ch}}$  axis. We fitted the distribution bin-by-bin by a Gaussian function. The mean was  $\langle N_{\text{ch}} \rangle_i$  and standard deviation gave the resolution. Assuming a linear correlation, the correlation factor from Eq. (7.8) was then determined as

$$\alpha_i = \langle N_{\text{ch}} \rangle_i / \langle N_i^{\text{corr}} \rangle.$$

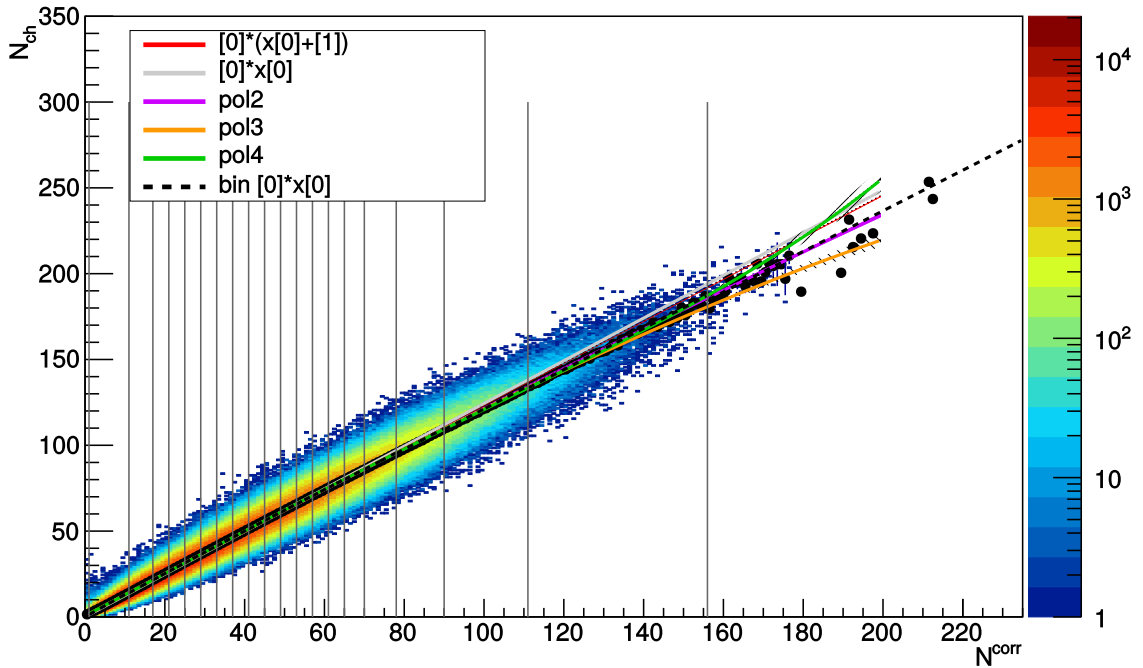


Figure 7.19:  $N_{\text{ch}} - N^{\text{corr}}$  correlation from the DPMJET MC production for the p-Pb period. Superimposed is the  $N^{\text{corr}}$  profile of the 2D distribution (black disks). Shown are also fits to the profile, see text for more details. The grey vertical lines denote the limits of  $N^{\text{corr}}$  bins used in the  $J/\psi$  signal extraction. The  $N_{\text{ch}} - N^{\text{corr}}$  correlation was weighted by the combined weight, using double exponential  $N^{\text{raw}}$  weight.

The  $N_{\text{ch}} - N^{\text{corr}}$  correlation scatter plot in DPMJET p-Pb production is shown in Fig. 7.19. We considered the following options to extract the correlation between  $N_{\text{ch}}$  and  $N^{\text{corr}}$ :

1. Linear fit to the distribution over the entire  $N^{\text{corr}}$  range. We used linear function with a small, non-zero  $N_{\text{ch}}$ -intercept  $\varepsilon$

$$f(N^{\text{corr}}; \alpha, \varepsilon) = \alpha(N^{\text{corr}} + \varepsilon),$$

$$N_{\text{ch}} = f(N^{\text{corr}}; \alpha, \varepsilon) \rightarrow \text{Eval}(N^{\text{corr}}). \quad (7.9)$$

Both  $\alpha$  and  $\varepsilon$  were let free.

2. Linear fit to the distribution over the entire  $N^{\text{corr}}$  range and with fixing the  $\varepsilon = 0$ . Used function has the form of Eq. (7.8).
3. Fit to the distribution in individual  $N^{\text{corr}}$  bins, fixing  $\varepsilon = 0$ . The used function has the form of Eq. (7.8).
4. Fit the distribution with a quadratic function with free parameters (i. e. the function is not forced to pass through the (0,0)). In such case we obtain  $N_{\text{ch}}$  as

$$N_{\text{ch}} = \text{pol2} \rightarrow \text{Eval}(N^{\text{corr}}). \quad (7.10)$$

5. Fit the distribution with a cubic function with free parameters:

$$N_{\text{ch}} = \text{pol3} \rightarrow \text{Eval}(N^{\text{corr}}). \quad (7.11)$$

6. Fit the distribution with a fourth order polynomial function with free parameters:

$$N_{\text{ch}} = \text{pol4} \rightarrow \text{Eval}(N^{\text{corr}}). \quad (7.12)$$

The fits are also shown in Fig. 7.19 (see the legend). At first glance, the quadratic function and bin-by-bin linear fits described the profile the best. This suggested that the linear correlation is broken in the Monte Carlo at high multiplicity. An additional test was done by comparing the  $\langle N_{\text{ch}} \rangle$  computed in each  $N^{\text{corr}}$  bin with the results of the projection into the  $N_{\text{ch}}$ -axis. The results can be found in Fig. 7.20 for p-Pb period and in Fig. 7.21 for Pb-p period (both for DPMJET production). At intermediate multiplicity, the bin-by-bin linear fits gave the closest value to the  $\langle N_{\text{ch}} \rangle$  extracted from the projection, but they deviated significantly at low and high multiplicity. In Pb-p, the statistics in the highest multiplicity bins was too limited for the fit to converge. From the fits over the full  $N^{\text{corr}}$  range, the ratios of the higher order polynomials divided by the projection were closest to unity. The fits were stable enough to allow us to compute the  $\langle N_{\text{ch}} \rangle$  in the highest multiplicity bin. Moreover, the quadratic function was less prone to fluctuations and displayed the most stable behaviour out of the three functions in both periods.

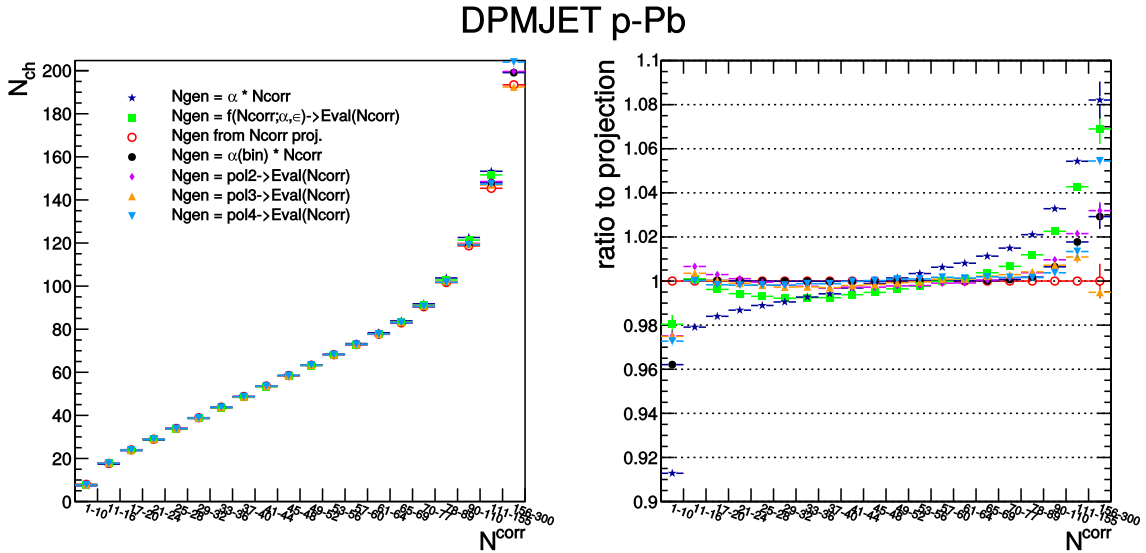


Figure 7.20:  $\langle N_{\text{ch}} \rangle$  computed for each  $N^{\text{corr}}$  bin in p-Pb. On left are the results obtained from different  $N_{\text{ch}} - N^{\text{corr}}$  correlation fits (see legend). The projections of  $N^{\text{corr}}$  intervals into the  $N_{\text{ch}}$  axis (the MC truth) is drawn in open red circles. The left plot shows the ratios of each of these distributions over the MC truth.

We therefore chose to use the quadratic correlation of  $N_{\text{ch}} - N^{\text{corr}}$  in our analysis (see Eq. (7.10)). Since our original hypothesis was that the two are proportional (see Eq. (7.8)), we opted to use the relative difference between the quadratic function and  $N_{\text{ch}} = \alpha \cdot N^{\text{corr}}$  in each bin as a systematic uncertainty. The correlation uncertainty in each bin is listed in Tab. 7.5.

## DPMJET Pb-p

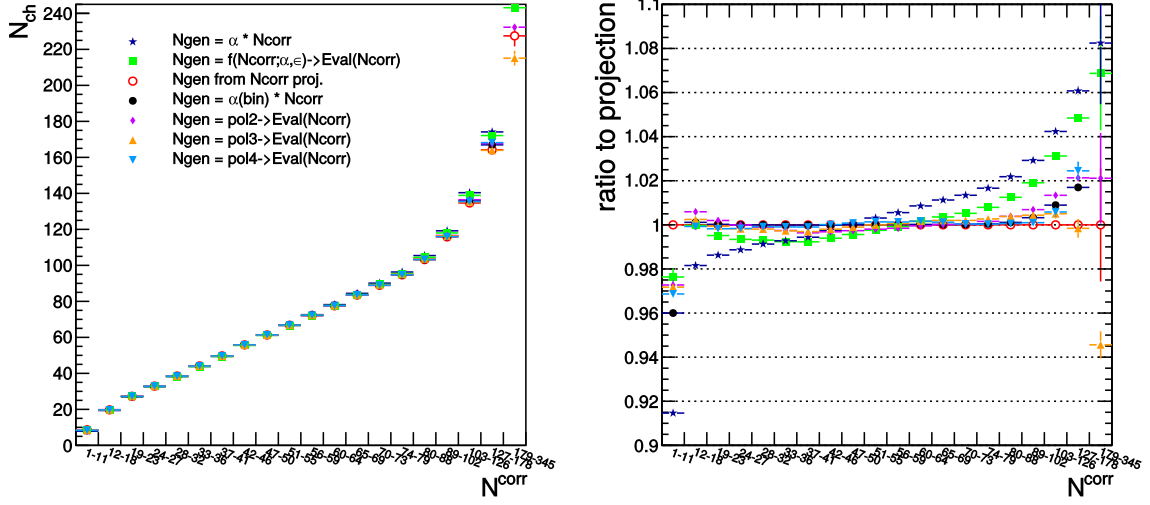


Figure 7.21:  $\langle N_{ch} \rangle$  computed for each  $N^{corr}$  bin in Pb-p. On left are the results obtained from different  $N_{ch} - N^{corr}$  correlation fits (see legend). The projections of  $N^{corr}$  intervals into the  $N_{ch}$  axis (the MC truth) is drawn in open red circles. The left plot shows the ratios of each of these distributions over the MC truth.

p-Pb		Pb-p	
$N^{corr}$ bin	syst. unc. (%)	$N^{corr}$ bin	syst. unc. (%)
1 – 10	6.4	1 – 11	6.9
11 – 16	2.5	12 – 18	2.8
17 – 20	1.6	19 – 23	2.0
21 – 24	1.2	24 – 27	1.5
25 – 28	0.8	28 – 32	1.1
29 – 32	0.5	33 – 36	0.8
33 – 36	0.2	37 – 41	0.5
37 – 40	0.1	42 – 46	0.3
41 – 44	0.3	47 – 50	0.1
45 – 48	0.5	51 – 55	0.1
49 – 52	0.7	56 – 59	0.3
53 – 56	0.9	60 – 64	0.5
57 – 60	1.1	65 – 69	0.7
61 – 64	1.3	70 – 73	0.9
65 – 69	1.5	74 – 79	1.1
70 – 77	1.8	80 – 88	1.3
78 – 89	2.2	89 – 102	1.7
90 – 110	2.9	103 – 126	2.3
111 – 155	3.9	127 – 178	3.2
156 – 300	5.8	179 – 345	4.9

Table 7.5: Systematic uncertainty on the  $N_{ch} - N^{corr}$  correlation in p-Pb and Pb-p.

### 7.3.3 The denominator $\langle dN_{\text{ch}}/d\eta \rangle$

The denominator in Eq. (7.3) is taken from an independent analysis [238]. The values for  $|\eta_{\text{lab}}| < 1$  are quoted in Tab. 7.6, as well as systematic uncertainties. In both periods, the uncertainty amounts to 4%.

collision system	$\langle dN_{\text{ch}}/d\eta \rangle  _{ \eta_{\text{lab}}  < 1}$
p-Pb	$20.33 \pm 0.83$
Pb-p	$20.32 \pm 0.83$

Table 7.6:  $\langle dN_{\text{ch}}/d\eta \rangle$  at midrapidity  $|\eta_{\text{lab}}| < 1$ .

### 7.3.4 Systematic uncertainty on the multiplicity measurement

#### 7.3.4.1 Uncertainty on the multiplicity axis construction

The uncertainty on the correlation was already discussed in Sec. 7.3.2.3. There are two more sources of uncertainty we will explore in this section: the uncertainty on the MC input and the uncertainty on the residual z-dependence, which was foreshadowed in Sec. 7.3.2.2.

#### Uncertainty on input

The uncertainty on input originates in the used generator and applied weights. We extracted the correlation using both DPMJET and EPOS productions for either period, which were corrected by one of the following  $N^{\text{raw}}$  weights<sup>4</sup>:

1.  $N^{\text{raw}}$  weights from TH1 at  $N^{\text{raw}} < 80$  and double exponential at  $80 < N^{\text{raw}} < 165$ .
2.  $N^{\text{raw}}$  weights from TH1 at  $N^{\text{raw}} < 80$  and Expo\*Pol2 at  $80 < N^{\text{raw}} < 165$ .
3. No  $N^{\text{raw}}$  weights applied.
4.  $N^{\text{raw}}$  double exponential weights as in 1. but with MC profiles correction.

In total we used eight different distributions per period, see Fig. 7.22 and 7.23. We studied this behaviour using only linear fits  $N_{\text{ch}} = \alpha \cdot N^{\text{corr}}$ , either global or in bins of multiplicity. The biggest effect stemmed from the generator type used, save for the highest multiplicity bin. We defined the systematic uncertainty as the maximal spread between values within one bin. In the case of global correlation factor  $\alpha_{\text{globalFixedTo0}}$ , the systematic uncertainty on input amounts to 2%. In multiplicity bins, the spread varies little with values up to 3%. We assigned the value extracted from the global fit to all multiplicity bins, as the global fit is more stable than the fits in bins and gives a good estimate in all bins. On a side note, we also included the results for the  $N^{\text{corr}}$  double exponential weight from the DPMJET production in the p-Pb period. The results are consistent with  $N^{\text{raw}}$  weights.

To conclude, we assigned the following input uncertainty to each multiplicity bin in the two periods:

$$\sigma_{\text{input}} = 2\%.$$

#### Uncertainty on residual z-vertex dependence

We investigated one more source of uncertainty - the residual z-vertex dependence of the profiles coming from the difference between the MC and the data. To control this effect, we fitted  $N_{\text{ch}} - N^{\text{corr}}$  in bins of  $v_z$ . We chose a step of  $\Delta v_z = 1$  cm. Here we considered only global fit  $N_{\text{ch}} = \alpha \cdot N^{\text{corr}}$ . The resulting  $\alpha$  distribution is shown in Fig. 7.24. The red line denotes the value integral in  $v_z$ . We extracted the systematic uncertainty due to the residual z-vertex dependence from the maximal spread of the results in bins:

$$\sigma_{\text{zVtx}} = 3\%.$$

<sup>4</sup>As we discussed previously, none of the other weights has sizeable effect on the distributions.

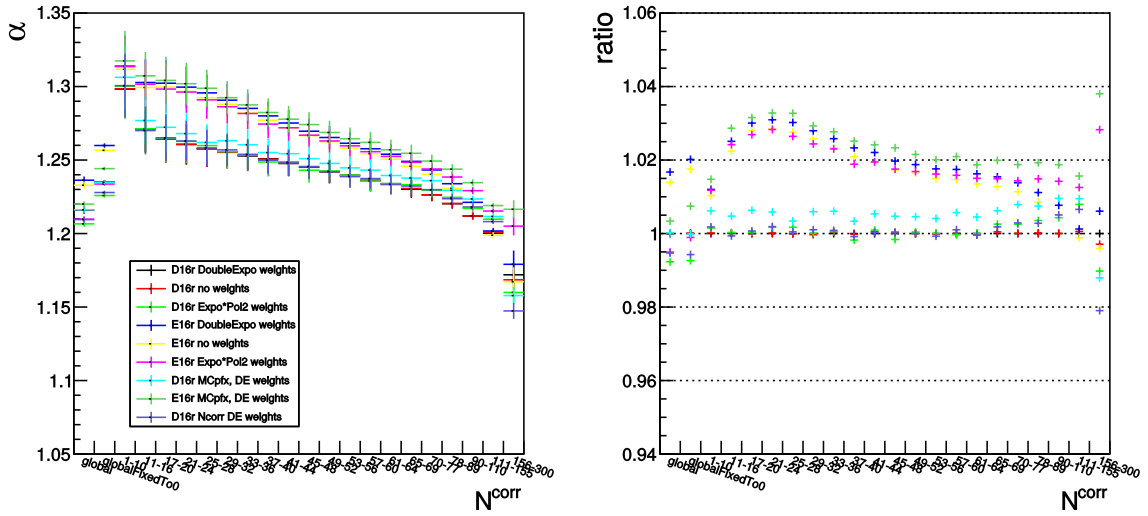


Figure 7.22: Systematic uncertainty on the MC input for the p–Pb period. The left-hand-side plots show the spread of the different correlation factor  $\alpha$  values in one period with varying generator and  $N^{\text{raw}}$  weights. The following distributions are shown: DPMJET with double exponential weights (black), DPMJET with no weights (red), DPMJET with Expo\*Pol2 weights (green), EPOS with double exponential weights (blue), EPOS with no weights (yellow), EPOS with Expo\*Pol2 weights (magenta). The last-but-one two are distributions obtained from distributions corrected by MC profiles: DPMJET with double exponential weights (turquoise), EPOS with double exponential weights (teal). The mauve datapoints show the results obtained with the  $N^{\text{corr}}$  double exponential weight. The plot on right shows the ratio of each of these distributions over the one obtained from DPMJET with double exponential weights.

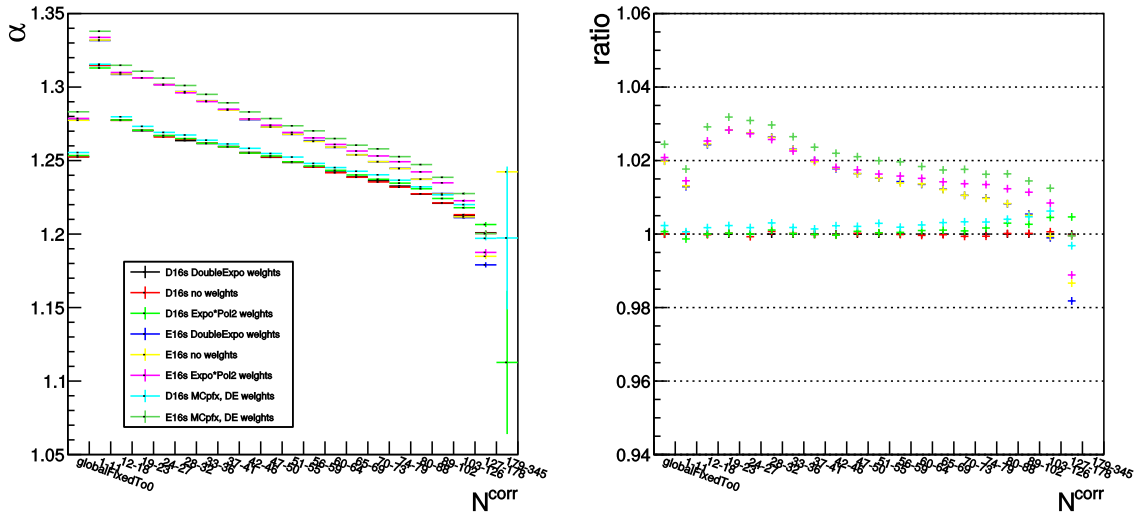


Figure 7.23: Systematic uncertainty on the MC input for the Pb–p period. The left-hand-side plots show the spread of the different correlation factor  $\alpha$  values in one period with varying generator and  $N^{\text{raw}}$  weights. The following distributions are shown: DPMJET with double exponential weights (black), DPMJET with no weights (red), DPMJET with Expo\*Pol2 weights (green), EPOS with double exponential weights (blue), EPOS with no weights (yellow), EPOS with Expo\*Pol2 weights (magenta). The last two are distributions obtained from distributions corrected by MC profiles: DPMJET with double exponential weights (turquoise), EPOS with double exponential weights (teal). The plot on right shows the ratio of each of these distributions over the one obtained from DPMJET with double exponential weights.

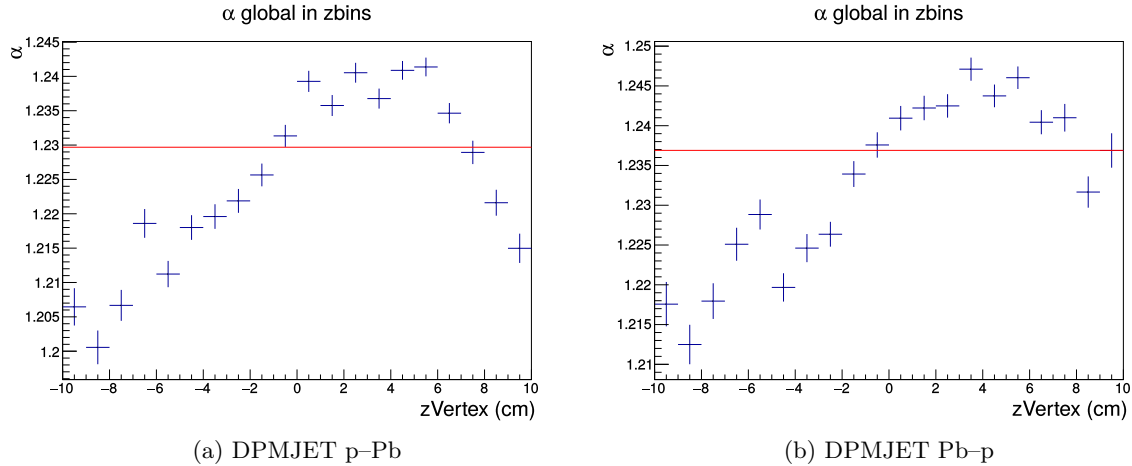


Figure 7.24:  $v_z$ -dependence of  $\alpha$  factor. The values were extracted from global fit with  $\varepsilon = 0$ . The red line shows the  $v_z$ -integrated value.

### 7.3.4.2 Uncertainty on the multiplicity bin-flow and pile-up

Especially with a very fine binning, such as the one used in our analysis, the bin-flow can have an important effect on final results both on the multiplicity determination as well as on the yield extraction. We took into account two possible sources of bin-flow:

- the randomisation in the correction method,
- the bin-edge effect.

Residual pile-up can be present in the data even after the pile-up cuts are applied. We used two different methods to evaluate the systematic uncertainty on residual pile-up:

- changing the applied SPD pile-up cut,
- toy MC, for details see Sec. 7.3.4.3.

To account for the uncertainty stemming from the randomisation of the correction applied to  $N^{\text{raw}}$ , we run the analysis task twice with the exact same setting, bearing in mind to assure enough time difference between the two tasks. This method resulted in two sets of output of equal size, but each event corrected with a different randomisation seed. The edge effect was tackled by repeating the same task but with shifting the entire  $N^{\text{corr}}$  axis by<sup>5</sup>

$$\text{bin}_{\text{offset}} = \pm 0.1.$$

We also varied the SPD pile up cut (for details on the cut variations, see Sec. 7.2.1.2). We compared the mean number of corrected tracklets  $\langle N^{\text{corr}} \rangle_i$  in each bin  $i$  extracted from each output. The uncertainty from either effect was found to be negligible and was not considered in the final systematic uncertainty.

### 7.3.4.3 Estimation of the possible remaining pile-up contamination

Event after pile-up removal cuts, the data may be biased by a residual pile-up contamination. The fraction of this residual pile-up was estimated by means of a toy Monte Carlo.

The toy MC was used to generate random pairs of  $(N^{\text{raw}}, v_z)$  following the distributions extracted from the data. The pile-up was added randomly to these pairs with a probability corresponding to the interaction rate  $\mu$  from the data. The  $(N^{\text{raw}}, v_z)$  pairs for these pile-up events were also taken to follow the same distributions. A mock-up of the multiplicity dependent SPD pile-up cut and of the SPD  $N_{\text{CL}} - N^{\text{raw}}$  cut was applied on the generated distributions.

The residual pile-up was evaluated from the ratio of all events passing the cuts divided by all simulated events. In all multiplicity bins except the last, the contribution of the remaining pile-up

<sup>5</sup>This was possible as by construction the  $N^{\text{corr}}$  were defined not as integer but as doubles. If they were defined as integers, we would have used a similar method but likely opted for integer shift.

was  $< 0.5\%$ , in agreement with results in Sec. 7.2.1.3. In the last multiplicity bin, the contribution jumped to 1% in p-Pb and 8% in Pb-p. However, the statistics at high multiplicity was limited, resulting in large fluctuations in the distributions. Taking into account these limitations, we did not assign an additional systematic on residual pile-up.

#### 7.3.4.4 Total systematic uncertainty

A list of all used uncertainties can be found in Tab. 7.7. The total uncertainty is computed as a square sum of all contributions as the different sources are uncorrelated. The total uncertainty ranges from 5.4 – 8.8% in p-Pb and 5.1 – 8.2% in Pb-p.

source	p-Pb	Pb-p
$N_{\text{ch}} - N^{\text{corr}}$ correlation	0.1 – 6.9%	0.1 – 6.4%
MC input	2%*	2%*
residual z-vertex dependence	3%*	3%*
$\langle dN_{\text{ch}}/d\eta \rangle$ [238]	4%*	4%*
total	5.4 – 8.8%	5.1 – 8.2%

Table 7.7: Sources of systematic uncertainties on the charged-particle multiplicity. Values marked with asterisk are correlated in multiplicity.

#### 7.3.5 Charged particle multiplicity

The multiplicity bins were defined using the dimuon triggered tracklet distribution, however the final  $\langle N_{\text{ch}} \rangle$  in each bin is determined from the MB distribution. Computing the multiplicity from MB data ensures possibility of comparing the results with theory and between experiments. The values of  $\langle N_{\text{ch}} \rangle$  in the two analysed periods can be found in Tab. 7.8. We recall that we computed the  $\langle N_{\text{ch}} \rangle$  taking the quadratic fit to the  $N_{\text{ch}} - N^{\text{corr}}$  correlation.

p-Pb				Pb-p			
$N^{\text{corr}}$ bin	$\langle N^{\text{corr}} \rangle$	$\langle N_{\text{ch}} \rangle$	$\frac{dN_{\text{ch}}/d\eta}{\langle dN_{\text{ch}}/d\eta \rangle}$	$N^{\text{corr}}$ bin	$\langle N^{\text{corr}} \rangle$	$\langle N_{\text{ch}} \rangle$	$\frac{dN_{\text{ch}}/d\eta}{\langle dN_{\text{ch}}/d\eta \rangle}$
1 – 10	5.43	7.25	0.18	1 – 11	5.86	7.85	0.19
11 – 16	13.47	17.25	0.42	12 – 18	14.97	19.23	0.47
17 – 20	18.49	23.46	0.58	19 – 23	20.99	26.72	0.66
21 – 24	22.49	28.40	0.70	24 – 27	25.49	32.31	0.80
25 – 28	26.49	33.32	0.82	28 – 32	29.99	37.87	0.93
29 – 32	30.49	38.23	0.94	33 – 36	34.49	43.42	1.07
33 – 36	34.49	43.12	1.06	37 – 41	38.98	48.93	1.21
37 – 40	38.49	48.01	1.18	42 – 46	43.97	55.06	1.36
41 – 44	42.48	52.87	1.30	47 – 50	48.48	60.56	1.49
45 – 48	46.48	57.73	1.42	51 – 55	52.96	66.01	1.63
49 – 52	50.49	62.58	1.54	56 – 59	57.47	71.50	1.76
53 – 56	54.48	67.41	1.66	60 – 64	61.96	76.93	1.89
57 – 60	58.48	72.23	1.78	65 – 69	66.94	82.94	2.04
61 – 64	62.48	77.04	1.90	70 – 73	71.48	88.39	2.18
65 – 69	66.96	82.41	2.03	74 – 79	76.42	94.32	2.32
70 – 77	73.34	90.03	2.22	80 – 88	83.76	103.08	2.54
78 – 89	83.04	101.55	2.50	89 – 102	94.77	116.14	2.86
90 – 110	98.27	119.50	2.94	103 – 126	111.93	136.31	3.36
111 – 155	123.68	149.02	3.67	127 – 178	139.80	168.55	4.15
156 – 300	168.87	200.27	4.93	179 – 345	191.87	227.10	5.59

Table 7.8: Mean corrected number of tracklets  $\langle N^{\text{corr}} \rangle$  and corresponding average number of charged particles  $N_{\text{ch}}$  in p-Pb and Pb-p periods.

## 7.4 J/ψ yields extraction

The J/ψ extraction was already described in the previous chapter (see Ch. 6). Here we will recall the most important formulæ.

The J/ψ yield  $Y_{J/\psi}$  is given as

$$Y_{J/\psi} = \frac{N_{J/\psi}}{A\varepsilon \cdot \text{BR}_{J/\psi \rightarrow \mu^+\mu^-} \cdot N_{\text{MB}}^{\text{eq}}}, \quad (7.13)$$

where  $N_{J/\psi}$  is the number of J/ψ in the analysed sample,  $A\varepsilon$  is the acceptance-efficiency of the detector,  $\text{BR}_{J/\psi \rightarrow \mu^+\mu^-}$  is the branching ratio of J/ψ decaying into a di-muon pair ( $5.961 \pm 0.033$ )% [1] and  $N_{\text{MB}}^{\text{eq}}$  is the number of the MB events equivalent to the analysed dimuon triggered sample.

We are ultimately interested in the relative yield in each multiplicity bin  $i$ , which is given as a ratio of the yield in a given bin to the total yield

$$Y_{J/\psi}^{R,i} = \frac{Y_{J/\psi}^i}{Y_{J/\psi}^{\text{tot}}}. \quad (7.14)$$

Since the detector effects do not change with multiplicity (will be verified in Sec. 7.4.1.2), the  $A\varepsilon$  factor will cancel out and we can compute the relative yields directly from ratio of the raw yields.  $\text{BR}_{J/\psi \rightarrow \mu^+\mu^-}$  cancels out too in Eq. (7.14). The two factors  $A\varepsilon$  and  $\text{BR}_{J/\psi \rightarrow \mu^+\mu^-}$  must be taken into account when computing the absolute yields.

The relative J/ψ yield was defined in Eq. (7.1):

$$Y_{J/\psi}^{R,i} = \frac{Y_{J/\psi}^i}{Y_{J/\psi}^{\text{tot}}} = \frac{N_{J/\psi}^i}{N_{J/\psi}^{\text{tot}}} \times \frac{N_{\text{MB}}^{\text{eq,tot}}}{N_{\text{MB}}^{\text{eq},i}} \times \frac{\varepsilon_{\text{MB}}^i}{\varepsilon_{\text{MB}}},$$

where  $N_{\text{MB}}^{\text{eq},i} = F_{\text{norm}}^i \times N_{\text{CMUL7}}^i$ , see Eq. (6.8).

### 7.4.1 J/ψ signal extraction

The J/ψ signal was extracted following the same method as in Sec. 6.2. In short, the J/ψ candidates were obtained by computing the invariant mass of the pairs of the opposite charge muon tracks that passed the selection criteria listed in Sec. 7.2.2. The number of J/ψ in the data was assessed by fitting the invariant mass spectra. The fitting functions combined functions describing the J/ψ and ψ(2S) signals with a background function. Several combinations of signal and background functions as well as different fit ranges were used to assess the systematic uncertainty on the signal extraction.

#### 7.4.1.1 Invariant mass fit

To fit the J/ψ signal, we used two functions each consisting of a Gaussian core and a set of tails in both lower and upper mass region: (i) Double Extended Crystal Ball function (CB2), and a (ii) NA60 function. The mass and width of the ψ(2S) peak was fixed to the J/ψ as

$$M_{\psi(2\text{S})} = M_{J/\psi} + (M_{\psi(2\text{S})}^{\text{PDG}} - M_{J/\psi}^{\text{PDG}}), \quad (7.15)$$

$$\sigma_{\psi(2\text{S})} = 1.05 \times \sigma_{J/\psi} \quad (7.16)$$

where PDG denotes the values given by the Particle Data Group [1]. The factor in Eq. (7.16) was obtained from pp data at 13 TeV [73]. Note the difference with Eq. (6.5) used in the pp analysis at  $\sqrt{s} = 5.02$  TeV. The statistics collected in 2015 at 13 TeV were enough to extract the widths of J/ψ and ψ(2S) from data. Hence all later analyses of forward J/ψ in ALICE such as this one now use the ratio extracted from ALICE data.

Due to limited statistics (particularly in multiplicity bins) and complicated fit function, the tails of the two functions needed to be fixed when fitting the invariant mass spectrum. Therefore it was necessary to also take into consideration the effect of the tails on the signal. This was handled by fitting the spectra multiple times with different set of tails in each fit. In the case of using the CB2 function, it was possible to fit the integrated spectra with free tails. We have performed such fit, however in the subsequent uncertainty evaluation the tails were always fixed. The tails needed to be always fixed when fitting with the NA60 function. Its very complex formula prevented us from

successfully fitting the invariant spectrum with free tails. We found that the tails presented the biggest contribution to the systematic uncertainty on signal extraction. To prevent biasing the results, we opted to use the equal number of tails from data and from MC. In total, we considered 6 sets of tails. 3 were issued from data and 3 issued from MC:

- tails extracted from data:
  - pp at  $\sqrt{s} = 13$  TeV (CB2),
  - p-Pb/Pb-p at  $\sqrt{s_{NN}} = 8.16$  TeV (CB2) fit to dataset without pile-up cuts and vertex selection [130],
  - p-Pb/Pb-p at  $\sqrt{s_{NN}} = 8.16$  TeV (CB2) fit to dataset with pile-up cuts and vertex selection;
- tails extracted from MC:
  - pp at  $\sqrt{s} = 13$  TeV (CB2),
  - p-Pb/Pb-p at  $\sqrt{s_{NN}} = 8.16$  TeV (CB2),
  - p-Pb/Pb-p at  $\sqrt{s_{NN}} = 8.16$  TeV (NA60).

Fig. 7.25 shows all applied tails for CB2 and NA60 signal functions.

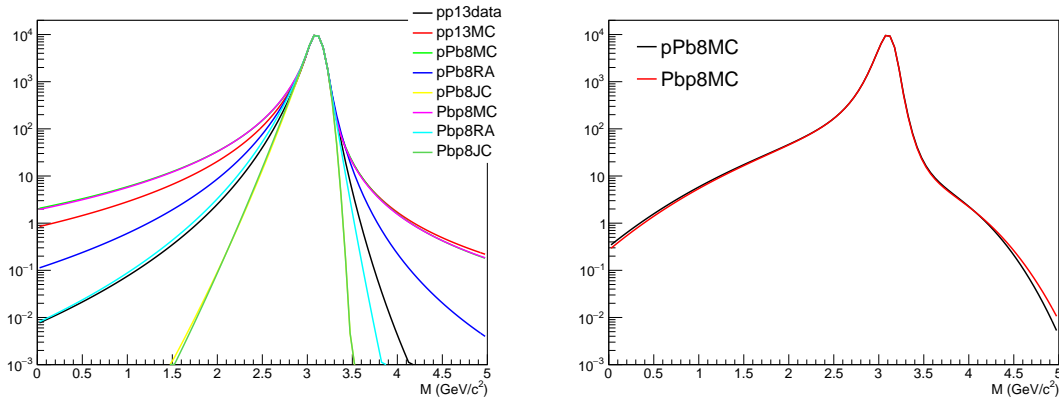


Figure 7.25: Comparison of tails used in the present analysis. Left plot shows the CB2 tails, right plots shows tails used for NA60 shape. Nomenclature: pp13data - extracted from pp data at 13 TeV, pp13MC - extracted from pp MC at 13 TeV, pPb8MC (Pb8MC) - extracted from p-Pb (Pb-p) MC at 8 TeV, pPb8RA (Pb8RA) - extracted from p-Pb (Pb-p) data at 8 TeV without pile-up or vertex cuts, pPb8JC (Pb8JC) - extracted from p-Pb (Pb-p) data at 8 TeV with the custom pile-up and vertex cuts used in this analysis.

For the background shape we considered (i) a double exponential function (DoubleExpo), and (ii) 4<sup>th</sup> order polynomial multiplied by exponential (ExpPol4). Other functions were also tested, the selected two were able to describe the background in all multiplicity bins. We used two fit mass ranges:

- $1.7 < M_{\text{inv}} < 4.8$  GeV/ $c$
- $2.0 < M_{\text{inv}} < 5.0$  GeV/ $c$

An example of integrated multiplicity fit is displayed in Fig. 7.26. Examples of signal at low, intermediate, and high multiplicity can be found in Fig. 7.27.

Taking into account two background shapes, two fit ranges and five sets of tail parameters for the CB2 signal shape adding up to 20 fits, and two background shapes, two fit ranges and one set of tail parameters for NA60 adding up to 4 fits, we obtained a set of 24 different fits. We verified that the biggest change in  $N_{J/\psi}$  stems from tails and thus that we do not bias the result by opting to use less NA60 fits than CB2. Results of these 24 different multiplicity integrated fits in the p-Pb and Pb-p period can be found in Fig. 7.28.

Analytic parametrisations of all the above listed functions can be found in App. A

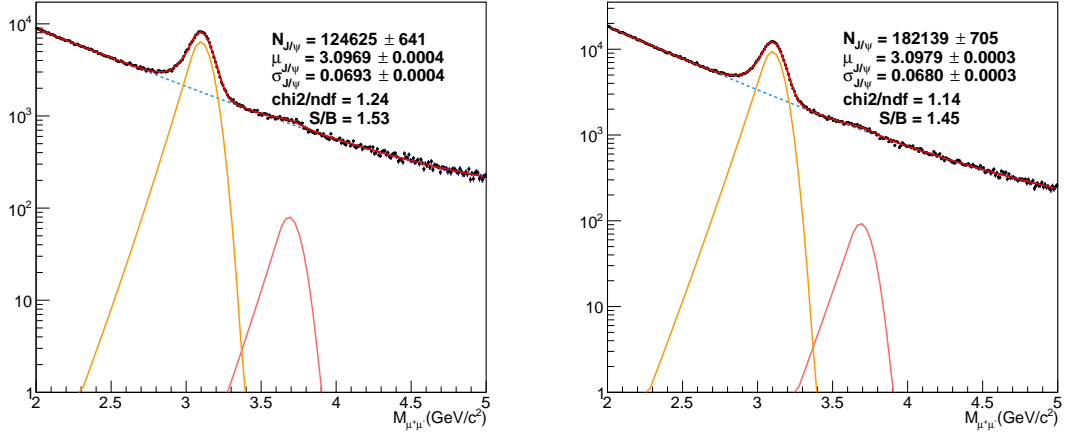


Figure 7.26: Example of signal extraction for the multiplicity integrated invariant mass spectra in p-Pb (left) and Pb-p (right). Used fit: combination CB2+DoubleExponential with p-Pb (Pb-p) tails extracted from data sample with vertex selection over the fit range  $2 < M_{\mu^+\mu^-} < 5 \text{ GeV}/c^2$ .

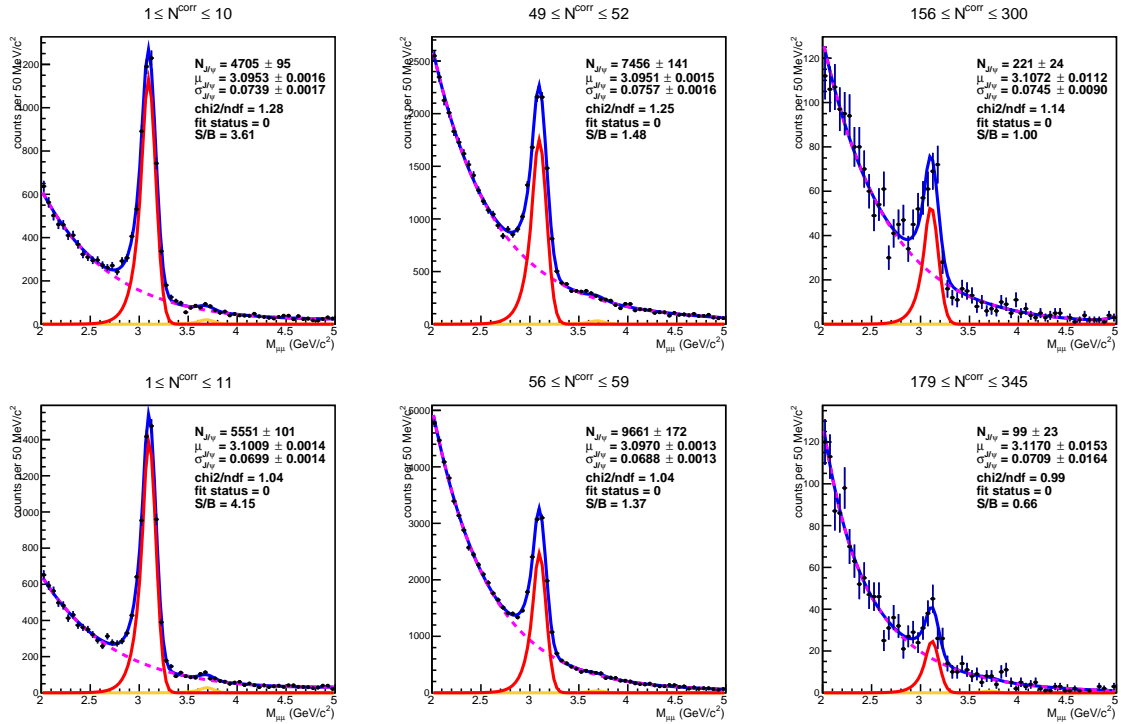


Figure 7.27: Examples of signal extraction at low, intermediate, and high multiplicity. Top row shows the p-Pb period, bottom row the Pb-p period. Used fit: combination CB2+Double Exponential with p-Pb (Pb-p) tails extracted from data sample with vertex selection over the fit range  $2 < M_{\mu^+\mu^-} < 5 \text{ GeV}/c^2$ .

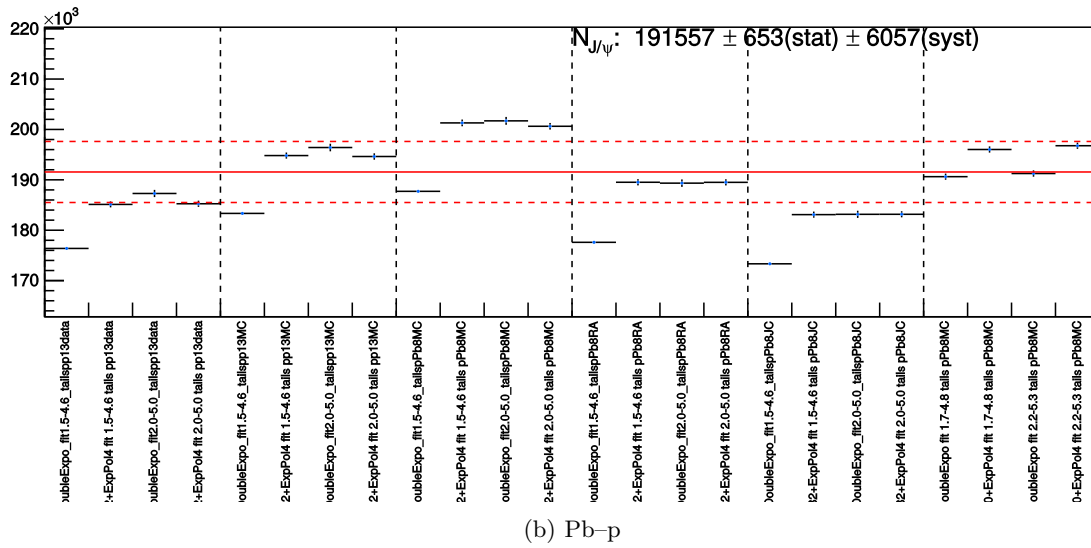
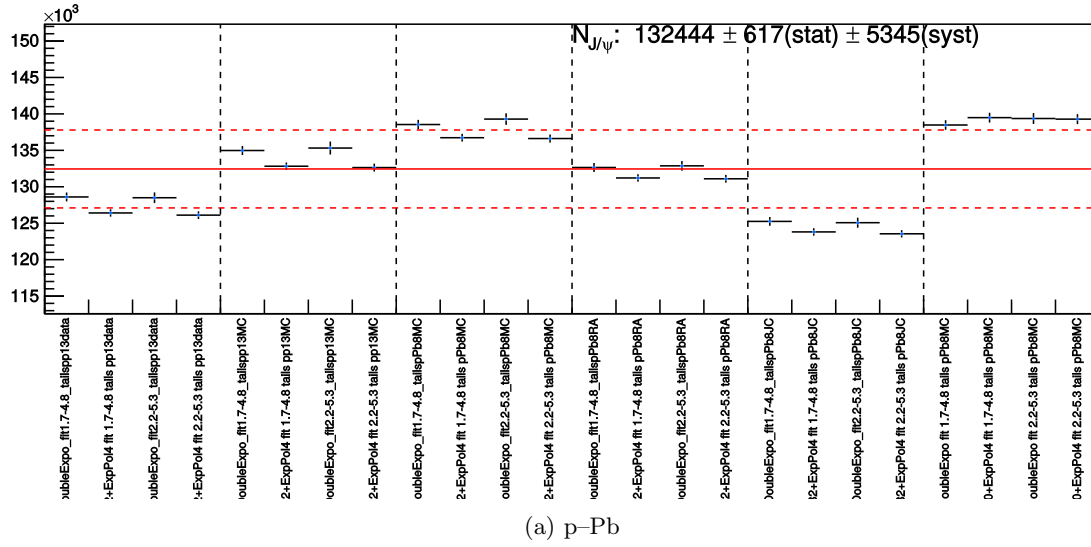


Figure 7.28: Signal extraction test set for integrated spectra. Dashed vertical lines show separate group of tests using a single set of tails.

### 7.4.1.2 Fits in bins of multiplicity

In the case of the multiplicity integrated fit, the  $J/\psi$  mass and width were left free. To ensure convergence of the fits in the individual multiplicity bins, we fixed the mass and the width of the  $J/\psi$  peak to the values extracted from the multiplicity integrated fit. We have previously verified that the fits in multiplicity bins gave constant mean and width if those were left free. Examples are shown in Fig. 7.29. The plots show the mean and the width for the two periods extracted by fitting the dimuon spectrum with CB2+DoubleExpo function. Both are constant in multiplicity. We have also checked that using another function (NA60) would give similar results.

The fact that the mean and width of the peak does not change in multiplicity means that the signal is constant in multiplicity and that the  $A\varepsilon$  and corresponding uncertainties cancel out in the relative yields.

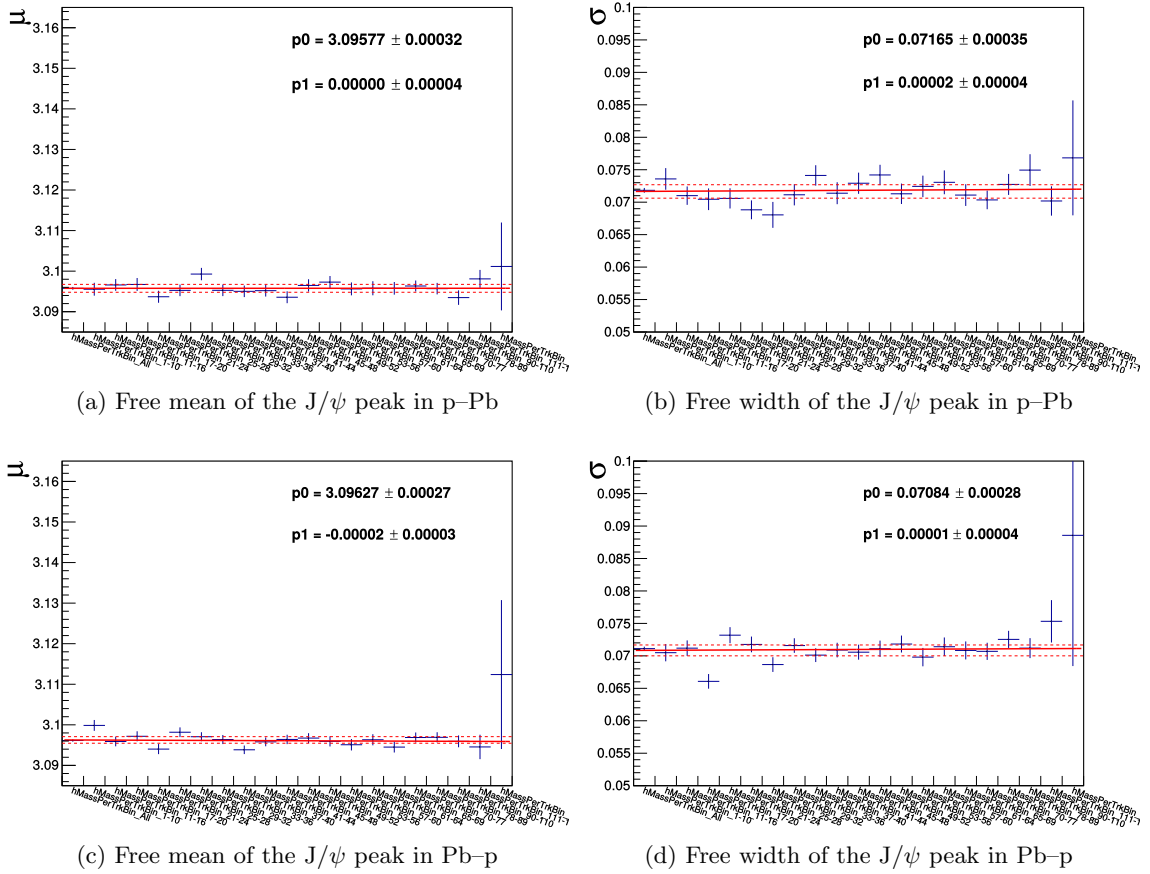


Figure 7.29: Values of free  $J/\psi$  mean and width in multiplicity bins.

The results of the extracted  $N_{J/\psi}$  are listed in Tab. 7.9. We verified the difference between the sum in bins and the integrated value. In both periods, the difference was smaller than the statistical uncertainty on the integrated case. Small difference was expected, its value depending on the correction used in SPD  $z$ -vertex equalisation. The reason of this was the exclusion of the lowest bin  $0 \leq N^{\text{corr}} < 1$  and possible fluctuations in fits. However, using maximal reference value to equalise the  $z$ -vertex we minimised the number of events with  $N^{\text{corr}} < 1$ .

### 7.4.1.3 Relative $J/\psi$ signal

The relative  $J/\psi$  signal in a bin  $i$  is defined as

$$N_{J/\psi}^R = \frac{N_{J/\psi}^i}{N_{J/\psi}^{\text{tot}}}. \quad (7.17)$$

p-Pb		Pb-p	
$N^{\text{corr}}$	$N_{J/\psi} \pm \text{stat} \pm \text{syst}$	$N^{\text{corr}}$	$N_{J/\psi} \pm \text{stat} \pm \text{syst}$
0-300	$132410 \pm 582 \pm 5204$	0-345	$192919 \pm 712 \pm 7205$
1-10	$4802 \pm 86 \pm 189$	1-11	$5706 \pm 92 \pm 211$
11-16	$5985 \pm 99 \pm 226$	12-18	$8064 \pm 113 \pm 297$
17-20	$5071 \pm 97 \pm 196$	19-23	$8181 \pm 116 \pm 299$
21-24	$5867 \pm 104 \pm 239$	24-27	$7793 \pm 114 \pm 286$
25-28	$6606 \pm 109 \pm 258$	28-32	$10867 \pm 139 \pm 403$
29-32	$7354 \pm 120 \pm 286$	33-36	$9905 \pm 133 \pm 369$
33-36	$7810 \pm 122 \pm 313$	37-41	$12962 \pm 156 \pm 485$
37-40	$7809 \pm 123 \pm 304$	42-46	$13913 \pm 162 \pm 517$
41-44	$7838 \pm 123 \pm 306$	47-50	$11104 \pm 146 \pm 415$
45-48	$7623 \pm 125 \pm 304$	51-55	$13590 \pm 167 \pm 507$
49-52	$7397 \pm 125 \pm 290$	56-59	$10188 \pm 146 \pm 381$
53-56	$6991 \pm 120 \pm 272$	60-64	$11864 \pm 159 \pm 443$
57-60	$6690 \pm 123 \pm 263$	65-69	$10756 \pm 154 \pm 410$
61-64	$5972 \pm 113 \pm 236$	70-73	$8052 \pm 133 \pm 301$
65-69	$6984 \pm 121 \pm 275$	74-79	$10524 \pm 155 \pm 394$
70-77	$9100 \pm 140 \pm 355$	80-88	$12590 \pm 173 \pm 471$
78-89	$9519 \pm 145 \pm 378$	89-102	$13349 \pm 180 \pm 513$
90-110	$8624 \pm 144 \pm 340$	103-126	$10022 \pm 161 \pm 376$
111-155	$4050 \pm 98 \pm 161$	127-178	$3259 \pm 98 \pm 122$
156-300	$236 \pm 22 \pm 11$	179-345	$107 \pm 18 \pm 5$
$\sum$ in bins	132328	$\sum$ in bins	192796
$\Delta$	82	$\Delta$	123

Table 7.9: Extracted number of  $J/\psi$  from p-Pb and Pb-p in the multiplicity integrated case and in individual multiplicity bins. We also show sum over all bins  $\sum$  and difference  $\Delta$  between  $\sum$  and integrated result.

To compute  $N_{J/\psi}^R$ , we started with all possible combinations of signal in each bin over integrated signal. We verified that the background signal is uncorrelated in multiplicity. The signal on the is constant in multiplicity and thus we correlate the signal part of the function between the numerator and the denominator.

This gave us 96 possible variations of  $N_{J/\psi}^R$ , 80 for the CB2 and 16 for the NA60 function. The mean over all possible combinations gave the central value, while the statistical uncertainty was given by the mean over all uncertainties. The systematic uncertainty was taken to be the standard deviation. The results for the two periods can be found in Tab. 7.10. An example of extraction of the relative  $N_{J/\psi}$  in bin is shown in Fig. 7.30.

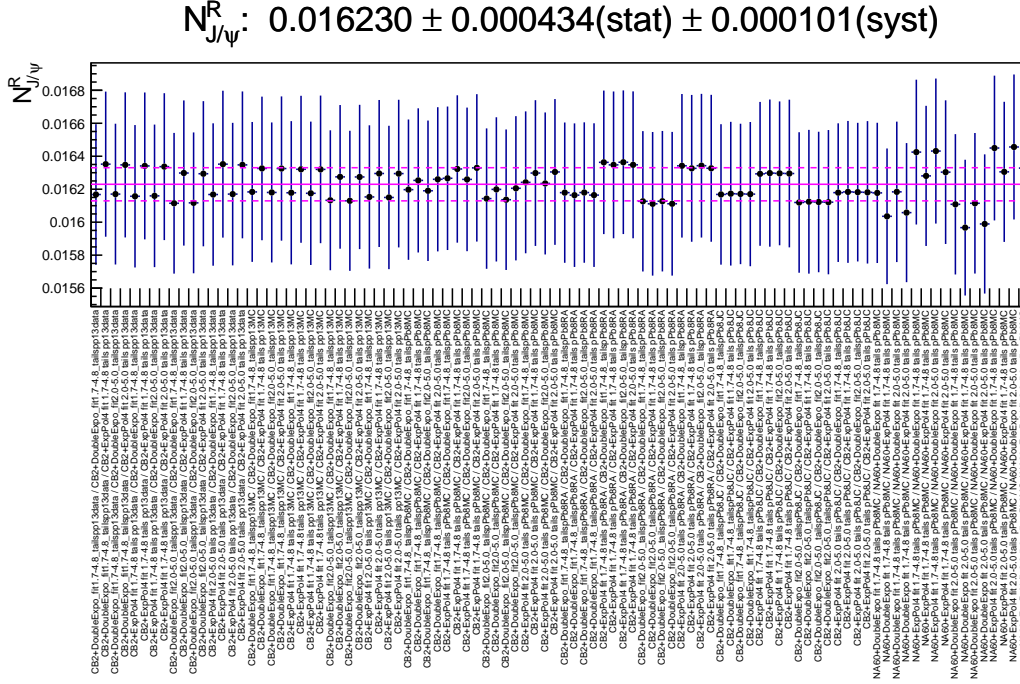


Figure 7.30: Relative  $N_{J/\psi}$  in the Pb–p period. The example show the one-but-last bin  $127 < N^{\text{corr}} < 179$ .

## 7.4.2 Event normalisation

The invariant  $J/\psi$  yields extracted from a dimuon triggered data sample needed to be normalised to a minimum bias sample. This normalisation was discussed in Sec. 6.4.1. here we will briefly repeat the most important formulæ. The number of equivalent MB events was defined in Eq. (6.8) as

$$N_{\text{MB}}^{\text{eq},i} = F_{\text{norm}}^i \times N_{\text{CMUL7}}^i.$$

### 7.4.2.1 Methods to compute $F_{\text{norm}}$

The methods to compute the  $F_{\text{norm}}$  were discussed in Sec. 6.4.1.1. From these methods, the online method could not be used in the multiplicity dependent analysis as the online scalers do not contain information on multiplicity in the event. Therefore we used the offline method only.

#### Offline method

The offline method consists of comparing the physics selected MB event sample to a subsample that also contains the 0MUL input. This can be done either directly (see Eq. (6.9)):

$$F_{\text{norm}}^{\text{off1},i} = \frac{N_{\text{MB}}^i}{N_{\text{MB}\&0\text{MUL}}^i},$$

p-Pb		Pb-p	
$N^{\text{corr}}$	$N_{J/\psi}^R \pm \text{stat} \pm \text{syst}$	$N^{\text{corr}}$	$N_{J/\psi}^R \pm \text{stat} \pm \text{syst}$
1-10	$(36.45 \pm 0.50 \pm 0.42) \cdot 10^{-3}$	1-11	$(30.09 \pm 0.37 \pm 0.18) \cdot 10^{-3}$
11-16	$(45.13 \pm 0.56 \pm 0.34) \cdot 10^{-3}$	12-18	$(42.34 \pm 0.43 \pm 0.20) \cdot 10^{-3}$
17-20	$(39.02 \pm 0.53 \pm 0.41) \cdot 10^{-3}$	19-23	$(43.09 \pm 0.44 \pm 0.20) \cdot 10^{-3}$
21-24	$(44.98 \pm 0.59 \pm 0.49) \cdot 10^{-3}$	24-27	$(40.74 \pm 0.45 \pm 0.21) \cdot 10^{-3}$
25-28	$(50.67 \pm 0.61 \pm 0.42) \cdot 10^{-3}$	28-32	$(57.07 \pm 0.52 \pm 0.27) \cdot 10^{-3}$
29-32	$(55.61 \pm 0.64 \pm 0.43) \cdot 10^{-3}$	33-36	$(50.69 \pm 0.51 \pm 0.39) \cdot 10^{-3}$
33-36	$(58.16 \pm 0.65 \pm 0.53) \cdot 10^{-3}$	37-41	$(67.97 \pm 0.56 \pm 0.37) \cdot 10^{-3}$
37-40	$(60.70 \pm 0.70 \pm 0.58) \cdot 10^{-3}$	42-46	$(72.54 \pm 0.58 \pm 0.38) \cdot 10^{-3}$
41-44	$(58.97 \pm 0.70 \pm 0.48) \cdot 10^{-3}$	47-50	$(57.15 \pm 0.55 \pm 0.40) \cdot 10^{-3}$
45-48	$(57.16 \pm 0.69 \pm 0.56) \cdot 10^{-3}$	51-55	$(69.54 \pm 0.60 \pm 0.86) \cdot 10^{-3}$
49-52	$(56.95 \pm 0.68 \pm 0.57) \cdot 10^{-3}$	56-59	$(52.91 \pm 0.57 \pm 0.26) \cdot 10^{-3}$
53-56	$(52.30 \pm 0.67 \pm 0.40) \cdot 10^{-3}$	60-64	$(61.66 \pm 0.59 \pm 0.30) \cdot 10^{-3}$
57-60	$(48.63 \pm 0.67 \pm 0.53) \cdot 10^{-3}$	65-69	$(56.71 \pm 0.61 \pm 0.39) \cdot 10^{-3}$
61-64	$(45.94 \pm 0.66 \pm 0.45) \cdot 10^{-3}$	70-73	$(40.98 \pm 0.54 \pm 0.21) \cdot 10^{-3}$
65-69	$(52.14 \pm 0.71 \pm 0.45) \cdot 10^{-3}$	74-79	$(54.86 \pm 0.61 \pm 0.71) \cdot 10^{-3}$
70-77	$(68.19 \pm 0.75 \pm 0.65) \cdot 10^{-3}$	80-88	$(64.75 \pm 0.67 \pm 0.34) \cdot 10^{-3}$
78-89	$(71.88 \pm 0.78 \pm 0.80) \cdot 10^{-3}$	89-102	$(67.86 \pm 0.68 \pm 0.35) \cdot 10^{-3}$
90-110	$(65.29 \pm 0.79 \pm 0.61) \cdot 10^{-3}$	103-126	$(51.21 \pm 0.64 \pm 0.30) \cdot 10^{-3}$
111-155	$(29.31 \pm 0.60 \pm 0.23) \cdot 10^{-3}$	127-178	$(16.23 \pm 0.43 \pm 0.10) \cdot 10^{-3}$
156-300	$(1.75 \pm 0.16 \pm 0.04) \cdot 10^{-3}$	179-345	$(0.54 \pm 0.09 \pm 0.01) \cdot 10^{-3}$

Table 7.10: Relative  $N_{J/\psi}$  per bin in p-Pb and Pb-p.

or via an intermediate trigger class such as CMSL as defined in Eq. (6.10)

$$F_{\text{norm}}^{\text{off2},i} = \frac{N_{\text{MB}}^i}{N_{\text{MB}\&0\text{MSL}}^i} \times \frac{N_{\text{CMSL7}}^i}{N_{\text{CMSL7}\&0\text{MUL}}^i}.$$

The trigger class used for this purpose is CINT7-B-NOPF-CENT. The one-step method suffers from the MB&0MUL count being too low, hence it is only used for verification.

Results of the two-step method for the multiplicity integrated case can be found in Fig. 7.31 and 7.32.

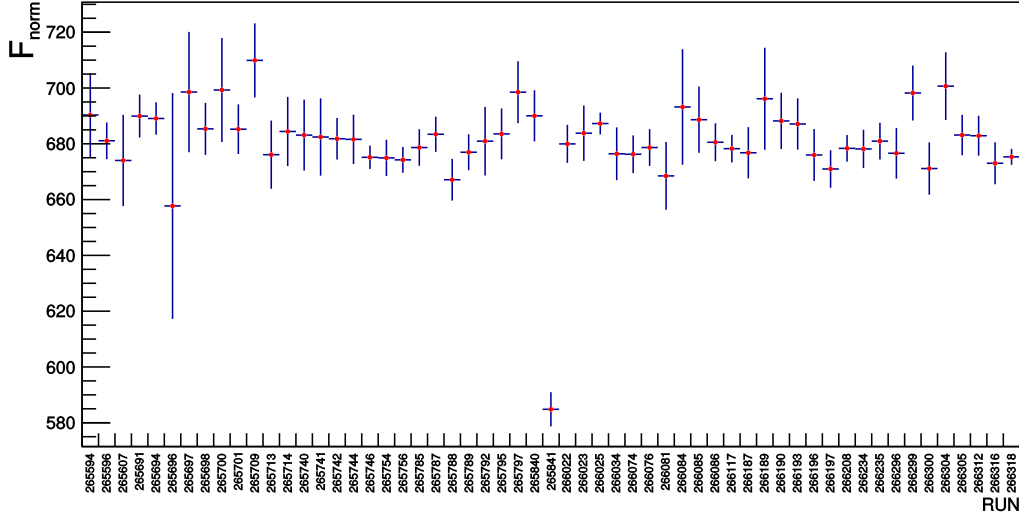


Figure 7.31: Dimuon trigger normalisation factor in p-Pb as a function of run, computed via the two-step offline method.

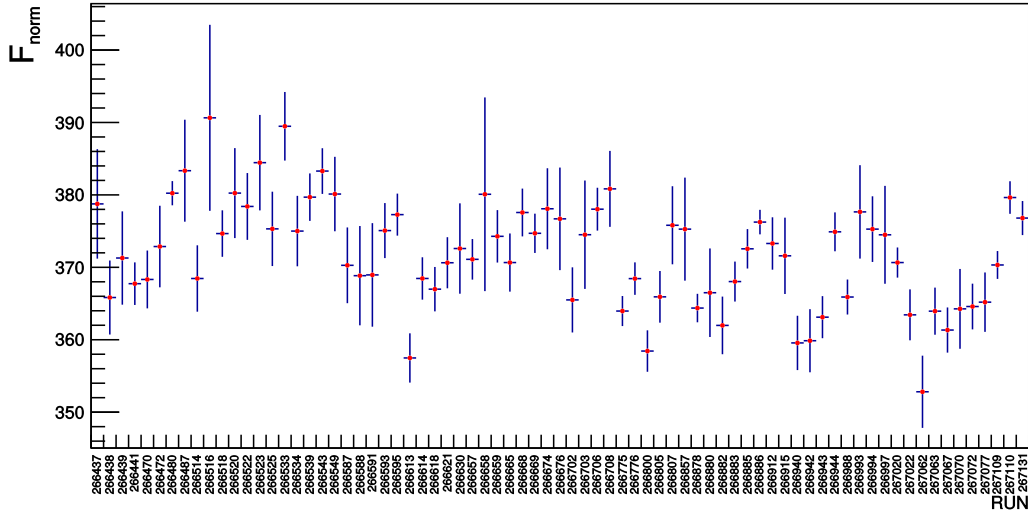


Figure 7.32: Dimuon trigger normalisation factor in Pb-p as a function of run, computed via the two-step offline method.

### Rescaling method

The two-step offline method was introduced to decrease the statistical uncertainty. However, it suffers from low statistics of the trigger classes in bins of multiplicity. To bypass this issue, an alternative

method to compute  $F_{\text{norm}}$  in multiplicity bins was proposed [221].

The multiplicity integrated  $F_{\text{norm}}^{\text{off2,tot}}$  (computed from Eq. (6.10)) is rescaled by a ratio of  $N_{\text{MB}}/N_{\text{CMUL7}}$  in each multiplicity bin divided by the same ratio multiplicity integrated. The rescaled normalisation factor  $F_{\text{norm}}^{\text{resc},j}$  in multiplicity bin  $j$  is computed as

$$F_{\text{norm}}^{\text{resc},j} = F_{\text{norm}}^{\text{off2,tot}} \times \frac{N_{\text{MB}}^j/N_{\text{CMUL7}}^j}{N_{\text{MB}}/N_{\text{CMUL7}}}. \quad (7.18)$$

The advantage of the rescaled method is that it has smaller uncertainties. This is because the method avoids using &0MUL and &MSL inputs, which may have very low statistics especially at high multiplicity. However, it assumes that the  $F_{\text{norm}}$  evolves with multiplicity in the same way as  $N_{\text{MB}}/N_{\text{CMUL7}}$ , which needed to be verified. In its original proposed form, the method also neglected any possible run-by-run fluctuations. We tested the proposed method, however instead of computing  $F_{\text{norm}}^{\text{resc},j}$  integrated over the full statistics we did the computation run-by-run, i. e. in each run  $i$  we computed

$$F_{\text{norm}}^{\text{resc},j,i} = F_{\text{norm}}^{\text{off2,tot}} \times \frac{N_{\text{MB}}^{j,i}/N_{\text{CMUL7}}^{j,i}}{N_{\text{MB}}^i/N_{\text{CMUL7}}^i}.$$

From there we computed the weighted average, using  $N_{\text{CMUL7}}^i$  in each run as weights.

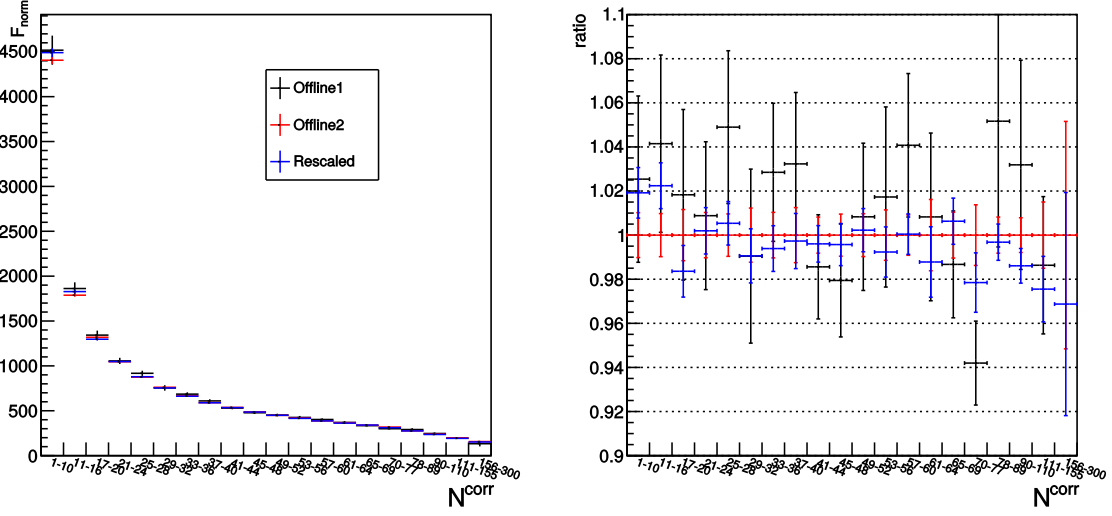
#### 7.4.2.2 Normalisation factor $F_{\text{norm}}$

We used three different approaches to compute the  $F_{\text{norm}}$ : the two-step offline method ( $F_{\text{norm}}^{\text{off2}}$ ), the one-step offline method ( $F_{\text{norm}}^{\text{off1}}$ ) to test the former, and the rescaling method ( $F_{\text{norm}}^{\text{resc}}$ ). Tab 7.11 compares the central values and the statistical uncertainties from the three methods in the p-Pb and Pb-p period. Visual comparison can be found in Fig. 7.33. The right panel shows the ratio of either method to the  $F_{\text{norm}}^{\text{off2}}$  as it is more robust than the other two, the uncertainties in this case are only computed from the uncertainty of the histogram in the numerator. One can see that the one-step method has larger uncertainties than the other two due to limited statistics. In p-Pb period, the one-step points mostly agree with the two-step method, while the  $F_{\text{norm}}^{\text{resc}}$  method gives systematically different result from  $F_{\text{norm}}^{\text{off2}}$  - higher at low and lower at high multiplicity, though compatible within the large uncertainties. In the Pb-p period, the one-step method gives systematic higher values of  $F_{\text{norm}}$  than the other two, while the  $F_{\text{norm}}^{\text{resc}}$  mostly agrees with the two-step method. All the points are within 2.5% from unity, which we will take as the systematic uncertainty (for both periods).

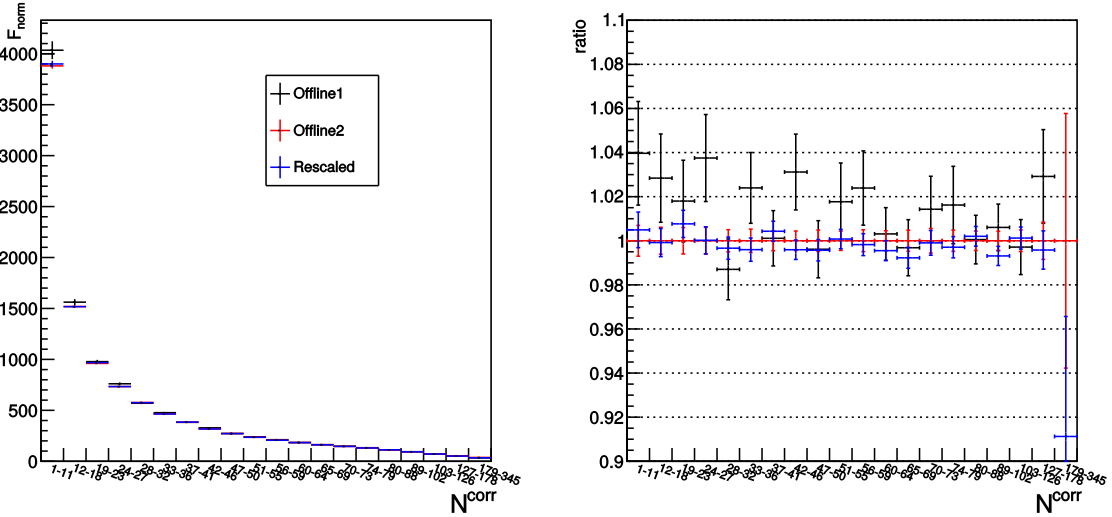
For the time being, we will consider  $F_{\text{norm}}^{\text{off2}}$  as central value. Part of the difference in the rescaled method may come from the fact that the multiplicity dependence is studied in MB triggered events instead of with MUL triggered events, while their multiplicity dependence differs.

p-Pb			Pb-p				
$N^{\text{corr}}$	$F_{\text{norm}}^{\text{offl}}$	$F_{\text{norm}}^{\text{off2}}$	$F_{\text{norm}}^{\text{resc}}$	$N^{\text{corr}}$	$F_{\text{norm}}^{\text{offl}}$	$F_{\text{norm}}^{\text{off2}}$	$F_{\text{norm}}^{\text{resc}}$
integrated	$681.22 \pm 6.21$	$679.10 \pm 1.53$	$679.10 \pm 1.53$	integrated	$371.59 \pm 1.14$	$371.06 \pm 0.42$	$371.06 \pm 0.42$
1 – 10	$4517.98 \pm 162.08$	$4406.09 \pm 44.91$	$4490.62 \pm 50.52$	1 – 11	$4034.81 \pm 87.78$	$3880.85 \pm 27.12$	$3900.00 \pm 31.35$
11 – 16	$1861.97 \pm 69.07$	$1787.81 \pm 17.47$	$1827.86 \pm 18.58$	12 – 18	$1561.94 \pm 29.58$	$1518.80 \pm 9.30$	$1517.56 \pm 9.69$
17 – 20	$1342.88 \pm 50.10$	$1318.74 \pm 15.30$	$1297.12 \pm 15.44$	19 – 23	$977.98 \pm 17.47$	$960.69 \pm 5.77$	$968.05 \pm 5.92$
21 – 24	$1055.42 \pm 34.77$	$1046.19 \pm 10.73$	$1048.24 \pm 11.00$	24 – 27	$760.59 \pm 13.95$	$733.08 \pm 4.45$	$733.23 \pm 4.49$
25 – 28	$917.43 \pm 28.92$	$874.59 \pm 8.42$	$879.28 \pm 8.62$	28 – 32	$569.51 \pm 8.07$	$576.99 \pm 2.91$	$575.05 \pm 2.91$
29 – 32	$754.35 \pm 30.34$	$761.60 \pm 9.35$	$754.43 \pm 9.34$	33 – 36	$476.85 \pm 7.30$	$465.69 \pm 2.46$	$463.81 \pm 2.46$
33 – 36	$685.28 \pm 20.29$	$666.30 \pm 6.88$	$662.24 \pm 6.91$	37 – 41	$382.71 \pm 4.79$	$382.28 \pm 1.73$	$383.93 \pm 1.74$
37 – 40	$609.72 \pm 18.54$	$590.65 \pm 7.38$	$589.06 \pm 7.39$	42 – 46	$328.04 \pm 5.31$	$318.13 \pm 1.41$	$316.83 \pm 1.41$
41 – 44	$529.48 \pm 12.88$	$537.21 \pm 4.40$	$535.08 \pm 4.45$	47 – 50	$271.91 \pm 3.55$	$272.96 \pm 1.33$	$271.79 \pm 1.32$
45 – 48	$477.77 \pm 12.76$	$487.80 \pm 4.66$	$485.71 \pm 4.66$	51 – 55	$239.48 \pm 4.06$	$235.31 \pm 1.03$	$235.50 \pm 1.03$
49 – 52	$452.25 \pm 14.86$	$448.53 \pm 4.36$	$449.53 \pm 4.39$	56 – 59	$211.78 \pm 3.40$	$206.83 \pm 1.03$	$206.47 \pm 1.03$
53 – 56	$425.57 \pm 16.80$	$418.34 \pm 4.78$	$415.14 \pm 4.76$	60 – 64	$184.31 \pm 2.18$	$183.74 \pm 0.84$	$182.91 \pm 0.83$
57 – 60	$402.73 \pm 12.11$	$386.96 \pm 3.54$	$387.14 \pm 3.55$	65 – 69	$162.54 \pm 2.08$	$163.06 \pm 0.78$	$161.80 \pm 0.77$
61 – 64	$369.87 \pm 13.84$	$366.84 \pm 5.93$	$362.37 \pm 5.86$	70 – 73	$147.82 \pm 2.15$	$145.74 \pm 0.82$	$145.60 \pm 0.82$
65 – 69	$334.10 \pm 8.31$	$338.60 \pm 3.52$	$340.73 \pm 3.55$	74 – 79	$133.04 \pm 2.26$	$130.92 \pm 0.63$	$130.53 \pm 0.63$
70 – 77	$299.77 \pm 6.44$	$318.24 \pm 4.38$	$311.39 \pm 4.28$	80 – 88	$112.39 \pm 1.24$	$112.33 \pm 0.50$	$112.56 \pm 0.50$
78 – 89	$290.76 \pm 15.01$	$276.47 \pm 2.26$	$275.59 \pm 2.27$	89 – 102	$93.84 \pm 0.98$	$93.27 \pm 0.40$	$92.63 \pm 0.41$
90 – 110	$246.67 \pm 10.99$	$239.05 \pm 1.88$	$235.72 \pm 1.88$	103 – 126	$71.10 \pm 0.89$	$71.31 \pm 0.35$	$71.39 \pm 0.36$
111 – 155	$194.55 \pm 6.23$	$197.25 \pm 2.96$	$192.42 \pm 2.93$	127 – 178	$52.55 \pm 1.05$	$51.06 \pm 0.43$	$50.84 \pm 0.44$
156 – 300	$132.89 \pm 30.29$	$156.83 \pm 8.09$	$151.92 \pm 7.93$	179 – 345	$33.19 \pm 7.74$	$37.57 \pm 2.17$	$34.23 \pm 2.04$

Table 7.11: Normalisation factor computed via the two-step offline method ( $F_{\text{norm}}^{\text{off2}}$ ), the one step offline method ( $F_{\text{norm}}^{\text{offl}}$ ) and the rescaling one ( $F_{\text{norm}}^{\text{resc}}$ ) per multiplicity bin for p-Pb and Pb-p data.



(a) Comparison of  $F_{\text{norm}}$  computed with one-step offline method, two-step offline method, and rescaling method in p-Pb. Right-hand-side plot shows ratio with respect to  $F_{\text{norm}}^{\text{off2}}$ . The errors represent errors of the  $F_{\text{norm}}$  in numerator normalised to the value of denominator.



(b) Comparison of  $F_{\text{norm}}$  computed with one-step offline method, two-step offline method, and rescaling method in Pb-p. Right-hand-side plot shows ratio with respect to  $F_{\text{norm}}^{\text{off2}}$ . The errors represent errors of the  $F_{\text{norm}}$  in numerator normalised to the value of denominator.

Figure 7.33: Comparison of  $F_{\text{norm}}$  in multiplicity intervals computed with three different methods.

### 7.4.3 Event selection efficiency

The event selection presented in Sec. 7.2 rejects events without a reconstructed vertex in the SPD or whose vertex does not pass the quality cuts. Moreover, the multiplicity measured in this analysis corresponds to a selected sub-sample. We perform the measurement in the class of non-single diffractive events (NSD). The computed multiplicity thus needs to be corrected by the efficiency of the MB selection of NSD events with reconstructed SPD vertex passing the vertex QA criteria.

#### 7.4.3.1 Multiplicity integrated event selection efficiency

The efficiency computation was performed in an independent analysis [238]. The efficiency was computed for one run in each period from two MC samples, one generated with HIJING and the other

with DPMJET. The estimation was performed from the ESD data<sup>6</sup>.

The vent selection efficiency for the NSD events with good reconstructed vertex [238] is

$$\varepsilon^{MB} = 97.4 \pm 1\%. \quad (7.19)$$

#### 7.4.3.2 Event selection efficiency compared between ESD and AOD

To compute the event selection efficiency in multiplicity bins, we adopted the same approach as was used in [238]. We considered event type selection (NSD) and vertex quality selection ( $N_{contributors}$  and resolution). As the integrated efficiency was estimated from the ESD data and we used AOD<sup>7</sup>, we could not use exactly the same selection criteria. To understand the effect this difference can have on the result, we first recomputed the integrated efficiency in p-Pb from the ESD for just the one run, using which the same data and DPMJET MC production as in []. Then we computed the efficiency for the same run but from AODs and from our DPMJET MC sample.

First we shall define the fraction of events without a selected vertex in the generated NSD sample

$$f_{noVtx}^{NSD} = \frac{N_{NSD}^{MC} - N_{sv}^{MC}}{N_{MB}^{MC}}, \quad (7.20)$$

where  $N_{NSD}^{MC}$  is the number of generated NSD events,  $N_{MB}^{MC}$  is the number of reconstructed events in MC passing the MB trigger, and  $N_{sv}^{MC}$  is the number of reconstructed MC events with selected vertex. The fraction of reconstructed events in MC without selected vertex is defined as

$$f_{noVtx}^{MB-MC} = \frac{N_{MB}^{MC} - N_{sv}^{MC}}{N_{MB}^{MC}}. \quad (7.21)$$

The MC efficiency for events without a vertex is

$$\rho_{MC} = \frac{f_{noVtx}^{MB-MC}}{f_{noVtx}^{NSD}}. \quad (7.22)$$

In AOD sample for run 266318:  $f_{noVtx}^{NSD} = 0.0125$ ,  $f_{noVtx}^{MB-MC} = 0.0042$ , hence  $\rho_{MC} = 33.88\%$ .

The number of reconstructed events in data without selected vertex is defined as

$$f_{noVtx}^{data} = \frac{N_{MB}^{data} - N_{sv}^{data}}{N_{MB}^{data}}, \quad (7.23)$$

where  $N_{MB}^{data}$  is the number of reconstructed MB events and  $N_{sv}^{data}$  is the number of reconstructed MB events with selected vertex. In AOD sample for run 266318:  $f_{noVtx}^{data} = 0.0177$ .

The vertex finding NSD event selection efficiency in [238] was defined as:

$$\varepsilon^{MB} = 1 + f_{noVtx}^{NSD} - f_{noVtx}^{data} / \rho_{MC}. \quad (7.24)$$

We use the same formula in our analysis in order to be able to use the values of  $\langle dN_{ch}/d\eta \rangle$  from the charged particle multiplicity analysis, which are more precise. The  $\varepsilon^{MB}$  estimated from DPMJET ESD files was [238]

$$\varepsilon_{ESD} = 0.9780.$$

The  $\varepsilon^{MB}$  estimated from our DPMJET AODs was

$$\varepsilon_{AOD} = 0.9779.$$

The two values were found to be consistent and hence we could safely use Eq. (7.24) on our AOD sample.

<sup>6</sup>ESD stands for Event Summary Data.

<sup>7</sup>AOD stands for Analysis Object Data and it is a more compact data format compared to the ESD.

### 7.4.3.3 Event selection efficiency in bins of multiplicity

We computed the event selection efficiency for each multiplicity bin from Eq. (7.24), using the full AOD dataset for each period. As first step, we computed the efficiency in each bin for each run. The final multiplicity dependent efficiency was taken as the weighted average over the whole period. We considered the CINT7-B-NOPF-MUFAST trigger class and the corresponding  $N_{\text{CINT7}}$  in each run as weights. This trigger class was used to compute the charged particle multiplicity. The uncertainty was taken from the weighted standard deviation.

For the multiplicity integrated case, we obtained

$$\text{p-Pb:} \quad \varepsilon^{MB} = 96.89 \pm 0.74 \%, \quad (7.25)$$

$$\text{Pb-p:} \quad \varepsilon^{MB} = 96.90 \pm 0.51 \%. \quad (7.26)$$

The results are consistent with (7.19). The multiplicity dependent efficiency for p-Pb is shown in Fig. 7.34 and for Pb-p in Fig. 7.35. In either period, the efficiency is  $< 1$  for the first two multiplicity intervals. This is due to the fact that at the lowest multiplicity, the vertex reconstruction algorithm has difficulties finding tracklets candidates to reconstruct the vertex. As the uncertainty is fully correlated in multiplicity, we will consider the 1% uncertainty on the  $\varepsilon^{MB}$  computed in [238].

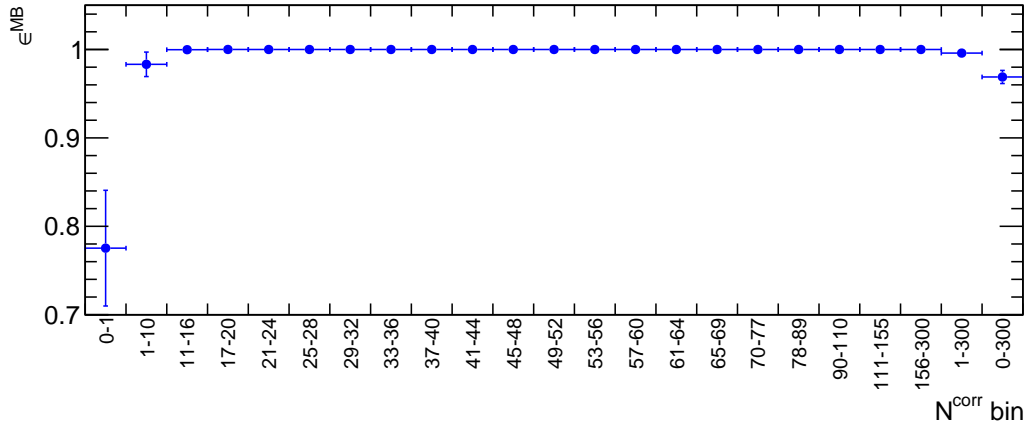


Figure 7.34: Multiplicity dependent vertex finding NSD event selection efficiency in p-Pb.

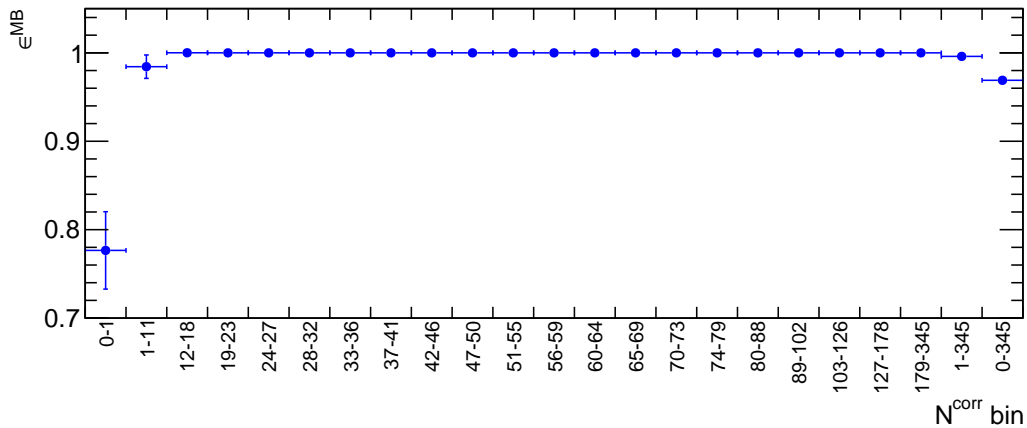


Figure 7.35: Multiplicity dependent vertex finding NSD event selection efficiency in Pb-p.

#### 7.4.4 Impact of the choice of the $\langle N_{\text{tr}} \rangle (v_z)$ equalisation reference value and the randomisation method

We re-analysed the data using the minimal correction with binomial smearing to study possible bias stemming for the data driven correction method. Using the minimum as a reference causes the  $N^{\text{corr}}$  distribution to narrow down compared to the  $N^{\text{raw}}$  distribution, see Fig. 7.9. As a result, the  $N_{\text{ch}} - N^{\text{corr}}$  correlation changes correspondingly. To achieve the best possible comparison, we multiplied the  $N^{\text{corr}}$  bin edges by a ratio of the minimum and maximum of the  $\langle N^{\text{raw}} \rangle (v_z)$  profile in the corresponding period. This resulted in the closest possible  $dN_{\text{ch}}/d\eta / \langle dN_{\text{ch}}/d\eta \rangle$  in the two analyses as possible, easing the comparison of the results.

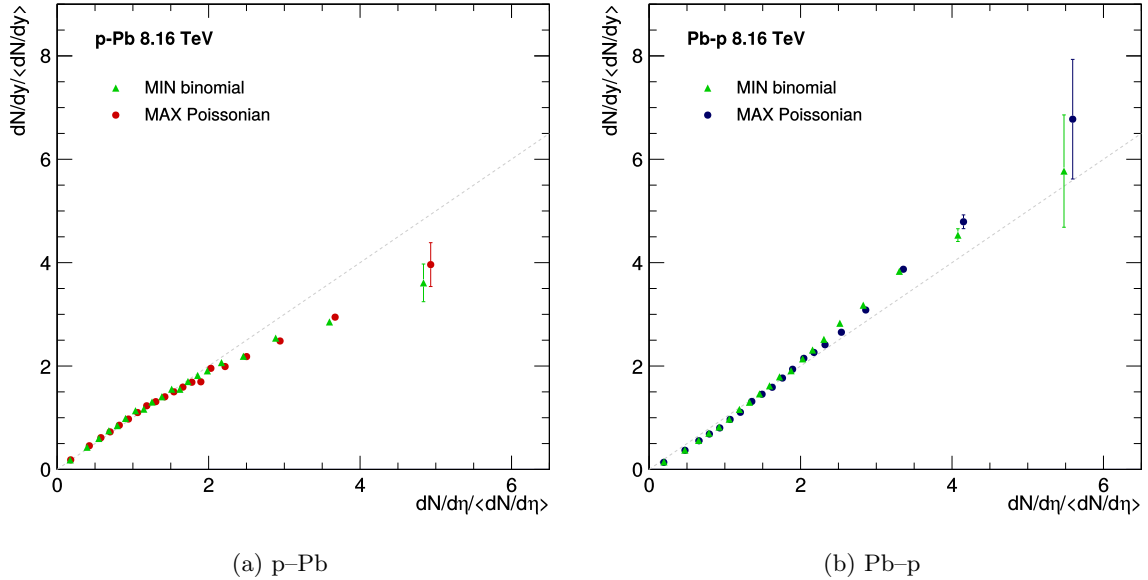


Figure 7.36: Comparison of the multiplicity dependent relative  $J/\psi$  yields obtained from Poissonian correction with respect of the  $\langle N^{\text{raw}} \rangle (v_z)$  maximum and binomial correction with respect to the  $\langle N^{\text{raw}} \rangle (v_z)$  minimum.

The comparison is shown in Fig. 7.36. The error bars show the statistical uncertainty of each point. The statistical uncertainties are partially correlated as the multiplicity bins are not the same in the two measurements.

Satisfying agreement is observed in both periods. The Pb-p results show a bit of tension at high multiplicity  $dN_{\text{ch}}/d\eta / \langle dN_{\text{ch}}/d\eta \rangle \gtrsim 4$ . At  $dN_{\text{ch}}/d\eta / \langle dN_{\text{ch}}/d\eta \rangle \sim 6$  the statistical uncertainty are very large and the data agree within the uncertainty. We considered these two scenario as extreme cases which serve to establish the corresponding systematic uncertainty, more in Sec. 7.4.5.3.

#### 7.4.5 Systematic uncertainty on the $J/\psi$ yields extraction

We consider the following sources of systematic uncertainty: signal extraction, normalisation, bin-flow and pile-up, and vertex equalisation. The global uncertainty on the NSD event efficiency correction is quoted separately. Tab. 7.12 shows contribution of different sources to the overall systematic uncertainty.

##### 7.4.5.1 Uncertainty in the signal extraction

This source of uncertainty was discussed in Sec. 7.4.1. The uncertainty on signal extraction was estimated by varying the combination of signal and background function in two mass fit ranges. The largest difference originated in the set of tails used in the fit and whether these tails were obtained from data or from MC. Therefore we made sure to include equal numbers of data tails and of MC tails.

The uncertainty on the multiplicity integrated yields amounts to 4% in p-Pb and 3.1% in Pb-p. The per-bin systematic uncertainties on absolute yields range between 3 – 4% and are quoted in Tab. 7.9. In case of the relative yields, we assumed that the yields are partially correlated in multiplicity

source	p-Pb		Pb-p	
	abs. yields	rel. yields	abs. yields	rel. yields
signal extraction	3.9 – 4.2% (4.0%)	0.8 – 2.3%	3.2 – 3.9% (3.1%)	0.5 – 1.9%
$F_{norm}$	2.5%		2.5%	
bin-flow	1%		1%	
pile-up	2%		2%	
vertex equalisation	—	0.1 – 2.6%	—	0.1 – 4.3%
event class normalisation [238]	1%*		1%*	

Table 7.12: Sources of systematic uncertainties. The values in parentheses correspond to the multiplicity integrated uncertainties related to the signal extraction. Values marked with asterisk are correlated in multiplicity.

(the signal is while the background is not). The per-bin uncertainty ranges between 0.8 – 2.3% in p-Pb and 0.5 – 1.9% in the Pb-p period.

#### 7.4.5.2 Uncertainty on the trigger class normalisation

The normalisation uncertainty was estimated from the combination of three  $F_{norm}$  calculation methods, see Sec 7.4.2. We studied the bin-by-bin spread of  $F_{norm}$  values computed from each of these methods. In both periods, all values are within 2.5% from central values, which we took as normalisation systematic.

#### 7.4.5.3 Uncertainty on the vertex equalisation

The multiplicity dependent relative yields were compared between the data corrected by the Poissonian vertex equalisation with respect to the maximum of the  $\langle N^{raw} \rangle (v_z)$  profile and the data corrected by the binomial vertex equalisation with respect to the minimum of the  $\langle N^{raw} \rangle (v_z)$  profile. The two extreme cases were visually compared in Sec. 7.4.4.

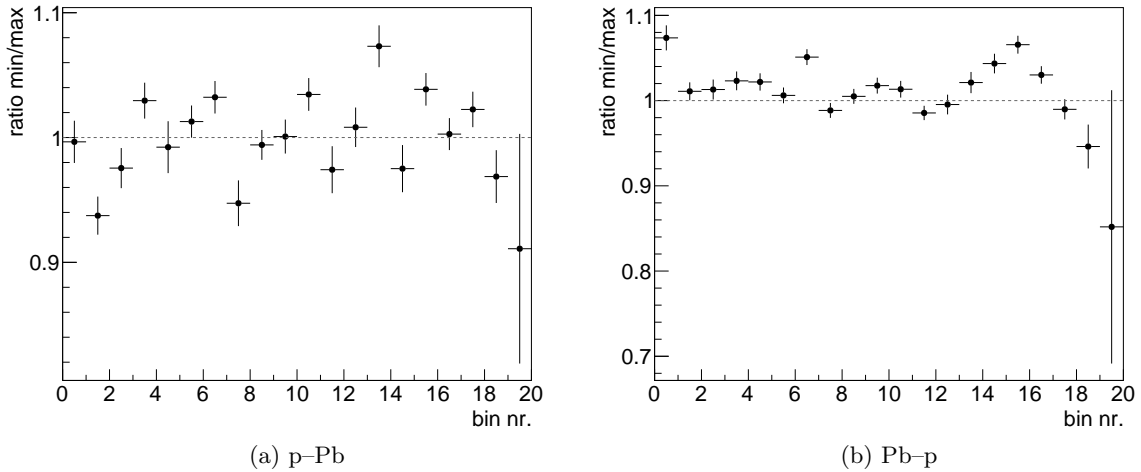


Figure 7.37: Ratio of relative  $J/\psi$  yields corrected with respect to the minimum and of the relative yields corrected with respect to the maximum of the  $\langle N^{raw} \rangle (v_z)$ .

Fig. 7.37 shows the ratio of the central values of the two distributions in p-Pb and in Pb-p. We will consider a conservative uncertainty, using the following assumptions:

- We neglect the difference in relative multiplicity, assuming that the two results are at the same  $dN_{ch}/d\eta / \langle dN_{ch}/d\eta \rangle$ . Such assumption increases the uncertainty.

- We consider the relative difference between the central values of the two distributions

$$\Delta_{J/\psi^R} = \frac{\left| (\langle dN/dy \rangle / \langle dN_{ch}/d\eta \rangle)^{\max} - (\langle dN/dy \rangle / \langle dN_{ch}/d\eta \rangle)^{\min} \right|}{(\langle dN/dy \rangle / \langle dN_{ch}/d\eta \rangle)^{\max}}$$

in each  $dN_{ch}/d\eta / \langle dN_{ch}/d\eta \rangle$  interval, neglecting the statistical uncertainty. The statistical uncertainty is partially correlated between the two distributions. Neglecting the statistical uncertainty maximises the uncertainty.

- We assume that the uncertainty is Gaussian.

The uncertainty on the equalisation computed from the difference of the central values

$$\sigma_{\text{equal.}} = \frac{\Delta_{J/\psi^R}}{\sqrt{12}}. \quad (7.27)$$

The results can be found in Tab. 7.13. We did not evaluate this uncertainty for the absolute  $J/\psi$  yields.

$\frac{dN_{ch}/d\eta}{\langle dN_{ch}/d\eta \rangle}$	p-Pb		Pb-p	
		syst. unc. (%)	$\frac{dN_{ch}/d\eta}{\langle dN_{ch}/d\eta \rangle}$	syst. unc. (%)
0.18		0.1	0.19	2.1
0.42		1.8	0.47	0.3
0.58		0.7	0.66	0.4
0.70		0.9	0.80	0.7
0.82		0.2	0.93	0.6
0.94		0.4	1.07	0.2
1.06		0.9	1.21	1.5
1.18		1.5	1.36	0.3
1.30		0.2	1.49	0.1
1.42		< 0.1	1.63	0.5
1.54		1.0	1.76	0.4
1.66		0.7	1.89	0.4
1.78		0.2	2.04	0.1
1.90		2.1	2.18	0.6
2.03		0.7	2.32	1.3
2.22		1.1	2.54	1.9
2.50		0.1	2.86	0.9
2.94		0.6	3.36	0.3
3.67		0.9	4.15	1.6
4.93		2.6	5.59	4.3

Table 7.13: Uncertainty on vertex equalisation.

#### 7.4.5.4 Uncertainty on the bin-flow and pile-up

The bin-flow and pile-up systematics on yields was obtained in a similar way as bin-flow uncertainty on the multiplicity determination, see Sec. 7.3.4.2.

In the case of bin-flow, we again took into account two possible effects - the bin-flow due to randomisation and the bin-edge effect. To do so, we compared the invariant yields  $N_{J/\psi}^i / N_{CMUL7}^i$  in each multiplicity bins for results of the same task but run with different randomisation seed and/or with a small shift on  $N^{\text{corr}}$  bins. We used the same bin shift as in the multiplicity part, i. e.  $\text{bin}_{\text{offset}} = \pm 0.1$ . We studied the maximal spread of the points within each multiplicity bin as well as the RMS, see

Fig. 7.38 and 7.39. The bottom plots show the ratio of output with different settings divided by the baseline results (i. e. no bin offset and with multiplicity dependent SPD pile-up cut). In the Pb-p period, the last multiplicity bin shows a large spread, this is however attributed to be due to signal extraction as the statistics is very limited in this bin. The bin-flow uncertainty was determined to be 1% in either period.

Pile-up systematic was also determined using similar method as in the multiplicity part. In this case we compared the invariant yields extracted from data obtained with three different SPD pile up configurations. The comparison of the yields can be found in Fig. 7.40 and Fig. 7.41. The bottom plots show the ratios of invariant yields from a given task output normalised by the baseline. The error bars represent error on the yields in numerator normalised by central value of the baseline. We studied the maximal spread of the points within each multiplicity bin as well as the RMS. For both periods, the pile-up uncertainty was determined to be 2%.

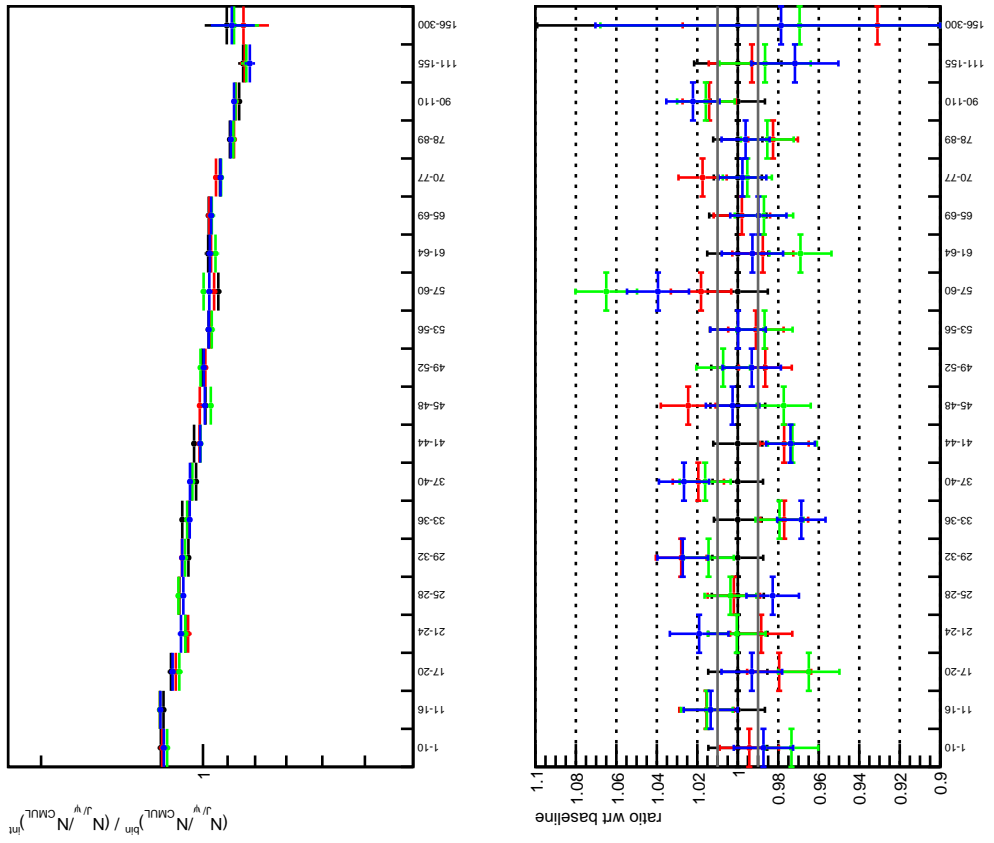


Figure 7.38: Bin-flow systematic uncertainty in p-Pb. The top left plot shows the invariant yields as a function of multiplicity for each of the task settings. Black points denote 'baseline', which is the standard settings used in the whole analysis, red is the same but with different randomisation seed, green and blue stand for yields obtained from running the task with -0.1 or +0.1 offset respectively. Top right is the same but for relative multiplicity dependent invariant yields. Bottom left and bottom right show ratio of the two with respect to the corresponding baseline.

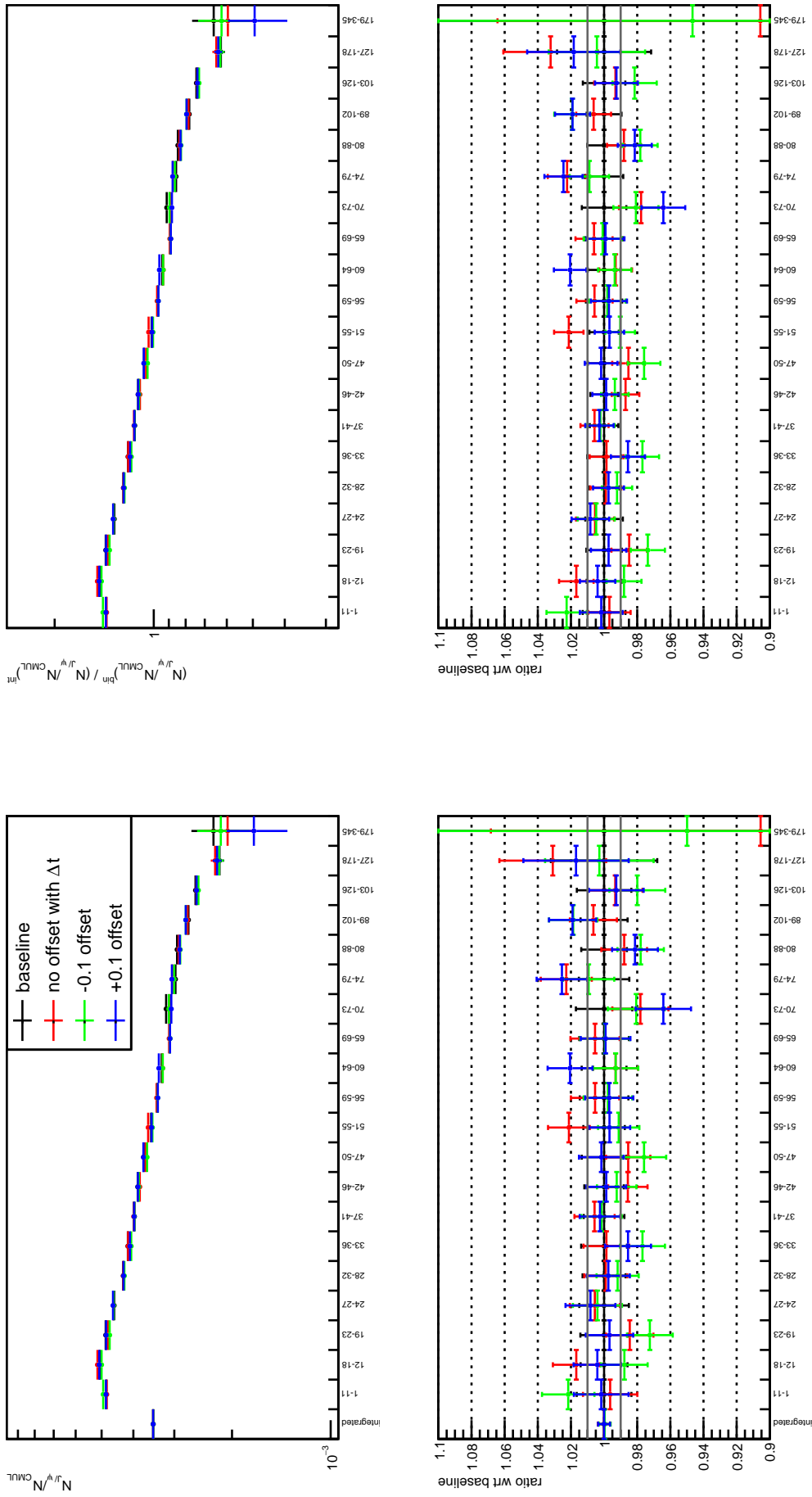


Figure 7.39: Bin-flow systematic uncertainty in Pb-p. The top left plot shows the invariant yields as a function of multiplicity for each of the task settings. Black points denote 'baseline', which is the standard settings used in the whole analysis, red is the same but with different randomisation seed, green and blue stand for yields obtained from running the task with -0.1 or +0.1 offset respectively. Top right is the same but for relative multiplicity dependent invariant yields. Bottom left and bottom right show ratio of the two with respect to the corresponding baseline.

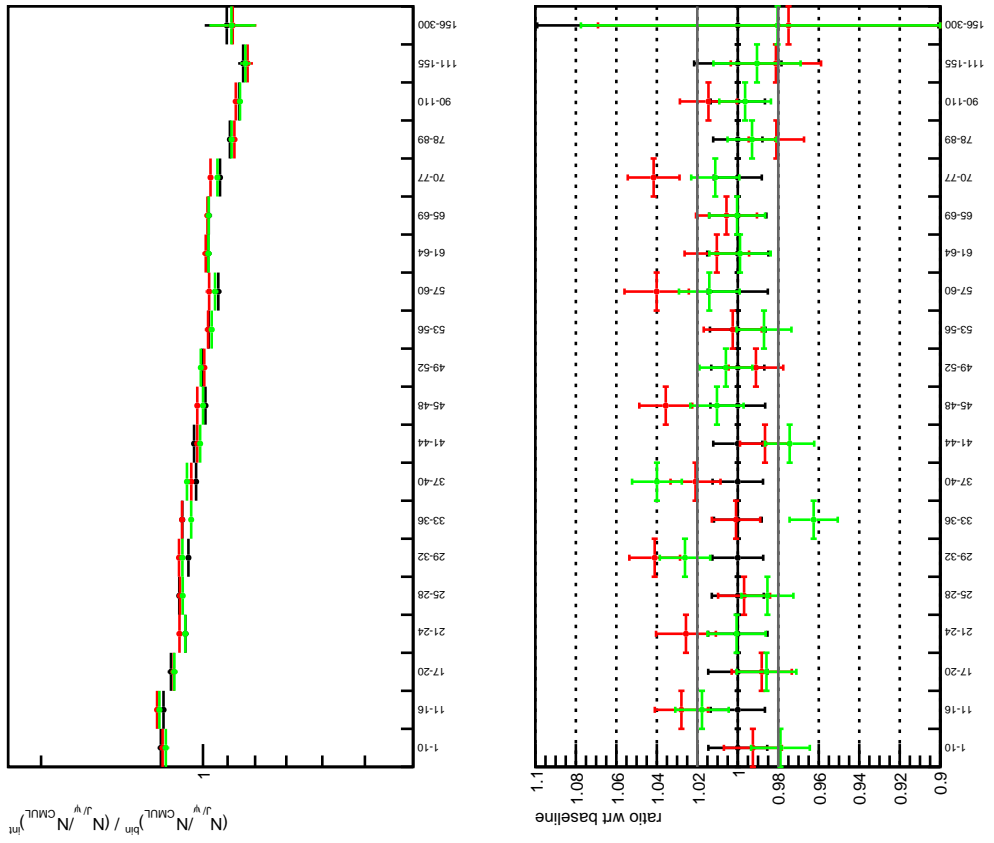


Figure 7.40: Pile-up systematic uncertainty in p-Pb. The top left plot shows the invariant yields as a function of multiplicity for each of the task settings. Black points denote 'baseline', which is the standard settings used in the whole analysis, red and green are extracted using SPD pile up cut with argument (3, 0.6) and (5, 0.8) respectively. Top right is the same but for relative multiplicity dependent invariant yields. Bottom left and bottom right show ratio of the two with respect to the corresponding baseline.

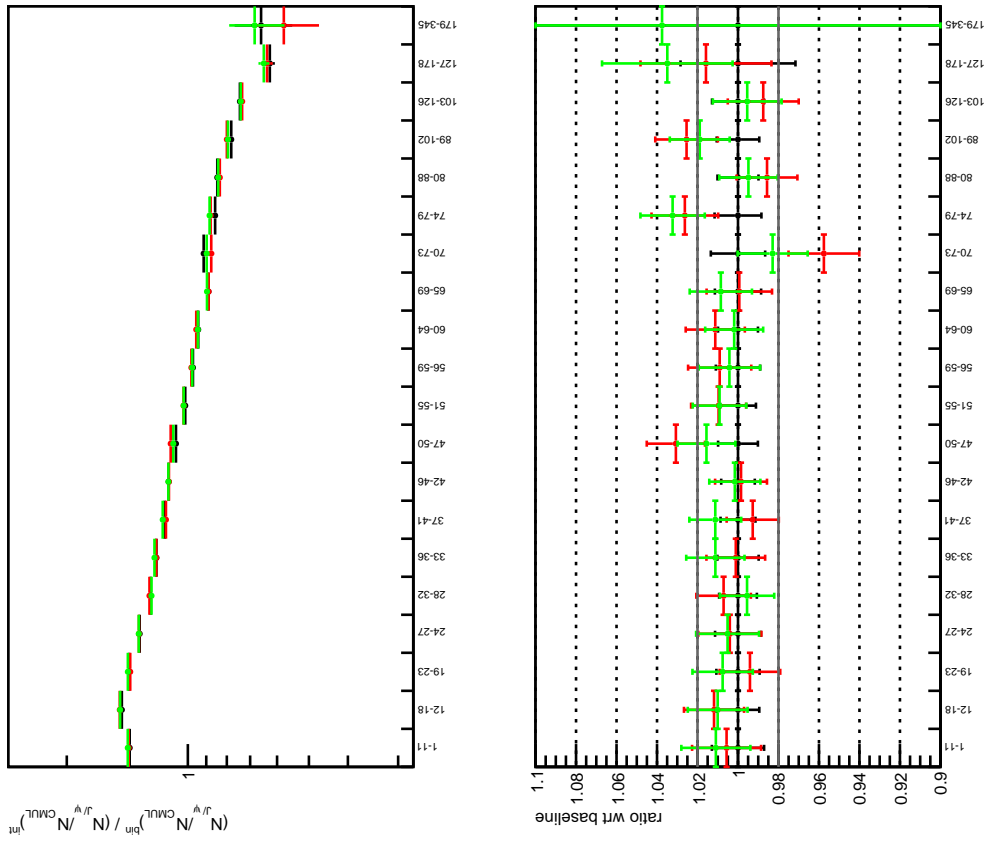
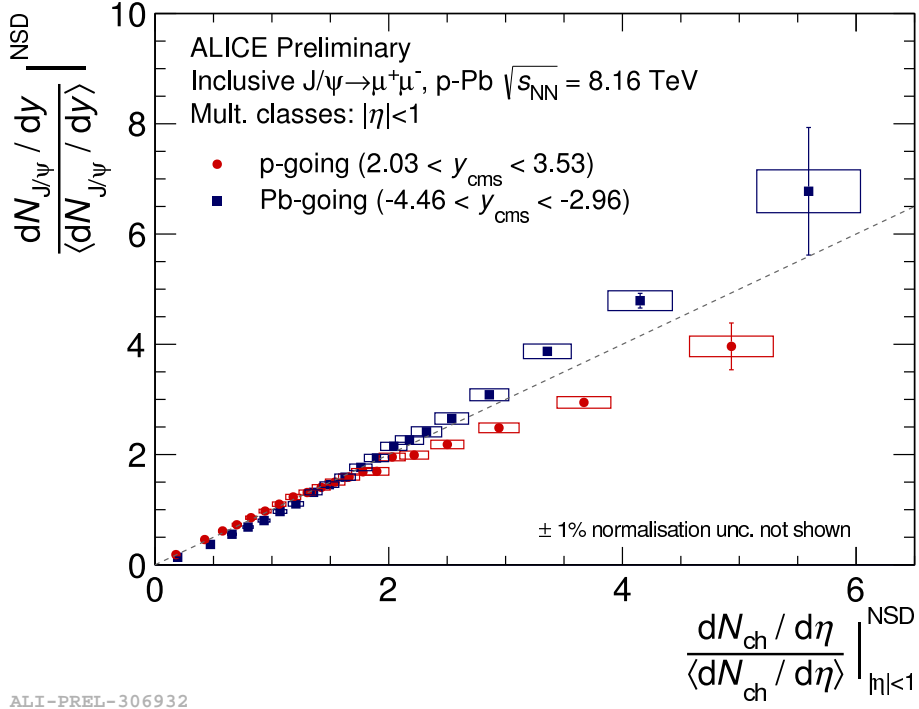


Figure 7.41: Pile-up systematic uncertainty in Pb-p. The top left plot shows the invariant yields as a function of multiplicity for each of the task settings. Black points denote 'baseline', which is the standard settings used in the whole analysis, red and green are extracted using SPD pile up cut with argument (3, 0.6) and (5, 0.8) respectively. Top right is the same but for relative multiplicity dependent invariant yields. Bottom left and bottom right show ratio of the two with respect to the corresponding baseline.

## 7.5 Multiplicity differential relative $J/\psi$ yields

Using the previously discussed ingredients, we computed the relative  $J/\psi$  yield as a function of the relative charged particle pseudorapidity density at forward rapidity  $2.03 < y_{\text{cms}} < 3.53$  and backward rapidity  $-4.46 < y_{\text{cms}} < -2.96$ . The results are shown in Fig. 7.42. The red data points represent the forward p-Pb yields. The blue data points represent the backward Pb-p yields. The dashed grey line is to draw the eye and represents the diagonal  $y = x$ . The values can be found in Tab. 7.14.



ALI-PREL-306932

Figure 7.42: Self-normalised  $J/\psi$  yields as a function of self-normalised charged particle multiplicity in p-Pb (p-going) and Pb-p (Pb-going) at  $\sqrt{s_{\text{NN}}} = 8.16$  TeV. The NSD and vertex normalisation uncertainty is quoted separately. The uncertainty on the multiplicity axis is partially correlated in multiplicity.

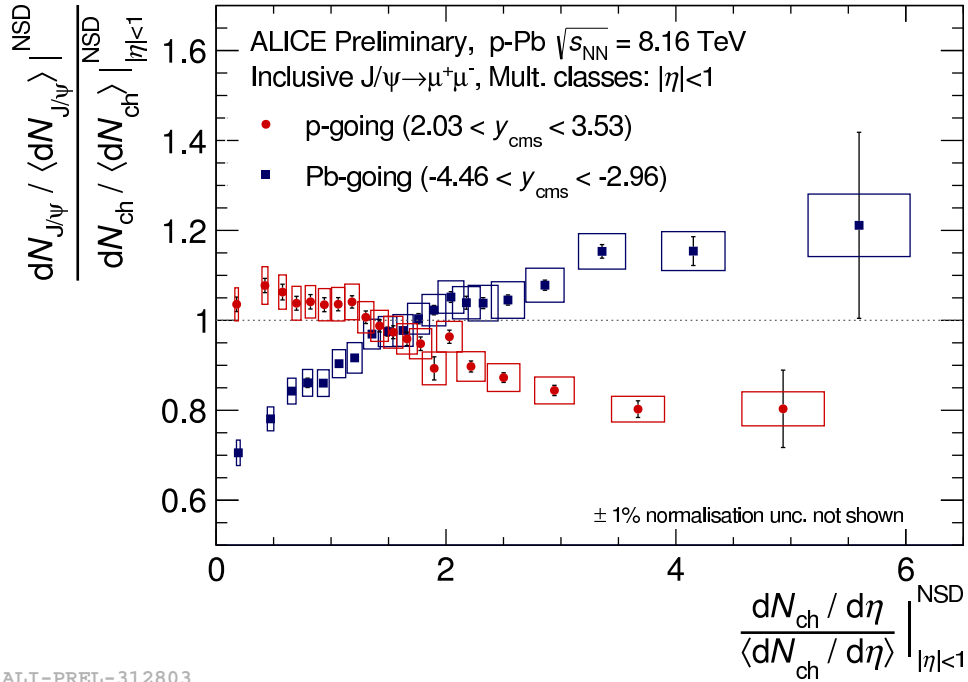
We observe a different behaviour of the relative yields at low and at high multiplicities. At low multiplicities, the relative yields demonstrate a linear increase with multiplicity regardless of the rapidity at which the  $J/\psi$  measurement was performed. At high multiplicity, we see two different trends. The forward yields show a slower-than-linear increase. The backward yields continue to rise linearly. Such behaviour is consistent with the expected CNM scenario (recall Sec. 2.4) - the  $J/\psi$  are suppressed due to the CNM effects at forward rapidity and the level of suppression increases with multiplicity. At backward rapidity, we see no difference between pp and p-Pb.

To better visualise the behaviour of the distributions, we divided the relative yields by the diagonal. The divided yields can be found in Fig. 7.43. The backward rapidity diagonal-divided yields are below the unity at low multiplicity. With increasing multiplicity, the relative yields increase and cross unity at  $\sim 1.5 \langle dN_{\text{ch}}/d\eta \rangle$ . The observed trend is consistent with linear increase with negative offset. The forward yields, on the other hand, decrease with multiplicity when divided by the diagonal and also cross unity at  $\sim 1.5 \langle dN_{\text{ch}}/d\eta \rangle$ . The crossing of the two rapidity measurements occurs at higher than the average multiplicity due to the fact that the  $J/\psi$  are produced in hard events. Hard events produce higher average multiplicities compared to minimum bias events [235].

We will compare our results to those from LHC Run 1 p-Pb at  $\sqrt{s_{\text{NN}}} = 5.02$  TeV [177] in the next section. However, we will first validate the analysis by comparing our results to the  $R_{\text{pPb}}$  and the centrality differential analysis.

p-Pb		Pb-p	
$\frac{dN_{ch}/d\eta}{\langle dN_{ch}/d\eta \rangle}$	$\frac{dN/dy}{\langle dN/dy \rangle} \pm \text{stat.} \pm \text{syst.}$	$\frac{dN_{ch}/d\eta}{\langle dN_{ch}/d\eta \rangle}$	$\frac{dN/dy}{\langle dN/dy \rangle} \pm \text{stat.} \pm \text{syst.}$
0.18	$0.185 \pm 0.003 \pm 0.007$	0.19	$0.136 \pm 0.002 \pm 0.005$
0.42	$0.458 \pm 0.007 \pm 0.018$	0.47	$0.370 \pm 0.004 \pm 0.013$
0.58	$0.614 \pm 0.010 \pm 0.022$	0.66	$0.555 \pm 0.006 \pm 0.019$
0.70	$0.726 \pm 0.011 \pm 0.026$	0.80	$0.685 \pm 0.008 \pm 0.024$
0.82	$0.855 \pm 0.013 \pm 0.030$	0.93	$0.802 \pm 0.008 \pm 0.028$
0.94	$0.974 \pm 0.015 \pm 0.034$	1.07	$0.966 \pm 0.010 \pm 0.033$
1.06	$1.100 \pm 0.016 \pm 0.040$	1.21	$1.105 \pm 0.010 \pm 0.041$
1.18	$1.231 \pm 0.016 \pm 0.047$	1.36	$1.315 \pm 0.011 \pm 0.045$
1.30	$1.311 \pm 0.018 \pm 0.045$	1.49	$1.454 \pm 0.015 \pm 0.050$
1.42	$1.405 \pm 0.019 \pm 0.049$	1.63	$1.589 \pm 0.015 \pm 0.057$
1.54	$1.501 \pm 0.022 \pm 0.055$	1.76	$1.767 \pm 0.020 \pm 0.060$
1.66	$1.592 \pm 0.025 \pm 0.056$	1.89	$1.938 \pm 0.020 \pm 0.066$
1.78	$1.687 \pm 0.027 \pm 0.060$	2.04	$2.149 \pm 0.024 \pm 0.074$
1.90	$1.695 \pm 0.049 \pm 0.069$	2.18	$2.263 \pm 0.031 \pm 0.078$
2.03	$1.956 \pm 0.030 \pm 0.069$	2.32	$2.412 \pm 0.028 \pm 0.092$
2.22	$1.990 \pm 0.027 \pm 0.073$	2.54	$2.654 \pm 0.029 \pm 0.103$
2.50	$2.183 \pm 0.027 \pm 0.077$	2.86	$3.084 \pm 0.032 \pm 0.108$
2.94	$2.485 \pm 0.034 \pm 0.088$	3.36	$3.872 \pm 0.051 \pm 0.132$
3.67	$2.946 \pm 0.068 \pm 0.105$	4.15	$4.791 \pm 0.133 \pm 0.180$
4.93	$3.962 \pm 0.424 \pm 0.187$	5.59	$6.776 \pm 1.157 \pm 0.389$

Table 7.14: Multiplicity dependent relative invariant  $J/\psi$  yields.



ALI-PREL-312803

Figure 7.43: Self-normalised  $J/\psi$  yields as a function of self-normalised charged particle multiplicity in p-Pb and Pb-p at  $\sqrt{s_{NN}} = 8.16$  TeV divided by the diagonal. The uncertainty on the multiplicity axis is partially correlated in multiplicity.

### 7.5.1 Comparison of invariant yields with $R_{pPb}$ analysis

We validated the multiplicity integrated invariant yields obtained from this analysis by comparing them with the values extracted in the  $R_{pPb}$  analysis [130]. The following formula was used to compute the yields:

$$Y(\Delta y) = \frac{N_{J/\psi}(\Delta y)}{A\varepsilon(\Delta y) \cdot F_{\text{norm}} N_{\text{MUL}} \cdot \Delta y}. \quad (7.28)$$

We used our values of  $N_{J/\psi}$ ,  $F_{\text{norm}}$  and  $N_{\text{MUL}}$  evaluated for our custom event selection (CPS and vertex cuts). The values of  $A\varepsilon$  as well as systematic uncertainties on the tracking efficiency, the trigger efficiency, and the trigger matching efficiency were adopted from [130]. The results of the two analyses are shown in Fig. 7.15, the values are listed in Tab. 7.15. The statistical uncertainties are fully correlated between the two analyses. The systematic uncertainties are almost fully correlated. The two measurements are in a good agreement, further validating the custom pile-up cuts used in our analysis.

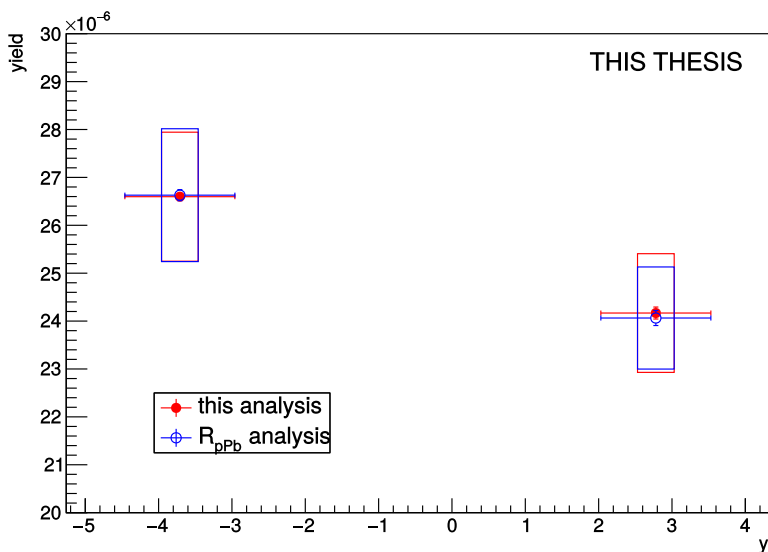


Figure 7.44: Multiplicity integrated invariant  $J/\psi$  yields in p–Pb and Pb–p at  $\sqrt{s_{\text{NN}}} = 8.16$  TeV. Full discs show results of this multiplicity analysis, open circles denote results from  $R_{pPb}$  analysis [239].

	p–Pb	Pb–p
this analysis	$2.42 \pm 0.01 \pm 0.12$	$2.66 \pm 0.01 \pm 0.13$
$R_{pPb}$ analysis [239]	$2.41 \pm 0.02 \pm 0.11$	$2.66 \pm 0.01 \pm 0.14$

Table 7.15: Multiplicity integrated invariant yields.

### 7.5.2 Comparison with results from the centrality dependent analysis

Another verification was performed by comparing the results of the multiplicity analysis with the centrality dependent results [234]. The centrality dependent analysis used the ZDC to determine the event multiplicity. The data were divided in centrality classes based on the deposited energy in the ZN calorimeters. ZNA was used for the p–Pb period and ZNC for the Pb–p period.

In order to compare the two analysis, we computed the correlation of  $dN_{\text{ch}}/d\eta / \langle dN_{\text{ch}}/d\eta \rangle$  with the ZN percentile. The correlation was studied in CINT7-B-NOPE-MUFAST triggered data. The correlation in the p–Pb period is shown as an example in in Fig. 7.45. We see that there is a weak

linear correlation, however the distribution is very wide. The systematic uncertainty on the correlation is thus large. We separated the two dimensional distribution into the same ZN percentile slices as were used in the centrality analysis. Then we projected the distributions into the multiplicity axis and extracted the mean and the width of the distribution in each slice.

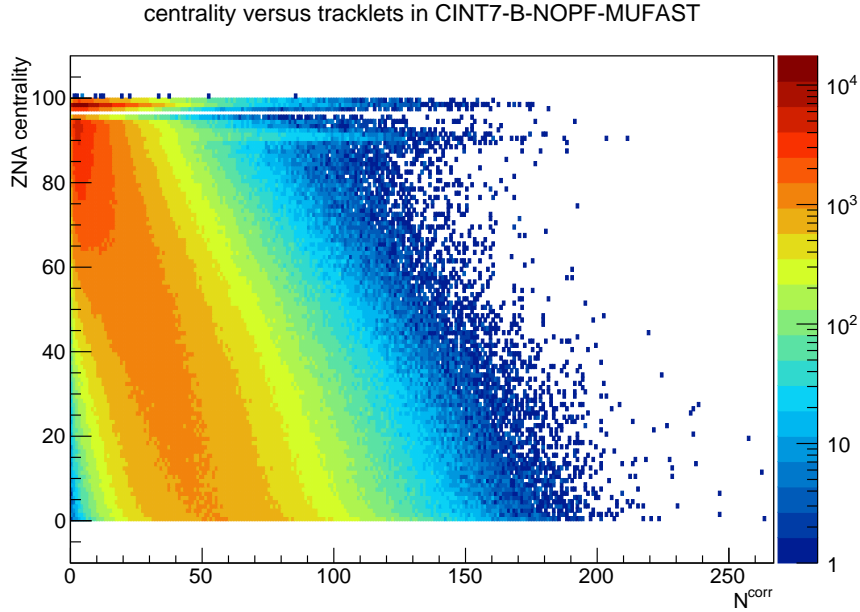
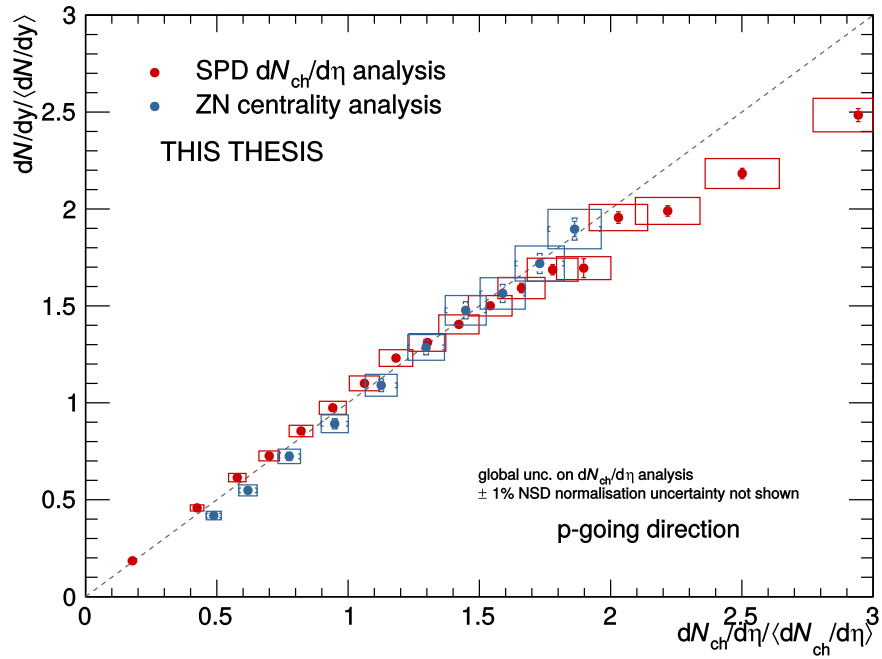


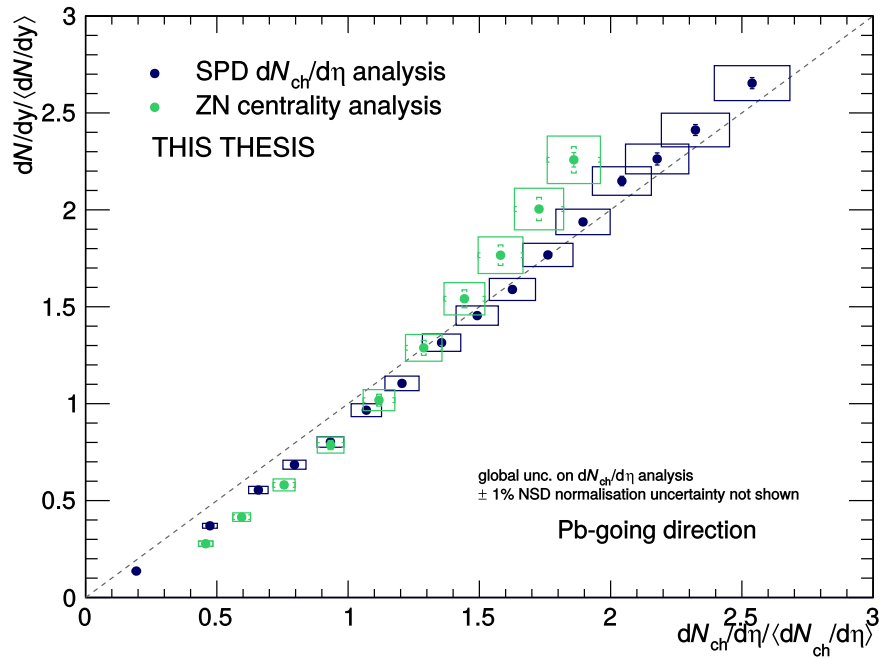
Figure 7.45: The correlation between the ZNA percentile and the  $N^{\text{corr}}$  in the CINT7-B-NOPF-MUFAST triggered p-Pb data sample.

We also had to calculate the relative yields  $dN/dy / \langle dN/dy \rangle$  since the centrality analysis studied absolute yields. In the multiplicity analysis, the multiplicity dependent yields were partially correlated with the integrated yields. We took this into account by computing two sets of systematic errors on the relative  $J/\psi$  signal - one set assuming the numerator and denominator are fully correlated and the other assuming they are fully uncorrelated. Apart from the signal extraction uncertainty, we also considered the uncertainty on  $F_{\text{norm}}$  and the uncertainty associated to pile-up, which we took from [234].

The comparison of the multiplicity and centrality dependent results in p-Pb and Pb-p is shown in Fig. 7.46. We did not draw the uncertainty on the correlation between ZN percentile and  $N^{\text{raw}}$ . The forward rapidity data show very good agreement between the two analyses. The backward rapidity data also agrees within uncertainties in the whole common multiplicity range. They show a bit of a tension in the lowest and highest multiplicity bins of the centrality analysis. This was also observed at 5.02 TeV [221]. This difference most likely comes from the fact that the last bin of the centrality analysis corresponds to several other bins in multiplicity and hence the relative yield is a linear combination of all the yields at high multiplicity. We also see the advantage of the multiplicity analysis - the centrality yields only reach to  $dN_{\text{ch}}/d\eta / \langle dN_{\text{ch}}/d\eta \rangle \sim 2$ .



(a) p-Pb

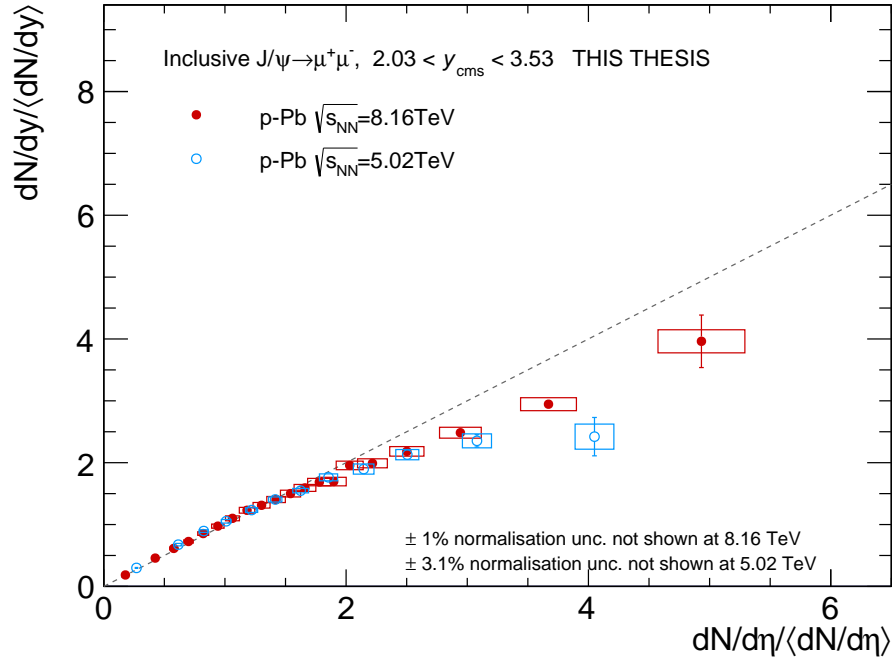


(b) Pb-p

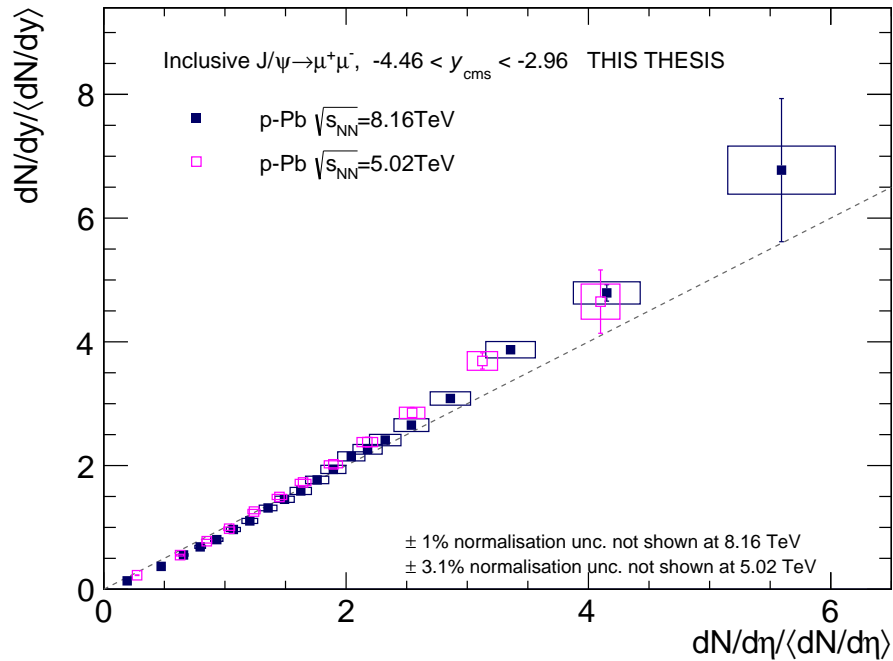
Figure 7.46: Comparison of multiplicity dependent results with results from centrality analysis. The boxes around the centrality dependent data points show the fully uncorrelated systematic uncertainty on the relative yields. The vertical brackets denote the fully correlated systematics on relative yields.

## 7.6 Comparison with other multiplicity dependent results

The multiplicity dependence of the relative  $J/\psi$  was previously measured in p-Pb in LHC Run 1 data at  $\sqrt{s_{NN}} = 5.02$  TeV [177]. Measurements in pp (multiplicity dependence), p-Pb ( $R_{pPb}$ ), and Pb-Pb ( $R_{PbPb}$ ) have shown that relative quantities are independent of the collision energy. Therefore we expected that the also these two analyses would give similar results.



(a) p-Pb



(b) Pb-p

Figure 7.47: Comparison of multiplicity differential relative  $J/\psi$  yields in p-Pb and Pb-p at  $\sqrt{s_{NN}} = 5.02$  [177] and 8.16 TeV.

We compared the new measurement with the previous one at 5.02 TeV. The comparison is shown in

Fig. 7.47. The new measurement extends the relative multiplicity reach up to of  $dN_{\text{ch}}/d\eta / \langle dN_{\text{ch}}/d\eta \rangle \sim 6$  within uncertainty. Contrast with the reach of the 5.02 TeV data which was  $dN_{\text{ch}}/d\eta / \langle dN_{\text{ch}}/d\eta \rangle \sim 4.5$ . The two measurements are in a good agreement in the backward rapidity region. In the forward region, they are consistent within uncertainties. Authors of [177] argued that the forward yields experience a saturation at high multiplicity. The results of the hereby presented analysis suggest that the increase is slower-than-linear, but do not support a saturation scenario.

## Summary

In this chapter, we presented the measurement of the multiplicity differential relative  $J/\psi$  yields in p-Pb collisions at  $\sqrt{s_{\text{NN}}} = 8.16$  TeV. The charged particle multiplicity was measured at midrapidity  $|\eta_{\text{lab}}| < 1$ . The inclusive  $J/\psi$  were measured in the rapidity region  $2.5 < y_{\text{lab}} < 4.0$ . Due to the asymmetry of the p-Pb collision, this allowed to probe two different centre-of-mass rapidity regions  $2.03 < y_{\text{cms}} < 3.53$  and  $-4.46 < y_{\text{cms}} < -2.96$ .

The yields show an increase with the multiplicity, that depends on the  $y$  of the  $J/\psi$  measurement but is independent of the collision energy. The relative yields were compared with the previous measurement at  $\sqrt{s_{\text{NN}}} = 5.02$  TeV. We found that correlating the relative yields with the relative multiplicity removes the energy dependence. The larger statistics in the 8.16 TeV sample allowed us to reach higher multiplicities and decrease the uncertainty in the common multiplicity range.

## MEAN TRANSVERSE MOMENTUM MEASUREMENT IN p–Pb COLLISIONS AT $\sqrt{s_{\text{NN}}} = 8.16$ TeV

In this chapter we will review the measurement of the  $J/\psi$  mean transverse momentum measurement  $\langle p_{\text{T}}^{J/\psi} \rangle$  and its dependence on the charged particle multiplicity at midrapidity. We will start by explaining the method used to extract the  $\langle p_{\text{T}}^{J/\psi} \rangle$ . We adopted the same technique that was developed in [221]. The method requires the dimuon data to be first corrected by the acceptance-efficiency of the detector. A two dimensional correction  $A\varepsilon(p_{\text{T}}, y)$  is considered.

From the  $A\varepsilon$  corrected dimuon data, we compute the mean transverse momentum invariant mass spectrum  $\langle p_{\text{T}}^{\mu^+\mu^-} \rangle(\mu^+\mu^-)$  as

$$\langle p_{\text{T}}^{\mu^+\mu^-} \rangle_i = \frac{\sum_{j=0}^{N_i^{\mu^+\mu^-}} p_{\text{T}}^j / A\varepsilon(p_{\text{T}}^j, y^j)}{\sum_{j=0}^{N_i^{\mu^+\mu^-}} 1 / A\varepsilon(p_{\text{T}}^j, y^j)}, \quad (8.1)$$

where  $N_i^{\mu^+\mu^-}$  is the number of dimuons in the given invariant mass bin  $i$ ,  $p_{\text{T}}^j$  and  $y^j$  are the transverse momentum and rapidity of the  $j$ -th dimuon pair in the invariant mass bin  $i$ . The denominator  $\sum_{j=0}^{N_i^{\mu^+\mu^-}} 1 / A\varepsilon(p_{\text{T}}^j, y^j)$  gives the effective number of entries in the bin  $i$ .

The  $\langle p_{\text{T}} \rangle$  spectrum is fitted in each multiplicity bin by the following function:

$$\begin{aligned} \langle p_{\text{T}}^{\mu^+\mu^-} \rangle(\mu^+\mu^-) &= \alpha^{J/\psi} \langle p_{\text{T}}^{J/\psi} \rangle \\ &+ \alpha^{\psi'} \langle p_{\text{T}}^{\psi'} \rangle \\ &+ \left(1 - \alpha^{J/\psi} - \alpha^{\psi'}\right) f(\langle p_{\text{T}}^{bkgd} \rangle), \end{aligned} \quad (8.2)$$

where  $\alpha^Q = S/(S+B)$  of given charmonium state was fixed to the value extracted from fitting the  $A\varepsilon$  corrected invariant mass spectrum. The  $\langle p_{\text{T}} \rangle$  of the background is described by a function  $f(\langle p_{\text{T}}^{bkgd} \rangle)$ .

We will describe the extraction of the  $J/\psi$  signal and the evaluation of systematic uncertainties. Finally we will present multiplicity differential results for the absolute  $\langle p_{\text{T}}^{J/\psi} \rangle$  and for the relative  $\langle p_{\text{T}}^{J/\psi} \rangle^R$ . We will compare our results with those from the previous p–Pb measurement [177, 221] at  $\sqrt{s_{\text{NN}}} = 5.02$  TeV.

### 8.1 Acceptance-efficiency correction

The dimuon spectrum needed to be corrected by the 2D acceptance-efficiency  $A\varepsilon$  of the spectrometer before we could compute the invariant mass and the corresponding  $\langle p_{\text{T}} \rangle$  profile in each interval. We used the  $A\varepsilon$  factor computed for the  $J/\psi$ . The computation of  $A\varepsilon$  for the p–Pb and Pb–p periods was executed centrally for all analysis on this datasample. The MC were produced following the

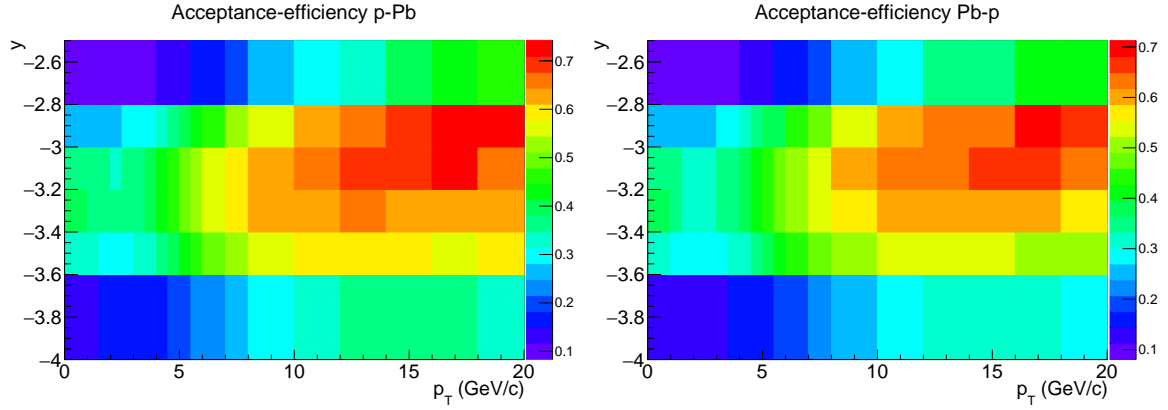


Figure 8.1: Double differential  $A\varepsilon(p_T, y)$  of the Muon Spectrometer in p-Pb and Pb-p at  $\sqrt{s_{\text{NN}}} = 8.16$  TeV.

iterative procedure described in Sec. 5.2. The  $A\varepsilon(p_T, y)$  maps for  $J/\psi$  computed in the kinematic range  $0 < p_T < 20$  GeV/c and  $2.5 < y_{\text{lab}} < 4$  are shown in Fig. 8.1 for the two rapidity intervals.

The fit function in Eq. (8.2) also includes a part that describes the  $\psi(2S)$  peak. This quantity is non-physical, as the spectrum is corrected by the  $A\varepsilon$  of the  $J/\psi$ . We need to however account for this contribution in order to properly describe the shape of the  $\langle p_T \rangle$  spectrum.

## 8.2 Mean transverse momentum extraction

The  $A\varepsilon$  corrected invariant yields are estimated using the same fit functions and their variations as in the relative yields analysis. We remind here which variations are considered:

- we describe the signal by a CB2 or a NA60 function,
- we vary 3 data tails and 3 MC tails,
- we describe the mass background by a Double Exponential or an Exp\*Pol4 function,
- we fit over the mass range  $1.7 < M_{\text{inv}} < 4.8$  GeV/c<sup>2</sup> or  $2.0 < M_{\text{inv}} < 5.0$  GeV/c<sup>2</sup>.

In addition, we also vary the  $\langle p_T \rangle$  of the background, considering that it can be described by a quadratic function or a product of a quadratic function and an exponential. Other functions were also tested, these two proved to be the most stable in all multiplicity bins and in both periods.

Example of the fit to the  $A\varepsilon$  corrected  $M_{\text{inv}}$  spectra and the corresponding  $\langle p_T \rangle$  fit can be found in Fig. 8.2. The multiplicity differential fits are shown in Fig. 8.3.

### Variation of invariant mass signal

Fixing the  $\alpha$  may lead to an artificial minimisation of the uncertainty on the fit and thus on the  $\langle p_T \rangle$ . Therefore we introduced an additional variation of  $\alpha$ , when we varied signal  $S$  by  $\pm 1\sigma$ . We considered the following:

- Any increase in  $S$  was compensated by a decrease of  $B$  of equal magnitude (and vice-versa) so that  $S + B$  is constant.
- $\psi(2S)$  has little effect on the overall fit - we did not vary  $\alpha^{\psi(2S)}$ .
- The statistical uncertainty on the signal  $\Delta S$  follows a Gaussian distribution around the mean value  $S$ . This cause the  $\alpha$  to vary by  $\delta_\alpha$ , which is randomly drawn from the Gaussian distribution with the mean  $S$  and width  $\Delta S$ .

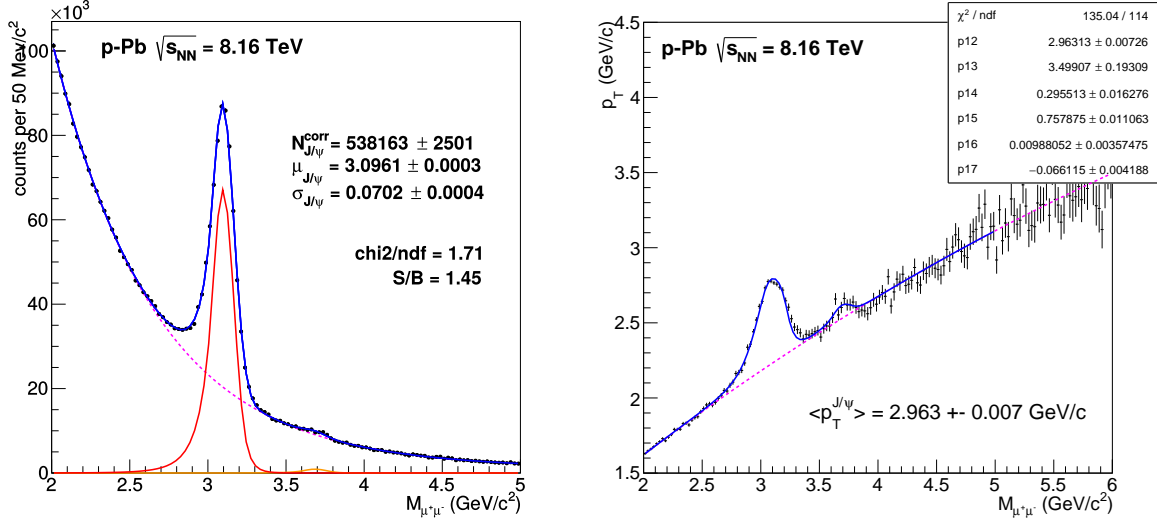


Figure 8.2: Fit to the multiplicity integrated,  $A\epsilon$  corrected invariant mass spectrum in p–Pb and the corresponding  $\langle p_T \rangle$  fit. The  $M_{\text{inv}}$  spectrum was fitted with a function combining a CB2 signal + double exponential background + tails extracted in cross section analysis in pp at 13 TeV over a fit range  $2 < M_{\text{inv}} < 5 \text{ GeV}/c$ . The  $f(\langle p_T^{bkgd} \rangle)$  was described by a product of quadratic and exponential function.

The function in Eq. (8.2) was varied by  $\delta_\alpha$  to

$$\begin{aligned}
 \langle p_T^{\mu^+ \mu^-} \rangle (\mu^+ \mu^-) &= \delta_\alpha * \alpha^{J/\psi} \langle p_T^{J/\psi} \rangle \\
 &+ \alpha^{\psi'} \langle p_T^{\psi'} \rangle \\
 &+ \left(1 - \delta_\alpha * \alpha^{J/\psi} - \alpha^{\psi'}\right) f(\langle p_T^{bkgd} \rangle),
 \end{aligned} \tag{8.3}$$

For each variation of Eq. (8.2), we considered the unmodified fit ( $\delta_\alpha = 1$ ) and five invariant mass signal variations of Eq. (8.3).

As we needed to control a very large number of fits, we introduced additional criteria - if those were not fulfilled the fit was rejected from the systematic uncertainty calculation:

1.  $0.5 < \chi^2/\text{ndf} < 4$ ,
2. fit must converge and have positive definite covariance matrix,
3.  $1.0 < \langle p_T \rangle < 4.0 \text{ GeV}/c$
4.  $0 < \delta_\alpha < 5$ .

The first and the second point were to quickly reject trials that could not be trusted. We also introduced the limits on  $\langle p_T \rangle$  to help the fits converge. In such case, a fit that would converge at a limit value of  $\langle p_T \rangle$  would not have a properly computed value and thus would be rejected by the third criterion. The last cut on  $\delta_\alpha$  was applied to prevent potential cases of  $S < 0$ . The upper limit was chosen arbitrarily and thus was selected to be large enough as to not bias the result.

### 8.2.1 Absolute $\langle p_T \rangle$ signal extraction

Fig. 8.4 shows the results of all variations of the integrated spectrum fit in p–Pb as an example. Tab. 8.1 lists the results integrated and bin-by-bin for the two periods. Note that the we do not give a value for the last bin in Pb–p as the variations of fit were particularly unstable.

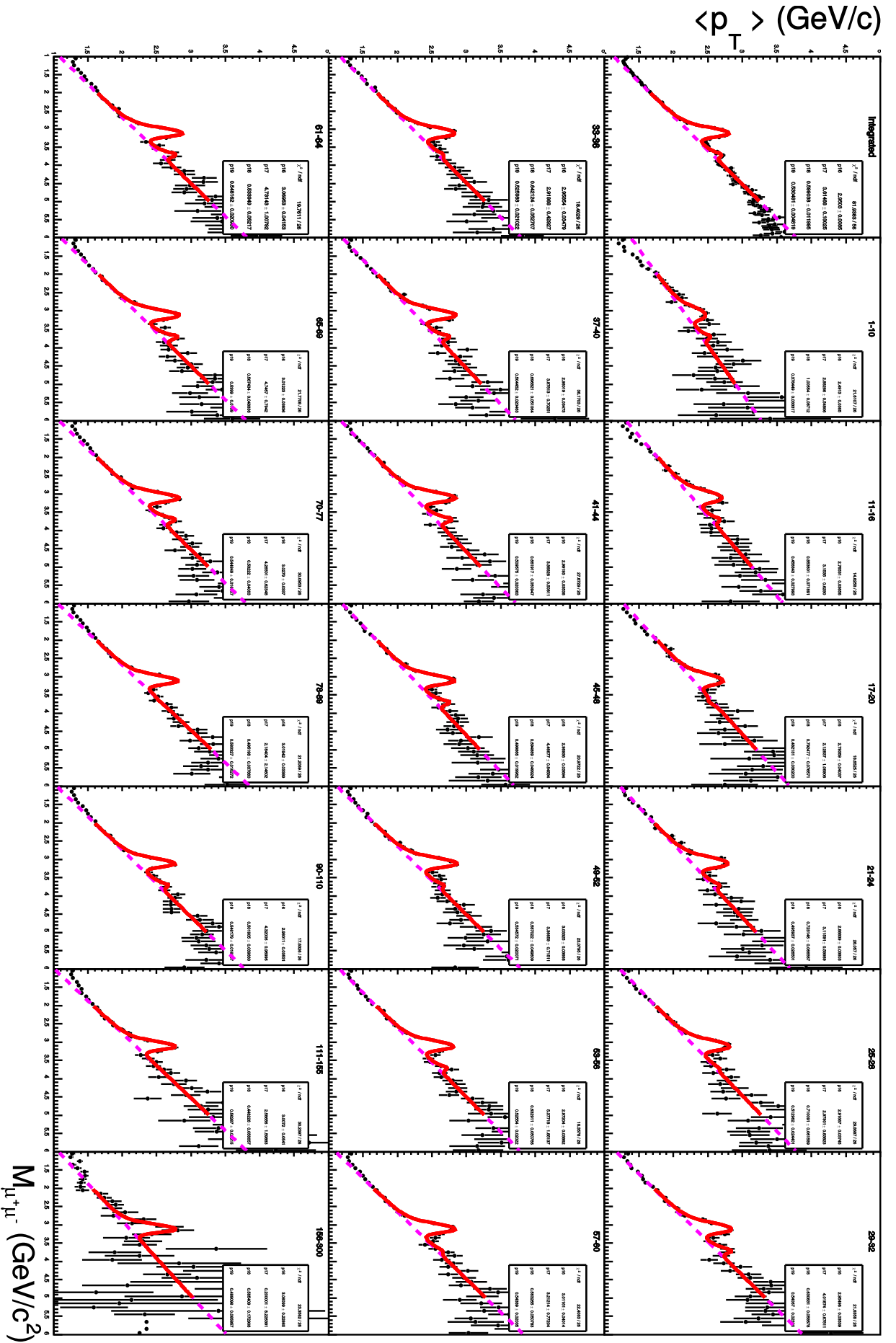


Figure 8.3: Example of  $\langle p_T \rangle$  fit to the p-Pb multiplicity dependent spectra using the following option:  $M_{\text{inv}}$  described by a combination of NA60 signal + double exponential background with MC tails,  $f(\langle p_T \rangle)$  described by a quadratic function multiplied by an exponential, fit over  $1.7 < M_{\text{inv}} < 4.8 \text{ GeV}/c^2$ .

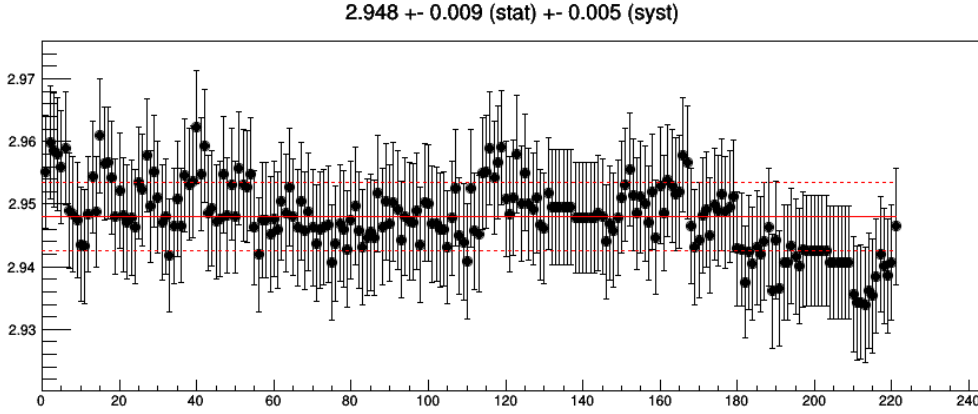


Figure 8.4:  $\delta_\alpha$  variations of  $\langle p_T \rangle$  fit to the multiplicity integrated spectrum in the p-Pb period. The points towards the right end that are systematically lower with respect to the rest correspond to fits with the NA60 signal shape.

p-Pb		Pb-p	
$\frac{dN_{ch}/d\eta}{\langle dN_{ch}/d\eta \rangle}$	$\langle p_T \rangle \pm \text{stat.} \pm \text{syst.} \text{ (GeV/c)}$	$\frac{dN_{ch}/d\eta}{\langle dN_{ch}/d\eta \rangle}$	$\langle p_T \rangle \pm \text{stat.} \pm \text{syst.} \text{ (GeV/c)}$
integrated	$2.948 \pm 0.009 \pm 0.005$	integrated	$2.662 \pm 0.007 \pm 0.005$
0.18	$2.496 \pm 0.037 \pm 0.006$	0.19	$2.212 \pm 0.037 \pm 0.010$
0.43	$2.745 \pm 0.038 \pm 0.008$	0.47	$2.469 \pm 0.031 \pm 0.005$
0.58	$2.784 \pm 0.046 \pm 0.025$	0.66	$2.514 \pm 0.032 \pm 0.009$
0.70	$2.860 \pm 0.041 \pm 0.015$	0.80	$2.514 \pm 0.033 \pm 0.009$
0.82	$2.915 \pm 0.041 \pm 0.013$	0.93	$2.628 \pm 0.029 \pm 0.006$
0.94	$2.956 \pm 0.038 \pm 0.018$	1.07	$2.629 \pm 0.032 \pm 0.007$
1.06	$2.949 \pm 0.038 \pm 0.012$	1.21	$2.675 \pm 0.028 \pm 0.010$
1.18	$2.950 \pm 0.037 \pm 0.013$	1.36	$2.656 \pm 0.028 \pm 0.016$
1.30	$2.998 \pm 0.038 \pm 0.014$	1.49	$2.721 \pm 0.032 \pm 0.014$
1.42	$2.966 \pm 0.040 \pm 0.013$	1.63	$2.667 \pm 0.029 \pm 0.008$
1.54	$2.993 \pm 0.039 \pm 0.016$	1.76	$2.696 \pm 0.034 \pm 0.014$
1.66	$2.972 \pm 0.042 \pm 0.012$	1.90	$2.708 \pm 0.031 \pm 0.014$
1.78	$3.019 \pm 0.043 \pm 0.016$	2.04	$2.722 \pm 0.034 \pm 0.020$
1.90	$3.077 \pm 0.045 \pm 0.017$	2.18	$2.779 \pm 0.039 \pm 0.017$
2.03	$2.993 \pm 0.041 \pm 0.016$	2.32	$2.716 \pm 0.034 \pm 0.017$
2.22	$3.030 \pm 0.036 \pm 0.020$	2.54	$2.770 \pm 0.030 \pm 0.023$
2.50	$3.013 \pm 0.035 \pm 0.015$	2.86	$2.716 \pm 0.029 \pm 0.033$
2.94	$2.967 \pm 0.036 \pm 0.016$	3.36	$2.743 \pm 0.034 \pm 0.024$
3.67	$3.014 \pm 0.054 \pm 0.031$	4.15	$2.681 \pm 0.059 \pm 0.029$
4.93	$2.974 \pm 0.218 \pm 0.088$	5.59	—

Table 8.1: Absolute  $\langle p_T \rangle$  values obtained from the  $\delta_\alpha$  variations. The last values bin in Pb-p did not properly converge, therefore we excluded it from the analysis. Uncertainty on the multiplicity not shown.

### 8.2.2 Relative $\langle p_T \rangle$ signal extraction

We also performed the same exercise to extract the relative mean transverse momentum in each multiplicity bin  $i$

$$\langle p_T \rangle^R = \langle p_T \rangle^i / \langle p_T \rangle^{MB}. \quad (8.4)$$

Here we used all variation as in Sec. 8.2.1. As in the relative yields analysis, we assumed that the signal shape is correlated in multiplicity. Therefore in the ratio we only allowed variations of:

- $M_{\text{inv}}$  background function,
- $M_{\text{inv}}$  fit range,
- $f(\langle p_T \rangle)$  background function,
- $\delta_\alpha$  randomisation.

The signal shape and tails must be the same in numerator and in the denominator. The bin-by-bin results of the fit are listed in Tab. 8.2.

p-Pb		Pb-p	
$\frac{dN_{\text{ch}}/d\eta}{\langle dN_{\text{ch}}/d\eta \rangle}$	$\langle p_T \rangle^R \pm \text{stat.} \pm \text{syst. (GeV/c)}$	$\frac{dN_{\text{ch}}/d\eta}{\langle dN_{\text{ch}}/d\eta \rangle}$	$\langle p_T \rangle^R \pm \text{stat.} \pm \text{syst. (GeV/c)}$
0.18	$0.847 \pm 0.010 \pm 0.003$	0.19	$0.831 \pm 0.011 \pm 0.004$
0.43	$0.931 \pm 0.010 \pm 0.003$	0.47	$0.928 \pm 0.009 \pm 0.003$
0.58	$0.944 \pm 0.012 \pm 0.007$	0.66	$0.944 \pm 0.009 \pm 0.004$
0.70	$0.970 \pm 0.011 \pm 0.005$	0.80	$0.944 \pm 0.010 \pm 0.004$
0.82	$0.989 \pm 0.011 \pm 0.005$	0.93	$0.987 \pm 0.008 \pm 0.003$
0.94	$1.003 \pm 0.010 \pm 0.006$	1.07	$0.988 \pm 0.009 \pm 0.003$
1.06	$1.000 \pm 0.010 \pm 0.005$	1.21	$1.005 \pm 0.008 \pm 0.004$
1.18	$1.001 \pm 0.010 \pm 0.005$	1.36	$0.998 \pm 0.008 \pm 0.006$
1.30	$1.017 \pm 0.010 \pm 0.005$	1.49	$1.022 \pm 0.009 \pm 0.006$
1.42	$1.006 \pm 0.010 \pm 0.005$	1.63	$1.002 \pm 0.008 \pm 0.003$
1.54	$1.015 \pm 0.010 \pm 0.006$	1.76	$1.013 \pm 0.010 \pm 0.006$
1.66	$1.008 \pm 0.011 \pm 0.005$	1.90	$1.017 \pm 0.009 \pm 0.005$
1.78	$1.024 \pm 0.011 \pm 0.006$	2.04	$1.023 \pm 0.010 \pm 0.008$
1.90	$1.044 \pm 0.012 \pm 0.006$	2.18	$1.044 \pm 0.012 \pm 0.007$
2.03	$1.015 \pm 0.011 \pm 0.006$	2.32	$1.020 \pm 0.010 \pm 0.007$
2.22	$1.028 \pm 0.009 \pm 0.007$	2.54	$1.041 \pm 0.009 \pm 0.008$
2.50	$1.022 \pm 0.009 \pm 0.005$	2.86	$1.020 \pm 0.008 \pm 0.013$
2.94	$1.007 \pm 0.009 \pm 0.006$	3.36	$1.030 \pm 0.010 \pm 0.009$
3.67	$1.022 \pm 0.015 \pm 0.011$	4.15	$1.007 \pm 0.019 \pm 0.011$
4.93	$1.010 \pm 0.069 \pm 0.030$	5.59	—

Table 8.2: Relative  $\langle p_T \rangle^R$  values obtained from the  $\delta_\alpha$  variations. The last values bin in Pb-p did not properly converge, therefore we excluded it from the analysis. Uncertainty on the multiplicity not shown.

### 8.3 Systematic uncertainty on $\langle p_T \rangle$

We considered the following sources of systematic uncertainty: signal extraction and the uncertainty on the acceptance efficiency  $A\varepsilon$ .

The uncertainty on the  $A\varepsilon$  relevant for the absolute  $\langle p_T \rangle$  originates in the following sources: i) the uncertainty on the tracking efficiency, ii) the uncertainty on the trigger efficiency, iii) the uncertainty

on the matching efficiency between the tracking and the trigger, and iv) the uncertainty on the MC input shapes. The first three were taken from [130] as a first estimate and apply only to the absolute results, i. e.  $\langle p_T \rangle$ . The uncertainty on the signal extraction and input shape were considered also for the relative  $\langle p_T \rangle^R$ .

source	p-Pb		Pb-p	
	$\langle p_T \rangle$	$\langle p_T \rangle^R$	$\langle p_T \rangle$	$\langle p_T \rangle^R$
signal extraction	0.2 – 3.0% (0.2%)	0.3 – 3.0%	0.2 – 1.2% (0.2%)	0.3 – 1.3%
tracking efficiency	1%*	—	2%*	—
trigger efficiency	2.6%*	—	3.1%*	—
matching efficiency	1%*	—	1%*	—
MC input	3.4%*	3.4%*	2.3%*	2.3%*
total	4.5 – 5.4% (4.5%)	3.4 – 4.5%	4.5 – 4.6% (4.5%)	2.3 – 2.6%

Table 8.3: Sources of systematic uncertainties. The values in parentheses correspond to the multiplicity integrated uncertainties related to the signal extraction. Values marked with asterisk are correlated in multiplicity.

### 8.3.1 Systematic uncertainty on signal extraction

The systematic uncertainty on  $\langle p_T \rangle$  signal extraction was discussed in the previous section. To summarise, we varied the background function, the fit range, and the signal fixed in  $\alpha^Q$ .

The uncertainty on absolute  $\langle p_T \rangle$  amounts to 0.2 % in both periods. The multiplicity differential uncertainties range between 0.2 – 3.0% in p-Pb period and 0.2 – 1.2% in the Pb-p period. The uncertainty on relative  $\langle p_T \rangle^R$  ranges between 0.3 – 3.0% in p-Pb and 0.3 – 1.3% in Pb-p. The values for each multiplicity bin can be found in Tab. 8.4. We recall that in Pb-p we excluded the last multiplicity bin as the result was deemed too unstable with the current method.

### 8.3.2 Systematic uncertainty on MC input

The uncertainty on the MC input shapes was described in Sec. 6.3.1. For the  $\langle p_T \rangle$  analysis, we modified the procedure in the following way:

1. We computed the corrected  $p_T$  or  $y$  differential spectrum as

$$N_{J/\psi}^{\text{corr}}(p_T/y) = \frac{N_{J/\psi}^{\text{raw}}(p_T/y)}{A\varepsilon(p_T/y)}.$$

2. We fitted the corrected spectra by a corresponding function used in the generation of the MC sample.
3. We split the data sample into low multiplicity part ( $N^{\text{corr}} < 54$  for p-Pb and  $N^{\text{corr}} < 62$  for Pb-p) and high multiplicity part ( $N^{\text{corr}} \geq 54$  for p-Pb and  $N^{\text{corr}} \geq 62$  for Pb-p) and fitted their one dimensional  $p_T$  and  $y$  distributions.
4. We again computed and subsequently fitted the corrected spectra.
5. We created ratios of the low (high) multiplicity functions divided by the corresponding 'default' function, we shall denote them  $f_{\text{low(high)}}^R(p_T)$  and  $f_{\text{low(high)}}^R(y)$ .
6. We defined weights for each  $p_T$  and  $y$  bin (we used fine binning for storing the information) as

$$w(p_T, y) = f_{\text{low(high)}}^R(p_T) \cdot f_{\text{low(high)}}^R(y)$$

7. We re-weighted the reconstructed and generated distributions in the MC using these weights.

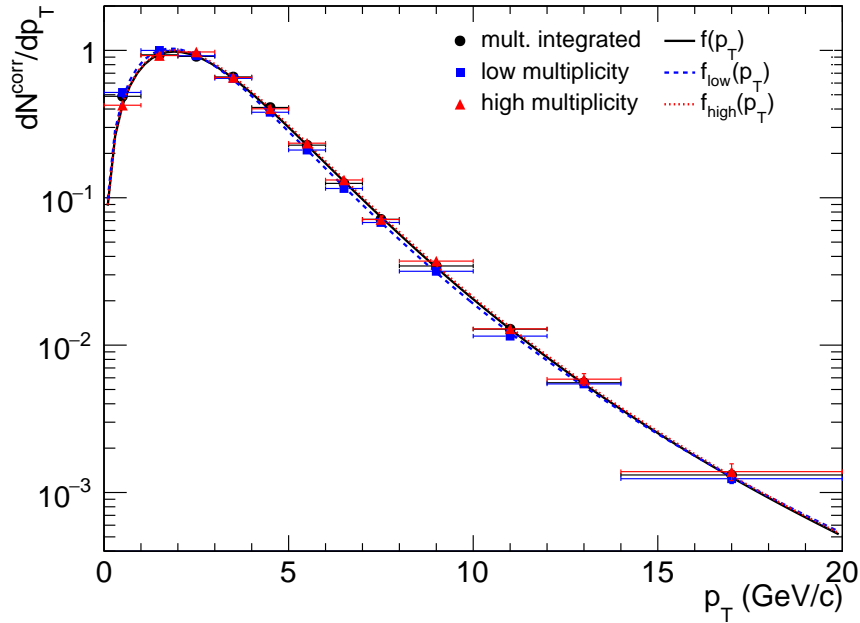
p-Pb			Pb-p		
$\frac{dN_{\text{ch}}/d\eta}{\langle dN_{\text{ch}}/d\eta \rangle}$	$\langle p_{\text{T}} \rangle$ unc. (%)	$\langle p_{\text{T}} \rangle^R$ unc. (%)	$\frac{dN_{\text{ch}}/d\eta}{\langle dN_{\text{ch}}/d\eta \rangle}$	$\langle p_{\text{T}} \rangle$ unc. (%)	$\langle p_{\text{T}} \rangle^R$ unc. (%)
integrated	0.2	—	integrated	0.2	—
0.18	0.2	0.4	0.19	0.5	0.5
0.43	0.3	0.3	0.47	0.2	0.3
0.58	0.9	0.7	0.66	0.4	0.4
0.70	0.5	0.5	0.80	0.4	0.4
0.82	0.4	0.5	0.93	0.2	0.3
0.94	0.6	0.6	1.07	0.3	0.3
1.06	0.4	0.5	1.21	0.4	0.4
1.18	0.4	0.5	1.36	0.6	0.6
1.30	0.5	0.5	1.49	0.5	0.6
1.42	0.4	0.5	1.63	0.3	0.3
1.54	0.5	0.6	1.76	0.5	0.6
1.66	0.4	0.5	1.90	0.5	0.5
1.78	0.5	0.6	2.04	0.7	0.8
1.90	0.6	0.6	2.18	0.6	0.7
2.03	0.5	0.6	2.32	0.6	0.7
2.22	0.7	0.7	2.54	0.8	0.8
2.50	0.5	0.5	2.86	1.2	1.3
2.94	0.5	0.6	3.36	0.9	0.9
3.67	1.0	1.1	4.15	1.1	1.1
4.93	3.0	3.0	5.59	—	—

Table 8.4: Systematic uncertainty on the absolute  $\langle p_{\text{T}} \rangle$  and relative  $\langle p_{\text{T}} \rangle^R$  extraction.

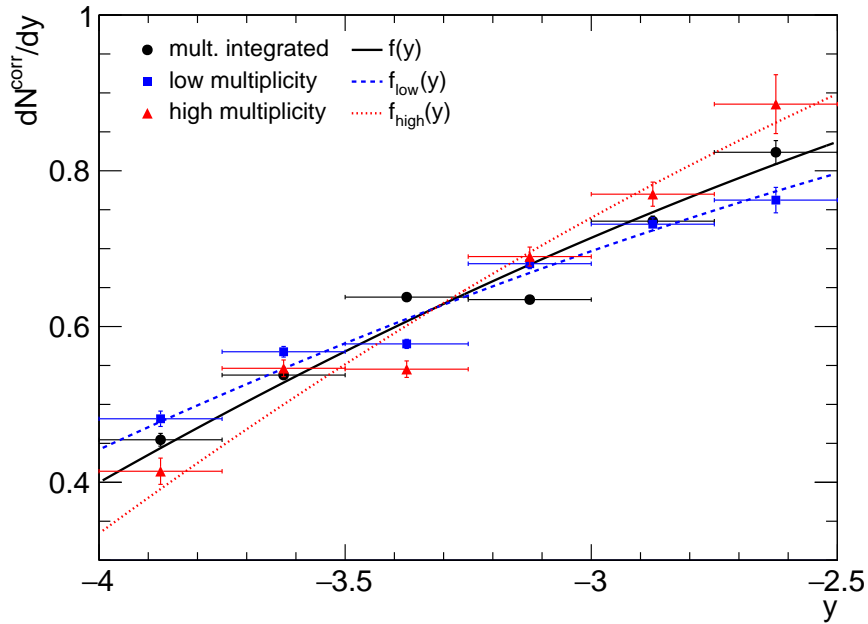
8. We extracted the new  $A\varepsilon(p_T, y)$ .

9. We re-evaluated the multiplicity integrated  $\langle p_T \rangle$  using the weighted  $A\varepsilon$ . We used the default signal extraction without the  $\alpha^Q$  variations.

Example of fits to the  $A\varepsilon$  corrected  $p_T$  and  $y$  spectra in the p-Pb period can be found in Fig. 8.5.



(a)  $p_T$  differential



(b)  $y$  differential

Figure 8.5:  $A\varepsilon$  corrected  $p_T$  and  $y$  spectra in p-Pb. The black distributions correspond to the multiplicity integrated spectrum. The blue and red data points show the high and low multiplicity distributions respectively. The corresponding fits are also drawn, see legend.

From all the possible combinations of weights issued from one period, we only consider those that take both the  $p_T$  and  $y$  dependent weights in the same multiplicity interval, i. e. i) the default unweighted distributions, ii)  $f_{\text{low}}^R(p_T) \cdot f_{\text{low}}^R(y)$ , and iii)  $f_{\text{high}}^R(p_T) \cdot f_{\text{high}}^R(y)$ . The uncertainty on MC input is taken as the maximal spread of the weighted results around the default one, see Fig. 8.6. We

consider the same uncertainty for both absolute  $\langle p_T \rangle$  and relative  $\langle p_T \rangle^R$ . The uncertainty amounts to 3.4% in the p–Pb and to 2.3% in the Pb–p period.

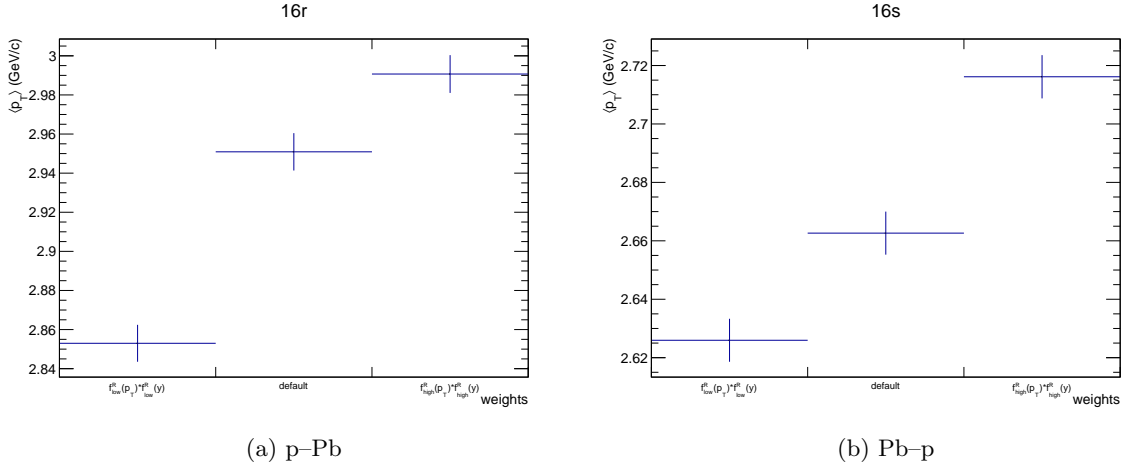


Figure 8.6: Spread of  $\langle p_T \rangle$  computed with different weight combination for the (a) p–Pb and (b) Pb–p data. Left is  $f_{low}^R(p_T) \cdot f_{low}^R(y)$ , centre is the default result, and on right is  $f_{high}^R(p_T) \cdot f_{high}^R(y)$ .

## 8.4 Results

Tab. 8.5 shows the multiplicity integrated  $\langle p_T \rangle$  values for the two periods. The multiplicity dependent results of  $\langle p_T \rangle$  distributions are shown in Fig. 8.7. The relative  $\langle p_T \rangle^R$  are shown in Fig. 8.8. The global, correlated part of the systematic uncertainty includes the contributions to the  $A\varepsilon$  uncertainty discussed in previous section. The systematic uncertainty on the multiplicity is partially correlated.

At low multiplicity, we observe an increase of  $\langle p_T \rangle$  in both periods. At multiplicities above the average, the distributions saturate. The  $\langle p_T \rangle$  in p–Pb is harder than in Pb–p. The suppression of forward  $J/\psi$  due to the CNM effects being stronger at low  $p_T$  is one contributing factor to this phenomenon. On the other hand, LHCb measured the  $p_T$ - and  $y$  double differential  $\langle p_T^{J/\psi} \rangle$  in pp collisions at  $\sqrt{s} = 7$  TeV [40]. In their paper, they showed that the  $\langle p_T \rangle$  decreases when measuring further away from midrapidity. Recall that the Pb–p are measured at a larger absolute rapidity than the p–Pb.

period	$\langle p_T \rangle \pm \text{stat.} \pm \text{syst.} \pm \text{global (GeV/c)}$
p–Pb	$2.948 \pm 0.009 \pm 0.005 \pm 4.5\%$
Pb–p	$2.662 \pm 0.007 \pm 0.005 \pm 4.5\%$

Table 8.5: Multiplicity integrated  $\langle p_T \rangle$  results. The global systematic uncertainty includes the uncertainty on the trigger, tracking, and trigger-track matching efficiencies, and on the MC input.

The present result show a similar trend to those observed at 5.02 TeV. The absolute  $\langle p_T \rangle$  is higher in the 8.16 TeV measurement. This is a consequence of the higher collision energy. The larger statistics of the new data sample allowed us to extend the multiplicity reach. Our systematic uncertainty is dominated by the uncertainty on the MC input and is larger than in the lower energy measurement. The relative  $\langle p_T \rangle^R$  are consistent within uncertainties.

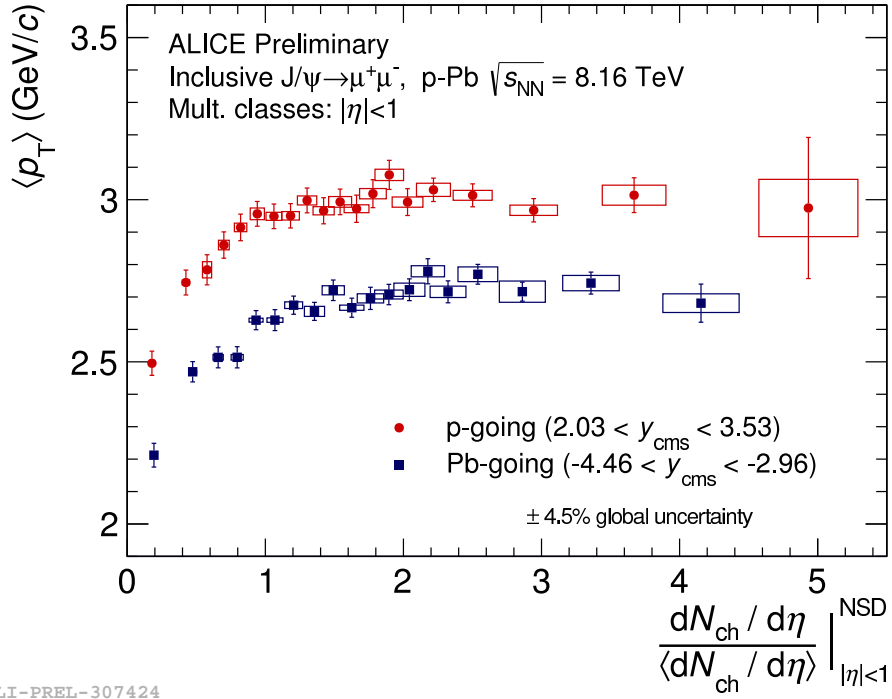


Figure 8.7: Multiplicity dependent  $\langle p_T \rangle$  results.

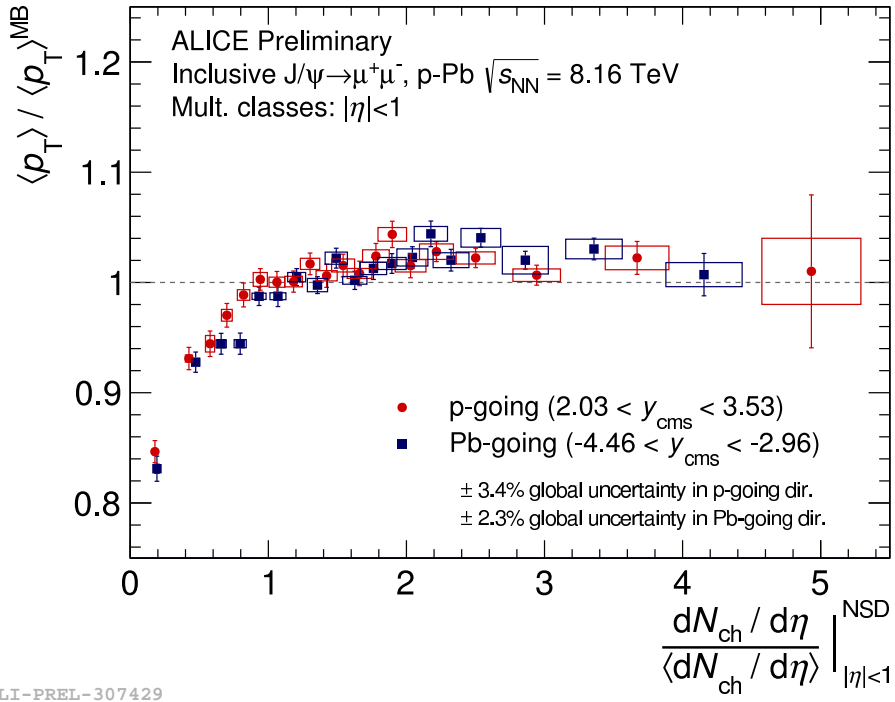
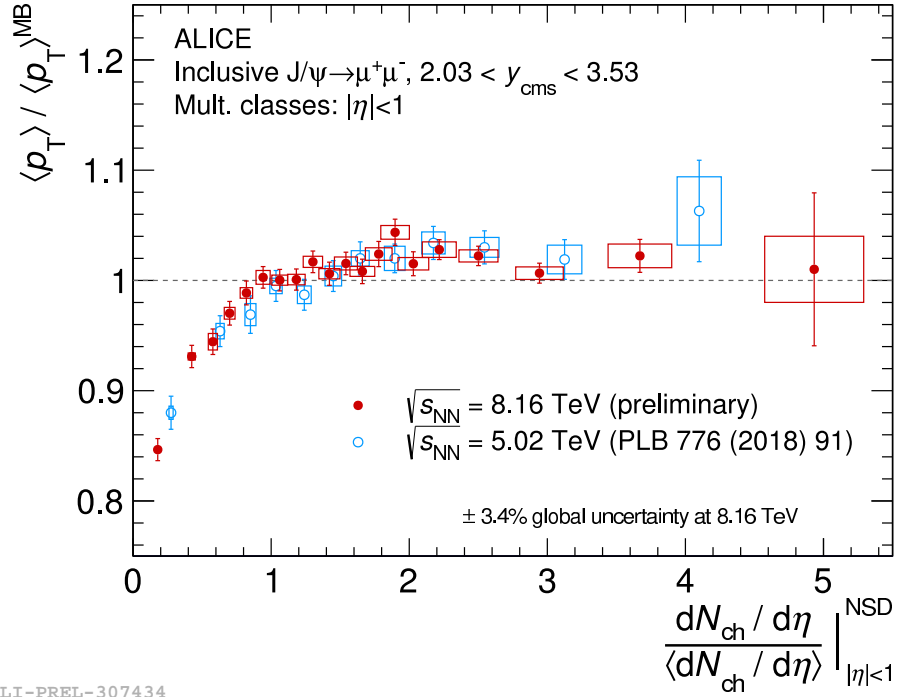
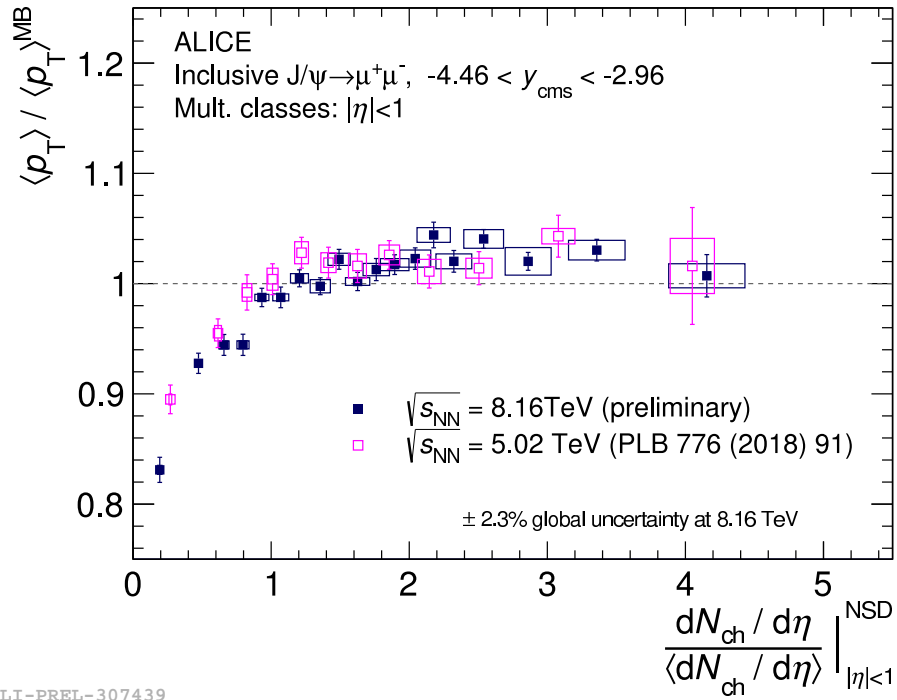


Figure 8.8: Multiplicity dependent  $\langle p_T \rangle^R$  results.



(a) p-Pb



(b) Pb-p

Figure 8.9: Comparison of  $\langle p_T \rangle^R$  in p-Pb and Pb-p at  $\sqrt{s_{\text{NN}}} = 5.02$  and 8.16 TeV.

## Summary

In this chapter, we presented the study of the multiplicity dependence of the mean  $J/\psi$  transverse momentum  $\langle p_T \rangle$  in p–Pb collisions at  $\sqrt{s_{NN}} = 8.16$  TeV. The applied method enabled us to extract  $\langle p_T \rangle$  at high multiplicities.

At low multiplicities, the  $\langle p_T \rangle$  increases steeply until it saturates at around relative multiplicity  $dN_{ch}/d\eta / \langle dN_{ch}/d\eta \rangle \sim 1$ . The  $\langle p_T \rangle$  is larger at forward rapidity than at backward rapidity, but qualitatively the behaviour is similar in the two rapidity intervals. Moreover, the results show qualitatively the same behaviour as was observed in lower energy p–Pb collisions at 5.02 TeV. The relative  $\langle p_T \rangle^R$  shows the same behaviour in the two rapidity intervals and is identical at the two energies. The  $\langle p_T \rangle^R$  saturates at around unity at  $dN_{ch}/d\eta / \langle dN_{ch}/d\eta \rangle \sim 1$ .



## CONCLUSIONS AND OUTLOOK

In the first part of this manuscript, we reviewed the theoretical background of the  $J/\psi$  production in pp, p–A and A–A collisions in collider experiments. The  $J/\psi$  measurements in pp challenge the present day QCD calculations. Their production involves QCD at hard and soft scales. Furthermore, one needs to take into account feed-down contributions of heavier  $c\bar{c}$  states and  $b$ -hadrons. Three principal models are commonly used to describe the prompt  $J/\psi$  cross section, all distinct in their treatment of the non-perturbative  $c\bar{c}$  pair hadronisation: the Colour Evaporation Model (CEM), the Colour Singlet Model (CSM), and the Non-Relativistic Quantum Chromodynamics (NRQCD). The non-prompt contribution  $b$ -to- $J/\psi$  is described by a first-order-next-to-leading-logarithm (FONLL) perturbative QCD (pQCD) calculations.

In p–A collisions, the presence of the nuclear matter affects the particle production thorough the whole collision. These so called cold nuclear matter (CNM) effects include modification of nuclear parton distribution functions (nPDFs), gluon saturation, or coherent energy loss to name a few. The magnitude of the CNM effects depends on the kinematic range of the measurement -  $p_T$  and rapidity in the the nucleus-nucleus centre-of-mass frame - and on the production process. Nevertheless, nuclear effects scale with energy of the collision. At present precision of our measurements, we clearly see the presence of the CNM effects at small  $x$  although we cannot conclude on which effects are those taking place.

Finally, the nuclear matter effects also apply in collisions of A–A. On top of the CNM effects, “hot” nuclear matter effects also affect the production of the  $J/\psi$  with respect to pp collisions. The latter are attributed to the deconfined state of matter - the Quark-Gluon Plasma (QGP) - produced in the A–A collision. Measurements of modification of  $J/\psi$  production aid to reveal formation of the deconfined medium on the system. At the LHC energies, two competing mechanism affecting the  $J/\psi$  yields are considered. The first is the screening of the  $c\bar{c}$  bound states by the free colour charges in the QGP and the consequent suppression of hadron yields. Second is the recombination of the free  $c$  and  $\bar{c}$  in the plasma. As in the case of the CNM effects, these hot effects also show dependence on  $p_T$  and  $y$ , and scale with energy. Furthermore, as the CNM effects in A–A cannot be decoupled from the effects due to presence of QGP, the interpretation of these results cannot be made without prior estimation of CNM effects in p–A.

Recently, we saw an onslaught of studies of correlations of hard and soft probes in pp and p–A systems. Contrary to what was believed, proton-proton events are more complicated as one collisions may involves multiple parton-parton interactions (MPI).  $J/\psi$  production is being studied in correlation with soft (charged particle multiplicity, angular correlations with charged hadrons) and hard processes (double  $J/\psi$  production,  $J/\psi - Z^0$  correlations, ...). Such observables are predicted to be sensitive to the production mechanism of the heavy flavour quark pair. Besides, the multiplicities attained in pp and p–Pb events at the LHC are above those measured in Au–Au at RHIC. Therefore it is interesting to investigate whether there could be QGP-like effects taking place also in those systems, such as the predicted suppression of  $J/\psi$  production in high multiplicity pp events. However, such behaviour has not been observed to date. Relative yields of open and hidden heavy flavoured hadrons have been studied as a function of relative multiplicity in pp and p–A by ALICE and CMS experiments at the LHC and by STAR at RHIC. Normalising the multiplicity to the average recovered in a given system at a given energy permits a direct comparison between different experiments and theory at various energies. The observed behaviour in either system is identical for all measurements in the same rapidity region regardless of the particle species. This suggests the phenomenon relates to the

production of the heavy quark pair rather than the hadronisation.

The second part of this thesis gives an overview of the ALICE experiment at the LHC. Detectors which are relevant for  $J/\psi$  measurements are described. The Muon Spectrometer is given a special attention as it is the main system which provided the data used in analyses presented in later chapters. We also explained the evaluation of acceptance-efficiency of the Muon Spectrometer and estimation of the uncertainty on tracking efficiency. The later incorporates the author’s personal contribution to estimation of the tracking efficiency systematic uncertainty in the data used later in the analysis of multiplicity differential  $J/\psi$  production in p–Pb collisions at  $\sqrt{s_{NN}} = 8.16$  TeV with ALICE at the LHC. This study, including creation of the ‘how-to’ documentation was performed as a part of author’s service task.

In the final part, we presented the two main subjects of this thesis which are the analysis of inclusive  $J/\psi$  production at forward rapidity in pp collisions at  $\sqrt{s} = 5.02$  TeV and the multiplicity differential  $J/\psi$  analysis in p–Pb collisions at  $\sqrt{s_{NN}} = 8.16$  TeV with ALICE at the LHC. These studies were based on the data from the ALICE Muon Spectrometer, collected during the LHC Run 2 data taking campaign.

Results of the pp analysis were discussed with similar measurements with ALICE at  $2.76 < \sqrt{s} < 13$  TeV in a paper entitled “Energy dependence of forward-rapidity  $J/\psi$  and  $\psi(2S)$  production in pp collisions at the LHC” [73]. The measurement was performed at forward rapidity  $2.5 < y < 4.0$ . The  $p_T$  differential cross section was further used as a reference for the  $R_{PbPb}$  measurement in Pb–Pb collisions at the same nucleon-nucleon centre-of-mass energy published in “ $J/\psi$  suppression at forward rapidity in Pb–Pb collisions at  $\sqrt{s_{NN}} = 5.02$  TeV” [100]. The inclusive  $J/\psi$  cross sections in pp were compared with theoretical models combining the NRQCD with CGC calculation for the small  $x$  gluon saturation in the incoming protons to describe the prompt contributions and a FONLL pQCD calculation to account for the  $b$ -hadrons feed down. The sum of these calculations agrees with the measurement at all energies. The evolution of the integrated cross section with  $\sqrt{s}$  was compared with CEM prediction, which qualitatively reproduces the measured shape of the dependence. The  $\psi(2S)$ -to- $J/\psi$  ratio computed at  $7 < \sqrt{s} < 13$  TeV presents a more rigorous test of the models as it allows for cancellation of various sources of systematic uncertainties both on data and on theory curves. The theoretical calculations overestimate this ratio. The mean transverse momentum  $\langle p_T \rangle$  of inclusive  $J/\psi$  shows a steady increase with collisions energy. Such hardening of the  $p_T$  spectra is believed to arise from the increase in production of  $b\bar{b}$  pairs with  $\sqrt{s}$  and to production of harder  $J/\psi$  with more energy being available in the system, resulting in potentially larger boost.

The p–Pb multiplicity dependent study was performed in two distinct rapidity regions of the yields measurement. At backward rapidity, the  $J/\psi$  were measured at  $-4.46 < y_{cms} < -2.96$ , while the forward rapidity yields were analysed at  $2.03 < y_{cms} < 3.53$ . The charged particle multiplicity was estimated from the SPD data at midrapidity  $|\eta| < 1$ . The 2016 p–Pb data were taken at high luminosities with high pile-up rate. We developed a custom event selection appropriate for this particular analysis in order to maximise our reach in multiplicity. The event selection applied in this analysis allowed for extraction of signal at nearly six times the average p–Pb charged particle multiplicity. The charged particle multiplicity was estimated from MC simulations, which present the leading contribution to the systematic uncertainty on multiplicity. The yields were normalised to the non-single diffractive event and corrected for the efficiency of the event selection. These corrections were taken from an independent analysis of the charged particle pseudorapidity density at midrapidity in p–Pb collisions at  $\sqrt{s_{NN}} = 8.16$  TeV (paper in preparation during writing of this manuscript). The self-normalised  $J/\psi$  yields display different behaviour at backward and forward rapidity. In the forward rapidity region, the increase with multiplicity is slower than linear. At backward rapidity on the other hand, the yields increase in a linear or even stronger-than-linear fashion with multiplicity. The increase in statistics enabled a decrease of systematic uncertainties on the yields with respect to the previous measurement at  $\sqrt{s_{NN}} = 5.02$  TeV from the LHC Run 1. The measurements at the two energies agree within uncertainties. The scaling in energy was expected from other relative results in pp (where similar measurements was performed at several energies), p–Pb, and Pb–Pb (for instance the  $R_{pPb}$  and  $R_{PbPb}$  also scale in energy). Theoretical calculations would be needed to understand the origin of the different behaviour in the two rapidity intervals. Our multiplicity integrated results are consistent with the measurement of the rapidity dependence of the  $R_{pPb}$  of inclusive  $J/\psi$  in the same data sample [130]. The  $R_{pPb}$  is suppressed at forward rapidity due to CNM effects, which is also a plausible explanation of the observed slower-than-linear increase of our forward

yields. Comparison with the preliminary results of the centrality dependent  $Q_{pPb}$  was also performed. The two measurements agree in the overlapping multiplicity interval. The advantage of our analysis is the extended multiplicity reach, which is almost doubled compared to the  $Q_{pPb}$  analysis.

The study of the  $\langle p_T \rangle$  of the inclusive  $J/\psi$  shows a saturation towards high multiplicity. Moreover, the shape of the  $\langle p_T \rangle$  evolution is identical between the two rapidity regions. As expected, the  $\langle p_T \rangle$  increases with the collision energy and with proximity to the midrapidity  $y \approx 0$ . The behaviour is independent of energy, as was also true for the yields.

In future measurements, it would be interesting to extend these studies into the beauty sector. Measurements of non-prompt  $J/\psi$  at midrapidity showed that the behaviour is compatible with the one observed for prompt  $J/\psi$  and prompt D-mesons. Besides, CMS studied the bottomonia multiplicity dependence and found similar behaviour as ALICE did for charmonia.

Correlating the multiplicity measured at forward rapidity with forward  $J/\psi$  allows for studies of possible auto-correlations. No such study was published to date for charmonia. However, measurements of open charmed hadrons and bottomia suggest that indeed behaviour consistent with such scenario is observed.

Last but not least, measuring the relative charged particle pseudorapidity density does not allow for direct comparison between pp and p-Pb data. The physics behind the different behaviour in pp and p-Pb is not the same in the two systems. Finding an observable that would relate to the same processes in both systems is an open question.



## Chapitre 1: Introduction

Le modèle standard est une théorie qui décrit les particules fondamentales et leurs interactions. Il contient l'interaction forte qui se manifeste par un échange de gluons colorés entre les particules chargées de couleur, c'est-à-dire les quarks et les gluons. Dans des conditions normales, les quarks sont toujours confinés dans des hadrons de couleur neutre. Cependant, en raison de la polarisation du vide QCD, le couplage s'affaiblit avec l'augmentation de l'énergie transférée dans les interactions. En conséquence, les quarks deviennent asymptotiquement libres aux hautes énergies. La matière hadronique connaît donc une transition vers un état de partons déconfinés, appelé Plasma de Quark Gluon (QGP).

Le QGP existait dans l'univers primordial quelques microsecondes après le Big Bang. Il peut être recréé en laboratoire lors de collisions d'ions lourds ultrarelativistes. Comme le QGP a une très courte durée de vie, il est impossible de mesurer ses propriétés directement. Au lieu de cela, nous mesurons des signatures indirectes de la formation du milieu déconfiné. La suppression de  $J/\psi$  est une de ces signatures et sera abordée dans le prochain chapitre.

## Chapitre 2: Production de $J/\psi$ dans des collisions de hadrons ultrarelativistes

Le  $J/\psi$  et d'autres charmonia ont été largement étudiés en collisions pp, p-A et A-A. Dans les collisions proton-proton, la production des  $J/\psi$  combine les processus à grands et à petits transferts d'impulsion. La mesure des taux de production de différents charmonia dans des gammes cinématiques spécifiques est nécessaire pour mieux contraindre les calculs théoriques décrivant les mesures de section efficace et de polarisation. La polarisation, en particulier, représente un défi pour les modèles actuels.

Dans les collisions noyau-noyau, les charmonia servent des sondes du milieu déconfiné. Les états liés  $c\bar{c}$  sont écartés dans le QGP. De plus, la régénération des charmonia à partir des (anti-)quarks charmés libres dans le milieu devient plus importante avec l'augmentation de l'énergie de la collision et joue un rôle important aux énergies du LHC.

Dans les collisions proton-noyau, les taux de productions sont modifiés par rapport aux taux dans les collisions de proton-proton. Cette modification est causée par des effets qu'on appelle des effets de la matière nucléaire froide (CNM effects). Les effets de suppression et d'augmentation observés par rapport à pp sont reproduits par les modèles prenant en compte différents effets CNM. Cependant, l'incertitude des mesures et des modèles ne permettent pas de déterminer l'importance relative des effets individuels. Des mesures plus précises seraient nécessaires pour déterminer quels effets jouent le rôle principal et dans quelles conditions.

## Chapitre 3: La production des quarks lourds en fonction de la multiplicité

Depuis le début de l'exploitation du LHC, il est devenu évident que les collisions proton-proton sont plus complexes qu'envisagé auparavant. Ceux-ci peuvent contenir de multiples interactions parton-parton. Cependant, les collisions pp restent le meilleur point de départ pour l'étude d'événements

plus complexes produits dans les collisions p–A et A–A. Par conséquent, il est nécessaire de bien comprendre les processus se déroulant dans les événements pp.

Des corrélations entre les hadrons de saveurs lourdes avec l'événement sous-jacent et/ou d'autres processus durs et mous sont essentielles pour mieux contraindre les modèles décrivant la production de sondes dures. Ils peuvent également nous aider à comprendre plus en détail les processus élémentaires intervenant dans une collision proton-proton.

Il existe de nombreux modèles théoriques qui étudient la production de charme en fonction de la multiplicité dans les collisions pp et p–A. Les modèles abordés dans ce travail utilisent les Interactions Partoniques Multiples (MPI) d'une manière ou d'une autre pour obtenir un bon accord avec les données. Ils incluent également d'autres processus durs et mous qui contribuent au comportement observé.

La mesure des mesons D et  $J/\psi$  dans les collisions pp a montré que la dépendance de leur production en fonction de la multiplicité ne provient pas des processus d'hadronisation. Elle est plutôt liée à la production de la paire de quarks lourds. Pour étudier les auto-corrélations possibles dans le cas où les hadrons et la multiplicité sont mesurés à la même rapidité, des études avec un écart en  $\eta$  ont été introduites. Les résultats sur les hadrons charmés à rapidité centrale ont montré que l'introduction d'un écart en  $\eta$  entre les mesures en pp n'a aucun effet sur la nature de l'augmentation des taux de production. Par contre, les résultats de CMS pour des  $\Upsilon$  suggèrent que, dans les collisions pp, les taux de production sont sensibles à l'intervalle de rapidité auquel la multiplicité est mesurée. De plus, l'écart en  $\eta$  joue un rôle dans les collisions p–Pb. Les mesons D montrent une augmentation plus forte lorsque la fenêtre de rapidité des mesures de taux de production et de multiplicité se chevauchent. On peut comprendre que cette différence a pour origine les effets collectifs se produisant dans les collisions p–Pb qui sont plus prononcées dans la région de rapidité centrale.

ALICE mesure les  $J/\psi$  à la rapidité vers l'avant et vers l'arrière en fonction de la multiplicité des particules chargées à rapidité centrale. Une telle mesure nous permet d'étudier les effets de CNM à une petite fraction de quantité de mouvement  $x$  de parton à l'intérieur du nucléon (sens vers l'avant). La mesure à une grande fraction de quantité de mouvement  $x$  (sens vers l'arrière) montre une augmentation cohérente avec celle observée pour les mésons D mesurés à rapidité centrale. Les données de CMS montrent également une plus forte suppression du taux de production vers l'avant lors d'événements à forte multiplicité, ce qui est attribué à la présence des effets CNM dans la région vers l'avant. La suppression des taux de production dans les collisions p–Pb par rapport à pp diffère entre  $J/\psi$  prompt et non prompt, suggérant différents effets CNM affectant chaque de ces deux contributions. Jusqu'à présent, aucune mesure de  $J/\psi$  vers l'avant n'a été effectuée en fonction de la multiplicité vers l'avant ou vers l'arrière. Une telle mesure fournira une autre pièce à ce casse-tête intéressant.

En complément, ALICE a également étudié des hadrons étranges en fonction de la multiplicité et a observé une transition douce lorsqu'on passe des collisions pp à faible multiplicité aux collisions centrales Pb–Pb. Cependant, l'augmentation de l'étrangeté observée avec l'activité d'un événement n'est pas attribuée à de multiples diffusions dures, comme c'est le cas pour le charme et la beauté, mais à une densité d'énergie plus élevée disponible pour la production de particules.

## Chapitre 4 et 5: Environnement expérimental

ALICE est une expérience dédiée aux ions lourds au LHC. Le détecteur se compose de près de vingt sous-systèmes regroupés en deux parties principales : le tonneau central à rapidité centrale  $|y| < 0.9$  et le spectromètre à muons dans la rapidité vers l'avant  $-4 < y < -2.5$ .

Le spectromètre à muons mesure les muons provenant de désintégrations de quarkonia, de mésons vecteurs de faible masse, de bosons de jauge, du Drell-Yan et de désintégrations des mesons D et B. Le spectromètre comprend un ensemble de chambres de trajectographie, un aimant dipolaire, un ensemble de chambres de déclenchement et un ensemble d'absorbeurs. Nous avons examiné le principe de fonctionnement des chambres de trajectographie et de déclenchement et expliqué la reconstruction des trajectoires de muons.

Pour calculer la section efficace de la production des particules mesurées dans le spectromètre à muons, nous devons calculer l'acceptance-efficacité  $A\epsilon$  du spectromètre et l'incertitude correspondante. L'incertitude systématique sur le facteur  $A\epsilon$  provient de plusieurs sources : les paramètres de distributions du MC, l'efficacité de reconstruction du système de trajectographe et de déclenchement, ...

Dans cette thèse, nous avons expliqué plus en détail l'estimation de l'incertitude sur l'efficacité de reconstruction du système de trajectographe et présenté les résultats obtenus pour la période de

données p-Pb à  $\sqrt{s_{\text{NN}}} = 8.16$  TeV. La méthode utilisée pour estimer l'incertitude sur l'efficacité de reconstruction du système de trajectographe repose sur la redondance des éléments de détection dans chacune des cinq stations de trajectographie. L'efficacité est calculée à partir des données et des simulations Monte Carlo dont les distributions étaient optimisées sur les données. L'incertitude sur l'efficacité de reconstruction du système de trajectographe correspond au rapport de l'efficacité obtenue à partir des données et de l'efficacité simulée.

## Chapitre 6: Section efficace $\sigma_{J/\psi}^{\text{pp}}$

Dans ce chapitre, nous avons examiné l'analyse de la production de  $J/\psi$  inclusive dans les collisions pp à  $\sqrt{s} = 5.02$  TeV. Les  $J/\psi$  ont été étudiés dans leur canal de désintégration en dimuon. La section efficace des  $J/\psi$  inclusifs a été mesurée dans la région de rapidité  $2.5 < y < 4.0$  et jusqu'à  $p_{\text{T}} = 12$  GeV/c. Les résultats sont illustrés sur la Fig. 9.1. Les résultats différentiels ont été comparés à des calculs NRQCD + FONLL afin de prendre en compte la contribution non-prompt dans les données. Un accord qualitatif et quantitatif a été observé entre les données et les courbes théoriques. Les résultats ont également été étudiés dans le contexte d'autres mesures d'ALICE à rapidité vers l'avant, à des énergies comprises entre  $2.76 \leq \sqrt{s} \leq 13$  TeV. La section efficace du  $J/\psi$  montre une augmentation constante avec  $\sqrt{s}$ . Un durcissement du spectre en  $p_{\text{T}}$  a également été observé avec une augmentation de l'énergie de collision. Ce dernier phénomène peut s'expliquer par une combinaison de deux effets. Premièrement, la production de  $b\bar{b}$  augmente avec l'énergie des collisions et entraîne une augmentation du nombre de  $J/\psi$  non-prompts créés à plus hauts  $p_{\text{T}}$ . Deuxièmement, étant donné que plus d'énergie est disponible pour la production de particules lors d'une seule collision, plus de  $J/\psi$  prompts sont créés à plus haut  $p_{\text{T}}$ . De plus, la section efficace intégrées en  $p_{\text{T}}$  et  $y$  à 5.02 TeV et la section efficace différentielle en  $p_{\text{T}}$  à 5.02 TeV ont été utilisées comme référence pour la mesure du  $R_{\text{AA}}$  à  $\sqrt{s_{\text{NN}}} = 5.02$  TeV.

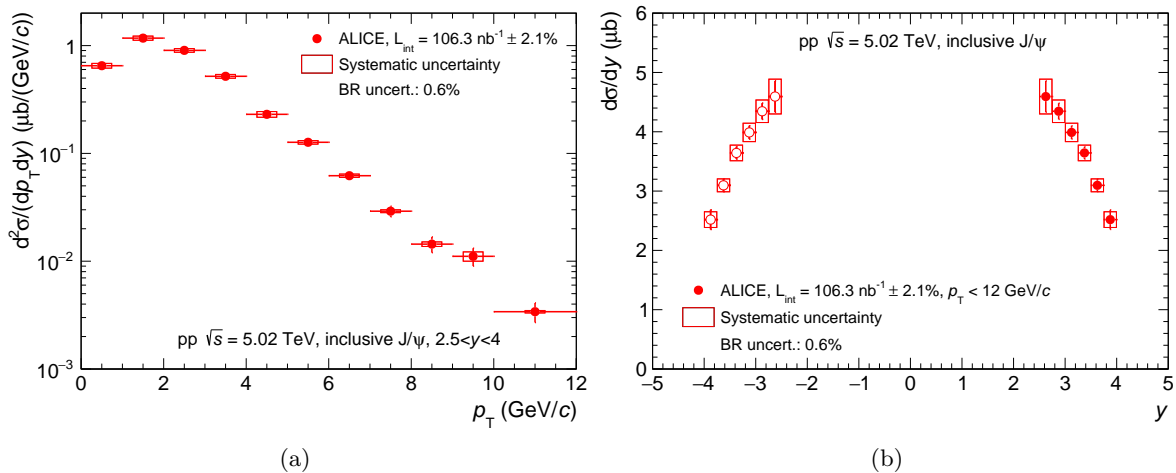


Figure 9.1: Section efficace inclusive de  $J/\psi$  différentielle en fonction de (a)  $p_{\text{T}}$  et (b)  $y$  dans des collisions pp à  $\sqrt{s} = 5.02$  TeV [73].

## Chapitre 7 et 8: Production de $J/\psi$ en fonction de la multiplicité dans les collisions p-Pb

Dans ce chapitre, nous avons présenté les taux de production relatifs différentiels de  $J/\psi$  en fonction de la multiplicité mesurés dans des collisions p-Pb à  $\sqrt{s_{\text{NN}}} = 8.16$  TeV. La multiplicité des particules chargées a été mesurée à rapidité centrale  $|\eta_{\text{lab}}| < 1$ . Les  $J/\psi$  inclusifs ont été mesurés dans la région de rapidité  $2.5 < y_{\text{lab}} < 4.0$ . En raison de l'asymétrie de la collision p-Pb cela a permis de sonder deux régions de rapidité du centre de masse différentes, à rapidité vers l'avant  $2.03 < y_{\text{cms}} < 3.53$  et à rapidité vers l'arrière  $-4.46 < y_{\text{cms}} < -2.96$ , voir Fig. 9.2.

Les taux de production montrent une augmentation avec la multiplicité, et dépend de la rapidité où sont mesurés les  $J/\psi$ . Une telle observation est compatible avec l'évolution de la suppression de  $J/\psi$

en fonction de la rapidité et mesuré dans les collisions p–Pb. Les comportements différents à rapidité vers l’avant ou vers l’arrière peuvent être expliqués par les effets de la matière nucléaire froide. Les taux de production relatifs ont été comparés à la mesure précédente à  $\sqrt{s_{\text{NN}}} = 5.02$  TeV. Nous avons constaté qu’en corrélant les taux de production relatifs et la multiplicité relative, la dépendance en énergie disparaît. La statistique plus importante de l’échantillon à 8.16 TeV nous a permis d’atteindre des multiplicités plus élevées et de réduire l’incertitude dans la plage de multiplicité commune.

Nous avons également étudié la dépendance en fonction de la multiplicité de l’impulsion transverse moyenne  $\langle p_T \rangle$  des  $J/\psi$  inclusifs dans les collisions p–Pb à  $\sqrt{s_{\text{NN}}} = 8.16$  TeV, voir Fig. 9.3. La méthode appliquée nous a permis d’extraire  $\langle p_T \rangle$  à des multiplicités élevées.

Lorsque la multiplicité est faible, le  $\langle p_T \rangle$  augmente fortement jusqu’à saturation autour de la multiplicité relative  $dN_{\text{ch}}/d\eta / \langle dN_{\text{ch}}/d\eta \rangle \sim 1$  et au-delà. Le  $\langle p_T \rangle$  est plus grand à rapidité vers l’avant qu’à rapidité vers l’arrière, mais qualitativement, le comportement est similaire dans les deux intervalles de rapidité. De plus, les résultats montrent qualitativement le même comportement que celui observé lors de collisions p–Pb à basse énergie à 5.02 TeV.

L’impulsion transverse moyenne relative  $\langle p_T \rangle^R$  montre le même comportement dans les deux intervalles de rapidité et est identique aux deux énergies. Le  $\langle p_T \rangle^R$  sature autour de l’unité pour la multiplicité moyenne  $dN_{\text{ch}}/d\eta / \langle dN_{\text{ch}}/d\eta \rangle \sim 1$ .

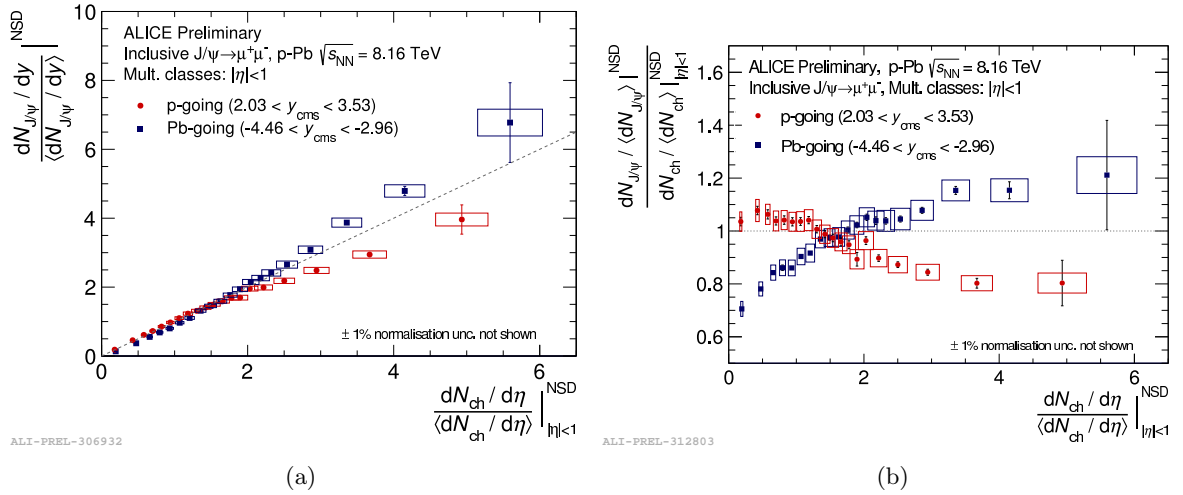
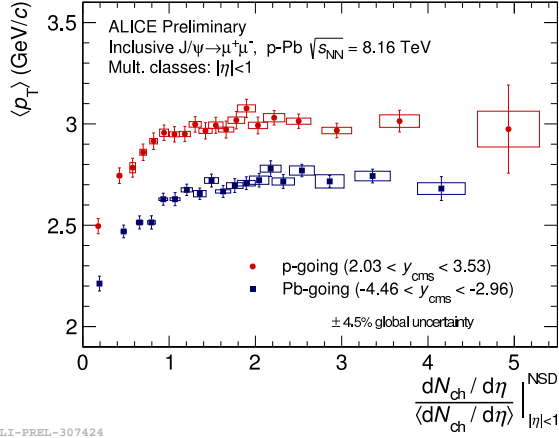
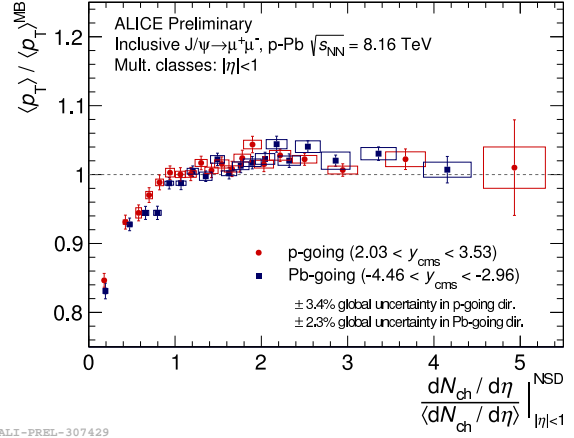


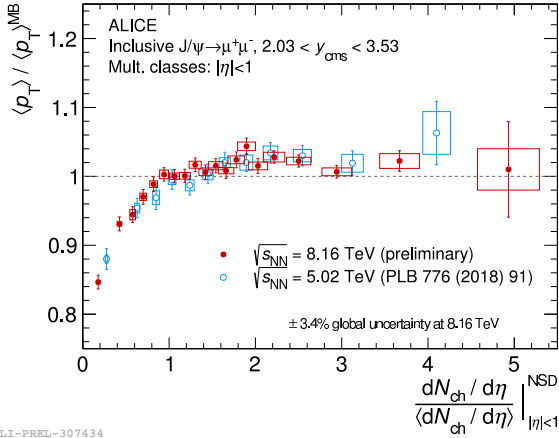
Figure 9.2: **(a)** Les taux de production des  $J/\psi$  en fonction de la multiplicité des particules chargées dans des collisions p–Pb à rapidité vers l’avant (rouge) et à rapidité vers l’arrière (bleu) à  $\sqrt{s_{\text{NN}}} = 8.16$  TeV. L’incertitude due à la normalisation et au vertex est citée séparément. L’incertitude sur l’axe de la multiplicité est partiellement corrélée en multiplicité. **(b)** Identique à (a) mais divisé par la diagonale.



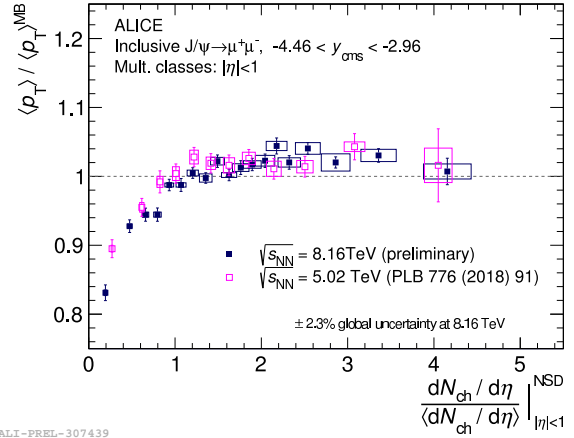
(a)



(b)



(c)



(d)

Figure 9.3: **(a)**  $\langle p_T \rangle$  absolu des  $J/\psi$  en fonction de la multiplicité relative des particules chargées. **(b)**  $\langle p_T \rangle^R$  relative des  $J/\psi$  en fonction de la multiplicité relative des particules chargées. **(c)**  $\langle p_T \rangle^R$  relative en fonction de la multiplicité à la rapidité vers l'avant dans les collisions p-Pb à 8.16 et 5.02 TeV. **(d)**  $\langle p_T \rangle^R$  relative en fonction de la multiplicité à la rapidité vers l'arrière dans les collisions p-Pb à 8.16 et 5.02 TeV.



## BIBLIOGRAPHY

- [1] **Particle Data Group** Collaboration, M. Tanabashi *et al.*, “Review of Particle Physics,” *Phys. Rev. D* **98** no. 030001, (2018) . 9, 11, 19, 20, 21, 93, 96, 152, 219, 229
- [2] D. Griffiths, *Introduction to elementary particles*. 2008. 10, 20, 229
- [3] **ATLAS** Collaboration, G. Aad *et al.*, “Observation of a new particle in the search for the Standard Model Higgs boson with the ATLAS detector at the LHC,” *Phys. Lett. B* **716** (2012) 1–29, [arXiv:1207.7214 \[hep-ex\]](#). CERN-PH-EP-2012-218. 10, 59
- [4] **CMS** Collaboration, S. Chatrchyan *et al.*, “Observation of a new boson at a mass of 125 GeV with the CMS experiment at the LHC,” *Phys. Lett. B* **716** (2012) 30–61, [arXiv:1207.7235 \[hep-ex\]](#). CMS-HIG-12-028, CERN-PH-EP-2012-220. 10, 59
- [5] **Belle** Collaboration, S. K. Choi *et al.*, “Observation of a resonance-like structure in the  $\pi^+\pi^-\psi'$  mass distribution in exclusive  $B \rightarrow J/\psi K^-\pi^+\pi^-\psi'$  decays,” *Phys. Rev. Lett.* **100** (2008) 142001, [arXiv:0708.1790 \[hep-ex\]](#). 10
- [6] **LHCb** Collaboration, R. Aaij *et al.*, “Observation of  $J/\psi$  Resonances Consistent with Pentaquark States in  $\Lambda_b^0 \rightarrow J/\psi K^- p$  Decays,” *Phys. Rev. Lett.* **115** (2015) 072001, [arXiv:1507.03414 \[hep-ex\]](#). 10
- [7] F. Mandl and G. Shaw, *Quantum field theory*. Wiley, 2nd ed ed., 2010. 11
- [8] S. Sarkar, H. Satz, and B. Sinha, “The physics of the quark-gluon plasma,” *Lect. Notes Phys.* **785** (2010) pp.1–369. 12, 13, 16, 219
- [9] Z. Fodor and S. D. Katz, “Critical point of QCD at finite T and  $\mu$ , lattice results for physical quark masses,” *JHEP* **04** (2004) 050, [arXiv:hep-lat/0402006 \[hep-lat\]](#). 12
- [10] **STAR** Collaboration, M. M. Aggarwal *et al.*, “An Experimental Exploration of the QCD Phase Diagram: The Search for the Critical Point and the Onset of De-confinement,” [arXiv:1007.2613 \[nucl-ex\]](#). 12, 219
- [11] J. D. Bjorken, “Highly Relativistic Nucleus-Nucleus Collisions: The Central Rapidity Region,” *Phys. Rev. D* **27** (1983) 140–151. 13, 45
- [12] M. L. Miller, K. Reygers, S. J. Sanders, and P. Steinberg, “Glauber modeling in high energy nuclear collisions,” *Ann. Rev. Nucl. Part. Sci.* **57** (2007) 205–243, [arXiv:nucl-ex/0701025 \[nucl-ex\]](#). 14, 219
- [13] **ALICE** Collaboration, B. Abelev *et al.*, “Centrality determination of Pb-Pb collisions at  $\sqrt{s_{NN}} = 2.76$  TeV with ALICE,” *Phys. Rev. C* **88** no. 4, (2013) 044909, [arXiv:1301.4361 \[nucl-ex\]](#). 14, 45
- [14] R. Vogt, *Ultrarelativistic heavy-ion collisions*. Elsevier, Amsterdam, 2007. 14, 20, 21, 24, 29, 229
- [15] S. Voloshin and Y. Zhang, “Flow study in relativistic nuclear collisions by Fourier expansion of Azimuthal particle distributions,” *Z. Phys. C* **70** (1996) 665–672, [arXiv:hep-ph/9407282 \[hep-ph\]](#). 16

- [16] **CMS** Collaboration, V. Khachatryan *et al.*, “Evidence for transverse momentum and pseudorapidity dependent event plane fluctuations in PbPb and pPb collisions,” *Phys. Rev. C* **92** no. 3, (2015) 034911, [arXiv:1503.01692](https://arxiv.org/abs/1503.01692) [nucl-ex]. 16
- [17] **ALICE** Collaboration, K. Aamodt *et al.*, “Higher harmonic anisotropic flow measurements of charged particles in Pb-Pb collisions at  $\sqrt{s_{NN}}=2.76$  TeV,” *Phys. Rev. Lett.* **107** (2011) 032301, [arXiv:1105.3865](https://arxiv.org/abs/1105.3865) [nucl-ex].
- [18] **ATLAS** Collaboration, G. Aad *et al.*, “Measurement of the azimuthal anisotropy for charged particle production in  $\sqrt{s_{NN}} = 2.76$  TeV lead-lead collisions with the ATLAS detector,” *Phys. Rev. C* **86** (2012) 014907, [arXiv:1203.3087](https://arxiv.org/abs/1203.3087) [hep-ex]. 16
- [19] C. Y. Wong, *Introduction to high-energy heavy ion collisions*. 1995. 16
- [20] P. Braun-Munzinger, K. Redlich, and J. Stachel, “Particle production in heavy ion collisions,” [arXiv:nuc1-th/0304013](https://arxiv.org/abs/nuc1-th/0304013) [nucl-th]. 17
- [21] R. C. Hwa and X. N. Wang, eds., *Quark-gluon plasma. Vol. 3*. 2004.
- [22] J. Stachel, A. Andronic, P. Braun-Munzinger, and K. Redlich, “Confronting LHC data with the statistical hadronization model,” *J. Phys. Conf. Ser.* **509** (2014) 012019, [arXiv:1311.4662](https://arxiv.org/abs/1311.4662) [nucl-th]. 17, 219
- [23] **ATLAS** Collaboration, G. Aad *et al.*, “Measurement of  $Z$  boson Production in Pb+Pb Collisions at  $\sqrt{s_{NN}} = 2.76$  TeV with the ATLAS Detector,” *Phys. Rev. Lett.* **110** no. 2, (2013) 022301, [arXiv:1210.6486](https://arxiv.org/abs/1210.6486) [hep-ex]. 17
- [24] **CMS** Collaboration, S. Chatrchyan *et al.*, “Study of  $Z$  production in PbPb and pp collisions at  $\sqrt{s_{NN}} = 2.76$  TeV in the dimuon and dielectron decay channels,” *JHEP* **03** (2015) 022, [arXiv:1410.4825](https://arxiv.org/abs/1410.4825) [nucl-ex]. 17, 18, 219
- [25] **ALICE** Collaboration, S. Acharya *et al.*, “Measurement of  $Z^0$ -boson production at large rapidities in Pb-Pb collisions at  $\sqrt{s_{NN}} = 5.02$  TeV,” *Phys. Lett.* **B780** (2018) 372–383, [arXiv:1711.10753](https://arxiv.org/abs/1711.10753) [nucl-ex]. 17
- [26] **SLAC-SP-017** Collaboration, J. E. Augustin *et al.*, “Discovery of a Narrow Resonance in  $e^+e^-$  Annihilation,” *Phys. Rev. Lett.* **33** (1974) 1406–1408. [Adv. Exp. Phys.5,141(1976)]. 19
- [27] **E598** Collaboration, J. J. Aubert *et al.*, “Experimental Observation of a Heavy Particle  $J$ ,” *Phys. Rev. Lett.* **33** (1974) 1404–1406. 19
- [28] S. L. Glashow, J. Iliopoulos, and L. Maiani, “Weak Interactions with Lepton-Hadron Symmetry,” *Phys. Rev.* **D2** (1970) 1285–1292. 19
- [29] J. Hořejší, *Fundamentals of electroweak theory*. 2002. 19
- [30] “The Nobel Prize in Physics 1976”. Nobelprize.org. Nobel Media AB 2014. Web. 26 Feb 2018..” [http://www.nobelprize.org/nobel\\_prizes/physics/laureates/1976/](http://www.nobelprize.org/nobel_prizes/physics/laureates/1976/). 19
- [31] G. S. Abrams *et al.*, “The Discovery of a Second Narrow Resonance in  $e^+e^-$  Annihilation,” *Phys. Rev. Lett.* **33** (1974) 1453–1455. [Adv. Exp. Phys.5,150(1976)]. 19
- [32] S. Okubo, “Phi meson and unitary symmetry model,” *Phys. Lett.* **5** (1963) 165–168. 20
- [33] G. Zweig, “An  $SU_3$  model for strong interaction symmetry and its breaking; Version 2,”. <http://cds.cern.ch/record/570209>.
- [34] J. Iizuka, “A systematics and phenomenology of meson family,” *Progress of Theoretical Physics Supplement* **37-38** (1966) 21–34, [/oup/backfile/content\\_public/journal/ptps/37-38/10.1143/ptps.37.21/2/37-38-21.pdf](http://oup/backfile/content_public/journal/ptps/37-38/10.1143/ptps.37.21/2/37-38-21.pdf). <http://dx.doi.org/10.1143/PTPS.37.21>. 20
- [35] **LHCb** Collaboration, R. Aaij *et al.*, “Measurement of the ratio of prompt  $\chi_c$  to  $J/\psi$  production in  $pp$  collisions at  $\sqrt{s} = 7$  TeV,” *Phys. Lett.* **B718** (2012) 431–440, [arXiv:1204.1462](https://arxiv.org/abs/1204.1462) [hep-ex]. 22

- [36] **LHCb** Collaboration, R. Aaij *et al.*, “Measurement of  $\psi(2S)$  meson production in pp collisions at  $\sqrt{s}=7$  TeV,” *Eur. Phys. J.* **C72** (2012) 2100, [arXiv:1204.1258 \[hep-ex\]](#). 22
- [37] **ALICE** Collaboration, B. Abelev *et al.*, “Measurement of prompt  $J/\psi$  and beauty hadron production cross sections at mid-rapidity in  $pp$  collisions at  $\sqrt{s} = 7$  TeV,” *JHEP* **11** (2012) 065, [arXiv:1205.5880 \[hep-ex\]](#). 22, 23, 219
- [38] **ATLAS** Collaboration, G. Aad *et al.*, “Measurement of the differential cross-sections of inclusive, prompt and non-prompt  $J/\psi$  production in proton-proton collisions at  $\sqrt{s} = 7$  TeV,” *Nucl. Phys.* **B850** (2011) 387–444, [arXiv:1104.3038 \[hep-ex\]](#). 23, 219
- [39] **CMS** Collaboration, V. Khachatryan *et al.*, “Prompt and non-prompt  $J/\psi$  production in  $pp$  collisions at  $\sqrt{s} = 7$  TeV,” *Eur. Phys. J.* **C71** (2011) 1575, [arXiv:1011.4193 \[hep-ex\]](#). 22, 23, 219
- [40] **LHCb** Collaboration, R. Aaij *et al.*, “Measurement of  $J/\psi$  production in  $pp$  collisions at  $\sqrt{s} = 7$  TeV,” *Eur. Phys. J.* **C71** (2011) 1645, [arXiv:1103.0423 \[hep-ex\]](#). 22, 28, 29, 116, 190, 219
- [41] **LHCb** Collaboration, R. Aaij *et al.*, “Measurement of forward  $J/\psi$  production cross-sections in  $pp$  collisions at  $\sqrt{s} = 13$  TeV,” *JHEP* **10** (2015) 172, [arXiv:1509.00771 \[hep-ex\]](#). [Erratum: *JHEP*05,063(2017)]. 22, 23, 28, 116, 219
- [42] A. Andronic *et al.*, “Heavy-flavour and quarkonium production in the LHC era: from proton–proton to heavy-ion collisions,” *Eur. Phys. J.* **C76** no. 3, (2016) 107, [arXiv:1506.03981 \[nucl-ex\]](#). 24, 30, 31, 219
- [43] C.-H. Chang, “Hadronic Production of  $J/\psi$  Associated With a Gluon,” *Nucl. Phys.* **B172** (1980) 425–434. 24
- [44] G. T. Bodwin, E. Braaten, and G. P. Lepage, “Rigorous QCD analysis of inclusive annihilation and production of heavy quarkonium,” *Phys. Rev.* **D51** (1995) 1125–1171, [arXiv:hep-ph/9407339 \[hep-ph\]](#). [Erratum: *Phys. Rev.*D55,5853(1997)]. 24
- [45] **CDF** Collaboration, F. Abe *et al.*, “ $J/\psi$  and  $\psi(2S)$  production in  $p\bar{p}$  collisions at  $\sqrt{s} = 1.8$  TeV,” *Phys. Rev. Lett.* **79** (1997) 572–577. 25, 219
- [46] M. Krämer, “Quarkonium production at high-energy colliders,” *Prog. Part. Nucl. Phys.* **47** (2001) 141–201, [arXiv:hep-ph/0106120 \[hep-ph\]](#). 25, 219
- [47] **CDF** Collaboration, T. Affolder *et al.*, “Measurement of  $J/\psi$  and  $\psi(2S)$  polarization in  $p\bar{p}$  collisions at  $\sqrt{s} = 1.8$  TeV,” *Phys. Rev. Lett.* **85** (2000) 2886–2891, [arXiv:hep-ex/0004027 \[hep-ex\]](#). 25, 219
- [48] M. Beneke and M. Krämer, “Direct  $J/\psi$  and  $\psi'$  polarization and cross-sections at the Tevatron,” *Phys. Rev.* **D55** (1997) 5269–5272, [arXiv:hep-ph/9611218 \[hep-ph\]](#). 25, 219
- [49] E. Braaten, B. A. Kniehl, and J. Lee, “Polarization of prompt  $J/\psi$  at the Tevatron,” *Phys. Rev.* **D62** (2000) 094005, [arXiv:hep-ph/9911436 \[hep-ph\]](#). 25, 219
- [50] **STAR** Collaboration, L. Adamczyk *et al.*, “ $J/\psi$  production at high transverse momenta in  $p + p$  and Au+Au collisions at  $\sqrt{s_{NN}} = 200$  GeV,” *Phys. Lett.* **B722** (2013) 55–62, [arXiv:1208.2736 \[nucl-ex\]](#). 25, 26, 219
- [51] **STAR** Collaboration, B. I. Abelev *et al.*, “ $J/\psi$  production at high transverse momentum in  $p+p$  and Cu+Cu collisions at  $\sqrt{s_{NN}} = 200$  GeV,” *Phys. Rev.* **C80** (2009) 041902, [arXiv:0904.0439 \[nucl-ex\]](#). 26, 219
- [52] **STAR** Collaboration, J. Adam *et al.*, “ $J/\psi$  production cross section and its dependence on charged-particle multiplicity in  $p + p$  collisions at  $\sqrt{s} = 200$  GeV,” [arXiv:1805.03745 \[hep-ex\]](#). 25, 26, 51, 219
- [53] **PHENIX** Collaboration, A. Adare *et al.*, “Measurement of Transverse Single-Spin Asymmetries for  $J/\psi$  Production in Polarized  $p + p$  Collisions at  $\sqrt{s} = 200$  GeV,” *Phys. Rev.* **D82** (2010) 112008, [arXiv:1009.4864 \[hep-ex\]](#). [Erratum: *Phys. Rev.*D86,099904(2012)]. 25, 26, 219

- [54] V. D. Barger, W.-Y. Keung, and R. J. N. Phillips, “On psi and Upsilon Production via Gluons,” *Phys. Lett.* **91B** (1980) 253–258. 25, 26, 219
- [55] V. D. Barger, W.-Y. Keung, and R. J. N. Phillips, “Hadroproduction of  $\psi$  and  $\Upsilon$ ,” *Z. Phys.* **C6** (1980) 169. 25
- [56] Y.-Q. Ma, K. Wang, and K.-T. Chao, “A complete NLO calculation of the  $J/\psi$  and  $\psi'$  production at hadron colliders,” *Phys. Rev.* **D84** (2011) 114001, [arXiv:1012.1030 \[hep-ph\]](#). 25
- [57] Y.-Q. Ma and R. Venugopalan, “Comprehensive Description of  $J/\psi$  Production in Proton-Proton Collisions at Collider Energies,” *Phys. Rev. Lett.* **113** no. 19, (2014) 192301, [arXiv:1408.4075 \[hep-ph\]](#). 25, 26, 115, 116, 219
- [58] **STAR** Collaboration, L. Adamczyk *et al.*, “ $J/\psi$  polarization in p+p collisions at  $\sqrt{s} = 200$  GeV in STAR,” *Phys. Lett.* **B739** (2014) 180–188, [arXiv:1311.1621 \[nucl-ex\]](#). 26
- [59] **PHENIX** Collaboration, A. Adare *et al.*, “Transverse momentum dependence of  $J/\psi$  polarization at midrapidity in p+p collisions at  $\sqrt{s} = 200$ -GeV,” *Phys. Rev.* **D82** (2010) 012001, [arXiv:0912.2082 \[hep-ex\]](#). 26
- [60] J. P. Lansberg, “ $J/\psi$  production at  $\sqrt{s}=1.96$  and 7 TeV: Color-Singlet Model, NNLO\* and polarisation,” *J. Phys.* **G38** (2011) 124110, [arXiv:1107.0292 \[hep-ph\]](#). 26
- [61] H. S. Chung, C. Yu, S. Kim, and J. Lee, “Polarization of prompt  $J/\psi$  in proton-proton collisions at RHIC,” *Phys. Rev.* **D81** (2010) 014020, [arXiv:0911.2113 \[hep-ph\]](#). 26
- [62] **ATLAS** Collaboration, G. Aad *et al.*, “Measurement of the differential cross-sections of prompt and non-prompt production of  $J/\psi$  and  $\psi(2S)$  in  $pp$  collisions at  $\sqrt{s} = 7$  and 8 TeV with the ATLAS detector,” *Eur. Phys. J.* **C76** no. 5, (2016) 283, [arXiv:1512.03657 \[hep-ex\]](#). 26, 27, 28, 219
- [63] **CMS** Collaboration, A. M. Sirunyan *et al.*, “Measurement of quarkonium production cross sections in  $pp$  collisions at  $\sqrt{s} = 13$  TeV,” *Phys. Lett.* **B780** (2018) 251–272, [arXiv:1710.11002 \[hep-ex\]](#). 27, 219
- [64] **CMS** Collaboration, V. Khachatryan *et al.*, “Measurement of  $J/\psi$  and  $\psi(2S)$  Prompt Double-Differential Cross Sections in  $pp$  Collisions at  $\sqrt{s}=7$  TeV,” *Phys. Rev. Lett.* **114** no. 19, (2015) 191802, [arXiv:1502.04155 \[hep-ex\]](#). 26, 27, 219
- [65] Y.-Q. Ma, K. Wang, and K.-T. Chao, “ $J/\psi(\psi')$  production at the Tevatron and LHC at  $\mathcal{O}(\alpha_s^4 v^4)$  in nonrelativistic QCD,” *Phys. Rev. Lett.* **106** (2011) 042002, [arXiv:1009.3655 \[hep-ph\]](#). 26, 27, 115, 116, 119, 219, 223
- [66] M. Cacciari, S. Frixione, and P. Nason, “The  $p_T$  spectrum in heavy flavor photoproduction,” *JHEP* **03** (2001) 006, [arXiv:hep-ph/0102134 \[hep-ph\]](#). 26, 27, 43, 219
- [67] M. Cacciari, S. Frixione, N. Houdeau, M. L. Mangano, P. Nason, and G. Ridolfi, “Theoretical predictions for charm and bottom production at the LHC,” *JHEP* **10** (2012) 137, [arXiv:1205.6344 \[hep-ph\]](#). 26, 27, 115, 116, 219
- [68] **ALICE** Collaboration, K. Aamodt *et al.*, “Rapidity and transverse momentum dependence of inclusive  $J/\psi$  production in  $pp$  collisions at  $\sqrt{s} = 7$  TeV,” *Phys. Lett.* **B704** (2011) 442–455, [arXiv:1105.0380 \[hep-ex\]](#). [Erratum: *Phys. Lett.*B718,692(2012)]. 26, 28
- [69] **CMS Collaboration** Collaboration, “Quarkonium production cross sections in  $pp$  collisions at  $\sqrt{s} = 13$  TeV,” Tech. Rep. CMS-PAS-BPH-15-005, CERN, Geneva, 2016. <https://cds.cern.ch/record/2145411>. 26, 28, 219
- [70] **LHCb** Collaboration, R. Aaij *et al.*, “Measurement of  $J/\psi$  production in  $pp$  collisions at  $\sqrt{s} = 2.76$  TeV,” *JHEP* **02** (2013) 041, [arXiv:1212.1045 \[hep-ex\]](#). 28
- [71] **LHCb** Collaboration, R. Aaij *et al.*, “Production of  $J/\psi$  and Upsilon mesons in  $pp$  collisions at  $\sqrt{s} = 8$  TeV,” *JHEP* **06** (2013) 064, [arXiv:1304.6977 \[hep-ex\]](#). 28

- [72] **ALICE** Collaboration, B. Abelev *et al.*, “Inclusive  $J/\psi$  production in  $pp$  collisions at  $\sqrt{s} = 2.76$  TeV,” *Phys. Lett.* **B718** (2012) 295–306, [arXiv:1203.3641 \[hep-ex\]](#). [Erratum: *Phys. Lett.*B748,472(2015)]. 28, 117
- [73] **ALICE** Collaboration, S. Acharya *et al.*, “Energy dependence of forward-rapidity  $J/\psi$  and  $\psi(2S)$  production in  $pp$  collisions at the LHC,” *Eur. Phys. J.* **C77** no. 6, (2017) 392, [arXiv:1702.00557 \[hep-ex\]](#). 93, 96, 112, 116, 117, 118, 119, 152, 196, 201, 223, 227
- [74] **ALICE** Collaboration, B. B. Abelev *et al.*, “Measurement of quarkonium production at forward rapidity in  $pp$  collisions at  $\sqrt{s} = 7$  TeV,” *Eur. Phys. J.* **C74** no. 8, (2014) 2974, [arXiv:1403.3648 \[nucl-ex\]](#).
- [75] **ALICE** Collaboration, J. Adam *et al.*, “Inclusive quarkonium production at forward rapidity in  $pp$  collisions at  $\sqrt{s} = 8$  TeV,” *Eur. Phys. J.* **C76** no. 4, (2016) 184, [arXiv:1509.08258 \[hep-ex\]](#). 28, 117
- [76] P. Artoisenet, J. P. Lansberg, and F. Maltoni, “Hadroproduction of  $J/\psi$  and  $\Upsilon$  in association with a heavy-quark pair,” *Phys. Lett.* **B653** (2007) 60–66, [arXiv:hep-ph/0703129 \[HEP-PH\]](#). 28, 219
- [77] J. M. Campbell, F. Maltoni, and F. Tramontano, “QCD corrections to  $J/\psi$  and Upsilon production at hadron colliders,” *Phys. Rev. Lett.* **98** (2007) 252002, [arXiv:hep-ph/0703113 \[HEP-PH\]](#). 28
- [78] P. Artoisenet, J. M. Campbell, J. P. Lansberg, F. Maltoni, and F. Tramontano, “ $\Upsilon$  Production at Fermilab Tevatron and LHC Energies,” *Phys. Rev. Lett.* **101** (2008) 152001, [arXiv:0806.3282 \[hep-ph\]](#). 28
- [79] J. P. Lansberg, “On the mechanisms of heavy-quarkonium hadroproduction,” *Eur. Phys. J.* **C61** (2009) 693–703, [arXiv:0811.4005 \[hep-ph\]](#). 28, 219
- [80] **LHCb** Collaboration, R. Aaij *et al.*, “Measurement of  $J/\psi$  polarization in  $pp$  collisions at  $\sqrt{s} = 7$  TeV,” *Eur. Phys. J.* **C73** no. 11, (2013) 2631, [arXiv:1307.6379 \[hep-ex\]](#). 29
- [81] **ALICE** Collaboration, B. Abelev *et al.*, “ $J/\psi$  polarization in  $pp$  collisions at  $\sqrt{s} = 7$  TeV,” *Phys. Rev. Lett.* **108** (2012) 082001, [arXiv:1111.1630 \[hep-ex\]](#). 29
- [82] **ALICE** Collaboration, S. Acharya *et al.*, “Measurement of the inclusive  $J/\psi$  polarization at forward rapidity in  $pp$  collisions at  $\sqrt{s} = 8$  TeV,” *Eur. Phys. J.* **C78** no. 7, (2018) 562, [arXiv:1805.04374 \[hep-ex\]](#). 29
- [83] M. Butenschoen and B. A. Kniehl, “ $J/\psi$  polarization at Tevatron and LHC: Nonrelativistic-QCD factorization at the crossroads,” *Phys. Rev. Lett.* **108** (2012) 172002, [arXiv:1201.1872 \[hep-ph\]](#). 29
- [84] B. Gong, L.-P. Wan, J.-X. Wang, and H.-F. Zhang, “Polarization for Prompt  $J/\psi$  and  $\psi(2S)$  Production at the Tevatron and LHC,” *Phys. Rev. Lett.* **110** no. 4, (2013) 042002, [arXiv:1205.6682 \[hep-ph\]](#).
- [85] H.-S. Shao and K.-T. Chao, “Spin correlations in polarizations of P-wave charmonia  $\chi_{cJ}$  and impact on  $J/\psi$  polarization,” *Phys. Rev.* **D90** no. 1, (2014) 014002, [arXiv:1209.4610 \[hep-ph\]](#). 29
- [86] T. Matsui and H. Satz, “ $J/\psi$  Suppression by Quark-Gluon Plasma Formation,” *Phys. Lett.* **B178** (1986) 416–422. 29, 30
- [87] R. L. Thews, M. Schroedter, and J. Rafelski, “Enhanced  $J/\psi$  production in deconfined quark matter,” *Phys. Rev.* **C63** (2001) 054905, [arXiv:hep-ph/0007323 \[hep-ph\]](#). 30
- [88] **ALICE** Collaboration, B. Abelev *et al.*, “Measurement of charm production at central rapidity in proton-proton collisions at  $\sqrt{s} = 2.76$  TeV,” *JHEP* **07** (2012) 191, [arXiv:1205.4007 \[hep-ex\]](#). 31, 219

- [89] A. Andronic, P. Braun-Munzinger, K. Redlich, and J. Stachel, “The statistical model in Pb-Pb collisions at the LHC,” *Nucl. Phys.* **A904-905** (2013) 535c–538c, arXiv:1210.7724 [nucl-th]. 30, 31, 33, 34, 220
- [90] X. Zhao and R. Rapp, “Medium Modifications and Production of Charmonia at LHC,” *Nucl. Phys.* **A859** (2011) 114–125, arXiv:1102.2194 [hep-ph]. 30, 33, 34, 220
- [91] X. Du and R. Rapp, “Sequential Regeneration of Charmonia in Heavy-Ion Collisions,” *Nucl. Phys.* **A943** (2015) 147–158, arXiv:1504.00670 [hep-ph]. 33, 34, 220
- [92] X. Du and R. Rapp, “ $\psi(2S)$  Production at the LHC,” *J. Phys. Conf. Ser.* **779** no. 1, (2017) 012042, arXiv:1609.04868 [hep-ph].
- [93] K. Zhou, N. Xu, Z. Xu, and P. Zhuang, “Medium effects on charmonium production at ultrarelativistic energies available at the CERN Large Hadron Collider,” *Phys. Rev.* **C89** no. 5, (2014) 054911, arXiv:1401.5845 [nucl-th]. 30, 33, 34, 220
- [94] E. G. Ferreira, “Charmonium dissociation and recombination at LHC: Revisiting comovers,” *Phys. Lett.* **B731** (2014) 57–63, arXiv:1210.3209 [hep-ph]. 30
- [95] E. G. Ferreira, “Excited charmonium suppression in proton–nucleus collisions as a consequence of comovers,” *Phys. Lett.* **B749** (2015) 98–103, arXiv:1411.0549 [hep-ph]. 30, 33, 34, 41, 42, 220
- [96] **NA50** Collaboration, B. Alessandro *et al.*, “psi-prime production in Pb-Pb collisions at 158-GeV/nucleon,” *Eur. Phys. J.* **C49** (2007) 559–567, arXiv:nucl-ex/0612013 [nucl-ex]. 32, 220
- [97] **PHENIX** Collaboration, A. Adare *et al.*, “ $J/\psi$  suppression at forward rapidity in Au+Au collisions at  $\sqrt{s_{NN}} = 200$  GeV,” *Phys. Rev.* **C84** (2011) 054912, arXiv:1103.6269 [nucl-ex]. 32, 33, 220
- [98] **PHENIX** Collaboration, A. Adare *et al.*, “ $J/\psi$  Production vs Centrality, Transverse Momentum, and Rapidity in Au+Au Collisions at  $\sqrt{s_{NN}} = 200$  GeV,” *Phys. Rev. Lett.* **98** (2007) 232301, arXiv:nucl-ex/0611020 [nucl-ex]. 32, 33, 34, 220
- [99] **ALICE** Collaboration, B. B. Abelev *et al.*, “Centrality, rapidity and transverse momentum dependence of  $J/\psi$  suppression in Pb-Pb collisions at  $\sqrt{s_{NN}}=2.76$  TeV,” *Phys. Lett.* **B734** (2014) 314–327, arXiv:1311.0214 [nucl-ex]. 33, 220
- [100] **ALICE** Collaboration, J. Adam *et al.*, “ $J/\psi$  suppression at forward rapidity in Pb-Pb collisions at  $\sqrt{s_{NN}} = 5.02$  TeV,” *Phys. Lett.* **B766** (2017) 212–224, arXiv:1606.08197 [nucl-ex]. 33, 34, 111, 196, 220
- [101] **ALICE** Collaboration, J. Adam *et al.*, “Inclusive, prompt and non-prompt  $J/\psi$  production at mid-rapidity in Pb-Pb collisions at  $\sqrt{s_{NN}} = 2.76$  TeV,” *JHEP* **07** (2015) 051, arXiv:1504.07151 [nucl-ex]. 33, 34, 220
- [102] **CMS** Collaboration, S. Chatrchyan *et al.*, “Suppression of non-prompt  $J/\psi$ , prompt  $J/\psi$ , and  $Y(1S)$  in PbPb collisions at  $\sqrt{s_{NN}} = 2.76$  TeV,” *JHEP* **05** (2012) 063, arXiv:1201.5069 [nucl-ex]. 33, 34, 220
- [103] X. Zhao and R. Rapp, “Charmonium in Medium: From Correlators to Experiment,” *Phys. Rev.* **C82** (2010) 064905, arXiv:1008.5328 [hep-ph]. 33, 34, 220
- [104] K. Zhou, N. Xu, and P. Zhuang, “Quarkonium Production and Medium Effects in High Energy Nuclear Collisions,” arXiv:1309.7520 [nucl-th]. 33, 34, 220
- [105] **STAR Collaboration** Collaboration, L. Adamczyk *et al.*, “Measurement of  $J/\psi$  Azimuthal Anisotropy in Au+Au Collisions at  $\sqrt{s_{NN}}=200$  GeV,” *Phys. Rev. Lett.* **111** (Aug, 2013) 052301. <https://link.aps.org/doi/10.1103/PhysRevLett.111.052301>. 33
- [106] **ALICE** Collaboration, E. Abbas *et al.*, “ $J/\psi$  Elliptic Flow in Pb-Pb Collisions at  $\sqrt{s_{NN}} = 2.76$  TeV,” *Phys. Rev. Lett.* **111** (2013) 162301, arXiv:1303.5880 [nucl-ex]. 33

- [107] **ALICE** Collaboration, S. Acharya *et al.*, “ $J/\psi$  elliptic flow in Pb-Pb collisions at  $\sqrt{s_{NN}} = 5.02$  TeV,” *Phys. Rev. Lett.* **119** no. 24, (2017) 242301, [arXiv:1709.05260 \[nucl-ex\]](#). 33, 34, 220
- [108] **ALICE** Collaboration, S. Acharya *et al.*, “ $D$ -meson azimuthal anisotropy in midcentral Pb-Pb collisions at  $\sqrt{s_{NN}} = 5.02$  TeV,” *Phys. Rev. Lett.* **120** no. 10, (2018) 102301, [arXiv:1707.01005 \[nucl-ex\]](#). 33
- [109] **ALICE** Collaboration, J. Adam *et al.*, “Centrality dependence of particle production in p-Pb collisions at  $\sqrt{s_{NN}} = 5.02$  TeV,” *Phys. Rev.* **C91** no. 6, (2015) 064905, [arXiv:1412.6828 \[nucl-ex\]](#). 35, 53
- [110] **H1** Collaboration, F. D. Aaron *et al.*, “Inclusive Deep Inelastic Scattering at High  $Q^2$  with Longitudinally Polarised Lepton Beams at HERA,” *JHEP* **09** (2012) 061, [arXiv:1206.7007 \[hep-ex\]](#). 36, 220
- [111] **European Muon** Collaboration, J. J. Aubert *et al.*, “The ratio of the nucleon structure functions  $F_{2n}$  for iron and deuterium,” *Phys. Lett.* **123B** (1983) 275–278. 36
- [112] K. Rith, “Present Status of the EMC effect,” *Subnucl. Ser.* **51** (2015) 431–449, [arXiv:1402.5000 \[hep-ex\]](#). 36
- [113] K. J. Eskola, P. Paakkinen, H. Paukkunen, and C. A. Salgado, “EPPS16: Nuclear parton distributions with LHC data,” *Eur. Phys. J.* **C77** no. 3, (2017) 163, [arXiv:1612.05741 \[hep-ph\]](#). 36, 37, 220
- [114] **PHENIX** Collaboration, A. Adare *et al.*, “Heavy-flavor electron-muon correlations in  $p+p$  and  $d+Au$  collisions at  $\sqrt{s_{NN}} = 200$  GeV,” *Phys. Rev.* **C89** no. 3, (2014) 034915, [arXiv:1311.1427 \[nucl-ex\]](#). 36, 45
- [115] E. Iancu and R. Venugopalan, “The Color glass condensate and high-energy scattering in QCD,” in *Quark-gluon plasma 4*, R. C. Hwa and X.-N. Wang, eds., pp. 249–3363. 2003. [arXiv:hep-ph/0303204 \[hep-ph\]](#). 38
- [116] F. Arleo and S. Peigne, “ $J/\psi$  suppression in p-A collisions from parton energy loss in cold QCD matter,” *Phys. Rev. Lett.* **109** (2012) 122301, [arXiv:1204.4609 \[hep-ph\]](#). 38
- [117] C. Lourenco, R. Vogt, and H. K. Woehri, “Energy dependence of  $J/\psi$  absorption in proton-nucleus collisions,” *JHEP* **02** (2009) 014, [arXiv:0901.3054 \[hep-ph\]](#). 39, 220
- [118] **PHENIX** Collaboration, A. Adare *et al.*, “Cold Nuclear Matter Effects on  $J/\psi$  Yields as a Function of Rapidity and Nuclear Geometry in Deuteron-Gold Collisions at  $\sqrt{s_{NN}} = 200$  GeV,” *Phys. Rev. Lett.* **107** (2011) 142301, [arXiv:1010.1246 \[nucl-ex\]](#). 38, 39, 40, 220
- [119] K. J. Eskola, H. Paukkunen, and C. A. Salgado, “EPS09: A New Generation of NLO and LO Nuclear Parton Distribution Functions,” *JHEP* **04** (2009) 065, [arXiv:0902.4154 \[hep-ph\]](#). 38, 39, 43, 44, 220
- [120] R. Vogt, “Shadowing and absorption effects on  $J/\psi$  production in dA collisions,” *Phys. Rev.* **C71** (2005) 054902, [arXiv:hep-ph/0411378 \[hep-ph\]](#). 38, 39, 220
- [121] D. Kharzeev and K. Tuchin, “Signatures of the color glass condensate in  $J/\psi$  production off nuclear targets,” *Nucl. Phys.* **A770** (2006) 40–56, [arXiv:hep-ph/0510358 \[hep-ph\]](#). 38, 39, 220
- [122] D. Kharzeev and K. Tuchin, “Open charm production in heavy ion collisions and the color glass condensate,” *Nucl. Phys.* **A735** (2004) 248–266, [arXiv:hep-ph/0310358 \[hep-ph\]](#). 38, 39, 220
- [123] **PHENIX** Collaboration, A. Adare *et al.*, “Transverse-Momentum Dependence of the  $J/\psi$  Nuclear Modification in  $d+Au$  Collisions at  $\sqrt{s_{NN}} = 200$  GeV,” *Phys. Rev.* **C87** no. 3, (2013) 034904, [arXiv:1204.0777 \[nucl-ex\]](#). 40, 220
- [124] B. Z. Kopeliovich, I. K. Potashnikova, and I. Schmidt, “Nuclear suppression of  $J/\psi$ : from RHIC to the LHC,” *Nucl. Phys.* **A864** (2011) 203–212, [arXiv:1012.5648 \[hep-ph\]](#). 40

- [125] B. Z. Kopeliovich, I. K. Potashnikova, and I. Schmidt, “ $J/\Psi$  production in nuclear collisions: Theoretical approach to measuring the transport coefficient,” *Phys. Rev.* **C82** (2010) 024901, [arXiv:1006.3042 \[nucl-th\]](#). 40
- [126] J. W. Cronin, H. J. Frisch, M. J. Shochet, J. P. Boymond, R. Mermod, P. A. Piroue, and R. L. Sumner, “Production of hadrons with large transverse momentum at 200, 300, and 400 GeV,” *Phys. Rev.* **D11** (1975) 3105–3123. 40
- [127] E. G. Ferreiro, F. Fleuret, J. P. Lansberg, N. Matagne, and A. Rakotozafindrabe, “Centrality, Rapidity, and Transverse-Momentum Dependence of Gluon Shadowing and Antishadowing on  $J/\psi$  Production in  $dAu$  Collisions at  $\sqrt{s}=200$  GeV,” *Few Body Syst.* **53** (2012) 27–36, [arXiv:1201.5574 \[hep-ph\]](#). 40
- [128] E. G. Ferreiro, F. Fleuret, J. P. Lansberg, and A. Rakotozafindrabe, “Cold nuclear matter effects on  $J/\psi$  production: Intrinsic and extrinsic transverse momentum effects,” *Phys. Lett.* **B680** (2009) 50–55, [arXiv:0809.4684 \[hep-ph\]](#). 40
- [129] **ALICE** Collaboration, J. Adam *et al.*, “Rapidity and transverse-momentum dependence of the inclusive  $J/\psi$  nuclear modification factor in p-Pb collisions at  $\sqrt{s_{NN}} = 5.02$  TeV,” *JHEP* **06** (2015) 055, [arXiv:1503.07179 \[nucl-ex\]](#). 41
- [130] **ALICE** Collaboration, S. Acharya *et al.*, “Inclusive  $J/\psi$  production at forward and backward rapidity in p-Pb collisions at  $\sqrt{s_{NN}} = 8.16$  TeV,” [arXiv:1805.04381 \[nucl-ex\]](#). CERN-EP-2018-101. 41, 42, 88, 91, 153, 176, 187, 196, 220
- [131] J. L. Albacete *et al.*, “Predictions for Cold Nuclear Matter Effects in  $p+Pb$  Collisions at  $\sqrt{s_{NN}} = 8.16$  TeV,” *Nucl. Phys.* **A972** (2018) 18–85, [arXiv:1707.09973 \[hep-ph\]](#). 41, 42, 220
- [132] J.-P. Lansberg and H.-S. Shao, “Towards an automated tool to evaluate the impact of the nuclear modification of the gluon density on quarkonium, D and B meson production in proton–nucleus collisions,” *Eur. Phys. J.* **C77** no. 1, (2017) 1, [arXiv:1610.05382 \[hep-ph\]](#). 43, 44, 220
- [133] Y.-Q. Ma, R. Venugopalan, K. Watanabe, and H.-F. Zhang, “ $\psi(2S)$  versus  $J/\psi$  suppression in proton-nucleus collisions from factorization violating soft color exchanges,” *Phys. Rev.* **C97** no. 1, (2018) 014909, [arXiv:1707.07266 \[hep-ph\]](#).
- [134] B. Ducloué, T. Lappi, and H. Mäntysaari, “Forward  $J/\psi$  production at high energy: centrality dependence and mean transverse momentum,” *Phys. Rev.* **D94** no. 7, (2016) 074031, [arXiv:1605.05680 \[hep-ph\]](#). 43
- [135] F. Arleo and S. Peigné, “Quarkonium suppression in heavy-ion collisions from coherent energy loss in cold nuclear matter,” *JHEP* **10** (2014) 073, [arXiv:1407.5054 \[hep-ph\]](#).
- [136] B. Chen, T. Guo, Y. Liu, and P. Zhuang, “Cold and Hot Nuclear Matter Effects on Charmonium Production in p+Pb Collisions at LHC Energy,” *Phys. Lett.* **B765** (2017) 323–327, [arXiv:1607.07927 \[nucl-th\]](#). 41, 42, 220
- [137] **ALICE Collaboration** Collaboration, “Preliminary Physics Summary: Inclusive  $J/\psi$  production at forward rapidity in p-Pb collisions at  $\sqrt{s_{NN}} = 8.16$  TeV,”. <https://cds.cern.ch/record/2244670>. 41, 220
- [138] **ALICE** Collaboration, J. Adam *et al.*, “Centrality dependence of inclusive  $J/\psi$  production in p-Pb collisions at  $\sqrt{s_{NN}} = 5.02$  TeV,” *JHEP* **11** (2015) 127, [arXiv:1506.08808 \[nucl-ex\]](#). 41, 42, 220
- [139] R. Vogt, “Cold Nuclear Matter Effects on  $J/\psi$  and  $\Upsilon$  Production at the LHC,” *Phys. Rev.* **C81** (2010) 044903, [arXiv:1003.3497 \[hep-ph\]](#). 41, 42, 220
- [140] F. Arleo, R. Kolevatov, S. Peigné, and M. Rustamova, “Centrality and pT dependence of  $J/\psi$  suppression in proton-nucleus collisions from parton energy loss,” *JHEP* **05** (2013) 155, [arXiv:1304.0901 \[hep-ph\]](#).

- [141] J. L. Albacete *et al.*, “Predictions for  $p$ +Pb Collisions at  $\sqrt{s_{NN}} = 5$  TeV,” *Int. J. Mod. Phys. E* **22** (2013) 1330007, [arXiv:1301.3395 \[hep-ph\]](#). 41, 42, 220
- [142] **LHCb** Collaboration, R. Aaij *et al.*, “Study of  $J/\psi$  production and cold nuclear matter effects in  $p$ Pb collisions at  $\sqrt{s_{NN}} = 5$  TeV,” *JHEP* **02** (2014) 072, [arXiv:1308.6729 \[nucl-ex\]](#). 43
- [143] **LHCb** Collaboration, R. Aaij *et al.*, “Prompt and nonprompt  $J/\psi$  production and nuclear modification in  $p$ Pb collisions at  $\sqrt{s_{NN}} = 8.16$  TeV,” *Phys. Lett. B* **774** (2017) 159–178, [arXiv:1706.07122 \[hep-ex\]](#). 43, 220
- [144] H.-S. Shao, “HELAC-Onia: An automatic matrix element generator for heavy quarkonium physics,” *Comput. Phys. Commun.* **184** (2013) 2562–2570, [arXiv:1212.5293 \[hep-ph\]](#). 43
- [145] H.-S. Shao, “HELAC-Onia 2.0: an upgraded matrix-element and event generator for heavy quarkonium physics,” *Comput. Phys. Commun.* **198** (2016) 238–259, [arXiv:1507.03435 \[hep-ph\]](#).
- [146] K. Kovarik *et al.*, “nCTEQ15 - Global analysis of nuclear parton distributions with uncertainties in the CTEQ framework,” *Phys. Rev. D* **93** no. 8, (2016) 085037, [arXiv:1509.00792 \[hep-ph\]](#). 43, 44, 220
- [147] B. Ducloué, T. Lappi, and H. Mäntysaari, “Forward  $J/\psi$  production in proton-nucleus collisions at high energy,” *Phys. Rev. D* **91** no. 11, (2015) 114005, [arXiv:1503.02789 \[hep-ph\]](#). 43
- [148] F. Arleo and S. Peigne, “Heavy-quarkonium suppression in p-A collisions from parton energy loss in cold QCD matter,” *JHEP* **03** (2013) 122, [arXiv:1212.0434 \[hep-ph\]](#). 43
- [149] M. Cacciari, M. Greco, and P. Nason, “The P(T) spectrum in heavy flavor hadroproduction,” *JHEP* **05** (1998) 007, [arXiv:hep-ph/9803400 \[hep-ph\]](#). 43
- [150] **CMS** Collaboration, A. M. Sirunyan *et al.*, “Measurement of prompt and nonprompt  $J/\psi$  production in pp and pPb collisions at  $\sqrt{s_{NN}} = 5.02$  TeV,” *Eur. Phys. J. C* **77** no. 4, (2017) 269, [arXiv:1702.01462 \[nucl-ex\]](#). 43, 44, 53, 220
- [151] **ATLAS** Collaboration, G. Aad *et al.*, “Measurement of differential  $J/\psi$  production cross sections and forward-backward ratios in p + Pb collisions with the ATLAS detector,” *Phys. Rev. C* **92** no. 3, (2015) 034904, [arXiv:1505.08141 \[hep-ex\]](#). 43
- [152] R. Vogt, “Shadowing effects on  $J/\psi$  and  $\Upsilon$  production at energies available at the CERN Large Hadron Collider,” *Phys. Rev. C* **92** no. 3, (2015) 034909, [arXiv:1507.04418 \[hep-ph\]](#). 43, 44, 220
- [153] F. Siegert, *Monte-Carlo event generation for the LHC*. PhD thesis, Durham U., 2010. [http://inspirehep.net/record/1296465/files/374132240\\_thesis.pdf](http://inspirehep.net/record/1296465/files/374132240_thesis.pdf). 45, 46, 220
- [154] M. Diehl and J. R. Gaunt, “Double parton scattering theory overview,” [arXiv:1710.04408 \[hep-ph\]](#). 45
- [155] R. Maciula, M. Luszczak, and A. Szczurek, “Production of charm quark/antiquark pairs at LHC,” *PoS QNP2012* (2012) 125, [arXiv:1207.6533 \[hep-ph\]](#). 45
- [156] E. R. Cazaroto, V. P. Goncalves, and F. S. Navarra, “Heavy quark production and gluon saturation in double parton scattering at the LHC,” *Phys. Rev. D* **88** no. 3, (2013) 034005, [arXiv:1306.4169 \[hep-ph\]](#). 46, 221
- [157] **LHCb** Collaboration, R. Aaij *et al.*, “Observation of double charm production involving open charm in pp collisions at  $\sqrt{s} = 7$  TeV,” *JHEP* **06** (2012) 141, [arXiv:1205.0975 \[hep-ex\]](#). [Addendum: *JHEP*03,108(2014)]. 45
- [158] **CMS** Collaboration, V. Khachatryan *et al.*, “Observation of Long-Range Near-Side Angular Correlations in Proton-Proton Collisions at the LHC,” *JHEP* **09** (2010) 091, [arXiv:1009.4122 \[hep-ex\]](#). 45

- [159] **CMS** Collaboration, S. Chatrchyan *et al.*, “Observation of long-range near-side angular correlations in proton-lead collisions at the LHC,” *Phys. Lett.* **B718** (2013) 795–814, [arXiv:1210.5482 \[nucl-ex\]](#).
- [160] **ALICE** Collaboration, B. B. Abelev *et al.*, “Long-range angular correlations of  $\pi$ , K and p in p-Pb collisions at  $\sqrt{s_{NN}} = 5.02$  TeV,” *Phys. Lett.* **B726** (2013) 164–177, [arXiv:1307.3237 \[nucl-ex\]](#).
- [161] **ATLAS** Collaboration, G. Aad *et al.*, “Observation of associated near-side and away-side long-range correlations in  $\sqrt{s_{NN}} = 5.02$  TeV proton-lead collisions with the ATLAS detector,” *Phys. Rev. Lett.* **110** no. 18, (2013) 182302, [arXiv:1212.5198 \[hep-ex\]](#).
- [162] **ATLAS** Collaboration, G. Aad *et al.*, “Measurement with the ATLAS detector of multi-particle azimuthal correlations in p+Pb collisions at  $\sqrt{s_{NN}} = 5.02$  TeV,” *Phys. Lett.* **B725** (2013) 60–78, [arXiv:1303.2084 \[hep-ex\]](#). 45
- [163] T. Lang and M. Bleicher, “Possibility for  $J/\psi$  suppression in high-multiplicity proton-proton collisions at  $\sqrt{s_{NN}} = 7$  TeV,” *Phys. Rev.* **C87** no. 2, (2013) 024907, [arXiv:1302.0655 \[hep-ph\]](#). 47
- [164] **ALICE** Collaboration, J. Adam *et al.*, “Centrality dependence of the charged-particle multiplicity density at midrapidity in Pb-Pb collisions at  $\sqrt{s_{NN}} = 5.02$  TeV,” *Phys. Rev. Lett.* **116** no. 22, (2016) 222302, [arXiv:1512.06104 \[nucl-ex\]](#). 47, 221
- [165] S. M. T. Sjöstrand and P. Z. Skands, “A Brief Introduction to PYTHIA 8.1,” *Comput. Phys. Commun.* **178** (2008) 852, [arXiv:0710.3820 \[hep-ph\]](#). 47, 48, 49, 51, 221
- [166] E. G. Ferreira and C. Pajares, “High multiplicity  $pp$  events and  $J/\psi$  production at LHC,” *Phys. Rev.* **C86** (2012) 034903, [arXiv:1203.5936 \[hep-ph\]](#). 48, 50, 51, 221
- [167] B. Z. Kopeliovich, H. J. Pirner, I. K. Potashnikova, K. Reygiers, and I. Schmidt, “ $J/\psi$  in high-multiplicity  $pp$  collisions: Lessons from pA collisions,” *Phys. Rev.* **D88** no. 11, (2013) 116002, [arXiv:1308.3638 \[hep-ph\]](#). 47, 48, 50, 51, 221
- [168] K. Werner, B. Guiot, I. Karpenko, and T. Pierog, “Analysing radial flow features in p-Pb and p-p collisions at several TeV by studying identified particle production in EPOS3,” *Phys. Rev.* **C89** no. 6, (2014) 064903, [arXiv:1312.1233 \[nucl-th\]](#). 47, 48, 50, 51, 53, 221
- [169] **ALICE** Collaboration, S. G. Weber, “Measurement of  $J/\psi$  production as a function of event multiplicity in  $pp$  collisions at  $\sqrt{s} = 13$  TeV with ALICE,” *Nucl. Phys.* **A967** (2017) 333–336, [arXiv:1704.04735 \[hep-ex\]](#). 47, 48, 50, 51, 221
- [170] **ALICE** Collaboration, J. Adam *et al.*, “Measurement of charm and beauty production at central rapidity versus charged-particle multiplicity in proton-proton collisions at  $\sqrt{s} = 7$  TeV,” *JHEP* **09** (2015) 148, [arXiv:1505.00664 \[nucl-ex\]](#). 47, 51, 52, 221
- [171] H. J. Drescher, M. Hladik, S. Ostapchenko, T. Pierog, and K. Werner, “Parton based Gribov-Regge theory,” *Phys. Rept.* **350** (2001) 93–289, [arXiv:hep-ph/0007198 \[hep-ph\]](#). 50, 53, 221
- [172] **ALICE** Collaboration, B. Abelev *et al.*, “ $J/\psi$  Production as a Function of Charged Particle Multiplicity in  $pp$  Collisions at  $\sqrt{s} = 7$  TeV,” *Phys. Lett.* **B712** (2012) 165–175, [arXiv:1202.2816 \[hep-ex\]](#). 50, 51, 221
- [173] P. Skands, S. Carrazza, and J. Rojo, “Tuning PYTHIA 8.1: the Monash 2013 Tune,” *Eur. Phys. J.* **C74** no. 8, (2014) 3024, [arXiv:1404.5630 \[hep-ph\]](#). 51
- [174] **ALICE** Collaboration, C. Jahnke, “ $J/\psi$  production as a function of event multiplicity in  $pp$  collisions at  $\sqrt{s} = 13$  TeV using EMCAL-triggered events with ALICE at the LHC,” in *14th International Workshop on Hadron Physics (Hadron Physics 2018) Florianopolis, Santa Catarina, Brazil, March 18-23, 2018*. 2018. [arXiv:1805.00841 \[hep-ex\]](#). <https://inspirehep.net/record/1671075/files/1805.00841.pdf>. 51

- [175] **STAR** Collaboration, R. Ma, “Measurement of  $J/\psi$  production in p + p collisions at  $\sqrt{s}=500$  GeV at STAR experiment,” *Nucl. Part. Phys. Proc.* **276-278** (2016) 261–264, [arXiv:1509.06440 \[nucl-ex\]](#). 51
- [176] **ALICE** Collaboration, J. Adam *et al.*, “Measurement of D-meson production versus multiplicity in p-Pb collisions at  $\sqrt{s_{NN}} = 5.02$  TeV,” *JHEP* **08** (2016) 078, [arXiv:1602.07240 \[nucl-ex\]](#). 52, 53, 221
- [177] **ALICE** Collaboration, D. Adamová *et al.*, “ $J/\psi$  production as a function of charged-particle pseudorapidity density in p-Pb collisions at  $\sqrt{s_{NN}} = 5.02$  TeV,” *Phys. Lett.* **B776** (2018) 91–104, [arXiv:1704.00274 \[nucl-ex\]](#). 53, 54, 121, 131, 174, 179, 180, 181, 221, 226
- [178] **ALICE** Collaboration, B. B. Abelev *et al.*, “Multiplicity dependence of the average transverse momentum in pp, p-Pb, and Pb-Pb collisions at the LHC,” *Phys. Lett.* **B727** (2013) 371–380, [arXiv:1307.1094 \[nucl-ex\]](#). 54, 221
- [179] **CMS** Collaboration, S. Chatrchyan *et al.*, “Event activity dependence of  $Y(nS)$  production in  $\sqrt{s_{NN}}=5.02$  TeV pPb and  $\sqrt{s}=2.76$  TeV pp collisions,” *JHEP* **04** (2014) 103, [arXiv:1312.6300 \[nucl-ex\]](#). 54, 55, 221
- [180] **ALICE** Collaboration, J. Adam *et al.*, “Enhanced production of multi-strange hadrons in high-multiplicity proton-proton collisions,” *Nature Phys.* **13** (2017) 535–539, [arXiv:1606.07424 \[nucl-ex\]](#). 55, 56, 221
- [181] **ALICE** Collaboration, B. B. Abelev *et al.*, “Multiplicity Dependence of Pion, Kaon, Proton and Lambda Production in p-Pb Collisions at  $\sqrt{s_{NN}} = 5.02$  TeV,” *Phys. Lett.* **B728** (2014) 25–38, [arXiv:1307.6796 \[nucl-ex\]](#). 55
- [182] **ALICE** Collaboration, J. Adam *et al.*, “Multi-strange baryon production in p-Pb collisions at  $\sqrt{s_{NN}} = 5.02$  TeV,” *Phys. Lett.* **B758** (2016) 389–401, [arXiv:1512.07227 \[nucl-ex\]](#). 55
- [183] **ALICE** Collaboration, B. B. Abelev *et al.*, “Multi-strange baryon production at mid-rapidity in Pb-Pb collisions at  $\sqrt{s_{NN}} = 2.76$  TeV,” *Phys. Lett.* **B728** (2014) 216–227, [arXiv:1307.5543 \[nucl-ex\]](#). [Erratum: *Phys. Lett.*B734,409(2014)]. 55
- [184] L. Evans and P. Bryant, “LHC Machine,” *JINST* **3** (2008) S08001. 59
- [185] **ATLAS** Collaboration, G. Aad *et al.*, “The ATLAS Experiment at the CERN Large Hadron Collider,” *JINST* **3** (2008) S08003. 59
- [186] **CMS** Collaboration, S. Chatrchyan *et al.*, “The CMS Experiment at the CERN LHC,” *JINST* **3** (2008) S08004. 59
- [187] **LHCb** Collaboration, A. A. Alves, Jr. *et al.*, “The LHCb Detector at the LHC,” *JINST* **3** (2008) S08005. 59
- [188] **ALICE** Collaboration, K. Aamodt *et al.*, “The ALICE experiment at the CERN LHC,” *JINST* **3** (2008) S08002. 59, 61, 63, 221
- [189] **ALICE** Collaboration, B. Abelev *et al.*, “Technical Design Report for the Upgrade of the ALICE Inner Tracking System,” *J. Phys.* **G41** (2014) 087002. 61
- [190] **ALICE** Collaboration, G. Dellacasa *et al.*, “ALICE technical design report of the inner tracking system (ITS),”. CERN-LHCC-99-12. 61
- [191] **ALICE** Collaboration, B. B. Abelev *et al.*, “Performance of the ALICE Experiment at the CERN LHC,” *Int. J. Mod. Phys.* **A29** (2014) 1430044, [arXiv:1402.4476 \[nucl-ex\]](#). CERN-PH-EP-2014-031. 61, 64, 69, 76, 229
- [192] E. Bruna, A. Dainese, M. Masera, and F. Prino, “Vertex reconstruction for proton-proton collisions in ALICE,” <https://cds.cern.ch/record/1225497>. 63
- [193] D. Elia, B. Ghidini, and M. Nicassio, “Measurement of pseudorapidity density of charged particles in proton-proton collisions with the ALICE Pixel detector,” <https://cds.cern.ch/record/1225499>. 64, 221

- [194] **ALICE Collaboration** Collaboration, G. Dellacasa *et al.*, *ALICE time projection chamber: Technical Design Report*. Technical Design Report ALICE. CERN, Geneva, 2000. <https://cds.cern.ch/record/451098>. CERN-OPEN-2000-183. 64
- [195] **ALICE Collaboration**, C. W. Fabjan *et al.*, “ALICE: Physics performance report, volume II,” *J. Phys.* **G32** (2006) 1295–2040. ALICE-TDR-13, CERN-LHCC-2005-030. 65
- [196] “ALICE Figure Repository.” <https://aliceinfo.cern.ch/Figure>. 65, 66, 221
- [197] **ALICE Collaboration**, P. Cortese, “ALICE transition-radiation detector,”. ALICE-TDR-9, CERN-LHCC-2001-021, LYCEN-2001-97. 65
- [198] A. Andronic and J. P. Wessels, “Transition radiation detectors,” *Nuclear Instruments and Methods in Physics Research A* **666** (Feb., 2012) 130–147, [arXiv:1111.4188](https://arxiv.org/abs/1111.4188) [physics.ins-det]. 65
- [199] **ALICE Collaboration**, G. Dellacasa *et al.*, “ALICE technical design report of the time-of-flight system (TOF),”. CERN-LHCC-2000-012. 65
- [200] **ALICE Collaboration**, P. Cortese *et al.*, “ALICE: Addendum to the technical design report of the time of flight system (TOF),”. CERN-LHCC-2002-016. 65
- [201] **ALICE Collaboration**, A. Alici, “The MRPC-based ALICE Time-Of-Flight detector: status and performance,” *Nucl. Instrum. Meth.* **A706** (2013) 29–32, [arXiv:1203.5976](https://arxiv.org/abs/1203.5976) [physics.ins-det]. 65
- [202] **ALICE Collaboration**, P. Cortese *et al.*, “ALICE technical design report on forward detectors: FMD, T0 and V0,”. CERN-LHCC-2004-025. 66, 67
- [203] **ALICE Collaboration**, E. Abbas *et al.*, “Performance of the ALICE VZERO system,” *JINST* **8** (2013) P10016, [arXiv:1306.3130](https://arxiv.org/abs/1306.3130) [nucl-ex]. CERN-PH-EP-2013-082. 66, 67, 68, 221
- [204] S. van der Meer, “Calibration of the effective beam height in the ISR,” Tech. Rep. CERN-ISR-PO-68-31. ISR-PO-68-31, CERN, Geneva, 1968. <http://cds.cern.ch/record/296752>. 67
- [205] **ALICE Collaboration**, J. Adam *et al.*, “Determination of the event collision time with the ALICE detector at the LHC,” *Eur. Phys. J. Plus* **132** no. 2, (2017) 99, [arXiv:1610.03055](https://arxiv.org/abs/1610.03055) [physics.ins-det]. 68, 221
- [206] **ALICE Collaboration**, G. Dellacasa *et al.*, “ALICE technical design report of the zero degree calorimeter (ZDC),”. CERN-LHCC-99-05. 69
- [207] **ALICE Collaboration**, “ALICE technical design report of the dimuon forward spectrometer,”. CERN-LHCC-99-22. 69, 71, 74, 75, 222
- [208] L. S. Azhgirey, I. S. Baishev, K. M. Potter, and V. V. Talanov, “Machine Induced Background in the Low Luminosity Insertions of the LHC,”. <http://cds.cern.ch/record/566824>. 71
- [209] A. Charpy, *Study of the muon production from open heavy flavours predicted by the Color Glass Condensate model in proton-proton and proton-lead collision with the ALICE muon spectrometer at LHC*. Theses, Université Paris Sud - Paris XI, Oct., 2007. <https://tel.archives-ouvertes.fr/tel-00188303>. 72, 222
- [210] V. P. Lizardo, *Inclusive  $J/\psi$  production measurement in Pb-Pb collisions at  $\sqrt{s_{NN}} = 2.76$  TeV with the ALICE Muon Spectrometer*. PhD thesis, Orsay, 2013. [http://inspirehep.net/record/1381338/files/Thesis-2013-Lizardo\\_2.pdf](http://inspirehep.net/record/1381338/files/Thesis-2013-Lizardo_2.pdf). CERN-THESIS-2013-377. 73, 84, 222
- [211] <http://www.saha.ac.in/web/henppd-introduction-detector-working>; Accessed: 2018-05-09. 73, 222
- [212] **ALICE Collaboration**, L. Aphecetche *et al.*, “Numerical Simulations and Offline Reconstruction of the Muon Spectrometer of ALICE,”. ALICE-INT-2009-044. 75

- [213] **ALICE** Collaboration, B. B. Abelev *et al.*, “Measurement of visible cross sections in proton-lead collisions at  $\sqrt{s_{NN}} = 5.02$  TeV in van der Meer scans with the ALICE detector,” *JINST* **9** no. 11, (2014) P11003, [arXiv:1405.1849](https://arxiv.org/abs/1405.1849) [nucl-ex]. CERN-PH-EP-2014-087. 76
- [214] **ALICE** Collaboration Collaboration, C. W. Fabjan, L. Jirdén, V. Lindstruth, L. Riccati, D. Rorich, P. Van de Vyvre, O. Villalobos Baillie, and H. de Groot, *ALICE trigger data-acquisition high-level trigger and control system: Technical Design Report*. Technical Design Report ALICE. CERN, Geneva, 2004. <http://cds.cern.ch/record/684651>. 76
- [215] H. Engel, T. Alt, T. Breitner, A. G. Ramirez, T. Kollegger, M. Krzewicki, J. Lehrbach, D. Rohr, and U. Keschull, “The alice high-level trigger read-out upgrade for lhc run 2,” *Journal of Instrumentation* **11** no. 01, (2016) C01041. <http://stacks.iop.org/1748-0221/11/i=01/a=C01041>. 76
- [216] Z. Conesa Del Valle, *Performance of the ALICE muon spectrometer. Weak boson production and measurement in heavy-ion collisions at LHC*. PhD thesis, SUBATECH, Nantes, 2007. <http://inspirehep.net/record/886889/files/CERN-THESIS-2007-102.pdf>. CERN-THESIS-2007-102. 80, 222
- [217] D. J. Lange, “The EvtGen particle decay simulation package,” *Nucl. Instrum. Meth.* **A462** (2001) 152–155. 80
- [218] E. Barberio and Z. Was, “PHOTOS: A Universal Monte Carlo for QED radiative corrections. Version 2.0,” *Comput. Phys. Commun.* **79** (1994) 291–308. CERN-TH-7033-93. 80
- [219] R. Brun, F. Bruyant, M. Maire, A. C. McPherson, and P. Zancarini, “GEANT3,”. CERN-DD-EE-84-1. 80
- [220] **GEANT4** Collaboration, S. Agostinelli *et al.*, “GEANT4: A Simulation toolkit,” *Nucl. Instrum. Meth.* **A506** (2003) 250–303. SLAC-PUB-9350, FERMILAB-PUB-03-339. 80
- [221] J. Martin Blanco, *Study of  $J/\psi$  production dependence with the charged particle multiplicity in p-Pb collisions at  $\sqrt{s_{NN}} = 5.02$  TeV and pp collisions at  $\sqrt{s} = 8$  TeV with the ALICE experiment at the LHC*. PhD thesis, SUBATECH, Nantes, 2016-01-25. <http://inspirehep.net/record/1503635/files/CERN-THESIS-2016-070.pdf>. CERN-THESIS-2016-070. 83, 84, 134, 161, 177, 181, 222
- [222] M. Lenhardt, *Étude du taux de production des  $J/\psi$  et muons simples en collisions proton-proton à l’aide du spectromètre à muons de l’expérience ALICE au LHC*. PhD thesis, SUBATECH, Nantes, 2011. <http://inspirehep.net/record/1186179/files/CERN-THESIS-2011-243.pdf>. CERN-THESIS-2011-243. 84
- [223] B. Audurier, *Étude de la production inclusive de  $J/\psi$  dans les collisions pp et Pb-Pb à  $\sqrt{s_{NN}} = 5.02$  TeV avec le spectromètre à muons de l’expérience ALICE au LHC*. PhD thesis, Nantes U., 2017. <http://www.theses.fr/s122944>. 84, 93, 98, 104, 111, 115
- [224] “Tracking efficiency determination.” <https://twiki.cern.ch/twiki/bin/viewauth/ALICE/MuonTrackingEfficiency>; Accessed:2018-05-09. 84
- [225] Phillipe Pillot, private communication (2017). 88, 91
- [226] “ALICE/LHCb joint public note,”. ALICE-PUBLIC-2013-002, LHCb-CONF-2013-013. 93, 113, 114, 223
- [227] R. Partridge *et al.*, “Observation of an  $\eta_c$  Candidate State with Mass  $2978 \pm 9$  MeV,” *Phys. Rev. Lett.* **45** (1980) 1150–1153. 96
- [228] “NA60 Collaboration website.”. <http://cern.ch/NA60>; Accessed: 2018-05-22. 96
- [229] M. Butenschoen and B. A. Kniehl, “Reconciling  $J/\psi$  production at HERA, RHIC, Tevatron, and LHC with NRQCD factorization at next-to-leading order,” *Phys. Rev. Lett.* **106** (2011) 022003, [arXiv:1009.5662](https://arxiv.org/abs/1009.5662) [hep-ph]. 115, 116, 119, 223

- [230] R. E. Nelson, R. Vogt, and A. D. Frawley, “Narrowing the uncertainty on the total charm cross section and its effect on the  $J/\psi$  cross section,” *Phys. Rev.* **C87** no. 1, (2013) 014908, [arXiv:1210.4610 \[hep-ph\]](#). 117, 223
- [231] **CDF** Collaboration, D. Acosta *et al.*, “Measurement of the  $J/\psi$  meson and  $b$ -hadron production cross sections in  $p\bar{p}$  collisions at  $\sqrt{s} = 1960$  GeV,” *Phys. Rev.* **D71** (2005) 032001, [arXiv:hep-ex/0412071 \[hep-ex\]](#). 117, 118, 223
- [232] **PHENIX** Collaboration, A. Adare *et al.*, “ $J/\psi$  production versus transverse momentum and rapidity in  $p^+p$  collisions at  $\sqrt{s} = 200$ -GeV,” *Phys. Rev. Lett.* **98** (2007) 232002, [arXiv:hep-ex/0611020 \[hep-ex\]](#). 117, 118, 223
- [233] **NA3** Collaboration, J. Badier *et al.*, “Experimental  $J/\psi$  Hadronic Production from 150-GeV/c to 280-GeV/c,” *Z. Phys.* **C20** (1983) 101. 117, 118, 223
- [234] **ALICE Collaboration** Collaboration, “Preliminary Physics Summary: Centrality dependence of inclusive  $J/\psi$  production in p-Pb collisions at  $\sqrt{s_{NN}} = 8.16$  TeV,” <https://cds.cern.ch/record/2272151>. 121, 123, 176, 177
- [235] **LEBC-EHS** Collaboration, M. Aguilar-Benitez *et al.*, “Comparative Properties of 400-GeV/c Proton - Proton Interactions With and Without Charm Production,” *Z. Phys.* **C41** (1988) 191. 123, 174
- [236] S. Roesler, R. Engel, and J. Ranft, “The Monte Carlo event generator DPMJET-III,” in *Advanced Monte Carlo for radiation physics, particle transport simulation and applications. Proceedings, Conference, MC2000, Lisbon, Portugal, October 23-26, 2000*, pp. 1033–1038. 2000. [arXiv:hep-ph/0012252 \[hep-ph\]](#). <http://www-public.slac.stanford.edu/sciDoc/docMeta.aspx?slacPubNumber=SLAC-PUB-8740>. 135
- [237] T. Pierog, I. Karpenko, J. M. Katzy, E. Yatsenko, and K. Werner, “EPOS LHC: Test of collective hadronization with data measured at the CERN Large Hadron Collider,” *Phys. Rev.* **C92** no. 3, (2015) 034906, [arXiv:1306.0121 \[hep-ph\]](#). 135
- [238] Valentina Zaccolo, private communication. 147, 150, 163, 164, 165, 167
- [239] Roberta Arnaldi, private communication. 176, 226

## LIST OF FIGURES

1.1	Elementary particles of the Standard Model [1]. . . . .	9
1.2	Feynman diagrams showing vacuum fluctuations at the lowest order in QCD. . . . .	11
1.3	Summary of measurements of $\alpha_s$ as a function of the energy scale $Q$ . Taken from [1]. . . . .	11
1.4	The QCD phase-space diagram. Modified from [10]. . . . .	12
1.5	Space-time evolution of a collisions of heavy-ion. Taken from [8]. . . . .	13
1.6	Schematic view of the initial geometry of a collisions of nuclei A and B at the impact parameter $b$ . Modified from [12]. . . . .	14
1.7	A sketch of a peripheral heavy ion collisions. The asymmetric overlap region gives rise to momentum anisotropy. . . . .	16
1.8	Relative particle production in central collisions at the LHC. Taken from [22]. . . . .	17
1.9	The $Z^0$ boson $R_{AA}$ values for the combination of the dimuon and dielectron channel as a function of the number of participants $N_{\text{part}}$ in Pb–Pb at $\sqrt{s_{\text{NN}}} = 2.76$ TeV. Taken from [24]. . . . .	18
2.1	OZI forbidden (left) and allowed (right) $c\bar{c}$ decay. . . . .	20
2.2	Spectroscopy of stable charmonia states. . . . .	21
2.3	The energy dependence of the $d\sigma_{b\bar{b}}/dy$ production cross section. Taken from [37]. . . . .	22
2.4	<b>(a)</b> The $p_T$ dependence of the fraction of non-prompt $J/\psi$ $f_b$ at midrapidity in pp at $\sqrt{s} = 7$ TeV measured in ALICE [37], ATLAS [38], and CMS [39]. <b>(b)</b> The $p_T$ dependence of fraction of non-prompt $J/\psi$ $f_b$ at forward rapidity in pp at $\sqrt{s} = 13$ TeV measured in LHCb [41]. . . . .	23
2.5	Examples of Feynman diagrams describing the charm quark pair creation in QCD. . . . .	23
2.6	<b>(a)</b> $p_T$ dependence of direct $J/\psi$ production in $p\bar{p}$ collisions at $\sqrt{s} = 1.8$ TeV at the Tevatron [45]. Visualised are colour singlet, colour octet and total contributions. Figure taken from [46]. <b>(b)</b> Polarisation of prompt $J/\psi$ (top) and $\psi(2S)$ (bottom) from 1.8 TeV $p\bar{p}$ collisions at the Tevatron. The coloured bands show different NRQCD predictions [48, 49]. Figure taken from [47]. . . . .	25
2.7	The $p_T$ differential $J/\psi$ cross section in pp collisions at $\sqrt{s} = 200$ GeV at the RHIC. Recent STAR results [52] are compared with previous STAR data [50, 51] and PHENIX data [53] at the same energy. Comparison with theoretical calculations [54–57] are shown. Figure taken from [52]. . . . .	26
2.8	<b>(a)</b> Prompt and non-prompt $J/\psi$ at $\sqrt{s} = 7$ TeV measured with ATLAS [62]. Prompt $J/\psi$ were compared with NRQCD calculation [65], non-prompt with FONLL calculation [66, 67]. <b>(b)</b> Prompt $J/\psi$ and $\psi(2S)$ at 13 TeV measured with CMS [63], compared with NRQCD calculation [65] (middle panel) and with data. at 7 TeV [64]. <b>(c)</b> Comparison between the ATLAS and the CMS data at $\sqrt{s} = 7$ TeV. . . . .	27
2.9	Non-prompt-to-inclusive $J/\psi$ fraction $f_b$ measured by CMS in pp at $\sqrt{s} = 7$ and 13 TeV [69]. . . . .	28
2.10	The LHCb $p_T$ -differential prompt $J/\psi$ production cross section in pp at $\sqrt{s} = 7$ TeV [40] compared with theoretical calculations [76–79]. . . . .	28
2.11	Polarisation parameter $\lambda_\theta$ of prompt $J/\psi$ measured by LHCb at forward rapidity [40]. . . . .	29
2.12	Schema of $J/\psi$ sequential suppression. Figure taken from [42]. . . . .	30
2.13	The total $c\bar{c}$ cross section in pp collisions. Figure taken from [88]. . . . .	31

2.14	<b>(a)</b> Measured over expected $J/\psi$ and $\psi(2S)$ as a function of the crossing length, which relates to centrality [96]. <b>(b)</b> Suppression of $J/\psi$ at mid- and forward rapidity as a function of centrality [97]. . . . .	32
2.15	<b>(a)</b> Comparison of $J/\psi$ suppression at forward rapidity between ALICE [99, 100] and PHENIX [97]. <b>(b)</b> Rapidity dependence of the $J/\psi$ suppression in Pb–Pb at $\sqrt{s_{NN}} = 2.76$ TeV measured with ALICE [99]. . . . .	33
2.16	<b>(a)</b> Prompt $R_{AA}$ at midrapidity as a function of $p_T$ at $\sqrt{s_{NN}} = 2.76$ TeV measured with ALICE [101] and CMS [102] compared to PHENIX results at $\sqrt{s_{NN}} = 200$ GeV [98]. Data are also compared with available theoretical calculation [90, 103, 104]. <b>(b)</b> Centrality dependent forward rapidity $R_{AA}$ at $\sqrt{s_{NN}} = 5.02$ TeV [100] compared with theoretical calculations [89–91, 93–95]. . . . .	34
2.17	The $p_T$ dependent $v_2^{J/\psi}$ at forward rapidity for semi-central (20–40%) Pb–Pb collisions at $\sqrt{s_{NN}} = 5.02$ TeV [107], compared with transport model calculations [91, 93]. . . . .	34
2.18	Parton distribution functions for valence quarks, sea quarks, and gluon at a scale $Q^2 = 10$ GeV [110]. . . . .	36
2.19	Schema of a typical $x$ dependence of a nuclear modification function in the EPPS16 parametrisation [113]. . . . .	37
2.20	The EPPS16 nuclear modification functions for gluons in the lead nucleus at the energy scale $Q^2 = 1.69$ and $10$ GeV <sup>2</sup> [113]. . . . .	37
2.21	The $J/\psi$ absorption cross section $\sigma_{abs}^{J/\psi}$ as a function of collision energy $\sqrt{s_{NN}}$ for free proton PDFs (top left) and for three different sets of nPDFs. Figures taken from [117].	39
2.22	Rapidity differential $R_{dAu}$ for $J/\psi$ measured in minimum bias collisions at $\sqrt{s_{NN}} = 200$ GeV with PHENIX. The data are compared to theoretical calculation combining EPS09 nPDFs with an absorption cross section (red lines) [119, 120], and with a saturation model (green lines) [121, 122]. Figure taken from [118]. . . . .	39
2.23	(Left) Rapidity differential $J/\psi$ $R_{dAu}$ for peripheral (top) and central (middle) collisions at $\sqrt{s_{NN}} = 200$ GeV measured by PHENIX. The data are compared to theoretical calculation combining EPS09 nPDFs with a absorption cross section (red lines), and with a saturation model (green lines). The ratio of the two centrality classes is shown in the bottom panel. Figure taken from [118]. (Right) $R_{dAu}$ of $J/\psi$ as a function of $p_T$ for (a) backward, (b) mid- and (c) forward rapidity in minimum bias d-Au collisions at $\sqrt{s_{NN}} = 200$ GeV measured by PHENIX. Figure taken from [123]. . . . .	40
2.24	The $J/\psi$ nuclear modification as a function of rapidity in Pb-Pb collisions at $\sqrt{s_{NN}} = 8.16$ TeV. ALICE data are compared with available theoretical calculations. The box around unity shows the correlated uncertainty. Figure taken from [137]. . . . .	41
2.25	The $p_T$ differential nuclear modification factor for inclusive $J/\psi$ measured in ALICE in p-Pb at $\sqrt{s_{NN}} = 8.16$ TeV. Data are in well described by all available models [131–136]. Figures taken from [130]. . . . .	42
2.26	Inclusive $J/\psi$ $Q_{pPb}$ as a function of $\langle N_{coll} \rangle$ at backward (left), mid- (centre) and forward (right) rapidity. The boxes centred at $Q_{pPb} = 1$ represent the relative uncertainties correlated over centrality. Comparison with theoretical calculations [95, 139–141] is shown. Figure taken from [138]. . . . .	42
2.27	The $p_T$ and centrality integrated $J/\psi$ nuclear modification factor $R_{pPb}^{J/\psi}$ in $\sqrt{s_{NN}} = 8.16$ TeV for prompt and non-prompt $J/\psi$ in LHCb. Figure taken from [143]. . . . .	43
2.28	The nucleon-nucleon centre-of-mass rapidity dependence of $R_{pPb}$ for prompt $J/\psi$ in p-Pb at $\sqrt{s_{NN}} = 5.02$ TeV measured by CMS. Data were compared with models including (anti)shadowing [119, 132, 146, 152]. Taken from [150]. . . . .	44
3.1	A sketch of a typical proton-proton collision at LHC. The green lines and ellipses indicate the two incoming protons, the light blue ellipses indicate the beam remnants. The event is visually separated into the hard part, which is in the top half of the figure, and the underlying event in the bottom half. The initial hard scattering, indicated by the big red blob, produces a parton shower. As the shower evolves, the products of the hard scattering decay and QCD radiation is emitted. The produced coloured partons eventually hadronise into colourless states, indicated by the light green ellipses. These states than may further decay into stable particles. The softer secondary hard scattering also produces a shower. Charged particles can also at any time emit electromagnetic radiation (yellow). Taken from [153]. . . . .	46

3.2	A diagram of single parton scattering (left) and double parton scattering (right). Taken from [156]. . . . .	46
3.3	Mean charged particle density normalised by the average number of participating nucleon pairs $\frac{2}{\langle N_{\text{part}} \rangle} \langle dN_{\text{ch}}/d\eta \rangle$ versus $\sqrt{s_{\text{NN}}}$ . Normalisation by $\frac{\langle N_{\text{part}} \rangle}{2}$ enables direct comparison of bulk particle production between different systems and energies. Taken from [164]. . . . .	47
3.4	Multiplicity-dependent self-normalised inclusive $J/\psi$ yields in pp collisions at $\sqrt{s} = 13$ TeV, measured at midrapidity. The measurement is compared with available calculations: percolation model by Ferreiro [166], EPOS3 [168], Pythia [165] and a calculation by Kopeliovich [167] (see legend). More details are given in text. Taken from [169]. . . . .	48
3.5	D- and B-meson relative yield as a function of the relative charged particle multiplicity at midrapidity calculated with the PYTHIA event generator [165]. The top row showcases the individual contributions to the total $c$ and $b$ quarks production. The bottom panel visualises the dependence of the increase on $p_{\text{T}}$ of the D-meson. . . . .	49
3.6	Self-normalised $J/\psi$ yields at mid- and forward rapidity as a function of relative charged particle multiplicity in pp collisions at $\sqrt{s} = 7$ TeV. Taken from [172]. . . . .	51
3.7	Average relative D-meson yields in $ y  < 0.5$ as a function of the relative charged particle multiplicity at midrapidity (a), and at backward rapidity (b). Compared are data measured in pp at $\sqrt{s} = 7$ TeV and p-Pb $\sqrt{s_{\text{NN}}} = 5.02$ TeV. The diagonal is shown as dashed line to draw the line. The bottom panel shows uncertainty on the B feed-down fraction. Taken from [176]. . . . .	52
3.8	Relative yields of charmed hadrons as a function of $dN_{\text{ch}}/d\eta / \langle dN_{\text{ch}}/d\eta \rangle$ in pp collisions at $\sqrt{s} = 7$ TeV. (a) shows inclusive $J/\psi$ at mid- and forward rapidity versus prompt D. (b) shows non-prompt $J/\psi$ at midrapidity versus prompt D. Taken from [170]. . . . .	52
3.9	Average relative D-meson yields in $ y_{\text{LAB}} < 0.5 $ as a function of the relative charged particle multiplicity at midrapidity (a), and at backward rapidity (b) measured in p-Pb $\sqrt{s_{\text{NN}}} = 5.02$ TeV. Data are compared to EPOS calculation with and without hydrodynamical evolution [168, 171]. The dashed line represents the diagonal $y = x$ and is shown to draw the eye. Taken from [176]. . . . .	53
3.10	$J/\psi$ at forward, mid-, and backward rapidity as a function of charge particle multiplicity measured at $ \eta  < 1$ . (a) Relative $J/\psi$ yields as a function of multiplicity. The diagonal is shown as dashed line to draw the line. (b) Relative $\langle p_{\text{T}} \rangle$ as a function of multiplicity at forward and backward rapidity, compared with results for charged hadrons at $ \eta_{\text{cms}}  < 0.3$ [178]. Taken from [177]. . . . .	54
3.11	The $\Upsilon(\text{ns})$ relative cross section versus transverse energy measured at forward rapidity $4 <  \eta  < 5.2$ (top row) and versus charged track multiplicity at midrapidity $ \eta  < 2.4$ (bottom row). The cross section was measured at midrapidity $ y_{\text{cms}}  < 1.93$ in pp collisions at $\sqrt{s} = 2.76$ TeV and in p-Pb collisions at $\sqrt{s_{\text{NN}}} = 5.02$ TeV. For $\Upsilon(1\text{s})$ , the results for Pb-Pb measurement at $\sqrt{s_{\text{NN}}} = 2.76$ TeV is also shown. Taken from [179]. . . . .	55
3.12	The relative yields of strange hadron compared to charged pions as a function of mean charged particle multiplicity $\langle dN_{\text{ch}}/d\eta \rangle$ . The shown yields were measured in pp, p-Pb, and Pb-Pb collisions. Taken from [180]. . . . .	56
4.1	The CERN accelerator complex. . . . .	60
4.2	The ALICE experiment in Run 2. . . . .	62
4.3	Layout of the ITS detector. Taken from [188]. . . . .	63
4.4	Schematic drawing of the tracklet reconstruction algorithm principle. Taken from [193]. . . . .	64
4.5	The specific ionisation energy loss $dE/dx$ in TPC as a function of momentum in Pb-Pb collisions at $\sqrt{s_{\text{NN}}} = 5.02$ TeV. The solid lines show the central value of the Bethe-Bloch parametrisation for a given particle. Taken from the ALICE Figure Repository [196]. . . . .	65
4.6	The TOF velocity $\beta$ as a function of momentum in Pb-Pb collisions at $\sqrt{s_{\text{NN}}} = 5.02$ TeV. Taken from the ALICE Figure Repository [196]. . . . .	66
4.7	Placement of the V0A and V0C arrays within the ALICE detector. Taken from [203]. . . . .	67
4.8	Time of flight of the particles detected in V0C versus V0A. The dashed line intersection represents the time of the collisions at the IP. Taken from [203]. . . . .	68
4.9	Layout of the T0 arrays inside the ALICE detector. Taken from [205]. . . . .	68
4.10	The p-Pb and Pb-p beam configuration in ALICE. . . . .	70

4.11	Schema of the Muon Spectrometer. . . . .	70
4.12	Schema of the front absorber of the Muon Spectrometer. Taken from [207]. . . . .	71
4.13	Schema of detection elements used in MCH. The quadrants used in the Stations 1 and 2 are shown on the left. The slats of the Stations 3, 4 and 5 are pictured on the right. Taken from [209]. . . . .	72
4.14	(a) Field configuration inside a MWPC. Taken from [210]. (b) Working principle of a MWPC inside the MCH. [211]. . . . .	73
4.15	Structure of the RPC in Muon Trigger. Taken from [207]. . . . .	74
4.16	Principle of the Muon Trigger online $p_T$ cut. Taken from [207]. . . . .	75
5.1	Example of $A\varepsilon$ of the Muon Spectrometer as a function of $p_T$ and $y$ . The top row shows the two dimensional $A\varepsilon(p_T, y)$ . The bottom row shows projections of $J/\psi$ acceptance (left) into the $p_T$ axis at $-3.6 < y < -3.0$ and (right) into $y$ axis at $2 < p_T < 4$ GeV/ $c$ . Taken from [216]. . . . .	80
5.2	Schema of the iterative tuning of the MC. . . . .	81
5.3	Schema of the MCH showing the arrangement of individual chambers and stations. Possible track passing responses are shown for Station 1. Stations 4 and 5 are considered as one ensemble (St45). Taken from [221]. . . . .	83
5.4	(Left) Correlated dead area and (right) anti-correlated dead area between the chambers of MCH. Taken from [221]. . . . .	84
5.5	Principle of the $p$ DCA selection criterion on the tracks reconstructed in the Muon Spectrometer. . . . .	85
5.6	Comparison of kinematic distributions in data (red) and MC (blue). The top row shows the individual distributions as a function of $p_T$ , $y$ , $\varphi$ and muon charge. The bottom row shoes corresponding ratios of data/MC. The distributions correspond to p-Pb data at $\sqrt{s_{NN}} = 8.16$ TeV. . . . .	86
5.7	Tracking efficiency estimated as a function of run in the p-Pb period at $\sqrt{s_{NN}} = 8.16$ TeV. The red points represent data while the blue points represent the MC. . . . .	87
5.8	Ratio of the tracking efficiency in data and MC as a function of detection element (DE) in Chamber 1. Corresponding to the p-Pb data at $\sqrt{s_{NN}} = 8.16$ TeV. . . . .	87
5.9	Ratio of the tracking efficiency in data and in MC in the p-Pb period as a function of run, $p_T$ , $y$ , and $\varphi$ . . . . .	89
5.10	Ratio of the tracking efficiency in data and in MC in the Pb-p period as a function of run, $p_T$ , $y$ , and $\varphi$ . The ratios were computed from the second reconstruction pass of the Pb-p data. . . . .	90
5.11	Ratio of the tracking efficiency in data and in MC in the Pb-p period as a function of run, $p_T$ , $y$ , and $\varphi$ . The ratios were computed from the third reconstruction pass of the Pb-p data. Courtesy of Philippe Pillot. . . . .	92
6.1	Schema of a decay of $J/\psi$ into a pair of opposite sign muons in the laboratory frame. . . . .	95
6.2	The dimuon invariant mass spectrum in pp collisions at $\sqrt{s} = 5.02$ TeV. . . . .	95
6.3	Example of CB2+VWG fit to the dimuon invariant mass spectrum over the range $2.1 < M_{inv} < 4.5$ GeV/ $c$ in pp collisions at $\sqrt{s} = 5.02$ TeV. . . . .	97
6.4	Number of $J/\psi$ integrated in $p_T$ and rapidity as a function of the fit trial in pp collisions at $\sqrt{s} = 5.02$ TeV. The solid red line shows the mean value averaged over all trials. The dashed lines show the standard deviation. . . . .	98
6.5	The evolution of $A\varepsilon$ with time in pp collisions at $\sqrt{s} = 5.02$ TeV. . . . .	100
6.6	The $p_T$ - and $y$ differential $A\varepsilon$ in pp collisions at $\sqrt{s} = 5.02$ TeV. (Left) $A\varepsilon$ as a function of $p_T$ , integrated over $2.5 < y < 4.0$ . (Right) $A\varepsilon$ as a function of $y$ , integrated over $0 < p_T < 12$ GeV/ $c$ . . . . .	100
6.7	Variation of MC shape within statistical uncertainty on data. Top row shows the $N_{J/\psi}^{corr}$ as a function of $p_T$ (left) and $y$ (right). The lines represent variations of the shape assuming Gaussian uncertainty, which are used to re-weight the MC. Bottom row shows the ratio of RMS over average of all re-weighted $A\varepsilon$ . More details in text. . . . .	102
6.8	The systematic uncertainty on $A\varepsilon$ associated to the MC input shape in pp collisions at $\sqrt{s} = 5.02$ TeV. The left column shows the $p_T$ differential uncertainty, while the right one shows the $y$ differential. The blue points correspond to the combinations of the extreme shapes. Courtesy of Philippe Pillot. . . . .	103

6.9	Estimated tracking efficiency in data and in MC in pp collisions at $\sqrt{s} = 5.02$ TeV. Courtesy of Benjamin Audurier and Philippe Pillot. . . . .	104
6.10	Ratio of estimated tracking efficiency in data and in MC versus $p_T$ (top), $y$ (middle), and $\varphi$ (bottom) in pp collisions at $\sqrt{s} = 5.02$ TeV. Courtesy of Benjamin Audurier. . .	105
6.11	The matching efficiency as a function of the matching $\chi^2$ cut for different track selection (left), for different $p$ selection (middle), and for different $p_T$ selection (right) in pp collisions at $\sqrt{s} = 5.02$ TeV. Courtesy of Benjamin Audurier. . . . .	107
6.12	Purity factor for CINT7 and CMUL7 trigger classes in pp at $\sqrt{s} = 5.02$ TeV as a function of time. . . . .	108
6.13	Pile-up factor for CINT7 and C0TVX trigger classes in pp at $\sqrt{s} = 5.02$ TeV as a function of time. . . . .	109
6.14	Pile-up factor for CINT7 and C0TVX trigger classes in pp at $\sqrt{s} = 5.02$ TeV as a function of time. . . . .	110
6.15	$\sigma_{\text{MUL}}$ calculated from the CINT7 and C0TVX trigger classes in pp at $\sqrt{s} = 5.02$ TeV as a function of time. . . . .	110
6.16	Differential inclusive $J/\psi$ cross section as a function of $p_T$ in pp at $\sqrt{s} = 5.02$ TeV [73].	112
6.17	Differential inclusive $J/\psi$ cross section as a function of $y$ in pp at $\sqrt{s} = 5.02$ TeV [73]. Filled and open markers denote the measured and mirrored points respectively. . . .	112
6.18	Differential inclusive $J/\psi$ cross section in pp collisions at $\sqrt{s} = 5.02$ TeV as a function $p_T$ and $y$ compared with interpolation done by ALICE and LHCb [226]. . . . .	114
6.19	Example fit of the function in Eq. (6.20) to the $p_T$ differential spectrum in pp collisions at $\sqrt{s} = 5.02$ TeV. . . . .	115
6.20	Differential inclusive $J/\psi$ cross section in pp collisions at $\sqrt{s} = 5.02$ TeV. Taken from [73]. . . . .	116
6.21	Inclusive $J/\psi$ cross section at forward rapidity as a function of collisions energy $\sqrt{s}$ . The band represents CEM calculation by Nelson et al. [230]. Taken from [73]. . . . .	117
6.22	Inclusive $J/\psi$ cross section at forward rapidity as a function of (a) $p_T$ and (b) $y$ . Taken from [73]. . . . .	118
6.23	$\langle p_T \rangle$ as a function of $\sqrt{s}$ . ALICE measurements at forward (full points) and midrapidity (open points) are compared with lower energy results from CDF [231], PHENIX [232], and NA3 [233]. Figure taken from [73] . . . . .	118
6.24	$\psi(2S)$ -to- $J/\psi$ ratio as a function of $p_T$ in pp at $\sqrt{s} = 13$ TeV, compared with NRQCD calculations [65, 229]. Figure taken from [73]. . . . .	119
7.1	. Pile-up selection criteria included in the AliPhysicsSelection. The red (magenta) curve shows the default cut used in the APS to clean the pile-up. Exemplar distributions corresponding to the Pb-p period. . . . .	123
7.2	$N_{\text{CL}}$ versus $N_{\text{tr}}$ SPD pile-up cut. The black line represents Eq. (7.4) and red line the alternative polynomial form proposed in Eq. (7.2.1.2) for the intermediate tracklet range. . . . .	125
7.3	Custom Physics Selection pile-up rejection cuts for CMUL events. . . . .	127
7.4	Comparison of $\langle N_{\text{tr}} \rangle$ extracted with CPS and APS in p-Pb and Pb-p in dimuon events. The top row shows the $\langle N_{\text{tr}} \rangle$ as a function of run with APS and with CPS. The bottom row shows the ratio of the CPS/APS distributions. . . . .	128
7.5	The $z$ -coordinate of the SPD vertex in p-Pb and Pb-p. The maximum of the distribution is shifted in both period with respect to the nominal interaction point. . . . .	130
7.6	Event averaged number of tracklets $\langle N_{\text{tr}} \rangle$ versus $z$ -coordinate of the SPD vertex $v_z$ before (blue) and after (red) the Poissonian correction using $v_z^0 = \text{Max}\{-10, 10\}$ . . . .	131
7.7	Number of tracklets $N_{\text{tr}}$ versus $v_z$ in CMUL7 triggered events in the p-Pb period. The top left (right) panel shows the distribution of raw (corrected) tracklets $N^{\text{raw}}$ ( $N^{\text{corr}}$ ). The bottom left plot shows projection of the top 2D distributions into the tracklets axis ( $N^{\text{raw}}$ in black or $N^{\text{corr}}$ in red, commonly denoted as $N_{\text{tr}}$ ). The bottom right plot shows the projections into the $v_z$ axis ( $N^{\text{raw}}$ in black or $N^{\text{corr}}$ in red). . . . .	132

7.8	Event averaged number of tracklets $\langle N^{\text{raw}} \rangle$ versus $v_z$ in CMUL7 and CINT7 triggered event samples. (a) $\langle N^{\text{raw}} \rangle$ vs $v_z$ in CMUL7 triggered events in p–Pb (LHC16r) and Pb–p (LHC16s) periods. The LHC16s period has overall larger multiplicity than LHC16r, which is the usual case in Pb–p collisions compared to p–Pb. (b) $\langle N^{\text{raw}} \rangle$ vs $v_z$ in CMUL7 triggered events in LHC16rs periods renormalised to unity. (c) $\langle N^{\text{raw}} \rangle$ vs $v_z$ in CINT7 triggered events in LHC16rs periods. (d) $\langle N^{\text{raw}} \rangle$ vs $v_z$ in CINT7 triggered events in LHC16rs periods renormalised to unity. (e, f) Comparison between renormalised $\langle N^{\text{raw}} \rangle$ vs $v_z$ in CMUL7 and CINT7 events in LHC16r and LHC16s respectively. The bottom panel shows the ratio of the two histograms. The ratio being consistent with unity, we apply the same correction to both CMUL7 and CINT7 in given period. . . . .	133
7.9	Left: $\langle N_{\text{tr}} \rangle$ as a function of $v_z$ in the p–Pb data sample. The $\langle N^{\text{raw}} \rangle (v_z)$ distribution (black) is compared to $\langle N^{\text{corr}} \rangle (v_z)$ corrected using minimum (blue), mean (green), and maximum (red). Comparison of $N^{\text{raw}}$ (black) distribution and $N^{\text{corr}}$ obtained using minimum (blue), mean (green), and maximum (red) in the p–Pb period. . . . .	134
7.10	Comparison of p–Pb data (red) and the corresponding DPMJET MC production (blue). In each plot, the bottom panel shows ratio of data/MC unless stated otherwise. (a) $\eta_{\text{lab}}$ distribution of reconstructed tracklets. (b) $\varphi$ distribution of reconstructed tracklets. The bottom panel show weighted ratio of data/MC; weights were number of MB events in each $\varphi$ bin. (c) $v_z$ distribution in $-20 < v_z < 20$ cm. (d) $N^{\text{raw}}$ distribution. . . . .	136
7.11	$\langle N^{\text{raw}} \rangle (v_z)$ profiles in p–Pb period. The top left plot shows the profiles compared between data and the two sets of MC. The top left shows ratio of data/DPMJET with a visible non-flat structure. Bottom left the same for data/EPOS, again a structure is present along z-vertex. Bottom right compares the two generated samples - we see that profiles from different MC are similar. . . . .	137
7.12	Same as Fig. 7.11 but for Pb–p period. . . . .	137
7.13	$\langle N^{\text{raw}} \rangle (v_z)$ (blue) and $\langle N^{\text{corr}} \rangle (v_z)$ (red) in DPMJET and EPOS Monte Carlo. . . . .	138
7.14	Ratio of MB events per run in data/MC. . . . .	139
7.15	Ratio of data/MC of z-vertex distributions. The red line shows the pol4 fit to the ratio. The fit was done over an extended range $-15 < v_z < 15$ cm to prevent edge effects at $v_z = \pm 10$ cm. Top left panel shows DPMJET p–Pb, top right panel DPMJET Pb–p, bottom left EPOS p–Pb, and bottom right EPOS Pb–p. . . . .	140
7.16	Function weights to correct $N^{\text{raw}}$ in the MC. Green line denotes the expo*expo fit. Both functions are fit in the range $60 < N^{\text{raw}} < 165$ . The vertical red chequered line shows the cut-off at $N^{\text{raw}} = 165$ above which the weights are set to 1. The middle panel shows the ratio of data/MC ratio histogram and the expo*expo function. The bottom panel shows the ratio of histogram and the expo*pol2 function. . . . .	141
7.17	Weighted $N^{\text{raw}}$ and $N^{\text{corr}}$ distributions in MC compared with the data. Used double exponential $N^{\text{raw}}$ weight. . . . .	142
7.18	Effect of run, z-vertex and $N^{\text{raw}}$ weights on tracklets distributions and profiles. Example shows DPMJET Pb–p. Note that black (no weight) points are hidden below the green (z-vertex weight) ones. Top row shows the $N^{\text{raw}}$ (left) and $N^{\text{corr}}$ distributions, the respective bottom panels show the ratio of the weighted distributions with respect to the unweighted one. Bottom row shows the $\langle N^{\text{raw}} \rangle (v_z)$ (left) and $\langle N^{\text{corr}} \rangle (v_z)$ (right). . . . .	143
7.19	$N_{\text{ch}} - N^{\text{corr}}$ correlation from the DPMJET MC production for the p–Pb period. Superimposed is the $N^{\text{corr}}$ profile of the 2D distribution (black disks). Shown are also fits to the profile, see text for more details. The grey vertical lines denote the limits of $N^{\text{corr}}$ bins used in the J/ $\psi$ signal extraction. The $N_{\text{ch}} - N^{\text{corr}}$ correlation was weighted by the combined weight, using double exponential $N^{\text{raw}}$ weight. . . . .	144
7.20	$\langle N_{\text{ch}} \rangle$ computed for each $N^{\text{corr}}$ bin in p–Pb. On left are the results obtained from different $N_{\text{ch}} - N^{\text{corr}}$ correlation fits (see legend). The projections of $N^{\text{corr}}$ intervals into the $N_{\text{ch}}$ axis (the MC truth) is drawn in open red circles. The left plot shows the ratios of each of these distributions over the MC truth. . . . .	145
7.21	$\langle N_{\text{ch}} \rangle$ computed for each $N^{\text{corr}}$ bin in Pb–p. On left are the results obtained from different $N_{\text{ch}} - N^{\text{corr}}$ correlation fits (see legend). The projections of $N^{\text{corr}}$ intervals into the $N_{\text{ch}}$ axis (the MC truth) is drawn in open red circles. The left plot shows the ratios of each of these distributions over the MC truth. . . . .	146

7.22	Systematic uncertainty on the MC input for the p–Pb period. The left-hand-side plots show the spread of the different correlation factor $\alpha$ values in one period with varying generator and $N^{\text{raw}}$ weights. The following distributions are shown: DPMJET with double exponential weights (black), DPMJET with no weights (red), DPMJET with Expo*Pol2 weights (green), EPOS with double exponential weights (blue), EPOS with no weights (yellow), EPOS with Expo*Pol2 weights (magenta). The last-but-one two are distributions obtained from distributions corrected by MC profiles: DPMJET with double exponential weights (turquoise), EPOS with double exponential weights (teal). The mauve datapoints show the results obtained with the $N^{\text{corr}}$ double exponential weight. The plot on right shows the ratio of each of these distributions over the one obtained from DPMJET with double exponential weights. . . . .	148
7.23	Systematic uncertainty on the MC input for the Pb–p period. The left-hand-side plots show the spread of the different correlation factor $\alpha$ values in one period with varying generator and $N^{\text{raw}}$ weights. The following distributions are shown: DPMJET with double exponential weights (black), DPMJET with no weights (red), DPMJET with Expo*Pol2 weights (green), EPOS with double exponential weights (blue), EPOS with no weights (yellow), EPOS with Expo*Pol2 weights (magenta). The last two are distributions obtained from distributions corrected by MC profiles: DPMJET with double exponential weights (turquoise), EPOS with double exponential weights (teal). The plot on right shows the ratio of each of these distributions over the one obtained from DPMJET with double exponential weights. . . . .	148
7.24	$v_z$ -dependence of $\alpha$ factor. The values were extracted from global fit with $\varepsilon = 0$ . The red line shows the $v_z$ -integrated value. . . . .	149
7.25	Comparison of tails used in the present analysis. Left plot shows the CB2 tails, right plots shows tails used for NA60 shape. Nomenclature: pp13data - extracted from pp data at 13 TeV, pp13MC - extracted from pp MC at 13 TeV, pPb8MC (Pbp8MC) - extracted from p–Pb (Pb–p) MC at 8 TeV, pPb8RA (Pbp8RA) - extracted from p–Pb (Pb–p) data at 8 TeV without pile-up or vertex cuts, pPb8JC (Pbp8JC) - extracted from p–Pb (Pb–p) data at 8 TeV with the custom pile-up and vertex cuts used in this analysis. . . . .	153
7.26	Example of signal extraction for the multiplicity integrated invariant mass spectra in p–Pb (left) and Pb–p (right). Used fit: combination CB2+DoubleExponential with p–Pb (Pb–p) tails extracted from data sample with vertex selection over the fit range $2 < M_{\mu+\mu^-} < 5 \text{ GeV}/c^2$ . . . . .	154
7.27	Examples of signal extraction at low, intermediate, and high multiplicity. Top row shows the p–Pb period, bottom row the Pb–p period. Used fit: combination CB2+Double Exponential with p–Pb (Pb–p) tails extracted from data sample with vertex selection over the fit range $2 < M_{\mu+\mu^-} < 5 \text{ GeV}/c^2$ . . . . .	154
7.28	Signal extraction test set for integrated spectra. Dashed vertical lines show separate group of tests using a single set of tails. . . . .	155
7.29	Values of free $J/\psi$ mean and width in multiplicity bins. . . . .	156
7.30	Relative $N_{J/\psi}$ in the Pb–p period. The example show the one-but-last bin $127 \leq N^{\text{corr}} < 179$ . . . . .	158
7.31	Dimuon trigger normalisation factor in p–Pb as a function of run, computed via the two-step offline method. . . . .	160
7.32	Dimuon trigger normalisation factor in Pb–p as a function of run, computed via the two-step offline method. . . . .	160
7.33	Comparison of $F_{\text{norm}}$ in multiplicity intervals computed with three different methods. . . . .	163
7.34	Multiplicity dependent vertex finding NSD event selection efficiency in p–Pb. . . . .	165
7.35	Multiplicity dependent vertex finding NSD event selection efficiency in Pb–p. . . . .	165
7.36	Comparison of the multiplicity dependent relative $J/\psi$ yields obtained from Poissonian correction with respect of the $\langle N^{\text{raw}} \rangle (v_z)$ maximum and binomial correction with respect to the $\langle N^{\text{raw}} \rangle (v_z)$ minimum. . . . .	166
7.37	Ratio of relative $J/\psi$ yields corrected with respect to the minimum and of the relative yields corrected with respect to the maximum of the $\langle N^{\text{raw}} \rangle (v_z)$ . . . . .	167

7.38	Bin-flow systematic uncertainty in p–Pb. The top left plot shows the invariant yields as a function of multiplicity for each of the task settings. Black points denote 'baseline', which is the standard settings used in the whole analysis, red is the same but with different randomisation seed, green and blue stand for yields obtained from running the task with -0.1 or +0.1 offset respectively. Top right is the same but for relative multiplicity dependent invariant yields. Bottom left and bottom right show ratio of the two with respect to the corresponding baseline. . . . .	170
7.39	Bin-flow systematic uncertainty in Pb–p. The top left plot shows the invariant yields as a function of multiplicity for each of the task settings. Black points denote 'baseline', which is the standard settings used in the whole analysis, red is the same but with different randomisation seed, green and blue stand for yields obtained from running the task with -0.1 or +0.1 offset respectively. Top right is the same but for relative multiplicity dependent invariant yields. Bottom left and bottom right show ratio of the two with respect to the corresponding baseline. . . . .	171
7.40	Pile-up systematic uncertainty in p–Pb. The top left plot shows the invariant yields as a function of multiplicity for each of the task settings. Black points denote 'baseline', which is the standard settings used in the whole analysis, red and green are extracted using SPD pile up cut with argument (3, 0.6) and (5, 0.8) respectively. Top right is the same but for relative multiplicity dependent invariant yields. Bottom left and bottom right show ratio of the two with respect to the corresponding baseline. . . . .	172
7.41	Pile-up systematic uncertainty in Pb–p. The top left plot shows the invariant yields as a function of multiplicity for each of the task settings. Black points denote 'baseline', which is the standard settings used in the whole analysis, red and green are extracted using SPD pile up cut with argument (3, 0.6) and (5, 0.8) respectively. Top right is the same but for relative multiplicity dependent invariant yields. Bottom left and bottom right show ratio of the two with respect to the corresponding baseline. . . . .	173
7.42	Self-normalised $J/\psi$ yields as a function of self-normalised charged particle multiplicity in p–Pb (p-going) and Pb–p (Pb-going) at $\sqrt{s_{NN}} = 8.16$ TeV. The NSD and vertex normalisation uncertainty is quoted separately. The uncertainty on the multiplicity axis is partially correlated in multiplicity. . . . .	174
7.43	Self-normalised $J/\psi$ yields as a function of self-normalised charged particle multiplicity in p–Pb and Pb–p at $\sqrt{s_{NN}} = 8.16$ TeV divided by the diagonal. The uncertainty on the multiplicity axis is partially correlated in multiplicity. . . . .	175
7.44	Multiplicity integrated invariant $J/\psi$ yields in p–Pb and Pb–p at $\sqrt{s_{NN}} = 8.16$ TeV. Full discs show results of this multiplicity analysis, open circles denote results from $R_{pPb}$ analysis [239]. . . . .	176
7.45	The correlation between the ZNA percentile and the $N^{corr}$ in the CINT7-B-NOPF-MUFAST triggered p–Pb data sample. . . . .	177
7.46	Comparison of multiplicity dependent results with results from centrality analysis. The boxes around the centrality dependent data points show the fully uncorrelated systematic uncertainty on the relative yields. The vertical brackets denote the fully correlated systematics on relative yields. . . . .	178
7.47	Comparison of multiplicity differential relative $J/\psi$ yields in p–Pb and Pb–p at $\sqrt{s_{NN}} = 5.02$ [177] and 8.16 TeV. . . . .	179
8.1	Double differential $A\varepsilon(p_T, y)$ of the Muon Spectrometer in p–Pb and Pb–p at $\sqrt{s_{NN}} = 8.16$ TeV. . . . .	182
8.2	Fit to the multiplicity integrated, $A\varepsilon$ corrected invariant mass spectrum in p–Pb and the corresponding $\langle p_T \rangle$ fit. The $M_{inv}$ spectrum was fitted with a function combining a CB2 signal + double exponential background + tails extracted in cross section analysis in pp at 13 TeV over a fit range $2 < M_{inv} < 5$ GeV/c. The $f(\langle p_T^{bgd} \rangle)$ was described by a product of quadratic and exponential function. . . . .	183
8.3	Example of $\langle p_T \rangle$ fit to the p–Pb multiplicity dependent spectra using the following option: $M_{inv}$ described by a combination of NA60 signal + double exponential background with MC tails, $f(\langle p_T \rangle)$ described by a quadratic function multiplied by an exponential, fit over $1.7 < M_{inv} < 4.8$ GeV/c <sup>2</sup> . . . . .	184

8.4	$\delta_\alpha$ variations of $\langle p_T \rangle$ fit to the multiplicity integrated spectrum in the p-Pb period. The points towards the right end that are systematically lower with respect to the rest correspond to fits with the NA60 signal shape. . . . .	185
8.5	$A\varepsilon$ corrected $p_T$ and $y$ spectra in p-Pb. The black distributions correspond to the multiplicity integrated spectrum. The blue and red data points show the high and low multiplicity distributions respectively. The corresponding fits are also drawn, see legend. . . . .	189
8.6	Spread of $\langle p_T \rangle$ computed with different weight combination for the (a) p-Pb and (b) Pb-p data. Left is $f_{\text{low}}^R(p_T) \cdot f_{\text{low}}^R(y)$ , centre is the default result, and on right is $f_{\text{high}}^R(p_T) \cdot f_{\text{high}}^R(y)$ . . . . .	190
8.7	Multiplicity dependent $\langle p_T \rangle$ results. . . . .	191
8.8	Multiplicity dependent $\langle p_T \rangle^R$ results. . . . .	191
8.9	Comparison of $\langle p_T \rangle^R$ in p-Pb and Pb-p at $\sqrt{s_{\text{NN}}} = 5.02$ and 8.16 TeV. . . . .	192
9.1	Section efficace inclusive de J/ $\psi$ différentielle en fonction de (a) $pt$ et (b) $y$ dans des collisions pp à $\sqrt{s} = 5.02$ TeV [73]. . . . .	201
9.2	(a) Les taux de production des J/ $\psi$ en fonction de la multiplicité des particules chargées dans des collisions p-Pb à rapidité vers l'avant (rouge) et à rapidité vers l'arrière (bleu) à $\sqrt{s_{\text{NN}}} = 8.16$ TeV. L'incertitude due à la normalisation et au vertex est citée séparément. L'incertitude sur l'axe de la multiplicité est partiellement corrélée en multiplicité. (b) Identique à (a) mais divisé par la diagonale. . . . .	202
9.3	(a) $\langle p_T \rangle$ absolu des J/ $\psi$ en fonction de la multiplicité relative des particules chargées. (b) $\langle p_T \rangle^R$ relative des J/ $\psi$ en fonction de la multiplicité relative des particules chargées. (c) $\langle p_T \rangle^R$ relative en fonction de la multiplicité à la rapidité vers l'avant dans les collisions p-Pb à 8.16 et 5.02 TeV. (d) $\langle p_T \rangle^R$ relative en fonction de la multiplicité à la rapidité vers l'arrière dans les collisions p-Pb à 8.16 et 5.02 TeV. . . . .	203
D.1	Comparison of $\eta$ distribution between data and DPMJET or EPOS. Bottom panel shows the ratio data/MC. . . . .	238
D.2	Comparison of $\varphi$ distribution between data and DPMJET or EPOS. Bottom panel shows the ratio data/MC. . . . .	238
D.3	Comparison of $v_z^{SPD}$ distribution between data and DPMJET or EPOS. Bottom panel shows the ratio data/MC. . . . .	239
D.4	Comparison of $N^{\text{raw}}$ distribution between data and DPMJET or EPOS. Bottom panels show the ratio data/MC. . . . .	240
D.5	Comparison of $N^{\text{corr}}$ distribution between data and DPMJET or EPOS. Bottom panels show the ratio data/MC. . . . .	241



## LIST OF TABLES

1.1	Properties of the fundamental interactions in the Standard Model [2]. . . . .	10
2.1	Characteristics of selected stable charmonia states. Masses were taken from [1], while radii were quoted from [14]. . . . .	21
2.2	Typical momentum fractions for forward $J/\psi$ ( $2.5 < y_{\text{lab}} < 4.0$ ) at the LHC. . . . .	37
4.1	Dimensions of individual layers of ITS [191]. . . . .	61
6.1	Definition of trigger classes used in $J/\psi$ analysis in pp collisions at $\sqrt{s} = 5.02$ TeV. . .	94
6.2	Number of $J/\psi$ extracted in $p_{\text{T}}$ bins integrated over $2.5 < y < 4$ and in bins of $y$ integrated in $p_{\text{T}}$ . . . . .	99
6.3	The $J/\psi$ acceptance-efficiency in $p_{\text{T}}$ bins integrated over $2.5 < y < 4.0$ and in bins of $y$ integrated in $p_{\text{T}}$ . . . . .	101
6.4	The systematic uncertainty on $A\varepsilon$ associated to the MC input shape as a function of $p_{\text{T}}$ (left) and $y$ (right). . . . .	103
6.5	The systematic uncertainty on trigger efficiency associated to the muon $p_{\text{T}}$ cut threshold in pp collisions at $\sqrt{s} = 5.02$ TeV. . . . .	106
6.6	Summary of systematic uncertainties on $J/\psi$ cross section. Values marked with asterisk are correlated in $p_{\text{T}}$ and $y$ . . . . .	111
6.7	The differential $J/\psi$ cross section extracted in $p_{\text{T}}$ bins integrated over $2.5 < y < 4$ and in bins of $y$ integrated in $p_{\text{T}}$ . . . . .	113
7.1	Definition of trigger classes used in $J/\psi$ multiplicity analysis in p-Pb collisions at $\sqrt{s_{\text{NN}}} = 8.16$ TeV. . . . .	122
7.2	Number of events in CMUL7 and CINT7 trigger samples in p-Pb and Pb-p after each pile-up cut. The cuts are applied sequentially, i. e. application of each of the cuts implies also application of the previously listed cuts. . . . .	126
7.3	Number of CMUL7 and CINT7 triggered events in p-Pb and Pb-p after each SPD vertex QA cut. . . . .	129
7.4	Minimal and maximal values of $\langle N_{\text{tr}} \rangle (v_z)$ in CMUL7 and CINT7 triggered data. . . .	134
7.5	Systematic uncertainty on the $N_{\text{ch}} - N^{\text{corr}}$ correlation in p-Pb and Pb-p. . . . .	146
7.6	$\langle dN_{\text{ch}}/d\eta \rangle$ at midrapidity $ \eta_{\text{lab}}  < 1$ . . . . .	147
7.7	Sources of systematic uncertainties on the charged-particle multiplicity. Values marked with asterisk are correlated in multiplicity. . . . .	150
7.8	Mean corrected number of tracklets $\langle N^{\text{corr}} \rangle$ and corresponding average number of charged particles $N_{\text{ch}}$ in p-Pb and Pb-p periods. . . . .	151
7.9	Extracted number of $J/\psi$ from p-Pb and Pb-p in the multiplicity integrated case and in individual multiplicity bins. We also show sum over all bins $\sum$ and difference $\Delta$ between $\sum$ and integrated result. . . . .	157
7.10	Relative $N_{J/\psi}$ per bin in p-Pb and Pb-p. . . . .	159
7.11	Normalisation factor computed via the two-step offline method ( $F_{\text{norm}}^{\text{off2}}$ ), the one step offline method ( $F_{\text{norm}}^{\text{off1}}$ ) and the rescaling one ( $F_{\text{norm}}^{\text{resc}}$ ) per multiplicity bin for p-Pb and Pb-p data. . . . .	162

7.12	Sources of systematic uncertainties. The values in parentheses correspond to the multiplicity integrated uncertainties related to the signal extraction. Values marked with asterisk are correlated in multiplicity. . . . .	167
7.13	Uncertainty on vertex equalisation. . . . .	168
7.14	Multiplicity dependent relative invariant $J/\psi$ yields. . . . .	175
7.15	Multiplicity integrated invariant yields. . . . .	176
8.1	Absolute $\langle p_T \rangle$ values obtained from the $\delta_\alpha$ variations. The last values bin in Pb-p did not properly converge, therefore we excluded it from the analysis. Uncertainty on the multiplicity not shown. . . . .	185
8.2	Relative $\langle p_T \rangle^R$ values obtained from the $\delta_\alpha$ variations. The last values bin in Pb-p did not properly converge, therefore we excluded it from the analysis. Uncertainty on the multiplicity not shown. . . . .	186
8.3	Sources of systematic uncertainties. The values in parentheses correspond to the multiplicity integrated uncertainties related to the signal extraction. Values marked with asterisk are correlated in multiplicity. . . . .	187
8.4	Systematic uncertainty on the absolute $\langle p_T \rangle$ and relative $\langle p_T \rangle^R$ extraction. . . . .	188
8.5	Multiplicity integrated $\langle p_T \rangle$ results. The global systematic uncertainty includes the uncertainty on the trigger, tracking, and trigger-track matching efficiencies, and on the MC input. . . . .	190

## FIT FUNCTIONS

## A.1 Extended Crystal-Ball

The function has the following seven parameters: normalisation factor  $N$ , two Gaussian core parameters (mean  $\bar{x}$  and width  $\sigma$ ), and four tail parameters ( $\alpha$ ,  $n$ ,  $\alpha'$  and  $n'$ ). The function is defined as:

$$f(x) = N \cdot \begin{cases} \exp\left(\frac{-(x-\bar{x})^2}{2\sigma^2}\right) & \text{for } \alpha' > \frac{x-\bar{x}}{\sigma} > -\alpha \\ A \cdot \left(B - \frac{x-\bar{x}}{\sigma}\right)^{-n} & \text{for } \frac{x-\bar{x}}{\sigma} \leq -\alpha \\ C \cdot \left(D + \frac{x-\bar{x}}{\sigma}\right)^{-n'} & \text{for } \frac{x-\bar{x}}{\sigma} \geq \alpha' \end{cases}$$

with

$$A = \left(\frac{n}{|\alpha|}\right)^n \cdot \exp\left(-\frac{|\alpha|^2}{2}\right), B = \frac{n}{|\alpha|} - |\alpha|$$

$$C = \left(\frac{n'}{|\alpha'|}\right)^{n'} \cdot \exp\left(-\frac{|\alpha'|^2}{2}\right), D = \frac{n'}{|\alpha'|} - |\alpha'|$$

## A.2 NA60

The function has the following eleven parameters: normalisation factor  $N$ , two Gaussian core parameters (mean  $\bar{x}$  and width  $\sigma$ ), and eight tail parameters ( $\alpha^L$ ,  $p_1^L$ ,  $p_2^L$ ,  $p_3^L$ ,  $\alpha^R$ ,  $p_1^R$ ,  $p_2^R$  and  $p_3^R$ ). The function is defined as:

$$f(x) = N \cdot \exp\left(-0.5 \left(\frac{t}{t_0}\right)^2\right)$$

with

$$t = \frac{x - \bar{x}}{\sigma}$$

and

$$\begin{cases} t_0 = 1 + p_1^L(\alpha^L - t)(p_2^L - p_3^L \sqrt{\alpha^L - t}) & \text{for } t < \alpha^L \\ t_0 = 1 & \text{for } \alpha^L < t < \alpha^R \\ t_0 = 1 + p_1^R(t - \alpha^R)(p_2^R - p_3^R \sqrt{t - \alpha^R}) & \text{for } t > \alpha^R \end{cases}$$

## A.3 Variable Width Gaussian

The function has the following four parameters: normalisation factor  $N$  and three parameters ( $\bar{x}$ ,  $\alpha$ ,  $\beta$ ). The function is defined as:

$$f(x) = N \cdot \exp\left(\frac{-(x - \bar{x})^2}{2\sigma^2}\right),$$

where

$$\sigma = \alpha + \beta \left(\frac{x - \bar{x}}{\bar{x}}\right)$$

## A.4 Double exponential

The function has the four parameters and is defined as:

$$f(x) = \exp(a + b * x) + \exp(c + d * x).$$

## IMPORTANT FORMULÆ

This appendix sums up the formulæ used in the analyses presented in this thesis.

**Weighted average**

Suppose we have a set of  $n$  values  $X = \{x_1, x_2, \dots, x_n\}$ . Each value  $x_i$  has an assigned weight  $w_i$ . The weighted average over the sample  $X$  is defined as

$$\langle x \rangle = \frac{\sum_{i=1}^n w_i \cdot x_i}{\sum_{i=1}^n w_i}. \quad (\text{B.1})$$

The quantities which are computed from Eq. (B.1) are:

- The mean of an observable, e. g. the number of  $J/\psi$  in a given  $p_T$ ,  $y$ , or multiplicity interval.
- The statistical uncertainty of the above mentioned observable in the same interval.

**Weighted standard deviation**

Suppose we have a set of  $n$  values  $X = \{x_1, x_2, \dots, x_n\}$ . Each value  $x_i$  has an assigned weight  $w_i$ . The weighted average of the sample is  $\langle x \rangle$ . There are in total  $M$  non-zero values assigned to the sample. The weighted standard deviation of  $X$  is defined as

$$\sigma_w(X) = \sqrt{\frac{\sum_{i=1}^n (x_i - \langle x \rangle)^2}{\frac{M-1}{M} \sum_{i=1}^n w_i}}. \quad (\text{B.2})$$

The quantities which were computed from Eq. (B.2) are:

- The systematic uncertainty of certain observables such as the number of  $J/\psi$  in a given  $p_T$ ,  $y$ , or multiplicity interval.



## LISTS OF ANALYSED RUNS

**C.1 LHC15n: pp data at  $\sqrt{s} = 5.02$  TeV**

ALICE collected pp data at 5.02 TeV between November 19, 2015 and November 23, 2015. The analysed data sample consist of 25 runs satisfying the QA section criteria:

244340, 244343, 244351, 244355, 244359, 244364, 244377, 244411, 244416, 244418, 244421, 244453, 244480, 244481, 244482, 244483, 244484, 244531, 244540, 244542, 244617, 244619, 244626, 244627, 244628.

**C.2 LHC16r: p–Pb data at  $\sqrt{s_{NN}} = 8.16$  TeV**

ALICE collected p–Pb data at 8.16 TeV from November 18, 2016 till November 25, 2016. The analysed data sample consists of 57 QA selected runs:

265594, 265596, 265607, 265691, 265694, 265696, 265697, 265698, 265700, 265701, 265709, 265713, 265714, 265740, 265741, 265742, 265744, 265746, 265754, 265756, 265785, 265787, 265788, 265789, 265792, 265795, 265797, 265840, 265841, 266022, 266023, 266025, 266034, 266074, 266076, 266081, 266084, 266085, 266086, 266117, 266187, 266189, 266190, 266193, 266196, 266197, 266208, 266234, 266235, 266296, 266299, 266300, 266304, 266305, 266312, 266316, 266318.

**C.3 LHC16s: Pb–p data at  $\sqrt{s_{NN}} = 8.16$  TeV**

ALICE collected Pb–p data at 8.16 TeV from November 26, 2016 till December 4, 2016. The analysed data sample consists of 75 QA selected runs:

266437, 266438, 266439, 266441, 266470, 266472, 266480, 266487, 266514, 266516, 266518, 266520, 266522, 266523, 266525, 266533, 266534, 266539, 266543, 266549, 266587, 266588, 266591, 266593, 266595, 266613, 266614, 266618, 266621, 266630, 266657, 266658, 266659, 266665, 266668, 266669, 266674, 266676, 266702, 266703, 266706, 266708, 266775, 266776, 266800, 266805, 266807, 266857, 266878, 266880, 266882, 266883, 266885, 266886, 266912, 266915, 266940, 266942, 266943, 266944, 266988, 266993, 266994, 266997, 267020, 267022, 267062, 267063, 267067, 267070, 267072, 267077, 267109, 267110, 267131.



## VALIDATION OF GENERAL EVENT MONTE CARLO PRODUCTIONS

Two sets of MC simulations were produced for our analysis, each using different generator. We performed a cross-check to make sure we can use both data samples from each generator. We will discuss the most critical checks. Neither of the generators describes the data precisely. The DPMJET generated samples describe the data to a better extent than the EPOS samples. We used both sets to prevent a possible bias coming from use of only one generator that does not describe data perfectly.

### $\eta$ distribution

Fig. D.1 contrasts the  $\eta$  distribution of reconstructed tracklets (in the SPD) between data and MC. We recall reader that the tracklets are counted within  $|\eta| < 1$ . While the DPMJET is able to reproduce the distribution in the p-Pb period in this range, it fares rather poorly in Pb-p. With EPOS, the situation is similar, when the p-Pb distribution is better simulated than the Pb-p. This may be hinting on issues with boost in the Pb-p samples. The strange behaviour of the Pb-p MC samples was reported to the experts. The origin is however unknown. In the  $|\eta| < 1$  region, the maximal deviation is  $\sim 5\%$ . We do not correct for this difference.

### $\varphi$ distribution

The  $\varphi$  distribution of reconstructed tracklets is rather well described, as can be seen in Fig. D.2. The bottom panels show ratio of the data/MC distributions. To evaluate the 'truthfulness' of the MC distributions, we computed the mean of the ratio weighted by number of MB counts in given bin. All distributions are within 3.5% from unity. We do not apply any correction on  $\varphi$ .

### $v_z^{SPD}$ distribution

Another important feature is the  $z$ -vertex distribution. It was noted early on during the MC preparation stage that the vertex distribution along the  $z$ -axis differs between MC and data (see Fig. D.3), the Pb-p are also shifted towards positive  $z$ . This can affect the  $N_{tr}$  in our samples, more so as we cut on  $z$ -vertex position. To correct this, we apply weights on  $v_z^{SPD}$  to bring it closer to data distribution.

### $N^{raw}$ and $N^{corr}$ distributions

We also verified if the produced shapes of tracklet distributions are true to reality. DPMJET is able to reproduce the shape to satisfactory level at intermediate multiplicity but not at low and high multiplicity. The  $N^{raw}$  distributions can be found in Fig. D.4,  $N^{corr}$  display the same behaviour, see Fig. D.5. EPOS gives a less satisfactory results. Either distribution does not reach far enough to ensure a clean determination of charged-particle multiplicity in the highest bin. We apply a weight to correct for the difference in  $N^{raw}$  and in  $N^{corr}$ .

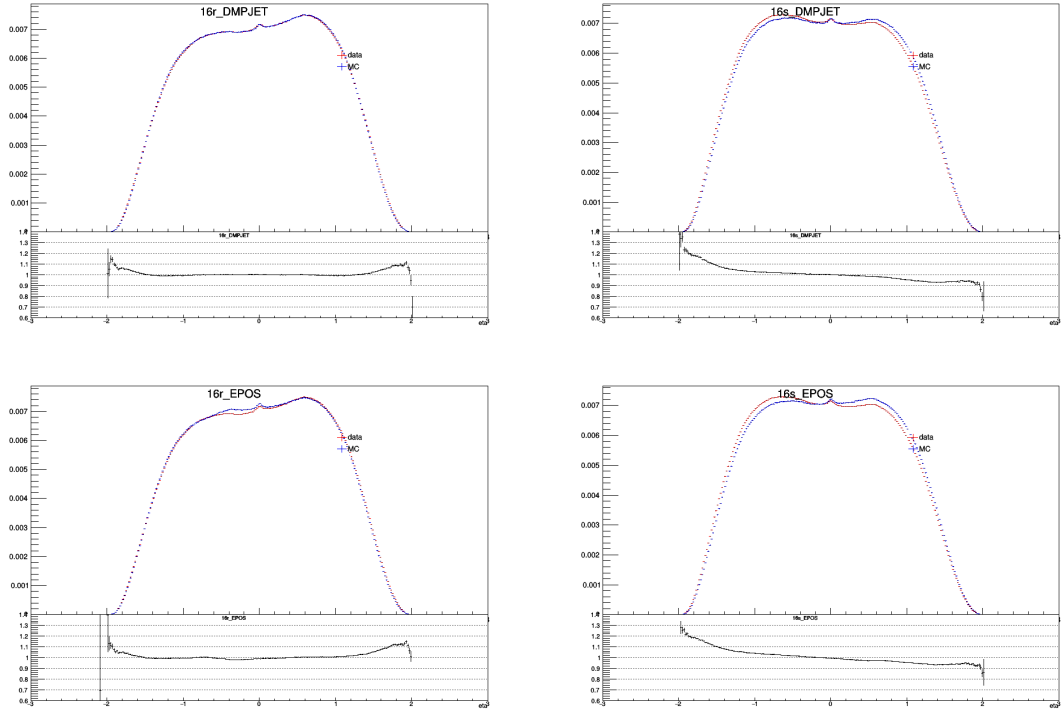


Figure D.1: Comparison of  $\eta$  distribution between data and DPMJET or EPOS. Bottom panel shows the ratio data/MC.

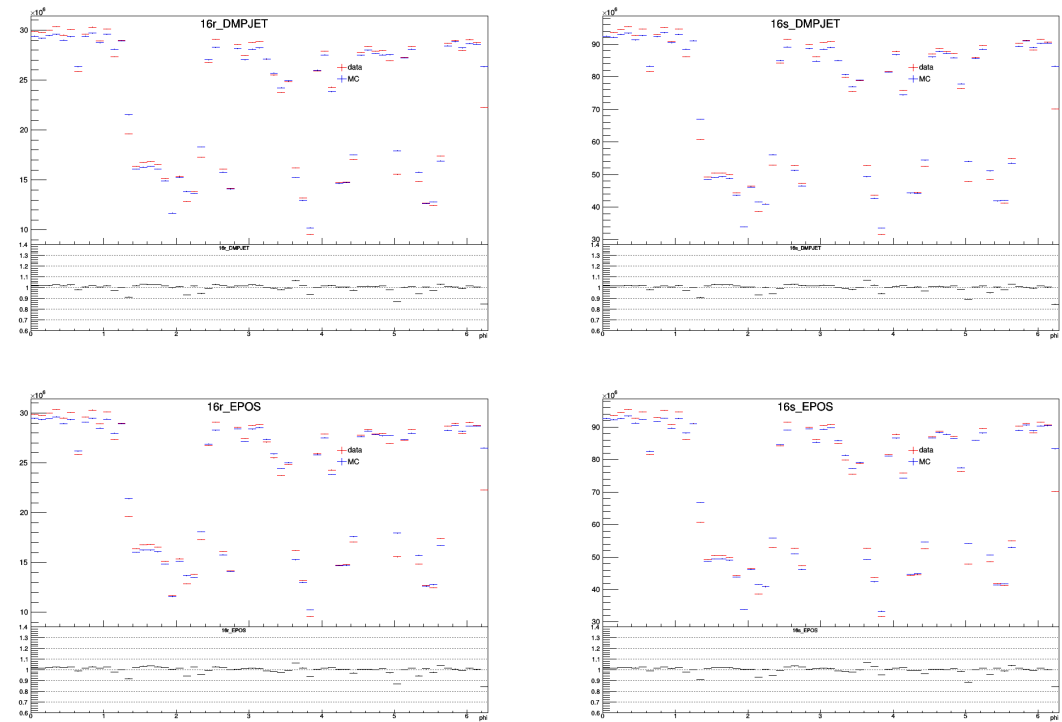


Figure D.2: Comparison of  $\varphi$  distribution between data and DPMJET or EPOS. Bottom panel shows the ratio data/MC.

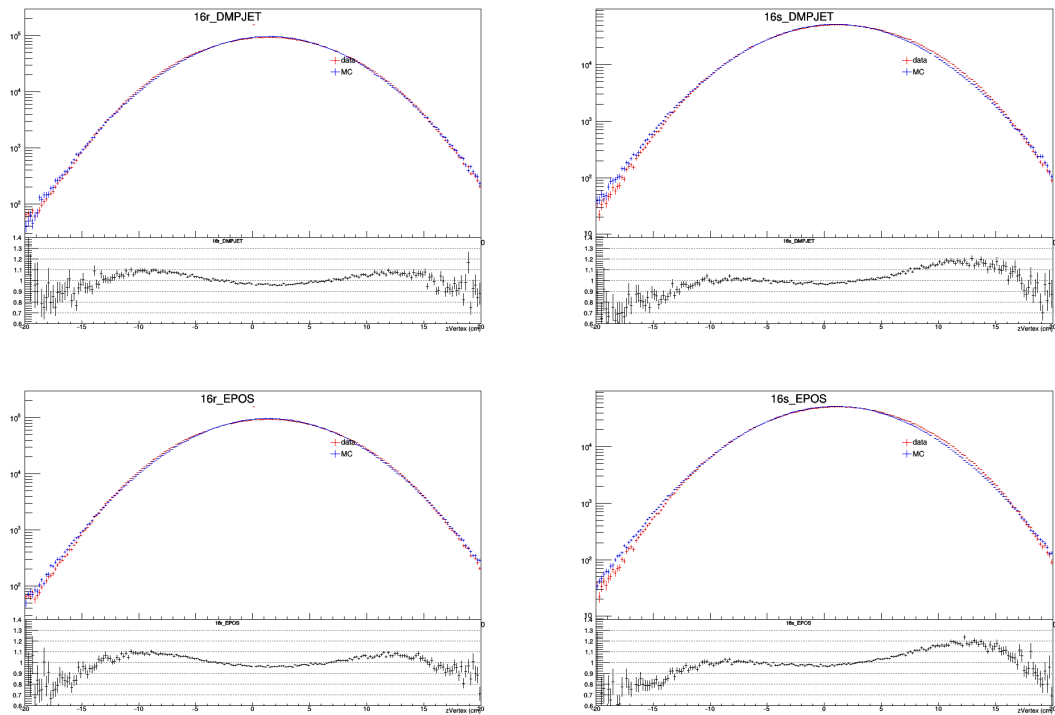


Figure D.3: Comparison of  $v_z^{SPD}$  distribution between data and DPMJET or EPOS. Bottom panel shows the ratio data/MC.

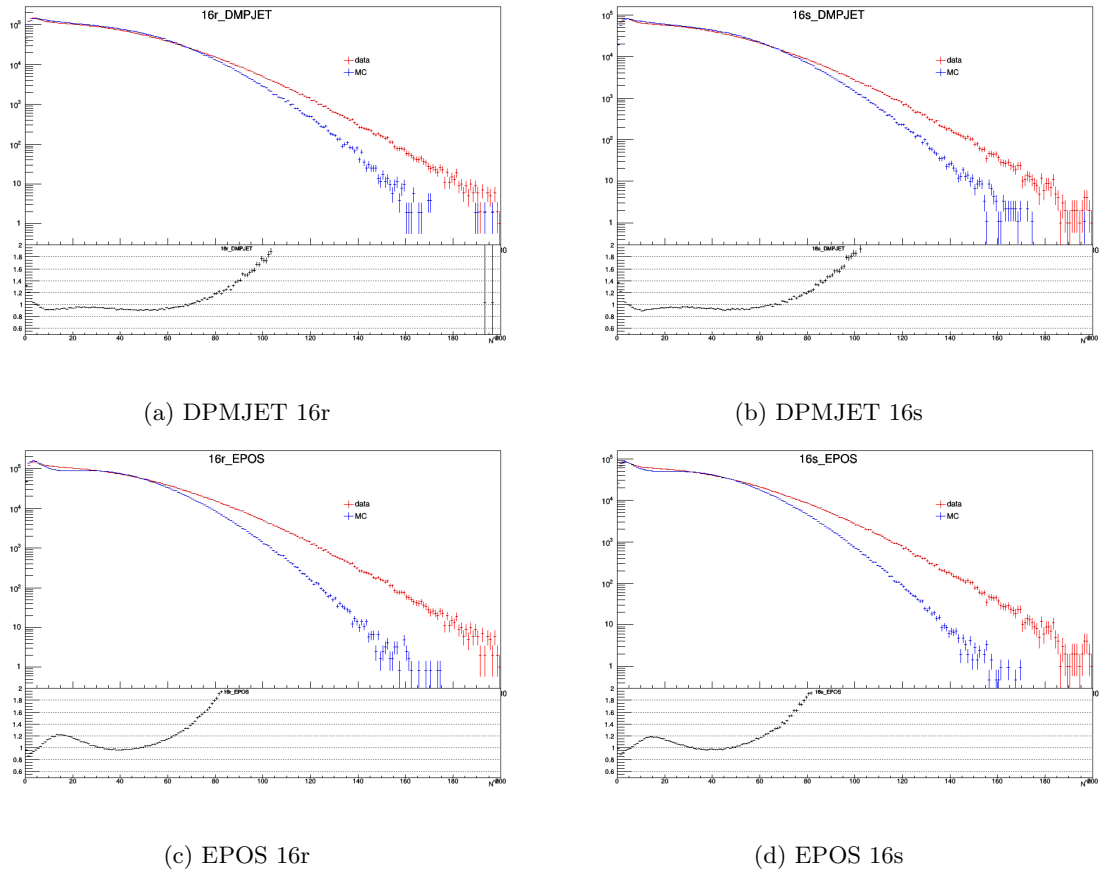
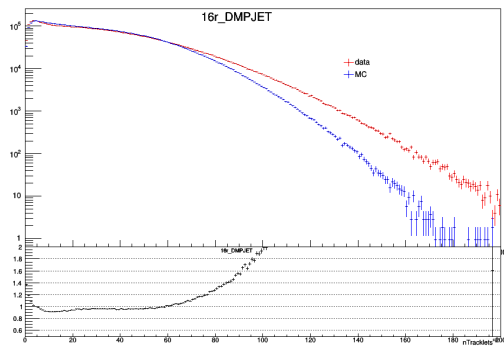
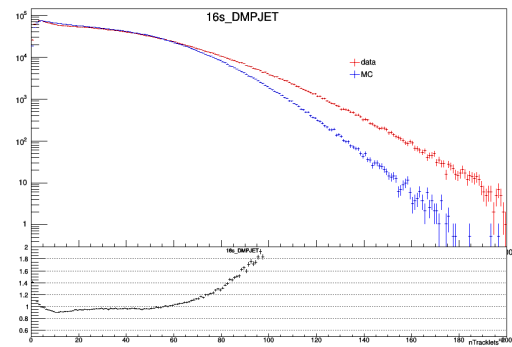


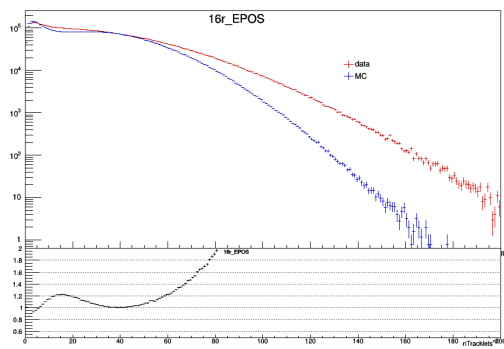
Figure D.4: Comparison of  $N^{\text{raw}}$  distribution between data and DPMJET or EPOS. Bottom panels show the ratio data/MC.



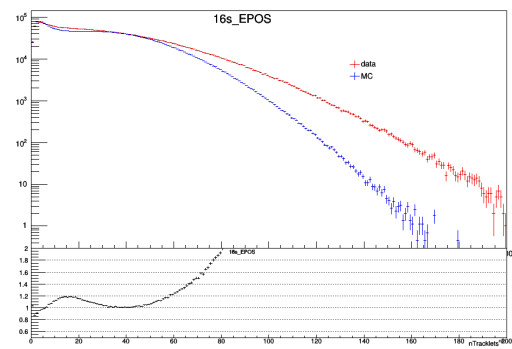
(a) DPMJET 16r



(b) DPMJET 16s



(c) EPOS 16r



(d) EPOS 16s

Figure D.5: Comparison of  $N^{\text{corr}}$  distribution between data and DPMJET or EPOS. Bottom panels show the ratio data/MC.

**Titre** : Etude de la production du  $J/\psi$  dans les collisions pp à  $\sqrt{s} = 5.02$  TeV et de la dépendance en multiplicité de la production du  $J/\psi$  dans les collisions p-Pb à  $\sqrt{s_{NN}} = 8.16$  TeV avec l'expérience ALICE au LHC

**Mots clés** : Multiplicité des particules chargées, collisions proton-noyau, quark charme,  $J/\psi$ , ALICE, LHC.

**Résumé** : L'expérience ALICE au CERN examine l'état de la matière QCD chaude et dense créée lors de collisions d'ions lourds ultra-relativistes - le plasma de Quark Gluon (QGP). En raison de sa courte durée de vie, le QGP ne peut être étudié que via ses signatures. La suppression de  $J/\psi$  a été proposée comme preuve de la formation du milieu déconfiné. Néanmoins, il est devenu évident que la réalité est bien plus complexe, car il existe d'autres mécanismes concurrents qui affectent la production de  $J/\psi$ . Pour comprendre quels effets agissant sur la production de  $J/\psi$  dans les collisions noyau-noyau résultent véritablement de la présence du QGP, ALICE étudie également la production de  $J/\psi$  en collisions pp et p-Pb. Le QGP ne devrait pas se former dans ces systèmes. De plus, les mesures de la production de  $J/\psi$  dans les collisions p-Pb peuvent révéler des informations sur les effets provenant de la liaison des nucléons dans le noyau, appelés effets de la matière nucléaire froide (CNM). L'objectif de cette thèse est d'étudier la production

de  $J/\psi$  à rapidité vers l'avant avec le spectromètre à muons ALICE. La section efficace de production  $J/\psi$  inclusive dans les collisions pp à  $\sqrt{s} = 5.02$  TeV, et sa dépendance en  $p_T$  et en rapidité, ont été examinées et comparées à des calculs théoriques ainsi qu'à des mesures à d'autres énergies du LHC. Les données sont bien décrites par la somme des calculs de pQCD pour les  $J/\psi$  prompts et de FONLL pour les  $J/\psi$  non-prompts. La production différentielle en multiplicité des  $J/\psi$  a été étudiée dans les collisions p-Pb et Pb-p à  $\sqrt{s_{NN}} = 8.16$  TeV, ainsi que le moment transverses moyen. La mesure montre un comportement dépendant de la rapidité pour les taux de production relatifs des  $J/\psi$ . Le moment transverses moyen des  $J/\psi$  est par contre identique dans les deux intervalles de rapidité mesurés. La nouvelle analyse a augmenté la précision et étendu la mesure à des multiplicités plus élevées par rapport à la mesure précédente à  $\sqrt{s_{NN}} = 5.02$  TeV. Nous constatons que les taux de production relatifs et le  $\langle p_t \rangle$  relatif sont indépendants de l'énergie du centre de masse.

**Title** : Study of the  $J/\psi$  production in pp collisions at  $\sqrt{s} = 5.02$  TeV and of the  $J/\psi$  production multiplicity dependence in p-Pb collisions at  $\sqrt{s_{NN}} = 8.16$  TeV with ALICE at the LHC

**Keywords** : Charged particle multiplicity, proton-nucleus collisions, charmed quark,  $J/\psi$ , ALICE, LHC.

**Abstract** : The ALICE experiment at CERN probes the state of hot and dense QCD matter created in ultrarelativistic heavy ion collisions - the Quark Gluon Plasma (QGP). Due to its short lifetime, the QGP can be studied only via its signatures. The suppression of  $J/\psi$  was proposed as a proof of formation of the deconfined medium. Nevertheless, it became clear that the real picture is far more complex as there are other competing mechanisms affecting the  $J/\psi$  production. To understand which effects acting on the  $J/\psi$  production in nucleus-nucleus collisions truly stem from the presence of the QGP, ALICE also studies the production of  $J/\psi$  in pp and p-Pb collisions. The QGP is expected not to form in these systems. Furthermore, measurements of the  $J/\psi$  production in p-Pb collisions can unveil information on the effects originating from the binding of the nucleons in the nucleus, referred to as the cold nuclear matter effects (CNM). The objective of this thesis is to study the production

of  $J/\psi$  at forward rapidity with the ALICE Muon Spectrometer. The inclusive  $J/\psi$  production cross section in pp collisions at  $\sqrt{s} = 5.02$  TeV, and its dependence on  $p_T$  and rapidity, were examined and compared with theoretical calculations as well as measurement at other LHC energies. The data are well described by a sum of pQCD calculations for prompt and FONLL calculations for non-prompt contribution. The multiplicity differential  $J/\psi$  production was studied in p-Pb and Pb-p collisions at  $\sqrt{s_{NN}} = 8.16$  TeV, as well as its mean transverse momentum. The measurement shows a rapidity dependent behaviour of relative  $J/\psi$  yields. The  $J/\psi$  mean transverse momentum on the other hand is identical in the two measured rapidity intervals. The new analysis increased the precision and extended the measurement to higher multiplicities compared to previous measurement at  $\sqrt{s_{NN}} = 5.02$  TeV. We find that both relative yields and relative  $\langle p_T \rangle$  are independent of centre-of-mass energy.

